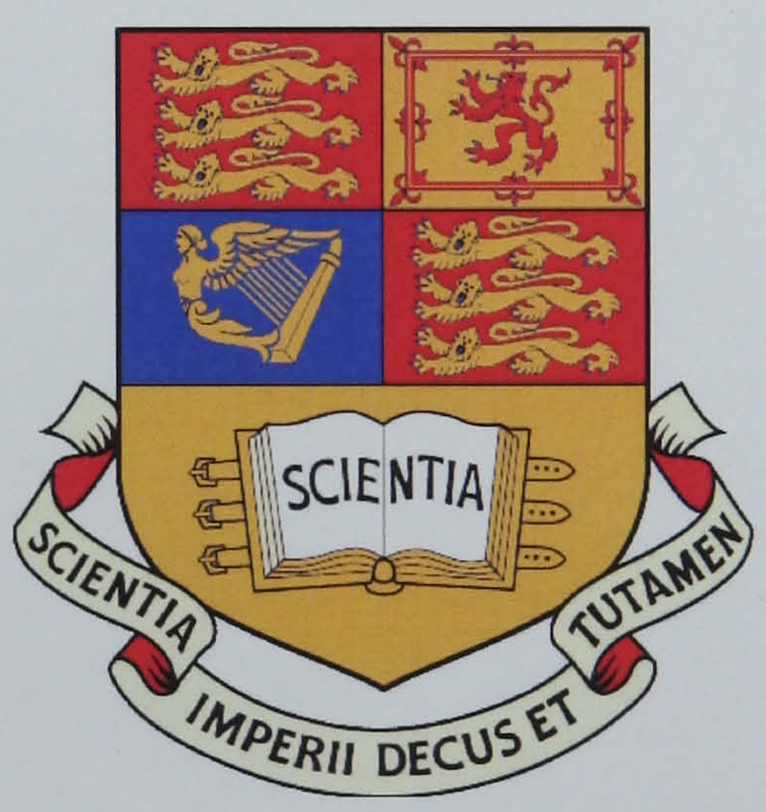
The Characterisation of Archaeological Glasses Using Advanced ~~Analytical~~ Analysis Techniques

Sean Diego McLoughlin

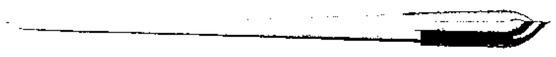
A thesis submitted for the degree of Doctor of Philosophy of the University of London and for the diploma of Imperial College of Science, Technology and Medicine



Department of Materials,
Imperial College of Science, Technology and Medicine,
Prince Consort Road,
London,
SW7 2BP.

October 2003

BRIT. LONDON. UNIV.



To my family

"Variety's the very spice of life,
That gives it all its flavour"

William Cowper, The Task (1785)

Acknowledgements

The list of acknowledgements in truth is endless, because I am thankful for every scrap of information, every result and every relevant shred of data that I have accumulated during this Ph.D project, and that's been a long process.

Firstly, I am indebted to my supervisors, Dr David McPhail, Prof Julian Henderson and Dr Phil Rogers, who started me off on the work and helped me wrap it all up. I am grateful to you all for your enthusiasm and your guidance and I have enjoyed the constructive energy of your different approaches and expertise.

Next I want to give my thanks to Nick Royall, John Wells, Richard Chater, Richard Sweeney, Mike Haddon, Robert Hill, Norman Charnley, Liz Morris, Chris Halls, Jill Hey, Ioan Notingher, Cheryl Haidon, Barry Coles, and Mark Tyrer. You have all been of immense help with the analytical techniques in the project and the necessary sample preparation.

I would like to thank my fellow PhD comrades, in particular Gene Lewis, a good friend and in many ways an inspiration. I am grateful to Chris Munnings, a man of many resources and one always willing to help. I would also like to express my gratitude to Sarah Fearn, with whom I have shared many interesting discussions on glass corrosion.

Thanks are due to Matilde Laurà. Your patience and encouragement have ensured that I complete the task. I'm waiting for you now!

Lastly I wish to thank my parents. Returning home for a period after all these years was a wonderful experience. Your unerring belief in me has been a significant driving force throughout the write-up.

Abstract

The present study is a collaborative interdisciplinary research project that aims to explore new areas of overlap between materials science and archaeometry. An analytical multi-technique materials science based approach has been applied to samples of archaeological glasses and glassmaking debris in order to answer questions of a historical and technological nature concerning ancient glass production. Novel high-resolution imaging techniques have also been used to shed light on aspects of the long-term weathering of these glasses.

Samples of archaeological glass and associated production debris were excavated from three locations at an Early and Middle Islamic industrial complex in Raqqa, Syria, dating from the late 8th- early 9th and 11th-12th centuries AD. There is clear evidence for primary and secondary production of glass over different time periods. This analytical project aims to contribute to the detailed picture of glass production which is emerging from investigations at Raqqa.

Chemical, physical, thermal and weathering characteristics of the samples have been measured using a range of analytical techniques. The chemical characterisation of Raqqa glass fragments using Electron Probe Microanalysis (EPMA) forms the basis of the present investigation. The major compositional groupings that emerge from the data suggest changes in glassmaking technology over time and experimentation with different raw ingredients. These points are studied further through experimental glasses melted from the original raw ingredients and through replica glasses mirroring the two major compositional groups. Analytical data collected on fragments of glass furnaces and casting trays has been coupled with theoretical models on glass viscosity and crystal growth with the aims of further identifying the remains, assessing refractory performance and establishing furnace temperatures at Raqqa.

Weathering characteristics have been assessed in the wider framework of glass corrosion studies; corroded Raqqa glasses are analysed and compared to replica ancient glasses excavated from a controlled glass burial experiment at Ballidon, UK, in order to investigate the complex processes of archaeological glass decay. New archaeometric applications for Field Emission Scanning Electron Microscopy (FE-SEM) and Focused Ion Beam (FIB) Microscopy have been developed to inspect the nature of sub-micron layered weathering formations in buried glasses.

Table of contents

Abbreviations, symbols and constants 11

Chapter 1 – Introduction 13

1.1 THE ROLE OF ARCHAEOLOGICAL SCIENCE 14

1.2 AN EXAMPLE OF CONSTRUCTIVE OVERLAP 14

1.3 AIMS AND OBJECTIVES OF THE THESIS 15

1.4 BIBLIOGRAPHY 18

Chapter 2 – A review of the literature 19

2.1 THE ARCHAEOMETRY OF GLASS 19

2.1.1 Assumptions on glass melting in antiquity 19

2.1.2 Analytical techniques for the characterisation of ancient glasses 20

2.1.2.1 Chemical analysis 20

2.1.2.2 Surface analysis 21

2.2 THE NATURE OF GLASS 21

2.2.1 Ionic mobility in silicate glasses 24

2.3 THE RAW MATERIALS OF EARLY GLASS PRODUCTION 25

2.3.1 Silica 26

2.3.2 Alkali 27

2.3.2.1 Compositional variability of alkali sources 28

2.4 COMPOSITIONAL CATEGORIES OF ANCIENT GLASSES 29

2.4.1 LMG vs. HMG 30

2.4.2 Compositional categories at Raqqa 31

2.5 PRIMARY GLASS PRODUCTION – EVIDENCE IN THE LEVANT 31

2.5.1 Tank furnaces 32

2.5.2 Production times and temperatures 32

2.6 PHYSICAL PROPERTIES OF GLASS 34

2.6.1 Viscosity 34

2.6.1.1 The Fulcher-Tammann equation 36

2.6.1.2 The Urbain method 38
2.6.2 Viscosity vs. workability 40
2.6.3 Crystallisation 40
2.6.3.1 The liquidus temperature 42
2.6.3.2 Nucleation rate 42
2.6.3.3 Growth rate 44
2.7 THE LONG-TERM CORROSION OF BURIED GLASSES 48
2.7.1 Atmospheric corrosion vs. reaction with aqueous solutions 48
2.7.2 Glass corrosion: mechanisms of decay 49
2.7.2.1 The thermodynamics of glass corrosion 49
2.7.2.2 Solubility of SiO_2 in aqueous solutions 52
2.7.2.3 Effect of pH of the solution on the solubility of SiO_2 52
2.7.2.4 Kinetics of dissolution 54
2.7.3 The long-term natural corrosion of glass 54
2.7.3.1 Structure of corrosion crusts 54
2.7.3.2 Chemical constitution of corrosion crusts 56
2.7.3.3 Burial experiments 57
2.7.3.4 Theories of layer formation 58
2.8 BIBLIOGRAPHY 60
Chapter 3 – Excavations and samples 67
3.1 RAQQA: A HISTORICAL INTRODUCTION 67
3.2 ARCHAEOLOGICAL INVESTIGATIONS AT RAQQA 68
3.3 MATERIALS SAMPLED 70
3.3.1 Glass from Tell Zujaj (TZ) and Tell Fukhkhar (TF) 70
3.3.2 Glass from Tell Belor (TB) 70
3.3.3 Furnace fragments and casting surfaces 70
3.3.4 Raw materials 73
3.3.4.1 The Salicornia experiment 73
3.3.5 Samples for corrosion studies 74
3.4 THE BALLIDON GLASS BURIAL EXPERIMENT 74
3.5 BIBLIOGRAPHY 77
Chapter 4 – Overview of experimental work 78
4.1 ANALYTICAL PROCEDURE 78
4.2 COMPOSITIONAL CHARACTERISATION 79

4.2.1 Inductively Coupled Plasma Atomic Emission Spectrometry (ICP-AES) 79
4.2.1.1 Sample preparation 80
4.2.1.2 Outline of technique 81
4.2.2 Electron Microscopy (EM) 81
4.2.2.1 Field Emission Scanning Electron Microscopy (FE-SEM) 81
4.2.2.1.1 The Field Emission Gun 82
4.2.2.2 Electron Probe Microanalysis (EPMA) 83
4.2.2.3 The interaction volume 83
4.2.2.4 X-ray detection: Energy Dispersive Spectrometry (EDS) 85
4.2.2.5 X-ray detection: Wavelength Dispersive Spectrometry (WDS) 85
4.2.3 Data calibration 86
4.2.3.1 EPMA inter-session data calibration 87
4.2.4 Data conversion 88
4.3 STRUCTURAL CHARACTERISATION 89
4.3.1 XRD 89
4.3.2 Thermal analysis 89
4.3.2.1 Differential Thermal Analysis (DTA) 89
4.3.2.2 Thermogravimetry (TG)/ Differential Thermogravimetry (DTG) 89
4.3.2.3 Differential Scanning Calorimetry (DSC) 90
4.4 REPLICA GLASSES 90
4.4.1 Experimental considerations 90
4.4.2 Batch preparation 91
4.4.3 Particle size analysis 92
4.4.4 Batch fusion and casting 92
4.4.5 Fining 93
4.4.6 Density measurements 94
4.5 CHARACTERISATION OF SURFACE CORROSION LAYERS 94
4.5.1 FE-SEM linescans 95
4.5.1.1 Quantifying the glass surface using FE-SEM linescans 95
4.5.2 Focused Ion Beam (FIB) Microscopy 98
4.5.2.1 The Liquid Metal Ion Source (LMIS) 99
4.5.2.2 Ion beam interaction with the surface 100
4.5.2.3 Scanning Ion Microscopy (SIM) 101
4.5.2.4 Secondary Ion Mass Spectrometry (SIMS) 102

4.5.2.4.1 The SIMS equation 102
4.5.2.4.2 Electron beam compensation 103
4.5.2.4.3 Static SIMS 104
4.5.2.4.4 Dynamic SIMS 106
4.5.3 Infrared Reflection Spectroscopy (IRRS) 107
4.5.3.1 Outline of technique 107
4.5.3.2 Interpretation of reflectance spectra of glass 108
4.6 BIBLIOGRAPHY 110

Chapter 5 – Compositional characterisation of glass from Raqqa ...112

5.1 TELL ZUJAJ 112
5.2 TELL FUKHKHAR 113
5.3 TELL BELOR 114
5.4 PRODUCTION WASTE 115
5.5 COMPOSITIONAL GROUPINGS 116
5.5.1 Type 3 vs. type 1 117
5.5.2 Type 4: experiment and recycling? 120
5.6 COLORANTS AND OPACIFIERS 122
5.7 REGIONAL COMPARISONS 125
5.8 BIBLIOGRAPHY 127

Chapter 6 – Experimental glassmaking and replica work 129

6.1 TYPE 1: QUARTZ AND SALICORNIA ASH 129
6.1.1 Salicornia ash analyses 129
6.1.2 Synthesised glasses 131
6.2 TYPE 1 VS. TYPE 3: REPLICA GLASSMAKING 132
6.2.1 Replica glasses 133
6.2.2 Viscosity 133
6.2.3 T_g 135
6.2.3.1 Comparison with excavated samples 137
6.2.4 Experimental casting 137
6.2.5 Experimental fining 139
6.2.6 Casting and fining properties 140
6.3 BIBLIOGRAPHY 142

Chapter 7 – Characterisation of production waste from Raqqa 143

7.1 GLASS ON VITRIFIED CA-RICH SUBSTRATES: CASTING TRAY OR FURNACE FRAGMENT? 143

7.1.1 Type A – TB6/TB2/TB5/TB9 143
7.1.2 Experimental casting 154
7.2 GLASS ON ALUMINO-SILICATE SUBSTRATES: FURNACE FRAGMENTS 155
7.2.1 Type B – TB13/TB14/TB7 155
7.2.2 Type C – TB19g/TB19y 161
7.2.3 A comparison of refractory performance 163
7.3 CHARACTERISTICS OF CRYSTAL GROWTH 165
7.3.1 Diopside 165
7.3.2 Wollastonite 167
7.3.3 Compositional considerations 167
7.3.4 Structural considerations 169
7.3.5 The kinetics of wollastonite precipitation 169
7.4 BIBLIOGRAPHY 174
Chapter 8 – The corrosion of buried glasses. Part 1: Ballidon 175
8.1 OPTICAL AND CHEMICAL CHARACTERISATION 175
8.1.1 B1 (Roman composition) 176
8.1.1.1 Compositional characteristics 177
8.1.2 B2 (Medieval composition) 181
8.1.2.1 Compositional characteristics 182
8.1.3 B3 (18th Century composition) 185
8.1.3.1 Compositional characteristics 187
8.2 STRUCTURAL CHARACTERISATION BY IRRS 188
8.2.1.1 B1 189
8.2.1.2 B2 189
8.2.1.3 B3 191
8.2.2 Quantification of peak shifts 192
8.2.2.1 Calibration 192
8.2.2.2 Interpretation and comparison with EDXA 194
8.3 THE CORROSION MECHANISMS OF BALLIDON GLASSES 197
8.4 BIBLIOGRAPHY 200
Chapter 9 – The corrosion of buried glasses. Part 2: Raqqa 201
9.1 CORROSION VS. COMPOSITIONAL TYPE 201
9.2 GROWTH IRREGULARITIES 207
9.2.1 Plugs 208
9.2.2 The effect of residual stresses 209

9.3 THE MACROSCOPIC EVOLUTION OF LAYER GROWTH 210
9.4 LAYER AND INTERLAYER STRUCTURE 214
9.5 CHARACTERISATION OF THE REACTION FRONT 216
9.6 INTERPRETING PERIODIC GLASS DISSOLUTION REACTIONS 219
9.7 THERMODYNAMIC APPROACH TO LAYER FORMATION 226
9.7.1 Methodology 227
9.7.2 The relationship between glass stability and layer thickness 228
9.8 THOUGHTS AND CONCLUSIONS 231
9.9 BIBLIOGRAPHY 232
Chapter 10 – Conclusions and suggestions for further work 234
10.1 SUGGESTIONS FOR FURTHER WORK 236
10.1.1 Trace element analysis 236
10.1.2 FIB-SIMS issues 236
10.1.3 Structural characterisation of glass corrosion 237
10.2 BIBLIOGRAPHY 238
Appendix 239
List of publications 247
List of figures and table captions 248

Abbreviations, symbols and constants

Å	Ångstrom
A	Ampere
AAS	Atomic absorption spectroscopy
AES	Auger Electron Spectroscopy
AMU	atomic mass unit
C	concentration
DSC	Differential Scanning Calorimetry
DTA	Differential Thermal Analysis
EDXA/EDS	Energy Dispersive X-Ray Analysis/ Spectrometry
EM	Electron Microscopy
EPMA	Electron Probe Microanalysis
FE-SEM	Field Emission Scanning Electron Microscopy
FIB	Focused Ion Beam
FT-IR	Fourier Transform Infrared Reflectometry
HMG	High Magnesia Glass
IC	Ion Chromatography
ICP-AES	Inductively Coupled Plasma Atomic Emission Spectrometry
IR	Infrared Reflectometry
IRRS	Infrared Reflection Spectroscopy
k	Boltzmann constant
KLS	Potash-Lime Silica (K_2O-CaO-SiO_2)
LA-ICP-MS	Laser Ablation Inductively-Coupled Plasma Mass Spectrometry
LEISS	Low Energy Ion Scattering Spectroscopy
LMG	Low Magnesia Glass
μm	micron
m/z	mass to charge ratio
MRN	Modified Random Network
NAA	Neutron Activation Analysis
nm	nanometre
N	molar fraction

NMR	Nuclear Magnetic Resonance
PIXE	Proton-Induced X-Ray Emission
ppb	parts per billion
ppm	parts per million
OES	Optical Emission Spectroscopy
R	gas constant
RBS	Rutherford Backscattering Spectrometry
RS	Raman Spectroscopy
RSD	Relative Standard Deviation
SD	Standard Deviation
SEM	Scanning Electron Microscopy
SIM	Scanning Ion Microscopy
SIMS	Secondary Ion Mass Spectrometry
SLS	Soda-Lime Silica (Na_2O-CaO-SiO_2)
SSMS	Spark Source Mass Spectrometry
TB	Tell Belor
TEM	Transmission Electron Microscopy
T_f	structure temperature
T_L	liquidus temperature
TF	Tell Fukhkhar
T_g	glass transition temperature
TG	Thermogravimetry
T_{Vmax}	time at maximum crystallisation rate
TZ	Tell Zujaj
UHV	Ultra High Vacuum
V	Volt
V	crystallisation rate
V_{max}	maximum crystallisation rate
WDS	Wavelength Dispersive Spectrometry
XAFS	X-Ray Absorption Fine-Structure
XPS	X-Ray Photoelectron Spectroscopy
XRD	X-Ray Diffraction
XRF	X-Ray Fluorescence
XRS	X-Ray Spectrometry
ΔG_a	free energy of activation
ΔS_f	entropy of fusion
ρ	density
η	viscosity

Chapter 1

Introduction

"*Materials science provides the methodology for reconstructing past societies...to assess how physical and chemical performance characteristics have influenced past technological choices*"[1].

Sillar and Tite's quote is an apt starting point as it exemplifies how the constructive overlap between many aspects of research of a scientific and anthropological or socio-historical nature is more important today than ever before and is reflected in the growing number of published technical and experimental studies that relate to the field of archaeological investigation. One of those areas of overlap is the study of ancient glass; over the past decades it has witnessed the evolution of more integrated approaches, which have enabled the enhanced assessment of ancient glassy materials production.

Over the last 40 years, there has been a discernible increase in the number of scholars who have focused their research on early industrial organisations, a field of study that has come to be known as archaeotechnology. Archaeologists have conducted fieldwork geared to the study of ancient technologies in a cultural context and have drawn on the laboratory analyses developed by materials scientists as one portion of their interpretative program.

This evolution reflects first of all the improved scientific understanding of the materials involved. This is particularly poignant in the case of glass, which remained a largely unexplained material in terms of structure and chemistry well into the 20th century. Secondly, the range of methods now available for scientific research on ancient materials allows a much broader spectrum of issues to be addressed. An ever-increasing number of analytical techniques are now employed in archaeometric studies. Developments in the breadth of research mirror the continuing expansion of analytical characterisation facilities available for scientific research on organic and inorganic materials. For example, research projects presented at the 33rd International Archaeometry Symposium held in Amsterdam in April 2002 involved over 40 analytical techniques applied to materials of an ancient or archaeological nature. This is a clear sign of the progress being made in the archaeological sciences and in the concurrently expanding goals of collaborative projects involving materials departments of many universities.

1.1 The role of archaeological science

The physical sciences can be applied to archaeology in three general areas[2]:

a) Geophysical analysis helps to identify and locate buried features that would otherwise be difficult to detect, even with aerial photography and detailed prospecting.

b) Physical methods of age determination provide a framework of absolute and worldwide chronology into which new items can be placed.

c) Analytical techniques in the examination of archaeological artefacts lead to informed conclusions on ancient technology and trade.

It is with this last point that the present study is concerned, and specifically the characterisation of ancient glass from an Islamic glass production centre at Raqqa in Syria. The three most prolifically excavated sites that have yielded glass in the Islamic world are Fustat (Old Cairo) in Egypt, Samarra in Iraq, and Nishapur in north-eastern Iran. Raqqa has already produced interesting results and "will probably establish itself as one of the most important glassmaking centres in the Islamic world"[3].

There are a number of problems related to the study of excavated Islamic glass. Only in exceptional cases do glass objects bear informative inscriptions providing names and dates. Both as luxury goods that were traded and exchanged and as simple containers for oils, perfumes and liquids of all kinds, Islamic glass circulated throughout the Islamic world and as far as south-eastern Asia, northern China and Europe. Glass was also shipped in large quantities as cullet (glass lumps and discarded broken vessels), suitable for remelting and making new glass inexpensively. Thus, the glass of a bottle created in Egypt, for example, may have been recycled as far as Central Asia; a new object may have been made that had a chemical composition usually ascribed to Egyptian vessels but a shape and decoration that suggested a different origin. While it clearly is problematic for scholars to determine their place or date of production, excavated objects may be of great help in better understanding the chronology and origin of Islamic glass.

1.2 An example of constructive overlap

One of the goals pursued in this work concerns an area of research that has received significant attention in the scientific community: the long-term corrosion of archaeological glasses. It is encouraging to notice the breadth of overlap between disciplines and the present thesis follows this current trend in archaeometric research. Long gone are the times when chemical data gathered on ancient artefacts provided an end in itself; the objectives of archaeometric studies now encompass much broader goals. The glass from Raqqa represents an unprecedented case

for the detailed comparison of different glassmaking traditions and technologies firstly within a single burial context, and secondly over multiple contexts spanning three centuries, and therefore representative of changes and continuity over time. Moreover, the Raqqa glasses offer an opportunity to assess the degree of influence that different compositional groups have had on long-term durability characteristics. Such information is rare because of constraints imposed on the corrosion analysis of archaeological specimens: corrosion rates cannot be calculated if the age of specimens is unknown; glasses cannot be confidently compared if they have different burial histories; a number of parameters affecting the corrosion characteristics can hinder any sound conclusions on long-term decay.

A multidisciplinary approach is important in the evaluation of technical data regarding archaeological materials. A multi-technique methodology has been selected, both for comparison and validation of chemical data and for a wider ranging spectrum of results. The utilisation of a broad array of established analytical techniques is adopted, alongside the development of novel techniques such as Field Emission Scanning Electron Microscopy (FE-SEM) and Scanning Ion Microscopy (SIM) with a Focused Ion Beam (FIB) workstation, for the evaluation of the glasses in this study.

1.3 Aims and objectives of the thesis

The current thesis is the result of a collaborative project involving the Materials Department of Imperial College, London and the Archaeology Department of Nottingham University and, as such, is aimed towards an interdisciplinary discussion of analytical data accumulated on materials of an archaeological nature. The methodology followed in all avenues of this investigation may be defined as 'reverse engineering': the archaeological glasses themselves represent an end product, and the aim of the study is to understand how they were made and what they were made from, i.e. the materials and conditions of their manufacture, and how they have degraded over time, i.e. their burial history and current state of decay. The objectives of the work are as follows:

1) Firstly, to chemically characterise a vast range of glass samples from different periods at Raqqa to further investigate the compositional groups* that have been tentatively suggested in previous studies[4, 5]. Data from several quantitative techniques will be cross-checked for validity and assessment of errors.

---

* Quantitative compositional studies have allowed historically coherent compositional groups to be determined and developed across time frames and geographical areas, which ultimately may permit the regional reconstruction of glass trade.

2) Secondly, to melt replica glasses from laboratory grade powders mirroring the compositional groups from Raqqa to explore possible technological inferences associated to the production of compositionally distinct glass types. Experimental melting of glasses using the supposed original raw materials of manufacture gathered on site will be attempted in order to confirm the reintroduction of a plant ash based recipe at Raqqa, to possibly confirm a local plant ash source and to shed light on plant ash preparation and variability.

3) Thirdly, to conduct a technical study of glassmaking debris from Raqqa such as furnace bricks, casting trays and refractory-glass interfaces in order to assess parameters involved in the manufacture of glass[†]. Structural and chemical studies of refractory ceramics will help to clarify the high temperature processes to which they have been exposed, and hence their scale of use. Mathematical viscosity models will be applied to furnace waste in order to predict a time scale for exposure to high temperatures on the basis of observations of wollastonite crystal growth at furnace brick-glass interfaces. In such a way casting surfaces can be distinguished from furnace debris in cases where this is not possible on the basis of visual examination alone.

4) Fourthly, to assess the long-term corrosion characteristics of Raqqa glasses in relation to composition and sample morphology. Archaeological glasses are under investigation as real time examples of long-term corrosion in a groundwater environment, which is something that cannot be realistically replicated in laboratory environments. With this in mind, replica ancient glasses unearthed from a glass burial experiment in Ballidon will be analysed in order to assess long-term corrosion rates, compare the influence of burial environments on corrosion and to examine the suitability of Infra-Red Reflection Spectroscopy (IRRS) as a technique for the non-destructive evaluation of corroded crusted glass surfaces. The novel combination of high-resolution electron and ion microscopy techniques applied to corroded archaeological glasses from Raqqa and Ballidon is intended to shed greater light on the physical structure of corroded glass and the chemical mechanisms that lead to the typical fine lamellar nature of glass crusts recovered from burial environments.

It is the aim of this thesis to explore the above four points with the sizeable sample set from Raqqa, an Islamic glass production site in Syria, which will be outlined in detail in Chapter 3.

[†] The growing number of experimental studies related to glass workshops and ancient production sites has increased understanding of the parameters of manufacture of ancient glasses.

As will become clear in later chapters, the strength of the samples from Raqqa lies in the fact that:

a) glass was produced at Raqqa from its raw ingredients, hence problems arising from the provenance of the materials sampled are eliminated.
b) well-defined compositional categories of glass have emerged in contemporaneous production from the same site in Raqqa.

Hence representative samples from these major compositional categories at Raqqa can be selected for comparative corrosion studies with the premise that:

a) they are characterised in detail.
b) they share the same burial history in the same location.

The fourth avenue of research will also make use of replica ancient glasses from a glass burial experiment in Ballidon, Derbyshire, UK. The glasses from Ballidon form a complementary line of glass corrosion studies for two reasons, namely that:

a) glasses buried under monitored conditions form the most suitable comparative framework for the interpretation of long-term decay effects on ancient glasses.
b) the buried glasses included replica specimens of typical Roman and Medieval compositions that can be relevantly compared to ancient glasses.

To the best of my knowledge, SIM and FE-SEM have not previously been applied to archaeological glass corrosion studies. It is through such novel combination of advanced analytical techniques, and with new data from Raqqa glasses, that this work aims to examine the mechanisms behind the formation of regular weathering layers observed in glasses excavated from archaeological contexts.

1.4 Bibliography

1. Sillar, B. and M.S. Tite, *The Challenge of 'Technological Choices' for Materials Science Approaches in Archaeology.* Archaeometry, 1999. **42**(1): p. 20.

2. Tite, M.S., *Methods of Physical Examination in Archaeology*. 1972, London: Seminar Press.

3. Carboni, S., *Archaeological Excavations of Islamic Glass*, in *Glass of the Sultans*, S. Carboni and D. Whitehouse, Editors. 2001, Metropolitan Museum of Art: New York. p. 24.

4. Henderson, J., *Archaeological and Scientific Evidence for the Production of Early Islamic Glass in al-Raqqa, Syria.* Levant, 1999. **31**: p. 225-240.

5. Henderson, J., *The Science and Archaeology of Materials*. 2000, London: Routledge.

Chapter 2

A review of the literature

The literature review encompasses a variety of topics that are relevant to the work in this study. An introduction to the techniques used in the archaeometry of glass and an outline of the chemistry of glass structure will be followed by a review of issues related to archaeotechnological studies of ancient glasses, with particular detail on the raw materials of early glass production, the chemical categorisation of ancient glasses and the archaeological evidence for their production. Sections outlining the physical properties of glass, including viscosity and crystal growth, and the corrosion of buried glasses will conclude the chapter.

2.1 The archaeometry of glass

Investigations of ancient glasses using a wide range of bulk compositional and surface analytical techniques have led to areas of research of a multidisciplinary nature that are pertinent to archaeology, archaeotechnology, conservation, analytical chemistry and materials science. The following research topics, of particular relevance to this thesis, will be outlined in detail:

a) The identification and sourcing of the raw materials used in glass production.
b) The chemical and physical characterisation of glass products at centres of glass production.
c) The assessment of long-term weathering mechanisms through the characterisation of corroded archaeological glasses.

2.1.1 Assumptions on glass melting in antiquity

The second point (b, above) is based on the premise that the use of a single specific combination of raw materials provides a chemical fingerprint of the glass, which can be specific to the time and place of manufacture. It is also based on the assumption that the total cationic content of the glass analysed is a product of the total cationic content of the batch of raw constituents introduced into the melt, minus the carbonates, sulphates and other volatile species that are expected to react away during the melting process. This is a significant assumption as examples of low quality and partially or incompletely fused glass are a common occurrence in ancient

glass technology, and has to be addressed in any attempt at analytical characterisation of such pieces. Rehren[1, 2] has suggested that early Egyptian glasses in particular were prone to incomplete fusion due possibly to limited furnace technology, and has proposed a 'partial batch melting' model for these glasses, whereby the composition of the melted glass develops along the eutectic troughs of the relevant ternary diagram. For the purposes of this study however, especially considering the large amounts of high quality glass excavated at Raqqa, 'total batch melting' has been assumed.

2.1.2 Analytical techniques for the characterisation of ancient glasses

The extensive variety of analytical techniques applicable to the elemental and surface study of glasses is tabulated in Table 2-1, based on the range outlined by Whan[3] in 1990. More techniques are available currently, in line with ongoing advances in technology and new developments in analytical chemistry and physics. Identifying a specific technique that proves well suited for any particular project is a topic that requires careful consideration, and needs to be defined at the outset. The choice of technique or techniques to be used is ultimately determined by availability, operating costs and sample preparation. Often in the characterisation of materials from ancient or archaeological contexts, considerations of sample destructiveness are of prime importance; non-destructive spectroscopy techniques are in fact routinely used for the preliminary assessment of surfaces where minimum sample damage is a crucial constraint.

2.1.2.1 Chemical analysis

Chemical analysis of ancient glass has moved from the use of arc emission spectroscopy and conventional wet chemistry in the period up to and including the 1960s[4] to the use of more automated techniques. Electron probe microanalysis (EPMA), scanning electron microscopy (SEM), X-ray fluorescence (XRF), neutron activation analysis (NAA), atomic absorption spectroscopy (AAS), inductively-coupled plasma-emission spectroscopy (ICPS), proton-induced x-ray emission (PIXE), mass spectrometry and ultra-violet and infra-red spectroscopy have been widely applied to the compositional analysis of ancient glass[5]. With such an array of data acquisition available, examples of studies comparing and contrasting compositional data acquired with two or more analytical techniques[6-8] are particularly useful in understanding the advantages and limitations of different methods.

Trace element analysis of ancient glasses has developed in recent years; lead isotope analysis and laser ablation inductively-coupled plasma mass spectrometry (LA-ICP-MS) in particular have allowed the determination of compositional groupings down to trace element level[9, 10].

A large body of chemical data has been published over the last few decades. Brill's[11] recently published monumental compendium of data covering 40 years of compositional analyses carried out at the Corning Museum of Glass should help greatly in building an ever more detailed picture of the development of glass technology.

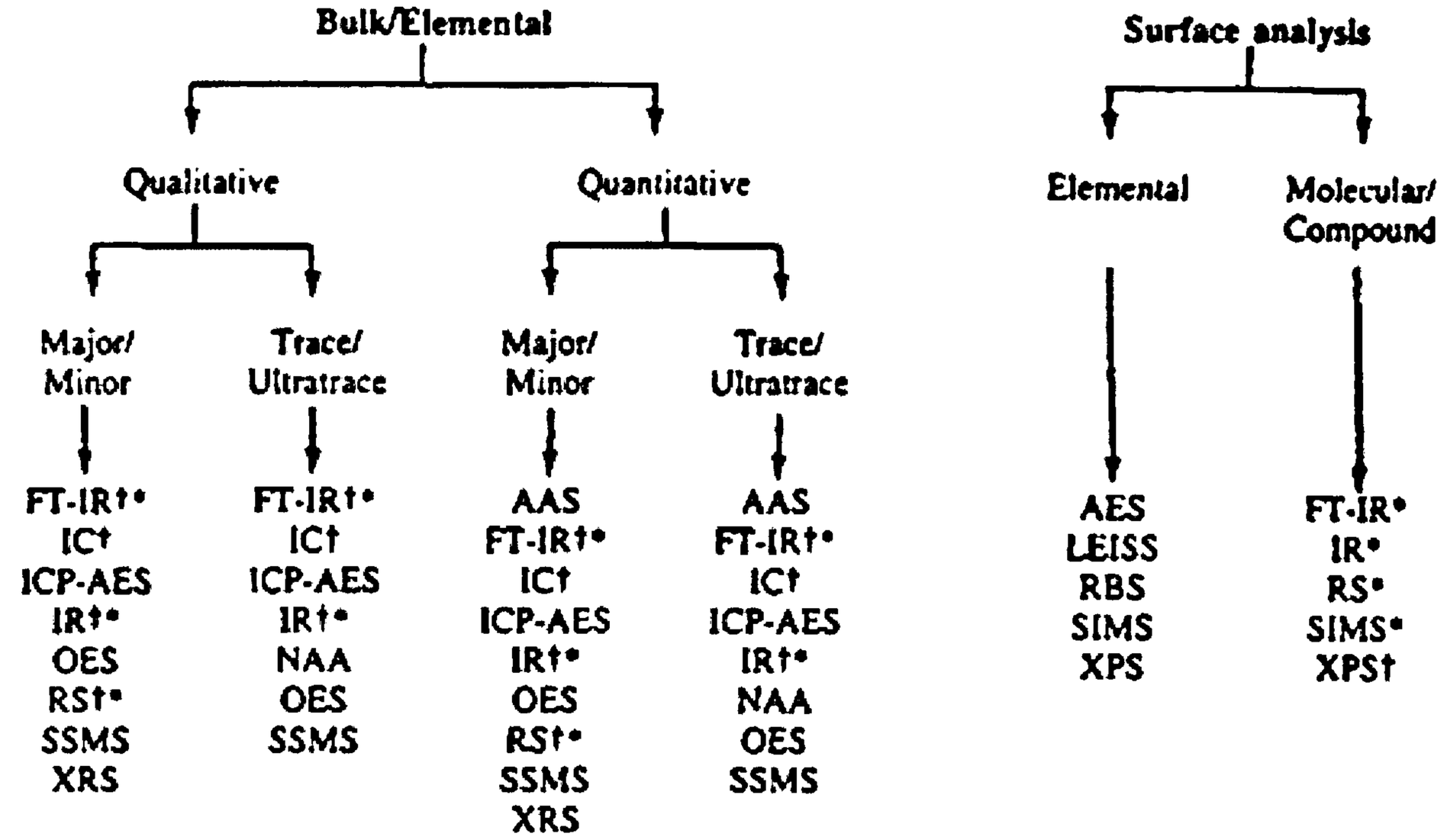


*Table 2-1: the range of analytical techniques applicable to the study of glasses, adapted from Wahn[3]. † denotes for limited elements only. * denotes under special conditions. The abbreviations used are listed on pages 11 and 12.*

2.1.2.2 Surface analysis

Growing interest in the corrosion of archaeological glasses has ushered more widespread applications of surface analytical techniques to archaeometry. As EPMA and SEM analyse only to a depth of 3-5μm of glass, they are also applicable to some surface work. Secondary ion mass spectrometry (SIMS), Auger electron spectroscopy (AES) and transmission electron microscopy (TEM) have all been applied to the study of buried glasses in conjunction with bulk compositional analyses[12].

2.2 The nature of glass

Glass is traditionally defined as "a material formed by cooling from the normal liquid state, which has shown no discontinuous change at any temperature, but has become more or less rigid through a progressive increase in its viscosity"[13]. According to the ASTM Standards for Glass, "glass is an inorganic product of fusion which has been cooled to a rigid condition without crystallisation"[14].

In other words, glass is an amorphous solid that has been cooled without the occurrence of crystallisation. At the glass transition temperature, known as T_g, glasses pass from exhibiting liquid-like properties to solid-like properties and vice versa, but one cannot talk of solidification or fusion as such. The glassy state in fact does not fit within the three classical states of matter because, although glasses possess the mechanical rigidity of crystals, they have the random or disordered structure of liquids.

The majority of glasses are a network of silica (SiO_2) and other metallic oxides in the roles of glass formers, intermediates and modifiers. Silica is the most common glass network former. In crystalline silica each silicon atom bonds with four oxygen atoms in the shape of $(SiO_4)^{4-}$ tetrahedra (see Figure 2-1). Each tetrahedron is held together tightly by strong covalent bonds and adjacent tetrahedra share one of the oxygen atoms to form a three-dimensional network, thus nullifying the strong negative charge of each tetrahedral group. Such a network has low mobility. On cooling relatively quickly from a molten state, the tetrahedra in fact do not rearrange themselves into an ordered structure. This is a glass of pure silica.

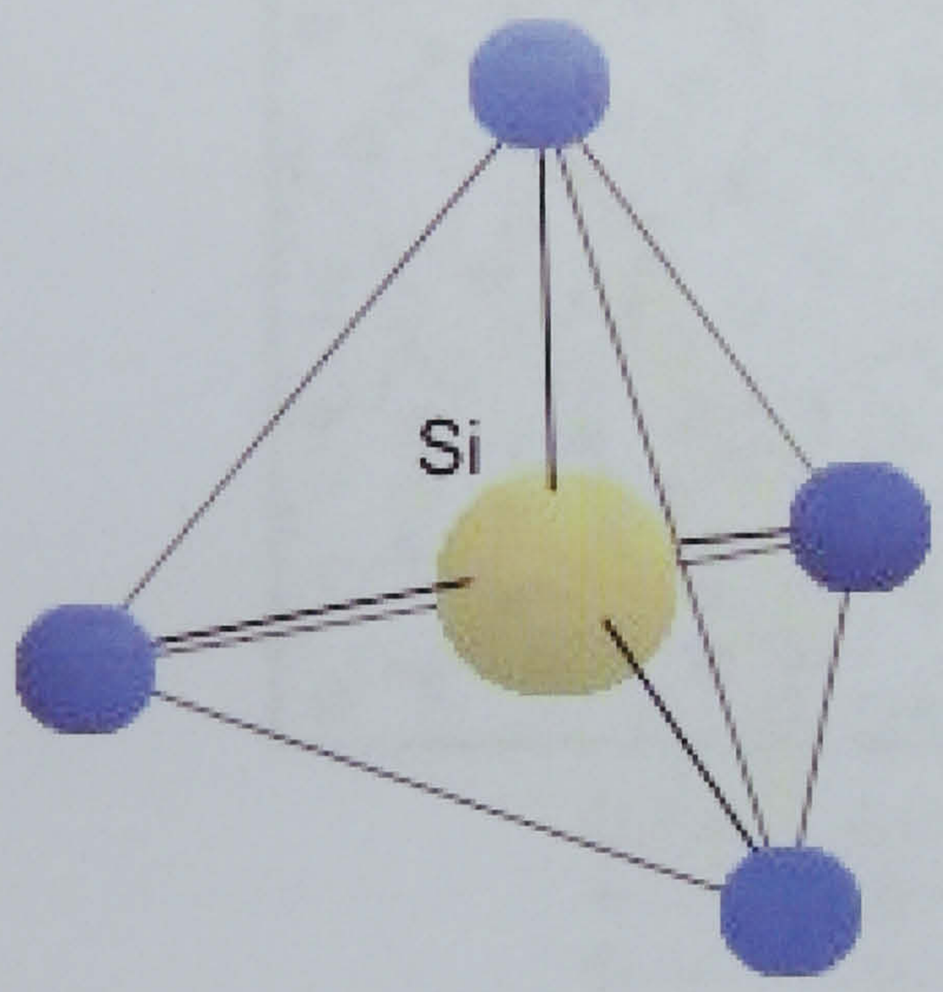


Figure 2-1: the silica tetrahedron, with four oxygen (O) atoms situated at equal distances from a central silicon (Si) atom, is the basic building block of silicate glasses. Ionic sizes are not to scale.

The structures of silicate glasses are based on the polymerising tendency of SiO_4 tetrahedra, which derives, in part, from the bonding properties of Si(IV) and the small ionic size of the silicon relative to that of oxygen. The bonding properties are deemed to rely primarily on the electronic polarity of the Si-O bond and the coordination number of oxygen atoms that surround the silicon atoms. Based on electronegativity values, the Si-O bond is approximately 88% ionic, indicating that the bond exhibits both ionic and covalent properties. The 12% covalent character helps to maintain the tetrahedra in the melt, making them the basic building blocks in silicate melts and glasses[15].

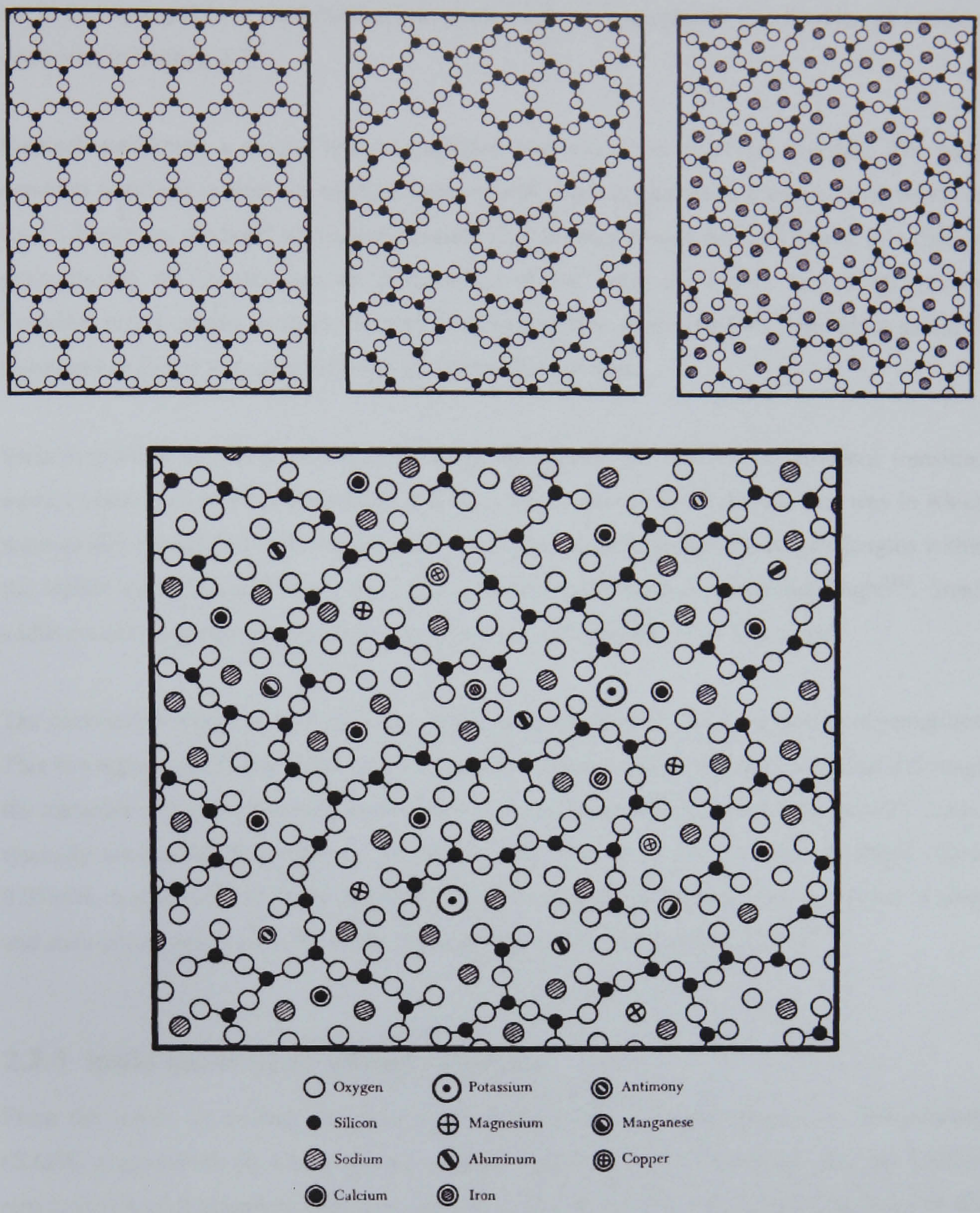


Figure 2-2: a schematic 2-D representation of the molecular structure of crystalline quartz (top left), silica glass (top centre), soda-silica glass (top right) and the more complex structure of a Roman glass, as suggested by Brill[17].

Pure SiO_2 melts at 1710°C, a temperature way above the capacity of an average furnace. In order to reduce the melting temperature of silica, fluxes are necessary. The most common flux is soda, or di-sodium oxide (Na_2O). Fluxes are network modifiers, monovalent alkali metal oxides that bond ionically with oxygen, locally disrupting bridging joints within the silica tetrahedral network and reducing the overall bond strength of glasses. Fluxes improve viscosity and thermal expansion but make crystallisation easier and affect chemical durability. The alkali ions

are in fact susceptible to leaching from the glass structure upon reaction with water, and will be dealt with in Section 2-7.

Network stabilisers, a second type of modifier, best solve this durability problem. The most common stabiliser is lime, or calcium oxide (CaO). CaO is present in glass in ionic bonds as Ca–O. However, the bond strength of bivalent Ca^{2+} is twice that of Na^{+} and results in a distinct strengthening of the structure on introduction of Ca^{2+} into the binary Na_2O-SiO_2 system. Trivalent metal oxides, such as alumina (Al_2O_3) and iron oxide (Fe_2O_3), enter glass as either stabilisers or fluxes and are referred to as intermediate oxides.

Soda-lime-silica (SLS) glasses are normally transparent and colourless. Bivalent transition metal oxides, such as FeO, ZnO, CuO and CoO, affect the colour of glasses. The way in which these oxides are bonded with oxygen results in a glass absorbing photons at wavelengths within the visible spectrum, and hence having a coloured appearance in transmitted light[16]. Small additions of manganese or antimony counteract the colouring effect of iron oxide.

The chemical structure of SLS glasses is made more complex by the introduction of impurities. This is a significant factor in the study of ancient glasses, where impurities introduced through the materials and manufacturing processes are present in significant quantities. Ancient glasses typically contain 10-15 compounds present in quantities above trace levels, i.e. above ~0.01-0.05wt%. A schematic example of the structural complexity of Roman glass compared to silica and soda-silica glass structures is illustrated in Figure 2-2, as suggested by Brill[17].

2.2.1 Ionic mobility in silicate glasses

From the results of nuclear magnetic resonance (NMR) and x-ray absorption fine-structure (XAFS) experiments on alkali silicate glasses, Greaves *et al.*[18] proposed that the bonding structure of multicomponent glasses is not totally disordered but can be described in terms of a modified random network (MRN). In the MRN model cation environments are restricted to percolation channels threading randomly through the network rather than being dispersed randomly through bonds with silica tetrahedra, reflecting the local geometry of crystalline silicates where layers of chains of corner-sharing SiO_4 units are cross-linked by ionically bonded alkali atoms. This concept is visualised in two dimensions in Figure 2-3. Similarly to crystalline silicates, the internetwork zones in silicate glasses are the basis for ionic diffusion, which ultimately undermines the stability of the structure and is the basis for glass corrosion (see Section 2.7); an alkali cation in a percolation channel in Figure 2-3 can jump to an adjacent site through the process of transferring its non-bridging oxygen bond to the next silicate group along the edge of the channel, causing a local rearrangement of the oxygen bonding structure in

the silicate groups that the cation has moved towards and away from. Such a process only requires oxygen atoms to 'flip' between bridging and non-bridging arrangements and acts as the basis for ion diffusion in glass.

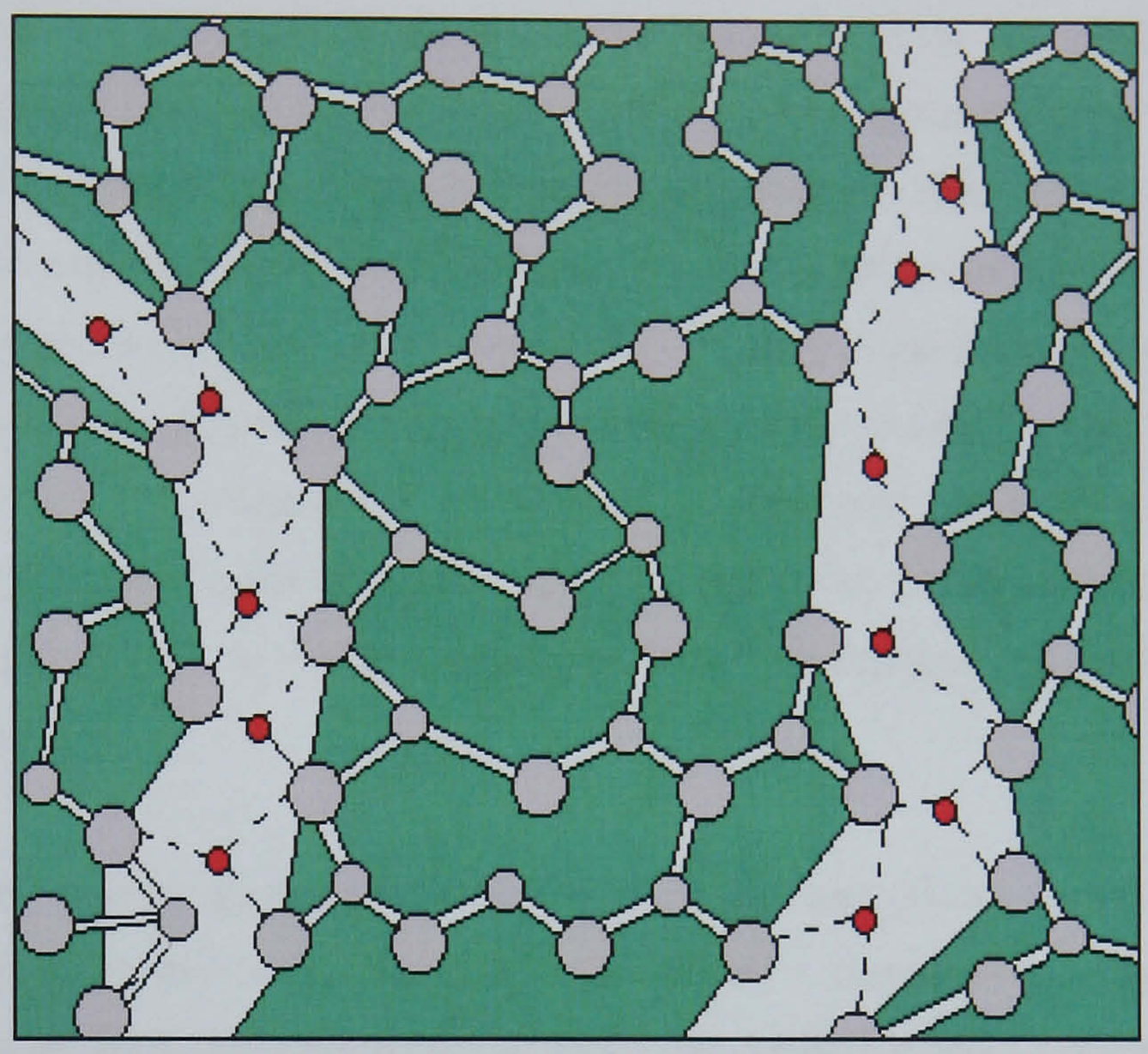


Figure 2-3: a schematic diagram of the MRN model of glass structure showing percolation channels formed by monovalent alkaline cations (in red) loosely bonded with oxygen atoms of surrounding silicate groups (in grey).

Ionic mobility in glasses is decreased when alkali cations of different sizes are present in the glass structure, particularly when they are present in equal amounts. The different ionic sizes cause interference in the percolation channels where local bond ordering energies are disturbed. This is known as the 'mixed alkali effect' and is responsible for greater long-term durability.

2.3 The raw materials of early glass production

Ascertaining the raw materials of glass production is complicated by a series of uncertainties. Henderson[19] outlined the two types of evidence for raw materials involved in early glassmaking. First are the remains of the raw materials from glassmaking sites; these can define the nature of the industry if their chemical relationships to products and by-products can be inferred. This is often not possible because of the restricted number of sites in which primary evidence for glass production has been found. Secondly, written descriptions of glass manufacture provide invaluable information about raw material use and furnace conditions for glass manufacture, but interpretation of the more ancient texts is problematic[20]. Nevertheless, successful replicative experimental studies based on written sources in antiquity are reported in the literature: glasses reproduced by Brill[21]according to recipes interpreted from Assyrian and

Mesopotamian texts dating to c. 700 BC closely mirrored the composition of analysed specimens from that period, and medieval glasses replicated by Jackson *et al.*[22] are based on 16th century guidelines given by Biringuccio.

The materials for ancient glass production were naturally occurring rocks and minerals, primarily a mixture of silica, soda and lime present in the right proportions to form a workable glass at attainable temperatures. There is widespread consensus that ancient glass was fused from only two raw ingredients, which (inadvertently it is thought) introduced a suitable quantity of fluxes and stabilisers; Brill's aforementioned replica experiments made use of two ingredients, similarly to 12th century glassmaking recipes reported by Theophilus[23]. It was not until the end of the 17th century that glassmakers appreciated that glass contained lime[24], although Brill has suggested the possibility of intentional three component batches by around the 12th-13th centuries[25]. In 1683 a first distinction between magnesia and potash in glasses was recorded by Bohn[26].

It is unclear from ancient glassmaking texts whether the ingredients, added in 'parts', were measured by volume or by weight; Smedley and Jackson[27] mention that Antonio Neri, in the 17th century, was probably the first author to report the weight of individual components to be added to the melt. They conclude that medieval plant ash-based glass recipes were measured by weight because volumes of sand and ash are susceptible to significant variations in weight per unit volume depending on the sand grain size and packing of the ash, and that this would affect the reproducibility of glass compositions. According to Brill[28], however, batches of natron-based Late Bronze Age glasses were probably measured out by volume, and his replication of Jalame glasses[35] is based on a 2:1 silica-containing ingredient to alkali ingredient recipe.

2.3.1 Silica

Sand is traditionally one of the main ingredients of early glass production. In the 1st century AD Pliny and Strabo quoted the mouth of the River Belus on the Syrian coast and the River Volturnus, northwest of Naples, as suitable sand deposits for glassmaking[24]. The River Belus remains the most frequently mentioned sand source in ancient texts and is often quoted in literature on glassmaking in the Levant. Reports by Turner[29] and Bezborodov[30] on analyses of sand gathered from the mouth of the River Belus indicate 8-10wt% CaO in the form of (often) microscopic shards of calcareous marine shells, 1-5wt% Al_2O_3 and minor Fe and Ti impurities. Most sands in fact contain varying amounts of feldspar and clay inclusions, which account for much of the Al_2O_3 and Fe_2O_3 in the final glass. Turner[29] concludes that although the ancient authors were possibly not aware of the advantageous properties of high-CaO containing sand, they were well aware that this particular sand produced glass of the desired quality. Crushed

quartz or flint was often substituted for sand to form glasses with a resulting lower Al_2O_3 impurity, although again this was not necessarily a conscious decision.

Purity and grain size are important parameters related to the silica source, as the former determines the extent of impurities that are introduced into the batch and the latter influences the rate at which the silica source reacts with other constituents at high temperatures; a suitably small grain size and narrow size distribution is desirable to promote rapid reactions in the melt.



Figure 2-4: present-day natron collection on the shores of the Wadi Natrun in Egypt. The image could represent the way the ancients collected and traded natron for use in glassmaking and soap manufacture.

2.3.2 Alkali

Two main types of alkali are reported in ancient glass production: the evaporite mineral natron (or trona, the sodium sesquicarbonate $Na_2CO_3.NaHCO_3.2H_2O$), which occurs as large scale deposits on the shores of dried salt-water lakes such as the Wadi Natrun in Egypt (see Figure 2-4), is discussed by Pliny, and the ashes of a variety of vegetable matter such as desert plants, seaweed, beech and oak trees etc. that are rich in Na compounds. The 'naga' plant referred to in Assyrian and Mesopotamian texts has been interpreted[21, 26] as a species within the genera *Salicornia* or *Salsola*, both of which grow abundantly in the desert margins of Iran, Iraq and Syria. *Salicornia* has been suggested as the alkaline component of plant ash glasses produced in desert regions of the Levant[29].

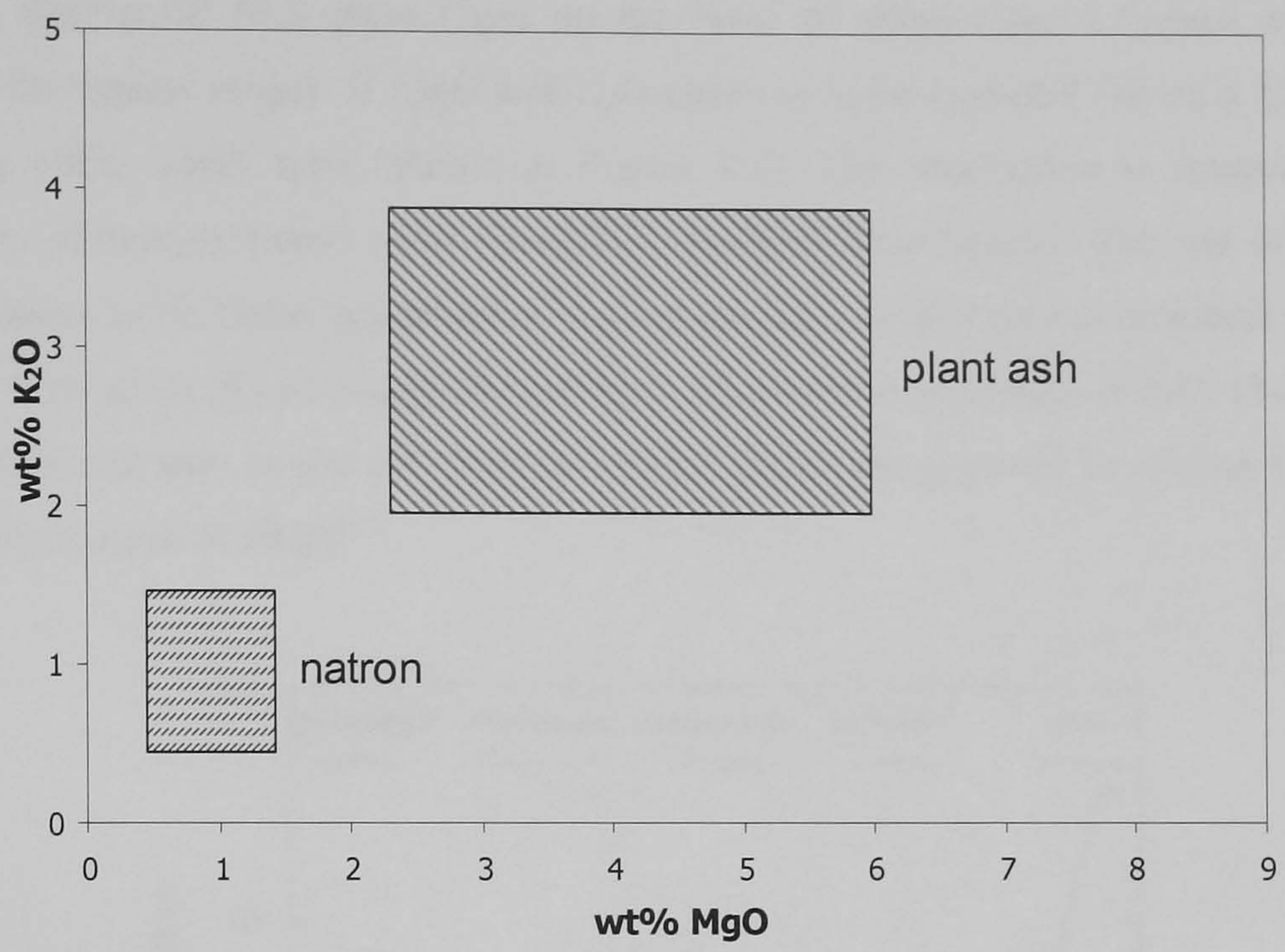


Figure 2-5: the variation in MgO and K_2O levels in SLS glass as a function of alkali source, according to Lilyquist and Brill[31].

2.3.2.1 Compositional variability of alkali sources

Carbonate, chloride and sulphate levels in natron analyses reported by Turner[29] varied enormously from trace level to major constituent, which would greatly influence the type of reaction taking place in the melt. The compositional variability associated with plant ashes makes the identification of a particular source or species elusive. Ashes from plants are highly variable in composition depending on a series of factors[19, 24]:

a) The physical environment in which the plant grows, as well as the time of year, affects the uptake and storage of nutrients.
b) The ways in which it is burned, refined or used alters the composition of the ash.
c) Different parts of plants have different chemical compositions.
d) There are differences between plants of the same species.
e) It is difficult to tell from the finished glass what the original proportions of sand to alkali were, what other substances were added, and which substances were lost in the reaction.

Because both alkali sources are naturally variable in composition, they are considered responsible for a degree of the compositional variability observed in ancient glasses (though one cannot exclude incomplete control over the glassmaking process as an important factor in this respect). Natron is the purer form of soda, hence natron based glasses typically contain much lower impurity levels of MgO, K_2O and, to a lesser extent, P_2O_5 than plant-ash glasses. It is thus

possible to distinguish SLS glass types on the basis of alkali type; Lilyquist and Brill[31] established the typical ranges of MgO and K_2O contents to be expected for early SLS glasses made using either alkali type (shown in Figure 2-5). This distinction is important in the classification of compositional types throughout antiquity (see below). The use of wood ash alkali introduces much higher quantities of K_2O to the glass so that typical medieval glasses are of a potash-lime-silica (KLS) compositional type. Appreciable quantities of P_2O_5 (3-8 wt%) are indicative of wood ash, or the ash from terrestrial plants (as opposed to marine vegetation), being the chief source of alkali[32].

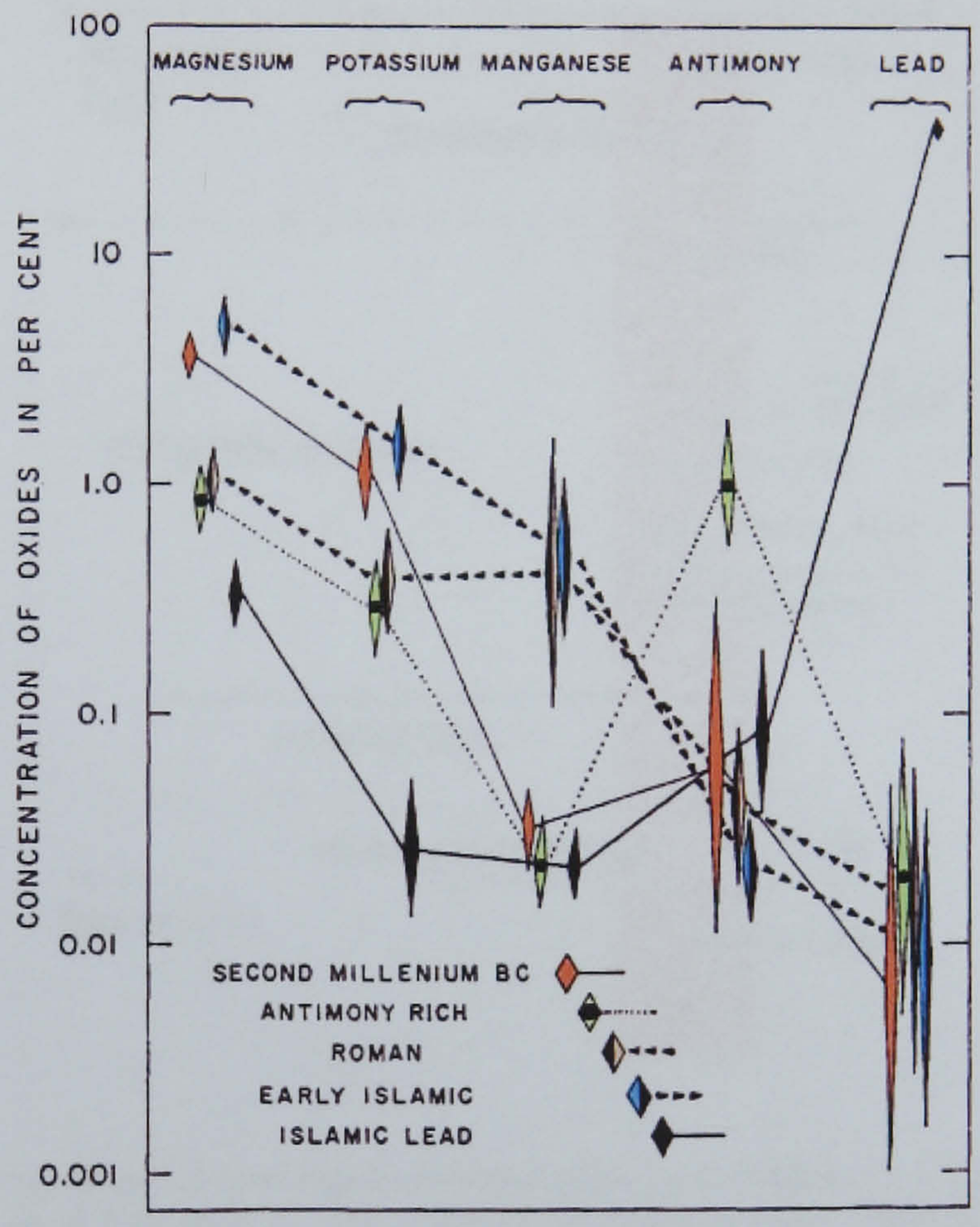


Figure 2-6: standard deviation ranges for concentrations of various metal oxides in the five main categories of Western ancient glass, as reported by Sayre and Smith[33].

2.4 Compositional categories of ancient glasses

The concentrations of the 10-12 major oxides serve as a basis for the classification of ancient glasses. A chemical classification can demonstrate that the artefact or sample under investigation belongs to a compositional glass category that was dominant over a certain period in a specific geographical region. Sayre and Smith[33] were the first, in 1961, to identify major compositional categories; they distinguished five groups ranging from the 2nd millennium BC to ~AD 1000 from different regions of the Near East and the Mediterranean on the basis of MgO, MnO, K_2O, Sb_2O_3 and PbO contents (Figure 2-6). They showed that a compositional transition

from natron to plant ash glasses had occurred between the Roman and Early Islamic periods across a wide geographical area. The categories drawn out by Sayre and Smith are still largely valid today even though the classification of ancient glass groupings has since been greatly refined by successive research. A more comprehensive picture of compositional glass categories over time has recently been supplied by Wedepohl[34] (Figure 2-7). He relates the groupings to the raw ingredients involved in their manufacture, so that natron based Roman glasses are 'soda lime' and Early Islamic plant ash glasses are 'soda ash'.

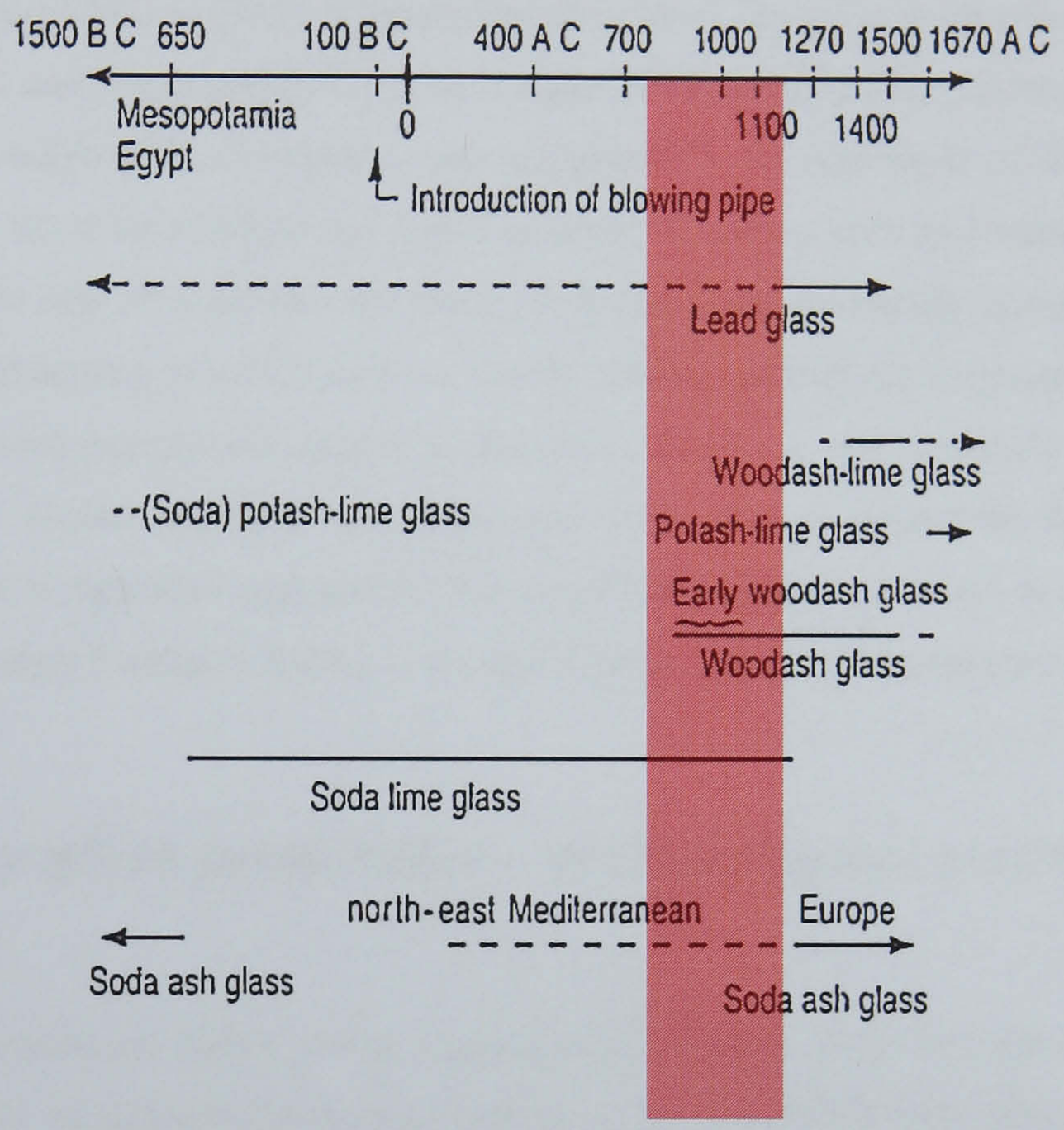


Figure 2-7: age ranges in which the major chemical glass compositions were produced in antiquity and medieval times, from Wedepohl[34]. The shaded area marks the time range for late Roman/ Early Islamic glasses from Raqqa in this study.

2.4.1 LMG vs. HMG

Of particular relevance to this study is the compositional overlap between 'soda lime' and 'soda ash' glasses, particularly in the north-eastern Mediterranean area. The increasingly large database for Byzantine and Islamic glass has revealed further examples of the two glassmaking traditions. Roman type glass was manufactured using natron along the Levantine coast between the 4th and 7th centuries[35] as were 5th century Byzantine glass tesserae from Israel[36], whilst a plant ash based glass was made further inland. A high MgO plant ash glass appears to be the earliest glass made c. 2500 BC, with glass beads having been found in Lower Mesopotamia[37]. Between the 8th and 10th centuries AD the high-MgO soda ash glass (HMG) gradually

supplanted and substituted for the low MgO soda lime glass (LMG) across the Islamic world[38-46], followed by a contemporary though different change- to wood ash- in Europe[34, 47, 48]. The exclusive use of plant ash glass in the Islamic period therefore represents a re-emergence of a dominant ancient technology, becoming almost the sole soda lime technology for several hundred years.

2.4.2 Compositional categories at Raqqa

The transition from LMG to HMG is particularly visible at the glass production site of Raqqa, where both LMG and HMG groups have been reported in simultaneous production at an 8th-9th century glass workshop[49]. Henderson has suggested[41] the presence of two 'workshop' compositions on the basis of MgO and Al_2O_3 contents. It will be seen in Section 5-1 that, with the new analytical data presented in this thesis, well-dated and chemically consistent groupings have emerged and serve a two-fold purpose. Compositional differences for glass used and made at Raqqa in separate periods are charted to interpret changes in raw materials over time. It is hoped that these detailed chemical investigations of the glass compositions from Raqqa will form the basis for comparative regional studies in northern Syria and beyond so as to investigate scientifically the significance of Raqqa as a major Islamic glass production centre.

2.5 Primary glass production – archaeological evidence in the Levant

Primary glass production refers to the manufacture of glass from its raw ingredients. An increasing number of primary production centres in the Near East have been excavated and published. Centres include a number of Roman and pre-Roman sites near the Wadi Natrun in Egypt[50], the Byzantine sites of Bet'Eliezer and Apollonia in Israel[51] and the Early Islamic site of Tyre in Lebanon[52]. On the basis of investigations of large-scale glassmaking centres, Freestone *et al.*[43] have suggested that primary glass production occurred in a relatively limited number of specialised locations close to the favoured sources of sand or alkali and away from inhabited areas. Once manufactured, the glass was broken up into large chunks and distributed to glass workshops where it was reheated and worked into vessels. The authors support their observations with the following arguments in favour of the division of production:

a) Roman glass composition is very homogeneous in terms of its chemical composition, which can be explained by the use of a small number of raw material sources mixed according to a simple recipe.

b) Peripheral areas such as Britain have not yielded unambiguous evidence for glass making as opposed to glass working. This is to be expected if the glass has been imported.
c) Ethnographic studies of glass production in modern India have highlighted a division of production: separate furnaces are used for glass making and glass working.

The trade and exchange of glass ingots is further evidence of the division of production. The 11th century Serç Limani shipwreck was found to contain a number of glass ingots[11]. It was presumably crossing the Mediterranean to deliver its consignment of ingots to glass workshops when it sank.

2.5.1 Tank furnaces

Many primary glass production centres in the Near East are characterised by the presence of one or more tank furnaces. Raw materials were placed inside these large, typically rectangular structures and fused in a single operation to form glass. This technique of glass manufacture stands in contrast to the two-stage process involving firstly the formation of a frit at temperatures between 750 and 900°C, followed by cooling, crushing and reheating to form a fully fused glass. Both procedures seem to have coexisted in antiquity; Roman fritting crucibles from the Wadi Natrun are reported by Saleh *et al.*[53], Brill's interpretation of 7th century BC Assyrian glassmaking texts includes a fritting stage[20] and medieval glasshouses used a two-step process to make their glass melts[47]. Tank furnaces were not designed to survive multiple firing cycles and were either rebuilt or abandoned after use; archaeological remains of primary production in tank furnaces come prevalently in the form of discarded or dismantled lumps.

2.5.2 Production times and temperatures

Theoretical reconstructions of tank furnaces have allowed the scale of operations to be more closely addressed: Gorin-Rosen reports 17 well-preserved tank furnaces at Bet Eli'ezer[51], represented in Figure 2-8. Each comprised a firing chamber, divided into two compartments, with separate openings, and a melting chamber measuring 2m x 4m. The fire in the firing chamber spread into the melting chamber and heated the raw materials placed there previously. Air circulation was provided by winds entering through the openings in the firing chamber. Gorin-Rosen hypothesises a manufacturing process lasting 10-14 days, and maximum temperatures of 1100°C. The scale of glass production capable at primary sites is often impressive; the great glass slab found at Bet She'arim weighs 8.8 tons and is thought to be an unsuccessful attempt at glassmaking in a tank furnace[44, 54], although no evidence of the furnace remains. Excavations of a 10th-11th century glassmaking site at Tyre in Lebanon have recently

identified the remains of four huge tank furnaces, the largest of which had the capacity to produce up to 37 tons of glass each time it was used[52].

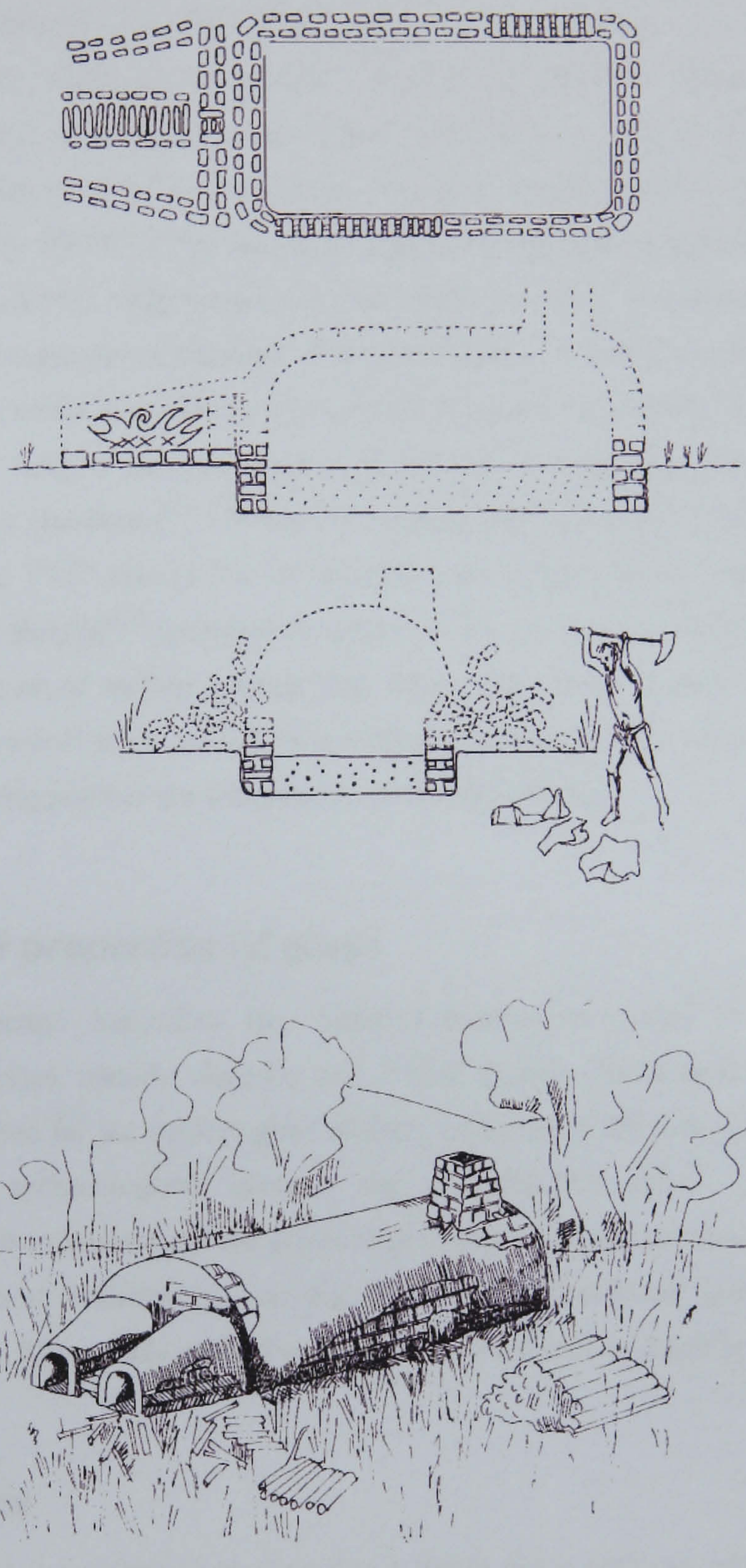


Figure 2-8: reconstitution of the plan and the sections of a tank furnace (top three images) from excavated remains at Bet Eli'ezer, Israel, as published by Gorin-Rosen[51]. The same author includes an artist's impression of how that tank furnace may have appeared when operational (bottom image).

Controversy exists in the literature regarding the temperatures reached during the glassmaking process. The maximum temperatures attained during glassmaking are ultimately restricted by

the performance characteristics of the furnace material – glass cannot be produced at temperatures higher than the melting temperatures of the furnace itself! The lowest possible temperature for the formation of a soda-lime-silica (SLS) glass is 725°C, which corresponds to the lowest ternary eutectic in the Na_2O-CaO-SiO_2 system (see Section 2.6.3.1), but the addition of other components alters this temperature significantly; Hlavác[55] reports experiments by Morey indicating that additions of Al_2O_3 higher than 2wt% to a three-component SLS glass cause a sharp increase in liquidus temperature. The effect of additions of 5wt% MgO is to lower the melting point by 100°C[2]. The results of gradient temperature experiments conducted by Brill[56] indicated that blue Egyptian glasses could form at 1060°C and colourless Roman glass at 1100°C; the experimental replication of Egyptian glass at Tell El-Amarna by Jackson *et al.*[57], although successful in producing glass, resulted in part of the replica furnace collapsing at 1150°C; Turner[29] doubted that temperatures above 1200°C could have been achieved before the 18th century, yet Henderson[58] reports that temperatures in excess of 1270°C had certainly been reached at the 7th-8th century site of Torcello, near Venice. In the 'partial batch melting' model proposed by Rehren[1, 2] (outlined in Section 2-1) glass formation is achieved through the progressive formation of molten pockets that follow the ternary eutectic troughs to higher temperatures. This would allow partial glass formation at significantly lower temperatures than the calculated melting point of the composition of the entire batch.

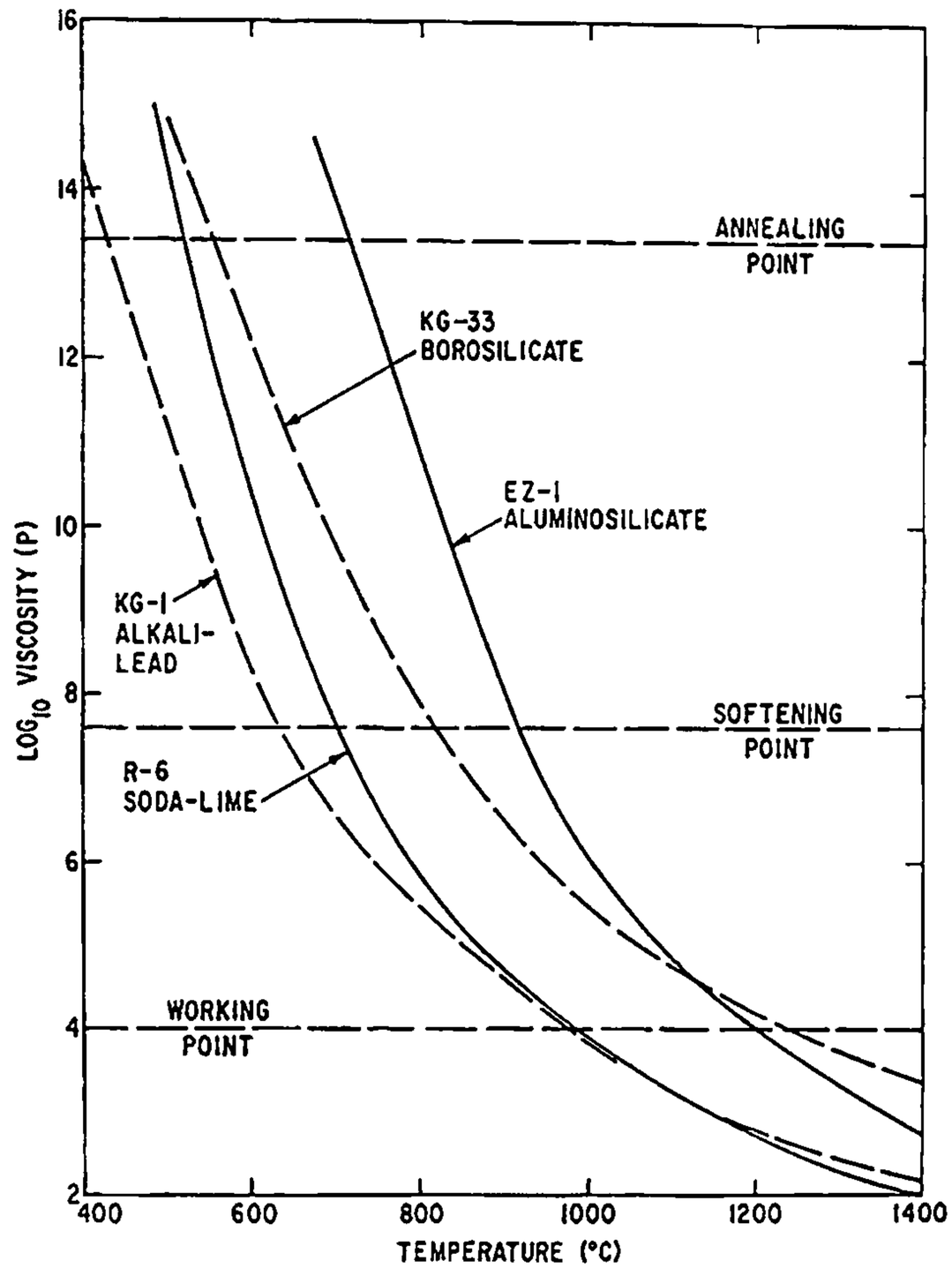
2.6 Physical properties of glass

The following section introduces two physical parameters related to high temperature glassmaking processes, namely viscosity and crystal growth. Mathematical models of these parameters developed for the modern glass industry constitute a theoretical framework that can be applied to archaeological glasses and glassmaking debris. This allows the archaeotechnologist to reconstruct the physical properties of materials associated with ancient glassmaking without necessarily carrying out often impractical and time consuming experimental work. The models applied in this thesis are outlined in detail below.

2.6.1 Viscosity

Viscosity describes the resistance to flow that a liquid poses with continued application of a force. The SI unit of viscosity (η) is the pascal-second, or Pa-s. The most common viscosity unit is the poise (P), which is equal to one tenth of a Pa-s. Viscosity is one of the most important working properties of glass, both technologically and historically, as it determines the melting conditions, working and annealing temperatures and workability of the melt. Once glass has been initially fused from its raw materials, one cannot really talk of melting temperatures, as it

shows no definable transition point between solid and liquid states at which the kinetic energy of molecules in the structure overcomes bonding forces.



Oxide (wt%)	Na_2O	MgO	Al_2O_3	SiO_2	K_2O	CaO	PbO	B_2O_3
Soda lime	15.2	3.6	1.7	72.6		4.6		0.8
Aluminosilicate	1.0		15.0	55.0	1.0	21.0		7.0
Alkali lead	9.0			77.0	5.0	1.0	8.0	
Borosilicate	7.0		1.0	68.0				24.0

Figure 2-9: viscosity-temperature plots for a range of commercial silicate glasses. Typical compositions are given below. From Doremus[14].

Glass instead undergoes an exponential increase in viscosity with decreasing temperature that fits an Arrhenius-type equation:

$$\eta = C\exp\left(\frac{Q}{RT}\right) \qquad [2.1]$$

where C is a constant and Q is the activation energy for viscous flow. Pure silica exhibits Arrhenian behaviour over the full range of temperatures for which data is available and thus a plot of $\ln\eta$ versus $1/T$ yields a straight line. Alkali silicates however show a change in Q with temperature. The temperature dependence of viscosity for several multicomponent silicate glasses is shown in Figure 2-9. The apparent activation energy is considerably larger in the low temperature region than at high temperatures, hence the deviation from a straight-line

relationship for multicomponent glasses. Hofmaier and Urbain[59] suggested that the higher than predicted activation energies encountered at lower temperatures may be attributed to the precipitation of a 'solid phase'.

The variation in Q with temperature for multicomponent glasses indicates that viscous flow in this case cannot be regarded as a simple activated process, but that it involves cooperative motion of more than one atom or molecule. The temperature dependence of viscosity does not fit any standard theoretical models and hence relationships have been determined with empirically derived equations. Owens-Illinois laboratories were the first to publish extensive data on viscosity measurements of SLS glasses in 1944[60]. Two important models that have since been developed will be considered in the light of this project and are outlined below.

2.6.1.1 The Fulcher-Tammann equation

The temperature dependence of viscosity varies widely for different groups of materials, and a number of models have been proposed to describe such dependence. For many glass forming melts the following equation proposed by Fulcher gives a very good representation of the variation of viscosity with temperature over a wide temperature range:

$$\eta = C\exp\left(\frac{Q}{R(T-T_0)}\right) \qquad [2.2]$$

where Q is the activation energy for viscous flow and T_0 is a temperature correction for a given melt composition required to fit data to a linear plot. The equation can be reduced to the Fulcher-Tammann relationship

$$\log\eta = -A + \frac{B}{T-T_0} \quad \text{or} \quad T = T_0 + \frac{B}{\log\eta + A} \qquad [2.3]$$

where A, B and T_0 are constants that can be calculated from at least three viscosity points. The relationship is valid only for temperatures above the glass transition temperature, T_g, because at lower temperatures the poor mobility of molecules necessitates the introduction of another variable, namely the structure temperature T_f, which may not correspond to the real temperature[61].

Lakatos *et al.*[62, 63] conducted viscosity measurements on multicomponent SLS glasses and derived empirical equations to calculate the constants in the Fulcher-Tammann equation. Thus:

$$\begin{aligned} B &= -6039.7\ Na_2O - 1439.6\ K_2O - 3919.3\ CaO + 6285.3\ MgO + 2253.4\ Al_2O_3 + 5736.4 \\ A &= -1.479\ Na_2O + 0.835\ K_2O + 1.603\ CaO + 5.494\ MgO - 1.518\ Al_2O_3 + 1.455 \\ T_0 &= -25.07\ Na_2O - 321.0\ K_2O + 544.3\ CaO - 384.0\ MgO + 294.4\ Al_2O_3 + 198.1 \end{aligned} \qquad [2.4]$$

The symbols Na_2O, K_2O, CaO, MgO and Al_2O_3 represent molecular contents in relation to one mole of silica. The effect of single oxides on viscosity was therefore calculated in terms of their relative content to silica, expressed as a measure of the change in temperature at which a specific viscosity is reached. The results are given in Figure 2-10 and it can be observed that:

a) The glass former SiO_2 and the intermediate Al_2O_3 increase viscosity. Al_2O_3 has about twice the viscosity-increasing effect of SiO_2.

b) The alkali oxides Na_2O and K_2O decrease viscosity and tend to make the glass 'longer'*. The viscosity-decreasing effect of K_2O is about half that of Na_2O.

c) The divalent oxides CaO and MgO have a strong viscosity decreasing effect at high temperatures and tend to make the glass 'short'*. MgO has about half the viscosity-decreasing effect of CaO, which increases viscosity at lower temperatures.

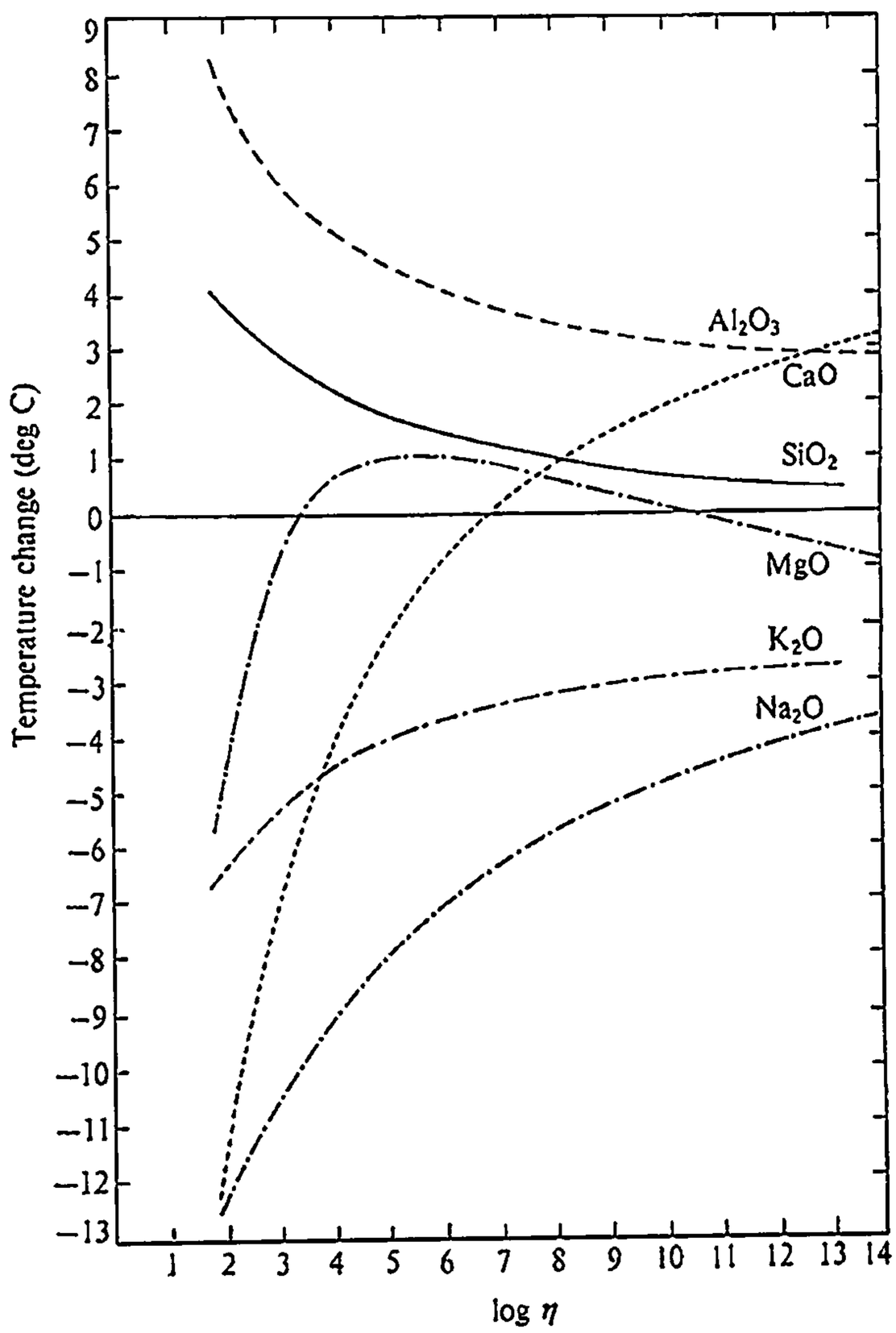


Figure 2-10: temperature change caused by an increase of 0.01 mole oxide/mole SiO_2 at different viscosities. From Lakatos[62, 63].

* 'Long' and 'short' are glassblowing terms that refer to the length of exposure at room temperature until a glass becomes too hard to be worked. A long glass thus allows more time for shaping than a short glass.

The authors state that, as standard deviations in the high temperature region were less than 1°C, and were approximately 1-1.5°C for the complete viscosity curve from 10^2 to 10^{13} poise, there is no need for more accurate formulae[64]. The validity of Lakatos' empirical formula has recently been confirmed by Dall'Igna *et al.*[61].

2.6.1.2 The Urbain method

The geologist Urbain developed a theoretical model to estimate the viscosity of molten magmas and silicate-based metallurgical slags. The model has since been adjusted and applied to a number of fields including ceramic processing and glass forming. The Urbain calculation[65] is based upon the statistical vacancy distribution and probability for the jump of one vacancy site to another within a silicate or an aluminosilicate melt, considered in terms of network formers, modifiers and amphoterics. The viscosity function he derived is:

$$\eta = AT\exp\left(\frac{1000B}{T}\right) \qquad [2.5]$$

where η is viscosity (in Pa-s), A and B are constants and T the temperature expressed in K. Urbain studied a series of ternary compositions and derived an empirical equation linking the two constants:

$$-\ln A = 0.2693B + 11.6725 \qquad [2.6]$$

Kalmanovitch and Frank[66] subsequently modified this relationship in order to make it applicable both to simple oxide glasses and complex silicate melts:

$$-\ln A = 0.2812B + 11.8279 \qquad [2.7]$$

The parameter B is a complex function of the chemical composition:

$$B = B_0 + B_1N + B_2N^2 + B_3N^3 \qquad [2.8]$$

where N is the molar fraction of network formers SiO_2 and TiO_2. Numerical values of B_i for i = 0,1,2,3 are interpolated by the following parabolic relations:

$$\begin{aligned} B_0 &= 13.8 + 39.5355\alpha - 44.049\alpha^2 \\ B_1 &= 30.481 - 117.1505\alpha + 129.9978\,\alpha^2 \\ B_2 &= -40.9429 + 234.0486\alpha - 300.04\,\alpha^2 \\ B_3 &= 60.7619 - 153.9276\alpha + 211.1616\,\alpha^2 \end{aligned} \qquad [2.9]$$

where $$\alpha = \frac{\sum \text{modifier oxides}}{\left(\sum \text{modifier oxides} + \sum \text{amphoteric oxides}\right)} \qquad [2.10]$$

and oxide totals are expressed as molar fractions. Kalmanovitch and Frank applied the modified Urbain model to fit over 400 measured viscosity curves of oxide glasses and coal ash melts in the temperature range 1250 to 1500°C with an R^2 value of 0.93. The Urbain formula is not particularly suited to viscosity values below about 10^7 poise because of the change in activation energy mentioned earlier but it nevertheless remains a widely used method for calculating theoretical viscosity.

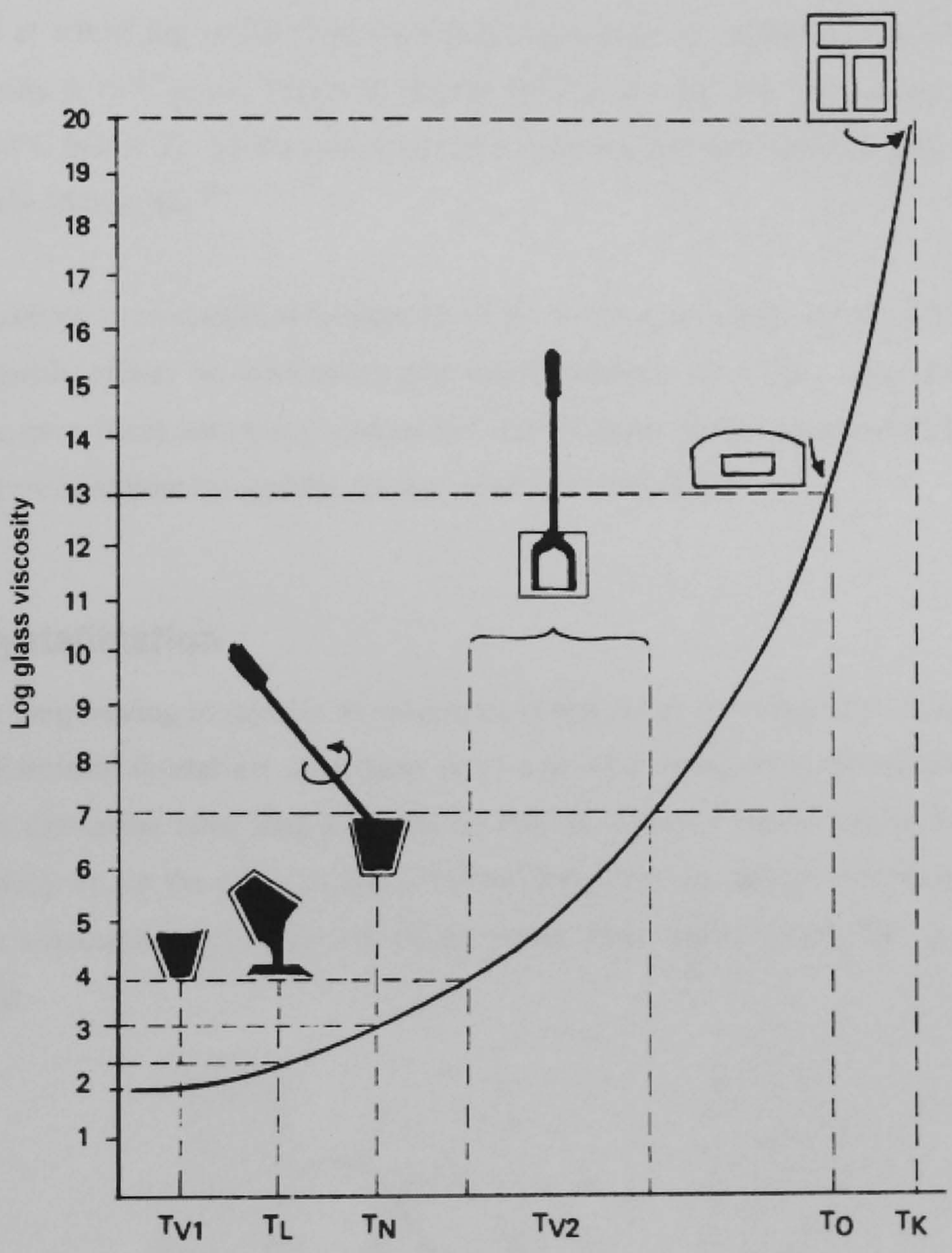


Figure 2-11: viscosity versus temperature in relation to glassmaking processes, as published by Bezborodov[30]. T_{V1} is the temperature at which glass flows similarly to water; T_L is the ideal casting temperature; at T_N glass can be gathered on to a pontil and blown; T_{V2} indicates the temperature range for mechanical forming processes; T_O indicates the annealing temperature and at room temperature (T_K) glass has the viscosity of most solids.

2.6.2 Viscosity vs. workability

The workability of glass as a function of its viscosity is given in Figure 2-11, from Bezborodov's comprehensive treatment of ancient glass properties[30]. The working point of a modern glass is defined as the temperature at which its viscosity is 10^4 poise, around 1000°C for most soda-lime-silica glasses. At such a viscosity glass can be readily formed or sealed[14]. The working point corresponds to the upper temperature limit of mechanical forming processes on Bezborodov's graph. Higher temperatures are required for manual forming (log η=3), when the glass needs to be gathered on to a pontil and removed from the furnace to be blown and marvered, and even higher temperatures for casting (log η=2.4). The softening point is the temperature at which log η=7.6. The annealing temperature is defined as the temperature at which viscosity is $10^{13.4}$ poise. This is to remove residual stresses from the cooling process and occurs 20-50°C below T_g. At the annealing point most stresses are removed from the glass in approximately 15 minutes[14].

Small fluctuations in composition brought about by minor components (Al_2O_3, MgO and K_2O) have appreciable effects on workability and would certainly have been observed by ancient glassmakers, even if not completely understood. The viscosity curves corresponding to different Raqqa glass compositional groupings are discussed in Section 6.2.

2.6.3 Crystallisation

Sufficiently long heating at suitable temperatures brings about crystallisation in glass, either in the form of isolated crystalline formations or as a layer growing from the surface. Industrial SLS glasses crystallise after long exposure in that temperature region where their viscosity allows forming, i.e. in the range of about 10^3-10^8 Pa-s. The crystals do not precipitate in the entire glass simultaneously; at certain points nuclei first appear which then grow into the ambient melt.

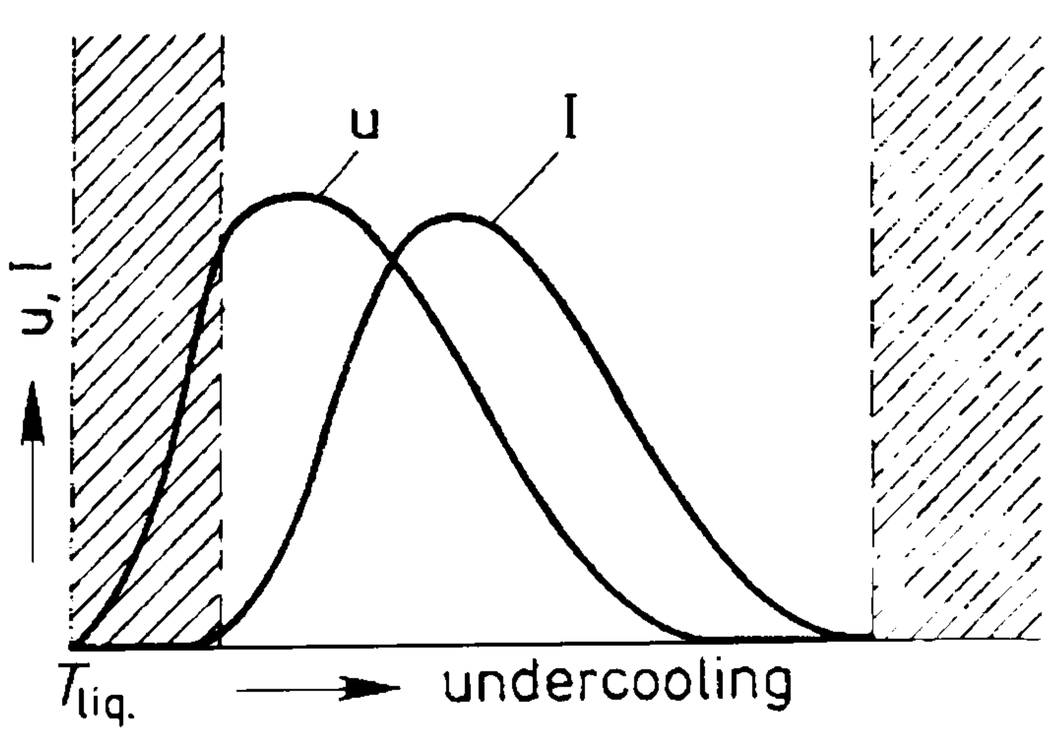


Figure 2-12: the temperature dependence of nucleation rate (I) and growth rate (u) of crystals in glasses, from Hlavác[55].

The crystallisation ability of glass can be characterised by the following parameters[55]:

1. The liquidus temperature
2. Nucleation rate
3. Crystal growth rate.

The nucleation rate is expressed by the number of nuclei created in a unit volume within a unit period of time. The rate of growth is given by the velocity at which the phase boundary advances into the melt, usually in $\mu m\ min^{-1}$.

The two quantities vary over a wide range according to glass composition; for a single glass they depend strongly on temperature, as illustrated in Figure 2-12. At liquidus temperature, they are both equal to zero, increase up to a maximum with decreasing temperature and then decrease asymptotically towards the temperature ordinate. The maximum in nucleation rate usually occurs at a lower temperature than the maximum in growth rate. This characteristic aids ready undercooling to the glassy state, whereas during reheating the tendency to crystallisation would be greater, since nuclei first arise that are then capable of further growth.

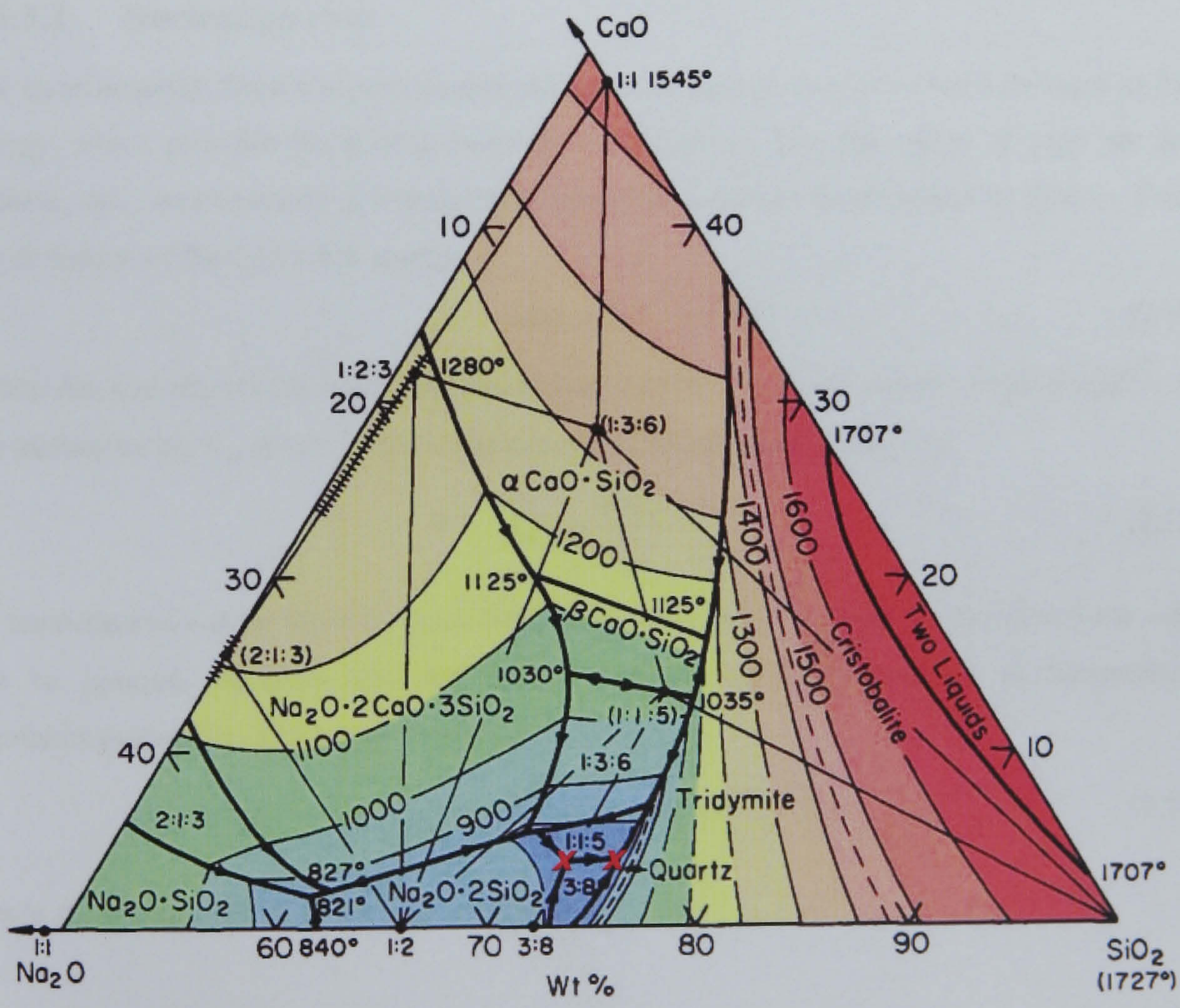


Figure 2-13: liquidus of the ternary SLS system of particular relevance to glass technology. The lowest ternary eutectics are situated at 755°C and are indicated by red crosses.

2.6.3.1 The liquidus temperature

The liquidus temperature (or melting point) is the temperature of equilibrium between the liquid and the crystalline phase. It is therefore the upper limit above which crystallisation can no longer occur. With SLS glasses, the liquidus temperature is usually in the range of 900-1200°C[55]. From the phase diagram one can determine the primary crystalline phase and also the sequence of the other phases separating during gradual cooling down of the melt. However, the sequence holds only for equilibrium conditions; this is not usually met in the case of glasses. The liquidus of the SLS system (given in Figure 2-13) shows two main eutectics at 755°C (for two compositions: 24.4-3.6-72.0 and 22.0-3.8-74.2 in wt% of Na_2O, CaO and SiO_2 respectively). SLS glasses, although modified by the introduction of small amounts of other oxides, belong essentially to a composition region in which tridymite or cristobalite (SiO_2), devitrite ($Na_2O.3CaO.6SiO_2$) and wollastonite ($CaO.SiO_2$) precipitate as crystalline phases. When the glass contains MgO, diopside ($CaO.MgO.2SiO_2$) frequently occurs. The presence of small amounts of other oxides in SLS glasses frequently results in the suppression of devitrite formation, so that cristobalite or β-wollastonite is often found in its place[16].

2.6.3.2 Nucleation rate

The transformation from a supercooled liquid to the crystalline state involves a decrease in free energy, which provides the driving force for solidification. The free energy change per unit volume, ΔG_V, on transforming a liquid to a crystalline solid can be estimated as follows. From the definition of the Gibbs free energy,

$$\Delta G_V = \Delta H_V - T\Delta S_V \qquad [2.11]$$

where ΔH_v and ΔS_v are the latent heat and entropy of fusion per unit volume, respectively[67]. At the melting point, T_m, $\Delta G_V = 0$; hence the entropy of fusion (ΔS_v) is given by:

$$\Delta S_V = \frac{\Delta H_V}{T_m} \qquad [2.12]$$

At temperatures not far from T_m the difference in the specific heats of the liquid and the solid can be ignored, therefore ΔH_v and ΔS_v are approximately independent of temperature. Combining equations 2.11 and 2.12 gives:

$$\Delta G_V = \frac{\Delta H_V (T_m - T)}{T_m} = \frac{\Delta H_V \Delta T}{T_m} \qquad [2.13]$$

where ΔT indicates the degree of undercooling.

The decrease in free energy in forming a spherical crystalline region of radius r is $4/3\pi r^3 \Delta G_V$. However, a crystal nucleus in a liquid involves the creation of a liquid-nucleus interface with an

associated surface energy (γ_{LN} per unit area), and is thus accompanied by an increase in free energy. The net change in free energy on forming the crystal nucleus is ΔG_{hom}[68],

$$\Delta G_{\text{hom}} = -\frac{4}{3}\pi r^3 \Delta G_V + 4\pi r^2 \gamma_{LN} \qquad [2.14]$$

which will achieve a maximum value when $\delta(\Delta G_{hom})/\delta r = 0$, i.e. when the crystalline 'embryo' attains a critical radius r^*, determined as:

$$r^* = \frac{2\gamma_{LN}}{\Delta G_V} \qquad [2.15]$$

Hence substituting for r and ΔG_V in equation 2.14 we obtain a final expression for the energy barrier to nucleation, ΔG^*_{hom},:

$$\Delta G^*_{\text{hom}} = \frac{16\pi \gamma_{LN}{}^3 T_m{}^2}{3\Delta H_V{}^2} \frac{1}{(\Delta T)^2} \qquad [2.16]$$

Thus the growth of a crystal nucleus depends on:

i. The formation of nuclei exceeding a critical size
ii. The extent to which a liquid is undercooled.

The rate of nucleation controls the rate of crystallisation of a supercooled liquid. The formation of a crystalline nucleus involves some structural rearrangement in the melt, requiring that atoms overcome the energy barriers that impede these rearrangements. This may involve a diffusion process (over small distances) or a reorientation of molecules into a configuration of greater stability. The rate at which the material can be transformed from a structure characteristic of a liquid to that of a crystal is proportional to an Arrhenius-type rate factor, $\exp(-\Delta G_D/RT)$, where ΔG_D is the activation energy associated with the structural rearrangement process, otherwise referred to as the kinetic barrier to nucleation. The rate factor decreases as temperature is reduced.

The rate of nucleation, I, is the number of stable nuclei to form per unit volume per second:

$$I = n\nu \exp\left(\frac{-N\Delta G^*_{\text{hom}}}{RT}\right) \exp\left(\frac{-\Delta G_D}{RT}\right) \text{nuclei m}^{-3}\ \text{s}^{-1} \qquad [2.17]$$

where n is the number of atoms per unit volume, ν is the vibrational frequency of atoms at the liquid-nucleus interface, N is Avogadro's number, ΔG^*_{hom} is the thermodynamic barrier to nucleation and ΔG_D is the kinetic barrier to nucleation.

The nucleation of crystals in oxide glasses has been recently reviewed by Gránásy and James[69], who consider and compare classical and non-classical nucleation models. In the classical approach, the nuclei are considered as spherical particles that show bulk properties up to a sharp interface. Steady state conditions for nucleation are assumed such that the steady state nucleation rate is expressed as:

$$J_{ss} = J_0 \exp\{-W^*/kT\} \quad [2.18]$$

where J_0 is the nucleation prefactor and W^* the work of formation of spherical nuclei, which is given as:

$$W^* = \frac{16\pi\gamma^3}{3\Delta g^2} \quad [2.19]$$

γ is the free energy of the crystal/glass interface, and $\Delta g \leq 0$ is the volumetric Gibbs free energy difference between the crystal and the undercooled liquid/glass. Gránásy et al.[70] provide experimental data for the free energy, γ, of the undercooled crystal/liquid interface for $CaO.SiO_2$ glasses, calculated at 434-749mJ/m^2.

2.6.3.3 Growth rate

The modelling of crystal growth is based on the following assumptions:

- Diffusion in the liquid is much more rapid than the reaction at the interface so that the growth rate is controlled by the crossing of atoms at the liquid-solid interface.
- Atoms in the liquid possess a free energy per unit mass higher than that possessed by atoms in the crystal by an amount equal to the bulk free energy of crystallisation, ΔG.

Once a stable nucleus has been established, the rate at which a crystal will grow is fixed by conditions of heat flow and rearrangement processes at the melt-crystal interface. According to Doremus[14], heat flow effects are expected to be found in crystallisation in glasses with growth rates higher than about 60μm/min, which is the case for alkali disilicate and borate glasses but does not really apply to SLS glasses as growth rates are significantly lower than 60μm/min.

The rate of crystal growth is determined by the rate of incorporation of molecules into the crystal from the melt. This process is illustrated in Figure 2-14. An atom or molecule must acquire an activation energy in order to detach itself from the attractions of neighbouring atoms of the liquid phase and form new bonds determined by the structure of the growing crystal. To cross an interface from liquid to crystal, an atom requires a free energy of activation ΔG_a, labelled as G_{LC} in Figure 2-14, and to cross from crystal to liquid a free energy of activation $G_{LC} + \Delta G = G_{CL}$. The net rate of crystal growth will be proportional to the difference between the frequency of liquid-solid transitions, ν_{LS}, and the frequency of solid-liquid transitions, ν_{SL}, where, according to Boltzmann's distribution law,

$$\nu_{LS} = \nu \exp\left(\frac{-\Delta G_a}{RT}\right) \quad [2.20]$$

and

$$\nu_{SL} = \nu \exp\left(\frac{-(\Delta G + \Delta G_a)}{RT}\right) \quad [2.21]$$

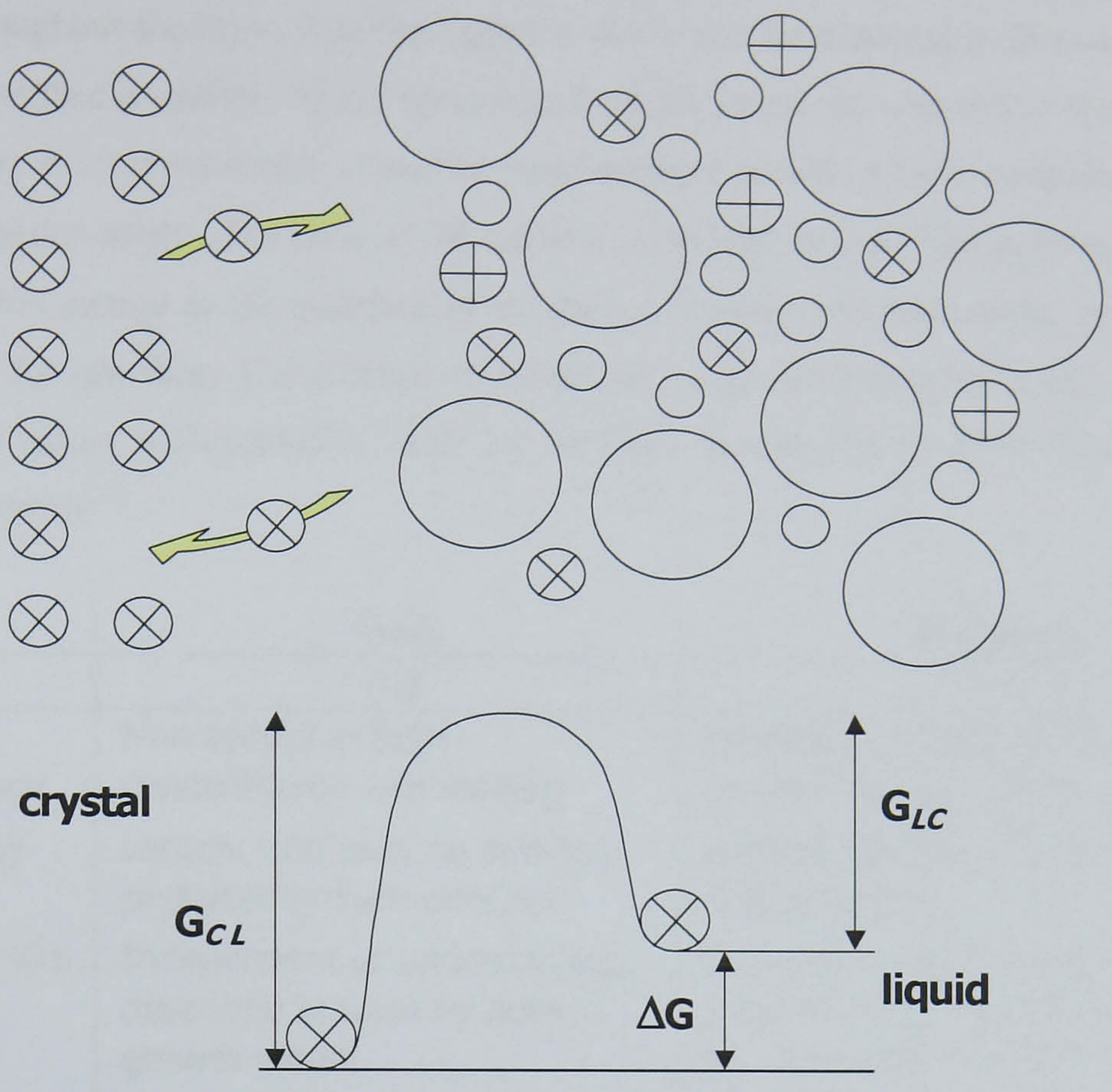


Figure 2-14: model for the precipitation of one of the constituents of a liquid mixture, adapted from Guillemet and Denoncin[74]. The activation energy necessary for an atom to cross from liquid to crystal is represented by G_{LC}. To cross from crystal to liquid an activation energy of $G_{LC} + \Delta G$ is required.

Therefore the rate of crystal growth, $V = fe\left(\nu_{LS} - \nu_{SL}\right)$, can be expressed as:

$$V = fe\nu \exp\left(\frac{-\Delta G_a}{RT}\right)\left[1 - \exp\left(\frac{\Delta G}{RT}\right)\right] \qquad [2.22]$$

where f is the fraction of crystal sites capable of accepting or releasing a molecule, e is the increase in length of the crystal after accepting a molecule and ν the vibrational frequency of molecules.

The crystal growth rate, because it is determined by parameters related to crystal-melt interface control, is also influenced by interface structure. Jackson's treatment of interface roughness[71] underlined the importance of the entropy of fusion in determining the interface structure and its influence on crystal growth. He found that the free energy change of an initially plane surface on adding molecules at random to the interface was proportional to a term α:

$$\alpha = \left(\frac{\Delta S_f}{R}\right)\xi \qquad [2.23]$$

where ΔS_f is the entropy of fusion , R is the gas constant and ξ the ratio of nearest neighbour sites parallel to the surface to the total number of nearest neighbour sites. The factor ξ is largest for the most closely packed planes of the crystal, for which it is ≥ 0.5. Jackson[72] then observed that, for $\Delta S_f/R < 2$, the interface is rough on an atomic level and liquid molecules can transform

to solid throughout the layer. A normal growth model can be expected in this case. For $\Delta S_f/R$ >4-6, the interface is smooth, so that molecules from the liquid can only be incorporated into the solid at steps in the solid surface, resulting in anisotropic growth, which is expected to follow a screw dislocation model. The ratio $\Delta S_f/R$ can also be written $\Delta H_f/RT$ and represents the ratio of the interaction energy at the interface to the thermal energy and reflects the ease of creating disorder at the interface. The contrast in behaviour of glass-forming materials with different entropies of fusion is illustrated in Table 2-2 for GeO_2 and $Na_2O{\cdot}SiO_2$ from Uhlmann's review of crystal growth[73].

System	GeO_2	$Na_2O{\cdot}SiO_2$
ΔS_f / R	1.3	4
Interface morphology	Nonfaceted in both crystallisation and melting	Faceted in crystallisation, nonfaceted in melting
Anisotropy	Largely isotropic; no strongly preferred growth direction	Anisotropic; growth preferentially in b direction
Interface site factor	Independent of undercooling; described in form by normal growth model	Increases with increasing undercooling; not well described by any standard kinetic model
Continuity at melting point	Crystallisation and melting data with continuous slope through T_m	Change in slope of kinetic data at T_m

Table 2-2: comparison of crystallisation and melting characteristics between GeO_2 and $Na_2O{\cdot}SiO_2$ on the basis of entropy of fusion. From Uhlmann[73].

The nature of the crystal-liquid interface has a decisive influence on the kinetics and morphology of crystallisation. Theoretical treatments of crystal growth have therefore focused on the relation between the nature of the interface and the predicted behaviour. The standard models for crystal growth from the melt are as follows:

a) Normal growth – the interface is pictured as smooth on an atomic scale, with a sizeable fraction of the interface sites being step sites where growth takes place. The growth rate is expressed as:

$$u = \nu a\left[1-\exp\left(\frac{\Delta G}{RT}\right)\right] \qquad [2.24]$$

where ν is the atom jump frequency at the interface and a the distance travelled by the interface.

b) Screw dislocation growth – this model views the interface as smooth but imperfect on an atomic scale, with growth taking place at step sites provided by screw dislocations intersecting the interface. The growth rate is given by:

$$u = f\nu a\left[1-\exp\left(\frac{\Delta G}{RT}\right)\right] \qquad [2.25]$$

where f is the fraction of preferred growth sites on the interface, given approximately as:

$$f \approx \frac{\Delta T}{2\pi T_m} \qquad [2.26]$$

Guillemet and Denoncin[74] have adapted the kinetic model of crystal growth for the precipitation of wollastonite in industrial SLS glasses. They modify equation 2.22 by substituting the gas constant, R, with the Boltzmann constant, k, and introducing an activity term, a, in the equation so that

$$V = fev \exp\left(\frac{-\Delta G_a}{kT}\right)\left[a - \exp\left(\frac{\Delta G}{kT}\right)\right] \qquad [2.27]$$

by assuming that if a pure liquid is involved, $a = 1$. The authors also assume that the reorientation and breaking of bonds necessary to incorporate a molecule into a crystalline structure are similar to movements involved in transport in the mass of the liquid and liken the activation energy term ($-\Delta G_a/kT$) to the viscosity η. They thus derive an empirical equation in which wollastonite growth rate, V (in m/s), is expressed in terms of undercooling, melt viscosity and CaO content:

$$V = 3.4\times10^{-4}\,\frac{(T_L - T)}{\eta}\left[1.5N_{CaO} - \exp\left[-\frac{4.73(1813 - T)}{T}\right]\right] \qquad [2.28]$$

$$\text{where } \frac{1}{T_L} = 5.04\times10^{-4} - 1.165\times10^{-4}\ln N_{CaO} \qquad [2.29]$$

T_L is the liquidus temperature for wollastonite growth (expressed in K)

N_{CaO} is the molar fraction of CaO in the glass

η is the viscosity of the glass (expressed in Pa-s)

Oxide	wt%
Na_2O	13 to 14
MgO	0 to 4.5
Al_2O_3	1 to 2.1
SiO_2	69 to 73
SO_3	0.13 to 0.3
K_2O	0.2 to 0.7
CaO	7 to 11
TiO_2	0.02 to 0.08
MnO	0 to 0.02
Fe_2O_3	0.03 to 0.01
BaO	0 to 0.9

Table 2-3: composition range of industrial SLS glasses studied by Guillemet and Denoncin[74].

The model represents wollastonite precipitation from a melt just above the liquidus temperature up to approximately 100K of undercooling. The compositional range investigated by Guillemet

and Denoncin is shown in Table 2-3. This adequately reflects the compositional range of SLS glasses from Raqqa, therefore their model has been applied in this study in Section 7.3.

2.7 The long-term corrosion of buried glasses

Glass is usually considered a highly non-reactive and durable material, hence its everyday use for storage purposes and drinking vessels. Because of its chemical inertness, the chemical durability of glass is concerned almost entirely with its reactivity with liquid water, aqueous solutions and water vapour, which in all these cases is extremely slow[14]. However, excavated archaeological glasses often exhibit a thick corrosion crust and in many cases have completely corroded. The complex corrosion mechanisms that occur at a glass surface when it reacts with water over long periods of time are of major interest to scientists and conservators alike. The characterisation of archaeological glass corrosion is therefore important in understanding the long-term reactions that occur in glasses during centuries of burial.

2.7.1 Atmospheric corrosion vs. reaction with aqueous solutions

Newton and Davison[75] report Harden's (1936) definition that: "The term 'weathering' is applied to any change for the worse on the surface… of glass that is caused, during the passage of time, by contact with outside influences… the term therefore covers a wide range of phenomena". However, the reaction of glass with water vapour in the ambient air, as opposed to with liquid water or aqueous solutions in the soil, is governed by different weathering mechanisms, as first indicated by Isard and Patel[76]. The two decay processes have increasingly been the subject of separate research programmes, for example recent International Glass Committee (ICG) publications on glass corrosion are divided according to corrosion in liquid water[77] and in humidity[78]. Newton[79] states that glasses tend to form a featureless fissured and pale coloured corrosion crust in the atmosphere and much darker crusts of a lamellar nature in soils. Cox and Cooper[80] observed that any weathering crusts forming in the atmosphere as a result of alkali and alkaline earth ions reacting with CO_2 and SO_2 do not have a laminated structure, which is instead a typical feature of buried glasses. Atmospheric weathering of glasses involves ion exchange but not congruent dissolution of the glass[14]. The degradation of glass in museum environments has been described in depth by Ryan[81], who noted the preferential formation of surface cracking, known as crizzling[82, 83], rather than a corrosion crust.

Although the two reaction mechanisms are based on the reaction between alkali ions in the glass and external water molecules, buried glasses are in permanent contact with an attacking aqueous solution, which generates a different chemical environment at the glass surface. An experiment by El-Shamy and Douglas[84] involved changing the rate of replenishment of the leaching

solution to study effects on alkali extraction. The results showed a marked increase in the amount of silica extracted as the number of replenishing times was decreased. Unless the leach solution is frequently renewed, the accumulation of alkali ions in the water leads to an increase in pH and a critical point is reached at pH>9 when the silica network is attacked (see below).

2.7.2 Glass corrosion: mechanisms of decay

The corrosion of glass is a slow, irreversible process that involves the hydration of its constituent species and the subsequent dissolution of the strongly bonded structure. Charles[85] described the corrosion process in terms of three chemical reactions:

a) the formation of a silanol group through penetration of water into the glassy network (where *R* denotes a monovalent alkali cation such as Na, K etc.)

$$\equiv Si-OR \;+\; H_2O \Rightarrow \equiv Si-OH \;+\; R^+ \;+\; OH^- \qquad [2.30]$$

b) the hydroxyl ion in solution disrupts a siloxane bond in the glass

$$\equiv Si-O-Si\equiv \;+\; OH^- \Rightarrow \equiv Si-OH \;+\; \equiv Si-O^- \qquad [2.31]$$

c) the non-bridging oxygen formed in reaction 2.31 interacts with a further molecule of water producing a hydroxyl ion, which is free to repeat reaction 2.31 again

$$\equiv Si-O^- \;+\; H_2O \Rightarrow \equiv Si-OH \;+\; OH^- \qquad [2.32]$$

This type of reaction breaks up the network, forming a 'gel' layer.

The first step in the reaction of water/aqueous solutions with an alkali silicate glass is generally assumed to be the exchange of alkali ions in the glass with hydrogen-bearing ions from the water:

$$Na^+(\text{glass}) \;+\; 2H_2O = H_3O^+(\text{glass}) \;+\; NaOH \qquad [2.33]$$

2.7.2.1 The thermodynamics of glass corrosion

Paul[86] predicted the durability of glasses from their chemical compositions and from thermodynamic hydration equations, where the free energy of hydration of the glass was correlated with the rate of alkali release from the glass into solution. According to Paul's method, the glass is treated as a homogenous mixture of structural species or units (Na_2SiO_3,

LONDON. UNIV.

SiO_2, etc). The thermodynamic stability is calculated by summing the free energies of the reactions of all structural species (expressed as molar fractions) present with water as given by:

$$\Delta G_{hyd} = \sum x_i \, (\Delta G_{hyd})_i \qquad [2.34]$$

where $(\Delta G_{hyd})_i$ is the free energy change of the thermodynamically most stable hydration reaction of component i at mole fraction x_i. For example, the hydration of SiO_2 is given by:

$$SiO_2 + H_2O \Leftrightarrow H_2SiO_3 \qquad [2.35]$$

where the forward reaction describes the dissolution process and the backward reaction describes the condensation reaction which is responsible for the formation of silica in the leached layers. The reaction is a description of the dynamic equilibrium set up at the interface of the glass surface and the leaching solution so that, for the reaction of silica and water, the equilibrium constant K is:

$$K = \frac{(\alpha_{H_2SiO_3})}{(\alpha_{SiO_2})(\alpha_{H_2O})} \qquad [2.36]$$

where α is the thermodynamic activity of the components in the mixture (or solution). Since silica and water are assumed to be in their standard state at 25°C (and are therefore unity), the equilibrium constant K is equal to $\alpha(H_2SiO_3)$. The relationship between the equilibrium constant and the free energy of the exchange reaction is given by:

$$\Delta G^\circ = -RT \ln K \qquad [2.37]$$

where ΔG° is the standard free energy of the reaction, R is the gas constant and T is the temperature in K.

Based on the free energy of hydration values of individual glass constituents, shown in Table 2-4, the overall free energy of hydration of any silicate glass composition can be calculated by taking into account ion exchange, matrix dissolution and surface layer formation mechanisms according to the method put forward by Jantzen[87]: network breaking structural species (e.g. Na_2O, CaO, etc.) are considered to be released into solution by ion exchange with protons from the solution. The polymerised silicate $(SiO_4)^{4-}$ structural units associated with the modifying species are considered to be released into solution or to form silanol bonds on the glass surface, where equations representing such exchange reactions are given respectively for the release of monovalent and divalent ions by:

$$R_2SiO_3 + 2H^+ \Leftrightarrow H_2SiO_3 + 2R^+ \qquad [2.38]$$

$$RSiO_3 + 2H^+ \Leftrightarrow H_2SiO_3 + R^{2+} \quad [2.39]$$

Glass Components	Hydrated Species	$(\Delta G_{HYD})_i$ (kcal/mol)
Na_2SiO_3	$Na^+.H_2SiO_3$	-28.815
K_2SiO_3	$K^+.H_2SiO_3$	-41.735
$CaSiO_3$	$Ca^{2+}.H_2SiO_3$	-16.116
$MgSiO_3$	$Mg^{2+}.H_2SiO_3$	-13.888
$MnSiO_3$	$Mn^{2+}.H_2SiO_3$	-14.871
Al_2O_3	$Al(OH)_3$	3.04
Fe_2O_3	$Fe(OH)_3$	15.5
P_2O_5**	$P^{5+}.H_3PO_4$	-55.93
TiO_2	$TiO(OH)_2$	15.99
SiO_2	H_2SiO_3	5.59

Table 2-4: calculated free energies of hydration for glass components, after Jantzen[87]. ** denotes value calculated by Cooper and Cox[104].

Dissolution of Fe_2O_3 and Al_2O_3 species, which form hydroxides or hydrates that participate in surface layer precipitation reactions, is expressed as:

$$R_2O_3 + 3H_2O \Leftrightarrow 2R^{3+}(OH)_3 \quad [2.40]$$

where R^{3+} is a trivalent cation.

Jantzen and Plodinec[88] correlated glass composition, structure and durability by considering the proportion of non-bridging oxygen bonds (NBO) in a glass network. The modified random network model (MRN) outlined in Section 2.2.1 shows that network modifying cations in a glass structure share similar environments (percolation channels) which are characterised by the presence of non-bridging oxygen bonds. The reaction mechanism is therefore directly related to glass composition and structure. The authors defined a formula for calculating the number of non-bridging oxygen atoms in silicate glasses as:

$$\begin{aligned} NBO = 2(BaO + CaO + FeO + K_2O + Li_2O + MgO + MnO + Na_2O + NiO + \\ - Fe_2O_3 - Al_2O_3) + 4(TiO_2 + ZrO_2 + UO_2)/\text{oxide mole sum} \end{aligned} \quad [2.41]$$

It is assumed that every molecule of monovalent and divalent oxide component contributes two non-bridging oxygen atoms while every Fe_2O_3 and Al_2O_3 component creates two bridging oxygen atoms due to the formation of tetrahedral $(AlO_4)^{5-}$ and $(FeO_4)^{5-}$ groups. Tetravalent ions such as Ti^{4+} are assumed to create four non-bridging oxygen atoms.

They then correlated the calculated free energy of hydration with the number of non-bridging oxygen atoms for 150 glass compositions and found there to be the following relationship with a degree of correlation of $R^2 = 0.72$:

$$\Delta G_{hyd} = -19.23\, NBO + 4.77 \qquad [2.42]$$

The correlation validates the relationship between their thermodynamic hydration model and the bond energetics of complex multicomponent glasses. As such, the model has frequently been referred to in subsequent literature. Conradt[89] has recently invoked the adoption of a more complete constitutional approach for glass corrosion and points out physical inconsistencies in the aforementioned thermodynamic approach; because the ΔG_{hyd} values are calculated based on tabulated standard data for vitreous, amorphous and crystalline compounds and the individual components are weighed according to the stoichiometry of the glass involved, the concept implies that the glass itself is a physical mixture of oxides and metasilicates and ignores the energy of vitrification present in glassy compounds. It is likely that further research in this field will focus accordingly on refining the thermodynamic principles in glass formation, although for the purpose of the present study the approach of Jantzen and Plodinec will be followed.

2.7.2.2 Solubility of SiO_2 in aqueous solutions

The relative insolubility of silica in water is one of the main factors in the corrosion of glass. When vitreous silica is brought into contact with water at ordinary temperatures the value of the equilibrium solubility is very low (<100ppm for vitreous silica), but it is the extremely slow rate of hydration that is responsible for this glass having a high resistance to the attacking water.

In principle the thermodynamic stability of a glass may be considered to be the stability of its component oxides, which in turn is a function of activity, a, of that particular oxide in glass and the equilibrium constants of hydration, ionisation and complexation. With the available thermodynamic data it is possible to calculate the various energy changes associated with these processes, and therefore the stability of the glass under various conditions can be judged.

2.7.2.3 Effect of pH of the solution on the solubility of SiO_2

As mentioned in Section 2.7.2.1, the reaction between water and silica may be expressed as:

$$SiO_2 + H_2O \Rightarrow H_2SiO_3 \qquad [2.43]$$

The solubility of SiO_2, in terms of H_2SiO_3 in solution, is independent of pH. But in the presence of alkali, additional silica passes into solution as silicate ions through the dissociation of silicic acid:

$$H_2SiO_3 \Rightarrow H^+ + HSiO_3^- \quad [2.44]$$

$$HSiO_3^- \Rightarrow H^+ + SiO_3^{2-} \quad [2.45]$$

And comparing the activities of each silicate species released into solution from vitreous silica:

$$a_{H_2SiO_3} = K = 10^{-4.098} \quad [2.46]$$

$$a_{HSiO_3^-} = K = 10^{-14.098} + pH \quad [2.47]$$

$$a_{SiO_3^{2-}} = K = 10^{-26.092} + 2pH \quad [2.48]$$

it is clear that one particular species will predominate for a given pH. For pH ≤ 9 the soluble portion of H_2SiO_3, reaching about $10^{-5.2}$ M, represents the minimum solubility. At pH values higher than 9 most of the silica that passes into solution is due to the formation of $HSiO_3^-$ and for pH ≥ 12, SiO_3^{2-} is the predominating species. Silica release is thus much higher at higher pH values ($>10^{-2}$ M). A stability diagram of quartz and vitreous silica in aqueous solution at 25°C is shown in Figure 2-15. All silica-based glasses will follow the same trend with respect to pH changes of the solution. Similarly, studies suggest[12] that for the variety of silicate glass systems studied worldwide, the leaching behaviour and decay mechanisms of many of these systems should be very similar.

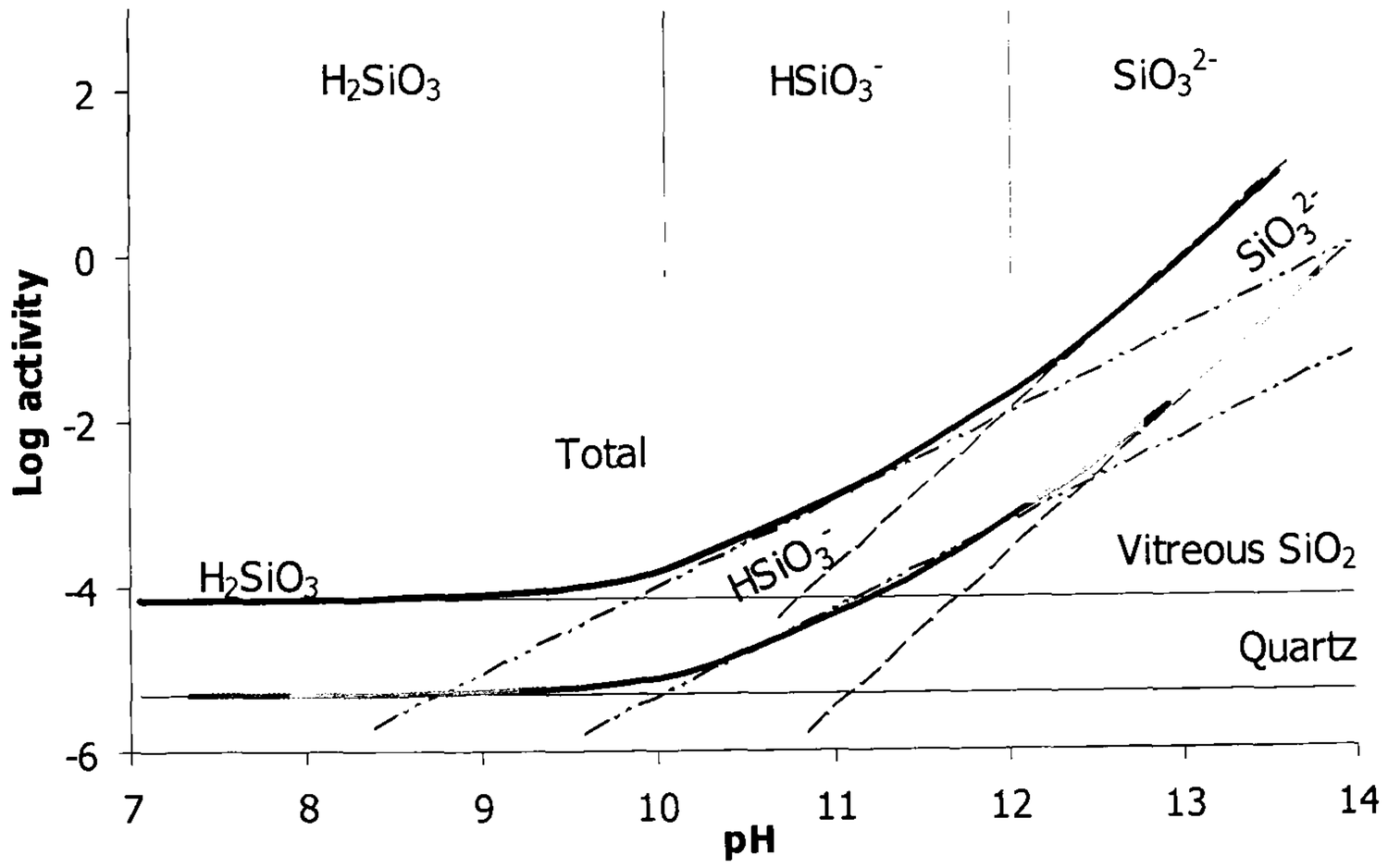


Figure 2-15: stability diagram of quartz (green line) and vitreous silica (red line) in aqueous solution at 25°C, after Paul[86].

2.7.2.4 Kinetics of dissolution

Experimental studies reported by Wicks[90] have shown that the total amount of alkali released from a glass, Q_{alk}, can be expressed by the rate reaction:

$$Q_{alk} = at^{1/2} + bt \qquad [2.49]$$

where a and b are constants and t indicates the time of leaching. As the initial ion exchange reaction is diffusion controlled leaching follows a square-root time dependency. In the longer term, the second part of equation dominates as the rate of release becomes linear with time. The parabolic to linear release rate of alkali is generally observed in many glass systems.

Recent studies on nuclear waste glasses [91, 92] have reinforced the notion that corrosion rates are slowed by the formation of the gel layer, which acts as a passivating layer through which ion diffusion is more difficult. It is thus generally accepted that glass corrosion processes reach steady-state conditions at longer time periods of exposure to aqueous solutions.

2.7.3 The long-term natural corrosion of glass

Archaeological glasses have proved a useful resource for weathering studies. In 1979 glass matrices were first proposed for the long term immobilization of high-level nuclear waste[88], leading a number of authors[93, 94] to advocate the use of archaeological glasses for predicting the long-term corrosion characteristics of glass. Although chemically complex in nature, glasses from well-dated archaeological contexts provide real examples of long-term natural decay through interaction with groundwater in soil environments that cannot be realistically replicated in laboratory environments[32]. Glass dissolution and mechanisms of alteration are mainly deduced from experimental studies based on simpler binary and ternary glasses. Information on natural alteration of glass over longer periods of time is also essential to check the validity of experimental models of dissolution[95].

2.7.3.1 Structure of corrosion crusts

Lopez *et al.*[96] recently stated that unanswered questions remain concerning the structure of the modified layers in corroded glasses. Advances in theories on weathering crust formation and the application of powerful new high-resolution imaging techniques have helped to characterise the complex chemical reactions taking place at the surface of buried glasses.

The beautiful iridescent appearance of many ancient glasses intrigued collectors for many years and was thought to be a lost secret in glassmaking practices[97]. As early as 1863 Brewster[98] observed that the iridescence was actually caused by diffraction effects arising from thin layers within a weathered crust. This conclusion was based on the idea that air gaps existed between

layers and the interference of light took place because of the great differences between the refractive index of the air and the corroded glass: he observed the complete extinction of colour when the glass was immersed in various liquids, suggesting a porous structure because water and other liquids could enter freely.

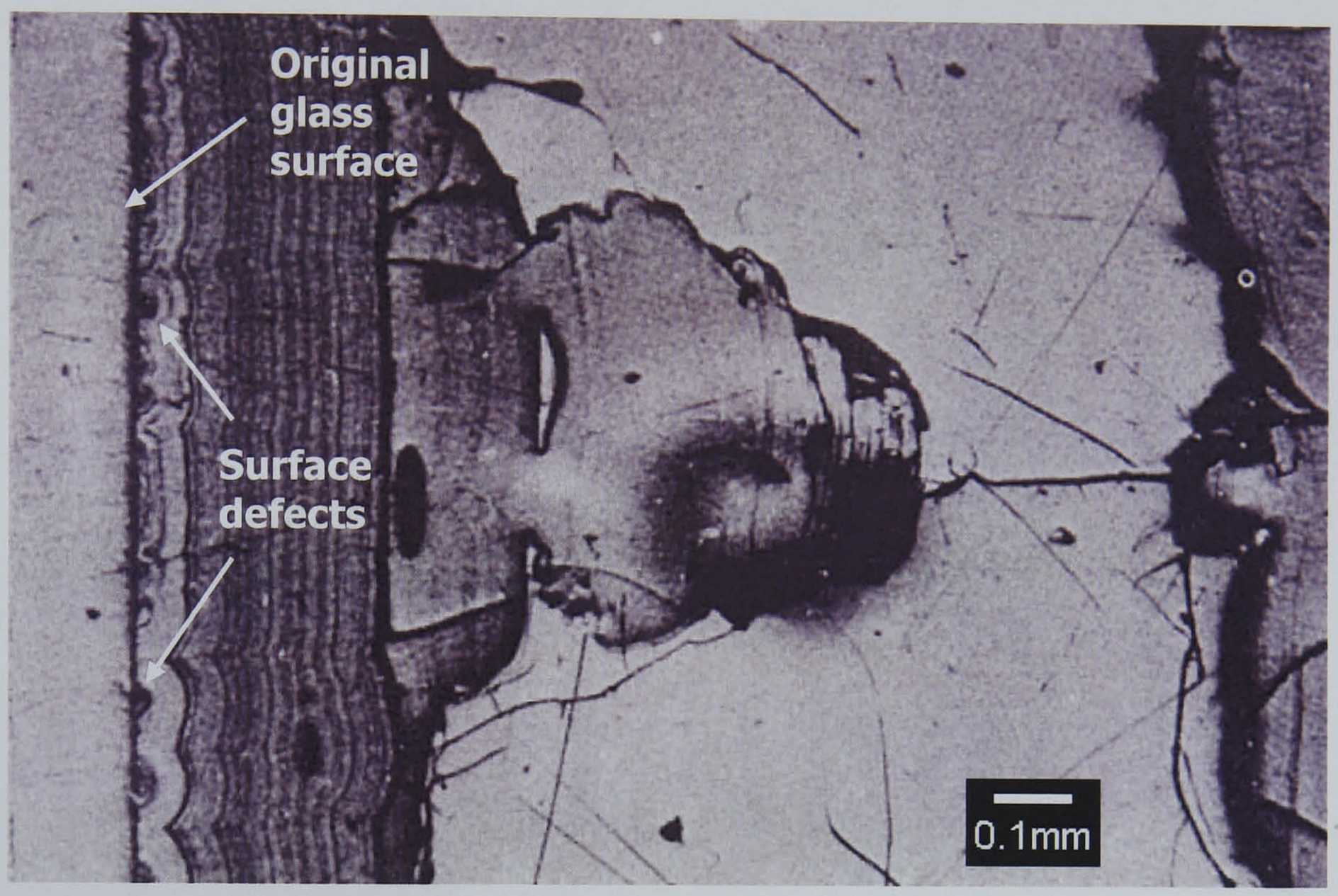


Figure 2-16: optical micrograph of a section through a KLS window glass buried for 288 years[97]. Layered corrosion develops from defects and irregularities at the outer surface, left, and begins to propagate hemispherically into the glass. In this sample, an irregular formation, centre, beneath the regularly formed layers, is reported.

In the 1950s Raw[99] and Geilmann[100] published detailed examinations of corroded crusts of buried medieval window glasses, showing the crust to be of a highly porous and very finely laminated nature that consisted of continuous and constantly spaced layers. Newton[101] reports that the reacted product loses 50-75% of its mass, despite having the same volume. Finely laminated crusts are reported by other authors[93, 97, 102] on buried KLS glasses.

Decomposition usually starts at a large number of centres on the surface and proceeds into the glass to form a series of hemispherical layered shells, which then coalesce so that, eventually, the layers are more or less parallel to the surface. Figure 2-16, published by Newton[97], is an optical micrograph of a section through a KLS window glass buried for 288 years. The upper surface of the cross-section in Figure 2-16 shows the typical hemispherical formation pattern just described.

Each layer possesses an individual physical identity, except for instances in which layers merge into each other, as has been illustrated by Newton[103]. In this publication Newton also included

an electron image of individual corrosion layers in cross-section (reproduced in Figure 2-17), taken along a crack that had formed transversely across the layers. He pointed out that the layered structure exists down the sides of the crack and that in this fractured area a 'substructure' is visible between adjacent layers. Newton hypothesised that the narrow bands between layers were air gaps that had filled with debris from the polishing operation.

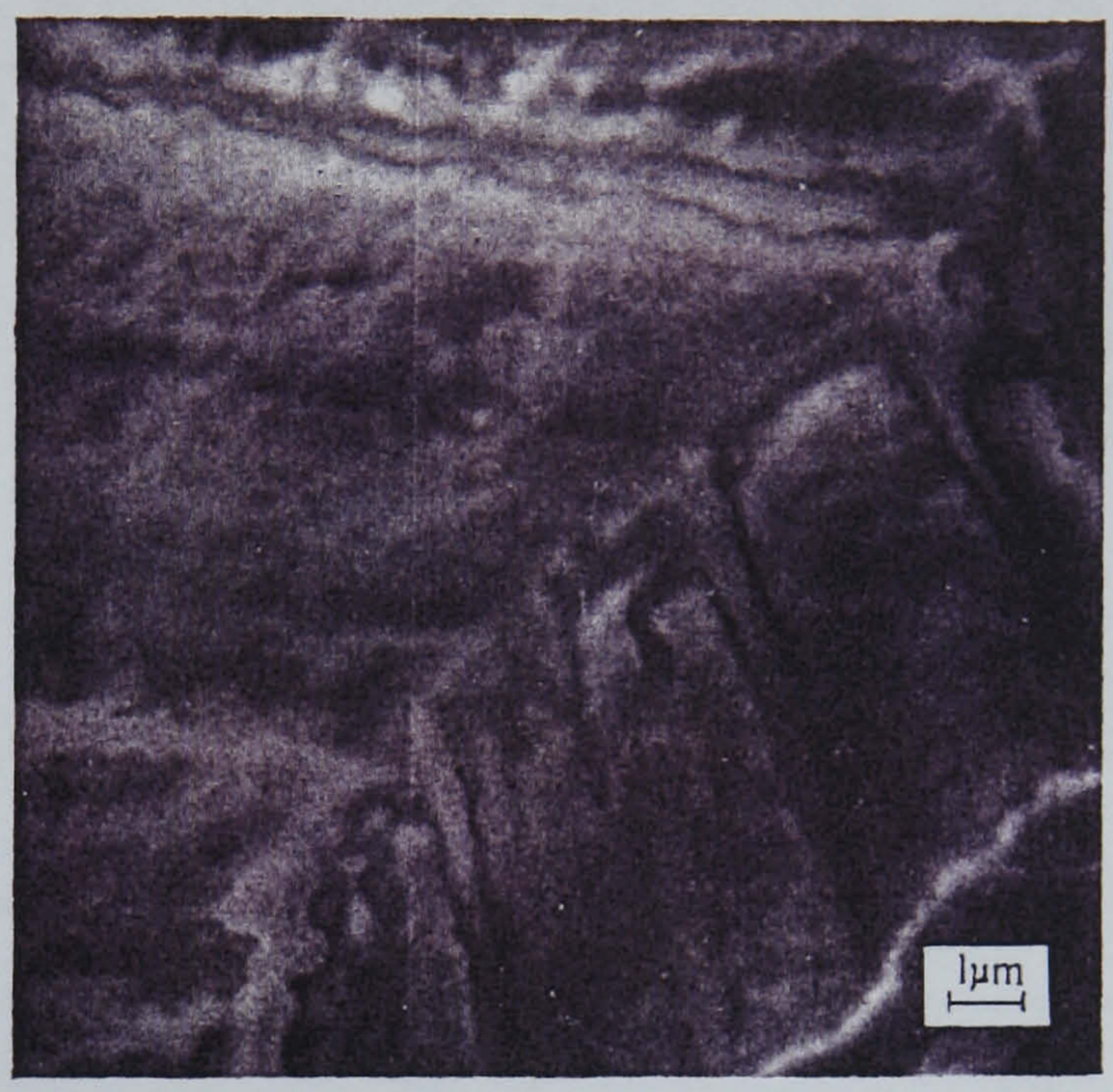


Figure 2-17: an electron image of individual corrosion layers in cross-section on the KLS glass shown in Figure 2-16.

Figure 2-18 is an electron image published by Macquet and Thomassin[93] of an individual corrosion layer of a corroded 10th century Carolingian glass. The authors point out the granular appearance of the layer surface. Cooper and Cox[104] found that soil corroded crusts of archaeological KLS and SLS glasses were essentially composed of a porous silica gel with typical pore diameters being <10nm, and with MnO_2 and calcium carbonate, phosphate and some sulphate precipitated within the pore spaces of the gel. Cox and Ford[32] report that x-ray and electron diffraction studies on several crusts revealed that their degree of crystallinity was either extremely low or undetectable.

2.7.3.2 Chemical constitution of corrosion crusts

A growing number of chemical analyses of crusts on archaeological glasses confirm that the corroded region is essentially depleted of network modifiers and stabilisers (Na_2O, K_2O, MgO, CaO), enriched in network formers (SiO_2 and Al_2O_3) and partially hydrated up to 20%. In 1973 El-Shamy[105] showed that the tendency for KLS glasses to form a crusted layer increased rapidly as the silica content fell below 66 mol%, the point at which every silicon atom in the glass becomes associated with a basic ion as its second neighbour.

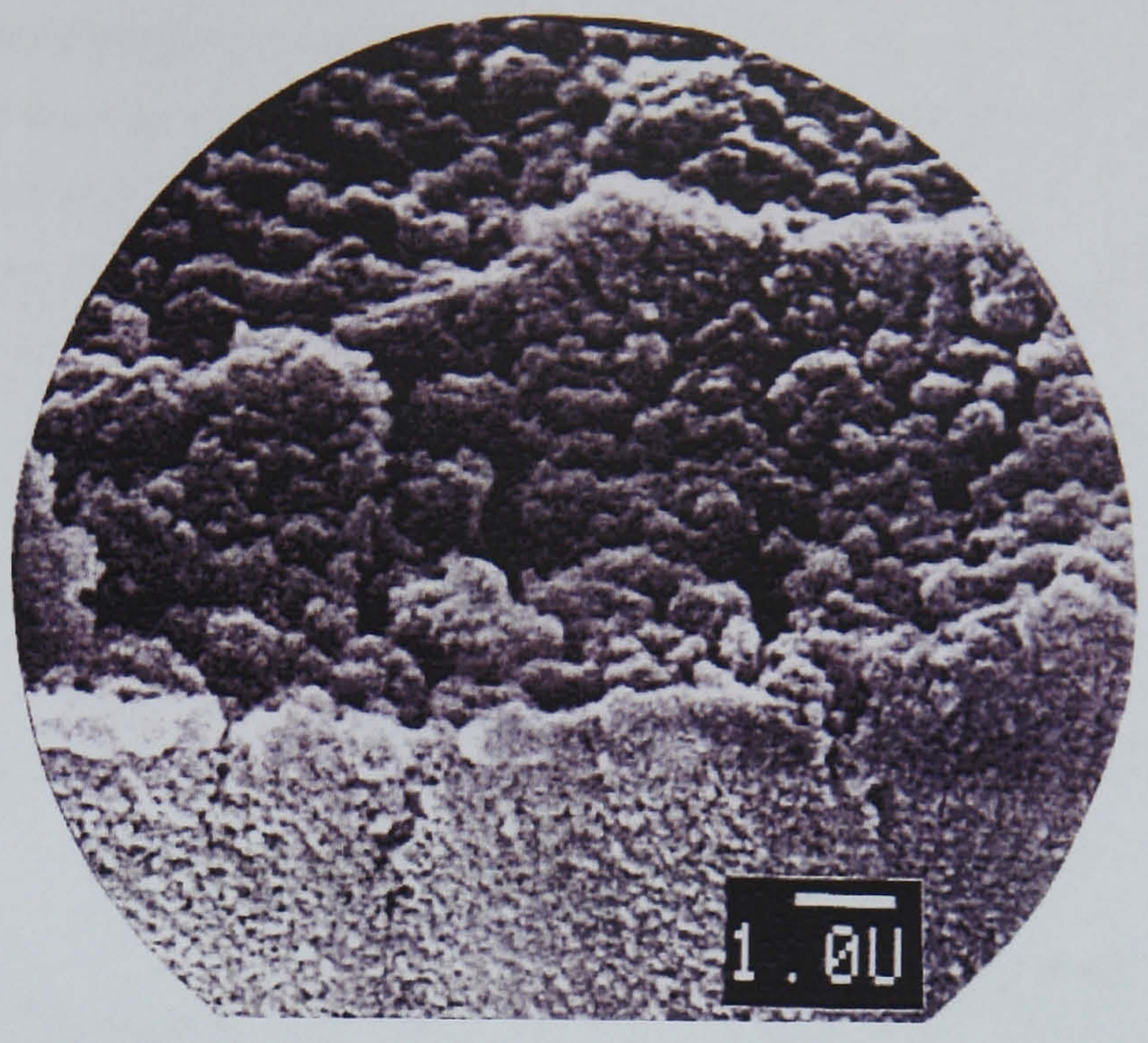


Figure 2-18: an individual corrosion layer of a corroded 10th century Carolingian glass[93]. The upper surface has a granular appearance

2.7.3.3 Burial experiments

First burial experiments have shown that laminated structures, as found on excavated glasses, can be simulated on model glasses by exposure to soil[106]. Cooper and Cox[104] found that above 85°C multi-layered crusts composed principally of clay minerals formed in water on KLS glasses. Their corrosion rate however was orders of magnitude greater than was observed on naturally corroded specimens.

Compositions of simulated high-level waste (HLW) form glasses have been the subject of numerous burial experiments, lasting typically up to five years. Wicks[90] summarised the altered regions in terms of precipitation and reaction zones that formed on a range of buried glasses, detected as the result of solution analyses and surface studies of buried waste glasses. A schematic representation of his observations is given in Figure 2-19. The zones are defined as follows:

- α_0 – *outermost precipitated salt layer*. Both amorphous and highly crystalline phases including chlorides, sulphates and silicates precipitate on the surface, largely from the surrounding solution rather than as result of leaching.
- α_1 – *precipitated glass layer*. Leaching of constituents from the glass leads to precipitation of silicate compounds from solution adjacent to the surface, which can act as a barrier against further water penetration and ion exchange. The layer is enriched in network formers and intermediates and possibly Ca.

- β_0 – *major depletion zone*. The region is significantly depleted in most constituents and is where the original glass surface (the a/b boundary) is located. In the case of glass compositions considered to be relatively unstable, this region is the result of dissolution and subsequent recondensation or reprecipitation of silicate compounds as the main reaction front moves deeper into the glass.
- β_1 – *gradient zone*. This region is where the main reaction front is located and is characterised by leaching gradients of alkaline components.
- β_2 – *diffusion zone*. This innermost leached glass layer defines the extent of water penetration into the glass ahead of the main dissolution reaction and is characterised by a concentration gradient of the most mobile alkaline components (Li, K or Na).

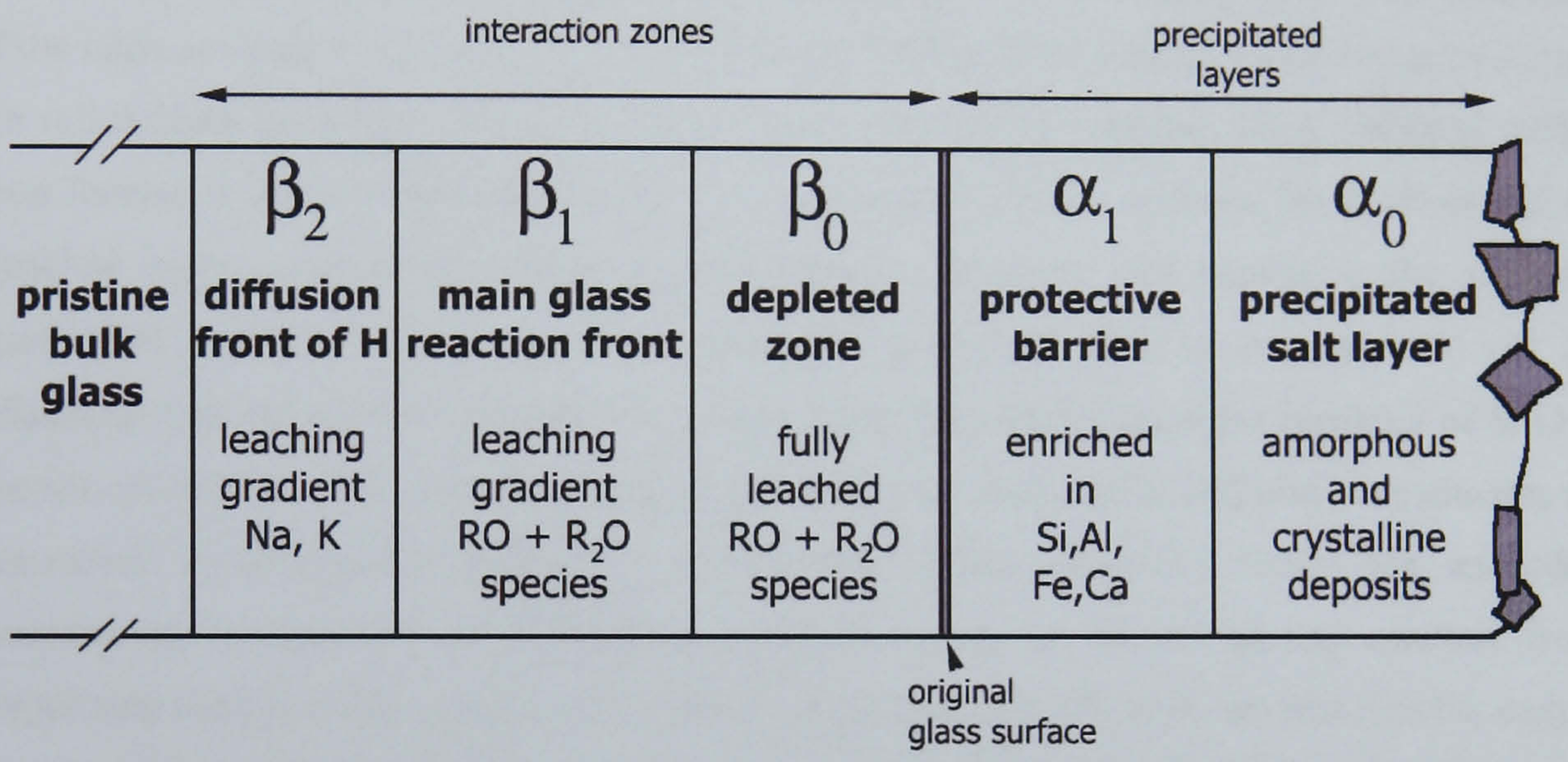


Figure 2-19: schematic diagram from Wicks[90] showing the main structural features of the altered layers found on buried glasses.

2.7.3.4 Theories of layer formation

In 1961 Brill and Hood[107] observed that in many cases the number of layers that had formed in the crust corresponded very closely to the years of burial and suggested that the formation process was a result of cyclic annual variation in humidity. They also proposed that glasses could be dated by counting the layers. Subsequent observations by Newton[97, 108] queried their hypothesis as he observed that the irregularity of layer formation often made counting very difficult. A number of authors pointed out a variety of inconsistencies in the growth of weathering layers [97, 103, 108-112], caused mainly by infiltration of manganese-rich compounds and several types of irregularities in the glass structure. Moreover, ancient glasses recovered from the seabed also exhibited a regular lamellar crust and thus in 1989 Cox and Ford[113] dismissed the idea that annual cycles were responsible for layer formation and suggested that the corrosion

process was of a geochemical nature, regulated by internal concentration gradients within the leached layer.

Another theory reported by Newton[79] suggested that the layers could be the result of mechanical deformation upon drying when samples were removed from their burial environments. Single layers would peel away as compressive stresses induced by alkali removal in the hydrated glass overcame the Young's modulus of the glass. This is highly unlikely however; the geochemical nature of glass corrosion suggests a very slow formation rate and the porous nature of the crust points to a redeposition process.

The reaction with groundwater is currently thought to involve mechanisms of ion exchange, congruent dissolution and precipitation/ recondensation[32, 80, 104]. Although shallow groundwater flow rates are highly variable and very difficult to estimate, the flow of water around a sample in soil is likely to be very low, except after heavy rain. Once a hydrated, alkali deficient surface has formed, a second stage, controlled by an interface reaction, reduces the thickness of the leached layer, thereby increasing the concentration gradient and regulating the diffusion controlled reaction. Under near static conditions a pH >7 is to be expected. At pH ≥ 9 dissolution of the glass forming network takes place, consequent upon the breaking of Si-O-Si bonds; congruent breakdown of the glass then ensues as alkali, silica and other constituents are extracted simultaneously (congruent dissolution). When solubility limits are exceeded, subsequent precipitation of dissolution products occurs at the advancing reaction front, regulating the pH of the attacking solution. Precipitation depends upon several factors, such as the extraction rate and solubility of the constituent oxides (especially SiO_2 and Al_2O_3) in the leachant.

Cyclic reaction conditions must be met in order for lamellar corrosion phenomena typical of buried glasses to occur. As the corrosion process involves dissolution and precipitation, a recurring balance needs to be established between the two processes. The conditions for lamellar crust formation in archaeological glasses are however not entirely clear in the literature, due to the number of variables involved and the sub-micron scale of the reaction front. Römich and Lopez[106] have recently advocated the closer determination of the structure of the alteration zone as a way of further understanding the long-term degradation effects of buried glasses. The characterisation of the reaction front of corroded archaeological glasses in the present study (in Section 9.7) has been conducted with this prompt in mind.

2.8 Bibliography

1. Rehren, T., *Rationales in Old World Base Glass Compositions.* Journal of Archaeological Science, 2000. **27**: p. 1225-1234.

2. Rehren, T., *New Aspects of Ancient Egyptian Glassmaking.* Journal of Glass Studies, 2000. **42**: p. 13-24.

3. Whan, R.E., *Materials Characterisation*, in *Metals Handbook.* 1990, American Society for Metals: Ohio. p. 5.

4. Caley, E.R., *Analysis of Ancient Glasses 1790-1957.* 1962, New York: The Corning Museum of Glass.

5. Henderson, J., *The Scientific Analysis of Ancient Glass and Its Archaeological Interpretation*, in *Scientific Analysis in Archaeology*, J. Henderson, Editor. 1989, Oxbow Books: Oxford. p. 30-62.

6. Verità, M., et al., *X-Ray Microanalysis of Ancient Glassy Materials: A Comparative Study of Wavelength Dispersive and Energy Dispersive Techniques.* Archaeometry, 1994. **36**(2): p. 241-251.

7. Hatcher, H., M.S. Tite, and J.N. Walsh, *A Comparison of Inductively-Coupled Plasma Emission Spectrometry and Atomic Absorption Spectrometry Analysis on Standard Reference Silicate Materials and Ceramics.* Archaeometry, 1995. **37**(1): p. 83-94.

8. Kuisma-Kursula, P., *Accuracy, Precision and Detection Limits of SEM-WDS, SEM-EDS and PIXE in the Multi-Elemental Analysis of Medieval Glass.* X-Ray Spectrometry, 2000. **29**: p. 111-118.

9. Aerts, A., et al., *Trace-Level Microanalysis of Roman Glass from Khirbet Qumrân, Israel.* Journal of Archaeological Science, 1999. **26**: p. 883-891.

10. Gratuze, B., *Obsidian Characterisation by Laser Ablation ICP-MS and Its Application to Prehistoric Trade in the Mediterranean and the Near East: Sources and Distribution of Obsidian within the Aegean and Anatolia.* Journal of Archaeological Sciences, 1999. **26**: p. 869-881.

11. Brill, R.H., *Chemical Analyses of Early Glasses*. Vol. I & II. 1999, Corning NY: Corning Museum of Glass.

12. Wicks, G.G., *US Field Testing Programs and Results.* Journal of Nuclear Materials, 2001. **298**: p. 78-85.

13. Jones, G.O., *Glass*. 1956, London: Methuen.

14. Doremus, R.H., *Glass Science*. 2nd ed. 1994, New York: John Wiley & Sons Inc. 215-240.

15. Gilliam, T.M. and C.M. Jantzen, *Waste Vitrification: Prediction of Acceptable Compositions in a Lime-Soda-Silica Glass-Forming System.* Materials Research Society Symposium Proceedings, 1997. **465**(Scientific Basis for Nuclear Waste Management XX): p. 87-93.

16. Volf, M.B., *Chemical Approach to Glass*. Glass Science and Technology. Vol. 7. 1984, Amsterdam: Elsevier Science Publishers.

17. Brill, R.H., *A Note on the Scientist's Definition of Glass.* Journal of Glass Studies, 1962. **4**: p. 127-138.

18. Greaves, G.N., et al., *A Structural Basis for Ionic Diffusion in Oxide Glasses.* Philosophical Magazine A, 1991. **64**(5): p. 1059-1072.

19. Henderson, J., *The Raw Materials of Early Glass Production.* Oxford Journal of Archaeology, 1985. **4**(3): p. 267-291.

20. Brill, R.H. *Some Chemical Observations on the Cuneiform Glassmaking Texts*. in *5th Congress AIHV*. 1970. Prague. p. 329-335.

21. Brill, R.H., *The Chemical Interpretation of the Texts*, in *Glass and Glassmaking in Ancient Mesopotamia*, A.L. Oppenheim, Editor. 1970, Corning Museum of Glass: New York. p. 105-128.

22. Jackson, C.M., et al. *Biringuccio on 16th Century Glassmaking*. in *13th Congress AIHV*. 1998. Venice. p. 335-340.

23. Freestone, I.C., *Theophilus and the Composition of Medieval Glass.* Materials Research Society Symposium Proceedings, 1992. **267**: p. 739-745.

24. Jackson, C.M., *A Compositional Analysis of Roman and Early Post-Roman Glass and Glassworking Waste From Selected British Sites*. PhD Thesis, 1992, Department of Archaeological Sciences,University of Bradford. p. 450.

25. Brill, R.H., *Scientific Investigations of the Jalame Glass and Related Finds*, in *Excavations at Jalame, Site of a Glass Factory in Late Roman Palestine*, G.D. Weinberg, Editor. 1988, University of Missouri Press. p. 257-294.

26. Turner, W.E.S., *Studies in Ancient Glasses and Glassmaking Processes. Part III. The Chronology of the Glassmaking Constituents.* Journal of the Society of Glass Technology, 1956. **40**: p. 39-52.

27. Smedley, J.W. and C. Jackson, *Medieval and Post-Medieval Glass Technology: Batch Measuring Practices.* Glass Technology, 2002. **43**(1): p. 22-27.

28. Brill, R.H., *Chemical Analyses of Some Glasses From Frattesina.* Journal of Glass Studies, 1992. **34**: p. 11-22.

29. Turner, W.E.S., *Studies in Ancient Glasses and Glassmaking Processes. Part V. Raw Materials and Melting Processes.* Journal of the Society of Glass Technology, 1956. **40**: p. 277-300.

30. Bezborodov, M.A., *Chemie und Technologie der Antiken und Mittelalterlichen Gläser*. 1975, Mainz: Verlag Philipp Von Zabern.

31. Lilyquist, C. and R.H. Brill, *Studies in Early Egyptian Glass*. 1993, New York: Metropolitan Museum of Art.

32. Cox, G.A. and B.A. Ford, *The Long-Term Corrosion of Glass by Groundwater.* Journal of Materials Science, 1993. **28**: p. 5637-5647.

33. Sayre, E.V. and R.W. Smith, *Compositional Categories of Ancient Glass.* Science, 1961. **133**: p. 1824-1826.

34. Wedepohl, K.H., *Chemical Composition of Medieval Glass from Excavations in West Germany.* Glastechnische Berichte Glass Science and Technology, 1997. **70**(8): p. 246-255.

35. Brill, R.H., *Scientific Investigations of the Jalame Glass and Related Finds*, in *Excavations at Jalame, Site of a Glass Factory in Late Roman Palestine*, G.D. Weinberg, Editor. 1998, University of Missouri Press. p. 257-294.

36. Freestone, I.C., M. Bimson, and D. Buckton. *Compositional Categories of Byzantine Glass Tesserae.* in *11th Congress AIHV.* 1988. Basel: Amsterdam AIHV Press. p. 271-279.

37. Moorey, P.R.S., *Ancient Mesopotamian Materials and Industries. The Archaeological Evidence*. 1994, Oxford: Clarendon Press.

38. Sayre, E.V. *Summary of the Brookhaven Program of Analysis of Ancient Glass*. in *Applications of Science in Examination of Works of Art*. 1965. Boston Museum of Fine Arts. p. 145-154.

39. Gratuze, B. and J.-N. Barrandon, *Islamic Glass Weights and Stamps: Analysis Using Nuclear Techniques.* Archaeometry, 1990. **32**(2): p. 155-162.

40. Henderson, J. *Glass Production in Raqqa, Syria: New Evidence for an Interim Assessment*. in *13th AIHV Congress*. 1995. Netherlands. p. 257-268.

41. Henderson, J., *Archaeological and Scientific Evidence for the Production of Early Islamic Glass in al-Raqqa, Syria.* Levant, 1999. **31**: p. 225-240.

42. Henderson, J., *Localised Production or Trade? Advances in the Study of Cobalt Blue and Islamic Glasses in the Levant and Europe*, in *Patterns and Process: A Festschrift in Honour of Edward V. Sayre*, L. van Zelst, Editor. 2003, Smithsonian Center for Materials Research and Education. p. 227-243.

43. Freestone, I.C., Y. Gorin-Rosen, and M.J. Hughes, *Primary Glass from Israel and the Production of Glass in Late Antiquity and the Early Islamic Period*, in *La Route du Verre: Ateliers Primaires et Secondaires du Second Millénaire av. J.-C. au Moyen Âge*, M.-D. Nenna, Editor. 2000, Maison de l'Orient Méditerranéen: Lyon. p. 65-85.

44. Freestone, I.C. and Y. Gorin-Rosen, *The Great Glass Slab at Bet She'arim, Israel: an Early Islamic Glassmaking Experiment?* Journal of Glass Studies, 1999. **41**: p. 105-116.

45. Brill, R.H., *Some Thoughts on the Chemistry and Technology of Islamic Glass*, in *Glass of the Sultans*, S. Carboni and D. Whitehouse, Editors. 2001, Metropolitan Museum of Art: New York. p. 25-45.

46. Brill, R.H., *Chemical Analyses of Some Glass Fragments from Nishapur in the Corning Museum of Glass*, in *Nishapur: Glass of the Early Islamic Period*, J. Kröger, Editor. 1995, Metropolitan Museum of Art: New York. p. 211-233.

47. Wedepohl, K.H. *The Change in Composition of Medieval Glass Types Occurring in Excavated Fragments from Germany*. in *13th Congress AIHV*. 1998. Venice. p. 253-257.

48. Jackson, C.M. *From Roman to Early Medieval Glasses: Many Happy Returns or a New Birth?* in *13th AIHV Congress*. 1995. Netherlands: Amsterdam AIHV Press. p. 289-301.

49. Henderson, J., *An Investigation of Early Islamic Glass Production at Raqqa, Syria.* Materials Research Society Symposium Proceedings, 1995. **352**(Materials Issues in Art and Archaeology IV): p. 433-444.

50. Nenna, M.-D., *Ateliers Primaires et Secondaires en Égypte*, in *La Route du Verre: Ateliers Primaires et Secondaires du Second Millénaire av. J.-C. au Moyen Âge*, M.-D. Nenna, Editor. 2000, Maison de l'Orient Méditerranéen: Lyon. p. 97-112.

51. Gorin-Rosen, Y., *The Ancient Glass Industry in Israel*, in *La Route du Verre: Ateliers Primaires et Secondaires du Second Millénaire av. J.-C. au Moyen Âge*, M.-D. Nenna, Editor. 2000, Maison de l'Orient Méditerranéen: Lyon. p. 49-63.

52. Aldsworth, F., et al., *Medieval Glassmaking at Tyre, Lebanon.* Journal of Glass Studies, 2002. **44**: p. 49-66.

53. Saleh, S.A., A.W. George, and F.M. Helmi, *Study of Glass and Glass-Making Processes at Wadi El-Natrun, Egypt in the Roman Period 30 B.C. to to 359 A.D.* Studies in Conservation, 1972. **17**: p. 143-172.

54. Brill, R.H., *A Great Glass Slab From Ancient Galilee.* Archaeology, 1967. **20**(2): p. 88-95.

55. Hlavác, J., *The Technology of Glass and Ceramics: An Introduction*. Glass Science and Technology. Vol. 4. 1983, Amsterdam: Elsevier Scientific Publishing Company.

56. Brill, R.H., *Ancient Glass*. Scientific American, 1963(Nov.): p. 120-130.

57. Jackson, C.M., P.T. Nicholson, and W. Gneisinger, *Glassmaking at Tell el-Amarna: an Integrated Approach.* Journal of Glass Studies, 1998. **40**: p. 11-23.

58. Henderson, J., *The Science and Archaeology of Materials*. 2000, London: Routledge.

59. Hofmaier, G. and G. Urbain, in *Science of Ceramics*. 1968, British Ceramics Society. p. 25.

60. Owens-Illinois Glass Composition Research Laboratories, *The Effect of Substituting MgO for CaO on Properties of Typical Soda-Lime Glasses.* Journal of the British Ceramic Society, 1944. **27**(8): p. 221-225.

61. Dall'Igna, R., et al., *Influence of Chemical Composition on Viscosity: Theoretical Formulations, Measuring Methods and Correlations Obtained From a Wide Database.* Rivista della Stazione Sperimentale del Vetro, 2002. **32**(4): p. 7-26.

62. Lakatos, T., L.-G. Johannson, and B. Simmingsköld, *The Effect of Some Glass Components on the Viscosity of Glass.* Glasteknisk Tidskrift, 1972. **27**(2): p. 25-28.

63. Lakatos, T., L.-G. Johannson, and B. Simmingsköld, *Viscosity Temperature Relations in the Glass System SiO_2-Al_2O_3-Na_2O-K_2O-CaO-MgO in the Composition Range of Technical Glasses.* Glass Technology, 1972. **13**(3): p. 88-95.

64. ibid.: p. 90.

65. Urbain, G., *Viscosity of Silicate Melts.* Journal of the British Ceramic Society, 1981. **80**: p. 139-147.

66. Kalmanovitch, D.P. and M. Frank, *An Effective Model of Viscosity for Ash Deposition Phenomena*, in *Mineral Matter and Ash Deposition*, R.W. Bryers and K.S. Vorres, Editors. 1990. p. 89-101.

67. Kingery, W.D., H.K. Bowen, and D.R. Uhlmann, *Introduction to Ceramics*. 2nd ed. 1976: John Wiley & Sons.

68. Pye, L.D., W.C. LaCourse, and H.J. Stevens, *The Physics of Crystalline Solids*. 1992, London: Taylor & Francis.

69. Gránásy, L. and P.F. James, *Non-Classical Theory of Crystal Nucleation: Application to Oxide Glasses: Review.* Journal of Non-Crystalline Solids, 1999. **253**: p. 210-230.

70. Gránásy, L., T. Wange, and P.F. James, *Kinetics of Wollastonite Nucleation in $CaO.SiO_2$ Glasses.* Journal of Chemical Physics, 1998. **108**(17): p. 7317-7326.

71. Jackson, K.A., *Nature of Solid-Liquid Interfaces*, in *Growth and Perfection of Crystals*, R.H. Doremus, B.W. Roberts, and D. Turnbull, Editors. 1958, Wiley: New York. p. 319.

72. Jackson, K.A., *On the Theory of Crystal Growth: Growth of Small Crystals Using Periodic Boundary Conditions.* Journal of Crystal Growth, 1958. **3-4**: p. 507.

73. Uhlmann, D.R., *Crystal Growth in Glass-Forming Systems: a Ten Year Perspective*, in *Nucleation and Crystallisation in Glasses*, J.H. Simmons, D.R. Uhlmann, and G.H. Beall, Editors. 1982, The American Ceramics Society: Columbus, Ohio. p. 80-124.

74. Guillemet, C. and J. Denoncin, *Kinetics of the Precipitation of Wollastonite in Industrial Soda-Lime-Silica Glasses*, in *Nucleation and Crystallization in Glasses*, J.H. Simmons, D.R. Uhlmann, and G.H. Beall, Editors. 1982, The American Ceramics Society, Inc.: Columbus, Ohio. p. 193-203.

75. Newton, R.G. and S. Davison, *Conservation of Glass*. 1989, London: Butterworth-Heinemann. p. 155.

76. Isard, J.O. and A.R. Patel, *A Comparison Between Weathering and Water Leaching Tests on Glasses of Simple Composition.* Glass Technology, 1981. **22**(6): p. 247-250.

77. Bange, K., et al., *Multi-Method Characterization of Soda-Lime Glass Corrosion Part 1. Analysis Techniques and Corrosion in Liquid Water. Report of the International Commission on Glass (ICG), Subcommittee of Technical Committee 19 "Glass Surface Diagnostics".* Glastechnische Berichte Glass Science and Technology, 2001. **74**(5): p. 127-141.

78. Bange, K., et al., *Multi-Method Characterization of Soda-Lime Glass Corrosion Part 2. Corrosion in Humidity. Report of the International Commission on Glass (ICG), Subcommittee of Technical Committee 19 "Glass Surface Diagnostics".* Glastechnische Berichte Glass Science and Technology, 2002. **75**(1): p. 20-33.

79. Newton, R.G., *The Durability of Glass - A Review.* Glass Technology, 1985. **26**(1): p. 21-38.

80. Cox, G.A. and G.I. Cooper, *Stained Glass in York in the Mid-Sixteenth Century: Analytical Evidence for its Decay.* Glass Technology, 1995. **36**(4): p. 129-134.

81. Ryan, J., *The Atmospheric Deterioration of Glass*. PhD Thesis, 1996, Materials Department, Imperial College: London. p. 251.

82. Rogers, P., D.S. McPhail, and J. Ryan, *A Quantitative Study of Decay Processes of Venetian Glass in a Museum Environment.* Glass Technology, 1993. **34**(2): p. 67-68.

83. Ryan, J., et al., *Glass Deterioration in the Museum Environment: A Study of the Mechanisms of Decay Using Secondary Ion Mass Spectrometry.* ICOM Committee for Conservation, 1996. **Vol. II**(11th Triennial Meeting of ICOM): p. 839-844.

84. El-Shamy, T.M., J. Lewins, and R.W. Douglas, *The Dependence on the pH of the Decomposition of Glasses by Aqueous Solution.* Glass Technology, 1972. **13**(3): p. 81-87.

85. Charles, R.J., *The Static Fatigue of Glass.* Journal of Applied Physics, 1958. **29**(1): p. 1549-1553.

86. Paul, A., *Chemical Durability of Glasses: a Thermodynamic Approach.* Journal of Materials Science, 1977. **12**: p. 2246-2268.

87. Jantzen, C.M., *Thermodynamic Approach to Glass Corrosion*, in *Corrosion of Glass, Ceramics and Ceramic Superconductors*, D.E. Clark and B.K. Zoitos, Editors. 1992, Noyes Publications: New Jersey. p. 153-217.

88. Jantzen, C.M. and M.J. Plodinec, *Thermodynamic Model of Natural, Medieval and Nuclear Waste Glass Durability.* Journal of Non-Crystalline Solids, 1984. **67**: p. 207-223.

89. Conradt, R., *A Proposition for an Improved Theoretical Treatment of the Corrosion of Multi-Component Glasses.* Journal of Nuclear Materials, 2001. **298**: p. 19-26.

90. Wicks, G.G., *Nuclear Waste Glasses: Corrosion Behaviour and Field Tests*, in *Corrosion of Glasses, Ceramics and Ceramic Superconductors*, D.E. Clark and B.K. Zoitos, Editors. 1992, Noyes Publications: New Jersey. p. 218-268.

91. Jégou, C., S. Gin, and F. Larché, *Alteration Kinetics of a Simplified Nuclear Glass in an Aqueous Medium: Effects of Solution Chemistry and of Protective Gel Properties on Diminishing the Alteration Rate.* Journal of Nuclear Materials, 2000. **280**: p. 216-229.

92. Grambow, B. and R. Müller, *First-Order Dissolution Rate Law and the Role of Surface Layers in Glass Performance Assessment.* Journal of Nuclear Materials, 2001. **298**: p. 112-124.

93. Macquet, C. and J.H. Thomassin, *Archaeological Glasses as Modelling of the Behaviour of Buried Nuclear Waste Glasses.* Applied Clay Science, 1992. **7**: p. 17-31.

94. Sterpenich, J. and G. Libourel, *Using Stained Glass Windows to Understand the Durability of Toxic Waste Matrices.* Chemical Geology, 2001. **174**: p. 181-193.

95. Sterpenich, J. and G. Libourel, *Crystal-Chemistry of Alteration Products of Medieval Stained-Glasses.* Mineralogical Magazine, 1998. **62A**(Pt. 3): p. 1456-1457.

96. Lopez, E., et al. *Special Corrosion Phenomena on Glass Objects*. in *Hyalos Vitrum Glass: History, Technology and Conservation of Glass and Vitreous Materials in the Hellenic World*. 2002. Athens: Glasnet Publications. p. 251-255.

97. Newton, R.G., *The Enigma of the Layered Crusts on Some Weathered Glasses. A Chronological Account of the Investigations.* Archaeometry, 1971. **13**(1): p. 1-9.

98. Brewster, D., *On the Structure and Optical Phenomena of Ancient Decomposed Glass.* Transactions of the Royal Society of Edinburgh, 1863. **23**: p. 193-204.

99. Raw, F., *The Long-Continued Action of Water on Window Glass: Weathering of the Medieval Glass at Weoley Castle, Birmingham.* Journal of the Society of Glass Technology, 1955. **39**: p. 128T-133T.

100. Geilmann, W., *Beiträge zur Kenntnis Alter Gläser iv. Die Zersetzung der Gläser im Boden.* Glastechnische Berichte, 1956. **29**: p. 145-168.

101. Newton, R.G. and S. Davison, *Conservation of glass*. 1989, London: Butterworth-Heinemann.

102. Gillies, K.J.S. and A. Cox, *Decay of Medieval Stained Glass at York, Canterbury and Carlisle. Part 2. Relationship Between the Composition of the Glass, its Durability and the Weathering Products.* Glastechnische Berichte, 1988. **61**(4): p. 101-107.

103. Newton, R.G., *Stereoscan Views of Weathering Layers on a Piece of Ancient Glass.* Glass Technology, 1972. **13**(2): p. 54-56.

104. Cooper, G.I. and G.A. Cox, *A Comparative Study of the Natural and Experimental Corrosion of Poorly Durable Potash-Lime-Silica Glasses.* Materials Research Society Symposium Proceedings, 1994. **333**: p. 525-531.

105. El-Shamy, T.M., *The Chemical Durability of K_2O-CaO-MgO-SiO_2 Glasses.* Physics and Chemistry of Glasses, 1973. **14**: p. 1-5.

106. Römich, H. and E. Lopez. *Research on Corrosion Phenomena of Archaeological Glasses*. in *Hyalos Vitrum Glass: History, Technology and Conservation of Glass and Vitreous Materials in the Hellenic World*. 2002. Athens: Glasnet Publications. p. 241-247.

107. Brill, R.H. and H.P. Hood, *A New Method for Dating Ancient Glass.* Nature, 1961. **189**: p. 12-14.

108. Newton, R.G., *Some Problems in the Dating of Ancient Glass by Counting the Layers in the Weathering Crust.* Glass Technology, 1966. **7**(1): p. 22-25.

109. Newton, R.G., *Some Further Observations on the Weathering Crusts of Ancient Glass.* Glass Technology, 1969. **10**(2): p. 40-56.

110. Newton, R.G. and G. Shaw, *Another Unsolved Problem Concerning Weathering Layers.* Glass Technology, 1988. **29**(2): p. 78-79.

111. Cox, G.A. and B.A. Ford, *The Influence of Inhomogeneities in Glass on the Morphology of the Weathering Layers.* Glass Technology, 1989. **30**(3): p. 113-114.

112. Cox, G.A. and A.-R. Khooli, *The Natural Corrosion of Glass: The Formation and Structure of Plugs.* Glass Technology, 1992. **33**(2): p. 60-62.

113. Cox, G.A. and B.A. Ford, *The Corrosion of Glass on the Sea Bed.* Journal of Materials Science, 1989. **24**: p. 3146-3153.

Chapter 3

Excavations and samples

This chapter will focus on the archaeological site of Raqqa, on the excavations conducted there and on the materials that were considered for analysis. Additional samples from a glass burial experiment in Ballidon will also be briefly outlined.

3.1 Raqqa: a historical introduction

The town of Raqqa (also known as Ar-Raqqah or Al-Raqqa) is situated in the Euphrates valley in northern Syria (Figure 3-1). The modern town has developed and expanded considerably within the last fifty years, due to stable economic conditions in Syria coupled with explosive demographic growth[1]. The original settlement dates back to Hellenistic times, more specifically to the 3rd century BC. Raqqa was a centre of industrial production between the late 8th and 13th centuries AD, in Early and Middle Islamic times.



Figure 3-1: political map of the Middle East. Inset, on right, a more detailed map of Syria showing underlined in red the location of Raqqa (Al Raqqa or Ar Raqqah) on the Euphrates River.

By the beginning of the 8th century, within 100 years of its birth, Islam controlled an empire that stretched from the western boundaries of China to the western tip of North Africa and Spain[2]. Syria became the centre of a new world order, with Damascus as the Islamic capital under the rule of the Umayyad dynasty of caliphs. Continuing internal struggles between different sects of Islam caused the collapse of the Umayyad dynasty in the mid-8th century in favour of the 'Abbasid dynasty, which moved the capital from Damascus to Baghdad. Al-Raqqa came to prominence as the residence of the 'Abbasid caliph Harun al-Rashid and was the centre of his area of influence between AD 796 and 808, after which he moved back to Baghdad. During this period a new walled city al-Rafika ("the companion") was built next to al-Raqqa, together with a complex of palaces and a substantial industrial area

3.2 Archaeological investigations at Raqqa

Excavations since 1982 have revealed the palace complexes at Raqqa and an industrial area consisting of a three-km strip of small tells, or artificial mounds, related to the manufacture of glass, glazes, ceramics and possibly metals[3]. A satellite image of Raqqa (Figure 3-2) shows the location of archaeological sites investigated. Since 1994 the Raqqa Ancient Industry Project has excavated the areas of glass production located at Tell Zujaj (Arabic for glass tell) of 8th-9th century date, Tell Fukhkhar (Arabic for pottery tell) of 11th century date and Tell Belor of 12th century date. A glass workshop was discovered at Tell Zujaj with the remains of two almost complete beehive-shaped three-chambered glass furnaces standing to 1.3m in height, plus the remains of two others. A furnace was located in each corner of the workshop. The workshop was sealed by a series of dumps that contained some 5 tons of tank furnace fragments, mainly of the broken floors, up to 1m in length, with raw green, purple, brown, blue and colourless glass colours adhering to them. The dumps of tank furnace fragments were contemporary with the workshop, suggesting strongly that both beehive and tank furnaces were in use at the same time[4]. Many large (up to 20cms in length) lumps of greyish glass frit were found in the dumps of material, showing that fritting also occurred in the same phase. Evidence for casting glass into blocks and the subsequent working of glass into finished vessels (moils, run-offs and dribbles of glass) was also found in the dumps. Archaeological dating of Tell Zujaj, partly based on deposits of coins and diagnostic pottery, suggests that the glass workshop and the dumping activities occurred within a short period of c. 30 years in the late 8th-early 9th centuries[5].

The evidence of the glass industry at Tell Fukhkhar, a site that dates to the 11th century, was far more limited[6]. It consisted of dumped tank furnace fragments with green raw glass attached and deposits of raw glass only. No furnaces or floors were discovered. The British Archaeological Mission to Raqqa 2000, at which I was present, focused on Tell Belor, where more large-scale dumping of tank furnaces was found. Large chunks of furnace floor up to

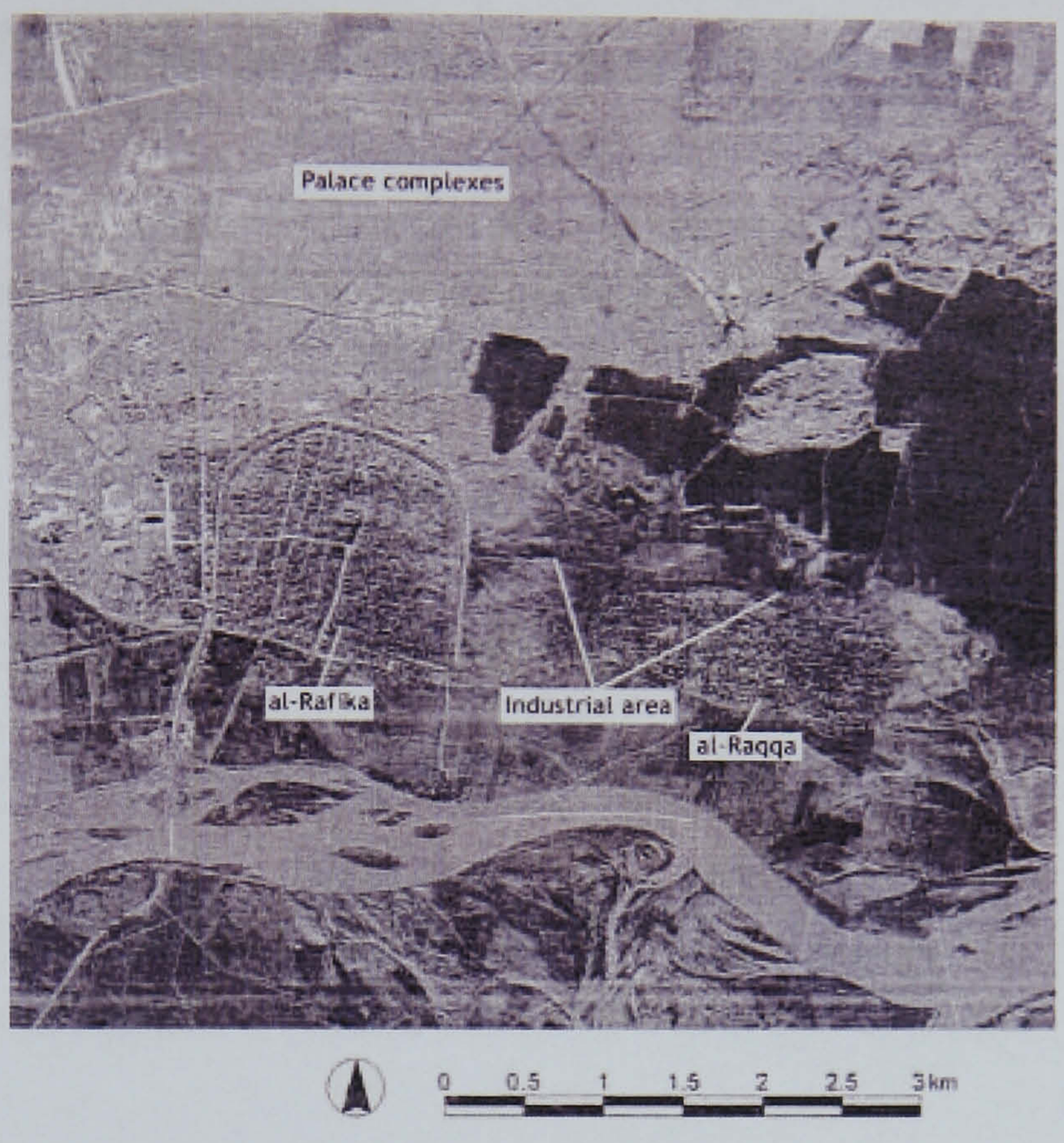


Figure 3-2: a Corona satellite photograph taken in 1967. It shows the environs of Raqqa, with the river Euphrates to the south; the characteristic horseshoe shaped walls of al-Rafika; al-Raqqa to the East; the industrial area extending from east to west north of al-Raqqa; and numerous Islamic industrial complexes to the north.

50cm in length were found, often with surfaces demarcated by the original position of bricks (Figure 3-3). Trickles of glass running in between bricks have formed channels beneath the floor that are visible in side view.



Figure 3-3: chunks up to 50cm in length of furnace base were found at Tell Belor. The flat upper surface (left) exhibits a thin vertical wall that marks the original position of refractory bricks. Glass trickles between the bricks have formed channels visible in side view (right).

3.3 Materials Sampled

Materials were sampled from all three sites at Raqqa. Internal political problems restricted the sample set that could be exported for analysis from Tell Belor. Glasses from Tell Zujaj and Tell Fukhkhar were made available for characterisation by Julian Henderson. A complete listing of analysed glasses from all three sites is given in Appendix 1.

3.3.1 Glass from Tell Zujaj (TZ) and Tell Fukhkhar (TF)

Production waste (moils, malformed pieces and raw chunks of glass adhering to furnace brick) from Tell Zujaj and Tell Fukhkhar was sampled for EPMA analysis along with bottles, goblets, jars, flasks, beakers, jug handles and a selection of vessel rim types. Tesserae and bracelets from Tell Fukhkhar were also selected for sampling. Window glass from Qasr al-Banât and from the 8th-9th century AD palace complexes was also sampled. A select group of samples was chosen for detailed corrosion studies once compositional analysis had been completed.

3.3.2 Glass from Tell Belor (TB)

In 2000 I selected glass from context 255, which was thought to be a glass dump as casting surfaces were found, along with cast and blown glass fragments and glassblowing scrap. From the evidence both casting and blowing were carried out together within the same phase or at least within a short distance of each other. Samples are listed below:

- TB2 – pale green/ purple glass attached to a limestone base
- TB5 – dark brown/ black glass attached to a limestone base
- TB6 – pale green glass attached to a limestone base
- TB7 – dark green glass attached to furnace fragment
- TB14 – green/purple glass attached to furnace floor.
- TB22a-k – 11 fragments of vessel glass were sampled from this context, nine pale green, one blue green and one dark green.

3.3.3 Furnace fragments and casting surfaces

Slabs of tank furnace wall and base of up to 50cm in length were found at Tell Belor. Three main types of industrial production debris were identified at Tell Belor and have been classed as types A to C.

A) Flat, cream or brown coloured slabs (Figure 3-4). They are thought to be casting surfaces (see below). The body is vitrified up to 1cm in thickness. The glass adhering to

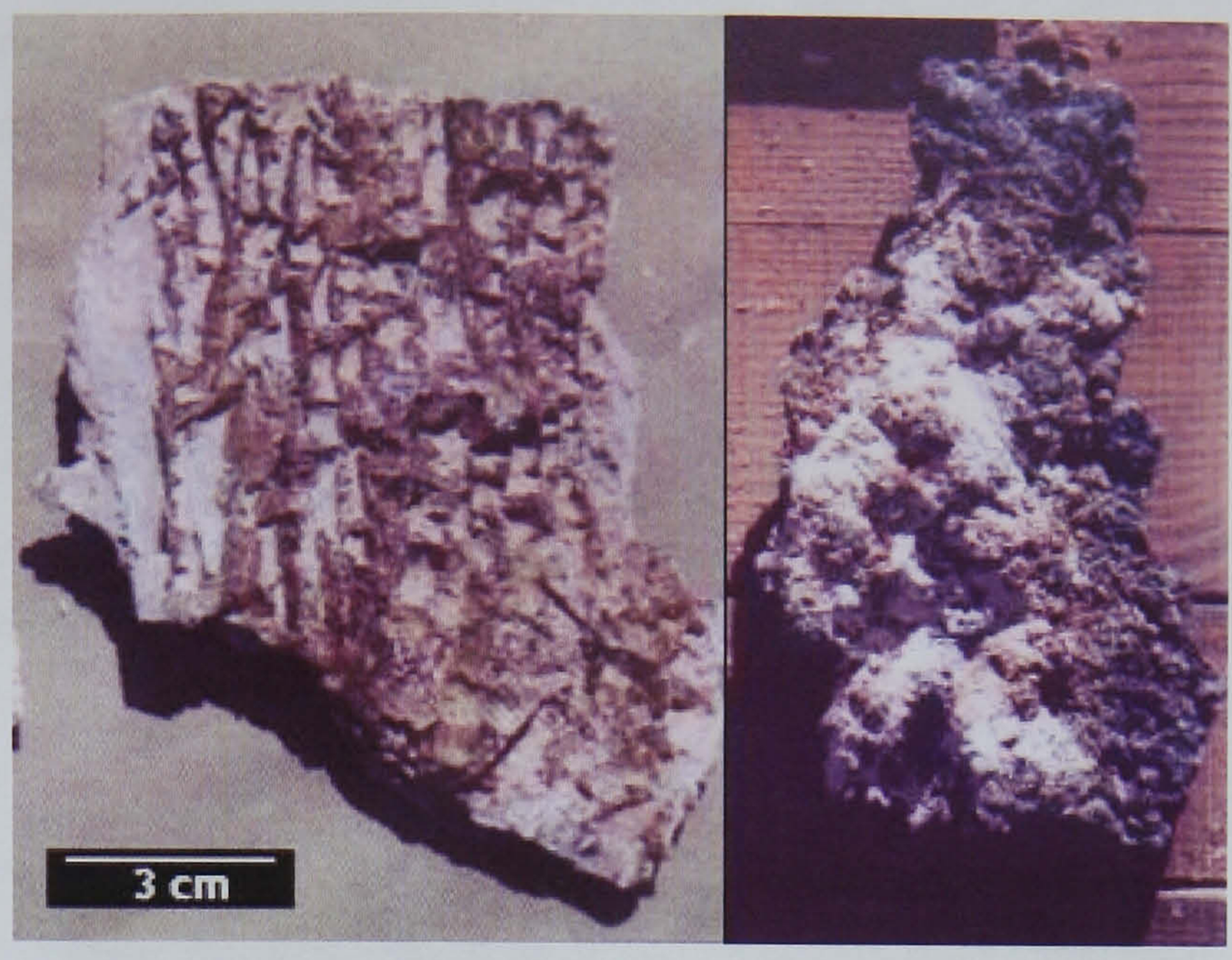


Figure 3-4: TB2, an example of type A production waste showing finely cracked, chiselled glass on upper surface (left) and limestone base (right).

the upper surface is pale green to purple-red in colour and is finely cracked in parallel lines along the surface. The undulating, bubbled pattern of vitrification on the calcined underside suggests it has been formed by heat contours. An example of a successful cast was found (TB9), supporting the hypothesis that these remains were originally casting surfaces. The upper surface is flat yet vitrified, and the extent of vitrification on the underside follows similar heat patterns. Samples of type A: TB2, TB5, TB6, TB9 (shown in Figures 3-4 and 3-5).

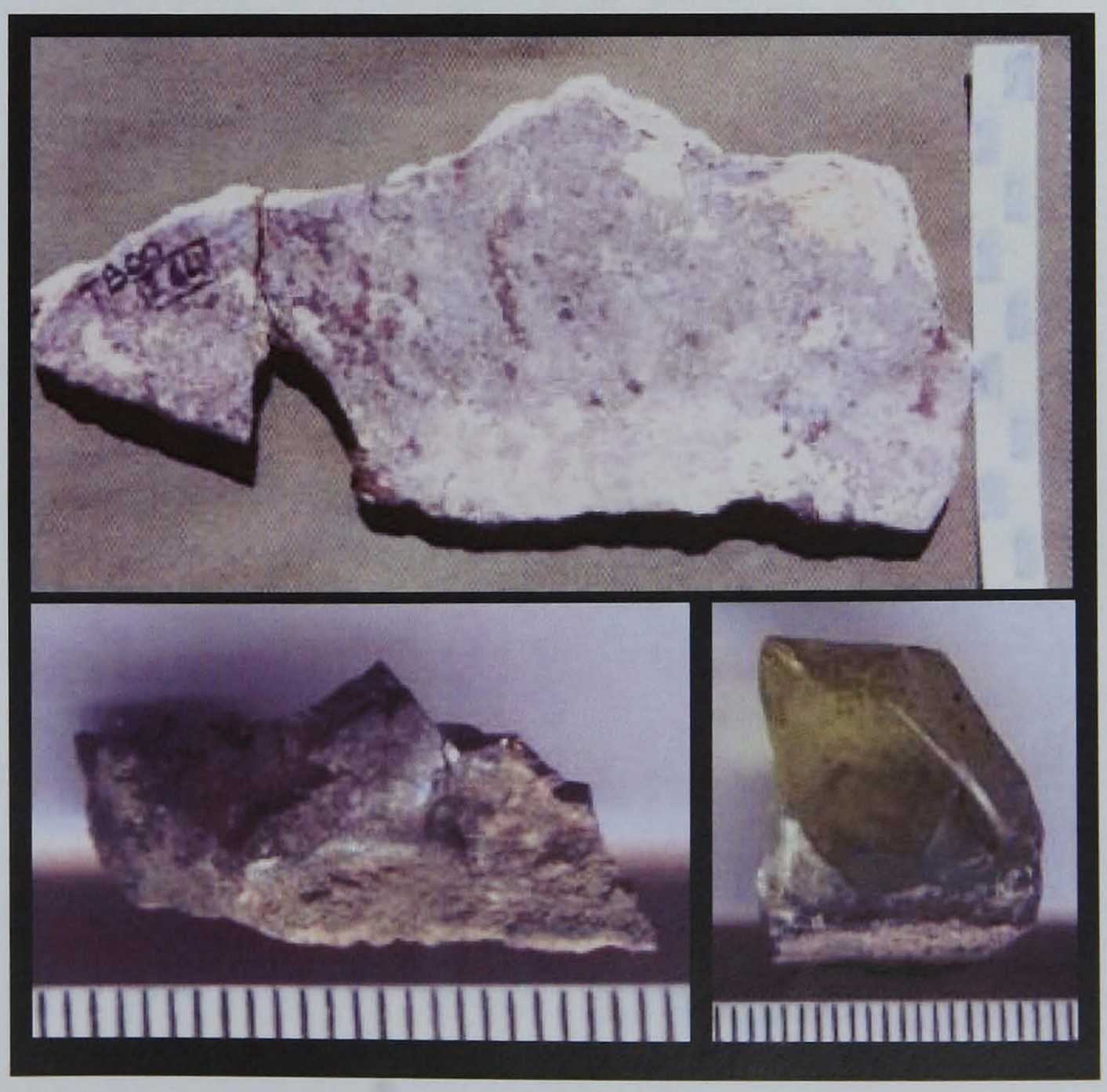


Figure 3-5: clockwise from top, samples TB9, TB6 and TB5 of production waste type A.

B) Large, sandy coloured chunks with glass adhering to the upper surface, thought to be remains of furnace floor (Figure 3-6). The pieces exhibit a thick zone of green vitrification, usually 2-4 cm in depth, demarcated at its lower extremity by a clear dark green line. Below this the substrate loses its green colour. The base of the pieces is of a burnt yellow clay consistency. Nearly all the adhering glass is bright green in colour. Chisel marks are clearly visible on the upper surface suggesting there were attempts, often successful, at removing the glass once it had cooled. Samples of type B: TB7, TB13, TB14 are shown in Figures 3-6 and 3-7).

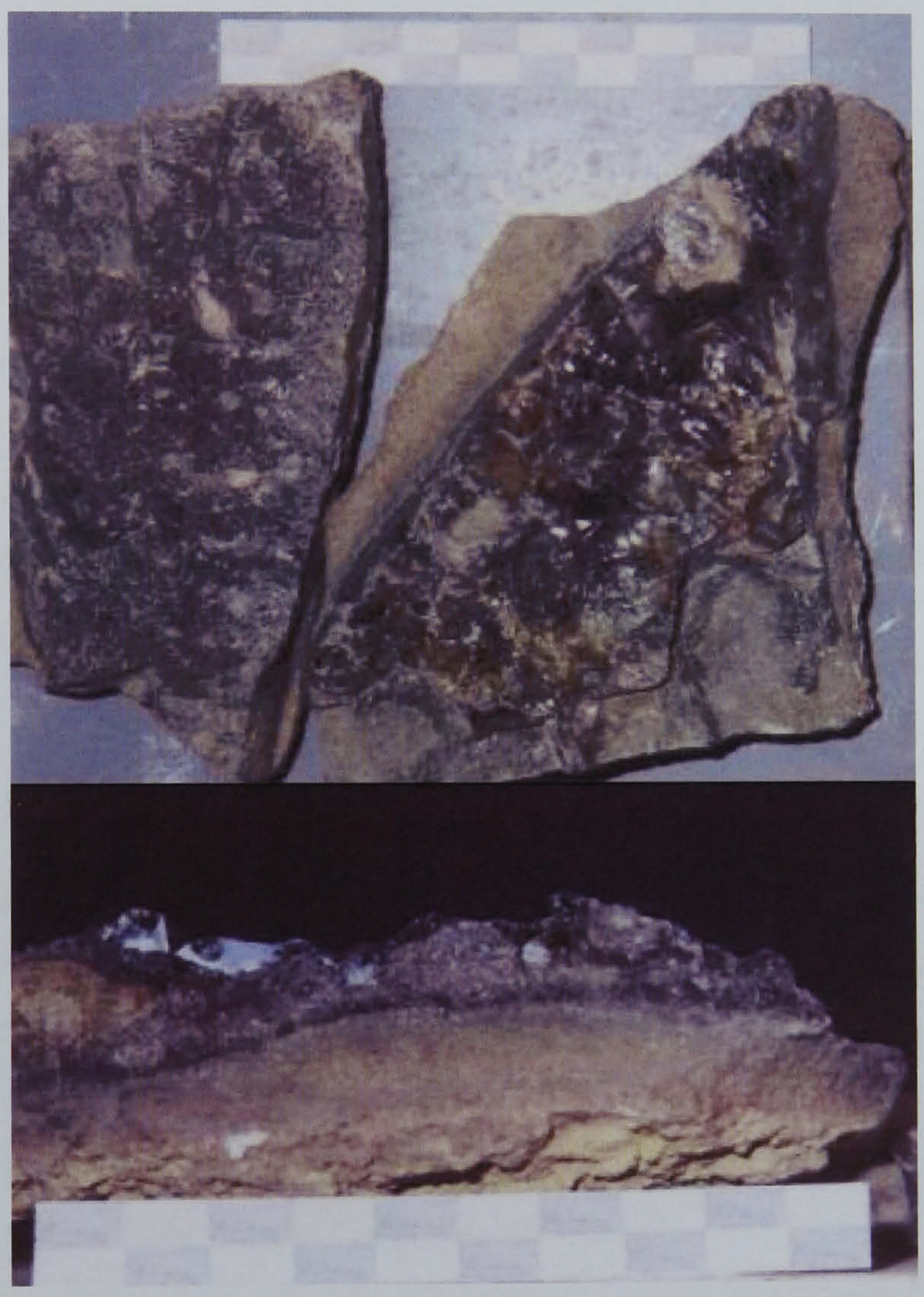


Figure 3-6: type B production waste consisting of furnace floor lumps that TB13 and TB14 were sampled from, viewed from above (top) and horizontally (bottom). A layer of dark green/ brown glass is still adhering to the upper surface. Chisel marks are visible, presumably as workers attempted to remove as much remaining glass as possible after cooling.

C) Yellow and green bricks approximately 4cm in thickness and of unspecified size (no complete bricks were found). The green brick is of a dense, heavy clay with white inclusions. The yellow brick is lighter. Samples of type C: TB19y (yellow), TB19g (green).

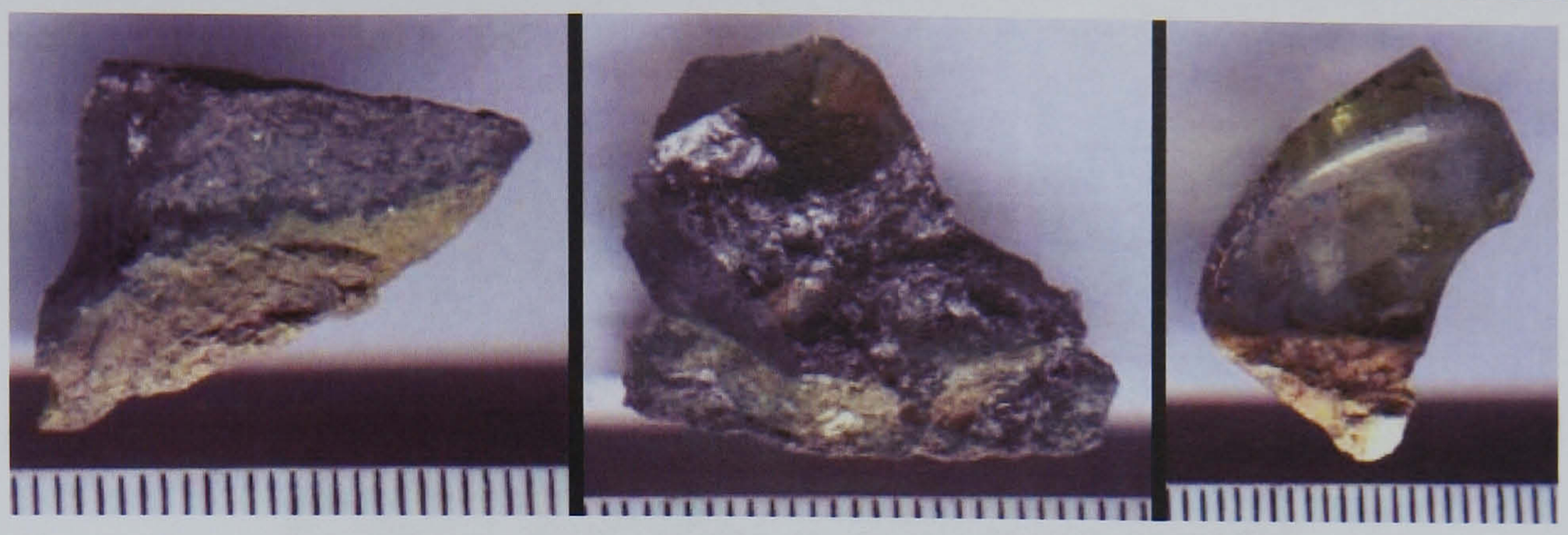


Figure 3-7: from left to right, samples TB13, TB14 and TB7 of production waste type B.

3.3.4 Raw materials

Pebbles of quartz were found amongst the furnace remains and embedded in incompletely fused glass fragments. Presumably the quartz had been collected from the nearby Euphrates, which even today provides a plentiful local supply. The floodplain area abounds with species of desert vegetation, amongst which the *Salicornia* is visibly the most abundant. Although it is impossible to state with certainty which plants were available to Islamic glassmakers over 10 centuries ago, providing climatic conditions have not changed dramatically since then, one may presume that the present vegetation can be a fairly accurate guide.

3.3.4.1 The *Salicornia* experiment

Approximately 10kg of *Salicornia* (the plant is shown in Figure 3-8) were picked from each of three locations at Raqqa in order to study the compositional variation of the presumed glassmaking raw ingredient. The locations are listed below

1) Tell Aswad (TA), at the edge of an irrigated field. The plants were a deep green colour with long spikes and were easily pulled out of the earth.
2) The Euphrates River (EU), on a raised bank. The plants were quite bushy, with thick stalks and more flowers on the extremities of the spiky stems.
3) Herakla (HE), in a dry field. The plants were very dry and dusty, and much smaller with thinner stalks.

The plants were hung to dry for three days, before which it was not possible to make them ignite. Two batches from each location were prepared, one being left intact and the other with the roots and the main stalk removed (labelled batches 1 and 2 respectively, so that for example *Salicornia* without roots and stalks from Tell Aswad is TA2 etc.). Each batch was placed in a wheelbarrow in a sunken pit and burned. A light, fluffy ash of a brown-grey colour resulted,

similar to that described by Brill in his experiments with *Salicornia* ashes[7], and was powdered and sieved before sampling.



Figure 3-8: typical appearance of Salicorna plant gathered at three locations at Raqqa and ashed.

3.3.5 Samples for corrosion studies

Once clear compositional groups had emerged from EPMA analyses of glasses from Tell Zujaj, it was noticed that samples from different groups exhibited clearly distinct weathering characteristics. Five glasses from Tell Zujaj were selected from the sample base for corrosion analysis on the basis that they share the same burial history and are representative of different compositional groups from the site. An additional sample was selected from Tell Fukhkhar. The samples are listed below and highlighted in red in Appendix 1.

- TZ76, 78, 79, 85, 143; TF211.

3.4 The Ballidon Glass Burial Experiment

A long-term glass burial experiment was started at Ballidon in Derbyshire in October 1970 by Fletcher[8] and continued since by Newton[9]. Sets of several types of newly made glass were

buried in soil with a pH value of 9.55-9.75 under a burial mound 4.6m x 1.2m. The intention was that a certain set should be excavated after burial periods of 1, 2, 4, 8, 16, 32, 64, 128, 256 and 512 years.

Newton[10] observed that six of the original nine types of glass chosen (including a replica Roman composition, high durability ovenware, modern plate glass and optical glass) showed no significantly visible signs of deterioration even after 16 years of burial and thus the original intention of the experiment, to assess the deterioration during burial, was partly frustrated by having chosen glasses which were too durable to reveal much information without the use of surface sensitive analytical techniques. Moreover, due to the ever-increasing time periods between excavations since its inception, problems had occurred in identifying the burial mound and in recovering all the samples in a particular set. Correct re-opening times of the mound over the years had also been either postponed or forgotten.

Oxide (wt%)	Glass #		
	1	2	3
Na_2O	18.2	2.6	0.7
MgO	0.5	4.7	5.4
Al_2O_3	3.6	4.3	3.5
SiO_2	68.5	50.1	46.5
P_2O_5	-	-	4.6
K_2O	1.3	16.7	16.4
CaO	7.3	18.6	21.6
MnO	0.34	0.36	-
Fe_2O_3	0.49	0.95	1.2
CoO	-	1.03	-
PbO	-	0.1	-
Total	100.23	99.44	99.9

Glass #	Years of burial		
	1	9	32
1	B1-1	B1-9	B1-32
2	B2-1	B2-9	B2-32
3	B3-1	B3-9	-

Table 3-1: reported compositions[8] of glasses recovered from Ballidon. The sample set is labelled according to type and burial time in years.

Nevertheless, two other buried glasses, which were replicas of poorly durable ancient compositions, showed clear signs of corrosion after 16 years. May 2002 saw the unearthing of the 32-year set (Set F), which was proudly attended by Newton himself (who by this time, as he had previously written[11], would be in his ninetieth year). The poorly durable glasses recovered in that session, along with their counterparts unearthed in 1971 (Set A described by Newton in 1981[12]) and 1979 (Set D unearthed by Hench[12]), form a significant sample set that has allowed for constructive comparative observations on the long-term decay during burial of controlled glass compositions. The Roman replica glass was also chosen for analysis because of its relevance to this project. A total of 8 glasses spanning over 30 years of burial were prepared

for analysis. Samples are labelled henceforth according to their compositional type and burial time in years. Compositions and burial times of samples, along with labels, are listed in Table 3-1. The glass sample types are as follows:

1 pale green glass of a typical SLS natron based Roman composition.

2 opaque dark blue glass of a typical KLS wood-ash based medieval composition.

3 green glass of a late 17th century composition, previously observed to form a highly layered corrosion crust. It was not possible to obtain a glass of this type unearthed in 2002.

3.5 Bibliography

1. Mannheim, I. and D. Winter, *Jordan, Syria & Lebanon Handbook*. 1998, Bath: Footprint Handbooks.

2. Ball, W., *Syria. A Historical and Architectural Guide*. 1998, New York: Interlink Books.

3. Henderson, J., *New Light on Early Islamic Industry: Excavations in Raqqa, Syria*, in *From River Trent to al-Raqqa*, R.J.A. Wilson, Editor. 1996, University of Nottingham. p. 59-71.

4. Henderson, J., *Localised Production or Trade? Advances in the Study of Cobalt Blue and Islamic Glasses in the Levant and Europe*, in *Patterns and Process: A Festschrift in Honour of Edward V. Sayre*, L. van Zelst, Editor. 2003, Smithsonian Center for Materials Research and Education. p. 227-243.

5. Henderson, J., *Archaeological and Scientific Evidence for the Production of Early Islamic Glass in al-Raqqa, Syria.* Levant, 1999. **31**: p. 225-240.

6. Tonghini, C. and J. Henderson, *An Eleventh Century Pottery Production Workshop at al-Raqqa: A Preliminary Report.* Levant, 1998. **30**: p. 113-127.

7. Brill, R.H., *The Chemical Interpretation of the Texts*, in *Glass and Glassmaking in Ancient Mesopotamia*, A.L. Oppenheim, Editor. 1970, Corning Museum of Glass: New York. p. 105-128.

8. Fletcher, W.W., *The Chemical Durability of Glass. A Burial Experiment at Ballidon in Derbyshire.* Journal of Glass Studies, 1972. **14**: p. 149-151.

9. Newton, R.G., *The Ballidon Glass Burial Experiment.* Glass Technology, 1985. **26**(6): p. 293.

10. Newton, R.G., *More Results from the Ballidon Glass Burial Experiment.* Glass Technology, 1988. **29**(3): p. 106-107.

11. Newton, R.G., *The Future of the Ballidon Glass Burial Experiment.* Glass Technology, 1992. **33**(5): p. 179-180.

12. Newton, R.G., *A Summary of the Progress of the Ballidon Glass Burial Experiment.* Glass Technology, 1981. **22**(1): p. 42-45.

Chapter 4

Overview of experimental work

The project began with the EPMA characterisation of glass from Tell Zujaj and Tell Fukhkhar. Then, following the British Archaeological Mission to Raqqa 2000, analyses focused on glasses from Tell Belor, their raw materials and associated furnace material. Replica glasses were produced and studied to help build up a detailed picture of glass production at Raqqa. The corrosion characteristics of the Raqqa glasses were studied in conjunction with buried glasses unearthed at Ballidon. A range of analytical techniques, each with its own advantages and limitations, has been applied in this project and will be outlined here. The novel archaeometric application of FE-SEM and FIB techniques to the study of ancient glass is highlighted.

4.1 Analytical procedure

A schematic of analytical procedure for all sample types in this study is illustrated in Figure 4-1. Due to the often small sample size (export restrictions prevented the exportation for analysis of samples heavier than ~3-4g from Raqqa), as much information as possible was gathered on archaeological samples before cross-sectioning for compositional analysis and preparation for other destructive techniques. When multiple techniques are applied to the same sample, it is important to take care that enough sample remains for each technique. An Astra 4400 scanner was used throughout to take detailed digital images of samples before and after analyses. This proved a very useful tool because images with a resolution limit <150μm were rapidly and easily acquired.

Optical microscopy was conducted on unaltered surfaces, cross-sections and thin sections. A Yamaha BH2 microscope equipped with Image Tool image collection software was used throughout, with the exception of the thin section analysis, which was conducted by Chris Halls of the Geology Department (Imperial College) on a ZEISS Axiotron microscope. Ballidon glasses were analysed by IRRS prior to cross-sectioning, after collaboration with L.L. Hench's group in the Materials Department (Imperial College) had made this technique available. The technique is outlined in Section 4.5.3. SIM was conducted on relevant glass samples, as no prior sample preparation was necessary. The technique is outlined in Section 4.5.2.

A range of techniques was applied to the different sample sets to yield information on composition, structure and surface alteration. All the techniques used are outlined in detail in this chapter.

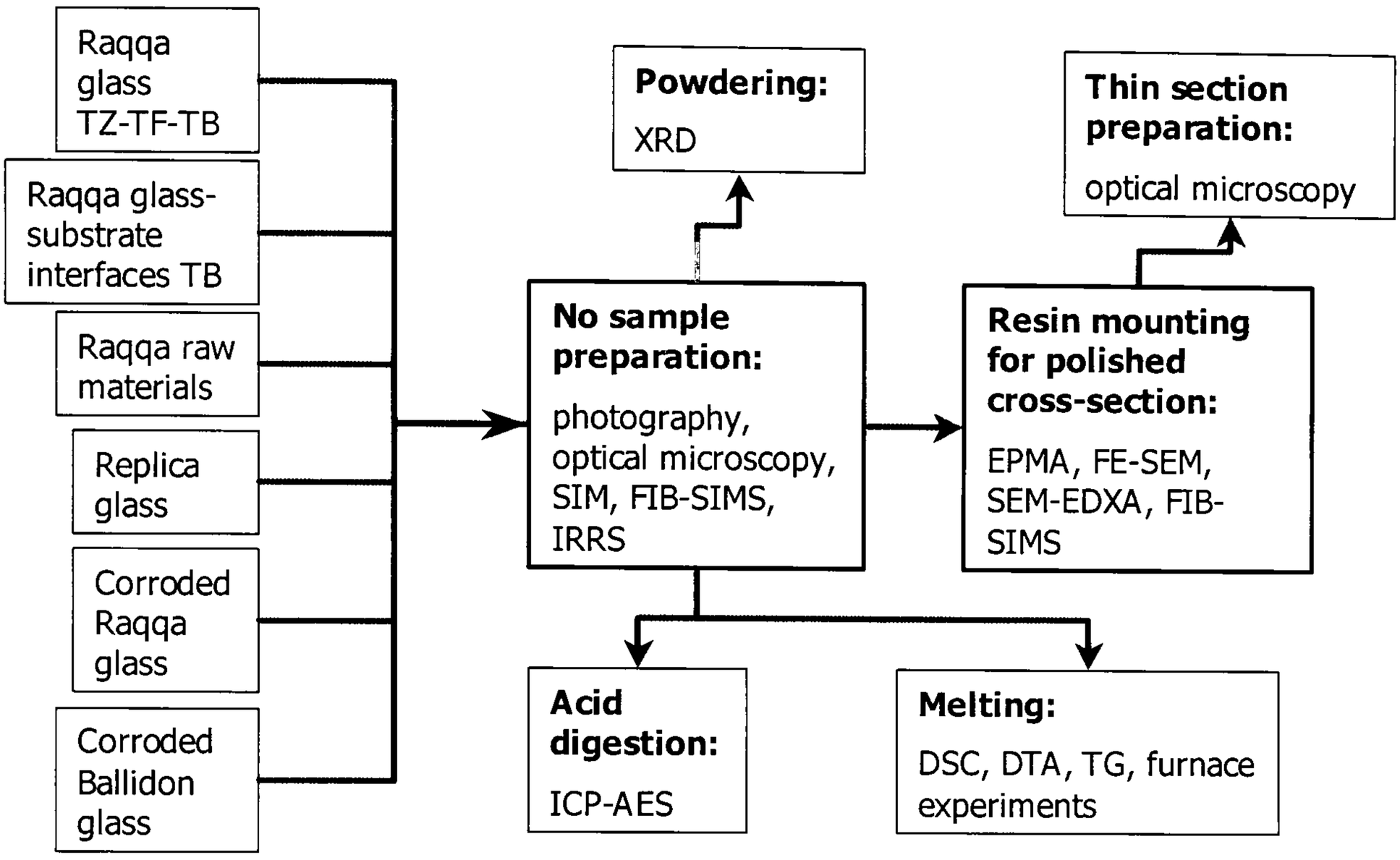


Figure 4-1: overview of experimental procedure for all samples in this study, according to sample preparation considerations.

4.2 Compositional characterisation

Bulk compositional data was gathered on a large selection of glasses and glassmaking debris from Raqqa and on glasses from Ballidon. The bulk compositional techniques utilised in this project were EPMA, SEM equipped with Electron Dispersive X-Ray Analysis (EDXA) and Inductively Coupled Plasma Atomic Emission Spectrometry (ICP-AES). For the electron beam techniques (EPMA and SEM-EDXA) samples were mounted in resin, polished and coated with a thin conductive layer of carbon or gold. For ICP-AES, samples were powdered and digested in nitric acid (HNO_3) prior to analysis. Details of techniques and relevant sample preparation are given below.

4.2.1 Inductively Coupled Plasma Atomic Emission Spectrometry (ICP-AES)

ICP-AES has been extensively used in the characterisation of a range of inorganic archaeological and geological materials. It is a powerful technique that offers simultaneous

quantitative analysis of over 70 elements with detection limits typically in the parts per million (ppm) to parts per billion (ppb) range.

4.2.1.1 Sample preparation

Sample preparation for silicate materials is a time-consuming process; fusion with lithium metaborate ($LiBO_2$) is necessary for complete digestion in HNO_3. Extreme care must be taken during the preparation phase to avoid losing any of the sample or contaminating any of the equipment. 100mg of sample are powdered and sieved through a 50μm stainless steel mesh, mixed with 500mg of $LiBO_2$ and heated in a graphite crucible to 950-1000°C for 20 minutes. The resulting fusion bead must be swirled around to ensure that the entire contents of the crucible are contained in the bead and rapidly poured into 100ml of 1.5M HNO_3. The solution is stirred continuously and, depending on the sample, complete acid digestion takes 1-12 hours. The solution is topped up to 250ml with deionised water and filtered into inert PDFE containers.

Prepared solutions were tested on the Fisons ARL 3580B ICP Analyser in the Geology Department (Imperial College) by Jill Hey and on the Varian Vista Pro ICP Spectrometer at the Natural History Museum, London, UK, by Cheryl Haidon. $LiBO_2$ and SiO_2 blanks were prepared for use as internal standards during the analyses. Both machines had been previously calibrated with various silicate rocks and accuracy of ±1% for major and minor elements (expressed in wt% oxide) and ±5-10% for trace elements (expressed in ppm) was recorded.

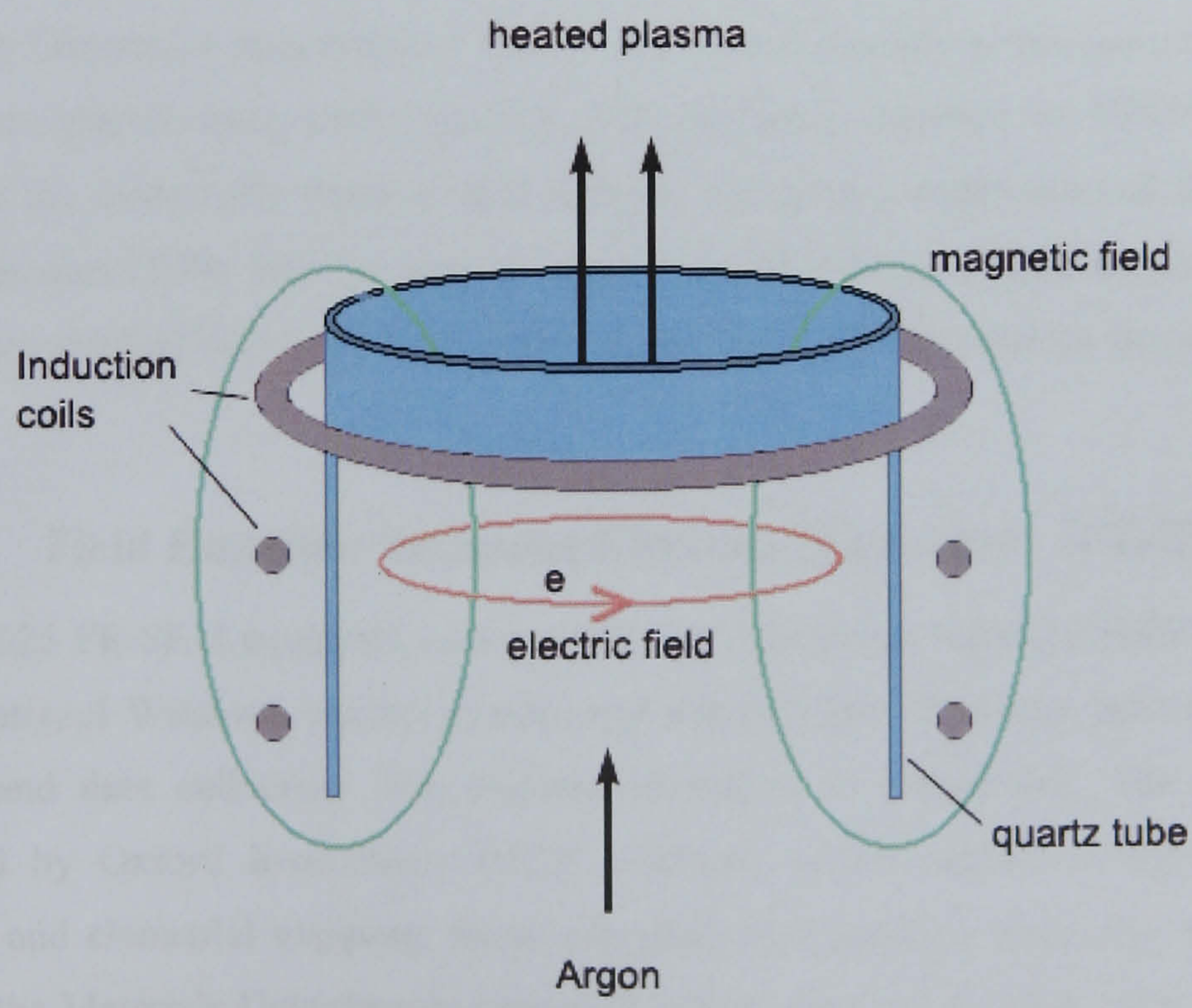


Figure 4-2: schematic of electric and magnetic fields that cause the plasma gas in ICP-AES.

4.2.1.2 Outline of technique

The sample solution to be analysed is introduced into a plasma where it is atomised. The plasma is a highly ionised gas with temperatures in the vicinity of 10,000K caused by the ionisation of argon. Argon gas flows axially through a quartz tube surrounded by an induction tube. When a high frequency current of up to 100A is made to flow in the water-cooled copper induction coils, oscillating magnetic fields are induced whose lines of force are oriented axially inside the quartz tube. The magnetic field in turn sets up an oscillating current in the ions and electrons of the support gas (argon), which causes the ionisation of the argon gas and resistive heating. Characteristic ultra-violet radiation corresponding to specific electron transitions of the atomic species present in the sample is emitted in quantities proportional to the amount of each species present. Qualitative and quantitative information is thus obtainable. Plasma production in ICP-AES is schematically illustrated in Figure 4-2.

4.2.2 Electron Microscopy (EM)

Electron microscopy is a powerful, versatile and widely used tool for imaging and gathering compositional data on a range of materials. The insulating properties of glass require samples to be well polished (to a 0.25μm finish) and coated with a conductive layer for satisfactory data acquisition. Silver dag was often applied to coated sample mounts to ensure good conduction. The quality of compositional data gleaned from x-ray analysis depends very much on the method of data collection: Wavelength Dispersive Spectrometry (WDS) is the more time-consuming technique but offers detection limits more than one order of magnitude lower than for Energy Dispersive Spectrometry (EDS), which is essentially semi-quantitative in nature. In this respect glasses from Tell Zujaj and Tell Fukhkhar analysed by EPMA (equipped with WDS) are the more fully characterised samples and form a compositional framework around which subsequent EDS data has been collated. The EM techniques used and the x-ray collection methods are detailed below, along with the calibration of EM data across the project.

4.2.2.1 Field Emission Scanning Electron Microscopy (FE-SEM)

A LEO 1525 FE-SEM equipped with an ultra high-resolution GEMINI field emission column, LEO32 integral Windows control system and thin-window EDS was used in this project for imaging and data collection. The machine is shown in Figure 4-3. The EDS interface is controlled by Oxford Instruments INCA software, which permits multiple point analysis, linescans and elemental mapping. Some compositional analyses were also conducted by J. J. Wells in the Materials Department (Imperial College) on a JEOL JSM-35CF scanning electron microscope equipped with EDS.

Samples were mounted in Scandiplex resin mixed in a 10:4 ratio with a hardening agent. When fully set, the mounts were polished to a 0.25μm diamond paste finish and coated with a thin conductive layer of carbon or coated with a layer of gold in cases where carbon content was sought. A beam current of $2x10^{-9}$A operating at 15kV was used throughout on the JEOL.



Figure 4-3: the LEO 1525 FE-SEM workstation equipped with an ultra high-resolution GEMINI field emission column and LEO32 integral Windows control system.

4.2.2.1.1 The Field Emission Gun

The FE-SEM is the result of advances in the emission sources used in electron microscopy for the generation of electrons. The conventional emission source is the thermoionic gun. The mitter is usually tungsten in the form of a wire bent into a hairpin, which is heated in a low vacuum (~10^{-3}-10^{-4} Pa) to approximately 2800K by the passage of a current while being held at a high negative potential with respect to the anode and the rest of the microscope. The thermoionic gun is limited in terms of the brightness of the beam it can produce, where brightness is a measure of how many electrons per second can be directed at a given area of the specimen[1]. Brightness is improved through the use of a field emission gun: the tungsten filament is prepared in the form of a sharp point, typically 0.1μm in diameter, so that an extremely high electric field (>10^{9} V/m) is generated at its tip. Quantum tunneling effects cause the release of electrons with well defined energies from the tip at much lower temperatures. As a result, brightness can be increased by a factor of a thousand or more compared with conventional thermoionic emission. This permits imaging at accelerating voltages much lower

than 10kV, resulting in better surface topography and higher image resolution because lower energy electrons are ejected from a smaller distance below the surface (see Section 4.2.2.3). Ultra-high-vacuum (UHV) conditions of $<10^{-7}$ Pa are necessary to preserve the fine point.

4.2.2.2 Electron Probe Microanalysis (EPMA)

A typical EPMA is equipped with multiple crystal spectrometers, containing a range of crystals so that the whole spectrum can be covered. A high degree of automation allows the recording of large amounts of compositional data, so that EPMA is a powerful analytical tool. Fragments of glass from Tell Zujaj and Tell Fukhkhar were analysed on a Cambridge Microscan 9 microprobe with two wavelength-dispersive spectrometers located at the Department of Earth Sciences at Oxford University, a machine that has yielded accredited, published results[2]. Batches of 18 samples were set in resin, polished to a 0.25μm diamond paste finish and carbon coated for analysis.

A defocused electron beam was fired at an accelerating voltage of 15kV onto a surface area of approximately 80μm in diameter and emitted x-rays counted for 100s. The migration of sodium and other lighter species away from the beam is minimised under diffuse beam conditions. The lower limits of oxide detection for the Cambridge Microscan 9 varied between 170ppm for CaO to 760ppm for Na_2O[2]. An accelerating voltage of 15kV was used to fire a diffused electron beam onto an area of about 80μm of the sample surface and x-rays emitted from the sample surface counted for 100s. Two analyses were conducted for each sample for all major and minor components in the glass

4.2.2.3 The interaction volume

Emitted electrons are accelerated through an aperture down the electron column and focused by condenser and objective lenses to a small spot on the sample surface 10nm to 1μm in diameter. These electrons penetrate into the sample and interact with atoms in the sample. The penetration depth depends on the atomic weight of the sample's constituents. The volume of atom-electron reaction is known as the interaction volume and limits the lateral resolution to 1-5μm[3]. It also implies that no useful analysis can be made of a region smaller than $1\mu m^3$. The interaction volume is illustrated in Figure 4-4. A range of secondary emissions are created and re-released from the sample surface.

a) Secondary electrons – low energy emissions (<50eV) generated by the ionisation of atoms on the surface. They give good topographical information about the sample surface.

b) Backscattered electrons – they are the result of violent collisions with atoms in the top third of the interaction volume and are scattered back out of the sample. As the proportion of backscattered electrons is dependent upon the mean atomic number of the sample, an increase in mean atomic number causes a sharp increase in brightness on the imaging screen, so that compositional differences are instantly visualised.

c) X-rays – when electron orbitals of atoms below the surface are ionised by high-energy electrons, the atoms become unstable and emit x-rays of energies and wavelengths characteristic of the emitting atom. When these are detected, they distinguish the emitting atom and therefore compositional data can be acquired through either wavelength or energy dispersive spectrometry methods.

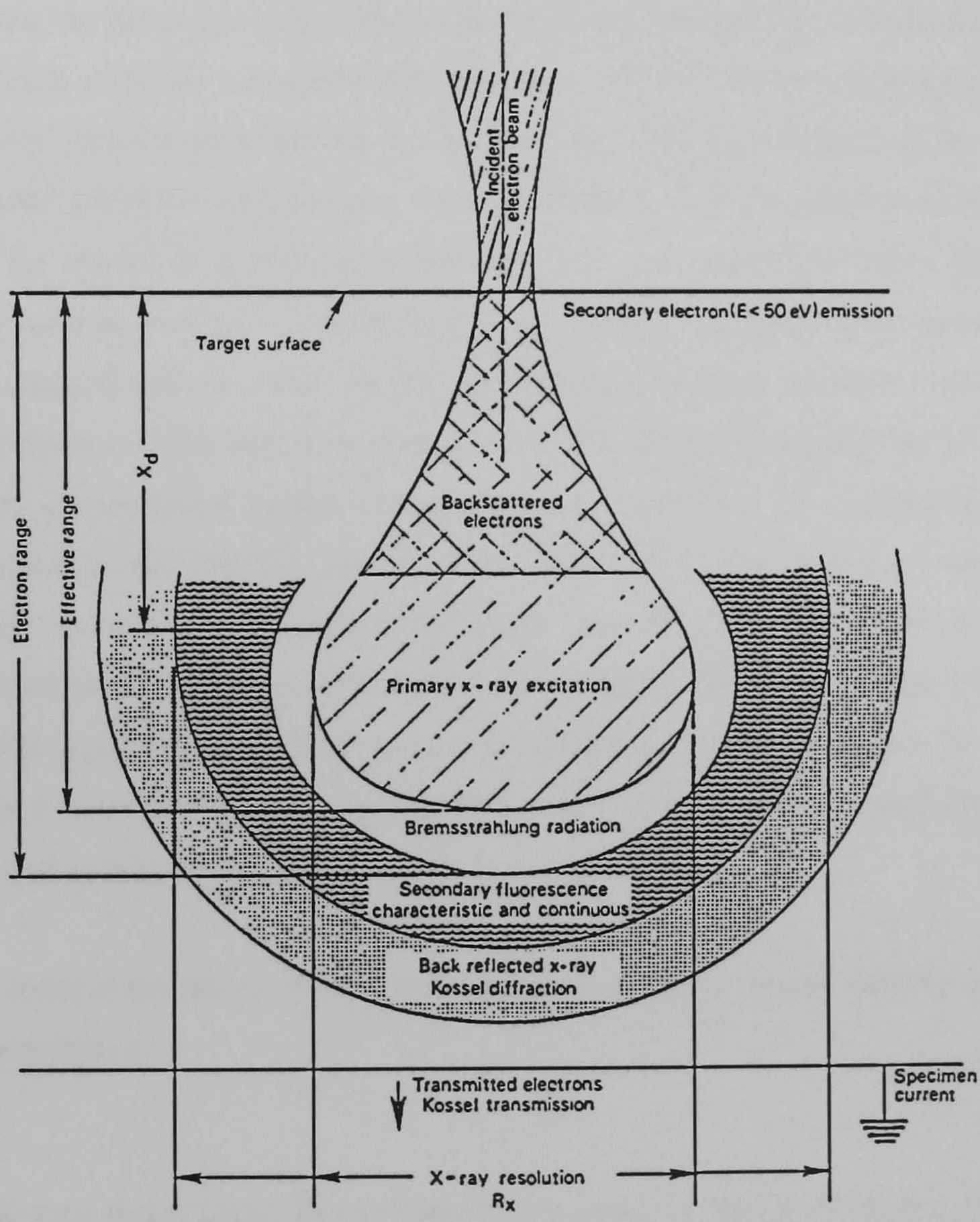


Figure 4-4: effects of the interaction of an electron beam with a solid, from Heinrich and Newbury[4]. X_d marks the limit of electron diffusion into the sample. The diagram shows the diameters of the excited volumes from which x-rays originate. X-ray resolution is thus limited laterally to a distance R_x.

The interaction volume establishes the effective minimum distance between adjacent points of a linescan that can be considered without overlap. A 15keV beam was used throughout for EDS chemical analyses because at this energy the interaction volume in glassy materials, calculated by the INCA software, has a maximum diameter of 3.5μm, compared to 4.5-5μm at 20keV. A

progressive loss in Na counts was observed when analyses were conducted at distances of 3.5μm or less apart, presumably due to the cumulative build up of charge with overlapping interaction volumes, hence a minimum distance of 3.7μm between points was fixed. Linescan procedures across cross-sectional corroded surfaces using FE-SEM are outlined in Section 4.5.1.1.

4.2.2.4 X-ray detection: Energy Dispersive Spectrometry (EDS)

EDS or EDXA is the most common compositional tool found with scanning electron microscopes and provides quantitative data quickly to a reasonable degree of accuracy (detection limits are typically 0.1-0.3wt%). The data takes the form of intensity as a function of wavelength. Each atom has a characteristic spectrum due to the unique arrangement of energy levels, hence the wavelength identifies the emitting atom and the intensity of the emitted lines determines, after corrective calculations, the concentration of their emitting atom. The x-rays are analysed by means of a detector, which consists of a crystal of silicon biased by gold electrodes on the front and rear surfaces. The emitted x-rays excite atoms in the detector that in turn eject an electron with the same kinetic energy as the original radiation minus the binding energy of the electron to the atom (the photoelectric effect). Free electrons lead to free electron-hole pairs that are separated by the internal bias and detected at the surface electrodes. The detector, coupled to the electron gun, is found inside the main ultra-high vacuum (UHV) chamber of the microscope and needs to be sealed from the vacuum by a thin window (a few μm in thickness), typically made of beryllium. The window absorbs all x-rays less than 1keV, hence elements lighter than sodium cannot be detected. Recent advances in thin window technology have allowed detection of elements down to carbon: this is the case for the FE-SEM workstation used in this study.

X-rays were counted for 50s at 15keV beam energy throughout. Beam stability was monitored using a cobalt standard.

4.2.2.5 X-ray detection: Wavelength Dispersive Spectrometry (WDS)

In WDS emitted x-rays are dispersed by an analysing crystal, via Bragg diffraction from its crystal lattice planes. The crystal is positioned mechanically at a point where only the desired wavelengths diffract, and different elements are analysed in turn. The diffracted x-rays are recorded in a detector and proportionally calculated as single element weight percentages from the counts obtained from a reference standard. Hence background is eliminated almost entirely and detection limits are in the ppm range.

4.2.3 Data calibration

For data calibration, analysis was first performed on Corning standard B, which represents a typical SLS composition, and standard deviations and relative errors calculated. The precisions are expressed as relative standard deviations (RSD):

$$\mathrm{RSD} = \frac{\mathrm{SD}}{\mathrm{mean}} \times 100\% \qquad [4.1]$$

and the accuracies as relative errors (RE):

$$\mathrm{RE} = \frac{|C_o - C_c|}{C_c} \times 100 \qquad [4.2]$$

where C_c is the certified composition

C_o the observed composition

SD is the standard deviation.

		WDS - EPMA				EDS - FE-SEM			
Oxide (wt%)	C_c (wt%)	C_o (wt%)	RE (%)	SD (wt%)	RSD (%)	C_o* (wt%)	RE (%)	SD (wt%)	RSD (%)
Na_2O	17.26	16.69	3.3	0.36	2.1	16.3	5.8	0.16	1.0
MgO	1.19	1.15	3.4	0.04	3.3	0.9	27.2	0.13	15.0
Al_2O_3	4.22	4.30	1.9	0.11	2.6	3.8	10.0	0.09	2.2
SiO_2	61.55	61.72	0.3	0.12	0.2	63.6	3.3	0.36	0.6
P_2O_5	0.84	0.76	9.5	0.05	6.2	0.3	64.3	0.07	23.3
SO_3	0.54	0.47	13.9	0.05	9.9	0.4	25.9	0.05	12.5
Cl	0.2	0.27	32.5	0.04	14.3	0.3	26.7	0.04	16.0
K_2O	1.1	1.04	5.9	0.04	3.7	0.9	15.2	0.04	4.1
CaO	8.71	8.65	0.7	0.12	1.3	8.5	2.6	0.02	0.3
TiO_2	0.1	0.07	30.0	0.02	24.7	0.3	246.7	0.14	41.7
MnO	0.28	0.24	16.1	0.03	11.3	0.2	13.1	0.02	8.6
Fe_2O_3	0.35	0.35	0.0	0.03	8.6	0.5	38.1	0.05	9.8
Cr_2O_3	0.05	0.02	60.0	0.02	86.6	nd	-	-	-
CoO	0.035	0.03	14.3	0.03	100.5	nd	-	-	-
NiO	0.09	0.05	50.0	0.03	58.8	nd	-	-	-
CuO	2.7	2.65	1.9	0.03	1.2	4.0	49.0	0.33	8.1
ZnO	0.2	0.18	10.0	0.02	8.5	nd	-	-	-
SnO_2	0.04	0.02	50.0	0.02	76.4	nd	-	-	-
Sb_2O_5	0.46	0.50	8.7	0.02	4.6	nd	-	-	-
BaO	0.14	0.10	28.6	0.02	23.1	nd	-	-	-
PbO_2	0.4	0.40	0.0	0.09	22.5	nd	-	-	-
Total	100.455	99.63				100.0			

Table 4-1: results of EPMA and FE-SEM calibration with Corning B glass standard. EPMA data is the mean of two WDS scans, FE-SEM data the mean of four EDS analyses. * denotes normalised data.

Results are presented for WDS and EDS calibration data in Table 4-1. The precisions are similar for the WDS calibration, being in the order of 1.3-4.1% for oxides present in larger proportions than 1wt%. The RSD values tend to increase with decreasing oxide content in the standard glass, which reflects the larger relative error that is associated with an equivalent variation in lesser components. The accuracy is also better for the major components, with RE values below 5% for the 5 major constituents. An error value of 3.3% was observed for Na_2O, which tends to migrate away from the beam if a small spot diameter is used[2, 5]. Larger errors are associated with the EDS data, which presented 10-27% RE values for oxides present in proportions of around 1wt%. Nevertheless, an RE value of 5.8% is reasonable for Na_2O, which was expected to vary more significantly.

As the Corning B standard was not available to calibrate the JEOL J35, Raqqa glasses TZ187, 188 and 189 were used as internal standards, based on the WDS data shown in Appendix 1. The samples were considered representative of compositional variation within the Raqqa dataset. Oxide totals were found to vary consistently and correlate well with the electron probe data. For comparative purposes EDS data has been normalised throughout.

Session	Average analytical total (wt%)	RSD analytical total (%)	Average SiO_2 total (wt%)	SD average SiO_2 total (wt%)	RSD average SiO_2 total (%)	Average SiO_2* total (wt%)	SD average SiO_2* total (wt%)	RSD average SiO_2* total (%)
1	102.93	0.5	70.91	2.82	4.0	67.98	2.73	4.0
2	97.28	1.0	66.37	2.67	4.0	69.09	2.34	3.4
3	99.39	0.4	69.03	2.72	3.9	69.64	2.86	4.1
4	104.01	0.9	72.77	3.70	5.1	68.75	3.69	5.4
5	101.06	1.1	69.09	1.97	2.9	68.03	1.78	2.6
6	100.86	0.4	67.56	2.76	4.1	66.71	2.86	4.3
7	97.89	0.5	66.56	1.12	1.7	68.67	1.35	2.0
SD across sessions (wt%)			**2.33**			**0.95**		
RSD across sessions (%)			**3.4**			**1.4**		

Table 4-2: calibration of SiO_2 totals across separate EPMA sessions. A discrepancy in SiO_2 calibration was found to influence the analytical totals for each session. By normalising SiO_2 content to 100%, the SD of analytical totals across sessions was reduced significantly without altering the distribution within single sessions.

4.2.3.1 EPMA inter-session data calibration

Calibration with the standard was performed for each of seven analytical sessions on the Cambridge Microscan electron microprobe. When it came to comparing results it was found that, although the average analytical total for each session was internally consistent (RSD ≤1.1%), the spread of totals across all sessions was over 6%, closely correlated to a shift

in average SiO_2 totals for each session. The Na and Ca signals were not found to vary in the same way. The spread was identified as the result of a 3% accuracy error for SiO_2 during calibration with the Corning B standard that had led to discrepancies in the analytical totals and was accounted for by normalising SiO_2 to 100% (labelled throughout as SiO_2*). The process is illustrated in Table 4-2. In this way the data is internally consistent as all totals are 100%, the variability of SiO_2 contents within single sessions remains almost constant ($SD_{Si} \cong SD_{Si*}$), but the overall SD of SiO_2 across all sessions is reduced by a factor of 2.4.

4.2.4 Data conversion

Compositional results are expressed in a variety of ways depending on the analysis technique used and the relevant output software. Glass compositions are normally expressed in terms of weight percentages of oxide components. However, molar quantities are important for the modelling of glass behaviour, and atomic percentages are useful for the interpretation of crystalline phases in cases where x-ray analysis is problematic. It is important that analytical results be correctly converted from one quantity to another.

Column	*1*	*2*	*3*	*4*	*5*	*6*	*7*	*8*	*9*
Oxide	atoms/ molecule	cations/ molecule	oxygens/ molecule	molecular wt oxide	wt% oxide	# mols oxide	mol% oxide	atom % cation	atom % oxygen
Na_2O	3	2	1	61.97	12.3	0.198	11.85	7.90	3.95
MgO	2	1	1	40.29	3.4	0.084	5.04	2.52	2.52
Al_2O_3	5	2	3	101.93	1.3	0.013	0.76	0.30	0.46
SiO_2	3	1	2	60.06	70	1.166	69.58	23.19	46.39
K_2O	3	2	1	94.19	2.5	0.027	1.58	1.06	0.53
CaO	2	1	1	56.07	10.5	0.187	11.18	5.59	5.59
Total					100	1.675	100	40.57	59.43
								Total = 100	

Table 4-3: an illustration of the method for data conversion followed in this study using a replica Raqqa HMG composition as an example.

An example of the method used in this study is given in Table 4-3 using the Raqqa HMG type 1 replica composition (see Table 4-4), and is explained as follows: to convert weight percent into molar percent, normalised oxide weight percent values (column 5) are divided by their individual molecular oxide weights (column 4) to express the molar quantity per unit weight of glass (column 6). Molar percentages are thus obtained (in column 7) by dividing the molar quantity of each oxide (in column 6) by the total molar quantity (at the base of column 6) and multiplying by 100. The atomic percentage of individual cations (column 8) is calculated by multiplying the molar percentage of each oxide (column 7) by the ratio of cations in that oxide (column 2) to the total number of atoms in the oxide (column 1). Correspondingly, the atomic

percentage of oxygen atoms for each oxide (column 9) is calculated by multiplying the molar percentage of each oxide (column 7) by the ratio of oxygen atoms in that oxide (column 3) to the total number of atoms in the oxide (column 1). The total sum of individual atomic percentages is equal to 100.

4.3 Structural characterisation

4.3.1 XRD

A Philips PW1720 diffractometer using Cu-Kα radiation was calibrated prior to data collection with a silicon reference and measurements of intensity versus 2θ were taken from 20 to 100° at 0.01° intervals every 5 seconds. Diffraction patterns were collected with the aid of Philips PC-APD software.

4.3.2 Thermal analysis

4.3.2.1 Differential Thermal Analysis (DTA)

Energy changes are measured in differential thermal analysis by monitoring the temperature difference between an inert reference material and the sample during controlled heating. Two thermocouples are connected to a voltmeter. One thermocouple is placed in an inert material such as Al_2O_3, while the other is placed in a sample of the material under study. As the temperature rises, there will be a brief deflection of the voltmeter if the sample is undergoing a phase transition. This occurs because the input of heat will raise the temperature of the inert substance, but be incorporated as latent heat in the material that is changing phase. The difference in temperature is recorded as a function of increasing temperature. When a temperature difference exists between sample and reference as a result of a chemical or physical change in the sample, a signal results which is recorded as a peak. In this way exothermic and endothermic reactions can be identified and monitored under inert, reducing or oxidising atmospheres.

4.3.2.2 Thermogravimetry (TG)/ Differential Thermogravimetry (DTG)

Thermogravimetry (TG) is a technique often used in conjuntion with DTA. Changes in the sample weight are recorded as a function of temperature, particularly at points in which the sample decomposes or melts. Differential thermogravimetry (DTG) converts the TG signal to its first derivative form to measure the rate of weight change with temperature.

A Stanton Redcroft TG 780 Simultaneous Thermal Analyser (TG-DTG-DTA) was used for analyses. Samples of up to 100mg in weight were heated to 1350°C in air or in an argon atmosphere at a 10°C/min heating regime. Al_2O_3 was used as a reference material. The simultaneous recording of two thermal processes on the same sample allows direct correlation of weight loss to reaction type, and thus clearer interpretation of complex thermal reactions.

4.3.2.3 Differential Scanning Calorimetry (DSC)

Differential scanning calorimetry (DSC) is similar to the DTA techniques described above in that a sample is heated at a controlled rate and heat energy measured against a reference alumina standard. In DSC identical temperatures are maintained at all times between the reference and the sample so that differences in heat energy between them can be measured. The amount of heat energy given or absorbed by the sample (expressed in $mcal \cdot s^{-1}$) is plotted against temperature. The technique is generally more sensitive than DTA and smaller sample sizes are required.

A Rheometrics Scientific DSC 1500 was used for analysis. Samples weighing 40-50mg were introduced to the furnace chamber and heated at 40°C/min.

4.4 Replica glasses

Most previous research concerning ancient and artistic glasses has utilised glass samples of similar composition to the actual objects that are under investigation. This approach has obvious advantages and has yielded much information, although it should be remembered that despite the similarity in chemical composition between the glass object and the replica glass, the nature of the replica glass will invariably differ to some extent from that of the original glass object.

4.4.1 Experimental considerations

Where archaeological samples are concerned, there are inevitably problems caused by the scarcity of materials available for destructive analysis and the often advanced state of corrosion they are in. Replicative work has proven advantageous in helping to answer many of the questions related to archaeological materials[6, 7], although it must be borne in mind that any replicative work will, at best, be approximate. This is due to differences in:

a) Raw materials: the use of chemically pure powders as raw materials, as opposed to the compositionally diverse raw materials used in antiquity, gives rise to simpler and more homogeneous structures with fewer impurities.

b) Crucibles: the melting of the glass batch, usually carried out in chemically inert platinum crucibles, as opposed to the original melting process which was carried out in refractory crucibles, will not suffer from any contamination effects. Saleh *et al.*'s work[8] shows some, albeit not significant, contamination from ancient Egyptian clay crucibles.

c) Furnaces: melting conditions in modern electric furnaces operating under controlled temperatures and oxidation conditions, as opposed to ancient wood or charcoal burning furnaces, are very different.

The quantity of minor and trace element impurities in the Raqqa glass would make complete replicative experiments difficult and time-consuming. Given the considerations listed above, a good balance between accuracy and practicality was achieved by considering only the 6 major glass oxides (SiO_2, Na_2O, CaO, MgO, Al_2O_3 and K_2O); they account for over 96.5% of the overall compositions and their viscosity effects in glass systems are extensively researched[9, 10]. Replica compositions of typical type 1 and type 3 glasses were made up according to Table 4-4. Compositions are based on type 1 HMG and type 3 LMG compositions from Tell Zujaj and Tell Fukhkar illustrated in Table 5-1. The differences in minor components (Mg, K, Al) are highlighted to indicate changes in production parameters that they may bring about.

Oxide (wt%)	I	III
Na_2O	12.3	13.3
MgO	3.4	0.5
Al_2O_3	1.3	3.2
SiO_2	70	73
K_2O	2.5	0.5
CaO	10.5	9.5
Total	100	100

Table 4-4: target compositions for type 1 HMG and type 3 LMG replicas.

4.4.2 Batch preparation

The batches were weighed from AnalaR, Aldrich and Hopkins & Williams pure oxide and carbonate powders. Carbonates evolve CO_2 upon heating to leave an oxide. For example:

$$CaCO_3 \rightarrow CaO + CO_2 \qquad [4.3]$$

The weight of evolved CO_2 needs to be accounted for at the weighing stage, so that the total weight of each carbonate is equal to the weight of the corresponding oxide multiplied by the ratio of atomic weights of carbonate to oxide. Thus, to make 100g of replica type 1 glass with

10.5g of CaO, 10.5 x 100/56 = 18.75g $CaCO_3$ are needed, where 100 is the atomic weight of $CaCO_3$ and 56 the atomic weight of CaO. As the K_2CO_3 and Na_2CO_3 used were in the form of hydrous compounds, they were first heated for 2 hours at 130°C to evaporate excess H_2O. Na_2CO_3 lost 8% of its original weight and K_2CO_3 lost 2.5% of its original weight through moisture evaporation. Batch compositions are given in Table 4.5. The components were weighed in turn on digital balances to an accuracy of ±0.05g, mixed and ball-milled in an inert HDPE container for 72 hours. Balls of Al_2O_3 were added to the batch before milling to aid homogenous mixing and grain size distribution.

Raw material (g)	I	III
Na_2CO_3	21.03	22.74
MgO	3.40	0.50
Al_2O_3	1.30	3.20
SiO_2	70.00	70.00
K_2CO_3	3.67	0.73
$CaCO_3$	18.75	16.95
Total	118.15	117.12

Table 4-5: batch compositions used to make 100g of type 1 HMG and type 3 LMG replicas.

4.4.3 Particle size analysis

A sufficiently fine particle size results in a surface area of the batch constituents that has an associated surface energy high enough to promote rapid reactions in the melt. Particle size analysis was carried out on the batch material to assess particle size distribution. A bimodal particle size distribution was found at approximately 2 and 10μm (Figure 4-5). Subsequent analysis revealed that the silica source used, when ultrasonically dispersed for 15 minutes, had a particle size of 10μm. The mean diameters of type 1 and type 3 replica batch particle size were 5.41μm and 5.62μm respectively.

4.4.4 Batch fusion and casting

30g batches of powder were heated in Pt-5%Au crucibles in a Carbolite RHF 1500 furnace. The crucibles were first left overnight filled with 5mol% HCl and rinsed in distilled water to remove any impurities. Batches were heated according to the following heating schedules: initially, melts were held at 700°C for two hours to allow CO_2 to evolve and then raised respectively to 1100°C, 1300°C, 1400°C and 1450°C for another two hours in order to establish at which temperature a satisfactory casting could be achieved.

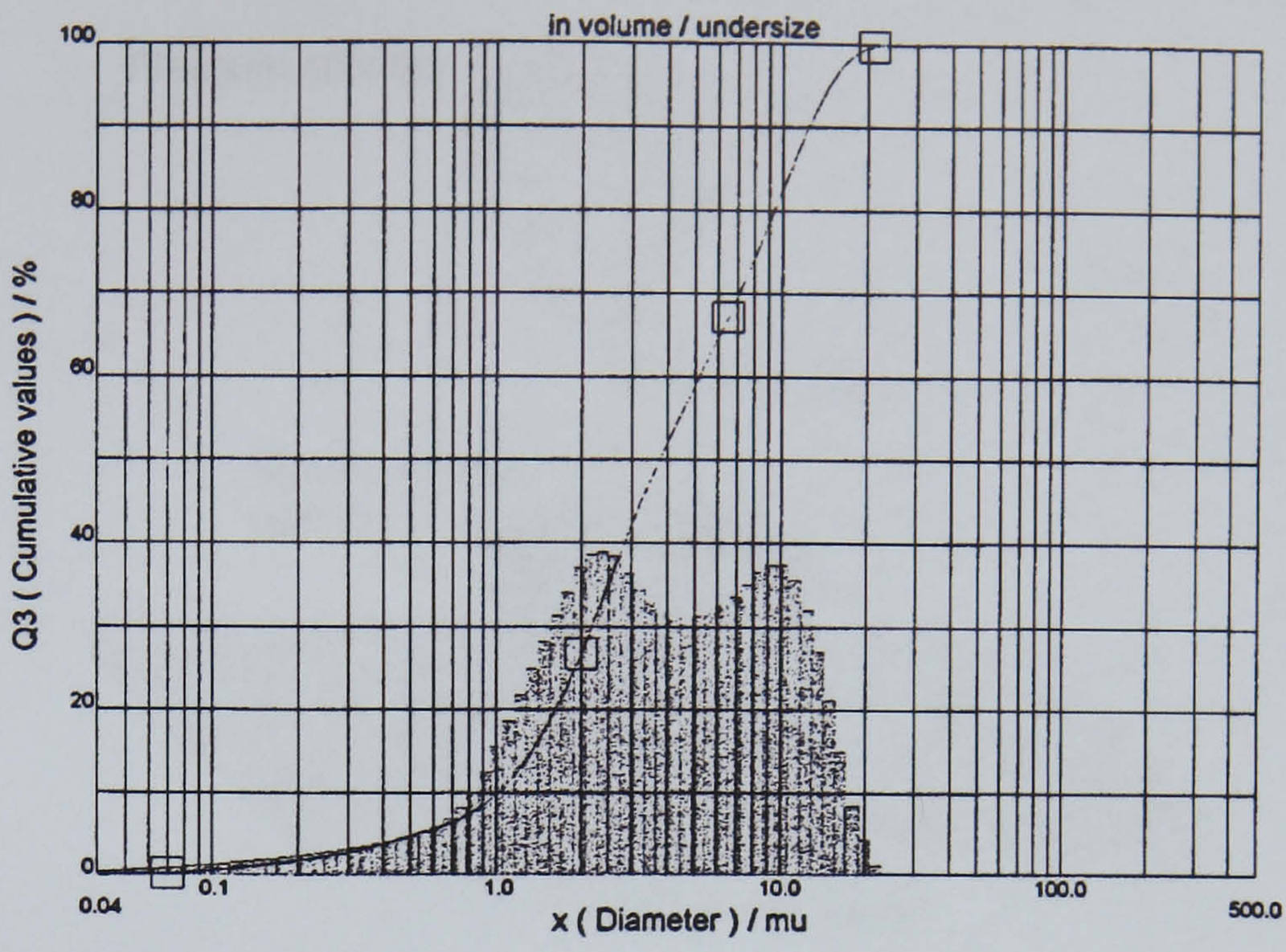


Figure 4-5: results of particle size analysis of powders used to make replica glasses. A bimodal distribution of grain size was found at approximately 2μm and 10μm.

At temperatures above 1300°C the tips of the iron tongs used to remove the crucible from the furnace and position it over the mould had to be coated in platinum foil to avoid the formation of Pt-Fe alloys and subsequent deterioration of the crucible. The crucible was quickly tipped and the glass cast into a stainless steel cylinder placed on a steel plate, both preheated to 500°C, and air cooled. Although glass should normally be furnace cooled to prevent stress cracking below T_g, the heat transmitted to the steel parts during the casting process slowed the cooling enough to ensure that the detrimental effects of rapid air cooling were avoided. The casting procedure is illustrated in Figure 4-6.

4.4.5 Fining

Fining refers to the removal of bubbles from the glass melt, and is dependent on viscosity among other factors. To compare the fining properties of the Raqqa replica types, four 30g batches of type 1 and type 3 replica composition were placed in alumina crucibles, heated to 700°C and held there for two hours, then heated to 1200°C and isothermally held. Single crucibles of each replica type were removed from the furnace after 100, 200, 300 and 1500 minutes at 1200°C and transferred to an annealing oven at 500°C for 30 minutes. The crucibles were then sectioned and the glass removed and polished for analysis.

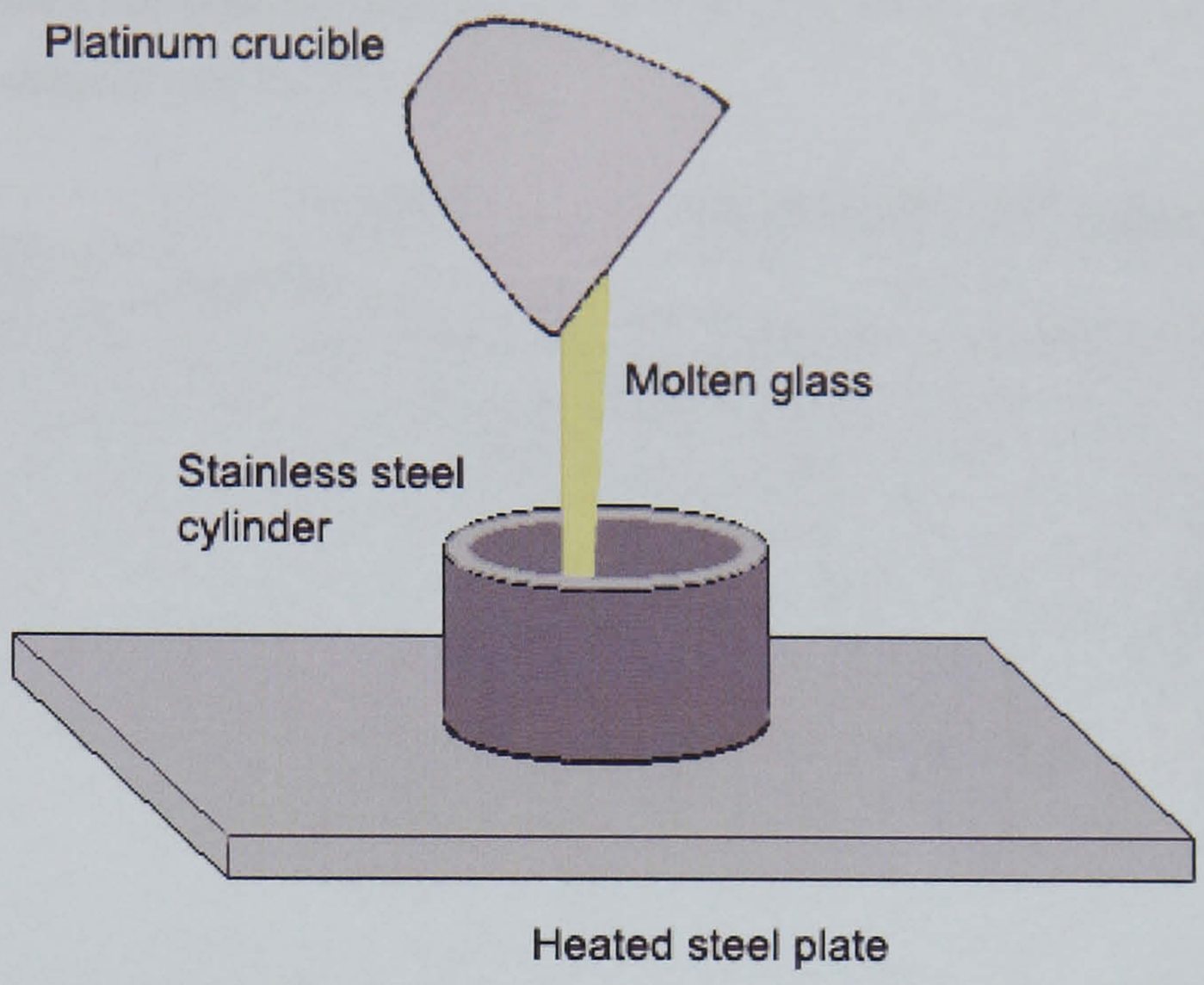


Figure 4-6: illustration of the casting process.

4.4.6 Density measurements

Density measurements were performed on fully dense cast samples and partially dense glasses from the fining experiment. Samples were immersed in distilled water and weights measured using Stanton Instruments Unimatic Scales (weight readings up to 0.0001g with an accuracy of ±0.0005g). Density was calculated according to the Archimedes method:

$$\rho = \frac{m}{V} = \frac{W_d}{W_w}\rho_{H_2O/T} = \frac{W_d}{W_d - (W_i - W_{i(C)})}\rho_{H_2O/T} \qquad [4.4]$$

where density, ρ, is the ratio between the dry weight, W_d, and wet weight, W_w, of a sample multiplied by the density of distilled water measured at the ambient temperature (a correction factor as the specific gravity of water changes with temperature). W_w is calculated as the difference between dry weight and the weight when immersed in distilled water, W_i. As the sample is held underwater in a cage, the immersed cage weight, $W_{i(c)}$, must be calculated separately and subtracted from W_i.

4.5 Characterisation of surface corrosion layers

The micron to sub-micron scale of corrosion layers was a serious obstacle to characterisation and will be dealt with in detail below. Corroded Raqqa samples were first inspected by optical microscopy and by SIM. Corroded Ballidon glasses were also analysed by IRRS. Polished

cross-sections were subsequently prepared for SEM-EDXA. SIMS analyses were attempted on corroded glass samples with the FIB system.

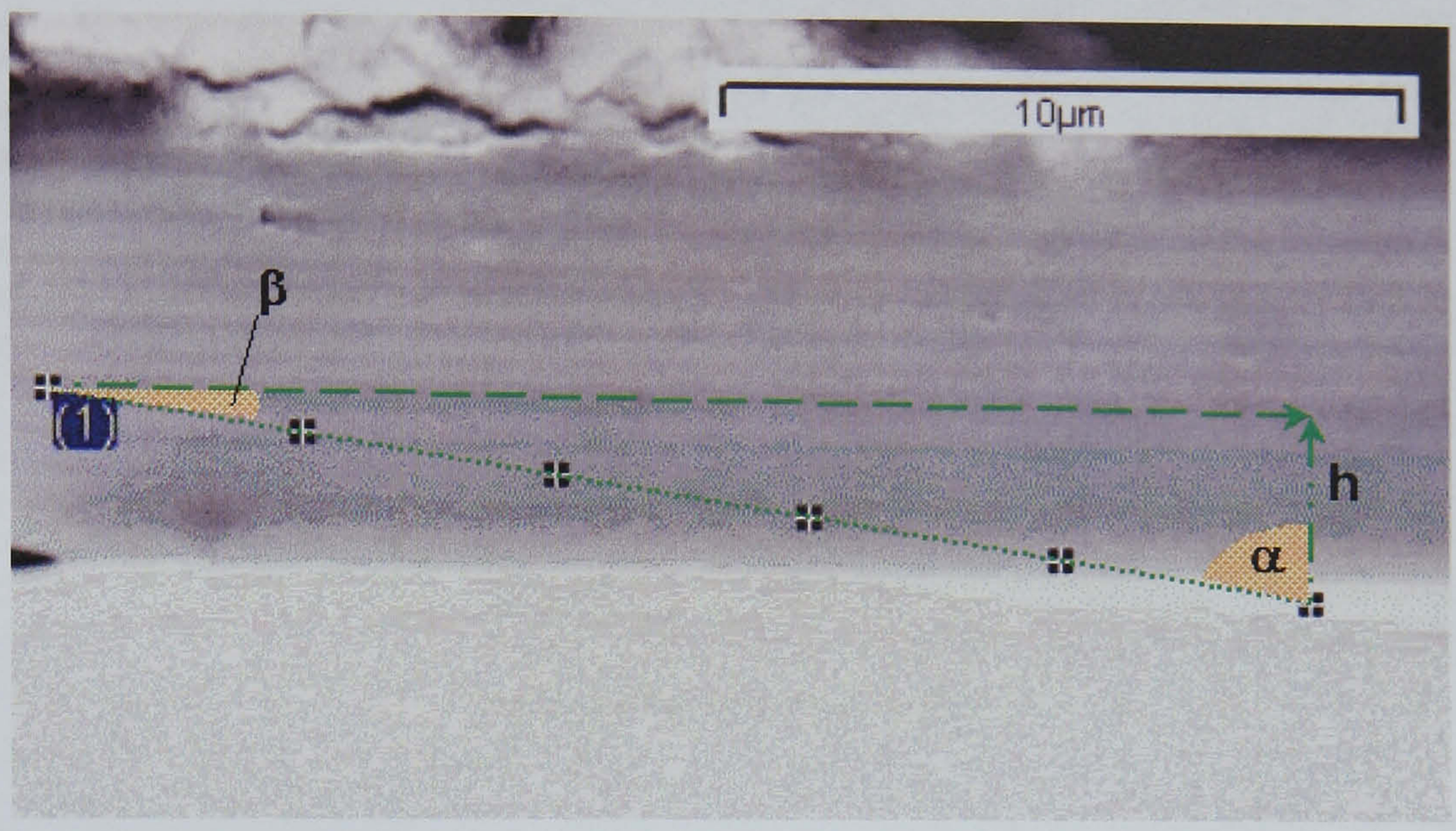


Figure 4-7: backscattered electron image of a polished cross-section of corroded crust on sample B2-9. Superimposed are six points of a linescan conducted across the glass/corrosion interface. The acute angle (β) that the linescan forms with respect to the interface axis means that six points can be acquired across an effective distance, h, perpendicular to the interface, without any overlap of individual interaction volumes.

4.5.1 FE-SEM linescans

Provided that compositional variation across interfaces and on outer surfaces, when viewed in cross-section, was homogeneous across a sufficiently large distance parallel to the interface itself, linescans could be taken at an acute angle with respect to the interface plane to maximise the number of data points representative of that interface. An example is given in Figure 4-7; six data points 3.7µm apart cross the glass-corrosion interface of Ballidon sample B2-9. The total distance perpendicular to the interface is represented by *h*, the product of the linescan length and the sine of the adjacent angle α or the cosine of the opposite angle β. In the example considered, β was measured at 11±1°; hence six data points represent an actual distance of 5x3.7·sin (11±1) or 3.5±0.3µm across the interface. Multiple linescans across the rest of the corroded layer provided a combined total of 20 points across the corroded surface region of B2-9.

4.5.1.1 Quantifying the glass surface using FE-SEM linescans

When linescans described above were conducted across the outer surface of corroded glass samples mounted in cross-section, interference with the data resulted from the epoxy resin adjacent to the surface in cross-section. This was due to the size of the interaction volume (3.5µm in diameter, as reported in Section 4.2.2.3), which led to the simultaneous generation of x-rays from the glass and the surrounding resin.

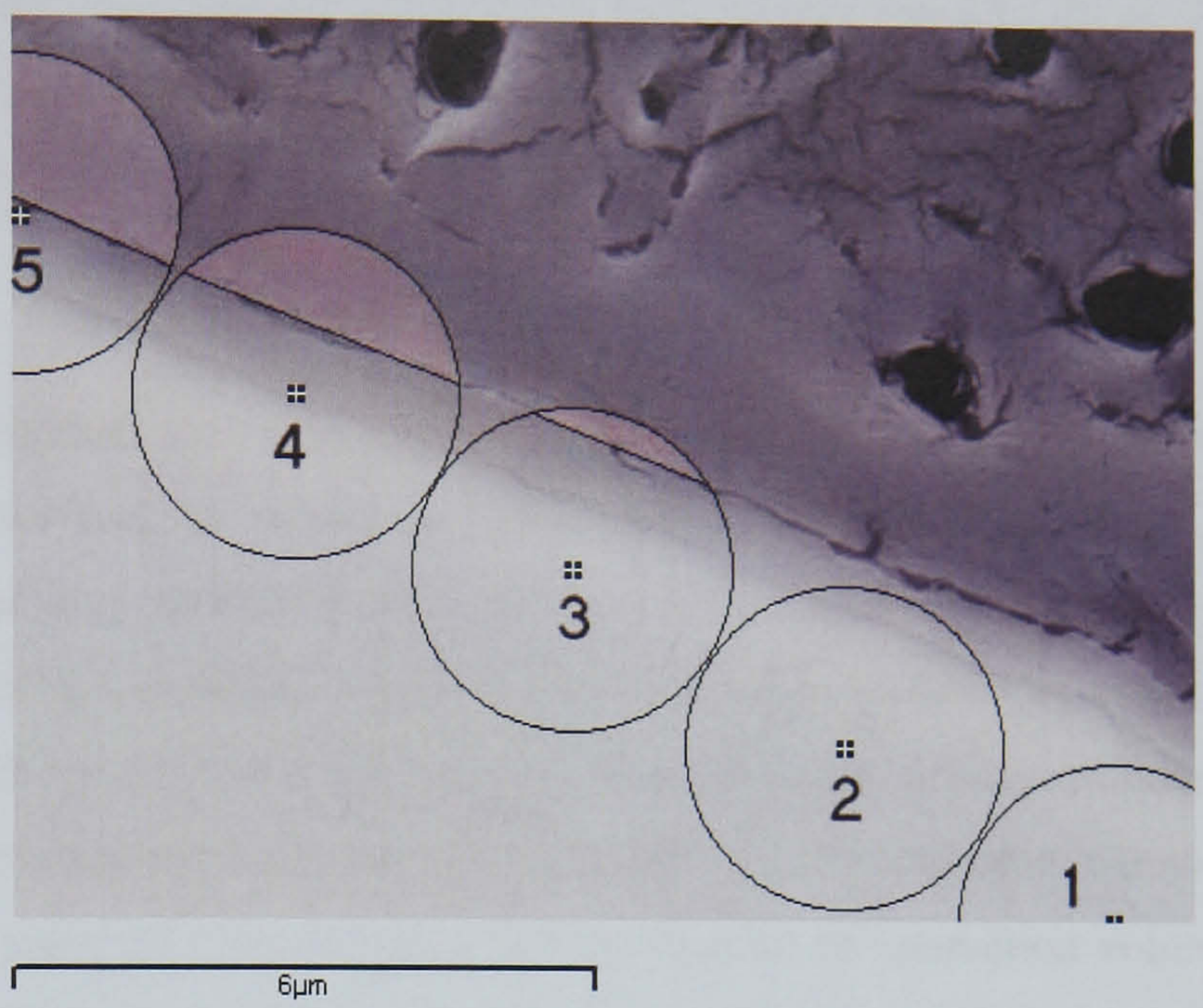


Figure 4-8: a backscattered electron image showing five points of a linescan conducted across the outermost depleted edge of B2-32, at a point where the corrosion crust had spalled away. A black circle represents the interaction volume for each analysis and the proportion of each volume generated from within the resin is coloured pink.

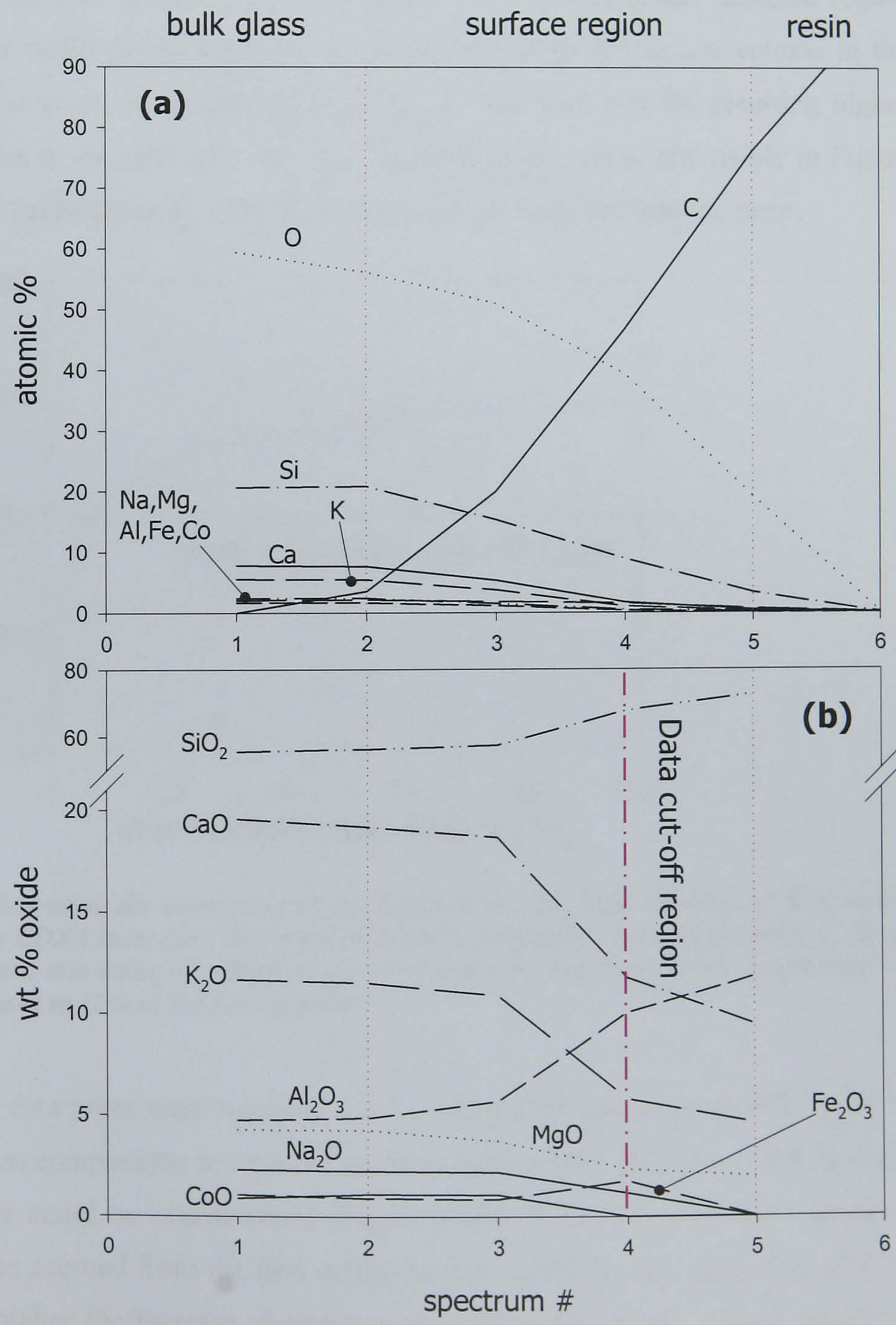


Figure 4-9: data from the linescan in Figure 4-8. The atomic percentages show an increasing proportion of C as the interaction volume moves over the edge of the glass into the surrounding resin (a). By removing the C data and converting and normalising counts to weight percentages of oxides, the composition of the outermost surface is characterised (b). Statistical errors for oxide determination become unacceptably high as the amount of C detected from the resin increases.

To illustrate the data manipulation involved for quantifying EDXA data gathered from the outermost 1-3μm of the specimen, an example is shown of a linescan conducted across the depleted surface of B2-32, which had been revealed after the corrosion crust had spalled away (shown in Figure 4-8).

The 3.7μm distance between individual spot analyses prevents interaction volume overlap but, as the points reach the outer surface, an increasing proportion of the interaction volume impinges upon the resin (shaded area in Figure 4-8). This results in an increasingly larger atomic percentage of C in the EDXA data and a subsequent decrease in values for all other constituents (Figure 4-9a). Thus in spectra 4 and 5, where significant interaction volume overlap with the resin has occurred, C constitutes respectively 50% and 75% of the total atomic count. These C values are higher than expected considering the actual fraction of interaction volume over the resin, and are due possibly to carbonaceous residues on the glass surface from the polishing process that increase the presence of C (although C in the actual depleted region cannot be ruled out), or could derive from the comparatively larger interaction volume in the resin with respect to the glass, given the lower density of the resin and the resulting higher electron scattering within it. Accordingly, the last data point (spectrum 6, not visible in Figure 4-8) yielded over 95% C although only 75% of its interaction volume fell into the resin.

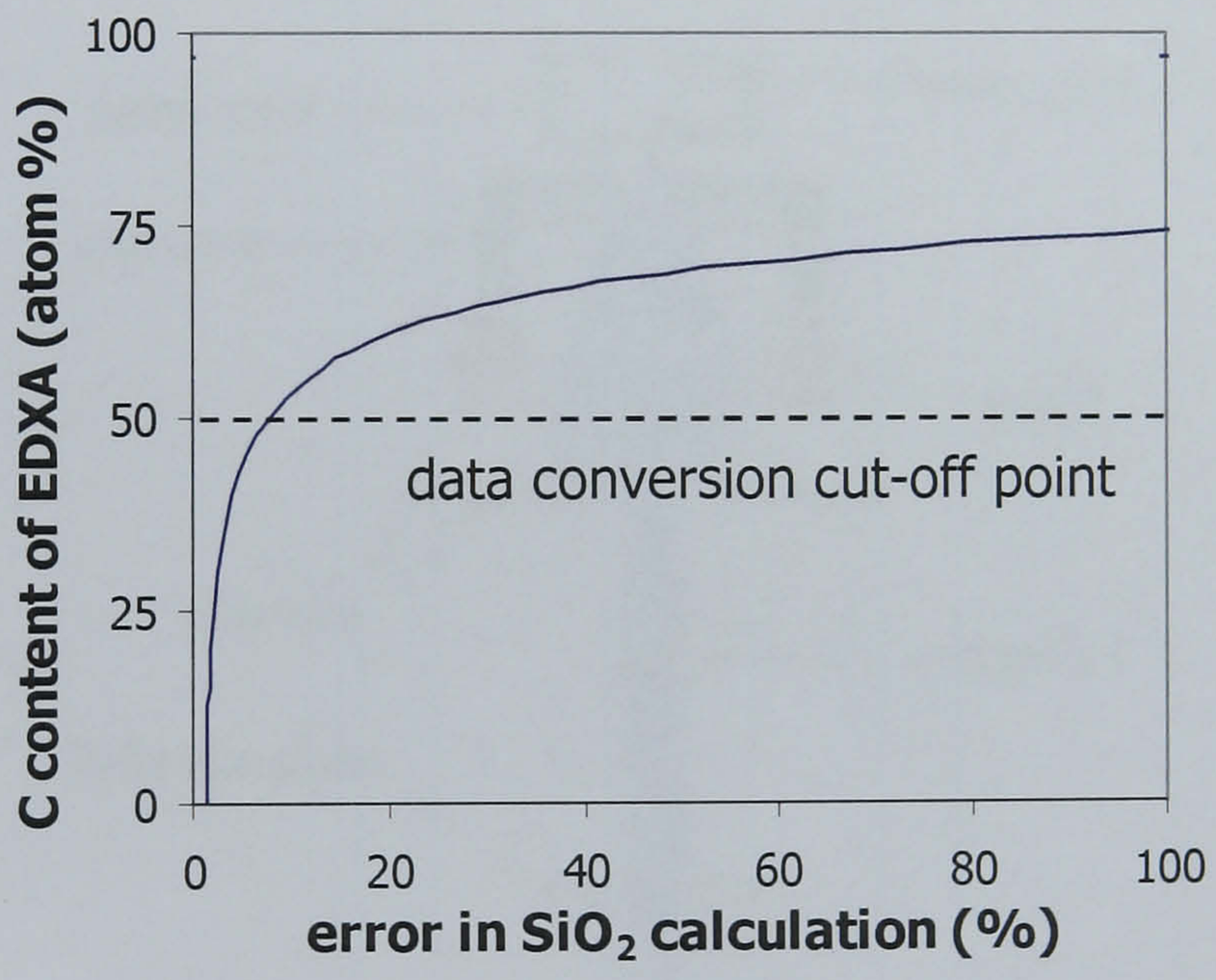


Figure 4-10: diagram illustrating the increasing errors involved in wt% determination of SiO_2 as the atomic% of C detected by EDXA increases. As errors increase dramatically above 50 atomic% C due to the decreasing SiO_2 counts, this value was fixed as the error limit for data conversion. The initial 3% error for SiO_2 had increased to 12% at the cut-off point.

The C counts for each data point were removed and the remainder converted to wt% oxide in order to express the glass composition in terms of its constituent oxides. In this way the depleted outermost surface layer could be characterised (Figure 4-9b). A limitation of this method is constituted by the errors accrued from the data manipulation: the higher the proportion of C in the original data, the higher the increase in errors associated to the oxides. This is shown in

Figure 4-10. The statistical error for SiO_2, for example, increases exponentially for increasing atomic percentages of C in the EDX data to be removed because Si, like other elements in the glass, represents an increasingly smaller proportion of the total data collected. Statistical errors with EDS data are in fact proportional to the square root of the number of counts[1]. Thus if 50% of atomic counts for a given total of counts are C, the resulting SiO_2 imprecision rises to ~12%, for 75% of atomic C percentage the error increases above 100%, which is clearly unacceptable. Therefore spectrum 4 in the aforementioned linescan represents the limit of glass composition determination within reasonable error (spectra 5 and 6 were not considered for this reason), and spectra 2-4 represent the depleted outer surface on sample B2-32 over an actual distance of 3x3.7 sin (15±1) = 2.9±0.3μm perpendicular to the surface. This process has been followed for all linescans conducted across glass surfaces mounted in cross-section.

4.5.2 Focused Ion Beam (FIB) Microscopy

Focused Ion Beam (FIB) systems have been commercially available since the late 1980s and are routinely used by the semiconductor industry[11]. In more recent years FIB technology has found more widespread use in a variety of applications. FIB technology has not previously been widely applied to archaeometric studies.

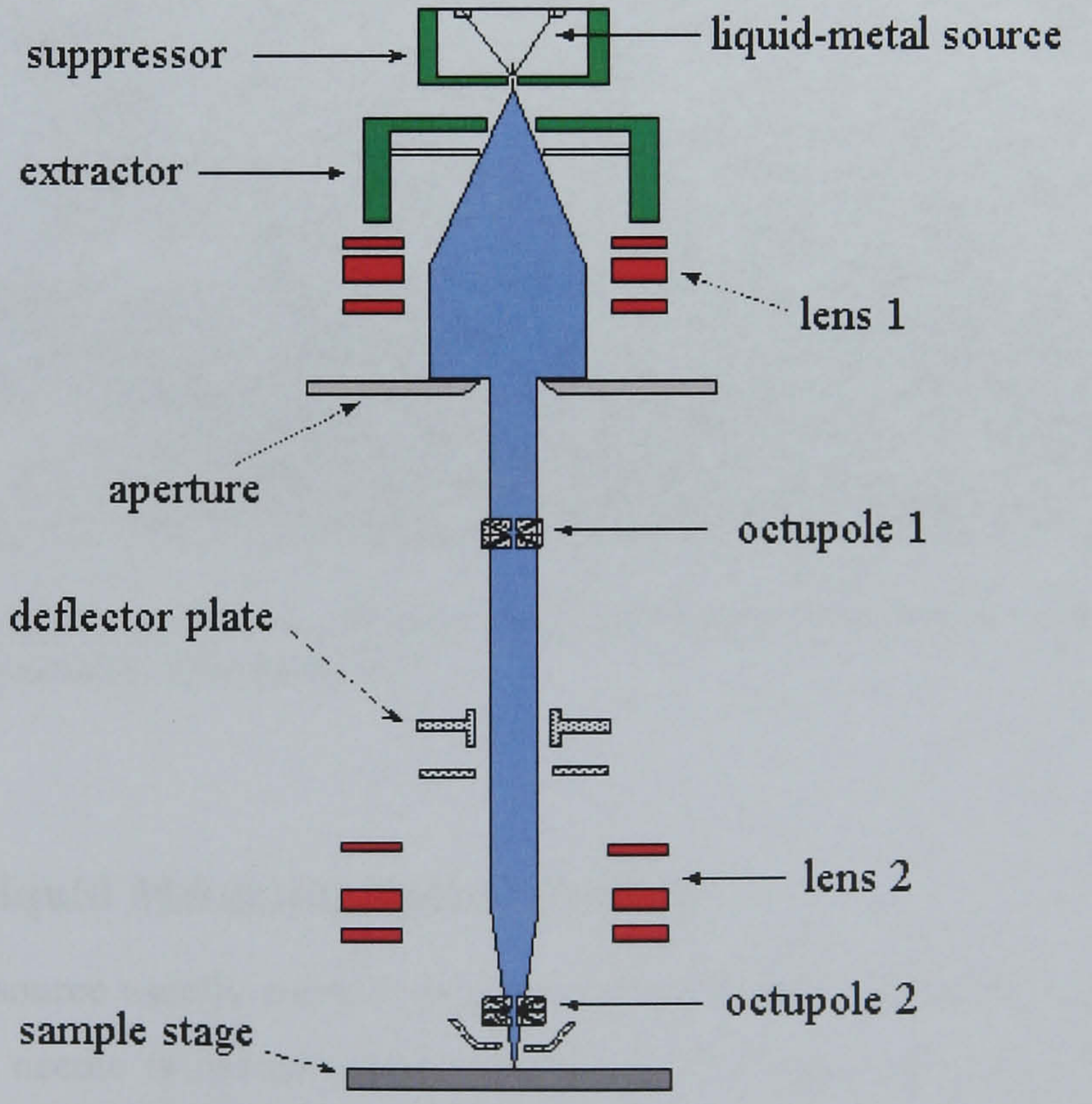


Figure 4-11: schematic diagram of an ion column in a focused ion beam spectrometer, based on Lehrer[12].

The construction of a FIB workstation is similar to that of an electron microscope and is illustrated in Figure 4-11. The sample is fixed on a multi-axis tilt stage located in a UHV

chamber. The chamber is connected to an ion column inside which ions are generated, accelerated and focused to a spot <1μm in diameter on the sample surface by a combination of lenses, octupoles and apertures. Ions are generated from a liquid metal ion source (LMIS). As the ion beam can be rastered across a surface area and the emitted species collected, the technique offers powerful ion and electron imaging capabilities.

An FEI Strata 200TEM Focused Ion Beam (FIB) microscope equipped with electron and ion detectors was used to study glass weathering layers and is shown in Figure 4-12. A low-energy (30keV) FIB column was generated from a liquid Ga source held at high vacuum (<7 x 10^{-7} mbar). Typical low beam intensities of 10-100pA were used for ion and electron imaging, and higher intensities of 500pA-20nA were used for ion milling and SIMS data collection.

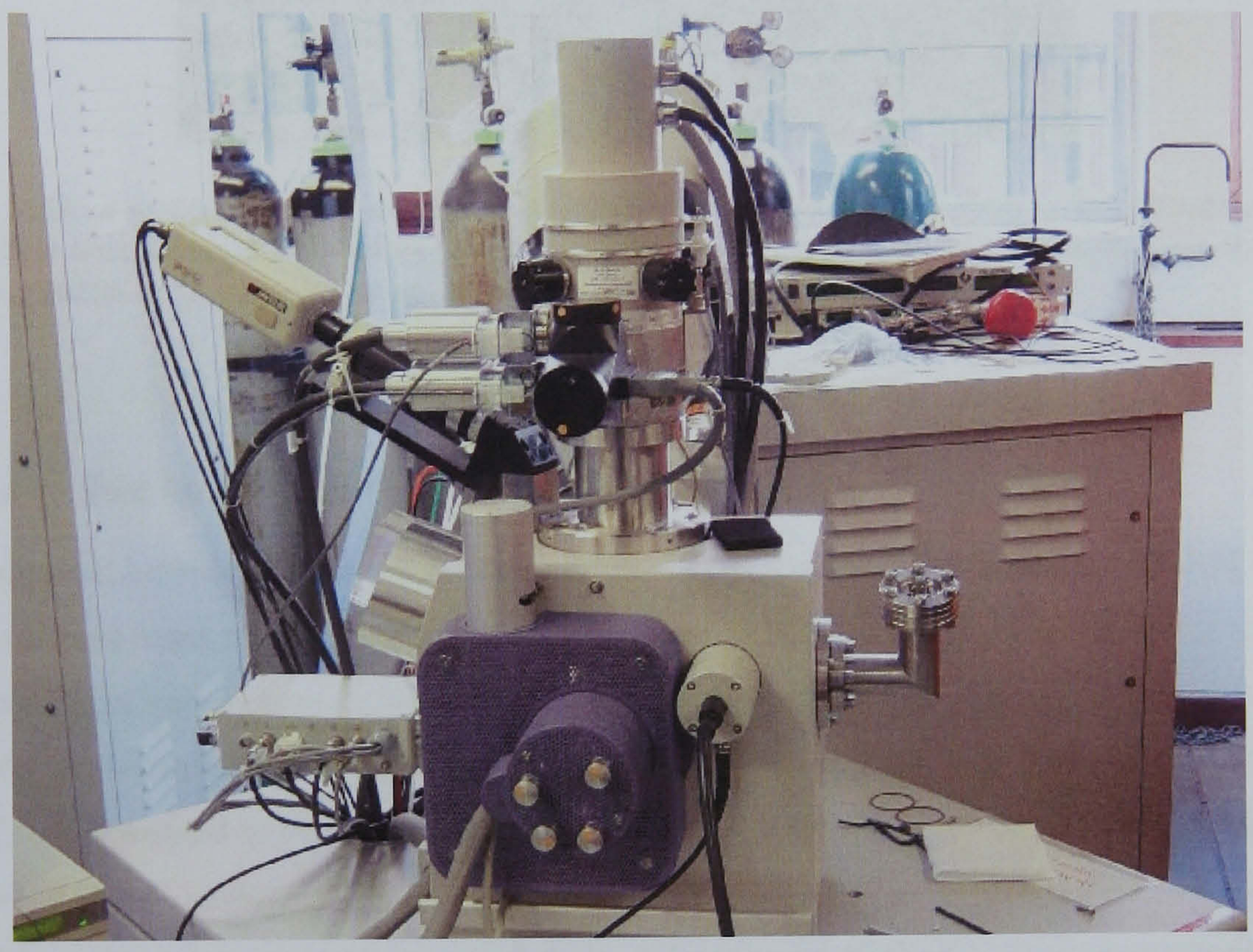


Figure 4-12: the ion column and main chamber of the FEI Strata T200 FIB workstation. The SIMS detector is visible as a separate unit, back right.

4.5.2.1 The Liquid Metal Ion Source (LMIS)

A liquid metal ion source usually consists of a metal-coated blunt needle with an end radius of around 10μm. The needle is heated to the melting point of the metal coating it and a high positive voltage (~2-10kV) is placed on it relative to a nearby extraction electrode. At the tip of the needle the liquid metal is drawn into a conical shape by the balance of electrostatic and surface tension forces and forms a very high electric field. The apex of the cone is so small (believed to be around 5nm in radius) that field evaporation takes place in much the same way as in field emission techniques (cf. FE-SEM outlined in Section 4.2.2.1); atoms or ions can

evaporate from a surface on which the potential barrier against evaporation has been lowered by the electric field. To make the ion beam stable, the liquid is confined to the surface of the needle. A typical LMIS is shown in Figure 4-13.

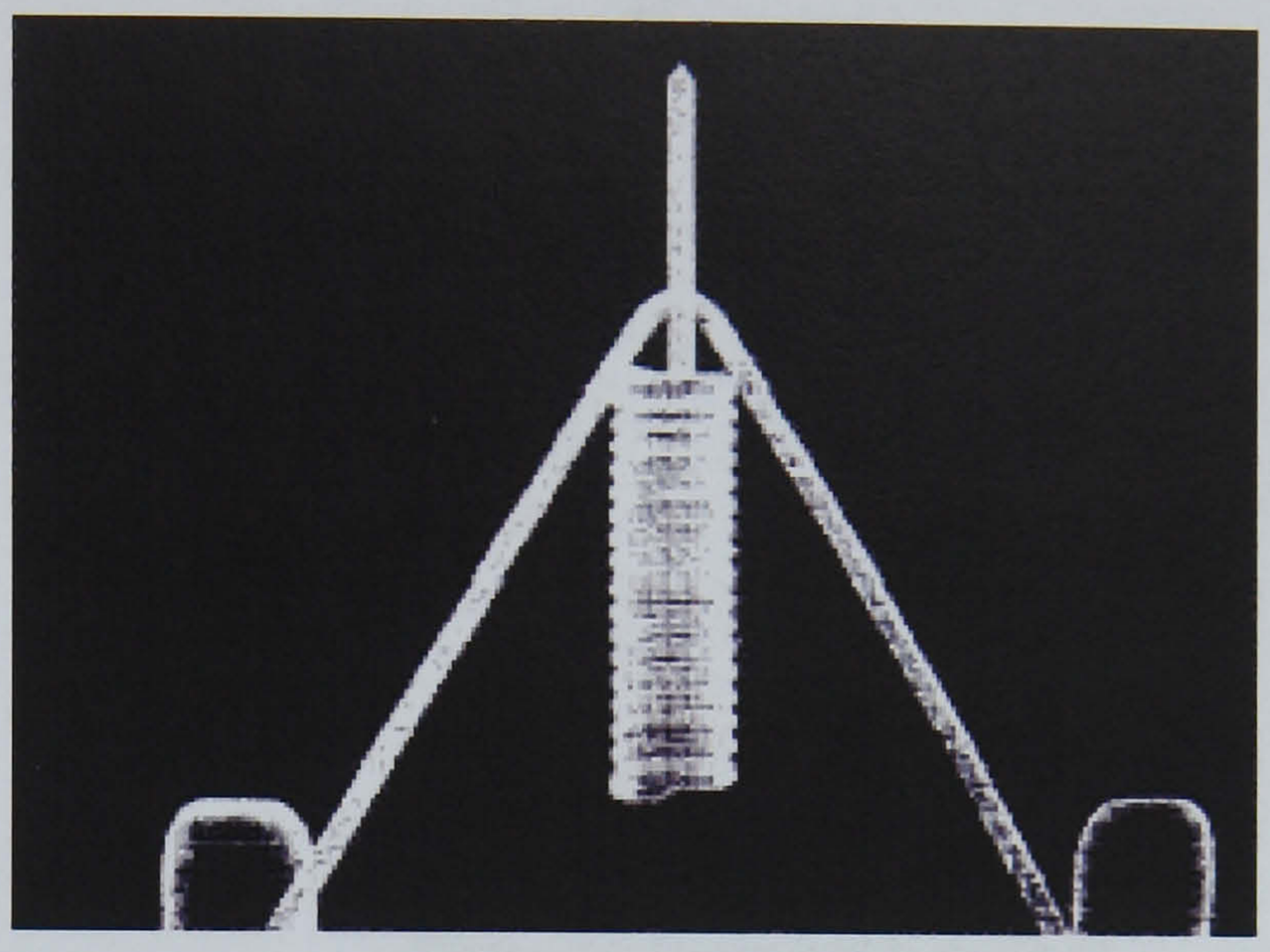


Figure 4-13: a typical liquid-metal ion source substrate showing a W needle and a spiral reservoir welded to a heating loop. The reservoir is approximately 3mm long and holds enough liquid Ga to last for about 1000h at 3μA extraction current[13].

4.5.2.2 Ion beam interaction with the surface

In its simplest terms, this technique involves the bombardment of the surface of a solid sample with a focused beam of mono energetic primary ions (at 30keV in the present case) in a vacuum. The transfer of momentum between the incoming ions and the constituent atoms leads to the emission of secondary species from the surface of the material. This process is known as sputtering (illustrated in Figure 4-14). The sputtered species may be neutral or charged particles. As the ion beam continues to raster across the surface of the sample, it sputters material from the surface. The charged particles can then be detected and analysed using conventional mass spectrometry analysis (see Section 4.5.2.4).

The bombarding ions, known as primary ions, lead to a series of effects on the surface. The implantation of the primary ions into the sample generates a collision cascade, whereby the kinetic energy of the bombarding ions is transferred via a series of collisions with the host atoms in the sample matrix. Recoil implantation and cascade mixing are two of the major interactions between the primary ion beam and the target atoms[14]. Recoil implantation occurs when there is direct collision of the primary ions with the sample atoms that are then driven further into the solid. Cascade mixing involves the collision of the primary ion and host atoms, which in turn continue to collide with the surrounding atoms. This continues until the system reaches equilibrium. After a period of continued bombardment, not only is the sample surface

damaged, but also its composition may vary compared to the bulk. This damaged region is known as the altered layer and is a limiting factor of depth resolution.

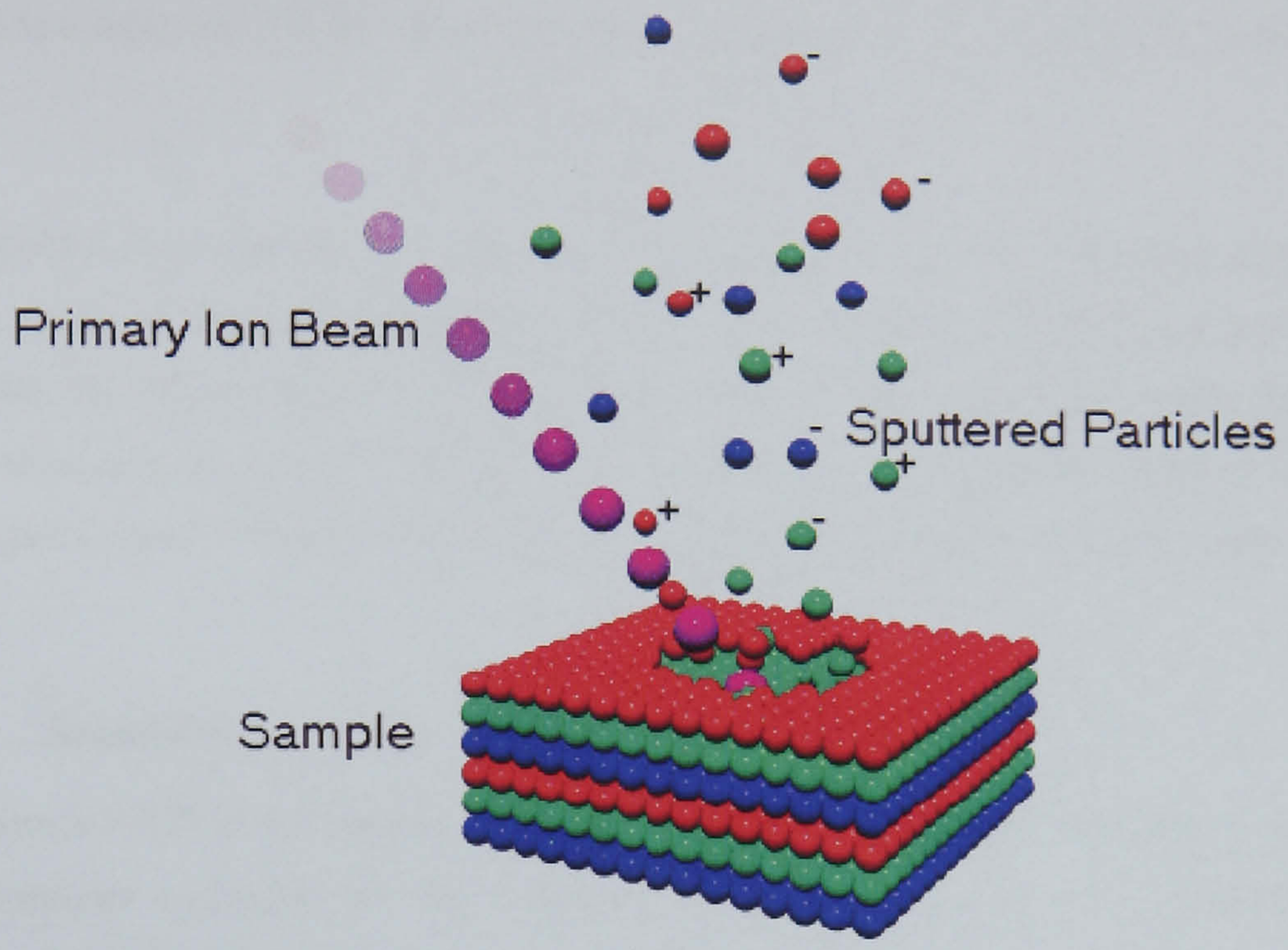


Figure 4-14: schematic of the sputtering process that occurs during ion beam bombardment[15].

4.5.2.3 Scanning Ion Microscopy (SIM)

Due to the focused nature of the beam, FIB systems have led to the development of ion microscopy. Scanning ion microscopy (SIM) is analogous to scanning electron microscopy (SEM). In both cases a beam of charged particles is focused onto the surface of a specimen or target and rastered across it. In the case of 20-30keV incident ion beam energies, the signals detected are secondary electrons and secondary ions emitted from a depth below the surface of the order of a fraction of a nanometre. As significantly more secondary electrons are emitted, they generally provide images of better quality and resolution compared to secondary ion images. The typical electron beam interaction volume can be several microns deep, so SIM is more sensitive to details of surface structure in the target than SEM. A high imaging resolution of 25-50nm is obtainable with a typical FIB system[13]. The ion-induced secondary electron yields are also very sensitive to changes in angle between the ion beam and the specimen surface, so that secondary electron images tend to have a very strong contrast. High-resolution secondary ion images of non-conducting materials such as glass are obtainable with SIM, as sample charging can be neutralised with a low energy electron beam that has little or no influence on the ion imaging collection efficiency. Thus it is not necessary to coat the specimens with carbon or gold prior to analysis.

As the ion beam causes rapid damage when it is rastered across very small areas (<15μm^2 in this study), minimal exposure to the beam is essential in order to preserve detailed morphological characteristics. Preliminary scans that were necessary in order to fine-tune focus and stigmation were kept to a minimum before the images were taken so as to avoid sputtering of the exposed surface.

Selected glasses from Tell Zujaj were mounted on adhesive conducting strips on an aluminium stage and placed in the vacuum chamber. As the corrosion crust is both fragile and brittle by nature, even the lightest handling operation caused extensive flaking. Fragments detached in this way were placed alongside the glass for inspection so that freshly exposed weathering morphologies could be viewed by rotating and tilting the stage relative to the ion beam.

4.5.2.4 Secondary Ion Mass Spectrometry (SIMS)

The FEI Strata 200TEM FIB system is also equipped with a quadrupole secondary ion detector and spectrometer controlled by the SIMSmap IIIxP Analysis system. The combination of secondary electron and secondary ion imaging with SIMS mass spectroscopy and depth profiling provides a particularly powerful analysis technique. However, much experimental work was necessary to optimise the newly acquired system for ancient glass analysis with mixed results. Maximising the secondary ion counts proved to be a delicate interplay between:

a) operating conditions – ion dose, ion detector settings (grid and front end voltages), electron beam settings (grid voltage and beam energy)
b) surface morphology
c) angle of tilt

4.5.2.4.1 The SIMS equation

Secondary ions are amongst the species emitted from the surface of a sample upon interaction with an ion beam, and are collected by the application of a suitable acceleration potential to the surface. The secondary ion yield is strongly influenced by the electronic state of the material being analysed, with consequent complications for quantitative analysis. The basic SIMS equation is:

$$I^m{}_s = I_p y_m \alpha^+ \theta_m \eta \qquad [4.5]$$

where $I^m{}_s$ is the secondary ion current of species m, I_p is the primary particle flux, y_m is the sputter yield, α^+ is the ionisation probability to positive ions, θ_m is the fractional concentration

of m in the surface layer and η is the transmission of the analysis system. Sputter yield, defined as the ratio of the number of atoms sputtered to the total number of incoming atoms, and ionisation probability, which corresponds to the fraction of ionised atoms, are the two fundamental parameters involved in SIMS. Positive or negative ions can be detected across the entire range of atomic weights.

4.5.2.4.2 Electron beam compensation

SIMS characterisation of insulating materials such as glass is problematic; build-up of charge under the ion beam causes a rapid rise in surface potential that energises emitted ions to levels outside the detection window of the detector, with a resulting drop in transmission. A common method of compensating for this is to flood the surface with a low energy electron beam (Figure 4-15). Charge neutralisation is generally achieved when there is a dynamic balance among the incident current (electron and ion currents), the emitted current (secondary ions and electrons) and leakage currents to ground.

The electron gun parameters (shown in Figure 4-16) were only vaguely outlined by the manufacturers, and needed to be optimised. The electron gun has to work at negative ion detector settings, presumably in order to avoid deflecting the beam away from the sample, which alone significantly suppresses the positive ion counts. The electron beam was found to compensate best when the electron current was fixed at approximately 100 times the ion beam current by balancing the electron beam settings (grid voltage and beam energy).

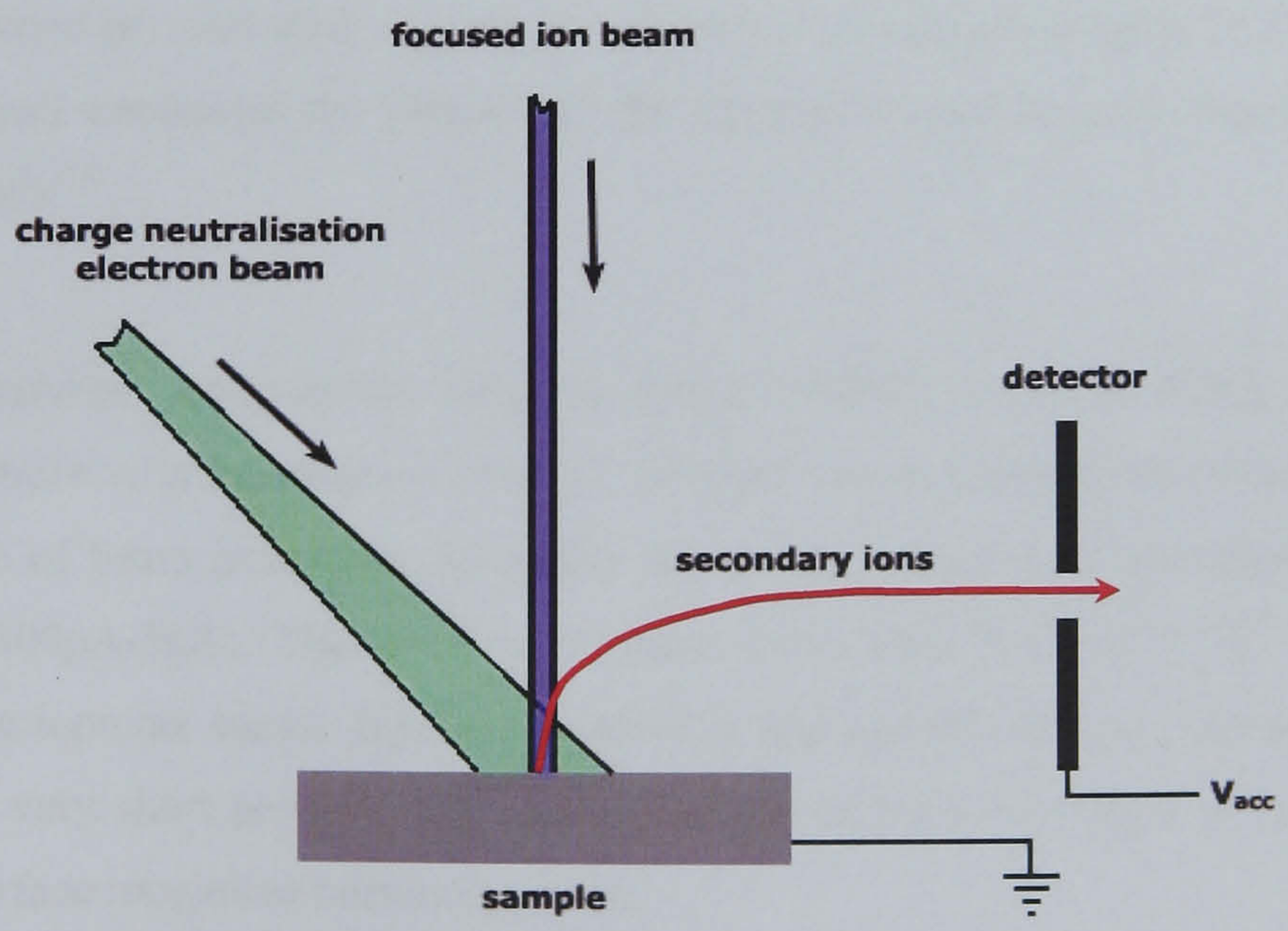


Figure 4-15: schematic of the operation of electron beam charge neutralisation.

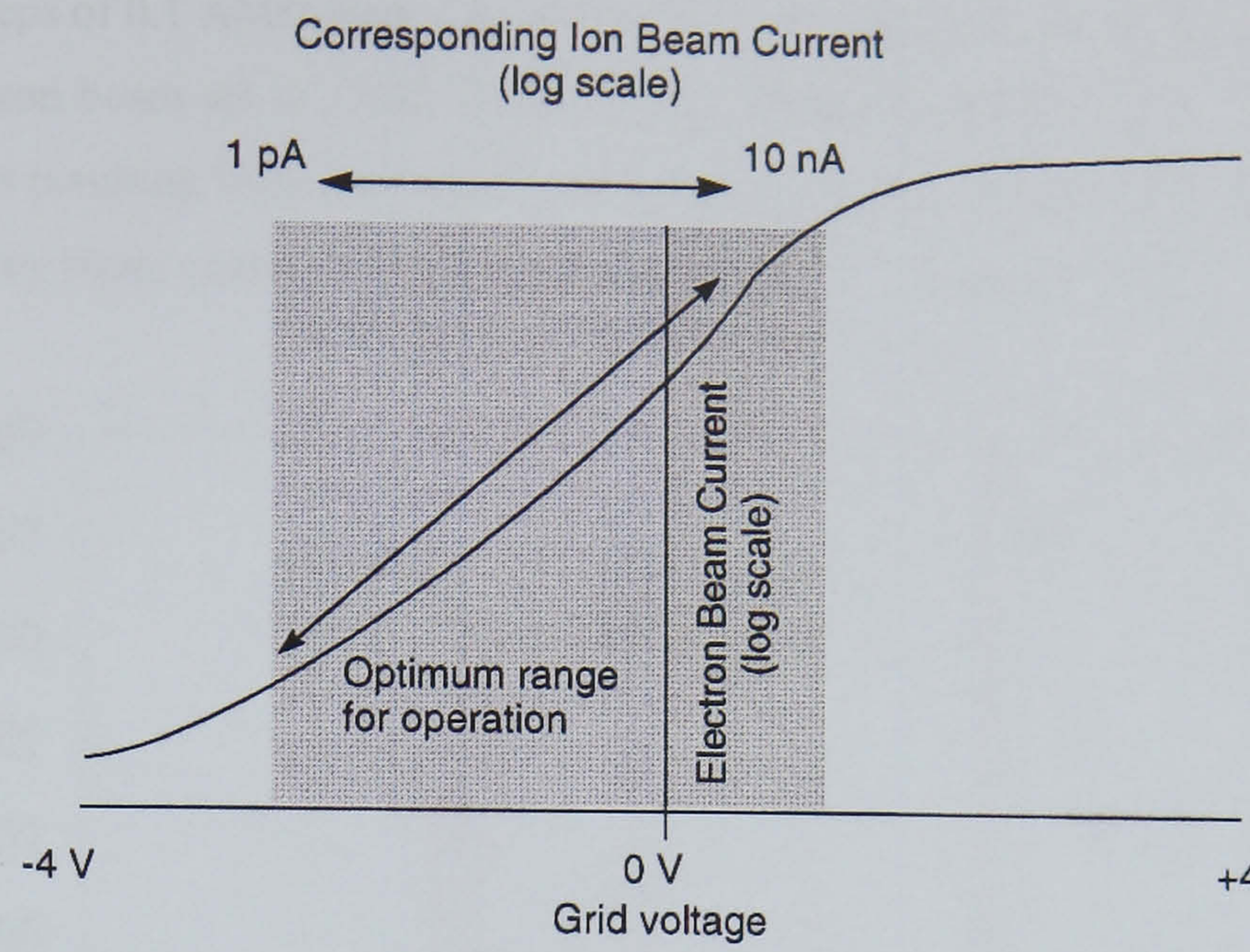


Figure 4-16: operating range of the electron gun, as outlined by the manufacturer, FEI. Charge compensation was thus obtained experimentally by adjusting electron gun grid voltage and setting electron beam current to appropriate values.

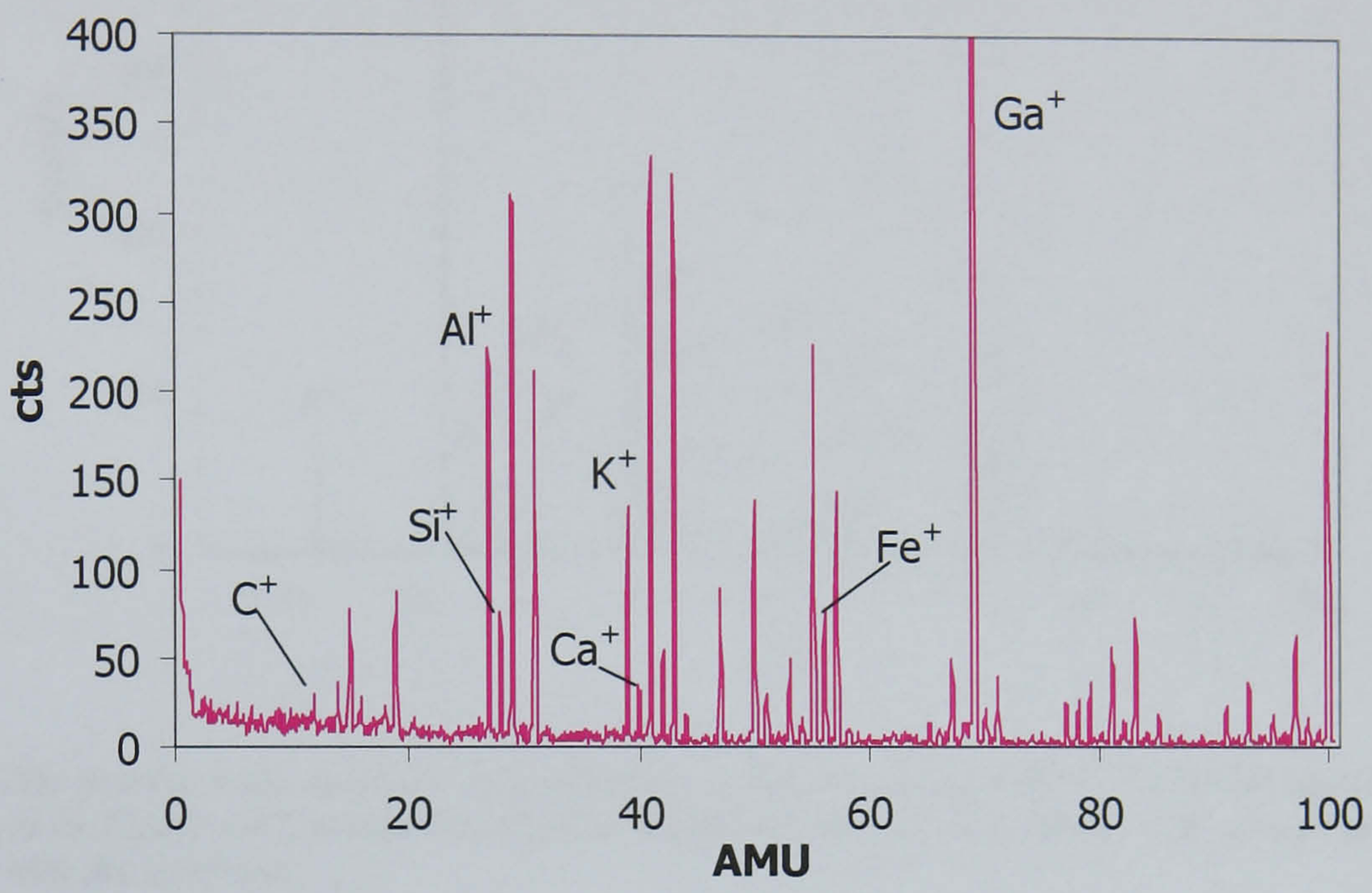
4.5.2.4.3 Static SIMS

Static SIMS involves collecting a mass spectrum of the sample surface over a predefined range of atomic mass units (AMU) where regions of damage to the topmost atomic layer do not overlap. For inorganic materials it is assumed that static conditions are about 1 $nA \cdot cm^{-2}$, with a total particle dose of about 10^{13} cm^{-2} (measured as the number of particles hitting the sample surface per second per unit area). Such a particle dose corresponds roughly to 1% of the surface atoms so at such conditions the lifetime of the topmost atomic layer is expected to be in the order of 10^3-10^5s[16].

The FIB workstation seems better suited to dynamic SIMS; the static SIMS conditions were difficult to achieve with the range of small (1-1000μm^2) surface areas that could be selected and with the range of beam intensities for which ion counts were clearly distinguishable from the background (300pA-5nA). The ion dose in many cases rose easily to $>10^{15}$ ions $cm^{-2} \cdot s^{-1}$, in which case the topmost atomic layer is expected to last seconds or less. This limited spectrum acquisition to very short periods with concurrent loss of peak resolution or to larger areas, in which case surface roughness became an issue.

If the beam energy of the charge neutralising electron beam was raised too much, the ionisation of CH^+ and CF^+ groups in the chamber suppressed yields from the sample. An example of this is a positive mass spectrum of B3-9 shown in Figure 4-17. Ions were counted for 0.02s in

incremental steps of 0.1 AMU from 1 to 100 on a 240μm^2 surface area with a 5nA ion beam and a 500nA electron beam set at 150eV beam energy. Although the spectrum is clean and counts are high, peaks resulting from the sample constituents are obscured by CH^+ and CF^+ peaks. The most satisfactory beam energy settings were found between 80 and 100eV.



m/z	species	m/z	species	m/z	species
15	CH_3^+	47	CFO^+	81	$C_6H_9^+$
19	H_3O^+	50	CF_2^+	83	$C_6H_{11}^+$
27	$C_2H_3^+$	53	$C_4H_5^+$	91	$C_7H_7^+$
29	$C_2H_5^+$	55	$C_4H_7^+$	93	$C_7H_9^+$,$C_3F_3^+$
31	CH_3O^+,CF^+	57	$C_4H_9^+$	95	$C_7H_{11}^+$
39	$C_3H_3^+$	67	$C_5H_7^+$	97	$C_7H_{13}^+$
41	$C_3H_5^+$	77	$C_6H_5^+$	100	$C_2F_4^+$
43	$C_3H_7^+$	79	$C_6H_7^+$		

Figure 4-17: positive mass spectrum of B3-9 taken with a 5nA ion beam and a 500nA electron beam set at 150eV beam energy. The CH^+ and CF^+ ion groups, listed in the table by increasing mass to charge ratio, interfere with the peaks from the glass.

With polished cross-sections reproducibility was more easily obtained for positive spectra. An example of this is given in Figure 4-18 for a polished section of sample TZ143. Analysis conditions are the same as for the previous sample except that electron beam energy is fixed at 100eV and the grid voltage adjusted to produce a 500nA electron beam. The peaks corresponding to the constituent cations in the glass are visible although CH^+ peaks are still seen to interfere and the $^{28}Si^+$ peak in particular in depressed. However, for irregular surfaces such as those of corroded glasses, microscopic roughness did not make any reproducible results possible.

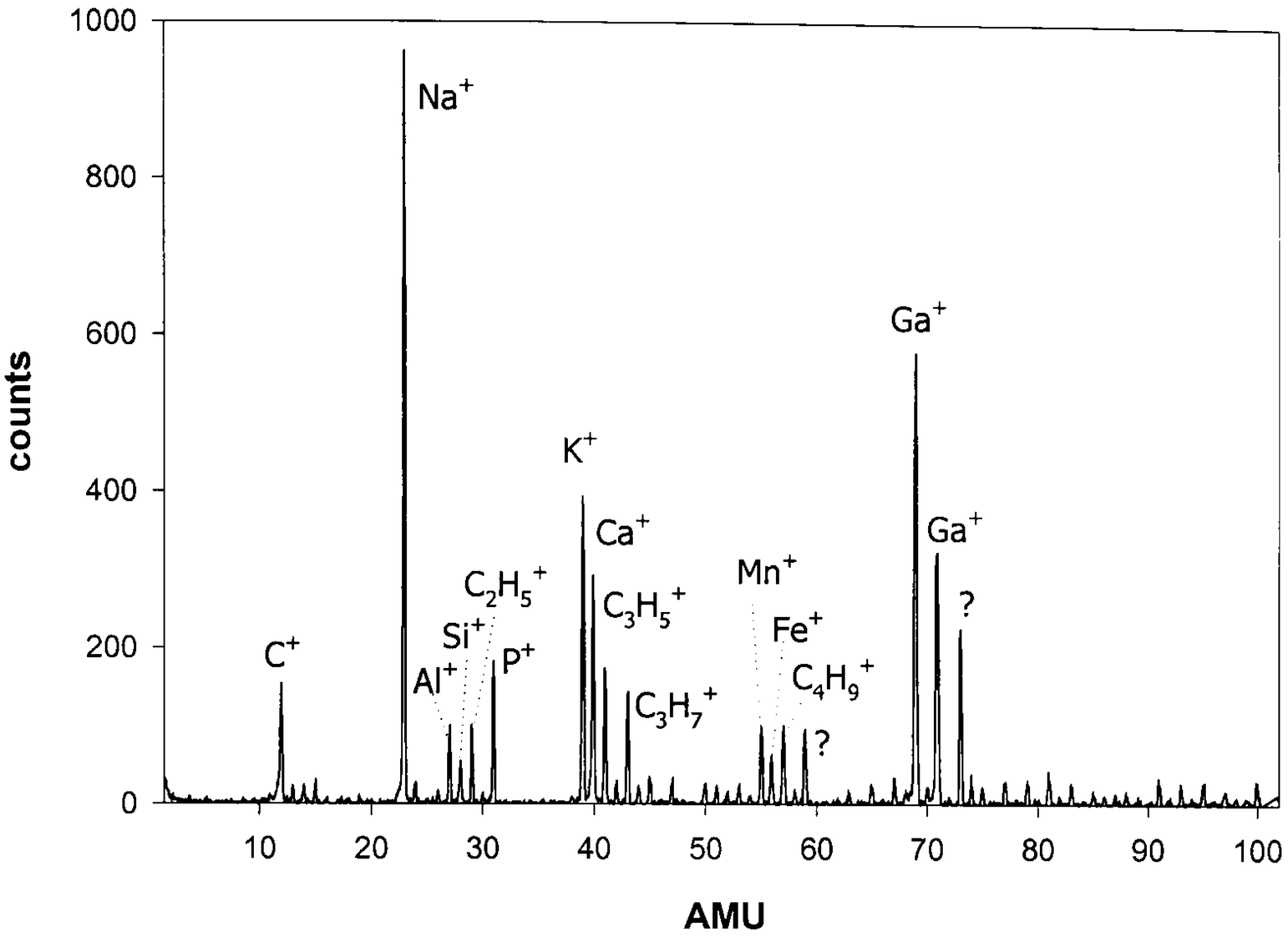


Figure 4-18: positive mass spectrum of a polished section of sample TZ143. Analytical conditions are the same as in Figure 4-17, except that electron beam energy is fixed at 100eV. CH^+ groups are seen to interfere with the spectrum.

4.5.2.4.4 Dynamic SIMS

In dynamic SIMS, as the damage to the surface from the continued sputtering of species results in the formation of a crater, the variation in counts with crater depth of selected atomic masses is charted to give a depth profile. The FIB mills very precise holes with near-vertical crater walls and proved very useful in exposing details below the surface (see Section 9-4). Beam intensities of >1nA were used for all milling operations. A crater aspect ratio of length:depth of at least 3:1 was necessary to maintain the walls coherently formed but it was observed that the base of the crater was often irregular. A typical uneven crater is shown in Figure 4-19. This is thought to be because the surface and structure of the sample were not homogeneous to begin with and because of beam instability caused by charging at the crater base. Uneven crater formation made data acquisition difficult and reproducibility unobtainable. In several attempts to acquire reproducible depth profiles, samples were coated with carbon or gold, painted with silver dag and *in situ* Pt deposition was carried out, all with less than satisfactory results. It would seem therefore that this bolt-on SIMS is ill equipped to deal with insulating, corroded materials and further work is necessary to develop a reproducible methodology for data acquisition.



Figure 4-19: secondary ion image of a 40x40µm crater viewed at 28°, on sample B3-9. The base is completely uneven and makes depth profile data interpretation very problematic.

4.5.3 Infrared Reflection Spectroscopy (IRRS)

4.5.3.1 Outline of technique

Infrared reflection spectroscopy (IRRS) has been used extensively for the quantitative analysis of leached surface layers on glass, as it is gives information about the structure of species in the outer 0.5µm of a sample. It is applicable to large or small glass surfaces, does not require a vacuum for operation, is rapid and inexpensive and requires only standard infrared spectrometers[17]. Infrared radiation is produced by electrically heating a Nernst filament (a high resistance, brittle element composed chiefly of Zr, Th and Ce oxides) or a rod of SiC. At temperatures between 1100 and 1800°C, depending on the filament material, the incandescent filament emits radiation over the whole infrared spectrum on to the sample[18]. The beam is dispersed by a prism or grating. A monochromator filters the reflected light through narrow exit slits to ensure that a detector can measure only the energy of radiation of a narrow frequency range at a time and transform it into an electrical signal. Data is represented as a plot of wavenumber against intensity. Specific molecular bonds vibrate when subject to radiation of certain infrared frequencies. The vibrations lead to changes in intensity at characteristic

wavenumbers and thus give rise to peaks on the plot, which can be used to identify the emitting species on the surface.

A Spectratech IR-Plan double beam infrared spectrometer was used for analysis of Ballidon glasses. The beam was aligned using a mirror reference standard and spectra gathered for freshly cleaved vitreous silica and Ballidon glasses by scanning an infrared beam of wavenumber 600-4000cm^{-1} over the sample surface. One sample of each composition was fractured prior to analysis in order to reveal a new surface. In this way corroded and unreacted surfaces were inspected. All the spectra were curve-fitted with a Lorentzian curve-fitting technique. The margin of error (measured as the width of the flat apex of the curve at high magnification) was found to be ± 3cm^{-1} for the S and NSX peaks and ±5cm^{-1} for the R peak (see below).

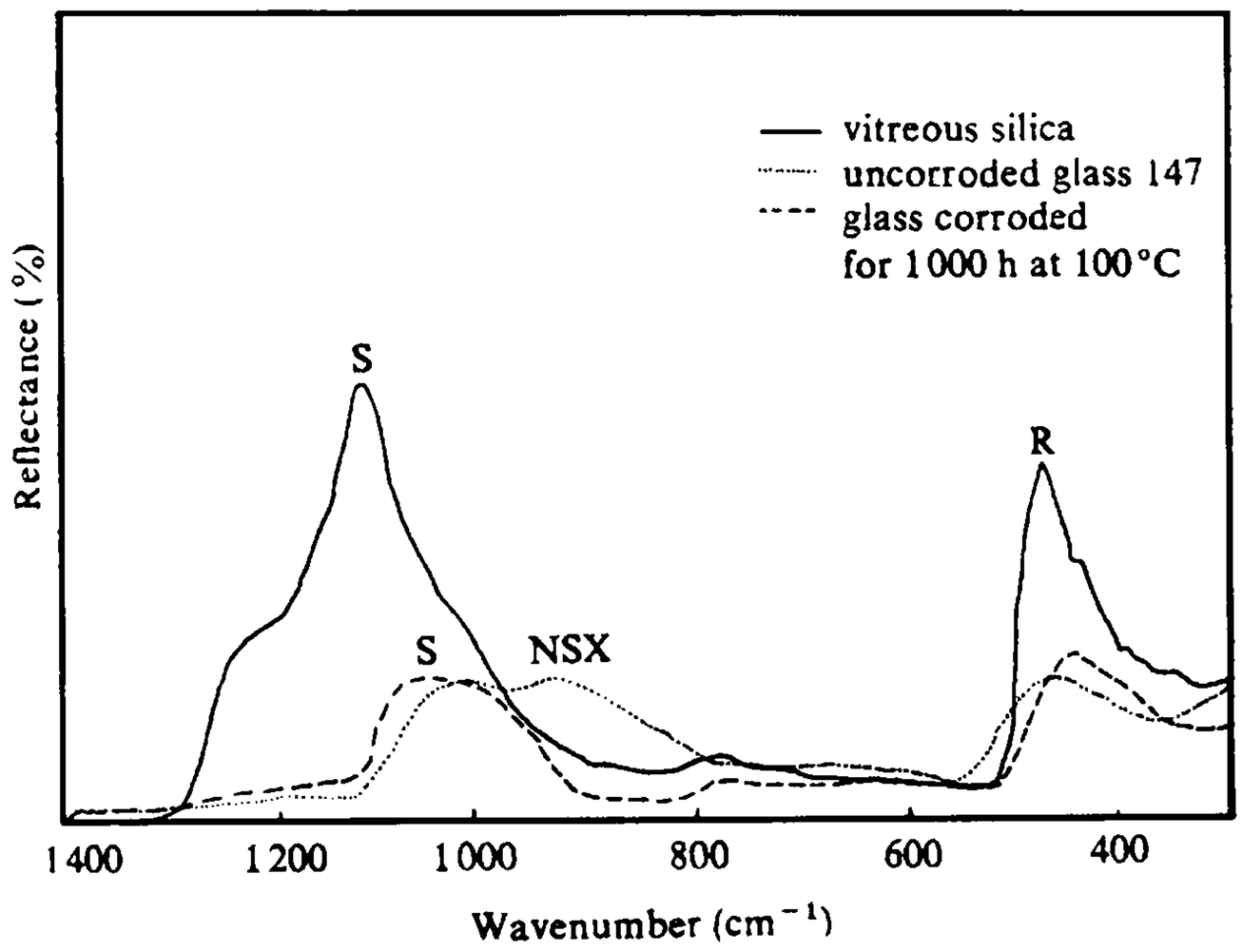


Figure 4-20: infrared reflection spectra of vitreous silica compared to a KLS glass before and after corrosion. From Hench et al.[19].

4.5.3.2 Interpretation of reflectance spectra of glass

The Y axis in an IRRS spectrum represents the relative reflectance of the sample in comparison to the mirror and is expressed as %R. 100% R implies that the radiation reflected from the specimen is equivalent in intensity to that reflected from the mirror. The main area of interest for determining the structural characteristics of glass lies in the region between 1200cm^{-1} and 400cm^{-1} as this is where the three major peaks related to glass structure are located (see Figure 4-20). The S peak at 1120cm^{-1} for vitreous silica is due to the Si-O-Si stretching vibrations in the glass network[19]. When network modifiers such as CaO or Na_2O are added to a glass the number of connecting Si-O-Si bonds in the glass structure decreases. With fewer Si-O-Si bonds in the network, vibrational interaction between the structural units is weaker and consequently

the location of the S peak vibrations decreases to a lower wavenumber. The S peak maximum was found to shift linearly for ternary SLS glasses with Na_2O contents up to 22 mol%[20]. Rocking vibrations of Si-O-Si bonds in the glass network give rise to the R peak that is situated at 480cm^{-1} for vitreous silica and, similarly to the S peak, at lower wavenumbers for the KLS glass in the figure. The presence of the network modifier in the glass decreases the intensity of the R peak and makes it broader.

Network modifying cations in the glass structure give rise to a second type of stretching vibration, Si-O-X, where X is any modifying cation such as Na, Ca, K or Mg. These vibrations, termed NSX, involve silicon ions bonded to non-bridging oxygens, i.e. oxygens that cannot form a link within the glass network because they are bonded to an alkali or alkaline earth cation as well as a Si ion. Because of the weaker bond, the NSX peak is located at a lower wavenumber, 960cm^{-1}, than the S peak.

A number of authors[20, 21] have reported an increase in the wavenumber of the S peak with increasing time of exposure to a leaching solution. This has been attributed to the formation of a silica-rich surface layer as alkali or alkaline earth cations are leached from the glass surface to be replaced by H^+ ions, H_3O^+ ions and/or water molecules. Similarly a decrease in the wavenumber location of the NSX peak has been attributed to a reduction in the concentration of modifying cations in the leached surface layers.

4.6 Bibliography

1. Goodhew, P.J. and F.J. Humphreys, *Electron Microscopy and Analysis,* Second Edition. 1988, London: Taylor & Francis Ltd.

2. Henderson, J., *Electron Probe Microanalysis of Mixed-Alkali Glasses.* Archaeometry, 1988. **30**(1): p. 77-91.

3. Scott, V.D., G. Love, and S.J.B. Reed, *Quantitative Electron Probe Microanalysis*. 1995, Ellis Horwood.

4. Heinrich, K.F.J. and D.E. Newbury, *Electron Probe X-Ray Analysis*, in *Materials Characterisation*. 1991, American Society for Metals: Ohio. p. 516-526.

5. Kuisma-Kursula, P., *Accuracy, Precision and Detection Limits of SEM-WDS, SEM-EDS and PIXE in the Multi-Elemental Analysis of Medieval Glass.* X-Ray Spectrometry, 2000. **29**: p. 111-118.

6. Merkel, J.F., *Reconstruction of Bronze Age Copper Smelting: Experiments Based on Archaeological Evidence from Timna, Israel*. 1982, UCL: London.

7. Jackson, C.M., P.T. Nicholson, and W. Gneisinger, *Glassmaking at Tell el-Amarna: an Integrated Approach.* Journal of Glass Studies, 1998. **40**: p. 11-23.

8. Saleh, S.A., A.W. George, and F.M. Helmi, *Study of Glass and Glass-Making Processes at Wadi El-Natrun, Egypt in the Roman Period 30 B.C. to to 359 A.D.* Studies in Conservation, 1972. **17**: p. 143-172.

9. Lakatos, T., L.-G. Johannson, and B. Simmingsköld, *Viscosity Temperature Relations in the Glass System SiO_2-Al_2O_3-Na_2O-K_2O-CaO-MgO in the Composition Range of Technical Glasses.* Glass Technology, 1972. **13**(3): p. 88-95.

10. Lakatos, T., L.-G. Johannson, and B. Simmingsköld, *The Effect of Some Glass Components on the Viscosity of Glass.* Glasteknisk Tidskrift, 1972. **27**(2): p. 25-28.

11. Young, R.J., *Application of the Focused Ion Beam in Materials Characterization and Failure Analysis.* Microsctructural Science, 1997. **25**: p. 491-496.

12. Lehrer, C., *http://www.iis-b.fhg.de/en/arb_geb/technology_an_fib.htm*. 2000.

13. Orloff, J., *High-Resolution Focused Ion Beams.* Review of Scientific Instruments, 1993. **64**(5): p. 1105-1130.

14. Benninghoven, A., F.G. Rudenauer, and H.W. Werner, *Secondary Ion Mass Spectrometry: Basic Concepts, Instrumental Aspects, Applications and Trends*. 1987, New York: Wiley.

15. *www.simsworkgroup.org*.

16. Vickerman, J.C. and A.J. Swift, *Secondary Ion Mass Spectrometry - the Surface Mass Spectrometry*, in *Surface Analysis - The Principal Techniques*, J.C. Vickerman, Editor. 1997, John Wiley & Sons: Chichester. p. 135-213.

17. Clark, D.E., C.G. Pantano, and L.L. Hench, *Corrosion of Glass*. 1979, New York: Books for Industry and The Glass Industry.

18. Cross, A.D. and R.A. Jones, *An Introduction to Practical IR-Spectroscopy*. 3rd ed. 1969, London: Butterworths.

19. Hench, L.L., R.G. Newton, and S. Bernstein, *Use of Infrared Reflection Spectroscopy in Analysis of Durability of Medieval Glasses, with Some Comments on Conservation Procedures*. Glass Technology, 1979. **20**(4): p. 144-148.

20. Clark, D.E., et al., *Quantitative Analysis of Corroded Glass Using Infrared Frequency Shifts*. Glass Technology, 1977. **18**(4): p. 121-124.

21. Salem, A.A., R. Kellner, and M. Grasserbauer, *Study of Corrosion Processes in Glass by a Multitechnique Approach. Part 2. Infrared Spectroscopy*. Glass Technology, 1994. **35**(3): p. 135-140.

Chapter 5

Compositional characterisation of glass from Raqqa

The compositional data has been combined with published analytical results on glass from Tell Zujaj, and is discussed together as a whole. Initial discussions will focus on the date of the glass (in this case by site). This will be followed by a breakdown of analytical data in relation to its composition, with implications for changes in raw materials used and glass production over time. The relationships between compositional types, vessel form and colour will also be discussed. All of the glasses analysed were of a soda-lime-silica composition with two exceptions: a tessera fragment from 11th century Tell Fukhkhar, which was found to be opacified with Pb-Sn oxide and therefore to contain a high level of PbO and an emerald green window fragment from 11th-12th century Qasr al-Banât (see Section 5.2) which was found to be of a PbO-SiO_2 composition.

5.1 Tell Zujaj

Figure 5-1 shows a plot of MgO and Al_2O_3 contents of 127 new analyses of 'Abbasid glass fragments from Tell Zujaj, along with previously analysed and discussed samples of cast glass, vessel glass and frit from Tell Zujaj and window and vessel glass from the contemporary palace complexes at Raqqa[1]. With the extra data, the major compositional groupings originally outlined are confirmed; both a low MgO SLS glass (LMG) and a high MgO SLS glass (HMG), respectively labelled Raqqa types 3 and type 1, were in use contemporaneously at Tell Zujaj. This underlines the fact that a plant ash based HMG recipe was in use at al-Raqqa by the early 9th century. The type 1 composition is present in a range of vessel forms and shapes and especially cast glass.

Chemical analysis of production waste included chunks of glass attached to tank furnace fragments of type 1 (analysis 82, analysis 3 and analysis 15), type 2 (analysis 77, analysis 5 and analysis 22), and type 4 (analysis 87 and analysis 17). In addition, chemical analysis of moils from blowing irons provides unambiguous evidence that glass of all four identified compositional types was being blown on or near the site. As well as Raqqa types 1 and 3

compositions, two possible 'workshop' compositional groups, type 2 and type 4 (including subtype 4a) have previously been tentatively suggested[1]. Originally types 4 and 4a were linked; with the extra samples reported here the group forms a negatively correlated cloud in Figure 5-1, evenly spread across a range of MgO and Al_2O_3 levels, and will be referred to henceforth as type 4. Eight samples fall into compositional type 2, which similarly forms a loose negative correlation between types 1 and 3 in Figure 5-1. The significance of these negative correlations is discussed in more detail in Section 5-5.

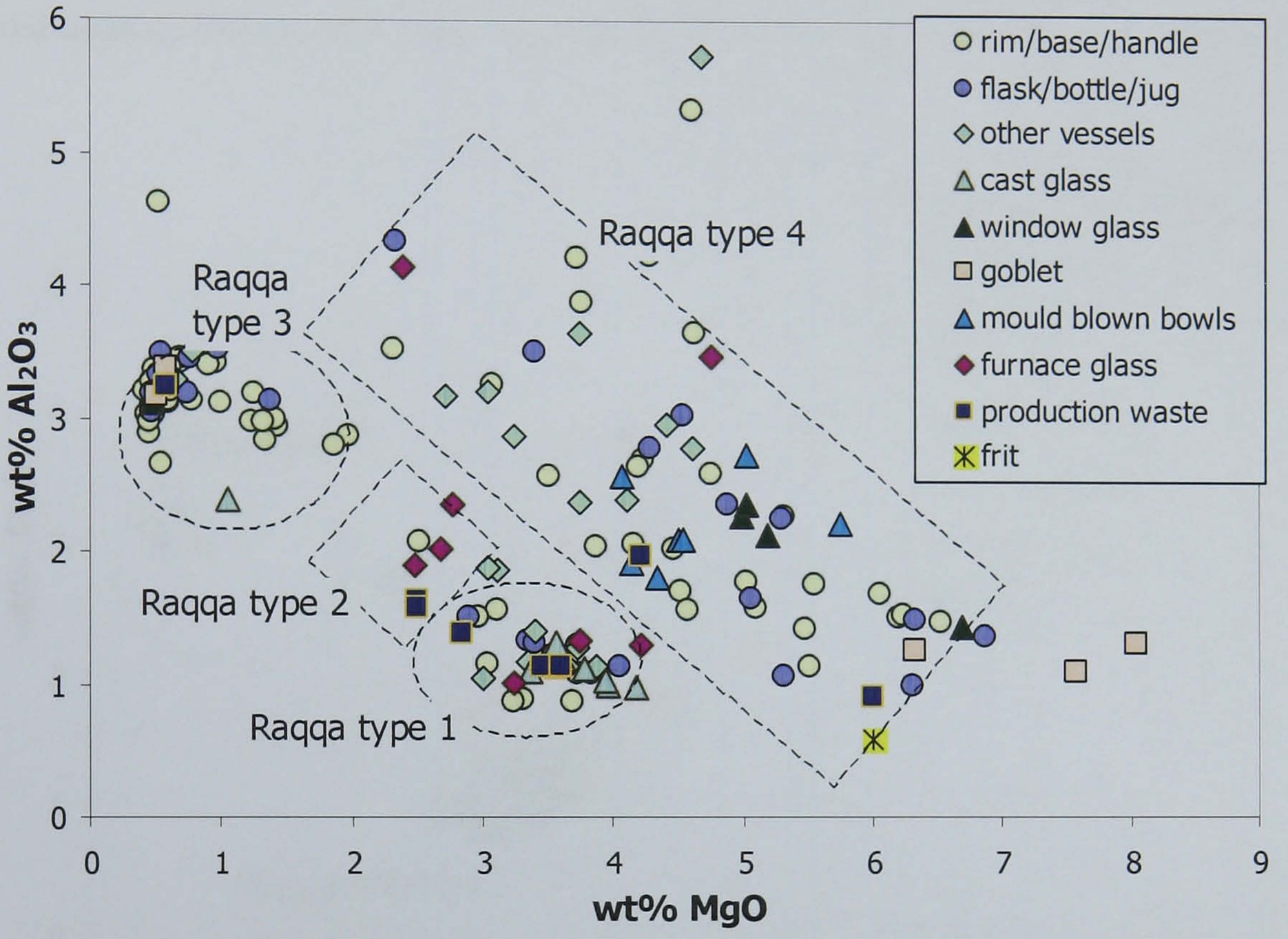


Figure 5-1: MgO vs. Al_2O_3 for 127 Tell Zujaj glass fragments. The plot includes previously published results[1] from Tell Zujaj and contemporary palace complexes at Raqqa.

5.2 Tell Fukhkhar

A plot of MgO and Al_2O_3 contents of 67 glass samples from Tell Fukhkhar is shown in Figure 5-2. Five analyses of Ayyubid window and vessel glass from the 11th-12th century Qas'r al-Banât, the princess's palace in al-Rafika, previously discussed[1], are also included. Over 75% of results fall into type 1, indicating that a general shift to that composition had occurred by the 11th century. The HMG is now prevalent for all object types and is graphically represented as subtype 1; it is compositionally distinct from its earlier HMG counterpart at Tell Zujaj (type 1) by virtue of its different Na_2O and CaO contents (see below).

Only four samples, one each from different typological groups, are natron glasses of type 3, which had clearly almost gone out of use by the 11th century at Tell Fukhkhar. Two miniature

bottle samples, one other vessel fragment and six highly coloured bracelets fall into the type 4 region. Another three samples are of type 2. The relatively low level of compositional variation amongst Tell Fukhkhar glass and the occurrence of production waste of subtype 1 (analysis 272, analysis 274 and analysis 275) and type 3 (analysis 273) suggest that the 13 samples of types 2 and 4 are not likely to have been produced at Tell Fukhkhar, but are more probably the result of recycling or re-use of earlier pieces. They are, in fact, compositionally identical to their 9th century equivalents at Tell Zujaj. The incidence of a piece of type 3 raw glass in the 11th century could imply that it was made in Raqqa, made elsewhere and imported or that it had been gathered together with the other (plant ash) raw glass and was made some 200-300 years earlier.

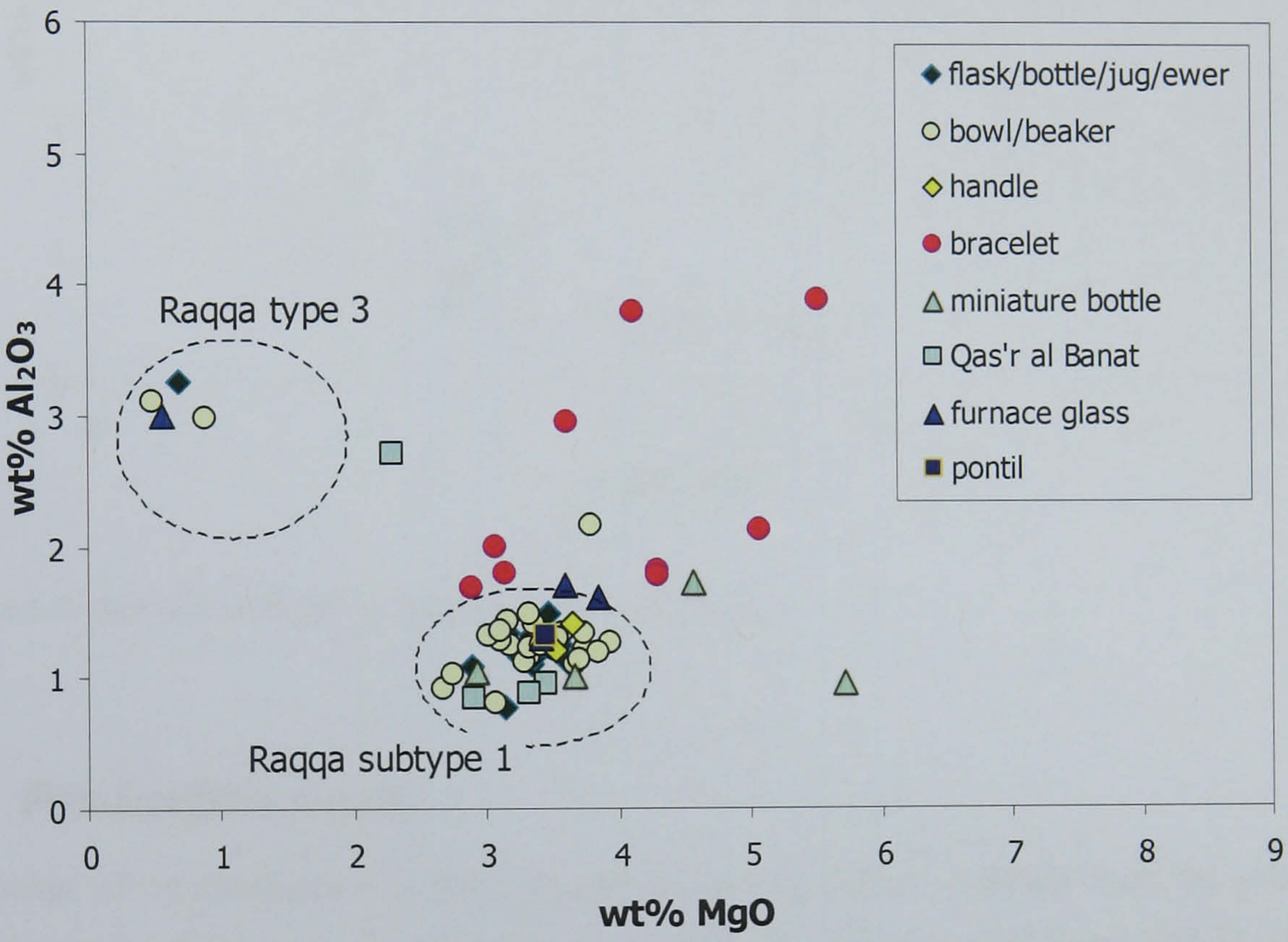


Figure 5-2: MgO vs. Al_2O_3 for 67 Tell Fukhkhar glass fragments. The plot includes previously published results[1] from contemporary Qas'r al-Banat.

5.3 Tell Belor

A plot of MgO and Al_2O_3 contents of 16 glass samples from Tell Belor is shown in Figure 5-3. The glasses associated with production waste type A (see Section 3.3.3), thought to be of cast glass, have been classed as furnace glass for reasons that will become clear in Chapter 7. The predominance of a subtype 1 composition, especially for blown glass vessels, is in accordance with results from Tell Fukhkhar, and underlines the continued dominance of a plant ash glass at Raqqa until at least the 12th century. One dark green vessel fragment (sample TB22h) does not fall into any of the compositional groupings, as it contains almost no MgO or K_2O (0.1wt%),

and could be an import. No other natron glasses were found at Tell Belor. Two samples fall into each of the compositional types, 2 and 4, indicating the continued spread of compositional variation at Raqqa.

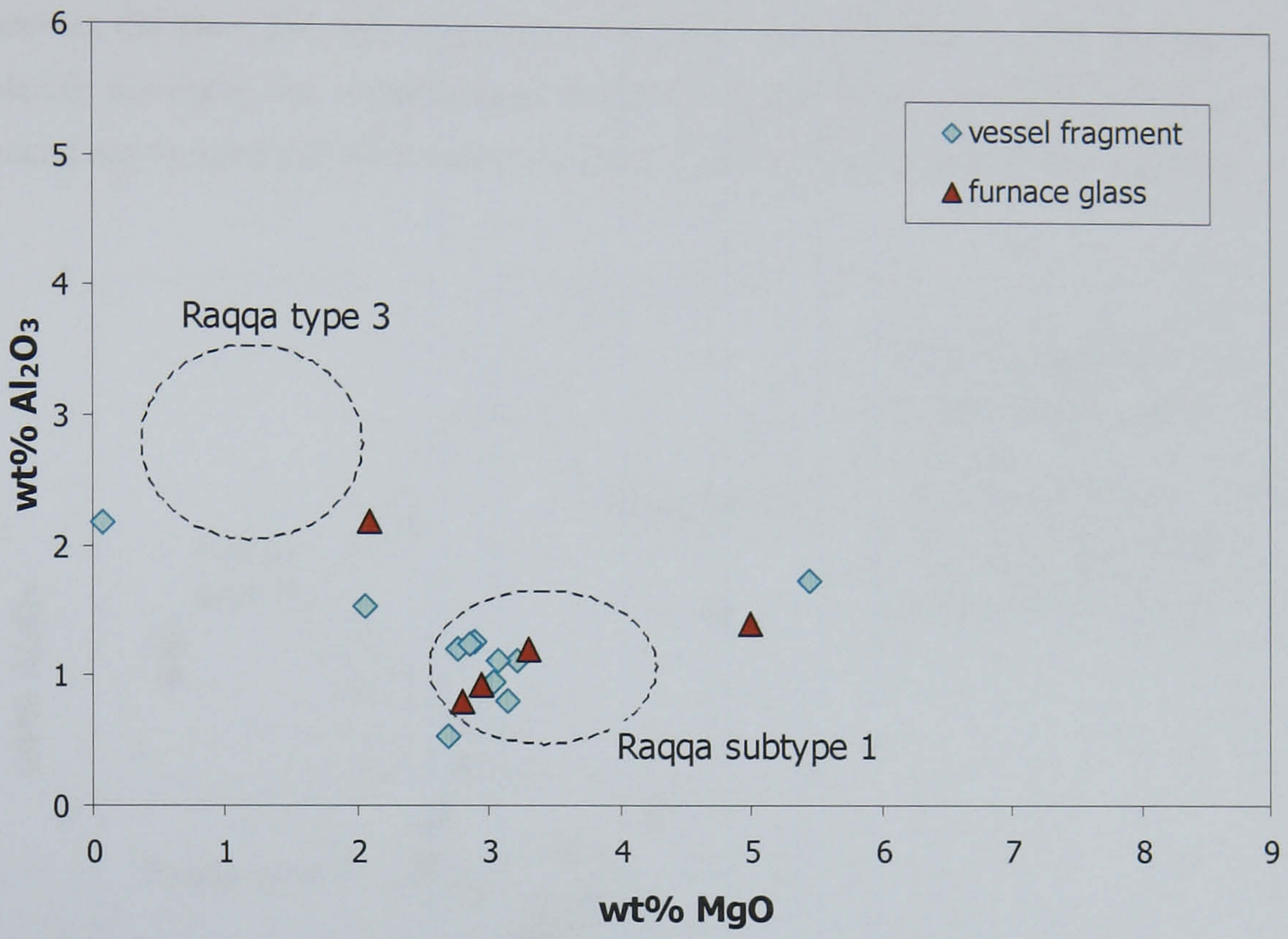


Figure 5-3: MgO vs. Al_2O_3 for 15 Tell Belor glass fragments.

5.4 Production waste

The range of compositions that has emerged from the analysis of debris from the primary manufacture/production and from the subsequent working of glass at Tell Zujaj, Tell Fukhkhar and Tell Belor, together with the large amount of archaeological evidence for primary glass production there, makes it reasonable to assume that the present sample set represents glass actually fabricated locally at Raqqa as opposed to pieces worked from glass imported from other glassmaking sites. Samples from primary and secondary glass production from all three sites at Raqqa are highlighted in Figure 5-4. Some doubts remain however, as there are not many immediately obvious stylistic traits amongst the finished vessels inspected from which to ascertain provenance with greater confidence, and no evidence for the primary production of type 3 was found at Tell Zujaj. But as such a compositionally wide-ranging series of primary and secondary production debris was found at Raqqa, a local production assemblage seems the most likely picture.

5.5 Compositional groupings

The size and breadth of the present database of analytical results have allowed the chemical compositions of Raqqa glasses to be considered as a whole, in an attempt to chemically characterise the glass that was made and used there. The interpretation of a database of such complexity involving the compositional analysis of glass from three archaeological sites of different dates forming part of the same industrial complex has not been published before.

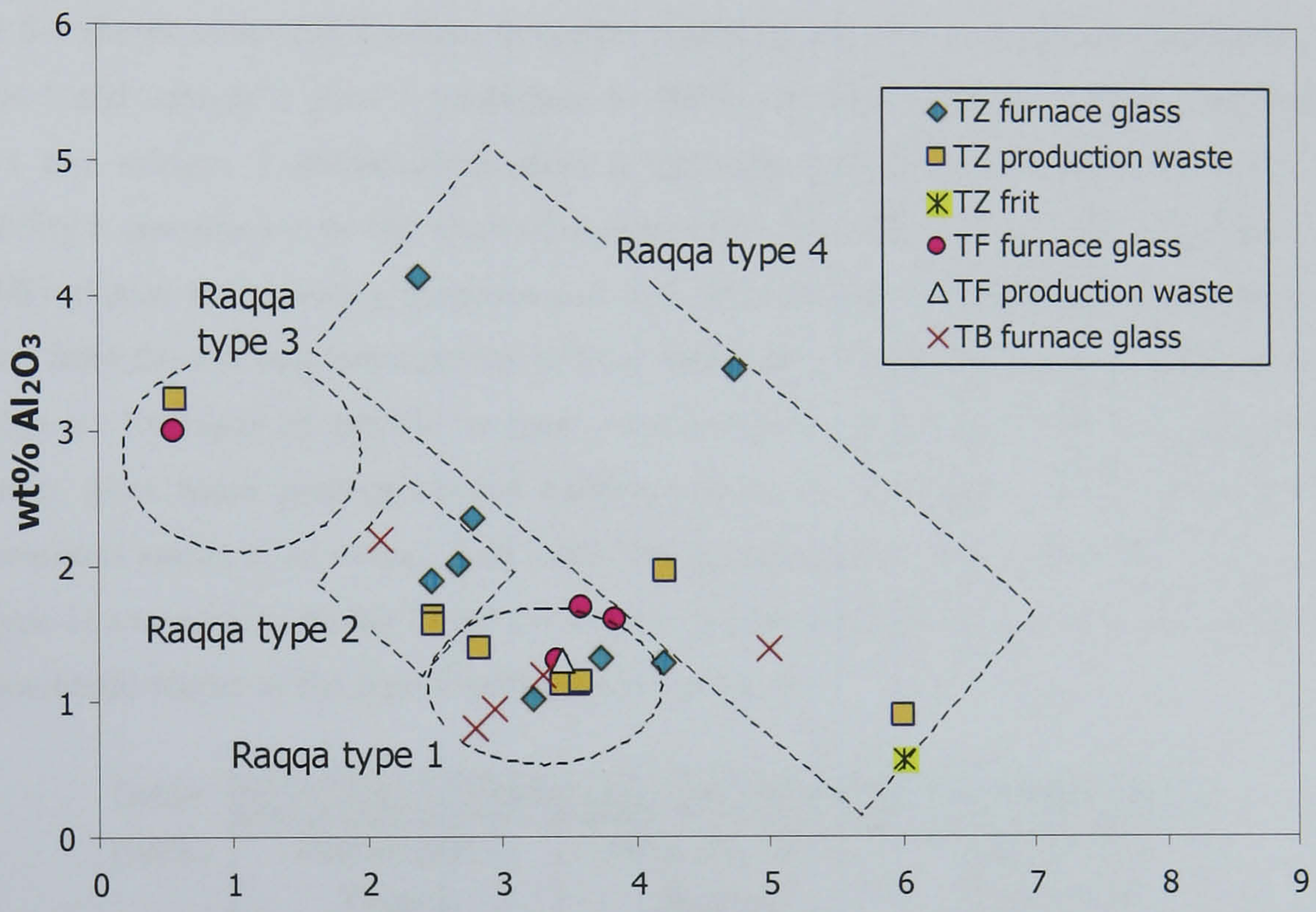


Figure 5-4: MgO vs. Al_2O_3 for primary and secondary production waste evidence from three Tells at Raqqa.

The samples analysed fall into one of four clear compositional groups consistent across all major and minor oxide components. Only minor and trace levels of the colorant oxides of Co, Zn, Cu, Fe and Mn cause less chemical homogeneity, but these are more likely to have been introduced in the batch separately in order to modify the colour of the glass. The full compositional plots incorporate a total of 258 samples. The two tightly clustered type 3 and type 1 compositional groups are loosely joined by type 2. The diffuse type 4 group extends from glasses containing high Al_2O_3 and high MgO to glasses which contain low Al_2O_3 and very high MgO (up to 8 wt%). The two oxides are clearly negatively correlated with each other.

The time-dependency of the clustering is unequivocal; almost all type 3 and type 4 glasses are from Tell Zujaj (8th-9th century), whereas the glasses from Tell Fukhkhar (11th century) and Tell Belor (12th century) are almost all of a type 1 composition (subtype 1 in Figures 5-2 and 5-3). At

Tell Zujaj the reported early use of type 1 is confirmed in a total of 34 samples. Although type 1 is clearly compositionally akin to the later subtype 1 glasses found at Tell Fukhkhar in terms of the alkali and silica sources used, type 1 and sub-type 1 are compositionally distinct in other ways (see below).

5.5.1 Type 3 vs. type 1

Table 5-1 shows mean and standard deviation values for the twelve major components of type 3, type 1 and subtype 1 glasses normalised to 100%. Only the contents of Fe_2O_3 and MnO in type 1 and subtype 1 compositions show a relatively high deviation from the mean. This variability is presumed to be the result of separate additions of Fe-rich and Mn-rich components to HMG glasses for colouring purposes and will be discussed in more detail in Section 5-6. It follows from the size and homogeneity of these three compositional types (1, sub-type 1 and 3) that they are the result of specific 'recipes', with seemingly very little variation in raw material selection, glass batch preparation and melting conditions. The high reproducibility of these compositions attests to an overall well controlled glassmaking process at Raqqa (for type 1 and sub-type 1) and perhaps on the Levantine coast (for type 3), in sharp contrast to the much wider compositional scatter of the type 4 workshop composition.

Oxide (wt%)	Tell Zujaj				Tell Fukhkhar	
	Natron glass **Type 3** (n=66)		Plant ash glass **Type 1** (n=36)		Plant ash glass **Subtype 1** (n=53)	
	wt %	+/-	wt %	+/-	wt %	+/-
Na_2O	13.82	0.88	13.7	1.11	12.18	0.95
MgO	0.73	0.35	3.55	0.33	3.38	0.28
Al_2O_3	3.19	0.28	1.17	0.17	1.24	0.17
SiO_2*	71.17	1.67	67.55	1.46	67.66	1.49
P_2O_5	0.1	0.05	0.29	0.04	0.27	0.03
Cl	0.73	0.11	0.79	0.16	0.73	0.08
SO_3	0.09	0.06	0.18	0.07	0.17	0.04
K_2O	0.61	0.21	2.47	0.19	2.48	0.33
CaO	9.07	1.09	8.51	1.02	10.18	1.00
TiO_2	0.05	0.01	0.06	0.01	0.06	0.01
MnO	0.04	0.04	1.2	0.62	1.09	0.51
Fe_2O_3	0.39	0.09	0.52	0.22	0.55	0.25
Total	100		100		100	

Table 5-1: mean values and standard deviations of the twelve major components of type 3 LMG and type 1 HMG from Tell Zujaj and subtype 1 HMG from Tell Fukhkhar and Tell Belor.

Type 3 is based on a 'late Roman' recipe and is equivalent in composition to late Roman and Byzantine glasses in the Levant region from Hermopolis[2], Jalame[3], Caesaria and Fustat[4], Bet Eli'ezer, Dor and Apollonia[5]. Brill[3] has established the probable raw ingredients of this glass: sand gathered from the banks of the Belus River in Israel gives rise to the c. 3-4 wt% Al_2O_3 impurity, and natron, a naturally pure form of soda, accounts for the low (0.5-1 wt%) MgO impurity. Shell fragments in the Belus River sand also provide the 8-10 wt% of CaO in type 3 glasses (see Figure 5-7).

Type 1 is made from different raw materials, namely quartz or some other purer source of silica such as chert, which accounts for the group's lower (1-1.4 wt%) Al_2O_3 content, and plant ash, which gives rise to a higher (3-4 wt%) MgO content and also an 8-10 wt% CaO content, similar to that of type 3. It is likely that ashes of the highly alkaline halophytic plant of the genus Salicornia, for example, were used as the alkali source at Raqqa[6].

A plot of MgO and K_2O contents confirms the use of different alkali source for type 1 and 3 glasses (Figure 5-5). The groupings sit comfortably within range limits of natron and plant-ash based glasses, as suggested by Lilyquist and Brill[7]. The frit sample in Figure 5-5 confirms that a plant ash glass was produced at Raqqa.

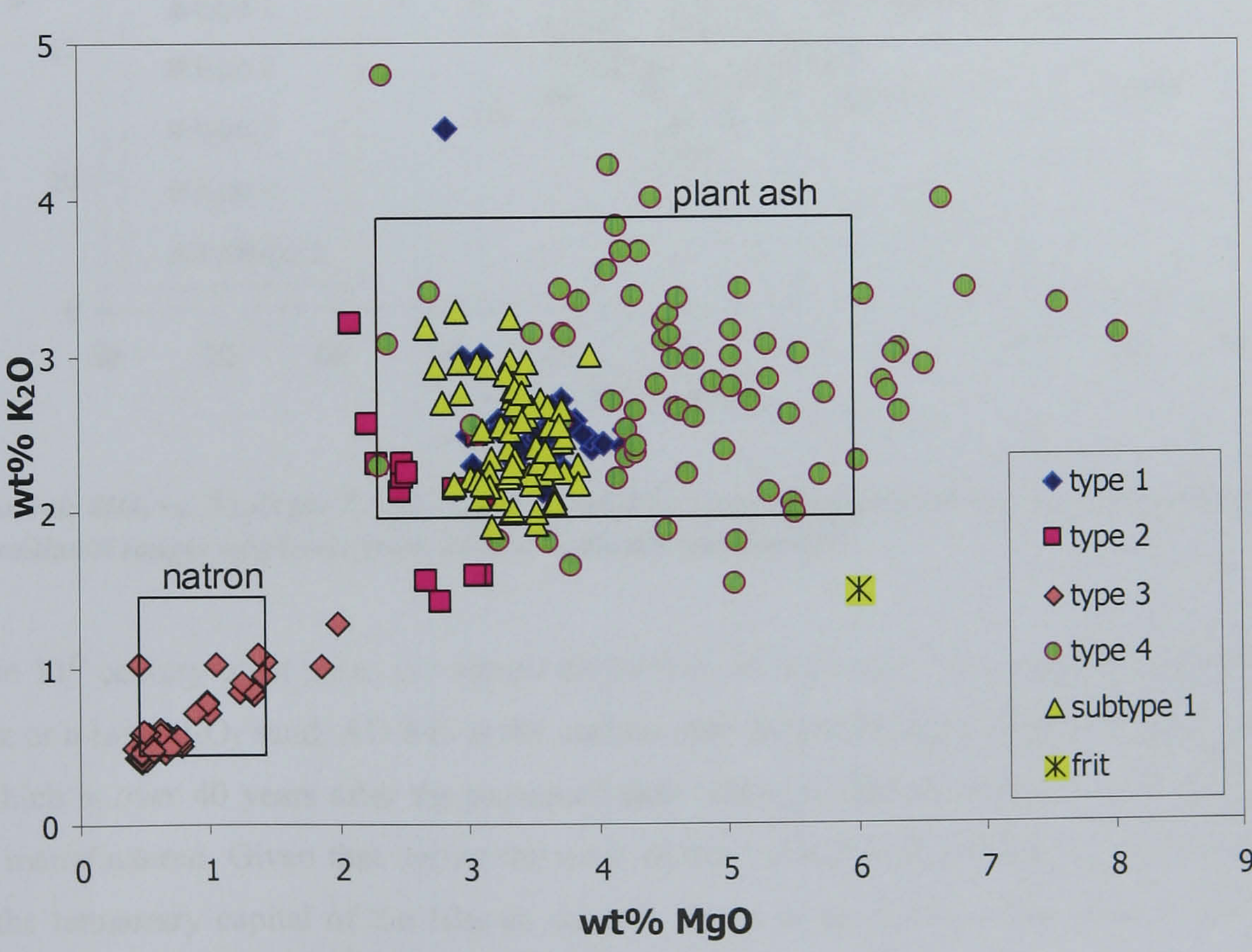


Figure 5-5: MgO vs. K_2O for Raqqa glasses divided by compositional grouping. Superimposed are the oxide ranges for SLS glasses of natron and plant-ash types according to Lilyquist and Brill[7].

The different alkali sources give rise to different Na_2O contents. Figure 5-6 is a bi-plot of the relative Na_2O and SiO_2 contents in the glass types. Superimposed on Figure 5-6 are the compositional ranges of glasses illustrated by Freestone *et al.*[8] from a range of earlier and contemporary sites. Type 3, which overlaps significantly with Late Roman and Byzantine glass from Ramla and Jalame, contains more SiO_2 than type 1; some type 1 overlaps comfortably with HMG glass from Banias. Subtype 1 glass contains generally less Na_2O than its 9th century counterpart, and higher CaO (Figure 5-7). Compositional differences between type 1 and its later subtype are therefore noticeable when these constituents are taken into consideration. The compositional differences suggest that a slightly different plant ash was used or prepared for the 11th century counterpart, or that they are just a product of the differences in plant ash over time.

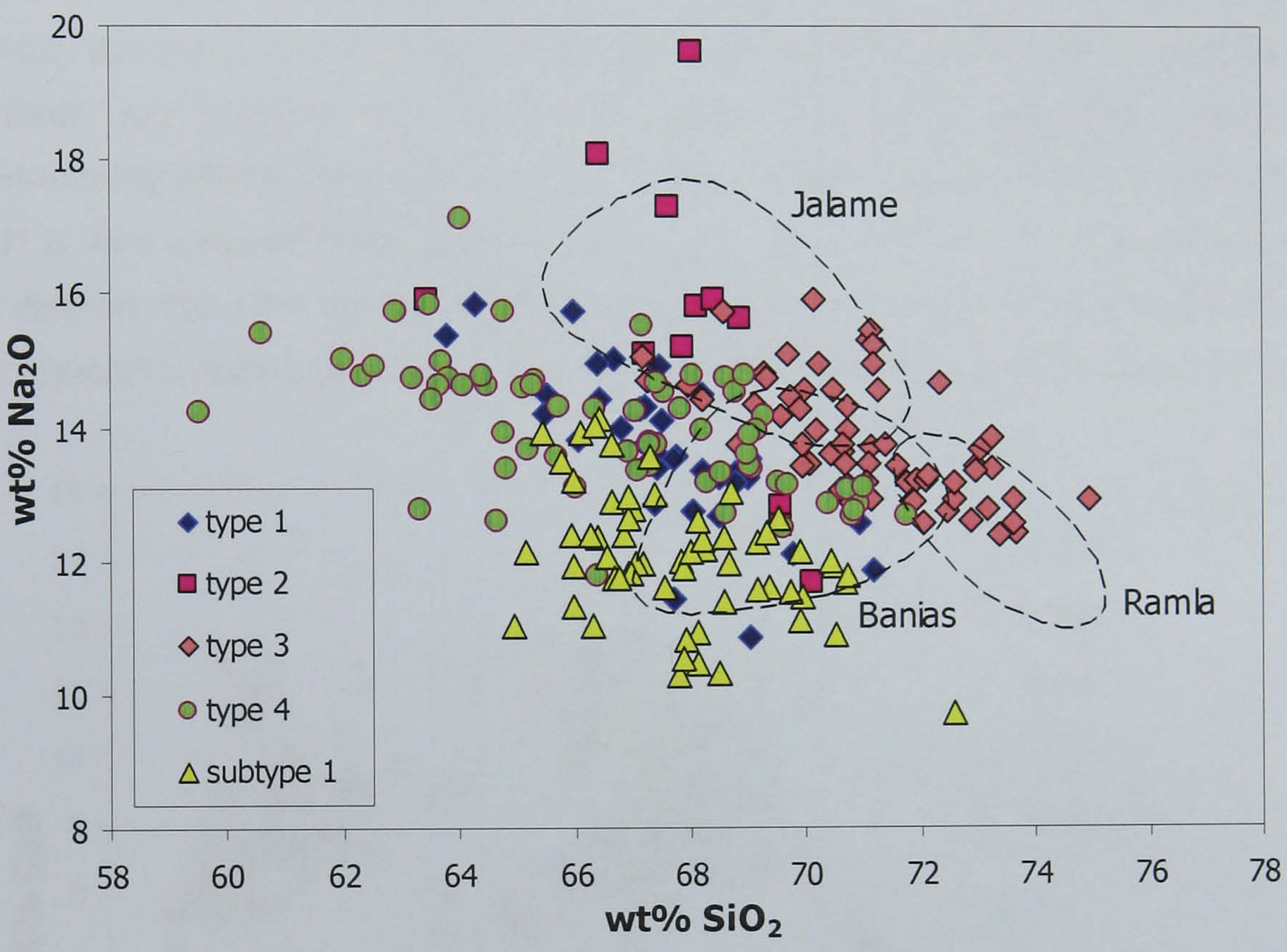


Figure 5-6: SiO_2 vs. Na_2O for Raqqa glasses divided by compositional grouping. Superimposed are the compositional ranges of glasses from Jalame[3], Ramla and Banias[8].

By the 11th century plant ashes are almost exclusively in use as the flux, coupled with crushed quartz or a low Al_2O_3 sand. AD 845 is the earliest date for published evidence of type 1 glass[9, 10], which is over 40 years after the presumed date when the glasses analysed from Tell Zujaj were manufactured. Given that during the reign of the 'Abbasid caliph Harun al-Rashid Raqqa was the temporary capital of the Islamic state, it comes as no surprise that there is analytical evidence for experimentation with new raw materials there.

5.5.2 Type 4: experiment and recycling?

The type 4 group is unusual because of its level of compositional variation, and by examining the variations across the group, a range of technological inferences can be drawn. The diffuse type 4 group can be distinguished compositionally from types 1 and 3 in terms of both the relative levels of components and the ways in which different components are correlated. Type 4 itself represents a dilution line in Figures 5-1 to 5-3 parallel to the line linking types 1 and 3 through type 2 and is similar in length, except that it includes a much wider range of Al_2O_3 and MgO levels. A dilution line is usually the result of balancing the amount of two substances against each other in varied and controlled proportions. Discussion will focus on type 4 because the number of samples in type 4 make the group a far more comprehensive case than 'type 2'. The characteristically low levels of CaO in type 2 glasses (shown in Figure 5-7) rule out the possibility that type 2 is the result of mixing type 1 and 3. How can the negative correlation be explained? Are different raw ingredients being balanced against each other? Are compositionally different glasses being mixed together or progressive quantities of cullet being added? Is there a natural balance of components? It is only as a result of manipulating such a large database that more precise correlations can be observed between components so as to better hypothesise the possible mineral and chemical associations of raw ingredients involved.

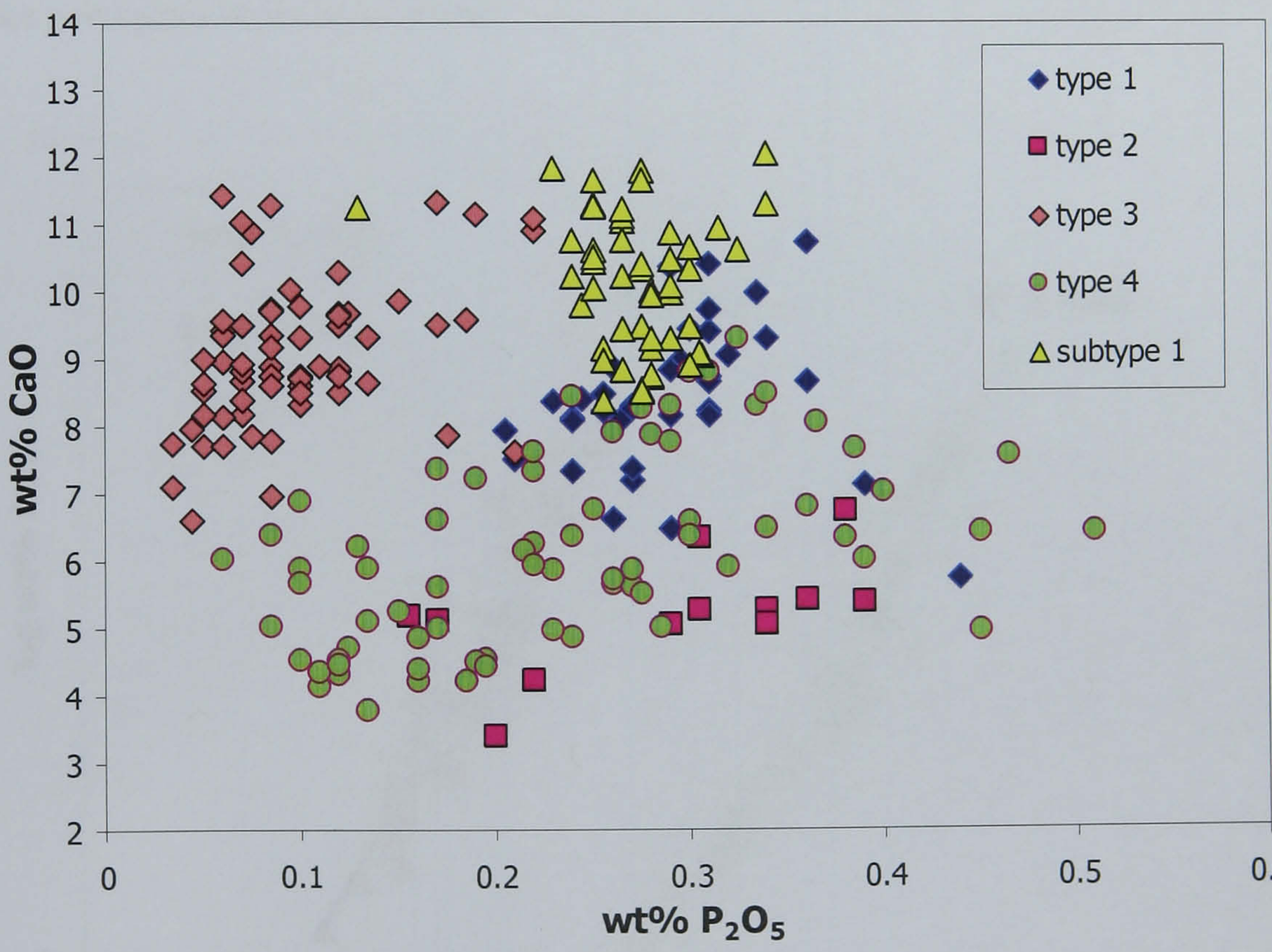


Figure 5-7: P_2O_5 vs. CaO for Raqqa glasses divided by compositional grouping.

Type 4 seems to be the result of experimentation with raw ingredients and of the subsequent recycling or re-use of cullet resulting from such experimentation. If a plant ash alkali based

glass does indeed make its first appearance at Raqqa, it represents the first recorded dominant use over a very wide area for centuries of such an ingredient. It seems logical then to assume a period of experimentation in which the glassmakers familiarised themselves with new glass properties and parameters in the glassmaking process that a new ingredient would have caused. Eventually they would aim to produce a glass that had not only the right technical properties and chemical stability but also the right compositional reproducibility for large-scale production. Logically, if one of the 'original' raw materials, sand, was mixed with a plant ash, this would result in the high Al_2O_3, high MgO type 4 glass. Clearly, the dilution of this glass with a second kind of glass made from quartz would lead to a reduction in the levels of Al_2O_3.

Glasses at the low Al_2O_3, high MgO end of type 4 contain the lowest levels of P_2O_5 and CaO (Figure 5-7), Fe_2O_3 and TiO_2 (Figure 5-8) and the highest SiO_2 levels (Figure 5-6). The very low (4 wt%) CaO content, which would render these glasses chemically less stable, is counter-balanced by a high MgO content (6-8 wt%), which acts as the main alkaline-earth modifier oxide. As with any new ingredient, the right dosage (proportion by weight) would need to be determined experimentally and balanced against other ingredients for optimum results. Assuming that plant ash replaced natron, and by weight perhaps the silica source (this would produce a chemical dilution line), the appropriate balance of R_2O and RO components to produce good glass could be achieved.

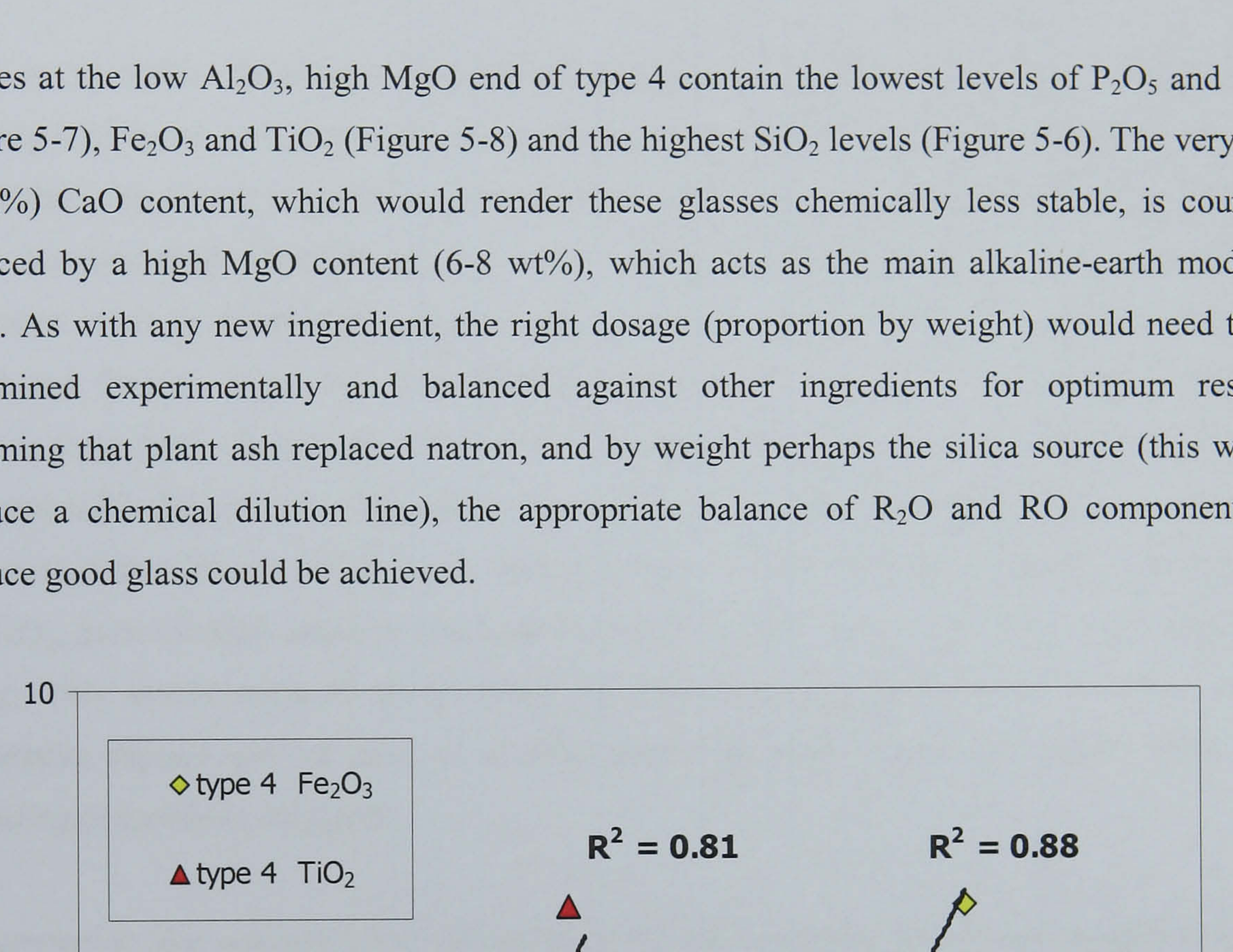


Figure 5-8: logarithmic plot of Al_2O_3 vs. Fe_2O_3 and TiO_2 for unintentionally coloured type 4 glasses with respective R^2 linear correlation coefficients. The close correlation between these compounds suggests a common mineralogical origin.

Let us consider the alkali used in more detail. The K_2O and MgO contents of type 4 glasses in Figure 5-5 clearly suggest that a plant ash flux is likely to have been used to make the glass. The clear positive correlation between MgO and K_2O observed in groups 1 and 3 is less well defined for the higher MgO levels found in type 4 glasses, indicating the possible addition of a separate Mg-rich component to a plant ash based glass. However, plant ash is also naturally variable in composition due to its organic nature and there is a possibility that a separate species was used. The use of a different genus of plant with a higher magnesia level is also likely for the high magnesia type 4 glasses. The variability of plant ash sources is discussed in further detail in Section 6.1.

Let us next consider the silica source: the associated Al_2O_3 content ranges from 1% (the typical impurity introduced with quartz or a purer silica source) to over 4% (a value similar to, if a little higher than, the typical impurity associated with sand). In other words there is a range of Al_2O_3 levels between those found in types 1 and 3. Al_2O_3 impurities in glass derive from mineral inclusions such as plagioclases that occur in sand, similarly to Fe_2O_3 and TiO_2 that are introduced through pyroxenes and ilmenite inclusions in sand[11, 12]. The high correlation between these three constituents for all type 4 glasses, denoted by linear R^2 coefficient values of 0.81 and 0.88 (Figure 5-8), links them strongly to the silica source and not to the alkali. It follows then that for increasing Al_2O_3 contents there is a corresponding increase in both Fe_2O_3 and TiO_2, from the high impurity levels associated with sand to the lower levels associated with quartz. This would seem to result from the increasing 'purification' of the glass by the progressive replacement of sand as a silica source by purer quartz (or glasses made with increasing proportions of quartz).

To summarise, the compositional variations observed for type 4 glasses are thought to be the result of experimentation first with raw ingredients and then with cullet. The addition of primary raw materials to the glass batch cannot however be ruled out. It is the glass working properties as determined by these raw materials plus any cullet that would have been of critical importance. It is probable, then, that even if cullet of the two 'end member' compositions (one with high levels of Al_2O_3 and the other with low levels) were mixed together, only a proportion of the glass that resulted would have had the desired working properties.

5.6 Colorants and opacifiers

Based on visual inspection, the colour was specified for all Raqqa glass samples by Julian Henderson prior to chemical analysis. 110 glass samples analysed from al-Raqqa are pale green, with a smaller number of aqua, other hues of green, brown, purple, blue and colourless. Uncoloured Raqqa glass is, like many ancient glasses, not truly colour-free but exhibits a light

greenish tint, indicative of a base Fe_2O_3 impurity. Hence palely coloured and colourless glasses in this study are considered 'unintentionally' coloured by the glassmaker in contrast to darker samples where the intentionality of producing a finished, coloured glass can be speculated.

Uncoloured type 3, type 1 and subtype 1 glasses typically contain 0.4-0.7 wt% Fe_2O_3 whereas uncoloured type 2 and type 4 glasses have increasing values of Fe_2O_3 from 0.5 to 2.3 wt% correlated to Al_2O_3 levels (see Figure 5-8). From the compositionally consistent Fe_2O_3 values of Raqqa glasses it seems clear when the oxide is present as a separate 'addition', perhaps as part of an Fe-rich colorant material or when it is present as an impurity; in Figure 5-9, a plot of Al_2O_3 against Fe_2O_3 contents for coloured and uncoloured Raqqa glasses, uncoloured glasses of types 1,2 and 4 define a positively correlated central zone which encompasses the aforementioned base Fe_2O_3 impurity of type 1 and subtype 1 and the steadily increasing iron contents of uncoloured type 2 and type 4 glasses. The majority of coloured glasses of these latter types plot visibly above the zone in Figure 5-9.

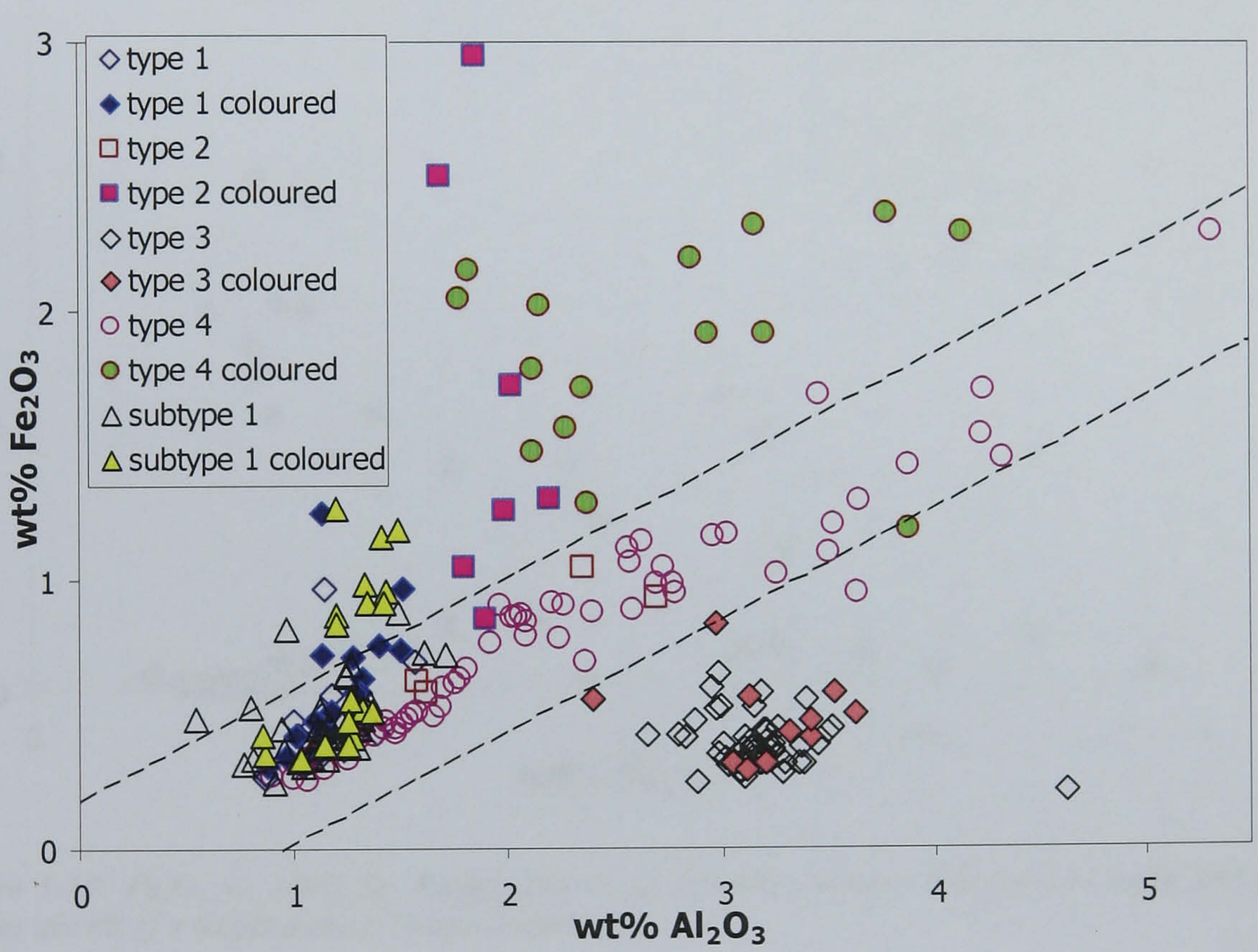


Figure 5-9: Al_2O_3 vs. Fe_2O_3 for Raqqa glasses divided by compositional grouping and coloration, as specified in the text. The positively correlated central zone formed by the uncoloured type 1, 2 and 4 glasses defines their natural Fe impurity. Samples above the zone have thus been coloured by additional Fe.

The presence of streaks of colour in some otherwise pale green glasses suggests that the colorants were added after the batch had fused and were sometimes inadequately mixed. However, since at least some of the glass analysed here was probably made using a single melt

in a tank furnace some of the streaking is also apparently due to variations in the oxidising/ reducing conditions in the furnace itself.

It is highly unlikely that MnO was introduced accidentally as an impurity. Early experimentation with plant ash at Tell Zujaj may have been accompanied by the early use of MnO at Raqqa; while present in type 3 glass only at trace levels, MnO seems to have been added to type 1 and type 2 glasses found at Tell Zujaj in significant quantities and to subtype 1 glasses found at Tell Fukhkhar (an average of 1.2 wt% for type 1, 1.1 wt% for subtype 1 and 2.15 wt% for type 2). MnO (an average 0.75 wt%) is also found in type 4 glasses and indicates the possibility of two separate traditions working side by side at al-Raqqa, certainly at Tell Zujaj, where evidence of primary glass production of different compositional types supports this hypothesis.

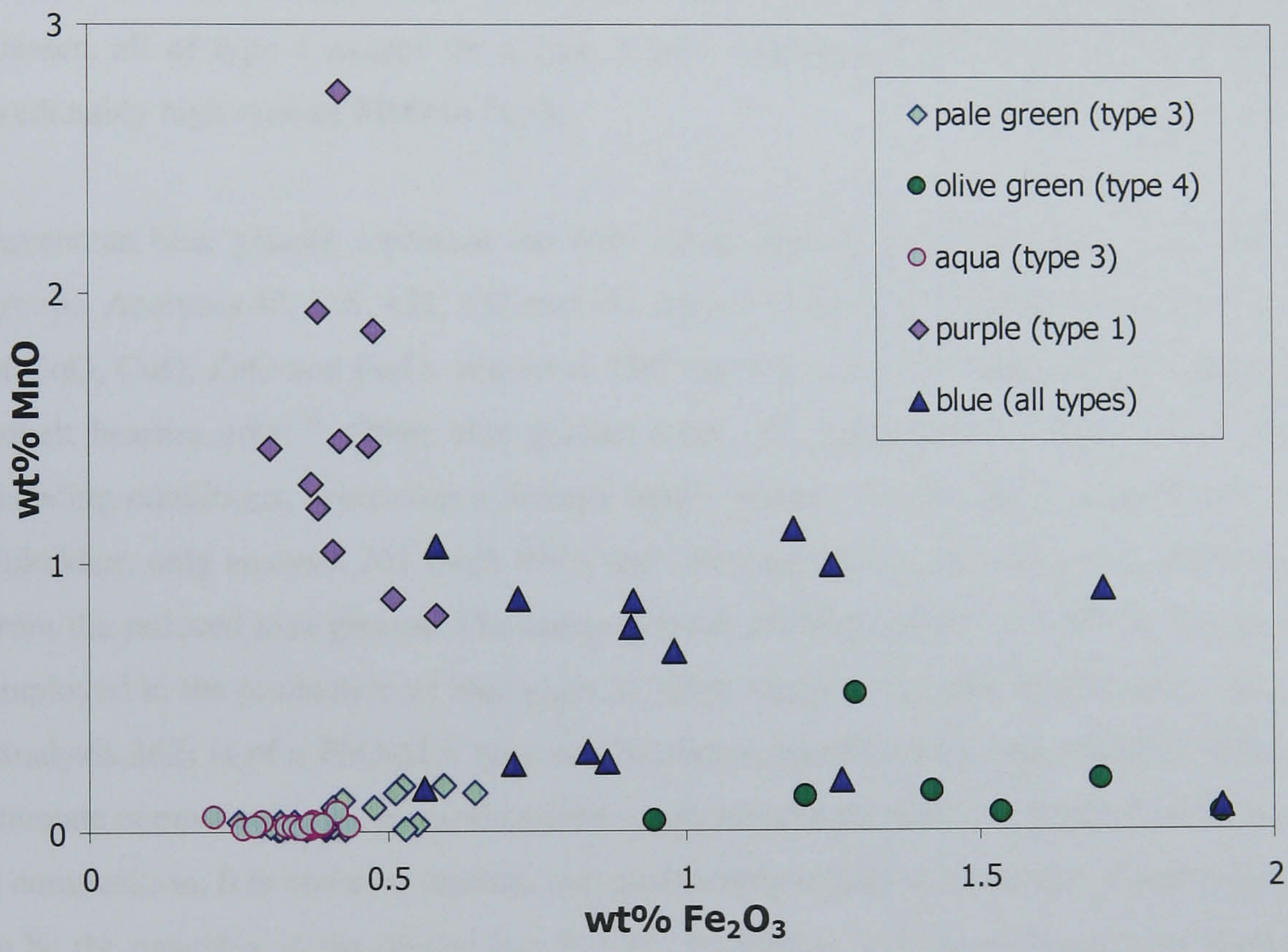


Figure 5-10: Fe_2O_3 vs. MnO for Raqqa glasses of different colours. Olive green, aqua and purple glasses are all of a single distinct compositional type.

At the same time that higher MnO levels are found in type 1 and type 4 glasses from Tell Zujaj, a famous Islamic chemist Jabir Ibn Haiyan was experimenting with glass production. Also known as Geber, he dealt in his writings with the use of manganese dioxide in glassmaking[13, 14]. He served under the patronage of the Barmaki Vizier during the 'Abbasid Caliphate of Harun al-Rashid and died in 803 when Harun was present in Raqqa. Traditonally Barmaki is said to be buried in al-Raqqa. Since Raqqa was the temporary capital of the Islamic caliphate under Harun al-Rashid, the incidence of increased MnO amongst Islamic glasses may be an

indication that its use formed part of glassmaking innovation/ re-introduction that occurred in Raqqa at this time – though the oxide had been used in earlier glass making technologies[15].

Intriguingly, there definitely seems to have been some degree of compositional specialisation with regard to colour at Raqqa (Figure 5-10). All aqua glasses are type 3 and have consistently low Fe_2O_3 contents (0.43 wt% is the highest value), slightly lower than their pale green type 3 equivalents superimposed in Figure 5-10. The overall compositional similarity between pale green and aqua type 3 glasses suggests that control over this particular colour was achieved (either deliberately or accidentally) in the furnace as a result of slight differences in the firing cycle including the oxidising-reducing conditions. Seven olive green glasses are however all of type 4 and have consistently low MnO and very high Fe_2O_3. They all sit at the low MgO, high Al_2O_3 end of type 4 and an Fe-rich raw material was possibly added deliberately to produce the colour. This again suggests that a distinct recipe was used in their production. Eleven purple glasses, all of type 1 except for a type 2 moil fragment, derive from both sites and have a predictably high ratio of MnO to Fe_2O_3.

Seventeen blue glasses represent the only colour type to span across all four compositional groups. Analyses 42, 118, 131, 132 and 133 from Tell Zujaj all contain anomalously high levels of CoO, CuO, ZnO and Fe_2O_3 and some PbO and were probably coloured by a combination of cobalt bearing ores[15]. Other blue glasses from Tell Zujaj seem to have been melted under reducing conditions, producing a ferrous oxide colorant. Of the seven blue glasses from Tell Fukhkhar, only analysis 261 (high PbO) and 250 (some CuO, ZnO and high MnO) are distinct from the reduced iron glasses. The compositional evidence points to different techniques being employed in the production of blue glass. A single opaque turquoise tessera from Tell Fukhkhar (analysis 262) is of a PbO-SLS type and has been opacified with lead stannate. When the lead stannate component was removed and the composition normalised, it adhered to the typical type 3 composition. It is however unusual compositionally in that lead stannate is not normally found to be the opacifier in the typical late Roman/ Byzantine tradition of tesserae production – it is normally calcium antimonate[15]. A window glass from Qas'r al-Banât is of a PbO-SiO_2 type[1].

5.7 Regional comparisons

A comparison of the chemical compositions of contemporary glass from other non-industrial sites in Raqqa and other areas of the Islamic world is a good way to assess the influence of the glass from the site. Compositional variations of type 1 and type 3 are reported for Late Byzantine and Islamic glass from Caesaria and Fustat respectively, published by Brill[4], and for contemporary and earlier glasses published by Freestone *et al.*[8]. Such data forms a chemical framework from which possible trade routes and distribution patterns may eventually be

assembled. An overall production model for SLS glasses involving a limited number of primary production centres where glass was fused from raw materials and a larger number of secondary production centres where glass was worked has been suggested for natron glass in the Levant[8]. Until more contemporary early Islamic primary and secondary glass production centres are discovered and excavated, and the industrial debris and glass products analysed, it is difficult to know whether it will be possible to distinguish between them analytically.

The scale and historical significance of the industrial complex at Raqqa and the presence of a glassmaking industry located side by side with contemporary ceramic and glaze manufacturing sites give weight to the idea that Raqqa may well have been one location where novel experimentation in the otherwise conservative field of glass production took place. The analysis of ten glass samples from the 8th-early 9th century palace complexes in al-Raqqa shows that type 3 was used for vessels and type 4 for the manufacture of windows. There is no evidence for the use of type 1. Analysis of five samples from 11th-12th century Qasr al-Banât reveals the use of a PbO-SiO_2 glass along with type 2 and type 1. The unusually high Na_2O content places these glasses in a separate compositional sub-group, but there are too few samples to draw conclusions.

One data set of chemical compositions of 9th-10th century unstratified glasses from Nishapur, Iran[16, 17] shows that coloured glasses tend to be of a sub-type of type 4, whereas another group of colourless glasses is compositionally distinct from types 1 and 4. This suggests that Nishapur could be a separate production centre, which used raw materials with slightly different compositions from those used at Raqqa.

Comparing the compositions of glasses from the early 11th century Serç Limani shipwreck[17] with those from Raqqa, only four examples of type 1 are to be identified. Almost all of the glasses analysed are of type 2, but are distinguishable compositionally from the Raqqa type 2 glasses; 89 samples fall into this type 2 variant but with higher CaO levels than in the Raqqa glasses (9.26wt%). A range of glass compositions has emerged from the shipwreck along with evidence for the use of 'new' (post-8th century experimental glass) compositions. The fact that the ship is thought to have loaded up on the Levantine coast[18] poses some intriguing questions on the provenance and the nature of the ingots or cullet it was carrying. To investigate fully the significance of the results reported here, similar analytical investigations need to be carried out on the evidence for glass production on contemporary and later Islamic industrial sites. It is hoped that, in this respect, further comparative analytical work will not only reveal more about the significance and influence of Raqqa as a glassmaking centre, but that it will also shed more light on the development of Islamic glassmaking across the Middle East.

5.8 Bibliography

1. Henderson, J., *Archaeological and Scientific Evidence for the Production of Early Islamic Glass in al-Raqqa, Syria.* Levant, 1999. **31**: p. 225-240.

2. Bimson, M. and I.C. Freestone. *The Discovery of an Islamic Glass-Making Site in Middle Egypt*. in *10th Congress AIHV*. 1985. Madrid. p. 237-243.

3. Brill, R.H., *Scientific Investigations of the Jalame Glass and Related Finds*, in *Excavations at Jalame, Site of a Glass Factory in Late Roman Palestine*, G.D. Weinberg, Editor. 1998, University of Missouri Press. p. 257-294.

4. Brill, R.H., *Some Thoughts on the Chemistry and Technology of Islamic Glass*, in *Glass of the Sultans*, S. Carboni and D. Whitehouse, Editors. 2001, Metropolitan Museum of Art: New York. p. 25-45.

5. Freestone, I.C. and Y. Gorin-Rosen, *The Great Glass Slab at Bet She'arim, Israel: an Early Islamic Glassmaking Experiment?* Journal of Glass Studies, 1999. **41**: p. 105-116.

6. Henderson, J., *The Raw Materials of Early Glass Production.* Oxford Journal of Archaeology, 1985. **4**(3): p. 267-291.

7. Lilyquist, C. and R.H. Brill, *Studies in Early Egyptian Glass*. 1993, New York: Metropolitan Museum of Art.

8. Freestone, I.C., Y. Gorin-Rosen, and M.J. Hughes, *Primary Glass from Israel and the Production of Glass in Late Antiquity and the Early Islamic Period*, in *La Route du Verre: Ateliers Primaires et Secondaires du Second Millénaire av. J.-C. au Moyen Age*, M.-D. Nenna, Editor. 2000, Maison de l'Orient Méditerranéen: Lyon. p. 65-85.

9. Sayre, E.V. *Summary of the Brookhaven Program of Analysis of Ancient Glass*. in *Applications of Science in Examination of Works of Art*. 1965. Boston Museum of Fine Arts. p. 145-154.

10. Gratuze, B. and J.-N. Barrandon, *Islamic Glass Weights and Stamps: Analysis Using Nuclear Techniques.* Archaeometry, 1990. **32**(2): p. 155-162.

11. Deer, W.A., R.A. Howie, and J. Zussman, *An Introduction to the Rock Forming Minerals*. 1966, London: Longman.

12. Bezborodov, M.A., *Chemie und Technologie der Antiken und Mittelalterlichen Gläser*. 1975, Mainz: Verlag Philipp Von Zabern.

13. Sarton, G., *Introduction to the History of Science*. Vol. 1. 1927, Baltimore: Carnegie Institute of Washington. 520-534.

14. Zahoor, A., *Muslim History: 570 - 1950 C. E.* 1992, Dresden: ZMD Corporation.

15. Henderson, J., *The Science and Archaeology of Materials*. 2000, London: Routledge.

16. Brill, R.H., *Chemical Analyses of Some Glass Fragments from Nishapur in the Corning Museum of Glass*, in *Nishapur: Glass of the Early Islamic Period*, J. Kröger, Editor. 1995, Metropolitan Museum of Art: New York. p. 211-233.

17. Brill, R.H., *Chemical Analyses of Early Glasses*. Vol. I & II. 1999, Corning NY: Corning Museum of Glass.

18. Henderson, J., *Tradition and Experiment in 1st Millennium AD Glass Production - the Emergence of Early Islamic Glass Technology in Late Antiquity.* Accounts of Chemical Research, in press.

Chapter 6

Experimental glassmaking and replica work

A series of experimental glasses were mixed firstly from raw materials sampled at Raqqa and secondly from pure oxide and carbonate powders to model LMG and HMG compositions from Raqqa. Glasses were experimentally melted and analysed in order to establish whether the plant ash ingredient was locally available and to further investigate the different Raqqa glass types in terms of their physical properties related to the glassmaking process.

6.1 Type 1: quartz and Salicornia ash

As outlined in Section 3.3.4, the presumed raw materials of glass manufacture at Raqqa were gathered on site and prepared for experimental replication.

6.1.1 Salicornia ash analyses

ICP-AES compositional data obtained from the six *Salicornia* batches collected and burnt at Raqqa is shown in Table 6-1. As the ashes did not digest fully in the acid prior to ICP analysis, complementary EDX analyses were conducted on two ashes and combined with the ICP data. Results for TA1 are shown in Table 6-2. Very little compositional variation is seen to be induced by the presence or lack of roots, indicating an even spread of elemental concentrations throughout the plant. This is in contrast to results published by Bezborodov[1] that gave higher Na_2O and Cl levels in ashes obtained from the whole *Salicornia* plant and significantly higher levels of eight other constituent metal oxides in the ashed roots. As the roots and main stem make up approximately 10% of the total weight of the plant, a higher variation in ash composition was expected.

It would seem logical to deduce that the entire plant was added, if nothing else to save part of the immense workload involved in gathering, drying and burning the plant. Although some compositional variation is noticeable between different locations, the general trend is similar;

the plants are very high in Ca, Mg, S and K with surprisingly little Na. Samples gathered by the irrigated field have the highest alkali content whereas the other two are more Ca-rich.

Element (wt%)	Sample					
	EU1	EU2	HE1	HE2	TA1	TA2
Na	1.01	0.82	2.45	3.03	2.59	2.27
Mg	4.37	4.16	5.70	5.61	6.70	6.61
Al	0.51	0.76	0.55	0.34	0.75	0.70
P	0.92	0.79	0.63	0.63	1.02	1.06
S	7.64	7.79	7.77	8.77	7.03	6.42
K	6.46	6.11	4.32	5.02	10.00	10.10
Ca	25.30	22.90	23.40	21.80	18.20	17.60
Ti	0.04	0.06	0.04	0.02	0.06	0.05
Mn	0.03	0.04	0.05	0.04	0.04	0.04
Fe	0.43	0.62	0.41	0.27	0.61	0.59
Cu	0.02	0.02	0.02	0.02	0.02	0.02
Zn	0.03	0.03	0.03	0.03	0.01	0.02
Sr	0.18	0.18	0.38	0.40	0.42	0.39
Total	46.93	44.27	45.75	45.98	47.45	45.88
Li*	3.6	4.3	18.6	23.7	21	20.7
V*	14.5	19.8	12.3	9.75	19.8	17.8
Cr*	27.5	38	17	11	17	28
Ni*	26	31	53	20	35	34.5
Ba*	144	185	55.7	40.5	49.5	46
Pb*	10.5	7.5	120	6	7.5	7.5

Table 6-1: ICP-AES results for Salicornia ash collected at Raqqa from the banks of the Euphrates River (EU), Herakla (HE) and Tell Aswad (TA). * denotes ppm. This data is compositionally incomplete because the samples were not fully digested in acid due to insoluble compunds in the ash.

The low levels of Na could be explained in a series of ways: the mineral content of organic species is affected by the conditions of the climate and soil in which they grow[2, 3], and hence these plants may have been picked at the wrong time of year. Furthermore, since this experiment I have seen ethnographic evidence of present day glassmakers in India slowly smoking their plants in a covered pit, rather than burning them in the open air. This would considerably lower the combustion temperatures involved and prevent the volatilisation of lighter species such as Na. Etegni and Cambell[4] showed that Na levels in wood ash were significantly lowered above combustion temperatures of 871°C, a temperature which is certainly achievable in an open fire. Moreover, one may conclude from the experiment that *Salicornia* is simply not the actual plant that was used as a raw ingredient in Islamic Raqqa.

Nevertheless, pellets of TA1 and HE1 were pressed for further analysis. An XRD scan of HE1 showed a 15-20% amorphous halo and the three major peaks were identified for $CaCO_3$, $CaSO_4$,

KCl, MgO and CaO. The ashes were calculated as oxide mixtures in a melt by removing C and S, which would leave the melt as CO_2 and SO_2, and Cl and I, which would also volatilise at high temperatures. These components accounted for almost 50% of the weight total. Thus a glass made with a 1:1 ash:quartz ratio was expected to contain ~67wt% SiO_2, 2wt% Na_2O, 6wt% MgO, 6.9wt% K_2O, 14.9wt% CaO and 1wt% Al_2O_3, a composition that would fall into the type 4 range were it not for the low Na and high K and Ca levels.

Element (wt%)	TA1	Oxide (wt%)	as oxide mixture with all	as oxide mixture -C,S,Cl,I	quartz	ash:quartz weight ratio 1:1	1:1*	2:1	2:1*
O	28.3*		-						
C	10.8*	CO_2	22.46						
Na	2.59	Na_2O	3.11	3.11		2.00	1.8	2.95	2.7
Mg	6.70	MgO	9.89	9.89	0.01	6.37	6.4	9.39	9.3
Al	0.75	Al_2O_3	1.26	1.26	0.25	0.97	1.3	1.31	1.7
Si	2.2*	SiO_2	4.25	4.25	99.6	66.83	68.4	51.28	54.8
P	1.02	P_2O_5	2.08	2.08		1.34	1.5	1.97	2.2
S	7.03	SO_3	15.63				nd		nd
Cl	6.0*	Cl	6.30				0.1		0.1
K	10.00	K_2O	10.73	10.73		6.90	5.8	10.18	8.8
Ca	18.20	CaO	22.68	22.68	0.01	14.60	13.5	21.52	19.4
Ti	0.06	TiO_2	0.09	0.09	0.01	0.06	0.1	0.09	0.1
Mn	0.04	MnO	0.05	0.05	0.01	0.04	0.1	0.05	0.1
Fe	0.61	Fe_2O_3	0.77	0.77	0.1	0.56	1.0	0.78	1.1
Sr	0.42	SrO	0.44	0.44		0.29	-	0.42	-
I	0.20	I	0.21						
Total	95.04		100	55.35	100	100	100	100	100

Table 6-2: ICP-AES results for TA1 Salicornia ash in wt% element (column 2) with missing values (denoted by *) from EDXA; TA1 is expressed as a normalised oxide mixture (column 4) with components that are lost during melting subtracted from the total (column 5); EPMA results for quartz from Raqqa are given in column 6; expected and experimentally obtained compositions of a glass made with ash:quartz ratios of 1:1 and 2:1 are given in columns 7-8 and 9-10 respectively. Experimental glasses (denoted by *) were analysed by EDXA.

6.1.2 Synthesised glasses

15g batches of ash and quartz (actually replaced by SiO_2 with 0.25 wt% Al_2O_3) in 2:1 and 1:1 weight proportions were made up, heated to 730°C for three hours and held overnight at 1200°C. Both batches formed a fully fused dark green glass. When analysed by SEM-EDXA, they corresponded closely to the calculated compositions. Relevant compositional data is given in Table 6-2.

It was thus possible to make a glass at 1200°C directly from its raw ingredients with no need for fritting, although the compositions resulting from 1:1 and 2:1 ash:quartz weight ratios did not match any compositions observed at Raqqa. The 1:1 glass is much closer in composition to

Roman mixed-alkali glasses reported from La Négade in France[5], particularly in light of the high P_2O_5 content, a characteristic of plants collected from inland terrestrial sites as opposed to marine environments (see Section 2.3.2.1). If extra Na were added to the batch to account for the Na presumed lost in the burning process, the 1:1 glass would fit a plant ash type composition, with nearly equivalent amounts of MgO and K_2O, close to type 1, but a high P_2O_5 content would remain.

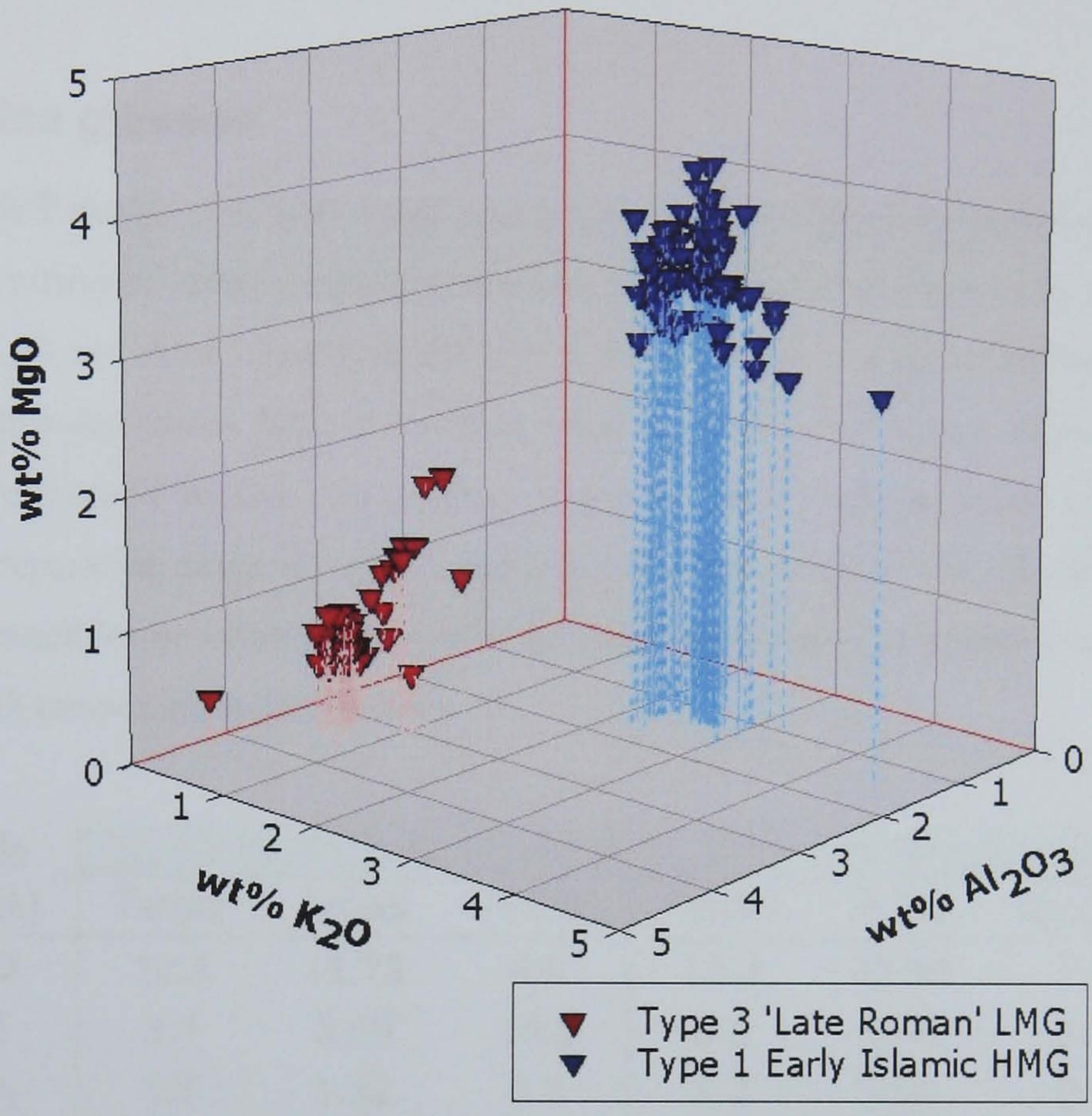


Figure 6-1: 3-D scatter plot of MgO, K_2O and Al_2O_3 levels for Raqqa LMG type 3 and HMG type 1.

The hypothesis that the locally abundant *Salicornia* was the raw ingredient of HMG glass recipes at Raqqa remains unresolved as a result of this experiment because the ashes of locally gathered plants contained the wrong balance of components to produce a Raqqa plant-ash glass composition. Improper alkali preparation may have been responsible for the lowered Na levels in the ash, and the mineral content of the ashes may well have been influenced by multiple sources of compositional variability known to exist for organic species. However, the high P_2O_5 content observed for all *Salicornia* batches prepared is in contrast with the consistently low (0.1-0.5 wt%) P_2O_5 levels in Raqqa glasses. This could suggest that the ashes to be used for glassmaking were not prepared from plants collected locally at Raqqa, which should in any case have contained significant amounts of P_2O_5 because they are terrestrial, but were procured from elsewhere, possibly from marine environments.

6.2 Type 1 vs. type 3: replica glassmaking

As discussed in Section 5.1.5.1, type 1 and type 3 can be clearly distinguished in terms of MgO, K_2O and Al_2O_3 contents, which relate to changes in the raw materials used to manufacture them. A 3-D plot of these components (Figure 6-1) underlines the compositional differences between them. Replica work was carried out to explore the differences in working properties that the compositional variation observed would have caused to the ancient glassmaker.

6.2.1 Replica glasses

The results of ICP analyses of type 1 and type 3 glass replica sample compositions are given in Table 6-3. The analytical data compares favourably with the target composition, although values of MgO and K_2O are lower than expected for both and show a range of RE values of 7.6 to 24%. Na_2O totals are also a little lower than expected, but with smaller relative errors (2.9-4.6%). The errors could be due to a number of factors other than analytical error: compound errors at the preparation stage (drying, weighing and transferring to the crucible), incomplete mixing in the crucibles or volatilisation from the melt, particularly as samples were only easily cast at very high temperatures (see below).

Oxide	I			III		
(wt%)	Target	Actual	RE (%)	Target	Actual	RE (%)
Na_2O	12.3	11.73	4.6	13.3	12.91	2.9
MgO	3.4	2.89	15.0	0.5	0.46	8.0
Al_2O_3	1.3	1.32	1.5	3.2	3.21	0.3
SiO_2	70	70.62	0.9	73	72.94	0.1
K_2O	2.5	2.31	7.6	0.5	0.38	24.0
CaO	10.5	10.83	3.1	9.5	9.51	0.1
TiO_2		0.06			0.08	
Fe_2O_3		0.12			0.12	
MnO		<0.05			<0.05	
P_2O_5		<0.05			<0.05	
Total		99.88			99.61	

Table 6-3: target compositions of type 1 and type 3 glasses and results of ICP-AES analyses of prepared samples. Relative errors are shown for the chemical data.

6.2.2 Viscosity

The theoretical viscosity-temperature curves for the type 1 and type 3 replica compositions were calculated using three models: Lakatos' empirical solution to the Fulcher-Tammann equation, the Urbain method and a set of results sent to me by N. T. Huff at the Owens-Corning Science

& Technology Center, Granville, Ohio. The Huff data is the average of four close-fitting curves that he calculated for the compositions from broad and narrow linear and non-linear equations. Standard deviations for averages values from Huff's data are 1-2°C for type 1 and 7-10°C for type 3. Unfortunately the equations were not disclosed to me and therefore the merits of the methodology he used cannot be discussed in this study but, given the range and validity of mathematical modelling methods which Owens-Corning has developed in the glass industry and Huff himself has recently reviewed[6], the data has been included on the assumption of its validity.

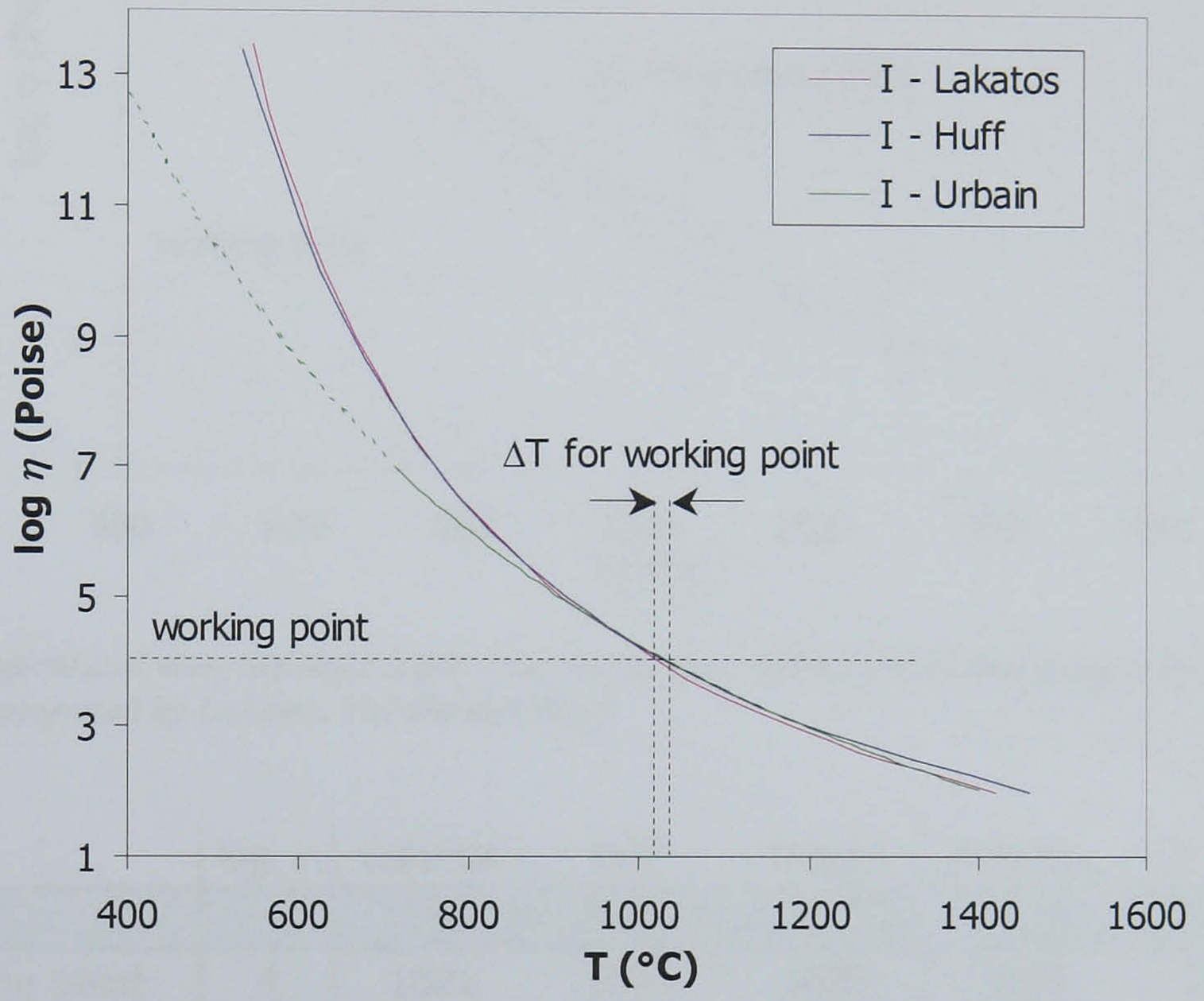


Figure 6-2: calculated viscosity-temperature curves for the replica type 1 HMG composition using data from models proposed by Lakatos, Urbain and Huff.

The plots are given in Figures 6-2 and 6-3 for type 1 and type 3, respectively. The three curves for type 1 are almost identical across the range of $\log\eta$ values 2-5. The overlap is very encouraging as it validates the idea of using several models in the first place. The working point ($\log\eta = 4$) is confined by the three curves to a narrow range of temperatures between 1021°C and 1035°C. For values of $\log\eta > 7$ the Urbain curve starts to deviate towards unrealistic values. No valid data therefore was gathered from the Urbain curve for the softening point and the annealing temperature. The Lakatos and Huff curves, however, are in close agreement for the softening point ($\log\eta = 7.6$) up to the annealing temperature at $\log\eta = 13.4$, expected at 547°C and 532°C respectively. The data does not fit nearly as well for type 3; the working point is anchored by the three curves across a temperature range of over 100°C, but nevertheless at consistently higher temperatures than for type 1. The Lakatos and Huff curves follow parallel but separate trajectories across the whole range and predict softening points of 741°C and 776°C, and annealing temperatures of 558°C and 566°C respectively. Again, these values are

higher than type 1. The Urbain data is again seen to deviate from data calculated from other models in the higher viscosity region. Relevant data to these plots is summed up in Table 6.4.

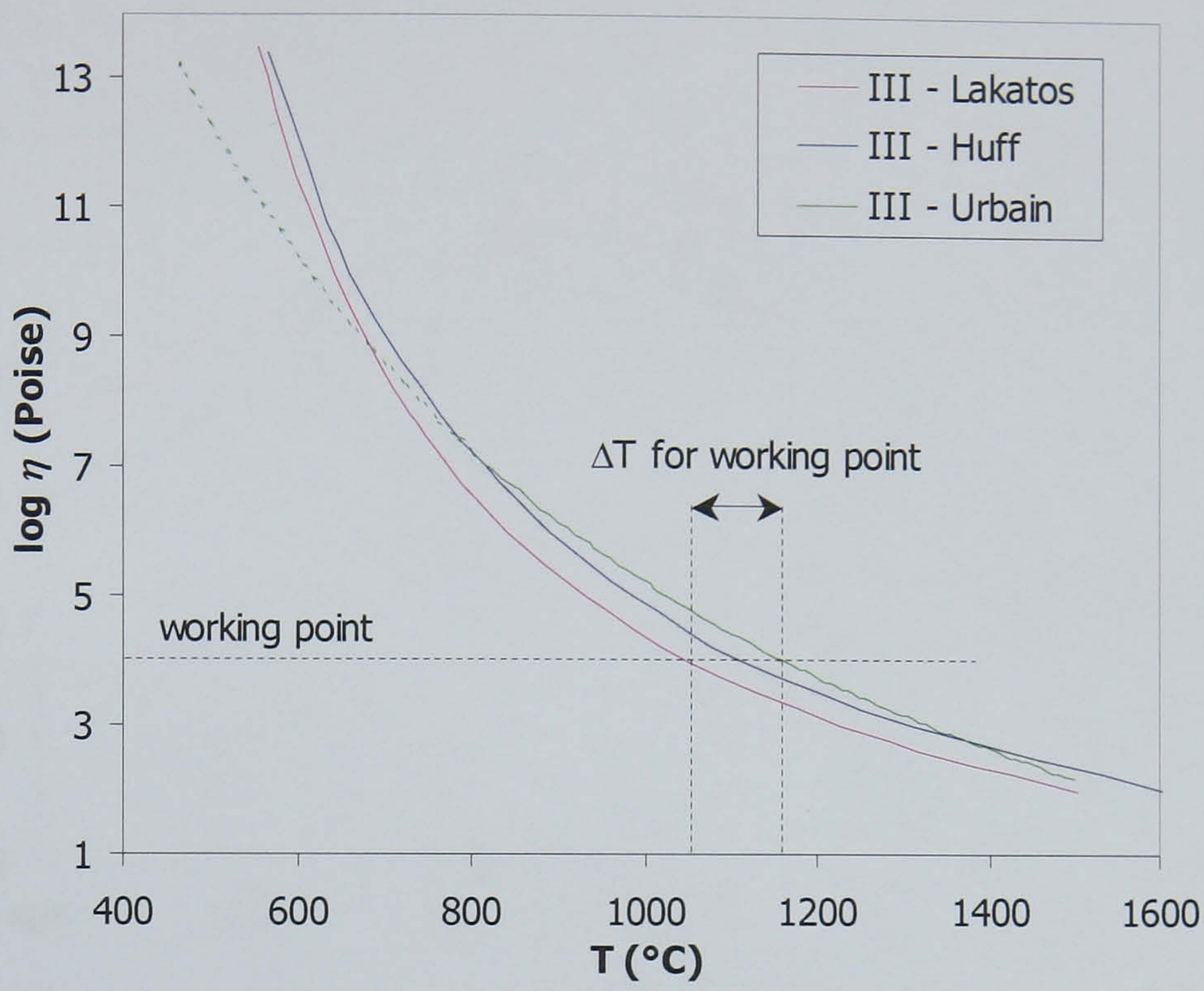


Figure 6-3: calculated viscosity-temperature curves for the replica type 3 LMG composition, using data from models proposed by Lakatos, Urbain and Huff.

	log η	Lakatos	Huff	Urbain	Average	SD (°C)
I						
working point	4	1021	1031	1035	1029	7.2
softening point	7.6	728	725	(666)	727	2.1
annealing T	13.4	547	532	na	540	10.6
III						
working point	4	1052	1117	1158	1109	53.5
softening point	7.6	741	776	(777)	759	24.7
annealing T	13.4	558	566	na	562	5.7

Table 6-4: theoretical working point, softening point and annealing temperature for type 1 and type 3 replica glasses according to viscosity models proposed by Lakatos, Huff and Urbain.

6.2.3 T_g

The glass transition temperature was measured by DSC for successfully cast replica samples (see below). The DSC output curves are shown in Figure 6-4 along with the construct lines to measure the onset of structural relaxation. Type 1 was found to have a T_g of 565 ±5°C and type 3 T_g was measured at 591 ±5°C. This corresponds closely to the annealing temperature

calculated from the viscosity curves; T_g is normally considered to be in the range of 30°C above the annealing temperature.

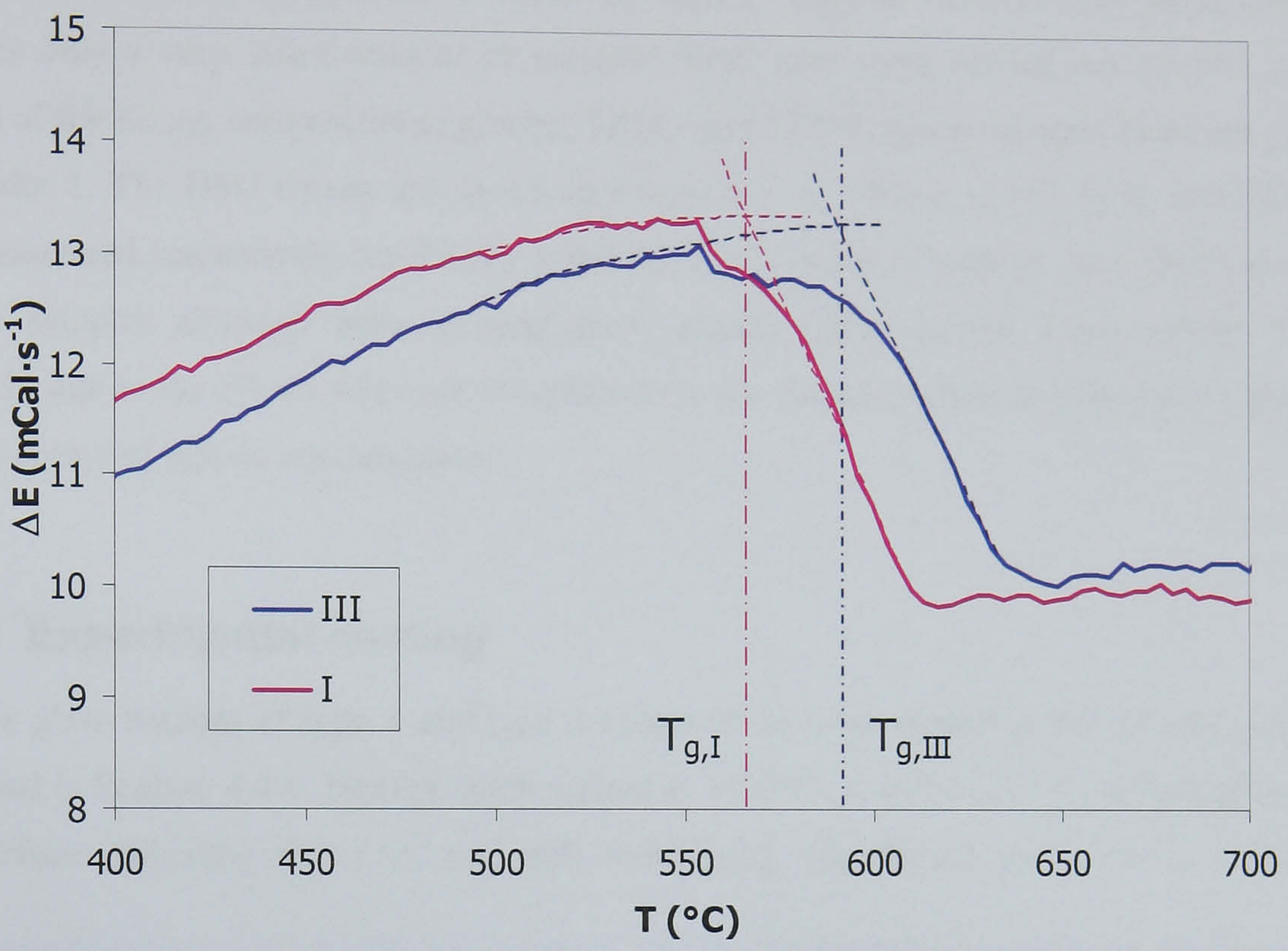


Figure 6-4: DSC curves of type 1 and type 3 replica glasses. The T_g values of the two glasses have been extrapolated from the intersection of the DSC curve tangents around the change in slope.

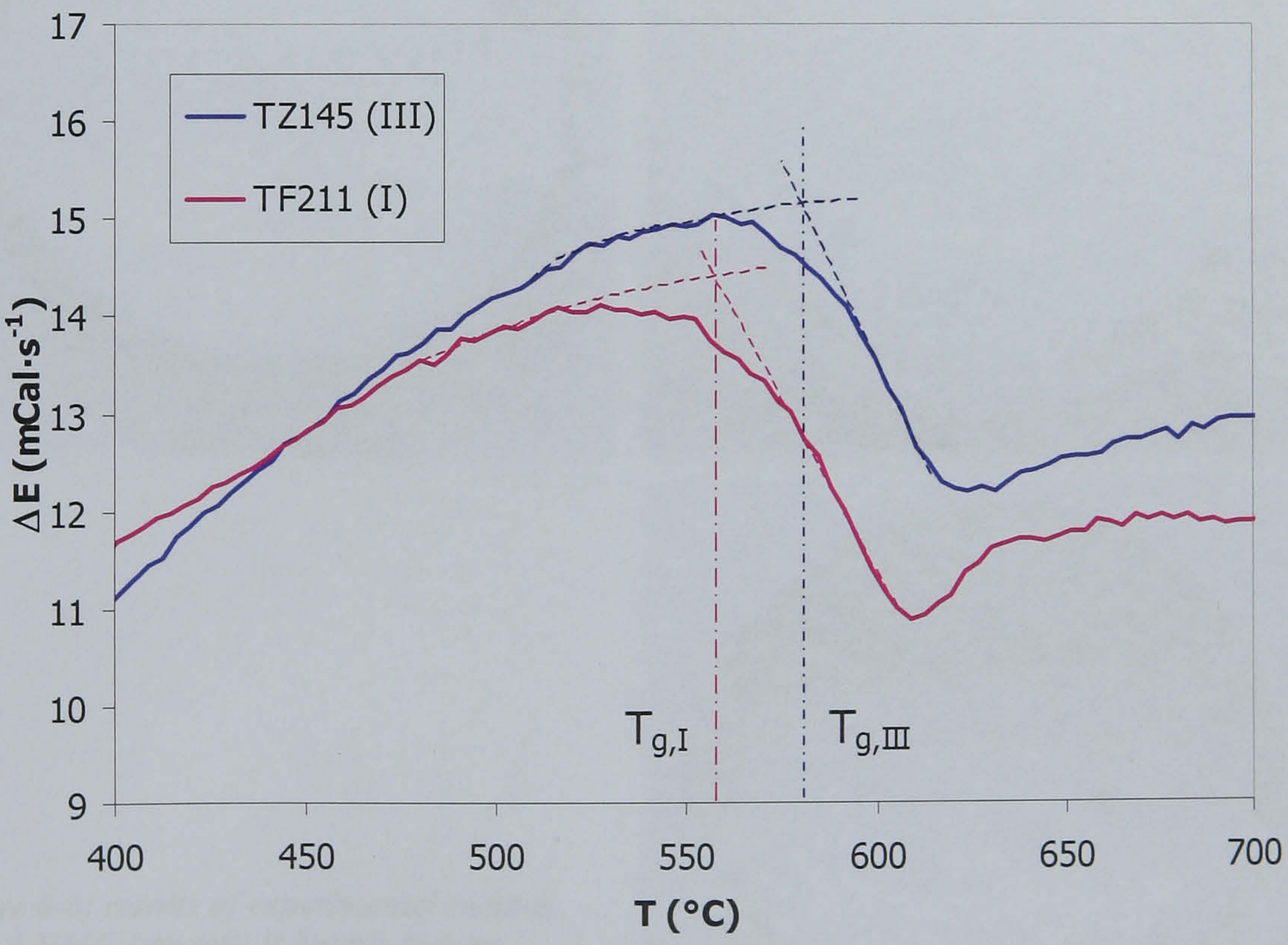


Figure 6-5: DSC curves of Raqqa samples TZ145 and TF211. The T_g values of the two glasses have been extrapolated from the intersection of the curve tangents around the change in slope.

6.2.3.1 Comparison with excavated samples

Of the thermal parameters, the glass transition temperature is the most straightforward to measure as scanning calorimetry is relatively quick, involves little sample preparation and requires only a very small amount of material. DSC runs were carried out on two samples typical of the Raqqa compositional groups: TZ143 and TF211, whose compositions are given in Appendix 1. The DSC curves are shown in Figure 6-5. T_g values of 557 ±5°C and 580 ±5°C were measured respectively for TZ143 and TF211. The results compare very favourably with replica samples although both archaeological glasses have slightly lower values. This is probably due to the effects of minor constituents in the Raqqa glasses that have been discarded in the simplified replica compositions.

6.2.4 Experimental casting

Replica glass batches of type 1 and type 3 composition were heated at the melting schedules indicated in Section 4.4.4. Neither batch melted at 1100°C. A distinctive foam was observed at the surface indicating that CO_2 was still volatilising. Significant quantities of unfused or

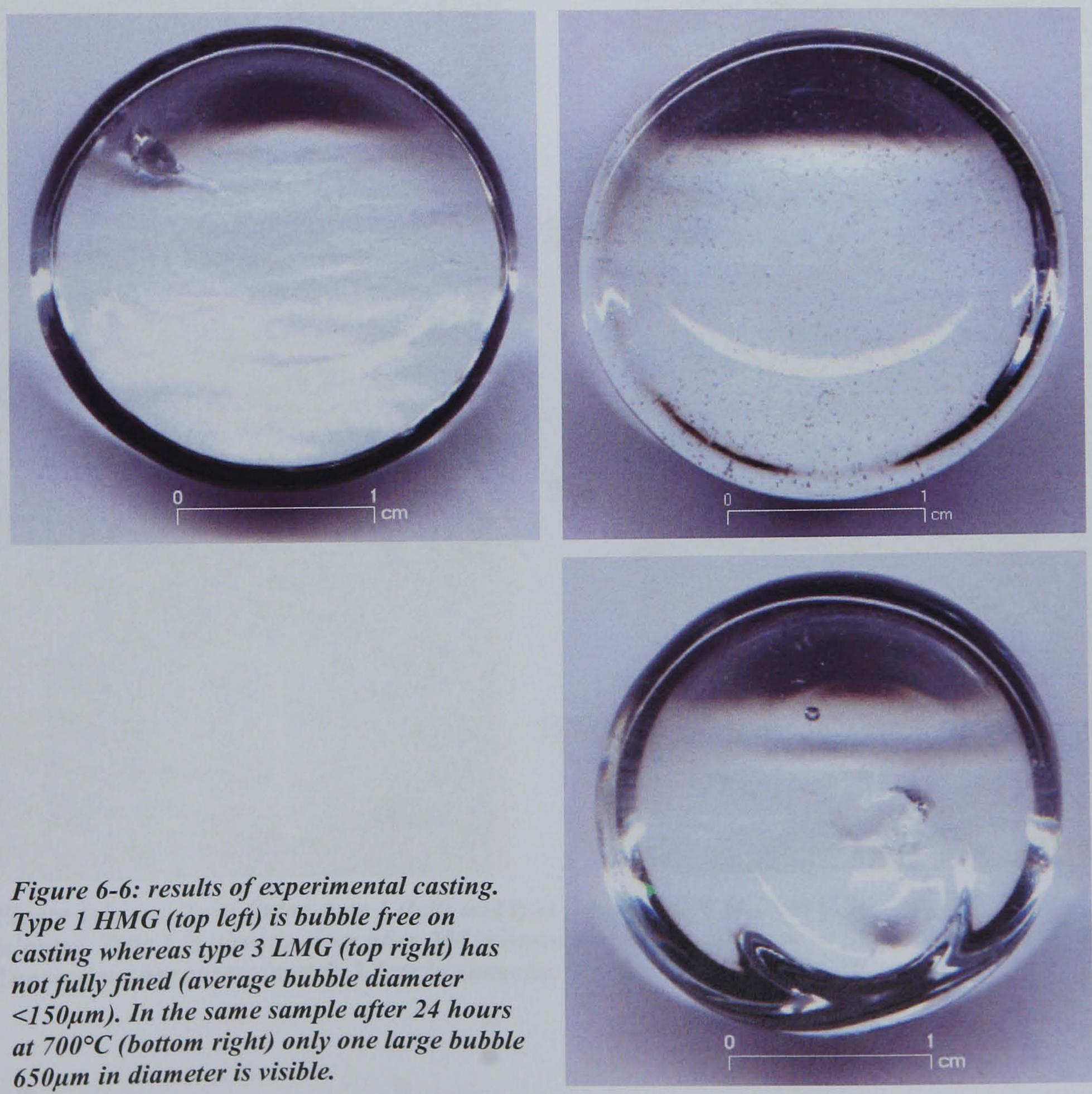


Figure 6-6: results of experimental casting. Type 1 HMG (top left) is bubble free on casting whereas type 3 LMG (top right) has not fully fined (average bubble diameter <150μm). In the same sample after 24 hours at 700°C (bottom right) only one large bubble 650μm in diameter is visible.

partially fused silica were also visible. At 1300°C a relatively clear, partially fined glass was produced in both cases, but on inspection under an optical microscope it was found to contain partially fused granules of silica. At 1400°C the glasses produced were clearer, although fining was still incomplete, and high enough viscous flow was attained to pour most of the glass from the crucible into the steel mould. At 1450°C a significant improvement in glass quality and viscous flow were noted and successful casts were achieved.

The glass flowed like hot syrup into the mould and the type 1 glass produced was free of bubbles. Type 3 was found to have a fine network of bubbles throughout, between 100 and 150μm in diameter. After this glass had been left for 24 hours at 700°C, the network of bubbles had disappeared and only one large bubble 650μm in diameter had coalesced. Images of samples cast at 1450°C are shown in Figure 6-6. Experimental results suggest a significant difference in fining properties between the replica types.

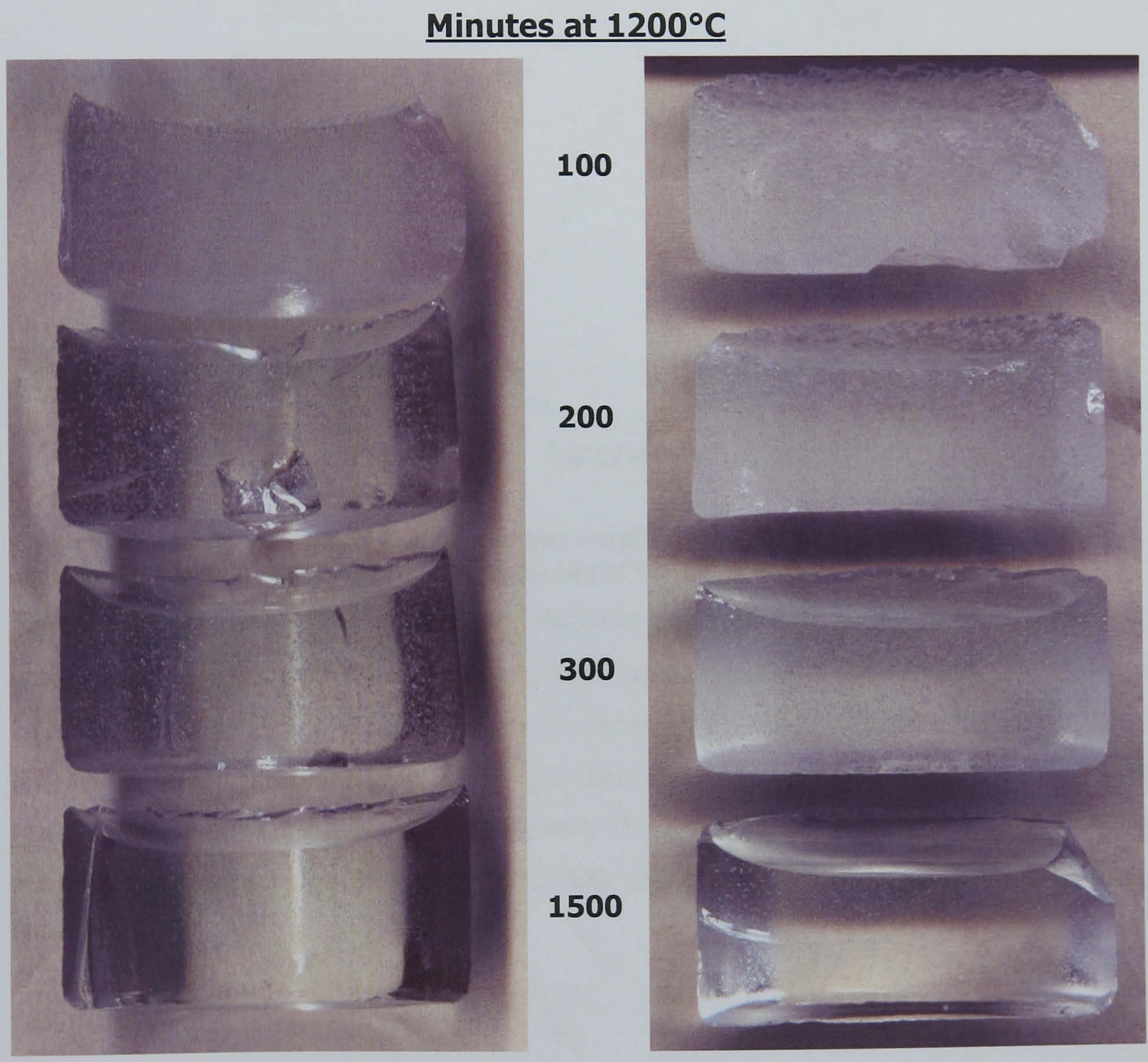


Figure 6-7: results of fining type 1 (left) and type 3 (right) held at 1200°C for 100, 200, 300 and 1500 minutes. Type 1 is already clear after 200 minutes whereas unfused silica grains are visible in type 3. The sections are approximately 2.5cm in diameter.

6.2.5 Experimental fining

Polished sections of type 1 and type 3 replica samples from the fining experiment outlined in Section 4.4.5 are shown in Figure 6-7. After 100 minutes neither glass had melted properly; the high percentage of unfused silica grains rendered the glasses opaque and grainy in appearance. After 200 minutes differences in glass quality became apparent, as type 1 had become transparent whereas type 3 remained opaque. An improvement was seen in type 3 after 300 minutes, but the glass quality was still poor. Type 1 by this stage has a fine network of bubbles in a clear matrix. After 1500 minutes type 1 had fined almost completely and a fine network of bubbles was still visible in type 3.

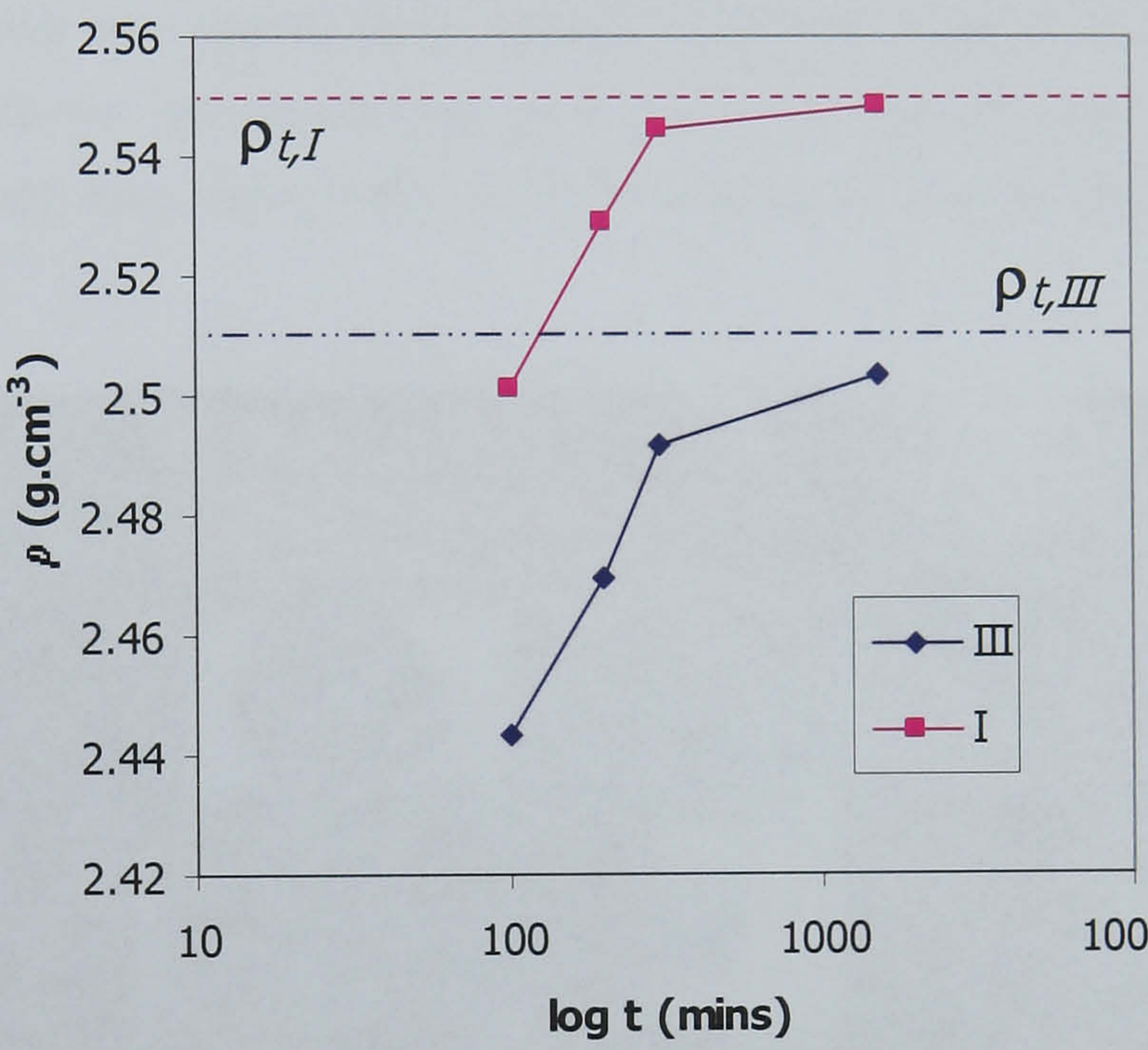


Figure 6-8: measured densities of type 1 and type 3 replica glasses against time held at 1200°C. Total densities, ρ_t, measured from fully dense samples cast at 1450°C, are indicated by dashed lines.

Fining rates were established after density data had been collected for the samples. The 'full' density (ρ_t) was measured from completely fined type 1 and type 3 glasses cast at 1450°C as 2.55 and 2.51 $g \cdot cm^{-3}$ respectively. Density measurements are plotted against the logarithm of time in Figure 6-8. From the graph it emerges that type 1 was much closer to full density than type 3 throughout the duration of the experiment. This can be directly related to viscosity, which is inversely proportional to the velocity of bubble movement through a melt given by Stokes' law:

$$\upsilon = \frac{2g\rho r^2}{9\eta} \qquad [6.1]$$

where g is the gravitational acceleration and r is the bubble diameter. For type 1 and type 3 glasses at 1200°C $\log\eta$ was found to be 3 and 3.4 respectively. The ratio of these two values is 2.5, which indicates that bubble removal is 2.5 times faster for type 1 than for type 3 for an equivalent bubble size.

6.2.6 Casting and fining properties

Viscosity is important in glassmaking as it defines the temperature range over which glass can be effectively cast and blown into finished articles and determines the rate at which gas bubbles escape from the melt. The workability range of replica type 1 is on average 80°C lower than for type 3, a significant difference when temperatures above 1000°C must be maintained. The replica type 3 glass also needed to be kept significantly longer at 1200°C in order to produce a sufficiently bubble-free glass. In Raqqa, such a relationship between composition and workability has greater implications for technological specialisation because the preparation of completely different raw ingredients is involved. Thus the adoption of a new glassmaking formula from different ingredients that produced a less viscous glass workable at lower temperatures would have implications on fuel economy as well as the quality of finished products.



Figure 6-9: cast glass from Raqqa for floor tile and tessera production with respective moulds in a display at the National Archaeological Museum in Aleppo, Syria.

Glass was cast mostly for floor tiles and tesserae (see Figure 6-9) and blown to make a range of utilitarian and decorative vessels. Fluidity is important in glass casting, more so than in blowing and other working techniques, where the glass is heated repeatedly as it is worked. Roman cast glass, for example, contains significantly higher levels of Na_2O than blown glass, to impart greater fluidity at lower temperatures for pouring or slumping in or over a mould[7]. The introduction of a less viscous glass would have been noticed by glassmakers and logically used for casting. Most of the cast glasses analysed from Tell Zujaj were in fact of a type 1

composition. It can thus be hypothesised that the general shift to a type 1 composition could be due not only to economic and political factors governing the procurement and availability of raw materials but also to technological factors related to the glassmaking process.

6.3 Bibliography

1. Bezborodov, M.A., *Chemie und Technologie der Antiken und Mittelalterlichen Gläser.* 1975, Mainz: Verlag Philipp Von Zabern.

2. Braunstein, H., *Biomass Energy Systems and the Environment.* 1981, Oxford: Pergamon Press.

3. Henderson, J., *The Raw Materials of Early Glass Production.* Oxford Journal of Archaeology, 1985. **4**(3): p. 267-291.

4. Etegni, L. and A.G. Cambell, *Physical and Chemical Characteristics of Wood Ash.* Bioresource Technology, 1991. **37**: p. 173-178.

5. Henderson, J., *Electron Probe Microanalysis of Mixed-Alkali Glasses.* Archaeometry, 1988. **30**(1): p. 77-91.

6. Choudhary, M.K. and N.T. Huff, *Mathematical Modeling in the Glass Industry: An Overview of Status and Needs.* Glastechnische Berichte Glass Science and Technology, 1997. **70**(12): p. 363-370.

7. Fischer, A. and W.P. McCray, *Glass Production Activities as Practised at Sepphoris, Israel.* Journal of Archaeological Sciences, 1999. **26**: p. 893-905.

Chapter 7

Characterisation of production waste from Raqqa

Furnace bricks, glass-furnace lining interfaces and casting trays from Tell Belor, sampled on site during the British Archaeological Mission to Raqqa 2000, and outlined and classified in Chapter 3, were analysed by various methods in order to establish their identity and to assess their performance characteristics in relation to glass manufacturing at Raqqa.

7.1 Glass on vitrified Ca-rich substrates: casting trays or furnace fragments?

7.1.1 Type A – TB6/TB2/TB5/TB9

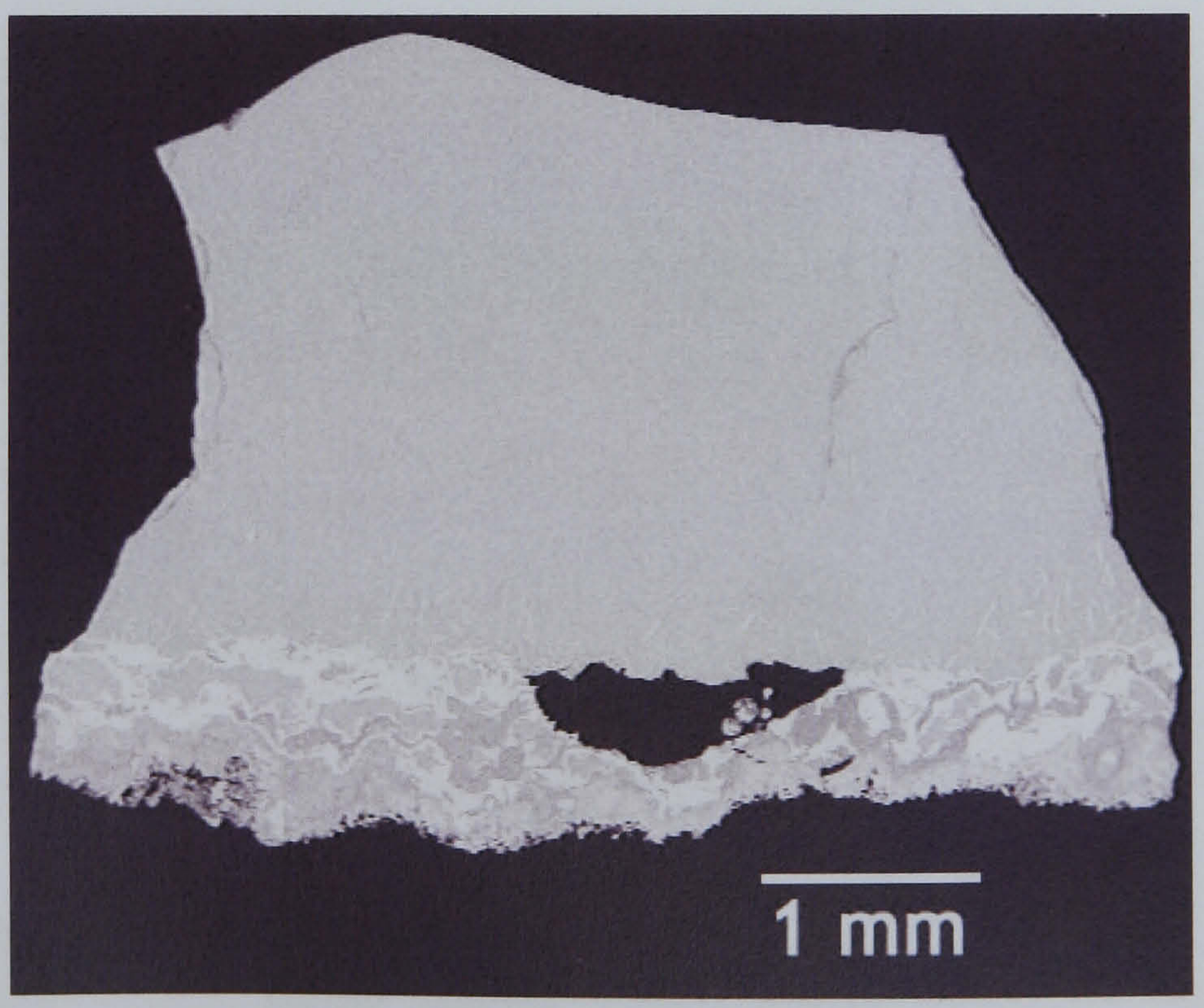


Figure 7-1: backscattered electron image of cross-section of TB6 showing reaction zone below interface.

TB6 presented a 0.5mm thick layer of vitrified substrate with glass still adhering to the upper surface. The bottom layer showed heat contours where the glass had come into contact with a white powder, causing the powder to react and vitrify. Figure 7-1 shows a multitude of phases in the 1mm thick 'reaction zone', above which a region of crystalline growth extends approximately 0.5mm into the bulk of the glass.

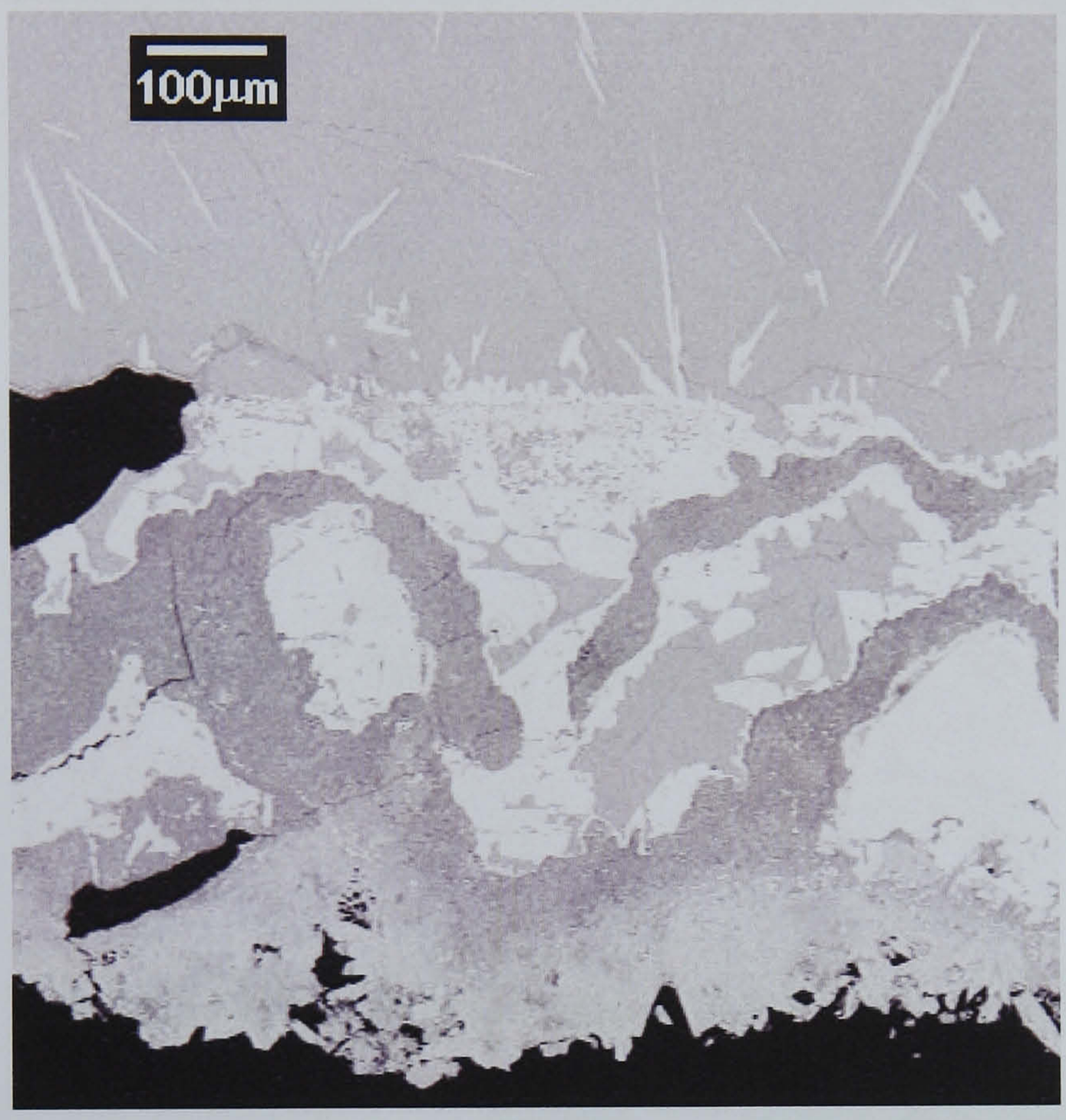


Fig 7-2: at higher magnification the different phases in the reaction zone of TB6 in Figure 7-1 are visible, as well as precipitated crystals in the glass.

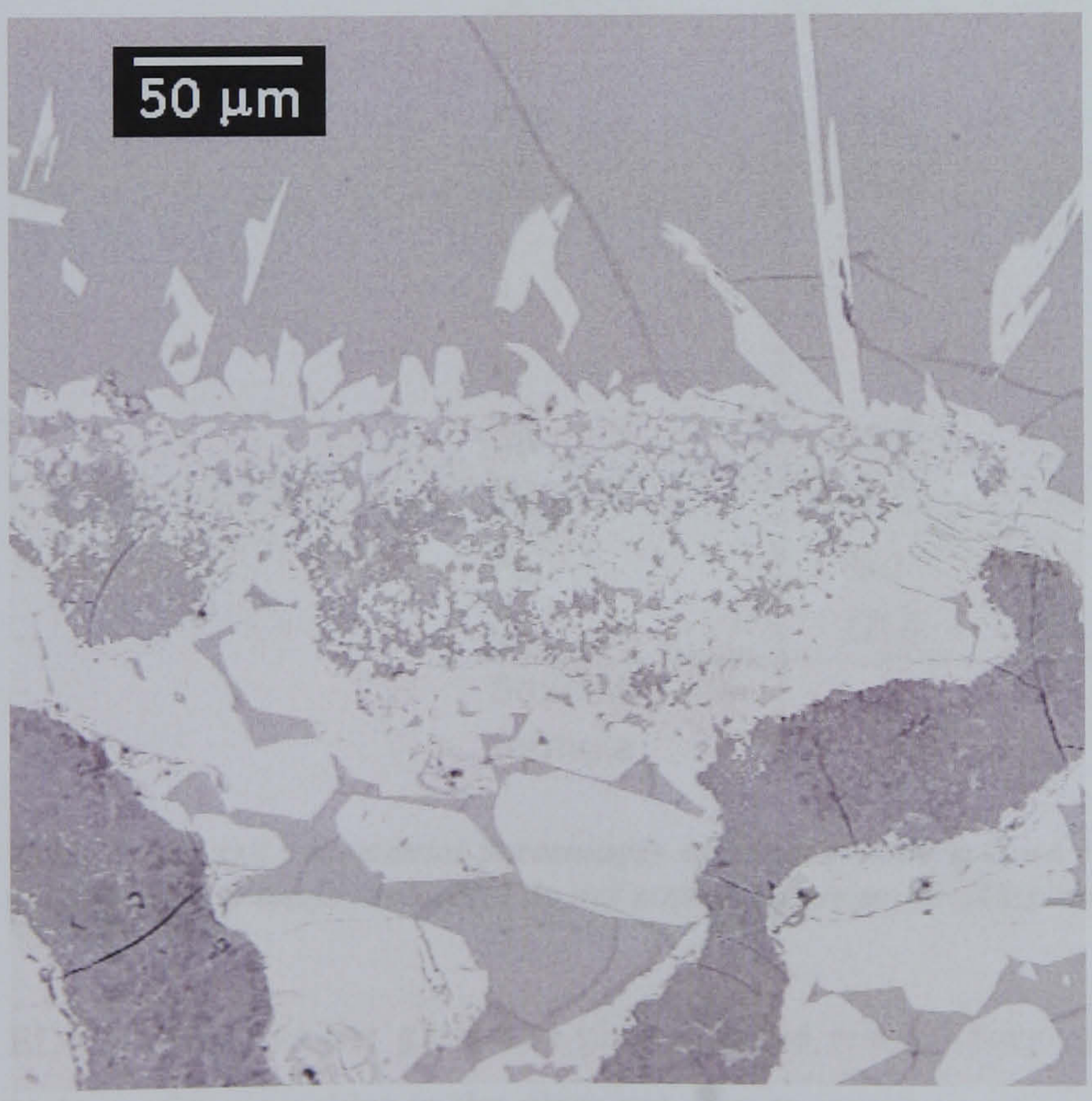


Figure 7-3: the minute granular phase can be seen at the reaction zone, as well as crystals heterogeneously precipitated from the boundary.

A closer look at the reaction zone (Figures 7-2 and 7-3) reveals a dark granular mottled phase layered between fused and partly fused white grains up to 100μm in diameter in a clear glassy matrix. Near the glass interface the glassy phase forms the matrix for much finer grains. From the interface thin elongated crystals, many with a compositionally distinct centre, rise into the glass bulk. The extent of vitrification, and hence the limit of interdiffusion, is marked at the low extremity of the reaction zone by a compositional gradient within the darker mottled phase.

Oxide	above interface		below interface	
(wt%)	1 mm	50 μm	200 μm	400 μm
Na_2O	11.7	12.8	13.0	13.3
MgO	2.9	2.9	2.0	2.9
Al_2O_3	0.9	1.0	3.8	1.8
SiO_2	70.7	67.7	68.3	69.1
P_2O_5	0.3	0.4	0.7	0.8
SO_3	0.1	0.1	0.4	0.5
Cl	0.7	0.7	1.1	0.6
K_2O	2.7	2.2	2.9	2.8
CaO	7.7	9.4	7.3	5.8
TiO_2	-	0.1	0.1	0.3
MnO	1.8	2.5	0.2	2.0
Fe_2O_3	0.4	0.2	0.2	0.1

Table 7-1: normalised EDXA data of glass above and below reaction boundary of TB6.

Element	wollastonite	
(atom%)	grains	crystals
Na	-	0.2
Mg	0.6	0.3
Si	24.0	24.5
P	-	0.2
S	-	-
K	-	-
Ca	24.3	25.3
Mn	0.1	0.4
Fe	0.1	-
O	*50.9*	*49.1*
Stoichiometric formula	$CaO.SiO_2$	

Table 7-2: EDXA elemental percentages of white phases around reaction zone of TB6, identified as wollastonite. O totals (in italics) do not match the proposed stoichiometry for reasons given overleaf.

EDXA results of the glass and phases in the reacted base are given in Tables 7-1 and 7-2. Values of most oxides in the glass are seen to increase with increasing depth at the expense of

CaO. This is due to the Ca-rich phases created in the reaction zone, which leave the glass locally depleted in Ca and correspondingly raise the levels of other components. This is particularly noticeable for Al_2O_3 and Na_2O, which are not present in any other phases. The pure Ca phase at the base of the reaction zone was identified as $CaCO_3$ through XRD analysis (in Figure 7-4). Two common polymorphs of $CaCO_3$, calcite and aragonite, were detected. Consequently, the powdered grains below the base of the reaction zone consist of unreacted $CaCO_3$, possibly a powdered limestone substrate on to which molten glass was poured. The reaction zone represents, therefore, the result of high temperature interaction between the molten glass and the calcareous substrate. Ca-rich products have in fact formed. The white grains in the reaction zone were identified as calcium silicates of the type $CaO.SiO_2$ on the basis of proportional atomic percentages of Ca and Si[ξ], known as wollastonite or parawollastonite, the low temperature $CaO.SiO_2$ polymorph stable below 1120°C[1]. Likewise, the crystals in the glass were found to have similar cationic proportions, but the highly directional morphology and the lower quantity of impurities compared to the grains rather suggest a more rapid growth mechanism. The rounded nature of the grains suggests a slower growth. Wollastonite is known to form preferentially to devitrite ($Na_2O.3CaO.6SiO_2$) in multi-component soda-lime-silica glasses[2]. Wollastonite precipitation in SLS glass systems will be dealt with in greater detail in Section 7.3.5.

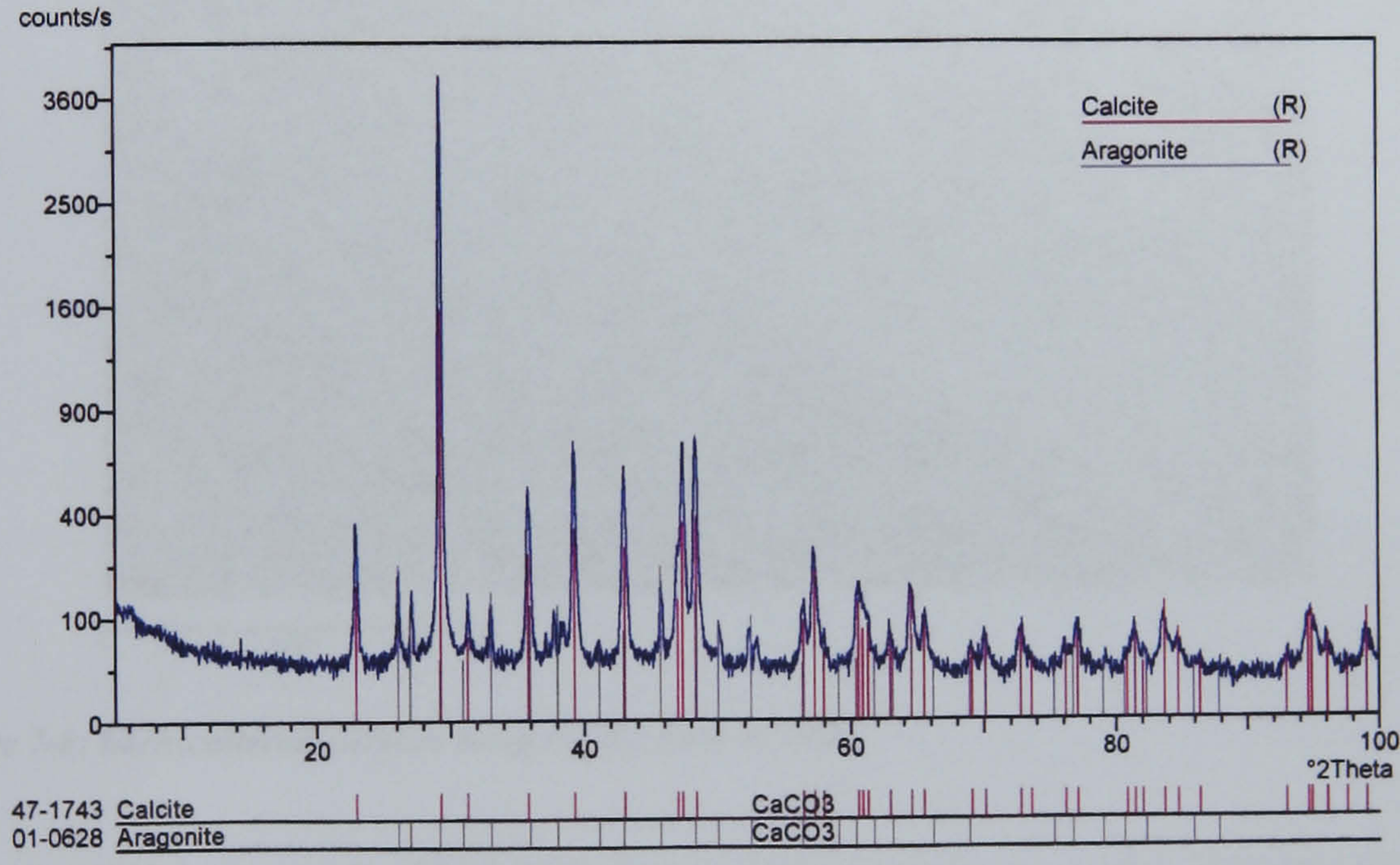


Figure 7-4: XRD results on the base of TB6 indicate it is a calcium carbonate ($CaCO_3$) consisting primarily of calcite with some aragonite.

[ξ] Quantification of O atoms is problematic due to the high analytical errors involved, so atomic O values were not considered. Phase identification based on cationic data is otherwise supported by observations, presented in Section 7.3.4, on the characteristic wollastonite morphology of crystals growing in the glass.

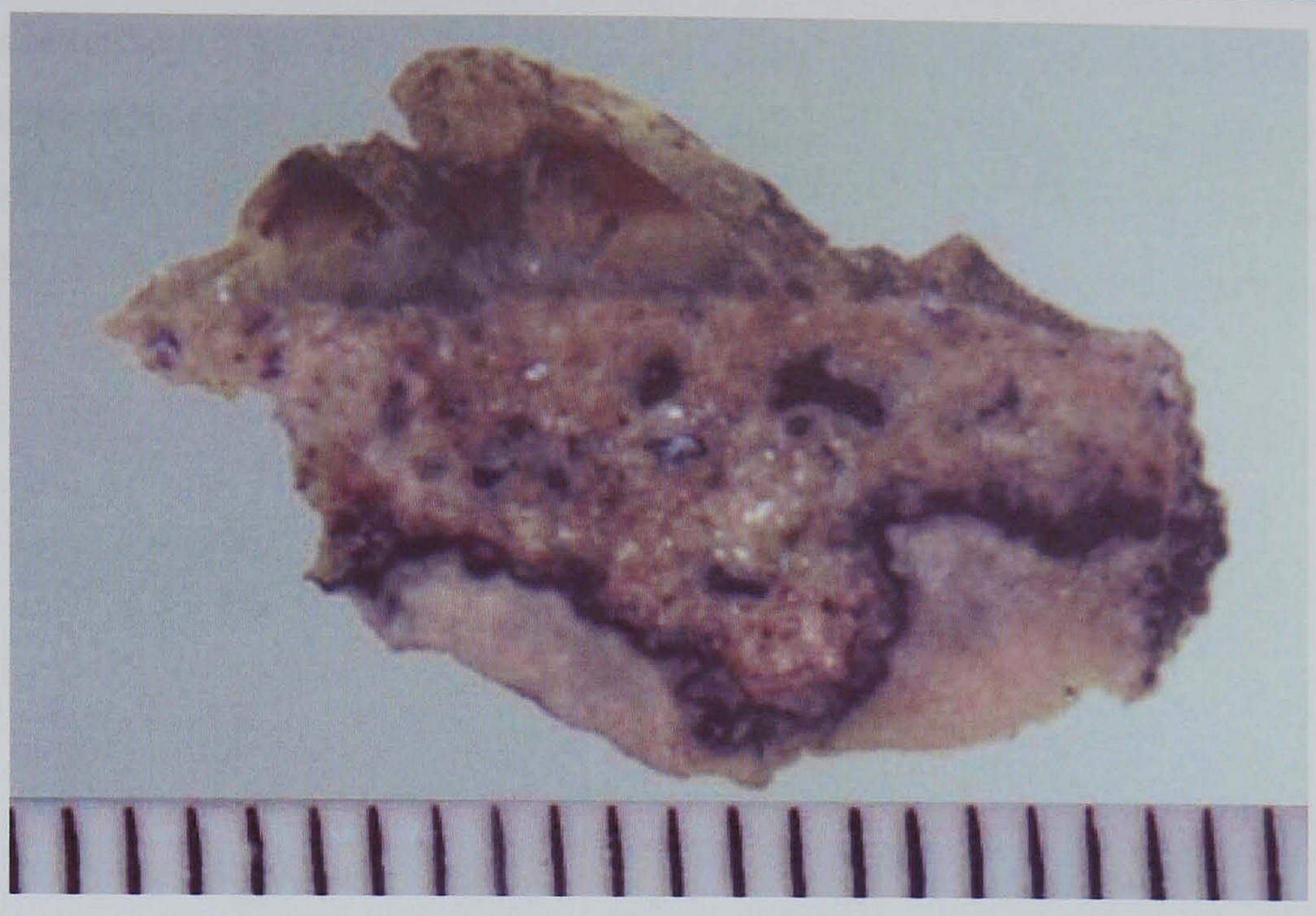


Figure 7-5: sample TB2 in polished cross-section. The limestone base, the vitrified reaction zone and browned glass above are visible

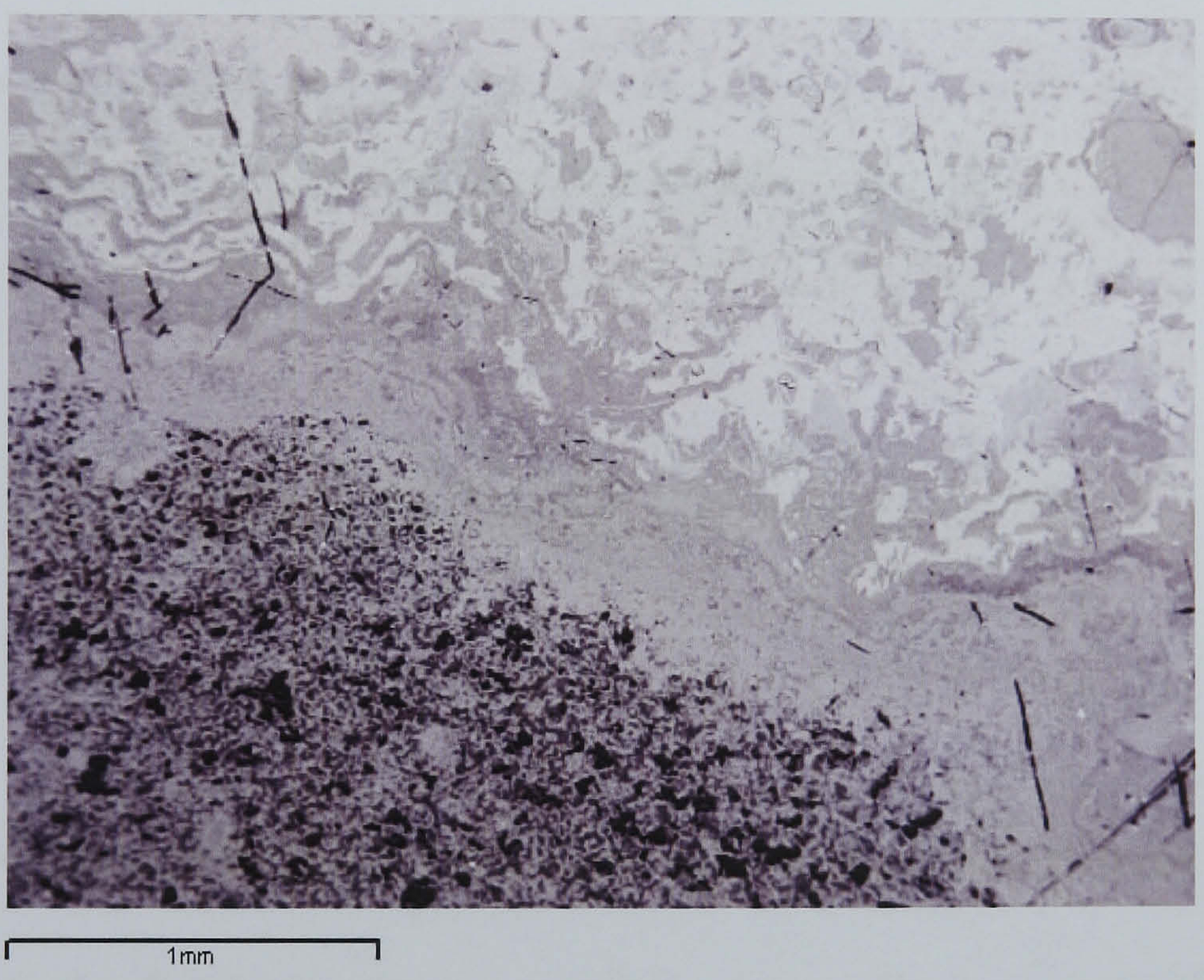


Figure 7-6: backscattered electron image of the base of TB2.

Similarly, TB2 is the result of high temperature interaction of glass with a limestone substrate. A cross-section of the piece (Figure 7-5) shows the limestone base, the 3-5mm thick vitrified reaction zone and the adhering glass above. The pale green glass changes to a dark brown colour approximately 1mm above the interface. The base shows a distinct border that marks the extent of reaction (Figure 7-6). EDXA data for TB2 shown in Tables 7-3 and 7-4 revealed a gradual interaction with Si from the almost pure $CaCO_3$ base. The bright phase throughout the vitrified region is a Ca-silicate that shows a considerable change in composition from the base

to the glass boundary. The glass-substrate interface (Figure 7-7) shows large Ca-rich inclusions in a Ca-silicate matrix and limited wollastonite precipitation in the glass. The glass composition changes with increasing distance from the interface, becoming gradually more enriched in MnO. This explains the brown tint observed 1mm above the interface. No Fe was detected in the glass.

Oxide (wt%)	Ca base	dark border	matrix base	matrix top
Na_2O	-	-	2.1	0.6
MgO	3.1	5.3	8.7	2.2
Al_2O_3	0.0	0.0	4.5	0.8
SiO_2	2.7	11.7	48.9	36.9
K_2O	-	-	0.4	-
CaO	94.2	83.0	32.6	31.3
TiO_2	-	-	0.3	-
MnO	-	-	0.9	1.1
Fe_2O_3	-	-	1.5	0.7

Table 7-3: normalised EDXA results for phases in the base and matrix composition of TB2.

Oxide (wt%)	glass (distance from interface) 100μm	1mm	2mm
Na_2O	11.9	11.6	10.9
MgO	3.5	3.4	3.3
Al_2O_3	0.9	0.9	1.2
SiO_2	70.2	70.2	70.5
Cl	0.7	0.6	0.6
K_2O	2.5	2.5	2.4
CaO	8.9	9.4	9.4
MnO	1.4	1.4	1.7

Table 7-4: normalised EDXA results for glass in TB2 at different points above the interface.

TB5 consists of a dark brown glass on a vitrified substrate. The cross-section (Figure 7-8) shows the irregularity of the interface: the reaction zone is irregularly distributed with large pockets of glass surrounded by reacted limestone. Widespread nucleation of wollastonite crystals is also visible. The pattern at the base is similar to TB2 and is shown in Figure 7-9: the dark layer at the very base of the figure is the extent of vitrification of the $CaCO_3$ base above which wollastonite grains have grown. In between the base and the glass a Ca-rich mottled phase predominates, with some rounded inclusions also visible. Compositional results are given in Table 7-5. The glass formed below the interface is significantly depleted in Na in favour of Si. The glass in the sample is finely cracked, producing single shards 40-200μm in size. This

would seem to indicate a rapid cooling regime and possibly quenching. A furnace base, on the other hand, would have slowly cooled glass attached to it.

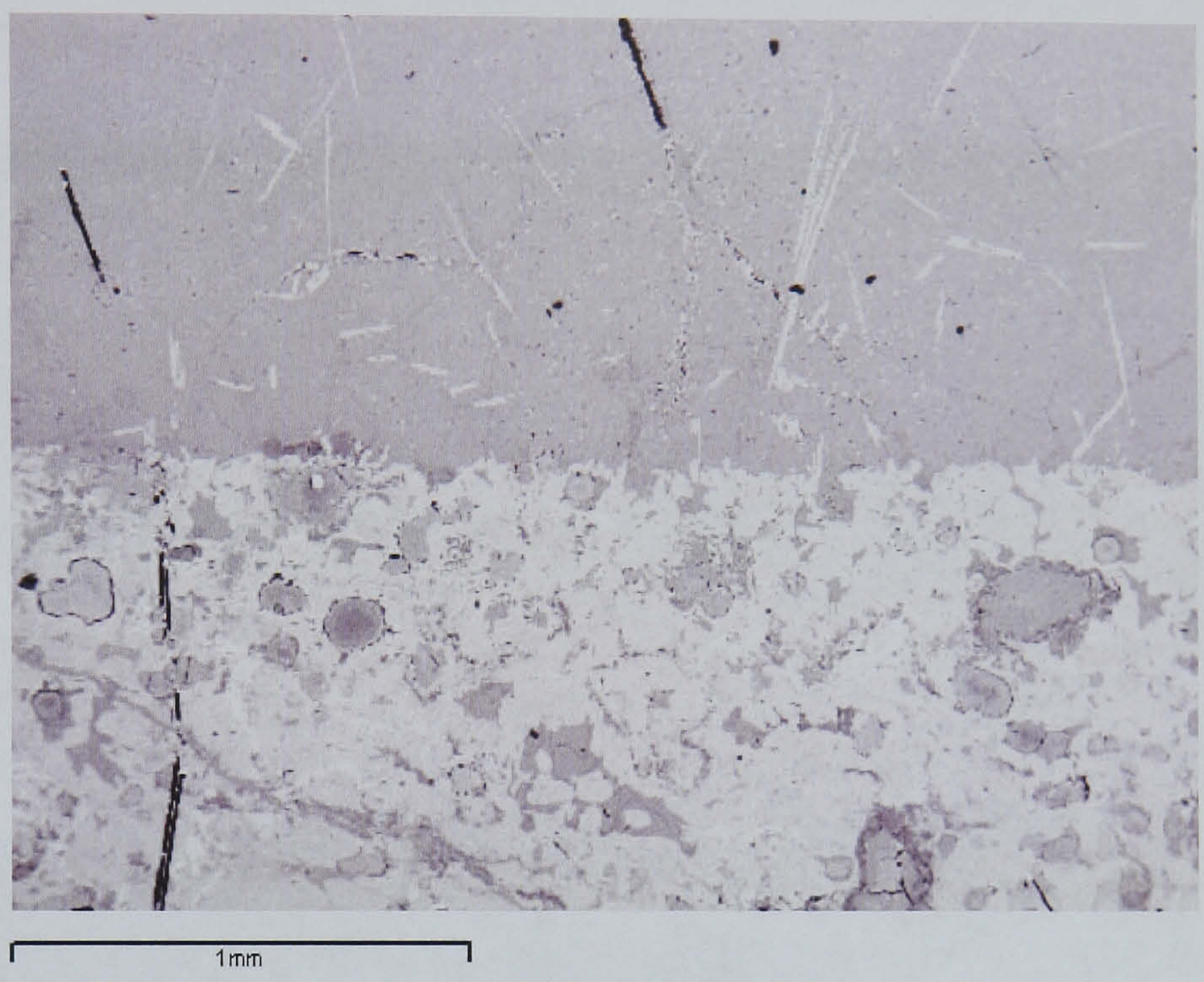


Figure 7-7: backscattered electron image of the glass-substrate interface of TB2. Limited wollastonite precipitation is observed in the glass.

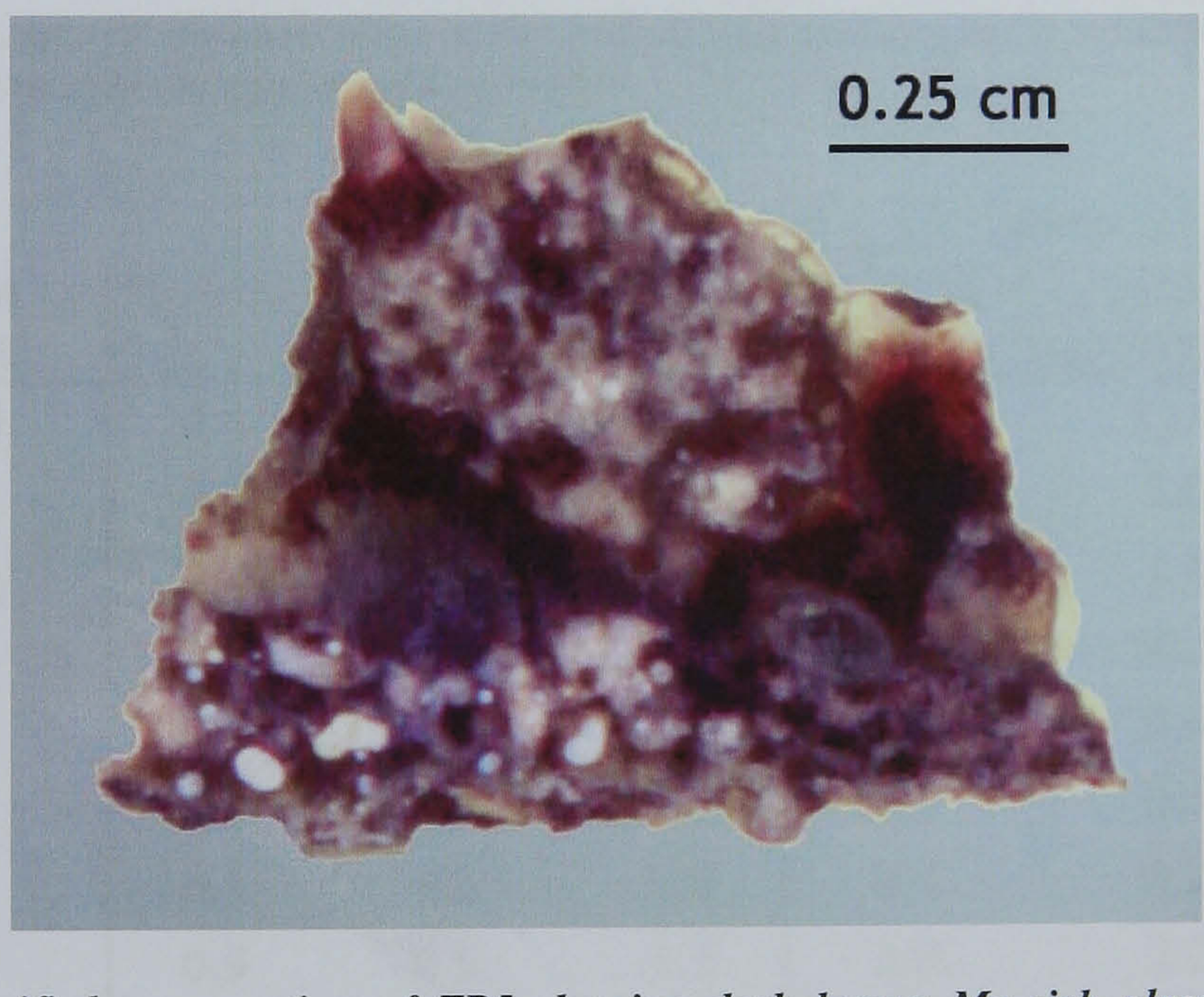


Figure 7-8: magnified cross-section of TB5 showing dark brown Mn-rich glass above a vitrified substrate.

The cracking has led to the formation of a number of channels that have permitted the movement of aqueous species around the borders of individual shards, promoting some alkali depletion of the glass. An elemental map of a cracked, wollastonite-rich area (Figure 7-10) revealed clear compositional differences: the wollastonite needles and the channel in the top right corner are rich in Ca and depleted in Na. High C counts in the channel indicate the

presence of $CaCO_3$ or organic Ca-rich species that have penetrated into the cracked glass network. Significant Na depletion at the edges of the channel is contrasted by O enrichment in this area, suggesting the presence of weathered species. Alkali depletion of glasses will be discussed in Chapters 8 and 9.

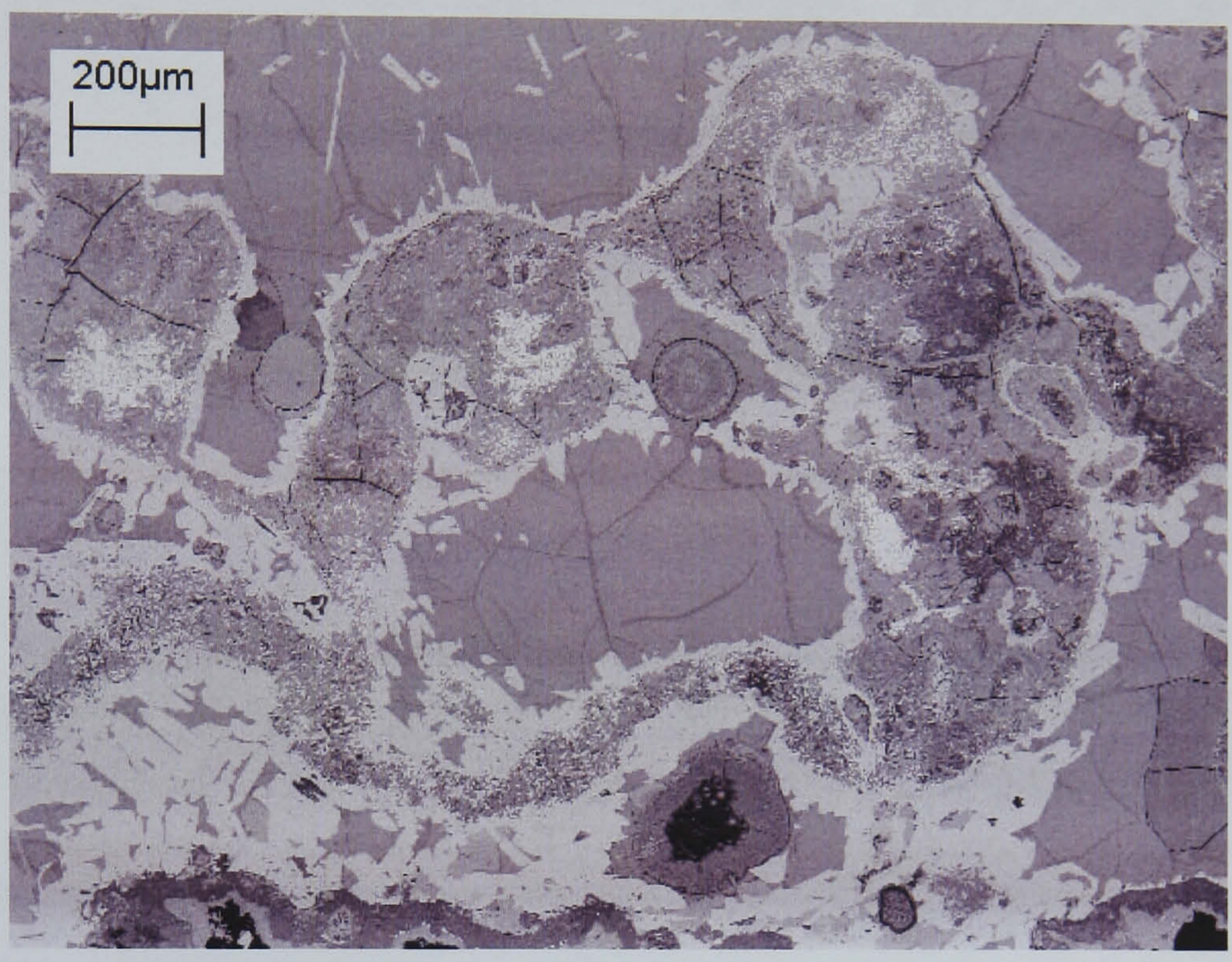


Figure 7-9: backscattered electron image of the base of TB5 showing the complex reacted phases and the nucleated wollastonite crystals in a glassy matrix.

Oxide (wt%)	Ca base	wollastonite grains	mottled phase	glass in reaction zone	glass above reaction zone
Na_2O	0.4	0.1	1.9	8.7	13.6
MgO	1.7	1.0	6.1	4.5	5.0
Al_2O_3	0.0	0.0	1.5	1.9	1.4
SiO_2	0.5	53.8	54.3	72.2	66.2
P_2O_5	0.4	0.0	1.0	0.4	0.4
SO_3	4.8	0.0	1.7	0.3	0.3
Cl	0.1	0.0	0.5	0.8	0.7
K_2O	0.9	0.0	1.5	2.8	3.0
CaO	91.0	44.2	27.8	6.0	6.3
MnO	0.0	0.9	2.5	1.7	2.4
Fe_2O_3	0.1	0.0	1.2	0.6	0.6

Table 7-5: normalised EDXA results for phases in the base and for the glass composition of TB5.

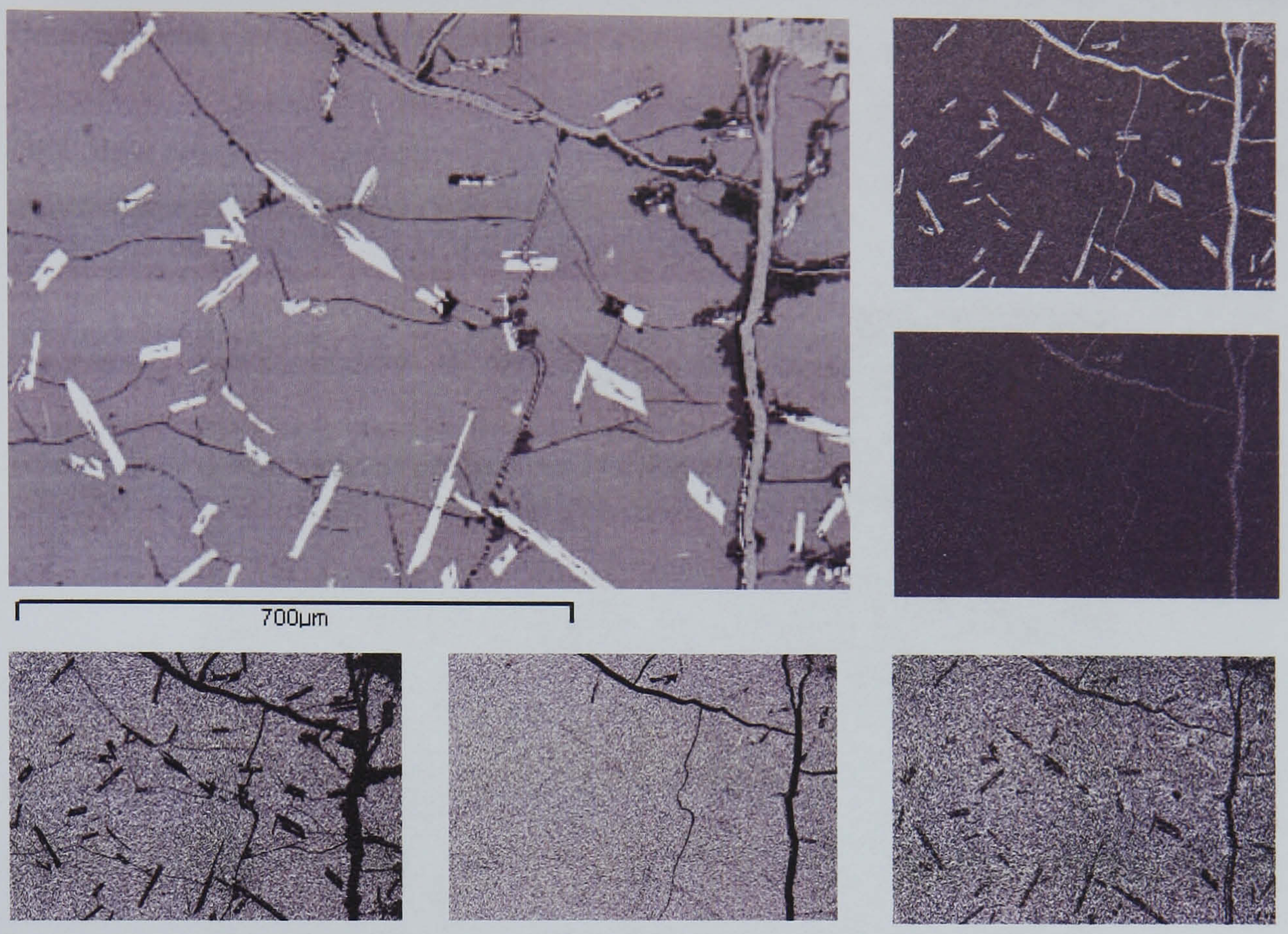


Figure 7-10: backscattered electron image (top left) of the cracks induced by wollastonite precipitation in TB5. Elemental maps of the image are shown clockwise, from top right, for Ca, C, O, Si and Na.



Figure 7-11: magnified cross-section of TB9 showing unreacted $CaCO_3$ base, vitrified body with darkened upper surface, and large pores in structure.

TB9 appears different to the previous fragments, as it is of a deep brown colour and had no glass adhering to its surfaces. The cross-section (Figure 7-11) revealed a vitrified structure, with a partially reacted, powdered base, and a darkened upper surface also visible. The top layer has been exposed to higher temperatures than the rest of the sample: viewed at higher magnification (Figure 7-12), it is 200-400µm thick and shows dendritic crystal growth in a vitreous matrix (a typical growth formation is illustrated in Figure 7-13) and a minor nucleated phase (the darker phase in Figure 7-12). A crystalline outer shell grows from its upper extremity. EDXA results for TB9 are given in Tables 7-6 and 7-7. The base was identified as gypsum ($CaSO_4$), calculated

from elemental proportions, mixed with SiO_2. The dendritic crystals exhibit the atomic proportions of the pyroxene mineral augite, $(Ca,Na,Mg,Fe,Mn,Ti)_2[(Si,Al)_2O_6]$. Although the O totals associated with the augite scan are not consistent with the expected stoichiometry, the close fit for all cationic components supports this identification.

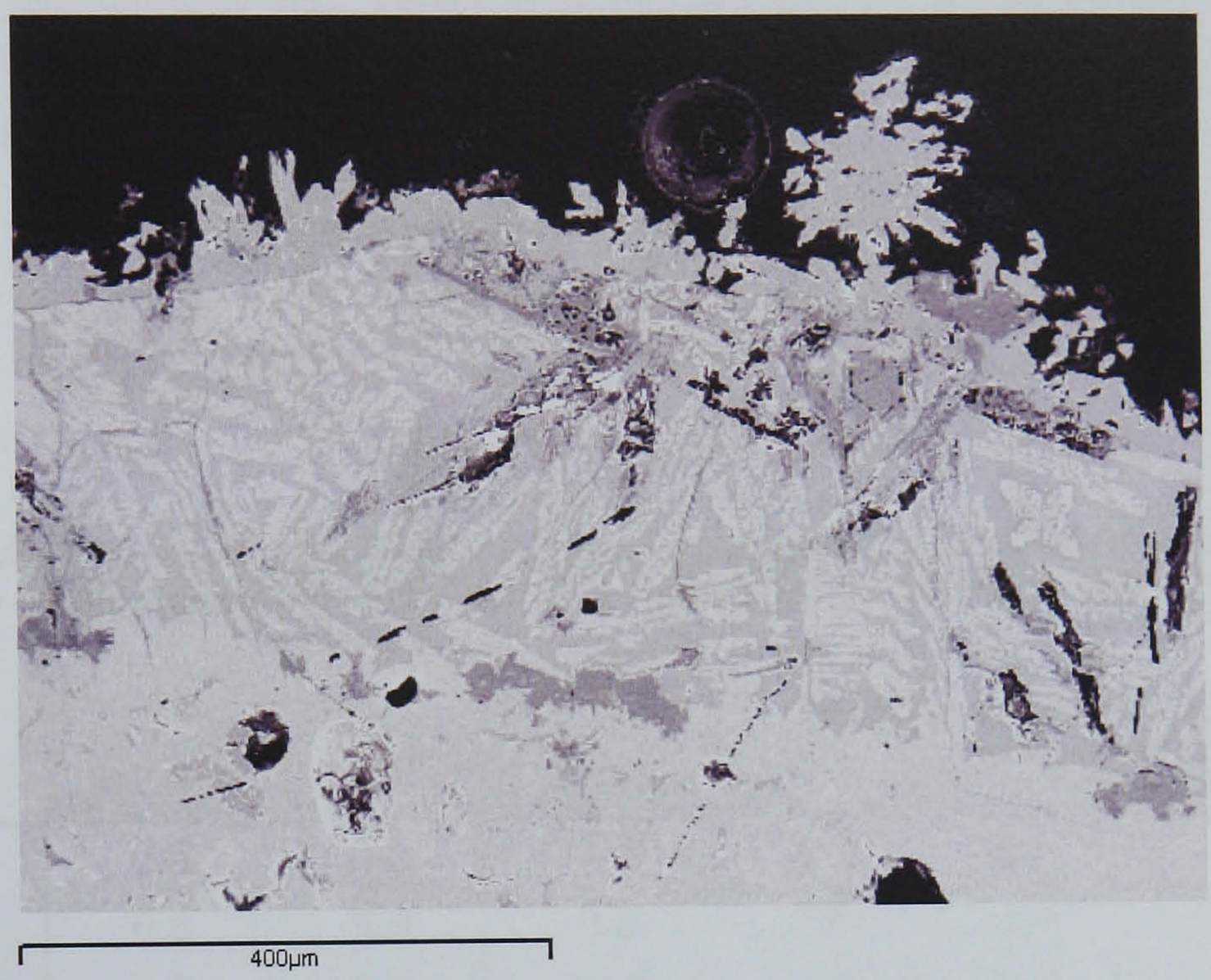


Figure 7-12: backscattered electron image of the top edge of TB9 showing precipitated crystals in a vitrified phase that stretches 400µm into the matrix below.

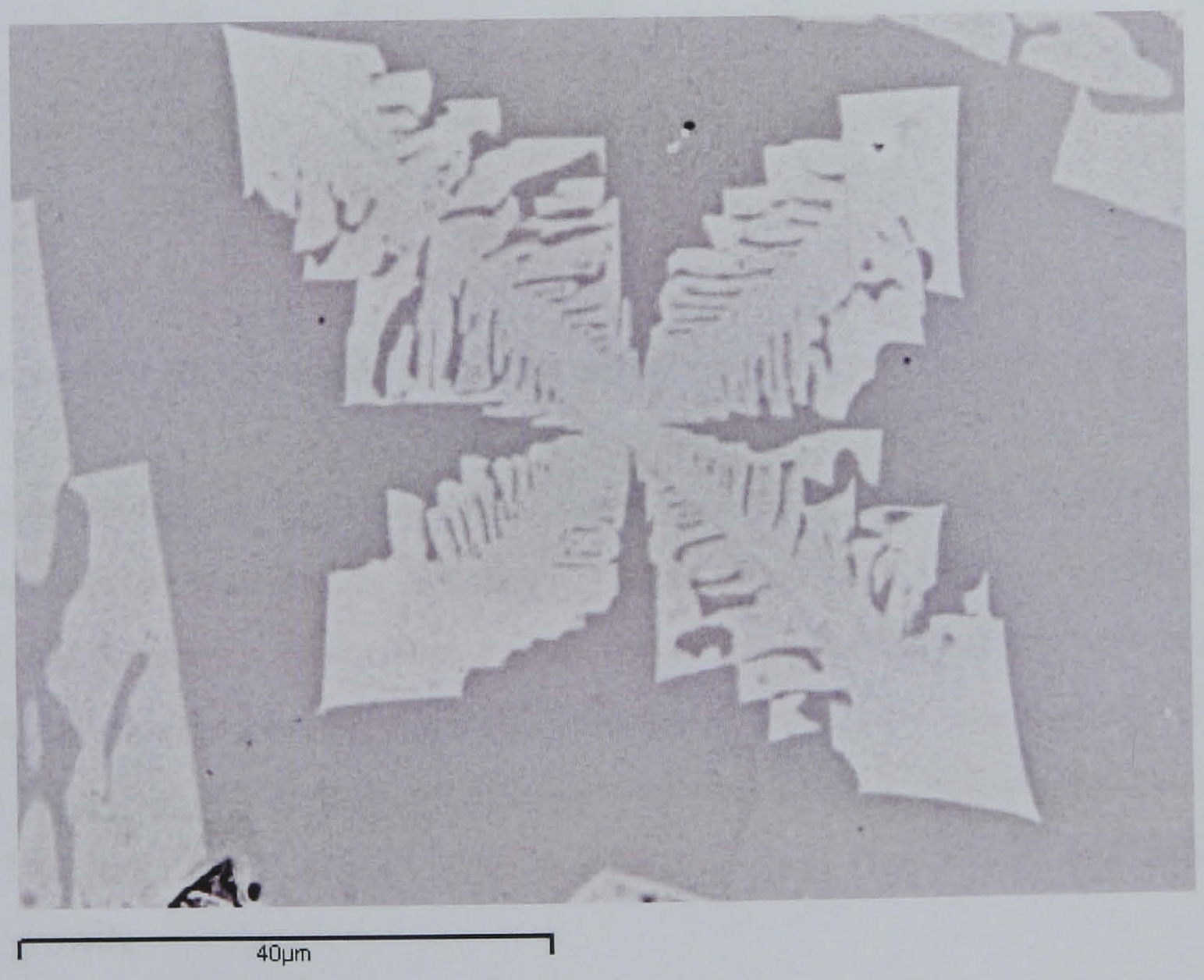


Figure 7-13: close-up of previous figure showing dendritic growth of a precipitated augite crystal.

Element (%)	Gypsum	Augite	
Na	-	1.5	
Mg	-	6.8	Calculations:
Al	-	1.8	Si+Al
Si	-	25.1	26.9
S	16.9	-	
Ca	16.4	10.8	Ca+Na+Mg+
Ti	-	0.6	+Fe+Mn+Ti
Fe	-	5.0	26.4
Mn	-	1.7	
O	*66.8*	*46.7*	
Stoichiometric formula	$CaSO_4$	$(Ca,Na,Mg,Fe,Mn,Ti)_2[(Si,Al)_2O_6]$	

Table 7-6: EDXA elemental percentages for gypsum and augite crystals identified at the base and upper surface of TB9 respectively. As for Table 7-2, O totals do not match their cationic equivalents.

Oxide	matrix		upper layer			
(wt%)	near base	near top	augite field	crystals	dark phase	Ca crystals
Na_2O	2.8	3.5	3.4	3.3	0.5	-
MgO	6.8	5.9	0.8	7.8	2.4	0.1
Al_2O_3	7.8	8.7	13.8	4.8	6.8	-
SiO_2	44.5	46.8	60.0	47.8	76.8	-
K_2O	0.3	0.9	6.1	0.4	7.2	-
CaO	33.8	29.0	2.6	31.3	1.9	98.6
TiO_2	0.3	0.3	1.6	-	-	-
MnO	0.2	1.0	2.5	1.5	-	-
Fe_2O_3	3.5	3.7	8.7	3.1	4.4	-
SrO	-	-	-	-	-	1.2

Table 7-7: normalised EDXA results for the vitreous matrix and the upper augite-rich layer of TB9.

The outermost crystalline layer was interpreted as $CaCO_3$, which is more stable at lower temperatures than the pure oxide. The glassy matrix of the layer contains significant levels of Ca, Mg, Fe and Al oxides. In the augite field, the results of mass transport are visible through variations in matrix composition; a general increase in levels of heavy elements (Ti,Fe,Mn) is observed in this phase, which is depleted in the components nucleating in augite and enriched in the others. The dark phase has nucleated possibly as a result of excess Si and K in the wake of bulk augite growth.

7.1.2 Experimental casting

In order to ascertain whether or not the samples analysed are indeed casting trays, 100g of a five-component SLS glass resembling a HMG composition (in wt%: 10.9 Na_2O, 2.8 MgO, 1.1 Al_2O_3, 76.2 SiO_2, 9 CaO) was cast on to a bed of powdered $CaCO_3$ at 1400°C and cooled in air. A temperature of 1400°C was necessary to achieve sufficiently low melt viscosity to allow flow from the crucible. No vitrification of the substrate was observed when the cast was removed from the $CaCO_3$ bed although the underside of the glass in contact with the $CaCO_3$ exhibited an opaque thin white layer. Viewed in cross-section, the underside of the glass showed a region of bulk crystallisation on average 50μm thick in which two crystalline phases are discernible (Figure 7-14). The brighter phase is wollastonite and the darker phase is of approximately a $Na_2O.2CaO.3SiO_2$ (NC_2S_3) composition (refer to Figure 2.13). Compositional results are given in Table 7-8.

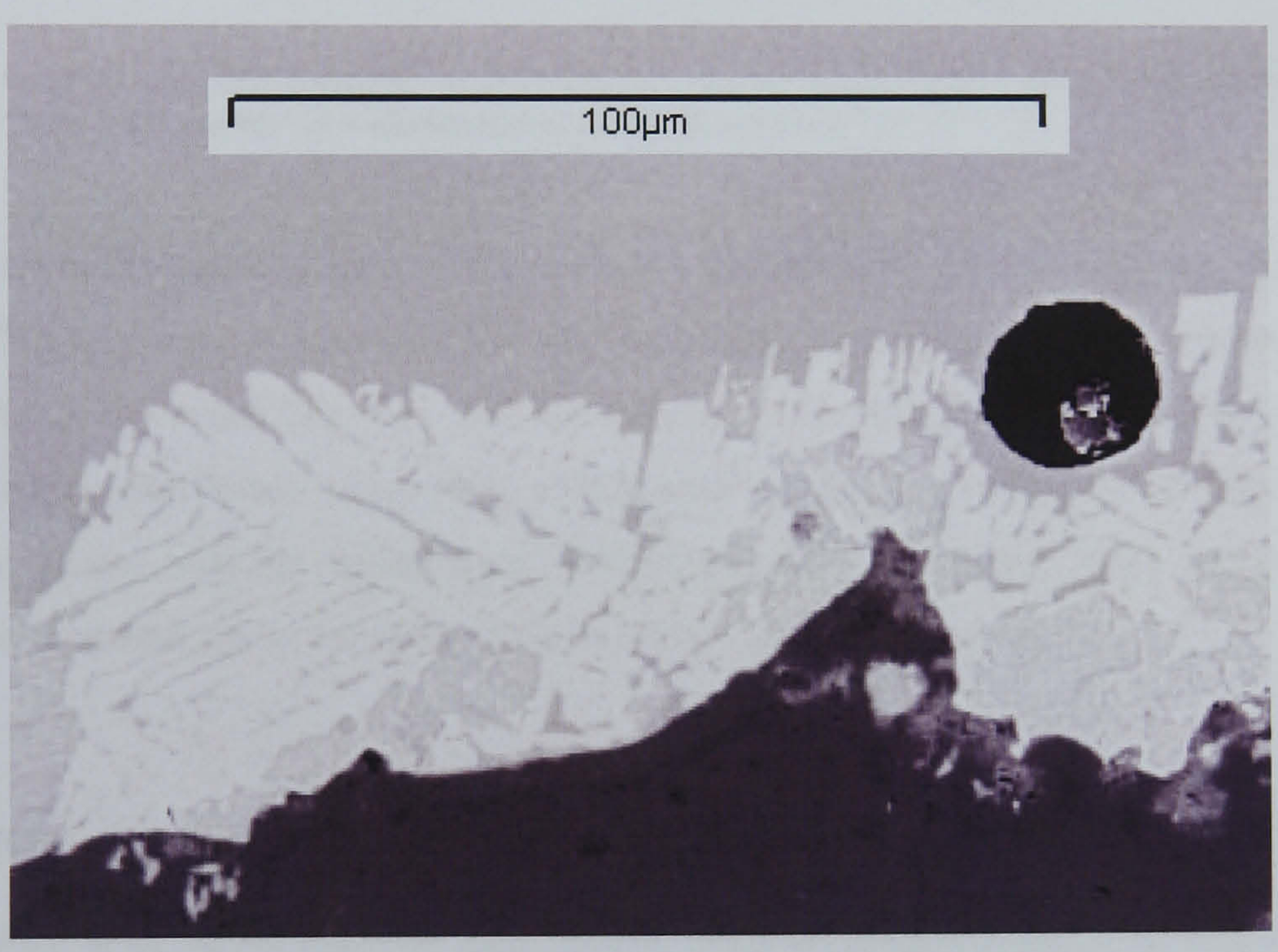


Figure 7-14: backscattered electron image of the reacted base of a SLS glass cast on to a $CaCO_3$ base at 1400°C showing bulk wollastonite (bright) and NC_2S_3 (dark) crystal growth.

The logical crystallisation sequence is as follows: as CaO is released from the carbonate and diffuses into the glass, NC_2S_3 and CS begin to crystallise at the glass surface when sufficient undercooling has been reached. This produces a Ca-depleted layer further into the glass. Once the temperature has decreased beyond the range for crystallisation, the glass is too viscous for any significant diffusion processes to take place. The glass took approximately 15 minutes to reach a temperature where it was cool enough to touch.

From these observations it seems likely that glass was cast on to TB9; the result of sudden contact with molten glass has isolated a molten zone in which the observed crystals have precipitated and limited the diffusion of Na from the glass to the top 400μm of the sample. The

glass would have cooled in a matter of minutes or hours even if a considerable amount was cast, which is still a much shorter timescale compared to the heating and cooling cycle used in a glass furnace. Hence the extent of reaction is not as marked as in other samples observed. More importantly for successful casting, the high melting point of TB9 (see Section 7.2.3) would have ensured that glass was cleanly removed from TB9 once it had cooled and could explain why no glass was found adhering to this sample.

Oxide (wt%)	bulk glass	above crystals	Wollas-tonite	NC_2S_3
Na_2O	10.9	8.6	0.0	13.4
MgO	2.8	3.1	1.0	0.0
Al_2O_3	1.1	1.2	0.0	1.1
SiO_2	76.2	79.6	54.6	53.4
CaO	9.0	7.5	44.4	32.2

Table 7-8: normalised EDXA results of the reacted base of a SLS glass cast on to a $CaCO_3$ base at 1400°C showing bulk growth of wollastonite and NC_2S_3 crystals.

The crystal morphology observed in the casting experiment and in TB9 suggests that, for TB6, TB2 and TB5, glass was not brought into sudden contact with $CaCO_3$ at high temperatures. This places in doubt the possibility that they are remains of casting trays. They are more probably fragments of furnace floors, which were coated with powdered $CaCO_3$ prior to introducing and heating the batch, possibly acting as a buffering layer between the glass and bricks. This observation is backed up by considerations of crystal growth in Section 7.3.

7.2 Glass on alumino-silicate substrates: furnace fragments

The fragments selected for analysis are from the different groups outlined in Section 3.3.3. All the furnace fragments analysed present the same phenomenon to differing extents: the heterogeneous precipitation of crystals at or near the glass-substrate boundary. Reported below are the observed characteristics.

7.2.1 Type B – TB13/TB14/TB7

TB13 and TB14 form part of the same furnace base assemblage. TB14 is a glass-substrate interface and TB13 a fragment of substrate. Cross-sectional profiles of the two samples are given in Figures 7-15 and 7-16 respectively, and compositional results obtained by EDXA and ICP-AES in Table 7-9.

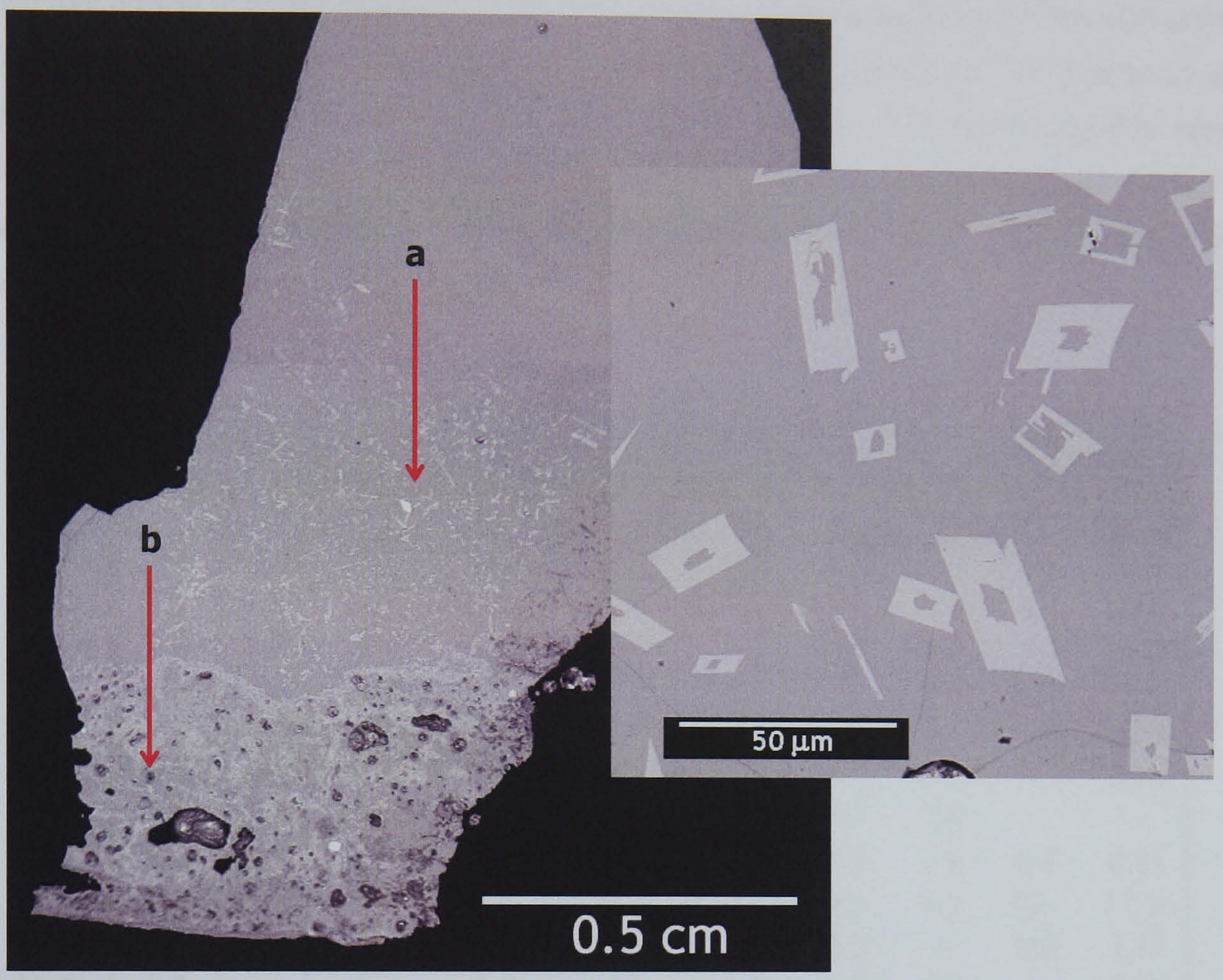


Figure 7-15: backscattered electron image of TB14 in cross-section showing the vitrified base and the glass above it. A magnified detail of the extended zone of wollastonite precipitation, visible up to 7mm above the interface, is shown in the backscattered electron image, right. The length and direction of two linescans shown in Figures 7-17 and 7-18 are marked a and b respectively.

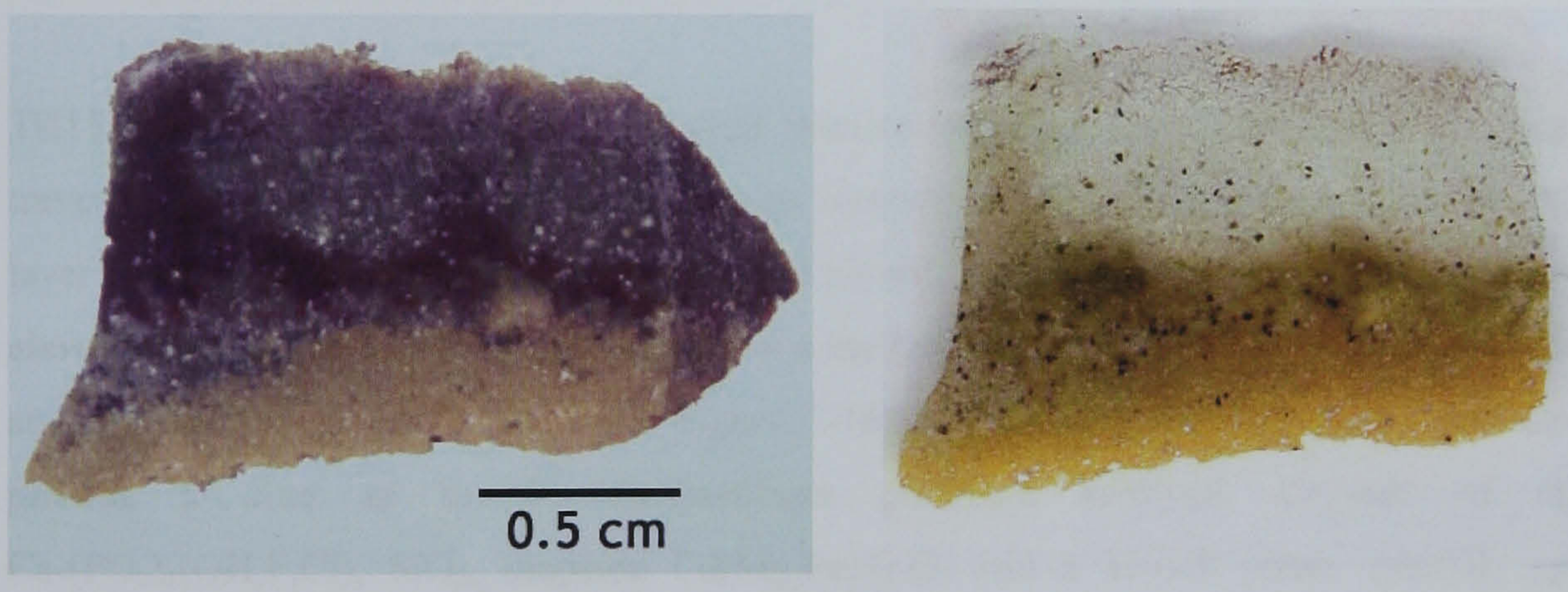


Figure 7-16: magnified cross-section of sample TB13 (left) showing the dark green layer that marks the limit of vitrification. This became clearly visible when a thin section of TB13 (right) was prepared.

In TB14 a zone of wollastonite crystals extends approximately 7mm into the glass above the glass-substrate interface. A zone of vitrification 4-5mm in thickness extends below the glass surface into the substrate. A 3mm linescan taken at 30µm intervals across the upper limit of crystal nucleation visible in Figure 7-15 revealed a marked compositional gradient across a 300µm distance (Figure 7-17). The glass matrix in the wollastonite precipitation region is particularly depleted in CaO, which has diffused to form the crystals. Other constituents are

therefore present in higher quantities in this area. An identical linescan across the glass-substrate interface revealed a similar 300µm-thick boundary layer that is highlighted by differences in MnO, Fe_2O_3 and Al_2O_3 (Figure 7-18). The data suggests that extensive interdiffusion has taken place between the glass and the substrate. The substrate is highly vitrified throughout the bulk, and regions of glassy phase lie in between the mineral phases. It is in fact characterised by high levels of Na_2O diffusing in from the glass.

	TB14					TB13				
Oxide (wt%)	Wollas-tonite	Glass			Substrate	Substrate (w.r.t vitrification limit)				
		clear	wollastonite field		<1mm	+5mm	+3mm	0	-5mm (base)	-5mm* (base)
			top	base						
Na_2O	0.1	12.1	12.4	12.2	10.2	12.4	10.4	9.7	2.9	3.92
MgO	0.7	2.1	2.2	2.3	2.2	1.7	1.9	1.8	5.0	5.60
Al_2O_3	0.0	2.2	2.9	3.5	10.7	7.1	8.3	7.0	14.1	14.09
SiO_2	50.4	66.3	65.7	64.6	53.9	66.2	67.2	69.0	54.8	49.27
P_2O_5	0.1	0.4	0.4	0.4	0.4	-	-	-	-	0.29
SO_3	0.0	0.4	0.4	0.5	0.1	-	-	-	-	0.26
Cl	0.0	0.6	0.4	0.4	0.2	0.6	0.7	0.8	-	-
K_2O	0.0	3.2	3.2	3.4	2.7	2.5	2.6	2.6	0.8	0.81
CaO	44.9	7.9	5.4	4.6	12.9	5.3	4.7	4.7	15.1	17.16
TiO_2	0.3	0.2	0.3	0.3	0.7	-	0.3	-	0.8	1.17
MnO	3.5	3.4	4.6	5.3	1.0	1.5	1.0	1.2	-	0.15
Fe_2O_3	0.0	1.3	2.0	2.4	5.1	2.6	3.0	3.2	6.5	6.94
										99.66

Table 7-9: normalised EDXA results of glass and substrate at different points in TB13 and TB14 and ICP analysis (*) of substrate base from TB13.

TB13 shows the extent of high temperature reaction in the substrate. The dark green layer that traverses the sample along its horizontal axis represents the extent of vitrification. Below this layer the base remains granular and porous in nature. A boundary is visible through the piece, above which crystals have precipitated from a melted matrix. This is visible in a cross-section and thin section of TB13, shown in Figure 7-16. The typology and morphology of crystals provide a clue as to the temperatures gradients involved. Crystals of apatite $Ca_5(PO_4)_3(OH,F,Cl)$, SiO_2, diopside $Ca(Mg,Fe)Si_2O_6$ and a Ti-rich phase, possibly sphene $Ca.Ti[SiO_4](O,OH,F)$, were detected in the first millimetre above the boundary. Further up, crystal nucleation is more pronounced and the matrix fully dense and vitreous. Diopside and wollastonite crystals have nucleated and grown from the matrix and around chromite ($FeCr_2O_4$) centres. The high melting temperature of chromite suggests that the crystals were present as inclusions in the brick prior to heating. The cubic spinel morphology of chromite is visible in Figure 7-19. Towards the top of TB13, diopside remains the only crystal present, along with strands of unidentified Mg-silicate crystal. The analytical data again suggests a bulk inter-diffusion of species, as compositional gradients are present throughout the sample.

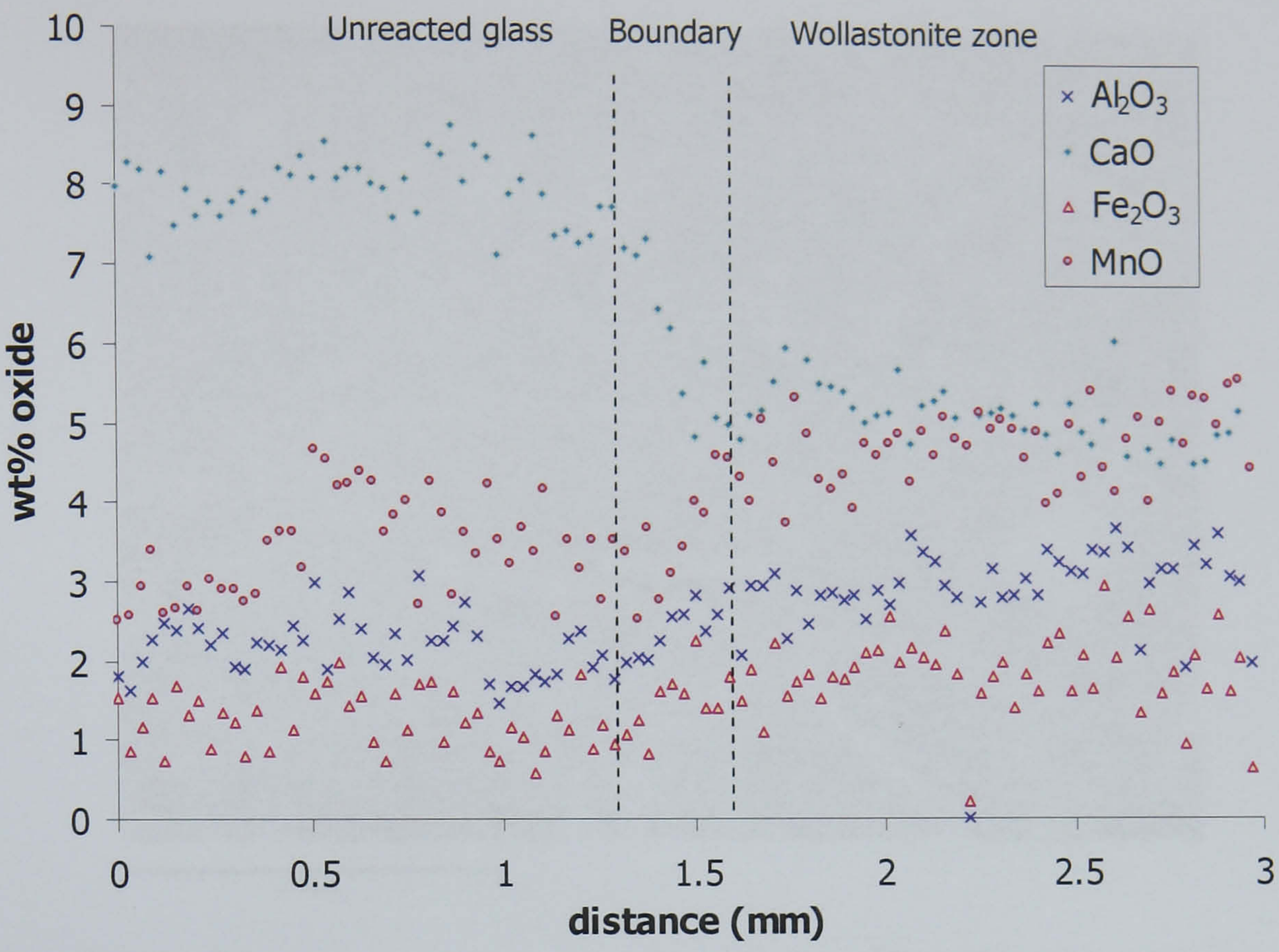


Figure 7-17: results of linescan a in Figure 7-15 across the upper boundary of the wollastonite precipitation layer in TB14. A 300µm boundary zone is visible.

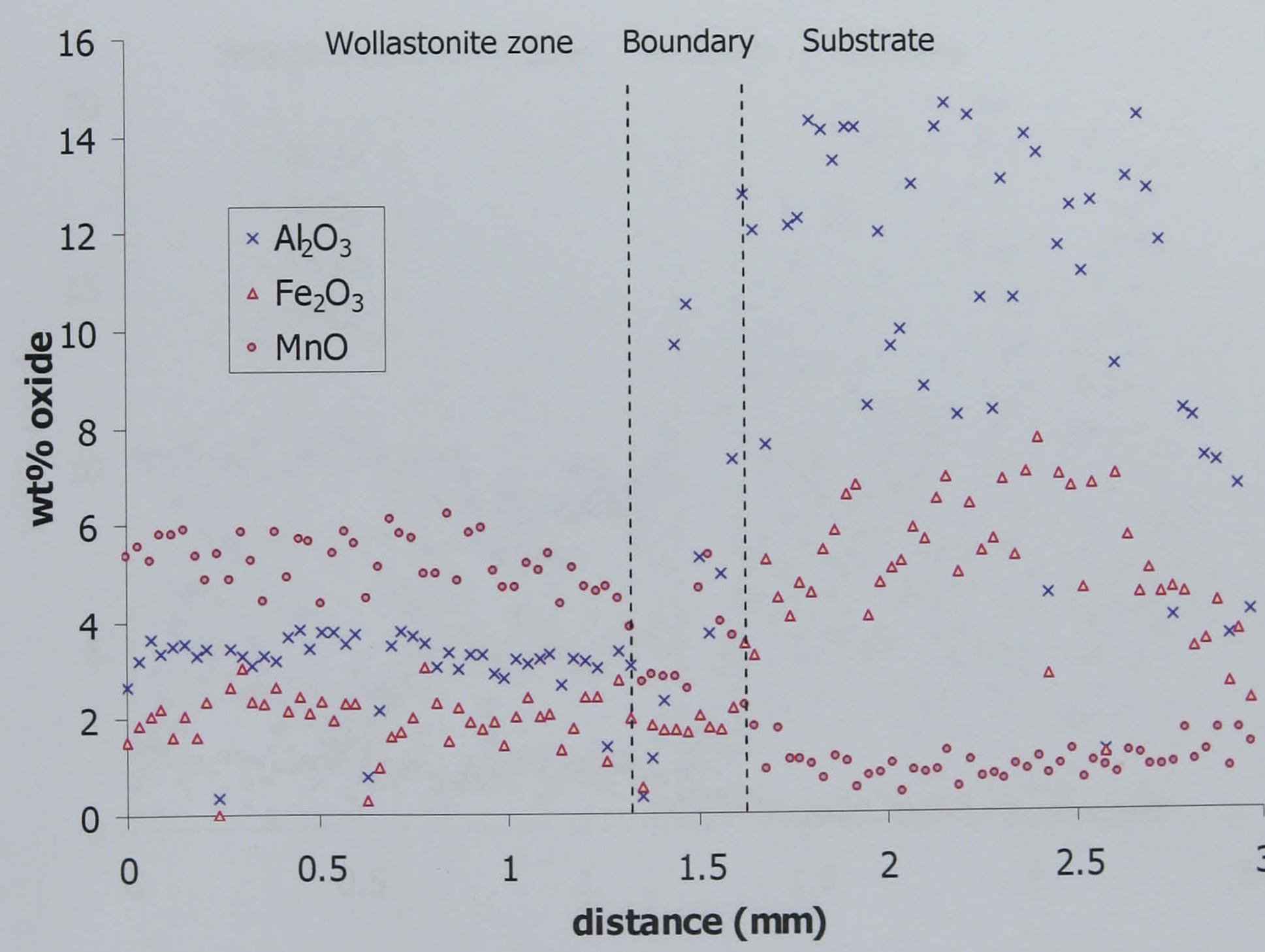


Figure 7-18: results of linescan b in Figure 7-15 across the glass-substrate interface of TB14. A 300µm boundary zone is again visible.

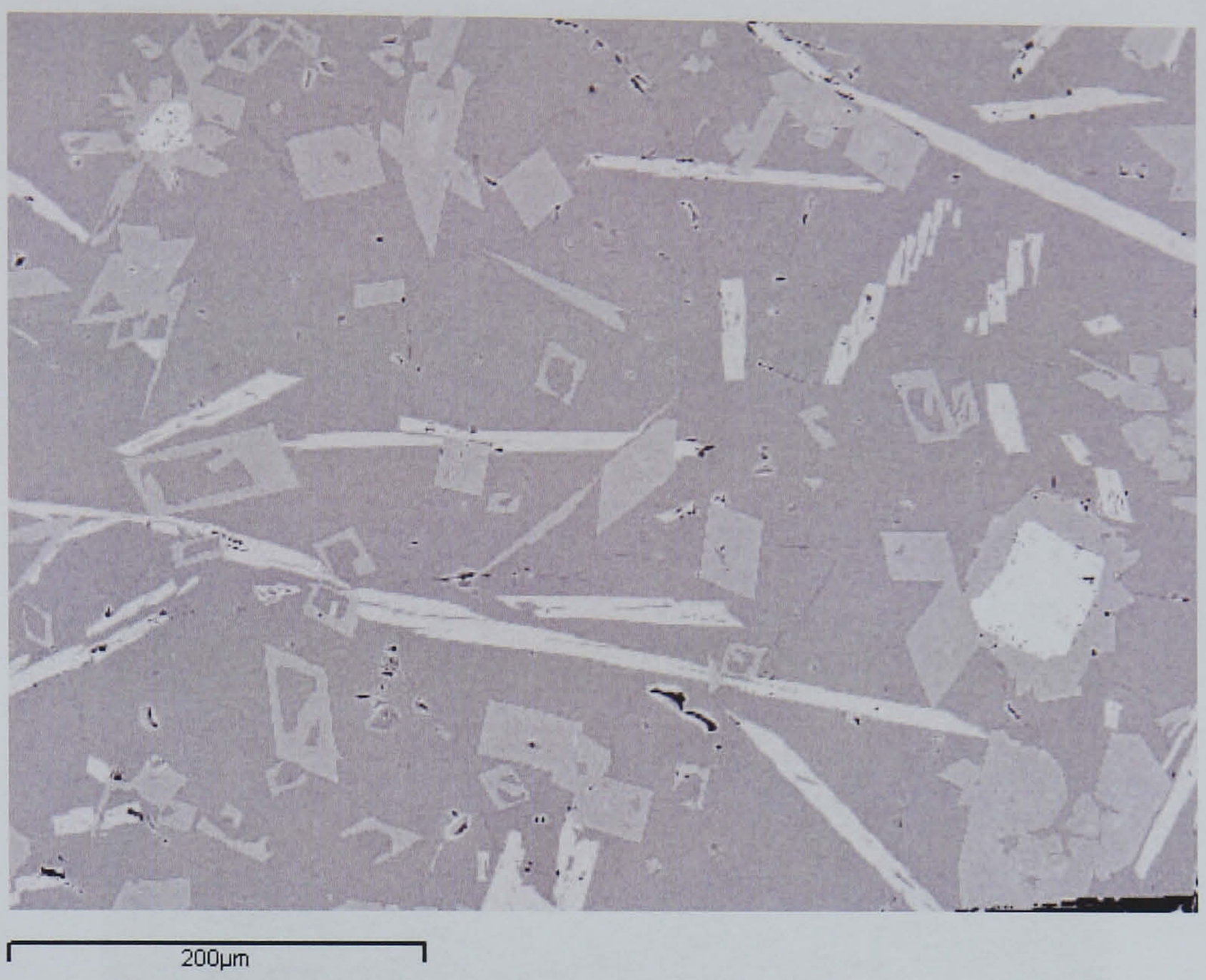


Figure 7-19: backscattered electron image of crystals nucleated in TB13. The matrix is fully dense and vitrified. Diopside can be seen growing from a chromite core (very bright cubic crystal on the right). The bright needle-shaped crystals are wollastonite.

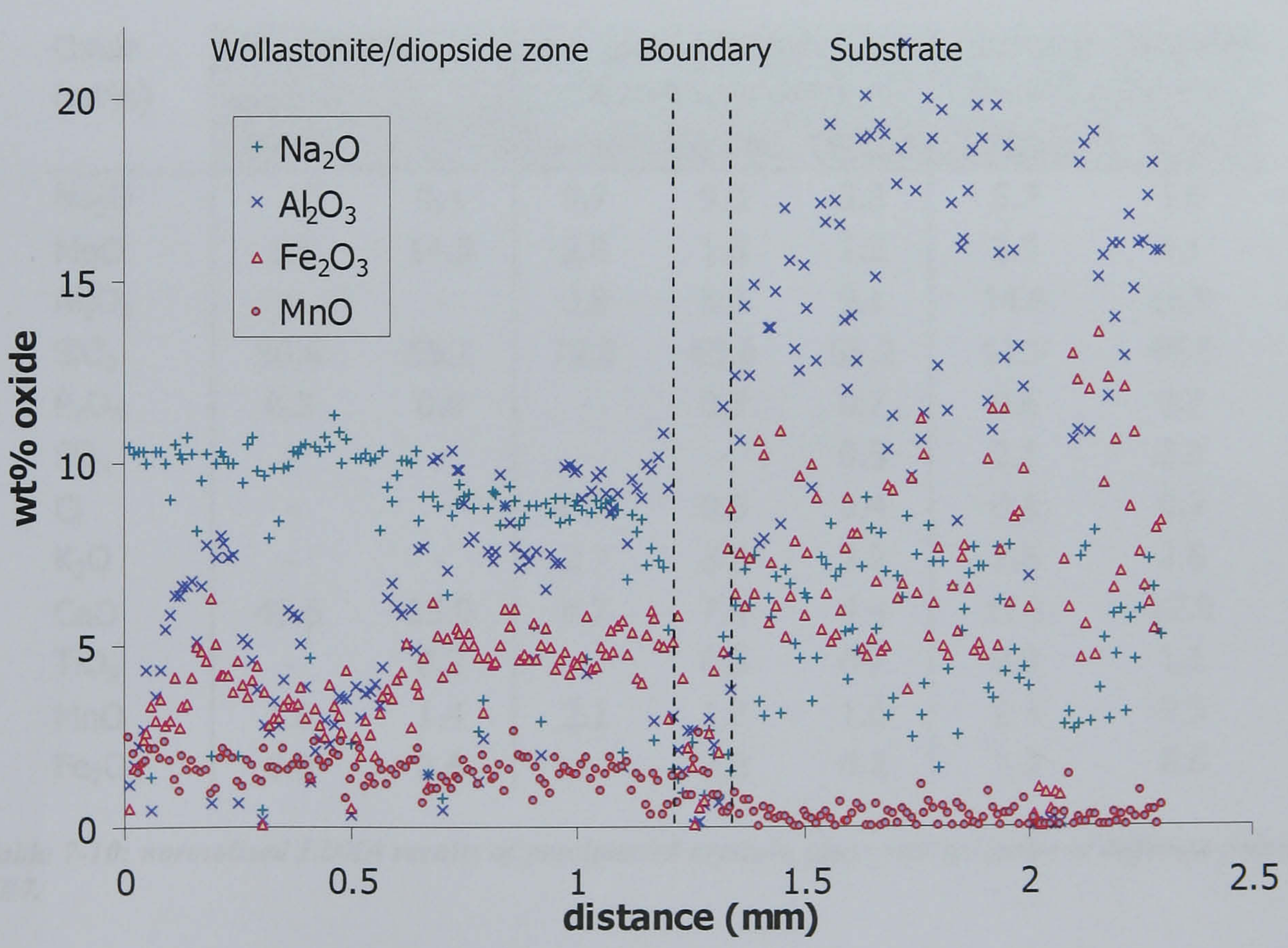


Figure 7-20: EDXA data of linescan across glass-substrate interface in TB7. The boundary zone consists of a 150µm thick layer of wollastonite precipitation.

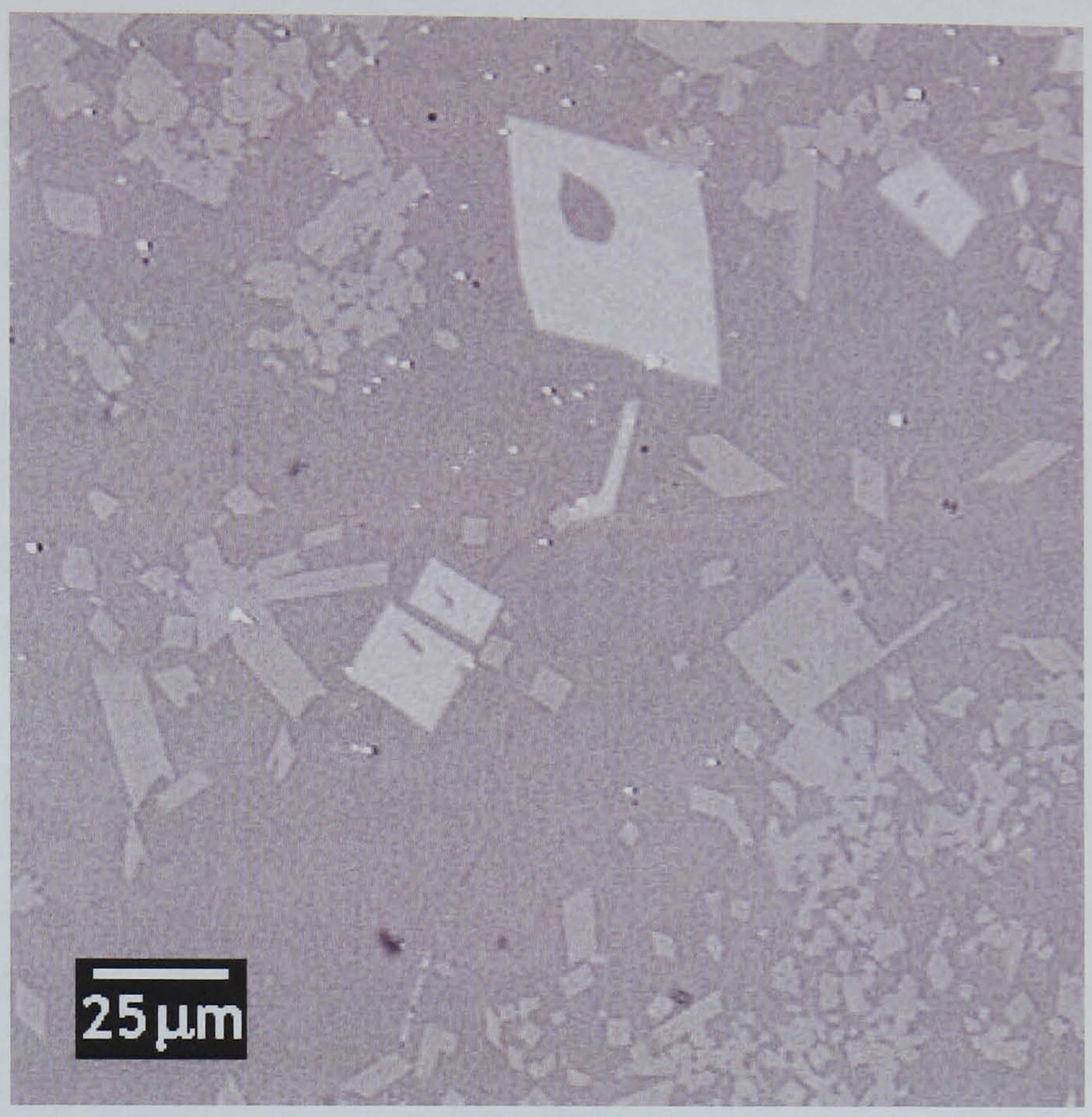


Figure 7-21: backscattered electron image of wollastonite (bright) and diopside (dark) crystals growing above the glass-substrate boundary in TB7.

Oxide (wt%)	crystals		glass (distance above boundary)			substrate (distance below boundary)	
	wollas-tonite	diopside	3mm	1mm	100µm	500µm	1mm
Na_2O	-	0.4	9.7	9.9	8.8	5.7	5.0
MgO	1.1	14.5	2.8	1.5	1.2	2.5	3.1
Al_2O_3	-	-	0.8	6.2	9.1	14.8	16.9
SiO_2	50.6	55.1	72.6	65.0	65.2	51.9	45.8
P_2O_5	0.3	0.8	-	0.7	0.7	0.6	0.7
SO_3	-	-	-	-	0.5	2.1	2.9
Cl	-	-	0.6	0.5	0.4	0.1	0.3
K_2O	-	-	2.7	3.0	3.2	2.8	2.6
CaO	45.6	25.0	8.7	7.4	4.4	11.1	12.8
TiO_2	-	0.2	-	0.3	0.7	0.9	1.1
MnO	1.6	1.4	2.1	1.7	1.6	0.3	0.3
Fe_2O_3	0.8	2.6	-	3.8	4.2	7.2	8.6

Table 7-10: normalised EDXA results of precipitated crystals, glass and substrate at different points in TB7.

TB7 is a glass-substrate that shows a clear boundary between the dark green glass and the yellow-tinted base (refer to Figure 3-7). A linescan taken at 100µm intervals across the boundary revealed mixed crystal precipitation extending 1-2mm into the glass and a vitrified substrate. The boundary (Figure 7-20), marked by variations in levels of Na_2O, Al_2O_3, Fe_2O_3

and MnO, consists of a 150μm thick wollastonitic zone, which lowers the oxide totals in the central section of the figure. The Ca-rich glass above the interface is the site of diopsode and wollastonite crystal growth (Figure 7-21). EDXA data of the glass, crystals and substrate analysed in TB7 is given in Table 7-10. The diffusion of Fe_2O_3 and Al_2O_3 into the glass, and of SiO_2 and Na_2O into the substrate, is evident.

The reason why diopside crystals have grown so readily in the glass of TB7 and not in the other samples may be attributable to the 3-4wt% Fe content of the glass. As outlined in Section 7.3, a larger degree of Fe cations can be substituted into the diopsiode structure than into wollastonite, and could explain why diopside growth is favoured in this composition.

7.2.2 Type C – TB19g/TB19y

The type C samples represent two furnace brick types found at Tell Belor. TB19g refers to the green brick and TB19y to the yellow brick. Both underwent analysis to establish whether they are of the same type as those found adhering to glass (types A and B), and to better assess the technology that was used in the construction of furnaces at Raqqa. EDXA data for the two bricks is given in Table 7-11 and their microstructure is shown in Figure 7-22. The two bricks are generally similar in composition, except for lower alkali levels and slightly lower levels of Al_2O_3 and higher CaO and SiO_2 in TB19y. The compositional similarities between TB19y and the unreacted substrate of TB13 are remarkable, suggesting that they belong to the same technological tradition. Similarly, the composition of TB19g is more akin to the unreacted base of TB7. As these two pairings are both between green and yellow pieces, the colour of the brick seems to be more dependent upon the oxidation state of Fe rather than composition.

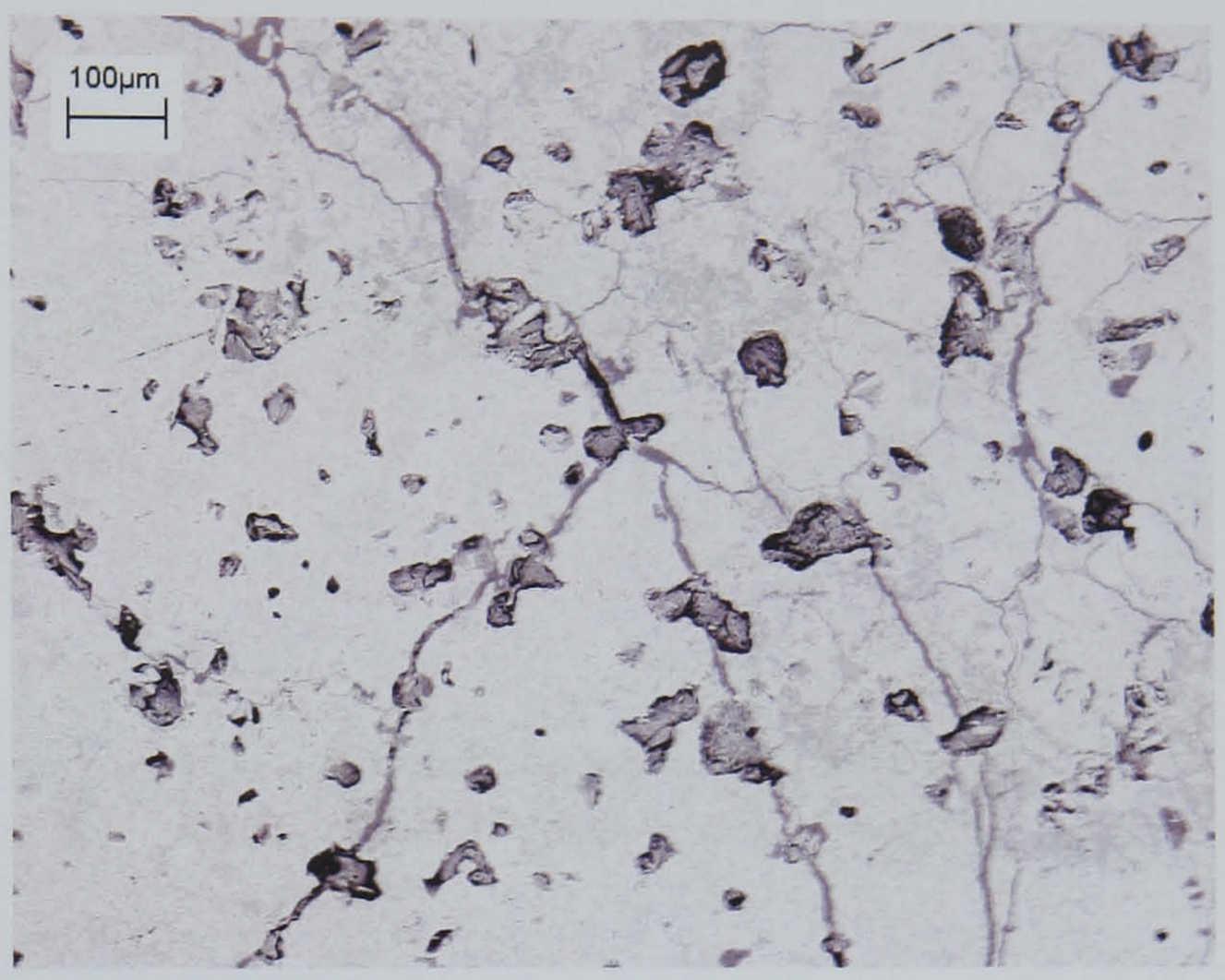
Oxide	S19 brick	
(wt%)	yellow	green
Na_2O	2.6	4.9
MgO	5.2	5.5
Al_2O_3	13.3	15.2
SiO_2	52.8	49.3
Cl	nd	0.4
K_2O	0.6	3.5
CaO	17.8	13.3
TiO_2	0.6	1.2
Fe_2O_3	7.0	6.7

Table 7-11: normalised EDXA results of TB19 yellow and green bricks.

The microstructure of TB19g has a granular appearance, with quartz grains and other Si-rich grains visible. Ti-rich grains (visible as bright spots) equivalent in composition to those

observed in TB13 point to the conclusion that raw ingredients with the same inclusions were used for both compositional brick types. TB19y presents a more homogeneously fused structure with fewer grains visible, suggesting it has been taken to a higher temperature than TB19g.

Figure 7-22: backscattered electron images showing the microstructure of TB19y (yellow brick, top) and TB19g (green brick, below). The more homogeneously fused structure of TB19y suggests it has been raised to a higher temperature than TB19g. Ti-rich grains in TB19g (small bright spots) suggest that the same materials source for furnace brick production were used as for TB13.



The above observation is confirmed by DTA and TGA analysis. In the DTA plot the various endothermic peaks correspond to physical processes, such as melting, and exothermic peaks indicate chemical reactions, such as oxidation or crystallisation. The relatively large endotherms for TB19g at 100°C and between 625°C and 725°C in Figure 7-23 indicate that it is losing more residual water and showing a greater degree of carbonate devolution than TB19y. The corresponding TGA plot in Figure 7-24 indicates that these two processes also lead to a weight loss of over 6% for TB19g compared to only 2% for TB19y. The latter sample shows a further weight loss beginning at 1000°C, suggesting it has reached temperatures similar to this before. It is speculated, therefore, that the two bricks belong essentially to the same technology,

prepared from similar raw materials, and that differences in previous heat exposure have led to their variation in appearance.

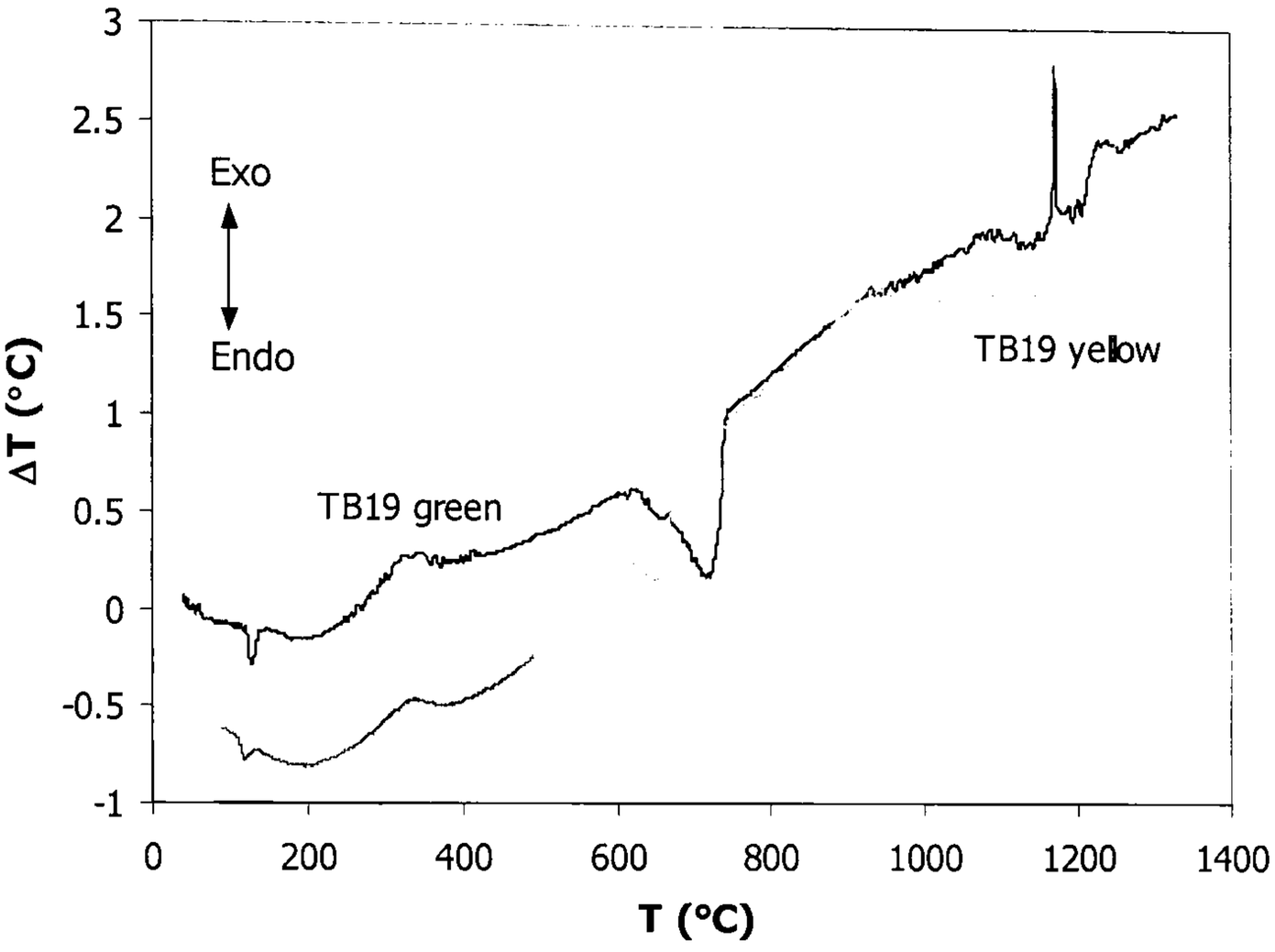


Figure 7-23: DTA scans of yellow brick TB19y and green brick TB19g.

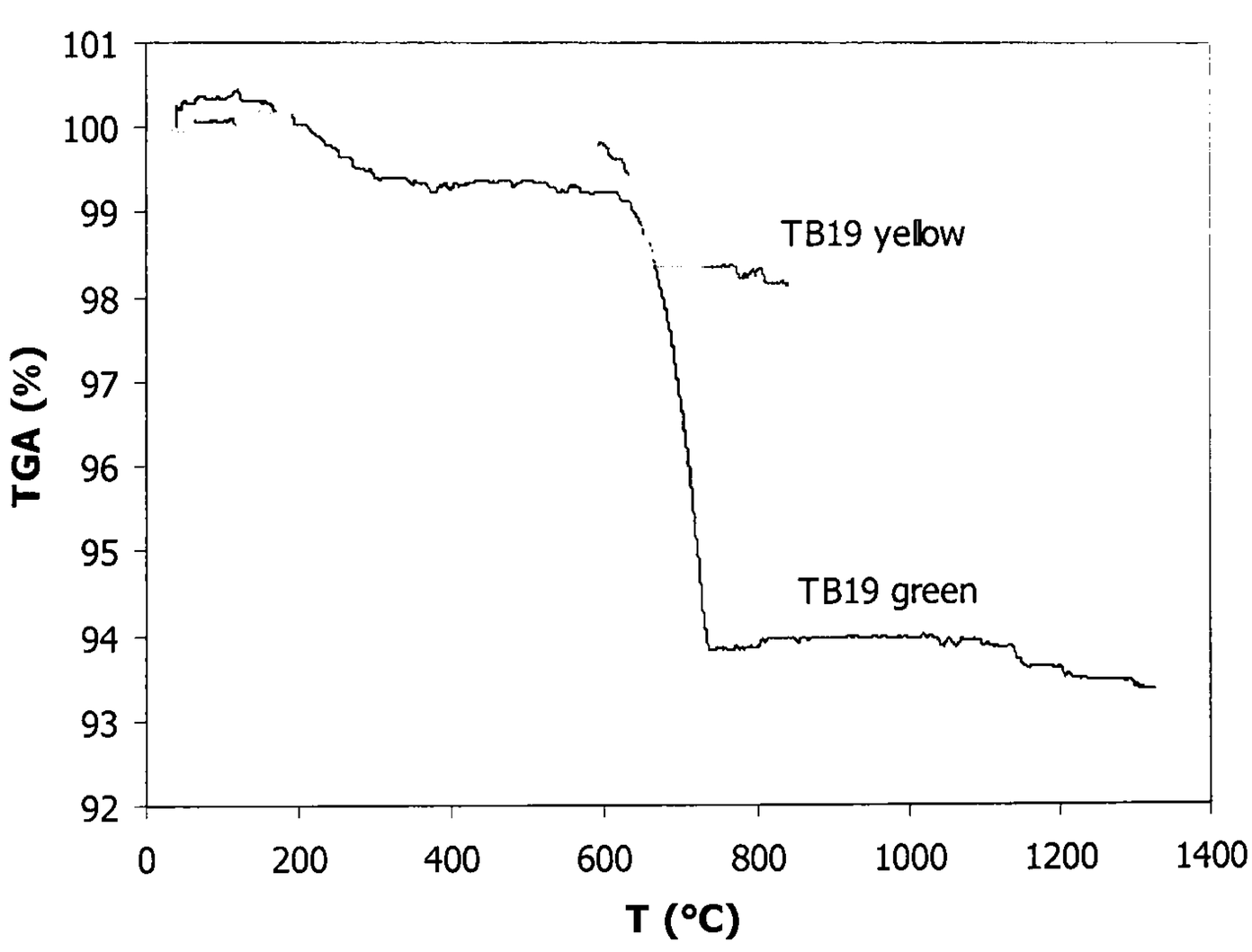


Figure 7-24: TGA scans of yellow brick TB19y and green brick TB19g.

7.2.3 A comparison of refractory performance

Samples from refractory types A and B (TB9, TB13) were analysed by DTA/TGA and compared to type C (TB19y) to assess their performance characteristics. The results of TGA and DTA are shown in Figures 7-25 and 7-26. Residual water in TB9 resulted in an endothermic DTA peak and a corresponding weight loss at 100°C. All three samples showed carbonate

devolution over a range of 70-100°C starting at 660°C, 640°C and 625°C for A, B and C respectively, which corresponded to weight loss of up to 3.5% for TB9, and melting began at 1140°C, 1160°C and 1180°C, again for A, B and C respectively. The endotherms for TB13 and TB19y at these temperatures corresponded to complete melting of the sample, which was also observed when the samples were heated directly in a furnace to 1200°C.

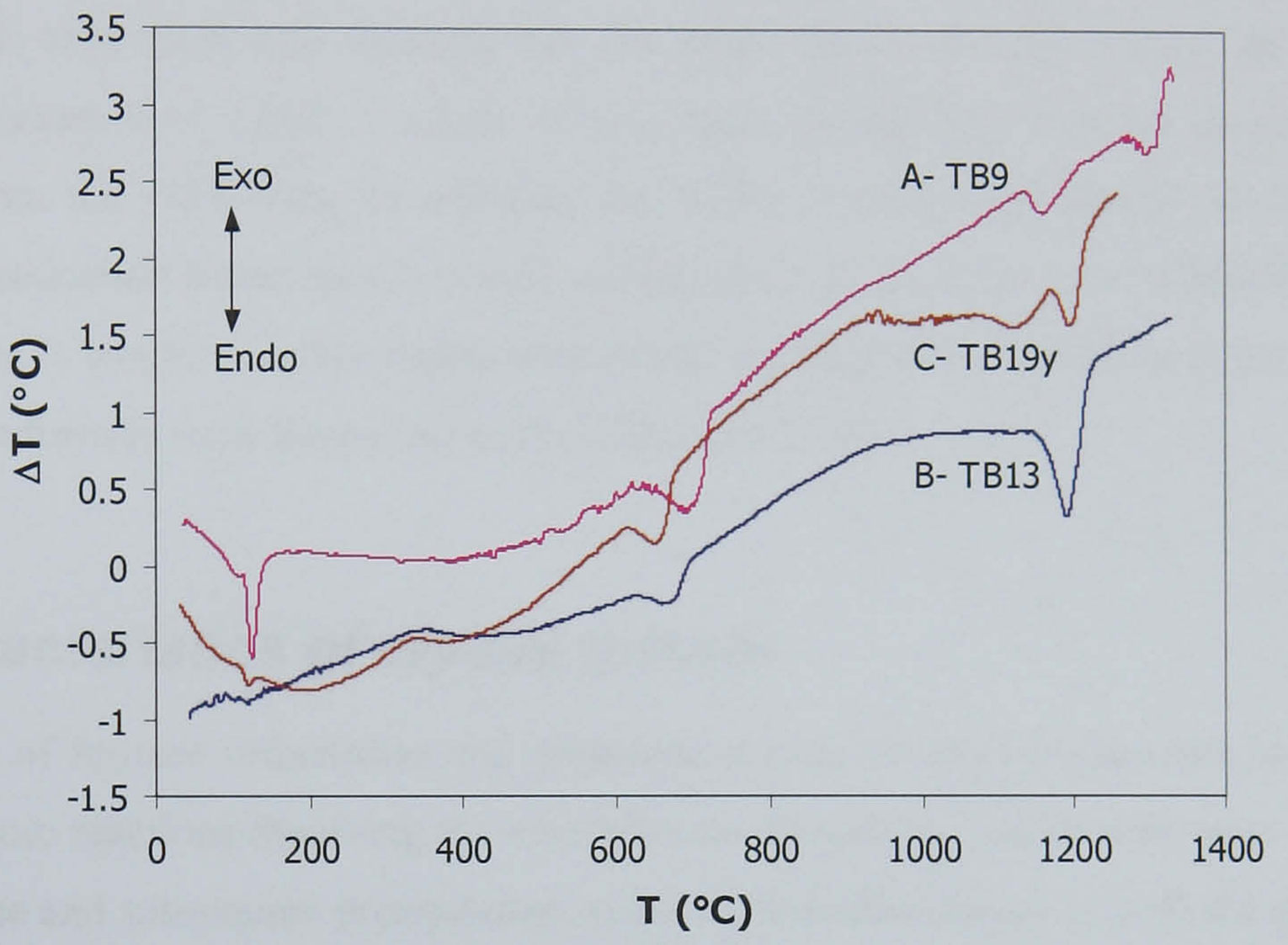


Figure 7-25: DTA results on fragments of production waste types A, B and C.

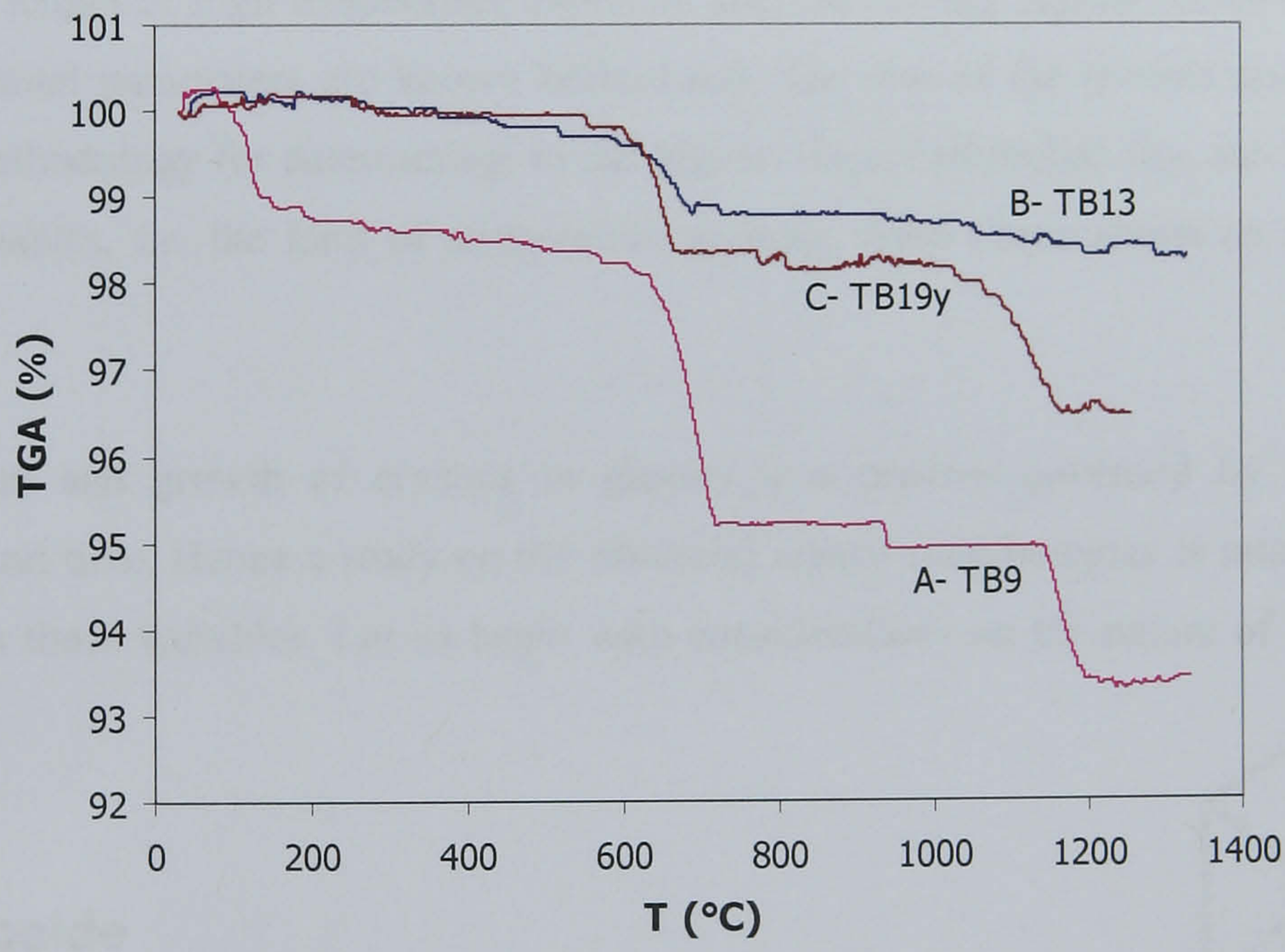


Figure 7-26: TGA results on fragments of production waste types A, B and C.

The TGA data for TB19y suggests widespread dissolution of the matrix at ~1050°C, which corresponds to a relatively small DTA endotherm. TB13 was found to melt completely at 1150°C when heated in a furnace. TB9, although it exhibits some melting at 1140°C, did not

melt fully until temperatures above 1300°C were reached. This corresponds to the highest temperature endotherm on the DTA graph.

It would seem logical to imply that temperatures at least up to, and possibly over, the melting temperatures of these fireclays must have been reached to cause extensive vitrification. Furnace temperatures at Raqqa in the region of 1150-1200°C are therefore proposed from the evidence discussed here. One must also presume that the glass cast on to TB9 was of an equal to or higher temperature than 1140°C, which is the onset of the first high temperature melting endotherm from the DTA data. In addition, the higher melting temperature of the lime-rich substrate of production waste type A would validate the use of limestone as a buffer material in the furnace, as it would possibly retard widespread melting of the bricks and the consequent collapse of the furnace once temperatures reached 1150-1200°C.

7.3 Characteristics of crystal growth

The exposure of furnace refractories and limestone powder to molten glass has brought about high temperature reactions involving the interdiffusion of species, partial melting or vitrification of the substrate and subsequent precipitation of solid crystalline phases in both the glass and the fused substrate. All the samples analysed showed the above phenomena to varying degrees depending on the type of substrate and glass brought into contact, the actual temperatures involved, the length of high temperature exposure and the cooling regime. Unfortunately only the compositional parameters are known beforehand. The aim of the present discussion is to establish a methodology for determining, to the highest degree of probability, the ranges of the unknown variables, i.e. the kind of temperature regimes, from observations on the chemical data.

The nucleation and growth of crystals in glasses is a process governed by composition, temperature and time. Hence a study on the observed crystal morphologies is intended to shed some light on those variables. Let us begin with considerations on the nature of diopside and wollastonite.

7.3.1 Diopside

Diopside minerals are members of the clinopyroxene group, a sub-set of the pyroxene group. Clinopyroxenes are chain silicates with a monoclinic unit cell structure (the diopside unit cell is illustrated in Figure 7-27) that have the formula $Ca(Mg,Fe^{2+},Mn)Si_2O_6$. Pyroxenes are formed by the linkage of SiO_4 tetrahedra by sharing two or four

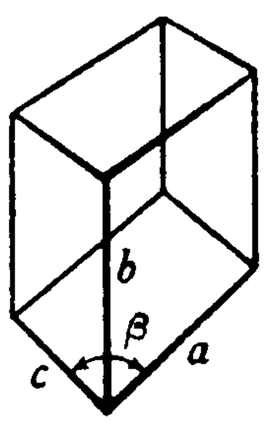


Figure 7-27: monoclinic unit cell structure of diopside. From Deer et al.[1].

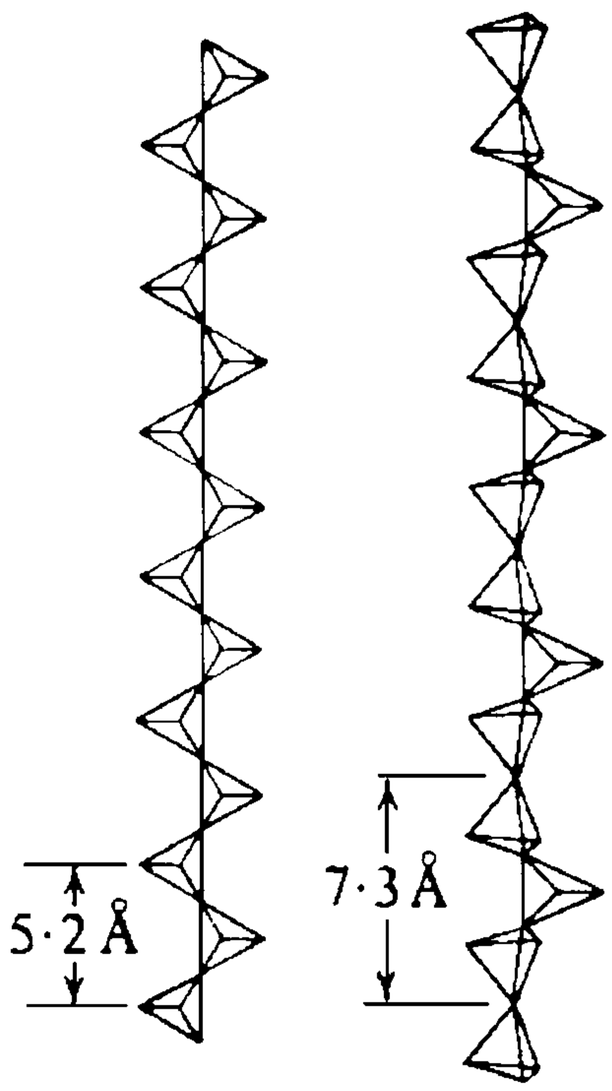


Figure 7-28: structure of chains of linked SiO_4 tetrahedra of composition $(SiO_3)n$ for diopside (left) and wollastonite (right) including unit cell measurements for each (from Deer et al.[1]).

corners to form continuous chains of composition $(SiO_3)_n$. In pure diopside the $(SiO_3)_n$ chains are linked laterally by Ca and Mg ions (Figure 7-28, left). A wide range of ionic substitutions is present in the clinopyroxenes; there is complete replacement of Mg by Fe^{2+} and of Fe^{2+} by Mn to form a solid solution series in the $CaMgSi_2O_6$-$CaFeSi_2O_6$ system (known as the diopside–hedenbergite series – Figure 7-29). The content of Mn is small (<0.25 wt% MnO) in the Mg-rich members of the series but often occurs in larger amounts in the more Fe-rich members (e.g. hedenbergites may contain up to 4 wt% MnO). The diopside–hedenbergite system has a binary character only for compositions having up to 60 mol% of the hedenbergite component. In the Fe-rich part, a wollastonite solid solution crystallises at liquidus temperatures and subsequently inverts to an Fe-rich clinopyroxene.

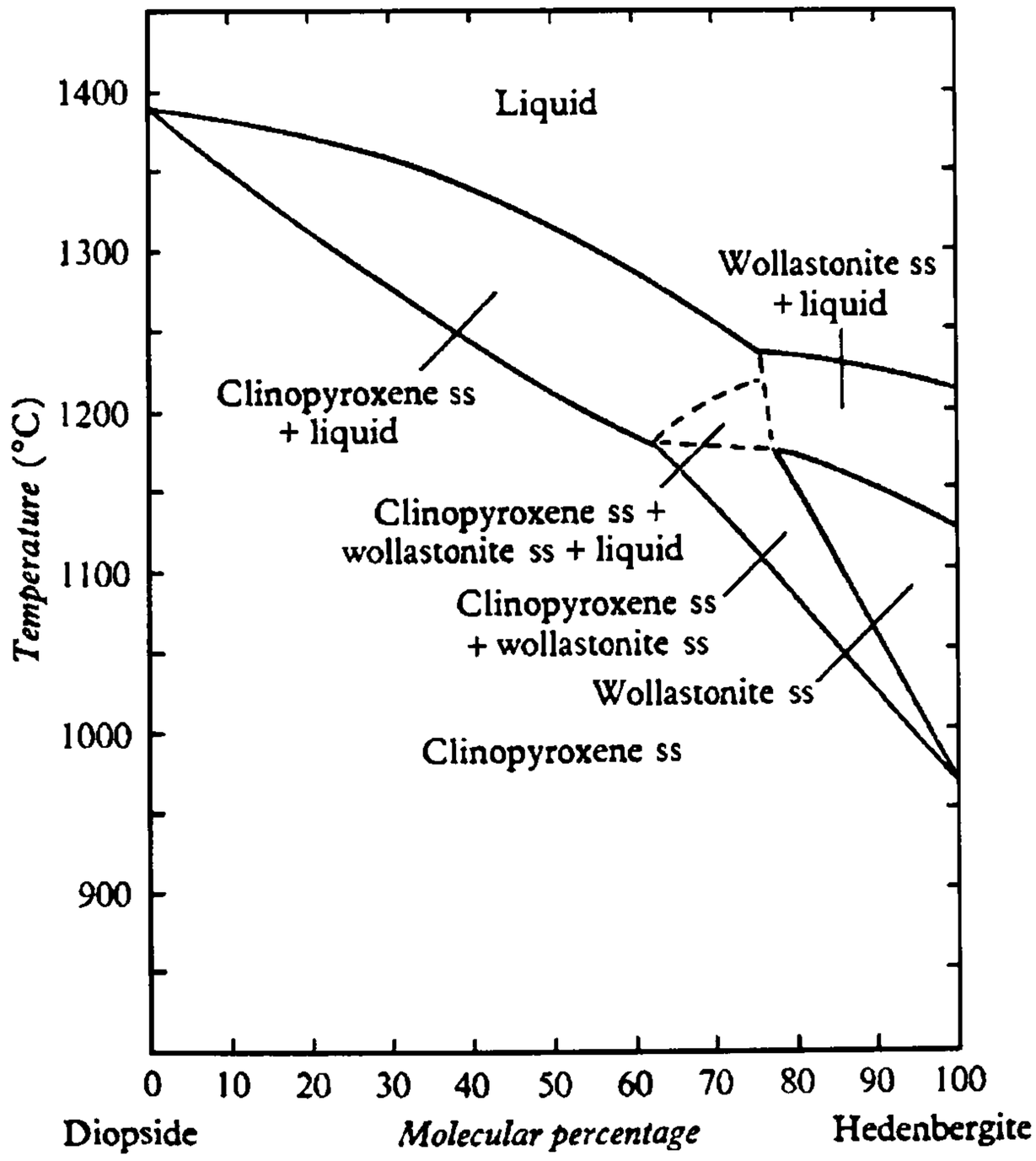


Figure 7-29: phase diagram for the $CaMgSi_2O_6$-$CaFeSi_2O_6$ (diopside-hedenbergite) system. From Deer et al. [1].

7.3.2 Wollastonite

Wollastonite ($CaSiO_3$) has a different type of infinite-chain structure from the pyroxenes (Figure 7-28, right). A chain of $(SiO_3)_n$ composition is formed by three SiO_4 tetrahedra per unit cell, arranged so that two of them are joined apex to apex and the third has an edge parallel to the chain direction. The high temperature polymorph, β-wollastonite, decomposes at 1120°C to α-wollastonite, more commonly referred to as wollastonite. Both structures are triclinic, although monoclinic formations have been observed in glasses[3]. Wollastonite is normally relatively pure although it can accept considerable amounts of Fe and Mn replacing Ca. It often occurs as a result of the reaction of quartz and calcite in metamorphosed limestones.

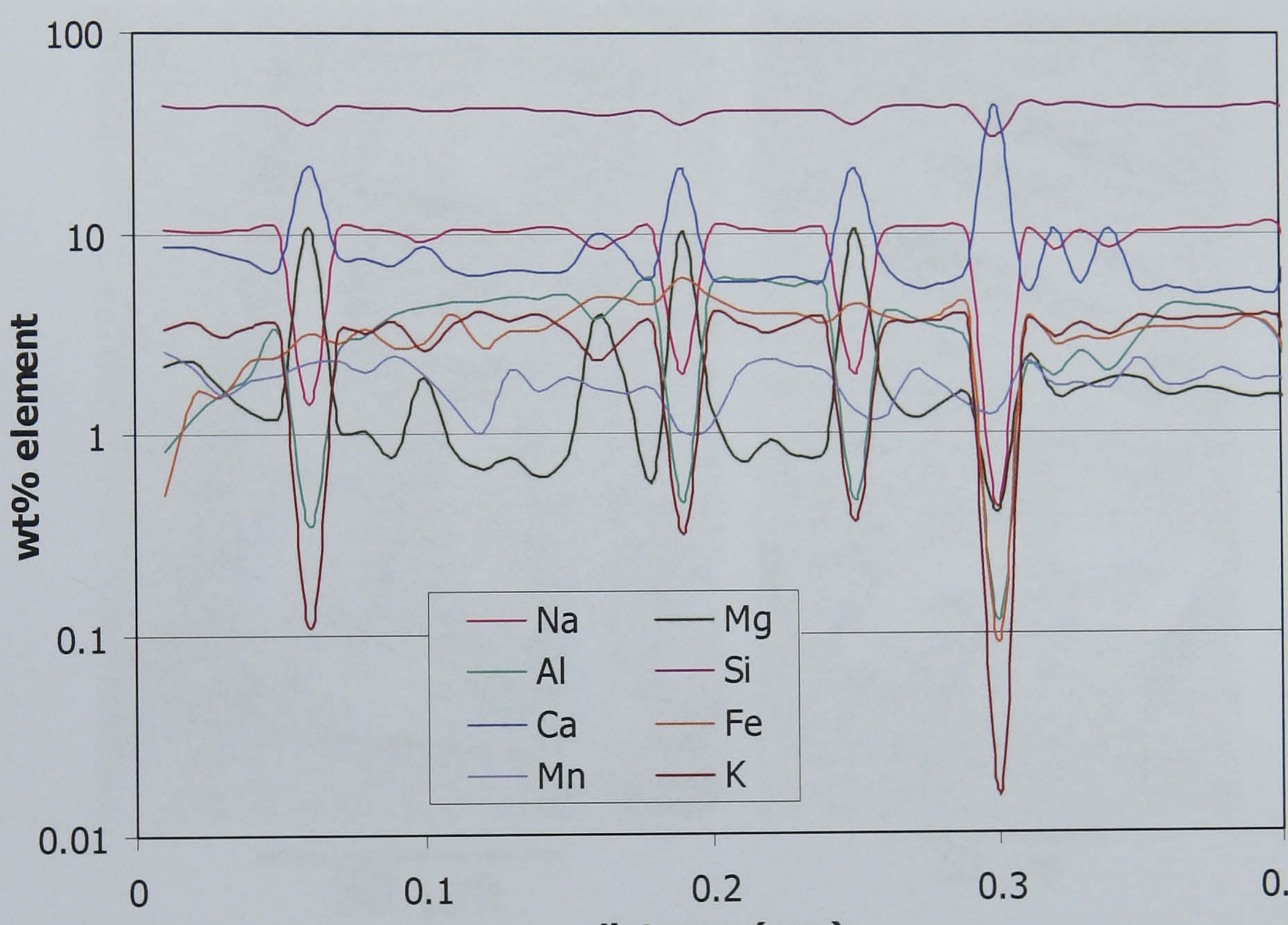


Figure 7-30: smoothed EDXA data of the first 400μm of the linescan in Figure 7-20 across diopside and wollastonite crystals in glass in TB7.

7.3.3 Compositional considerations

Some compositional overlap exists therefore in the two crystal types, and this is evident when the crystal growth in Raqqa fragments is considered. The reasons behind the observed wollastonite precipitation are explained by the local Ca enrichment of the glass adhering to the substrate; this pushes the composition into a β-wollastonite area in the ternary diagram, from which wollastonite crystals would result at temperatures below 1120°C. For the samples in direct contact with limestone, the glass becomes supersaturated with respect to Ca and causes

wollastonite precipitation. The contemporaneous precipitation of diopside is brought about by contact with refractory material richer in Mg and Fe, which favours the solid solution containing these elements. A detail of the first 400µm of the linescan in Figure 7-20, expressed in log wt% of elements, which was conducted across the crystal-rich zone of TB7, illustrates this point (represented in Figure 7-30). The first three crystals are diopside and are encountered at 60µm, 100µm and 250µm distance. The monovalent cations, Na^{+} and K^{+}, and the trivalent cation Al^{3+} are significantly reduced in quantity in the diopside, as they do not fit into the structure. The same is observed for a wollastonite crystal situated at 300µm, except that the values for these species are even lower than in the diopside, and other divalent species (Mg, Fe^{2+}) are also reduced. Only Mn remains in the wollastonite structure.

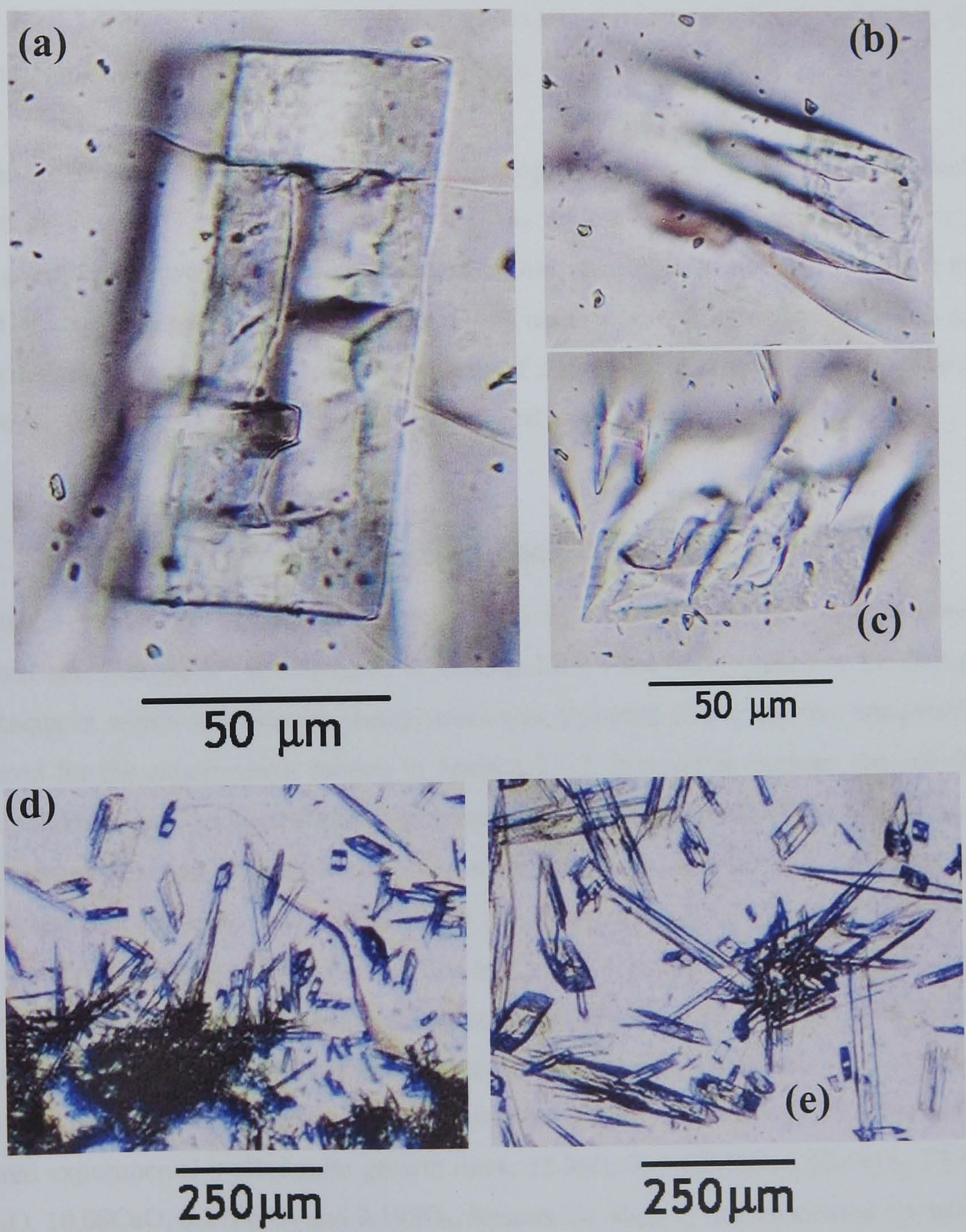


Figure 7-31: transmitted light photomicrographs of wollastonite structures in TB14 in thin section. Laths are faceted in structure and grow anisotropically, often around a liquid core (a). Wall thickness is seen to taper with length (b) and to form irregularly (c). Needles have nucleated at the glass-substrate interface (d) and at inhomogeneities in the glass (e).

7.3.4 Structural considerations

According to observations by Guillemet and Denoncin[3], at temperatures just below T_L wollastonite crystals have the appearance of laths, often with facets. The morphology changes with undercooling of 85°C, which roughly corresponds to the maximum crystallisation rate, V_{max}; at lower temperatures they become elongated in the form of needles. As observed in the previous paragraphs, wollastonite (and diopside) crystals have grown both as laths, reflecting the different temperature regimes. In many cases they have not formed homogeneously; Figure 7-31 shows variations of wollastonite formations viewed in an optical thin section. A hollow centre is often observed with faceted internal surfaces (Figure 7-31a), which can also be seen to taper with depth (Figure 7-31b). In other cases the outer surfaces are faceted in appearance (Figure 7-31c). Needle formations grow heterogeneously at the glass-substrate boundary (Figure 7-31d) or from inclusions in the glass (Figure 7-31e).

The reasons for this can be explained by considering the high melting entropy of wollastonite, reported by Jackson[4] as 4.73. In general, crystals with a high melting entropy show facets during growth and grow in an anisotropic manner. As the number of sites at the surface that are capable of accepting new molecules increases with undercooling[3], crystals with a high melting entropy favour a lateral growth mechanism around a liquid core. This is indeed the case with many of the precipitated wollastonite crystals studied here.

7.3.5 The kinetics of wollastonite precipitation

The kinetic model for wollastonite precipitation in industrial SLS glasses developed by Guillemet and Denoncin[3] and outlined in Section 2.6.3.3 has been applied to the five glasses from Raqqa in which wollastonite precipitation was observed and to the five-component SLS glass used for the experimental casting in Section 7.1.2. In order to perform the calculations, weight percentages of unreacted glass compositions were first converted to molar fractions for consitituent oxides, and N_{CaO} expressed on a molecular basis. According to equation 2-29, T_L was extrapolated for each composition from the slope of $\ln(N_{CaO})$ versus $10^4/T_L$. Viscosity values were then calculated from the Lakatos and Urbain models outlined in Section 2.6.1 and converted into SI units to establish the wollastonite growth rate, V, in $m \cdot s^{-1}$ in equation 2-28 that was converted to $\mu m \cdot min^{-1}$. To calibrate the procedure, the calculation was also performed for the following glass composition, expressed in wt% oxide, for which the authors have published measured experimental wollastonite growth rates: $13.3Na_2O$, $3.62MgO$, $1.02Al_2O_3$, $71.67SiO_2$, $0.19K_2O$, $10.08CaO$, $0.27Fe_2O_3$ and $0.19SO_3$. Results for N_{CaO}, T_L and calculated viscosity at T_L are given for seven glasses in Table 7-12. The viscosity modelling introduces some approximation to the data as values of Fe_2O_3, P_2O_5, MnO, TiO_2, SO_3 and Cl were discarded in

the Lakatos model and hence the molar fractions were representative of 95-97% of the totals. The Urbain method has the advantage of including all oxides, with only the Cl values discarded.

Sample	TB2	TB5	TB6	TB7	TB14	SLS	G&D
N_{CaO}	0.100	0.067	0.082	0.093	0.086	0.095	0.106
T_L (°C)	1022	949	985	1007	994	1012	1034
log η at T_L (poise)	4.1	4.5	4.4	4.4	4.2	4.4	3.9

Table 7-12: molar fraction of CaO, the derived liquidus temperature and corresponding calculated viscosity for seven glasses showing wollastonite precipitation. SLS is the five-component glass used for the experimental casting in Section 7.1.2. G&D denotes the composition studied by Guillemet and Denoncin[3].

Despite the approximation, the values of V calculated with Lakatos viscosity data fall within 40% of the published measured values; a maximum value of 1.6 $\mu m \cdot min^{-1}$ was found at 957°C for Guillemet and Denoncin's composition compared with their measured value of 2.7 $\mu m \cdot min^{-1}$ at 960°C, a relative error of 40%. The reaction tapers to near-zero values at around 800°C, which is also in line with their observations. Calculated growth curves with Lakatos data for all seven glasses are shown in Figure 7-32. Values of V calculated with Urbain viscosity data gave a maximum of 2.1 $\mu m \cdot min^{-1}$ at 945°C. This equated to a relative error of 22%, approximately half the error obtained with Lakatos data, and hence these values shall be used for the following discussion. Calculated growth curves with Urbain data for all seven glasses are shown in Figure 7-33.

According to Figure 7-33, the growth rate for the cast SLS glass shows a maximum of 0.16 $\mu m \cdot min^{-1}$ at 940°C. In theory the glass would have to be kept at 940°C for over 2 hours to produce the 50µm-long wollastonite crystals that are observed in Figure 7-14. This is clearly not the case. In reality a significant amount of Ca diffusion has taken place in the temperature region of 1200-1400°C during the first instants of contact between the glass and the $CaCO_3$ base, supersaturating the glass with respect to CaO. A higher molar fraction of CaO at the contact interface would increase T_L and simultaneously decrease the corresponding viscosity value associated with it, affecting the magnitude and temperature range of the wollastonite growth rate. In fact by adjusting N_{CaO} to 0.2, a considerably conservative estimate of the bulk CaO content of the crystalline zone given the near total wollastonite crystal density in this region, T_L increased to 1200°C and the growth rate increased by over two orders of magnitude. The adjusted values suggest that the observed bulk crystallisation of wollastonite occurred within the first seconds after casting once Ca had diffused several microns into the glass, and is therefore a reason why none of the interfaces studied could have been a casting tray.

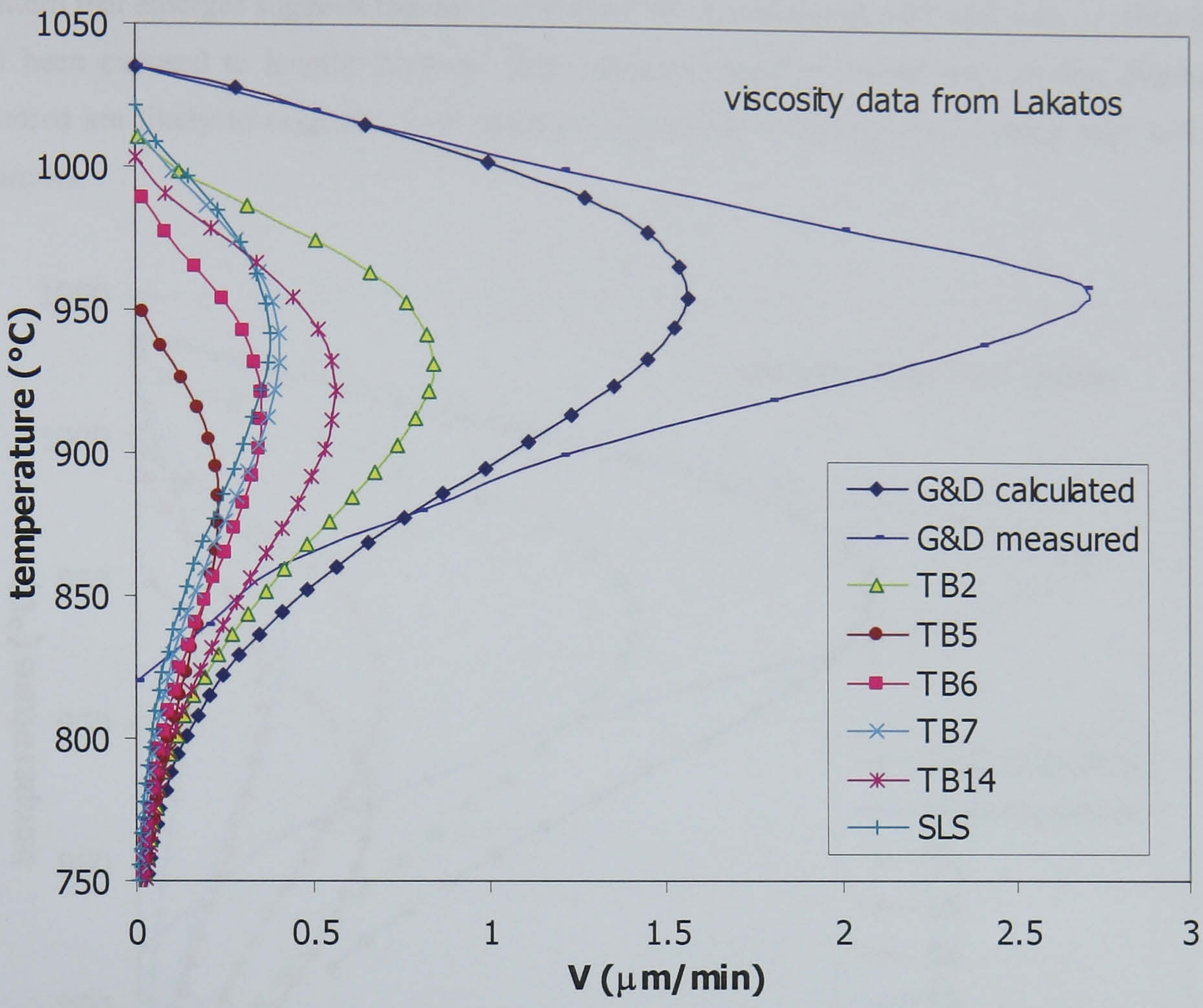


Figure 7-32: calculated growth rates of precipitated wollastonite crystals, following the equations published by Guillemet and Denoncin and using viscosity values calculated from the Lakatos model.

The interplay between temperature and viscosity fixes both upper and lower limits on temperatures at which crystals could grow at given CaO concentrations. The *minimum* exposure to crystallisation temperatures can be extrapolated for the Raqqa samples by considering the amount of time it would take at the temperature for maximum crystallisation rates (T_{Vmax}) for the longest observed needles (of length L_{max}) to form. As mentioned earlier, a needle-like morphology is favoured at V_{max}. It is probable that exposure times would have been much longer, as any positive or negative deviation from T_{Vmax} would decrease the crystallisation rate significantly.

Data for exposure to crystallisation temperatures is given for five Raqqa glasses in Table 7-13. Agreement between V_{max} and T_{Vmax} values obtained from Lakatos and Urbain viscosity data is good, except for TB5 where a large time discrepancy is caused by significantly different values of V_{max} (0.23 and 0.66 $\mu m \cdot min^{-1}$ for Lakatos and Urbain models respectively). Errors of ±10°C for T_{Vmax} and ±5-10μm for L_{max} are attributable to imprecision in the measuring process. Nonetheless, the data indicates that the wollastonite needles observed in the glasses could only be the result of ~7-16 hours of reaction at T_{Vmax}. Longer times are likely as deviations of ±40°C from T_{Vmax} halve the crystallisation rate and thus double the necessary exposure time. The

pattern that emerges suggests that all five samples have similar exposure histories, i.e. they have all been exposed to lengthy heating. This constitutes another reason why all five fragments studied are likely to originate from furnaces exposed to a heating cycle lasting days and not minutes.

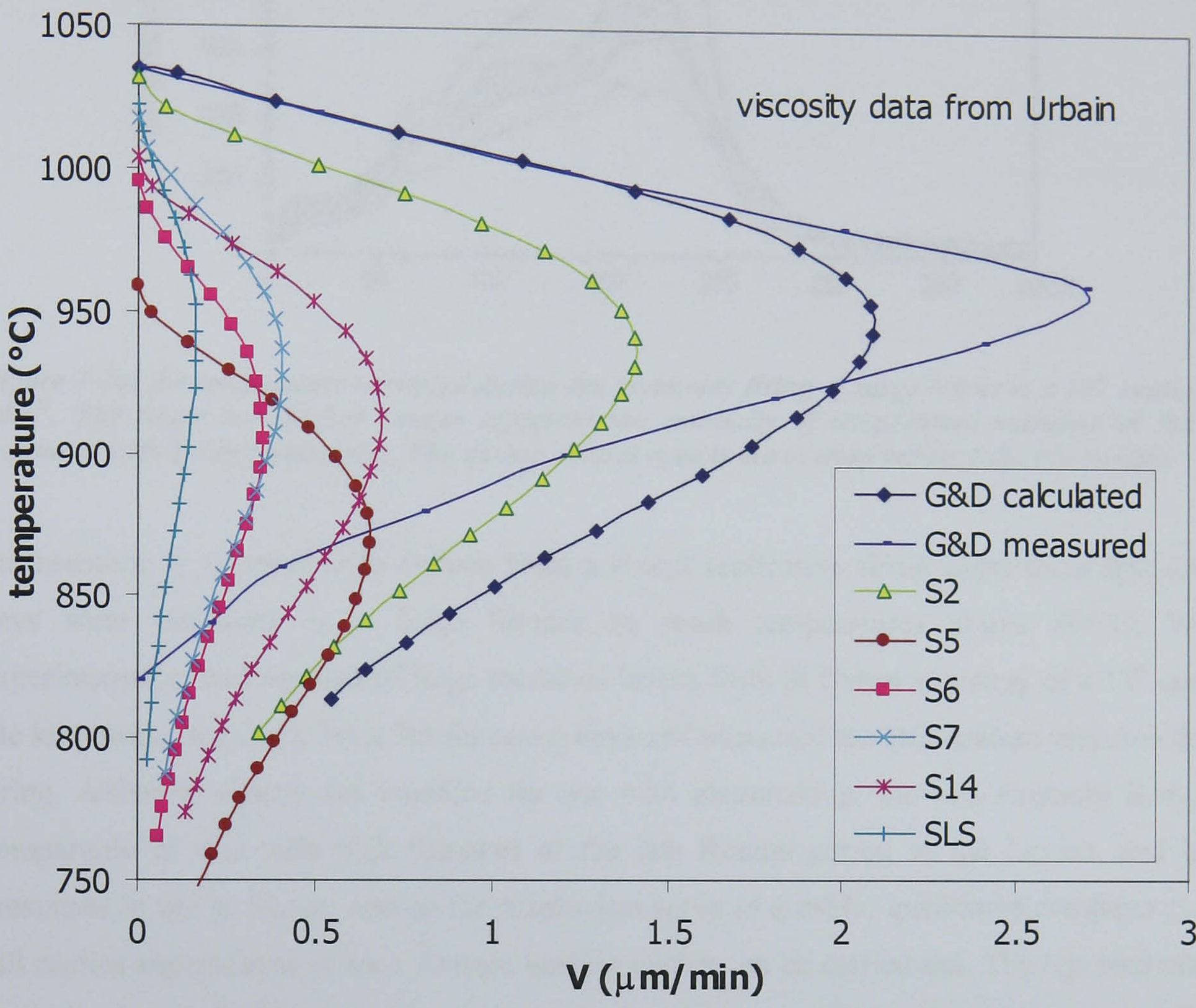


Figure 7-33: calculated growth rates of precipitated wollastonite crystals, following the equations published by Guillemet and Denoncin and using viscosity values calculated from the Urbain model.

Sample		TB2	TB5	TB6	TB7	TB14
L_{max} wollastonite (μm)		591	663	208	282	408
Lakatos	V_{max} (μm·min^{-1})	0.84	0.23	0.35	0.41	0.56
	T_{Vmax} (°C)	932	885	922	937	922
	t at T_{Vmax} (hrs)	11.7	48.0	9.9	11.5	12.1
Urbain	V_{max} (μm·min^{-1})	1.4	0.66	0.35	0.41	0.69
	T_{Vmax} (°C)	942	869	905	927	914
	t at T_{Vmax} (hrs)	7.0	16.7	9.9	11.5	9.9

Table 7-13: the maximum observed length of wollastonite needles in five Raqqa furnace glasses. V_{max}, T_{Vmax} and time at T_{Vmax} for the observed wollastonite growth are calculated from Guillemet and Denoncin's growth model using viscosity data according to Lakatos, above, and Urbain, below.

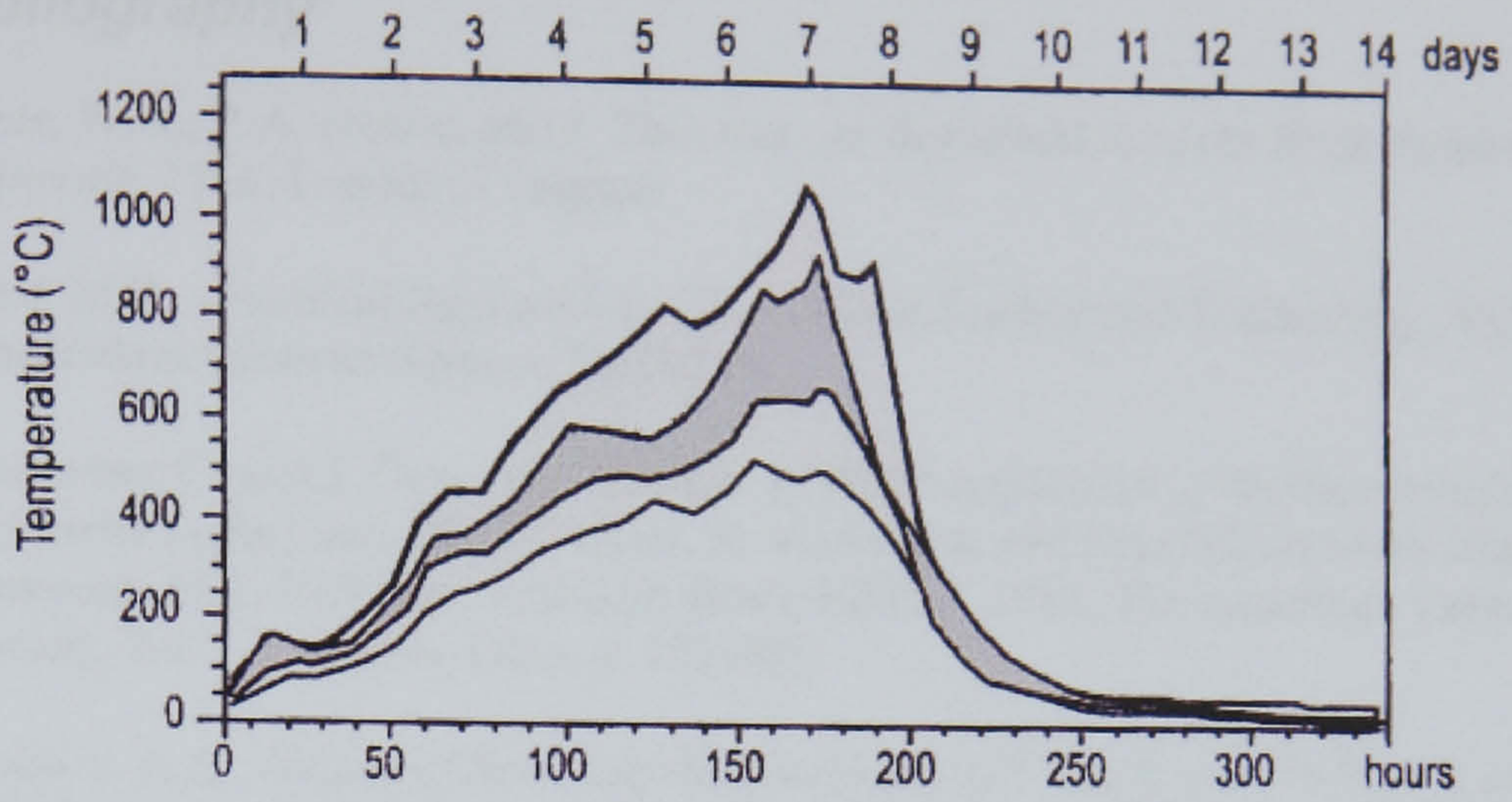


Figure 7-34: the temperature variation during the seven-day firing of large bricks in a 13th century tile kiln[5]. The lower and higher ranges represent the extremity of temperature variation in the kiln measured with 17 thermocouples. The darker central area is the overlap between the two ranges.

Furthermore, it is possible to deduce from a recent replicative firing experiment that several days were necessary in a large furnace to reach temperatures above 800°C; Wolf[5] experimentally fired replicas of large medieval bricks from St Urban in a copy of a 13th century tile kiln measuring 3m x 3m x 3m for seven days and measured the temperature variation during firing. Although clearly not intended for use with glassmaking, the kiln structure is at least comparable in size with tank furnaces of the late Roman period in the Levant, and hence presumed in use at Raqqa, and so the results can serve as a useful qualitative comparison until full replica experiments of tank furnace heating cycles can be carried out. The reported heating cycle is shown in Figure 7-34. Wolf noticed a wide temperature distribution in different locations in the kiln and a gradual increase of temperatures of 3-6°C·h^{-1}. After six days, temperatures above 800°C were reached and maintained for 24 hours, after which a slow cooling followed. Temperatures dropped rapidly only a day after the end of heating, suggesting that maximum temperatures were held for approximately 48 hours. This is the kind of time scale calculated for wollastonite crystal growth in glasses from Guillemet and Denoncin's model. No firm clues, therefore, can be gleaned from this model regarding the overall duration of the glass furnace heating cycle, but one can say with a degree of certainty from these results that at least 5-10 days would have been necessary to melt the raw ingredients. A recent ethnographic study of glassmaking in India[6] reports that three tons of glass are melted at one time inside a furnace with a floor size of 2.2m x 3.8m in a process lasting three to four days. If anything up to ten tons of glass were melted in a single operation in tank furnaces at Raqqa, the heating cycle must have taken significantly longer.

7.4 Bibliography

1. Deer, W.A., R.A. Howie, and J. Zussman, *An Introduction to the Rock Forming Minerals*. 1966, London: Longman.

2. Volf, M.B., *Chemical Approach to Glass*. Glass Science and Technology. Vol. 7. 1984, Amsterdam: Elsevier Science Publishers.

3. Guillemet, C. and J. Denoncin, *Kinetics of the Precipitation of Wollastonite in Industrial Soda-Lime-Silica Glasses*, in *Nucleation and Crystallization in Glasses*, J.H. Simmons, D.R. Uhlmann, and G.H. Beall, Editors. 1982, The American Ceramics Society, Inc.: Columbus, Ohio. p. 193-203.

4. Jackson, K.A., *Nature of Solid-Liquid Interfaces*, in *Growth and Perfection of Crystals*, R.H. Doremus, B.W. Roberts, and D. Turnbull, Editors. 1958, Wiley: New York. p. 319.

5. Wolf, S., *Estimation of the Production Parameters of Very Large Medieval Bricks From St. Urban, Switzerland.* Archaeometry, 2002. **44**(1): p. 37-65.

6. Kock, J. and T. Sode, *Medieval Glass Mirrors in Southern Scandinavia and Their Technique, as Still Practiced in India.* Journal of Glass Studies, 2002. **44**: p. 79-94.

Chapter 8

The corrosion of buried glasses

Part 1: Ballidon

The three glass compositions from Ballidon mentioned in Section 3.4 were analysed by optical microscopy, IRRS, SIM and FE-SEM with EDXA. Because of the non-destructive nature of IRRS, it was used before any sample preparation was necessary. The present study aims to assess the utility of IRRS in the surface characterisation of corroded glasses from burial contexts; the importance of accurate non-destructive analysis is often paramount where archaeological or conservation contexts are concerned due to considerations such as the paucity of finds for analysis, their heavily altered and fragile condition or the high value of the material to be analysed.

I felt that the long-term burial experiment at Ballidon was an appropriate starting point for glass corrosion studies, particularly given the three replica ancient glass compositions buried there and the unique length of the experiment (now in its 33rd year), and thus the relevance of its findings to informing both the scientific and the archaeological community. The analysis of the Ballidon glasses also served as a basis for comparison between the different analytical techniques selected for the characterisation of corroded glass surfaces. This allowed a methodology for the determination of chemical variation in the corroded areas to be developed and to be subsequently applied to corroded specimens from Raqqa.

Results are presented below in turn for each composition as different corrosion morphologies have evolved. Attention will be focused on the extent of corrosion versus burial time for each composition and then comparatively between the different compositions. The cross-technique validity of compositional characterisation of buried corroded glasses using IRRS and EDXA will also be examined.

8.1 Optical and chemical characterisation

The unaltered bulk EDXA results of the three glass compositions given in Table 8-1 fall within expected error margins for major and minor oxides of reported results, although the reported 0.49wt % Fe_2O_3 content was not detected for B1. This anomaly notwithstanding, the bulk data

points to the chemical homogeneitiy of the original glass batches that the samples were melted from.

Oxide	B1		B2		B3	
(wt%)	Rep.	EDX	Rep.	EDX	Rep.	EDX
Na_2O	18.2	18.1	2.6	2.2	0.7	0.7
MgO	0.5	0.5	4.7	3.8	5.4	4.4
Al_2O_3	3.6	4.0	4.3	4.7	3.5	3.3
SiO_2	68.5	69.2	50.1	53.4	46.5	51.1
P_2O_5	-	-	-	-	4.6	5.6
K_2O	1.3	1.0	16.7	15.9	16.4	14.2
CaO	7.3	6.6	18.6	17.6	21.6	19.6
MnO	0.34	0.6	0.36	0.7	-	-
Fe_2O_3	0.49	nd	0.95	1.1	1.2	1.2
CoO	-	-	1.03	0.8	-	-
PbO	-	-	0.1	nd	-	-
Total	100.23		99.79		99.9	

Table 8-1: reported compositions of Ballidon glasses B1, B2 and B3 and corresponding normalised bulk EDXA results in this study.

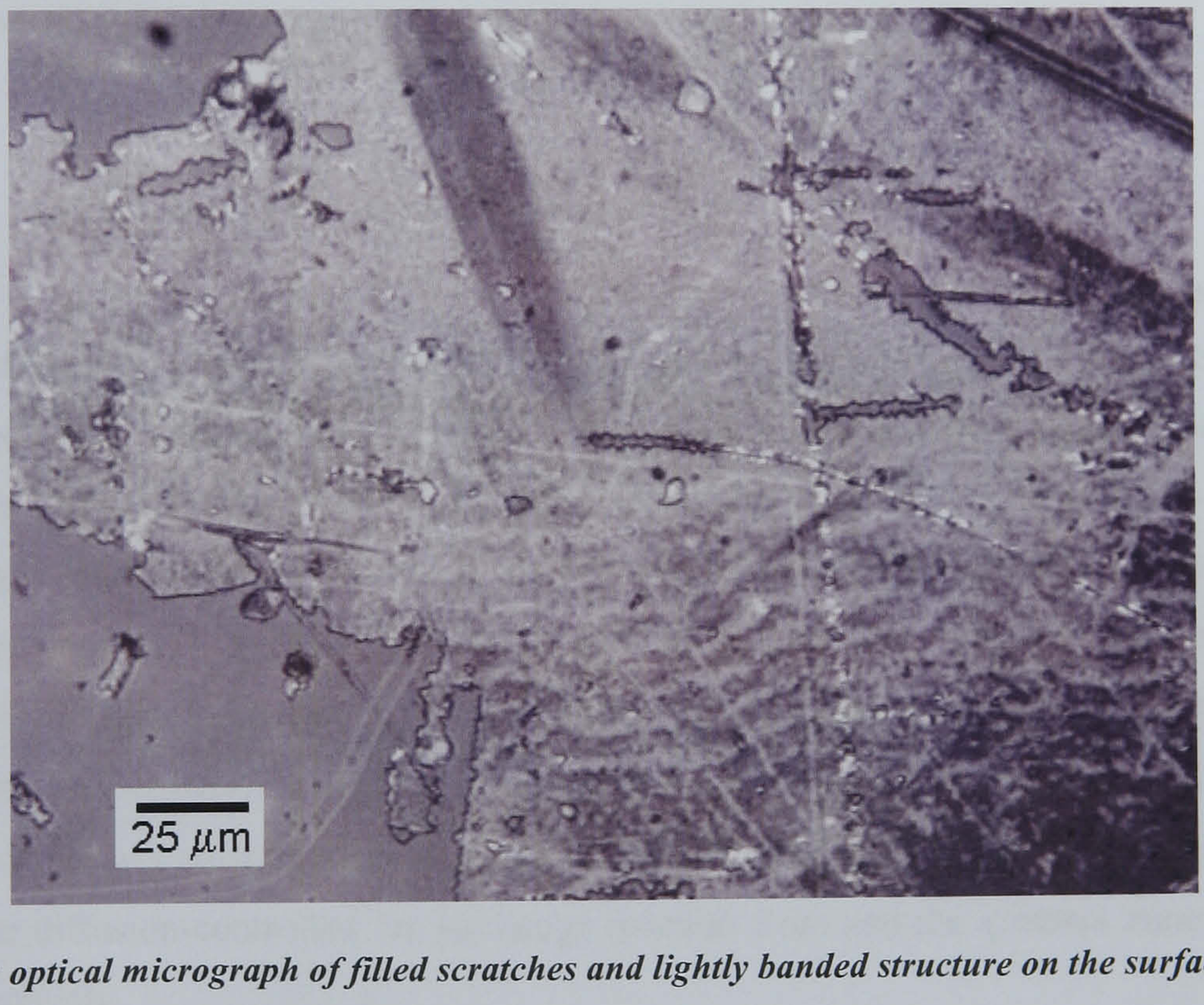


Figure 8-1: optical micrograph of filled scratches and lightly banded structure on the surface of B1-32.

8.1.1 B1 (Roman composition)

Newton[1] observed some iridescence after eight years of burial but stated that of the ancient glass replica compositions it was by far the most durable. Evidence of this was gleaned from microscopic observation and chemical analysis. The smooth surface of all three B1 samples was

in fact well preserved, with a lightly banded iridescent skin and some filled scratches on B1-32 the only feature of note (Figure 8-1).

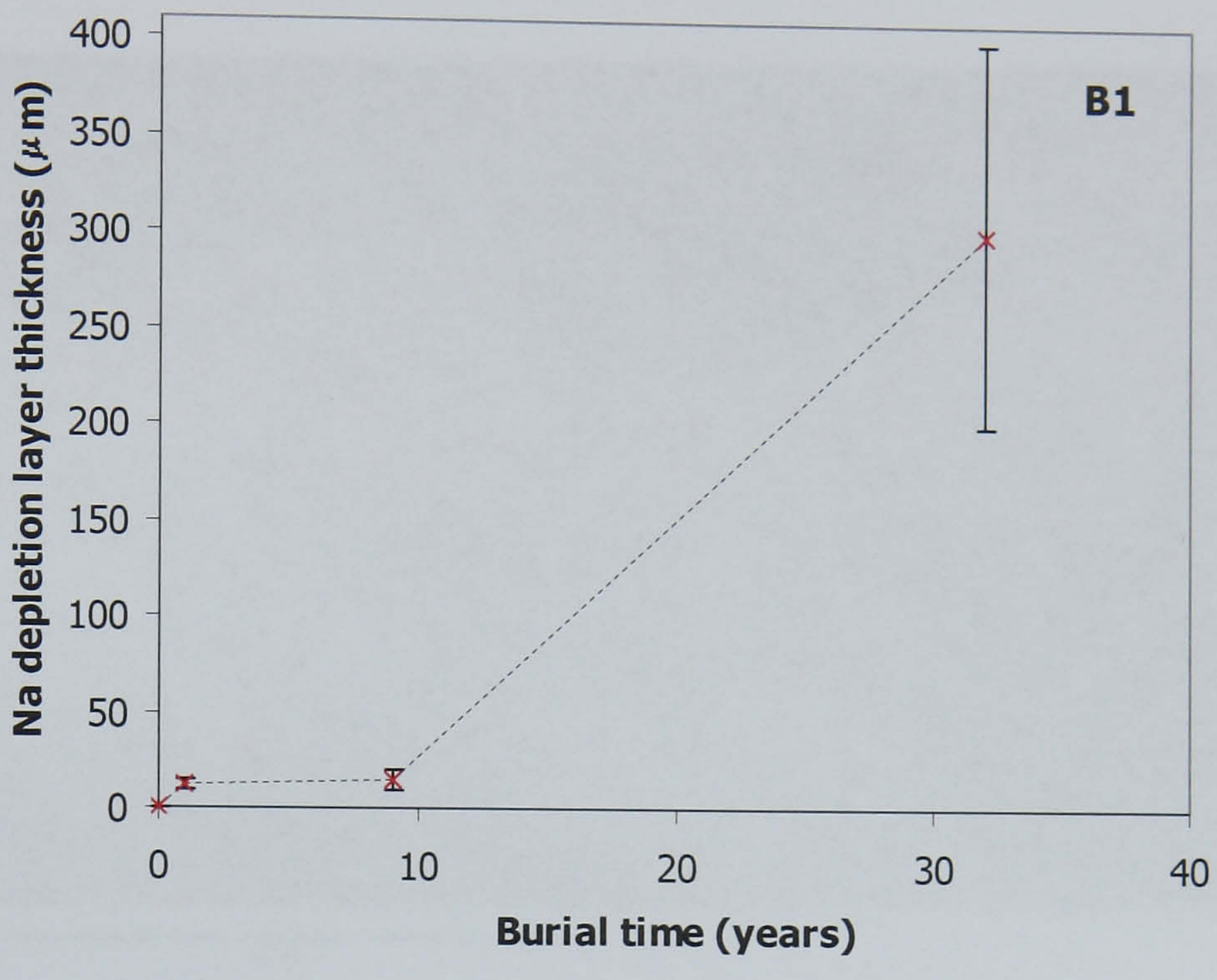


Figure 8-2: Na depleted layer thickness versus burial time for B1 samples. A marked increase in the depleted layer is seen after 32 years.

8.1.1.1 Compositional characteristics

B1 did not form a corrosion crust as such, but presented a surface depleted principally in Na, the main modifier cation. The thickness of the Na depleted region was measured for each sample as the distance from the onset of lowered Na_2O values to the outer surface (results are shown in Figure 8-2). The region was found to be similar in thickness for B1-1 and B1-9 (10-20μm) but nearly 400μm thick in places for B1-32, and littered with bright Fe-rich precipitates visible in backscattered electron mode (Figure 8-3). A linescan across the depleted region of B1-32 (Figure 8-4) reveals that Na_2O levels stabilise to ~12wt% forming an extended gradient zone over 400μm thick in places and fall to zero across the outermost 20μm, leading to a significant Si, Ca and K surface enrichment. These two regions correspond to β_2 and β_1 in Figure 2-19 that indicate the diffusion-controlled ion exchange reaction front and the gradient zone of leached glass respectively.

The reaction products can be divided into distinct regions that are formed according to different reactions: a first gradient zone (β_2) of ion exchange, where part of the mobile Na^+ cations have been replaced with H^+ ions, a second gradient zone where the difference in Na concentration across it is controlling network breakdown and a third zone nearest the surface (β_0) where Na^+

and Mg^{2+} are leached completely and a silicate skin is left (or may have re-precipitated from solution). Because the ion exchange and network dissolution reactions are independent of each other they have progressed into the glass at different rates.

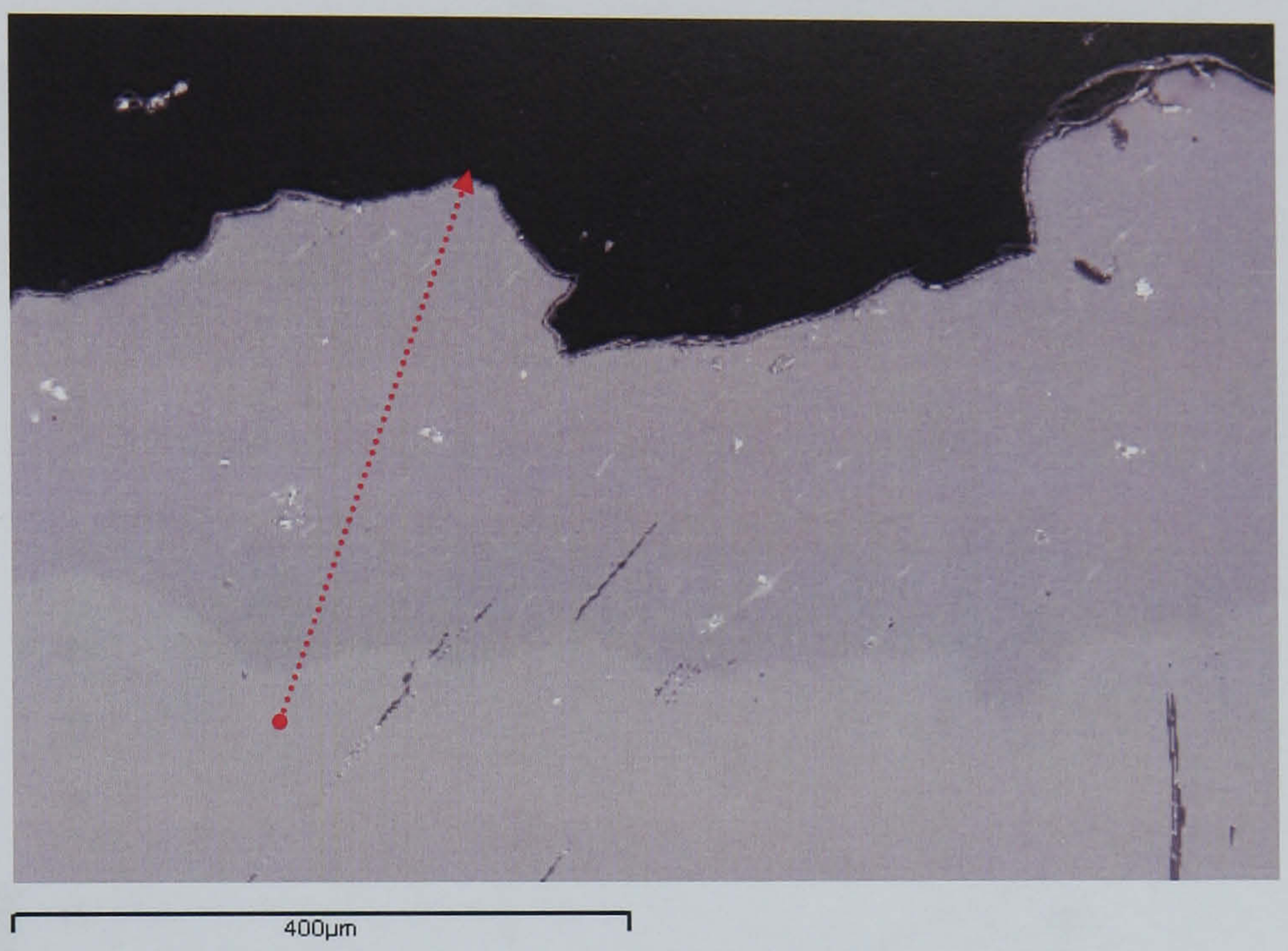


Figure 8-3: backscattered electron image of the outer surface of B1-32 in cross-section. The Na depleted zone appears darker than the unreacted bulk glass and bright Fe-rich precipitates are visible. The red arrow indicates the direction and length of a linescan shown in Figure 8-4.

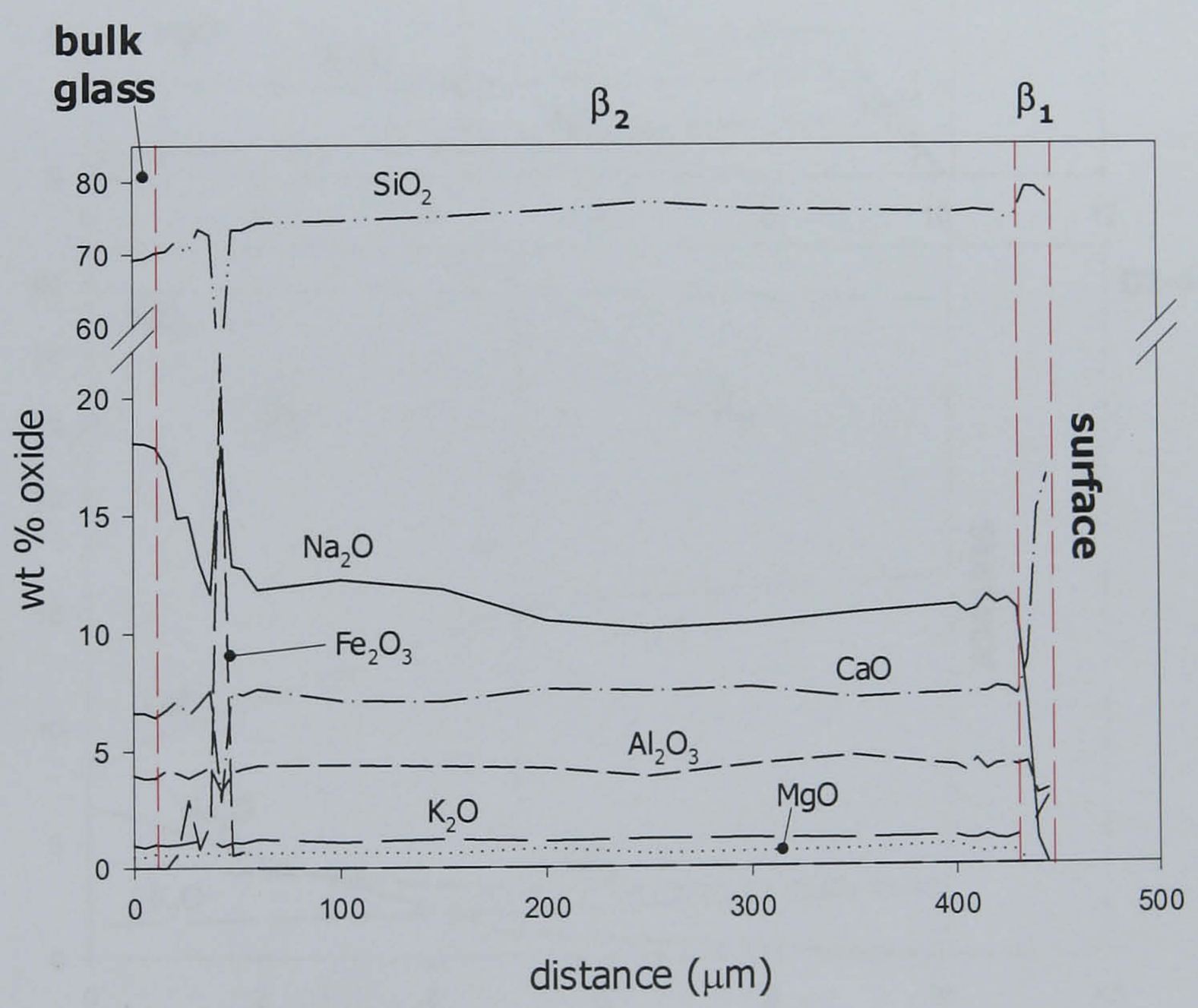


Figure 8-4: linescan across a 400µm-wide area of the Na depleted region of B1-32 in Figure 8-3. Na_2O levels stabilise at 12 wt% across this area until the outer 20µm, across which complete Na depletion is seen to take place.

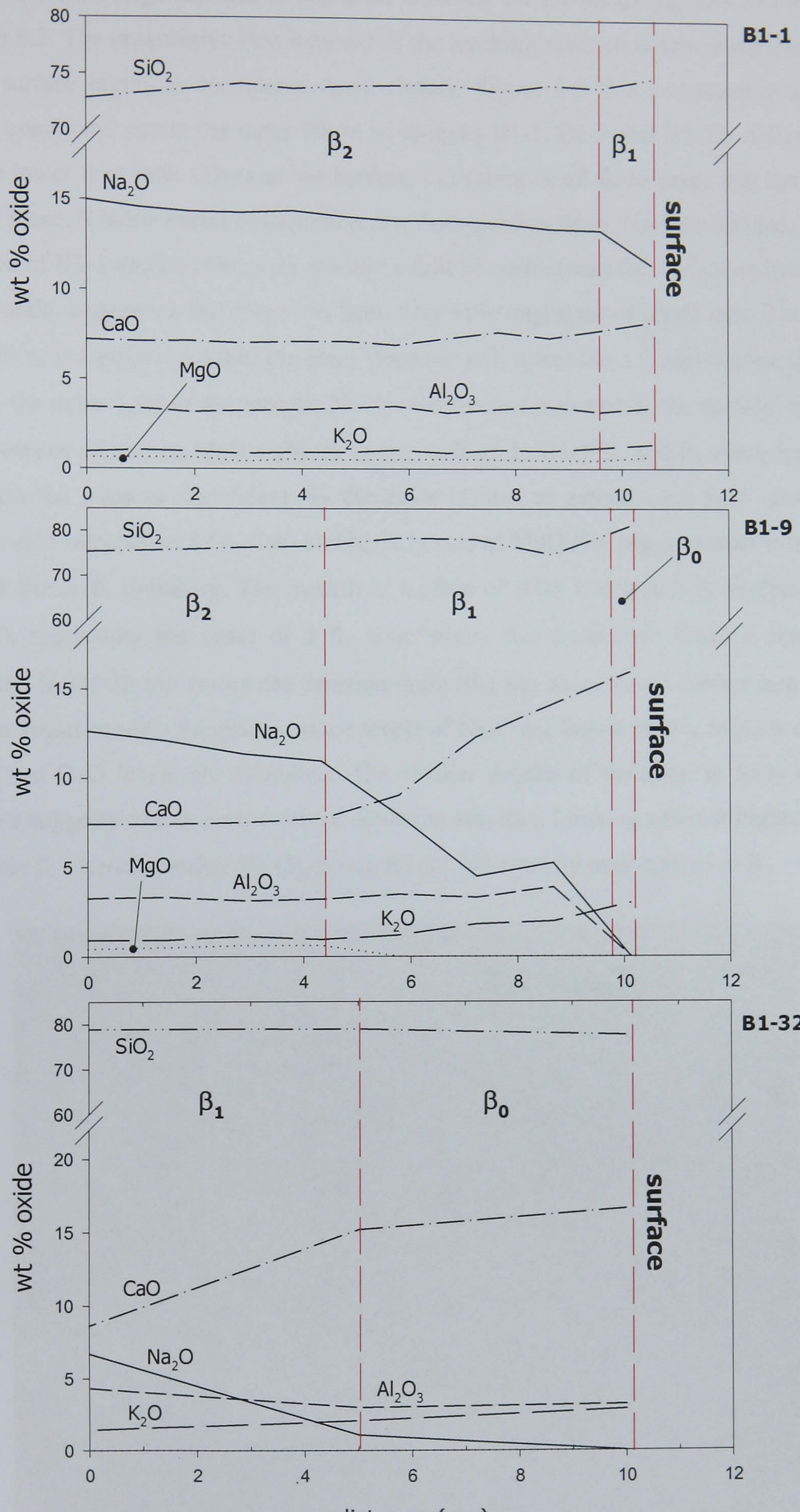


Figure 8-5: comparative linescans across the outer 10μm of the surfaces of B1-1, B1-9 and B1-32. The selective leaching of alkali and alkaline earth constituents is seen to progress with time in this region.

The reasons for the large increase in depletion thickness for B1-32 are explained in more detail in Section 8.3. The progressive development of the leaching reaction is seen more clearly when the near surface region is considered more closely. Figure 8-5 is a comparative diagram of linescans conducted across the outer 10μm of samples B1-1, B1-9 and B1-32. Although Na_2O levels are lower than bulk values at the surface, indicating in all three cases that ion exchange has taken place, it is the extent of depletion that distinguishes them. Na_2O levels are ~11wt% at the surface of B1-1 and no change in contrast could be seen across the surface in backscattered electron mode, suggesting that there had been very little migration of alkali ions. The diffusion reaction front has progressed into the glass (forming a β_2 zone) but a gradient zone (β_1) is only visible in the outer 1μm of the sample. No dissolution has occurred at the surface, highlighted by the presence of mobile MgO right up to the surface. In B1-9 β_2 and β_1 zones have moved further into the glass as significant Na depletion is seen to extend over 5μm into the glass forming a skin enriched in SiO_2, CaO and K_2O. Levels of MgO that begin to taper to zero in this area mark the β_2/β_1 boundary. The outermost surface of B1-9 is completely depleted in Na_2O and MgO, suggesting the onset of a β_0 zone where the dissolution reaction has come to completion. In B1-32 the completed reaction zone (β_0) has also moved further into the glass; more than 10μm beneath the glass surface levels of Na_2O are below 6wt%, MgO is completely removed and CaO levels are increased. The smaller degree of variation in SiO_2 across this region also suggests a more fully evolved depletion reaction. Looking again at Figure 8-4 it can be seen that β_1 extends another 10-15μm into B1-32 followed by over 300μm of β_2.

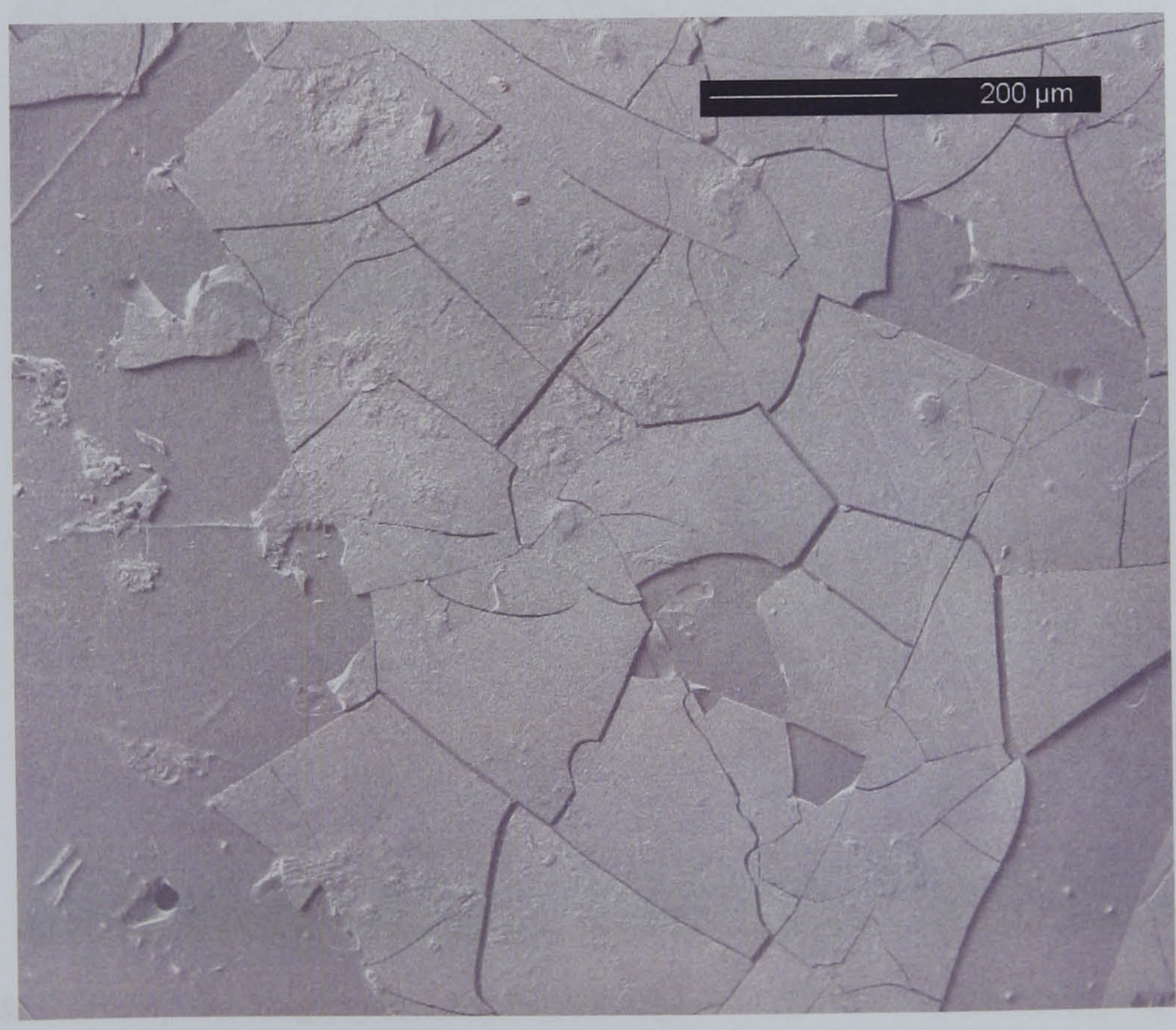


Figure 8-6: secondary ion image of cracked crusted surface of B2-1.

8.1.2 B2 (Medieval composition)

B2 is a typical example of medieval KLS glasses, which are known to be readily susceptible to corrosion and surface crust formation upon burial[2]. It came then as no surprise that the surface of B2-1 (Figure 8-6) was already covered with an opaque crust approximately 6-18μm thick.

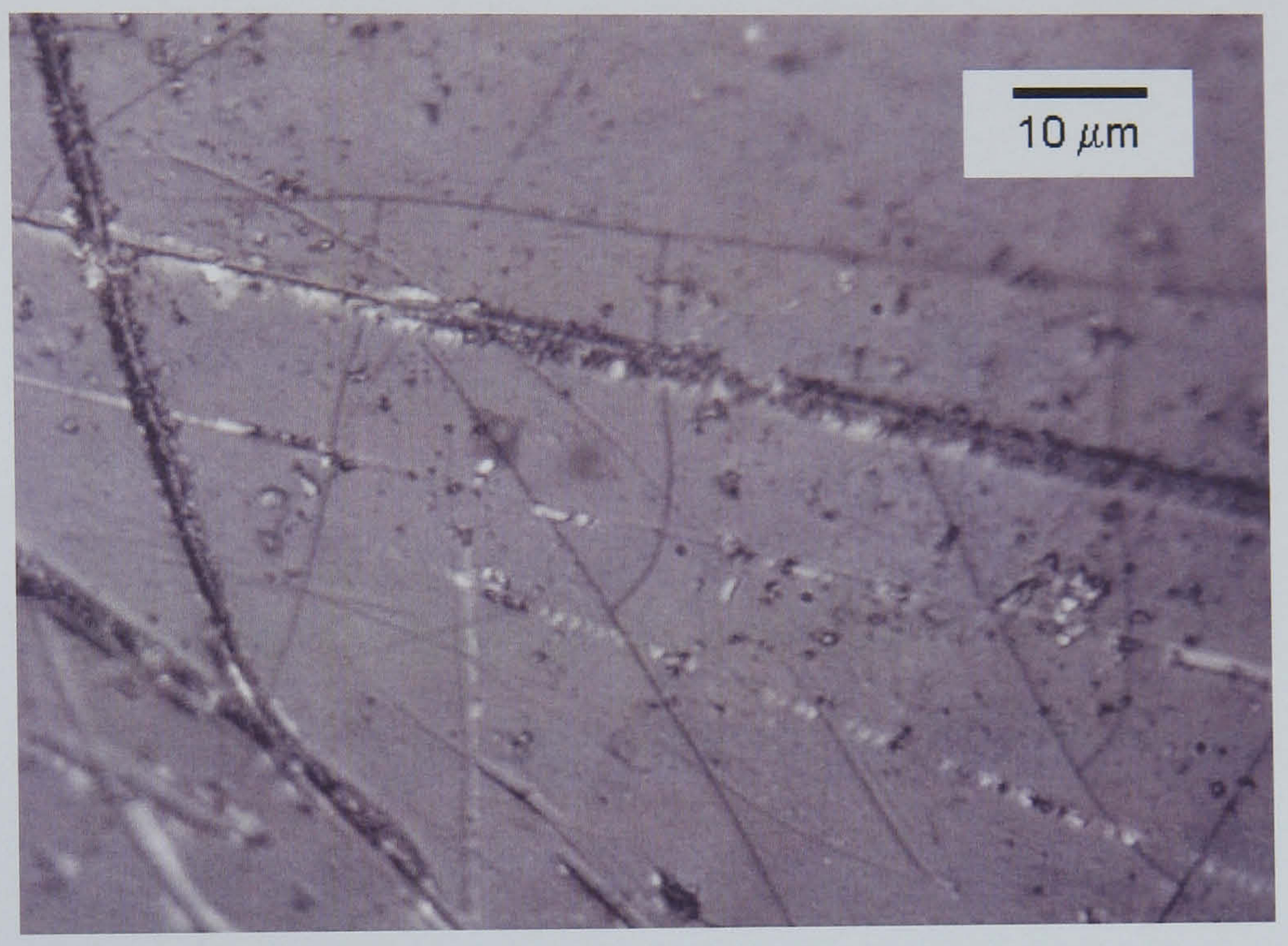


Figure 8-7: optical micrograph of cracked crusted surface with filled scratches on the surface of B2-9.

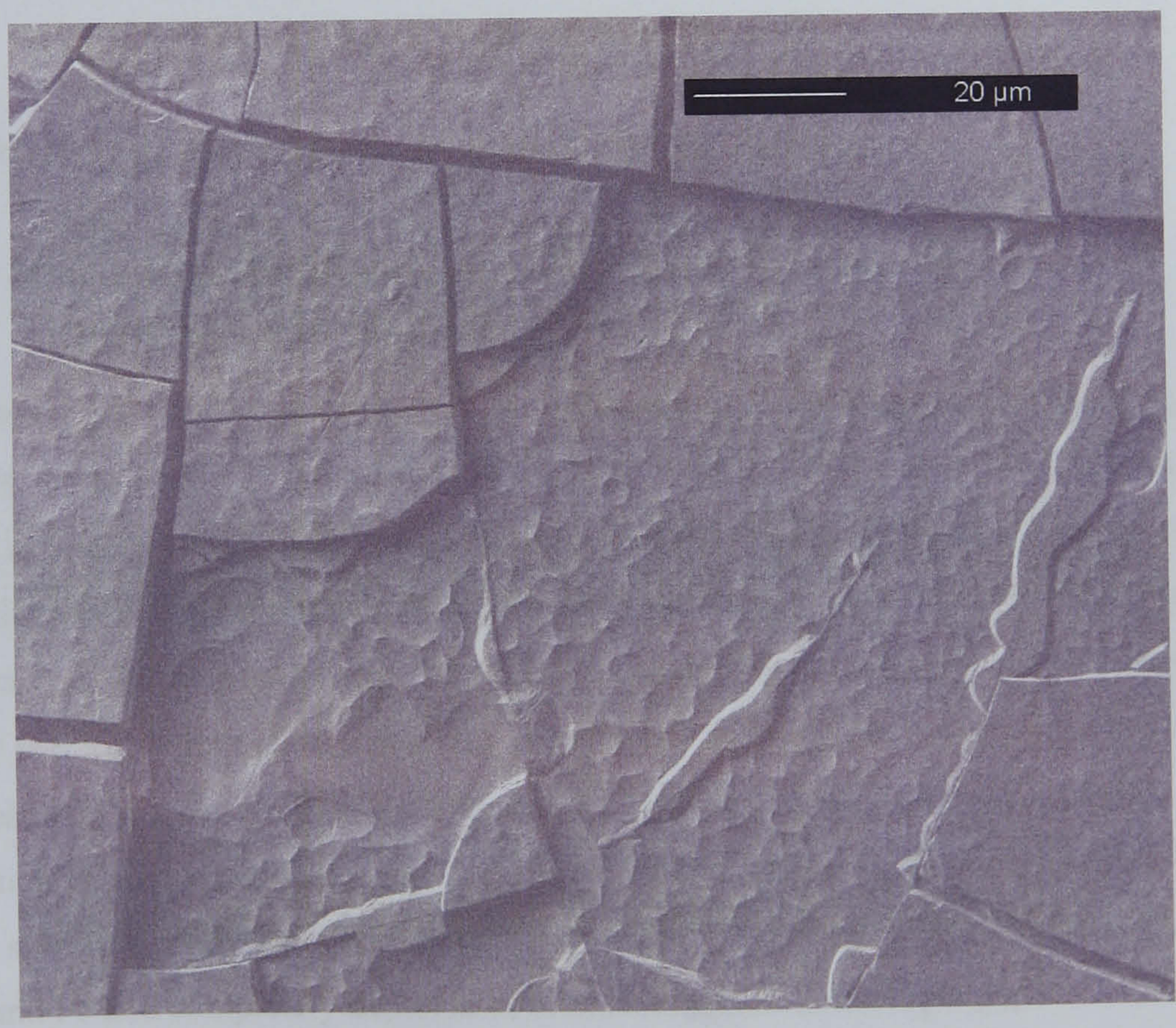


Figure 8-8: secondary ion image of cracked crusted surface of B2-32. The pitted surface of the glass is visible below the crust.

Although filled scratches were seen on the surface of B2-9 (Figure 8-7) and pitting was clearly visible on the newly exposed weathered surface of B2-32 (Figure 8-8), which indicates the progressive attack of the silicate network over time, the extent of corrosion was not found to increase with increasing burial time. The crust remained stable in thickness at 5-20μm for all three samples (Figure 8-9) suggesting that the formation of a corrosion crust has acted to slow the rate of the degradation process.

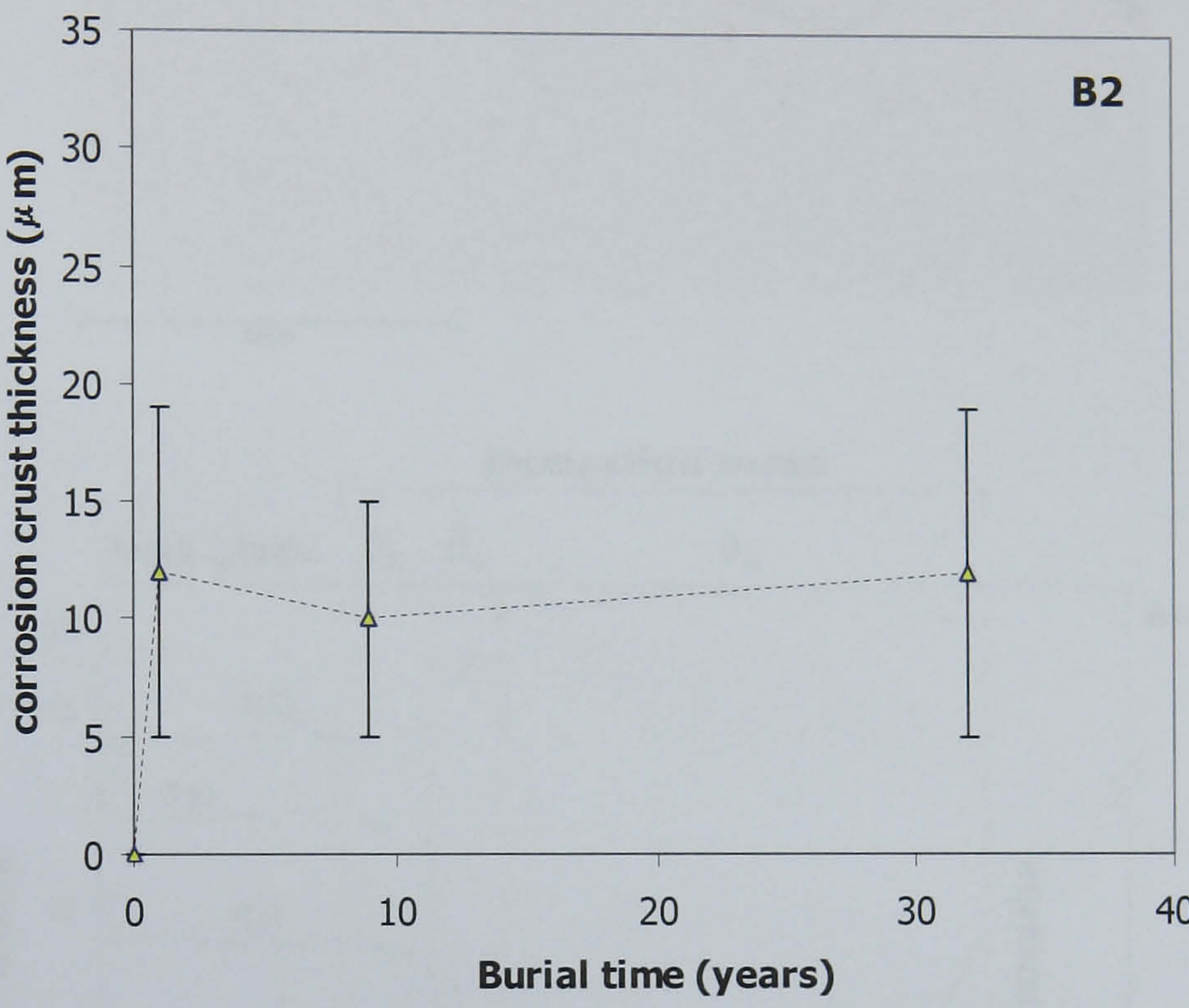


Figure 8-9: corrosion crust thickness versus burial time for B2 glasses.

8.1.2.1 Compositional characteristics

The corrosion crust on B2 glasses could be readily distinguished from the unreacted glass when viewed in cross-section. Backscattered electron images and corresponding compositional linescans across the crusts of B2-1 and B2-9 are given in Figure 8-10 and 8-11 respectively. The data highlights the different mechanisms that operate with corrosive crust formation as opposed to the gradual leaching observed for B1: the change in composition across the glass-crust boundary is abrupt and thus the gradient zone (β_1) is compressed to within 2-3μm. Alkali ions are not leaching out in significant proportions prior to the dissolution of the network and the re-precipitation of a corrosion crust enriched in Si, Al and Fe and significantly depleted in all RO and R_2O species (except for ~1wt% MgO). The outer edge of the crust was particularly rich in both Al and Fe and completely depleted of alkali and alkaline earth species.

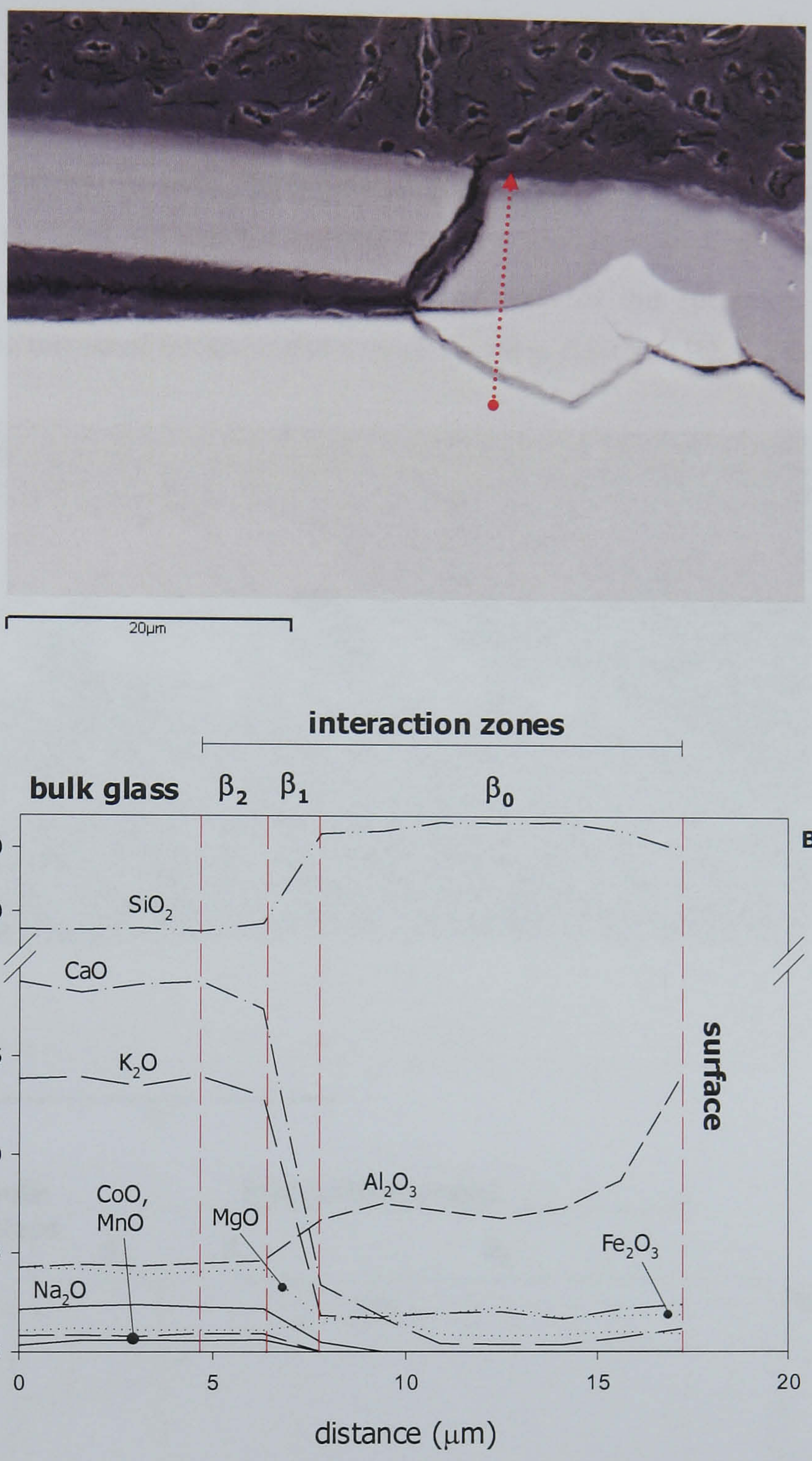


Figure 8-10: backscattered electron image of the corrosion crust formed on B2-1, viewed in cross-section (top). The dotted red arrow indicates the length and direction of the linescan, the data for which is given below the image.

A backscattered electron image of the corrosion crust of B2-9 in cross-section (Figure 8-11) suggests that after 9 years of burial the corrosion crust had started to acquire a fine, compositionally banded structure. It is unclear from the image whether these layers are physically separated from each other, and the perceived thickness of individual layers is seen to vary within the crust. No compositional differences between layers were detectable due to the large size of the analytical interaction volume relative to the thickness of individual layered bands, but a linescan across the crust reveals similar compositional gradients across the boundary to B2-1 (in Figure 8-10), and similar Si, Al and Fe enrichment within the crust. The

outer edge of the crust is exceptionally rich in Ca, and this is probably due to the calcite deposit (with some Sn, possibly detected as the result of deconvoluted x-ray lines) adhering to it rather than to material leached out of the glass. The crust is otherwise depleted in RO and R_2O components and follows the same compositional trend as B2-1 (Si, Al and Fe-rich). The crust on B2-32 visible in Figure 8-8 was not detected when mounted in cross-section and therefore no compositional data could be gleaned for the crusted zone of this specimen, although it is presumed from the measured thickness that a similar trend to B2-1 and B2-9 is to be expected.

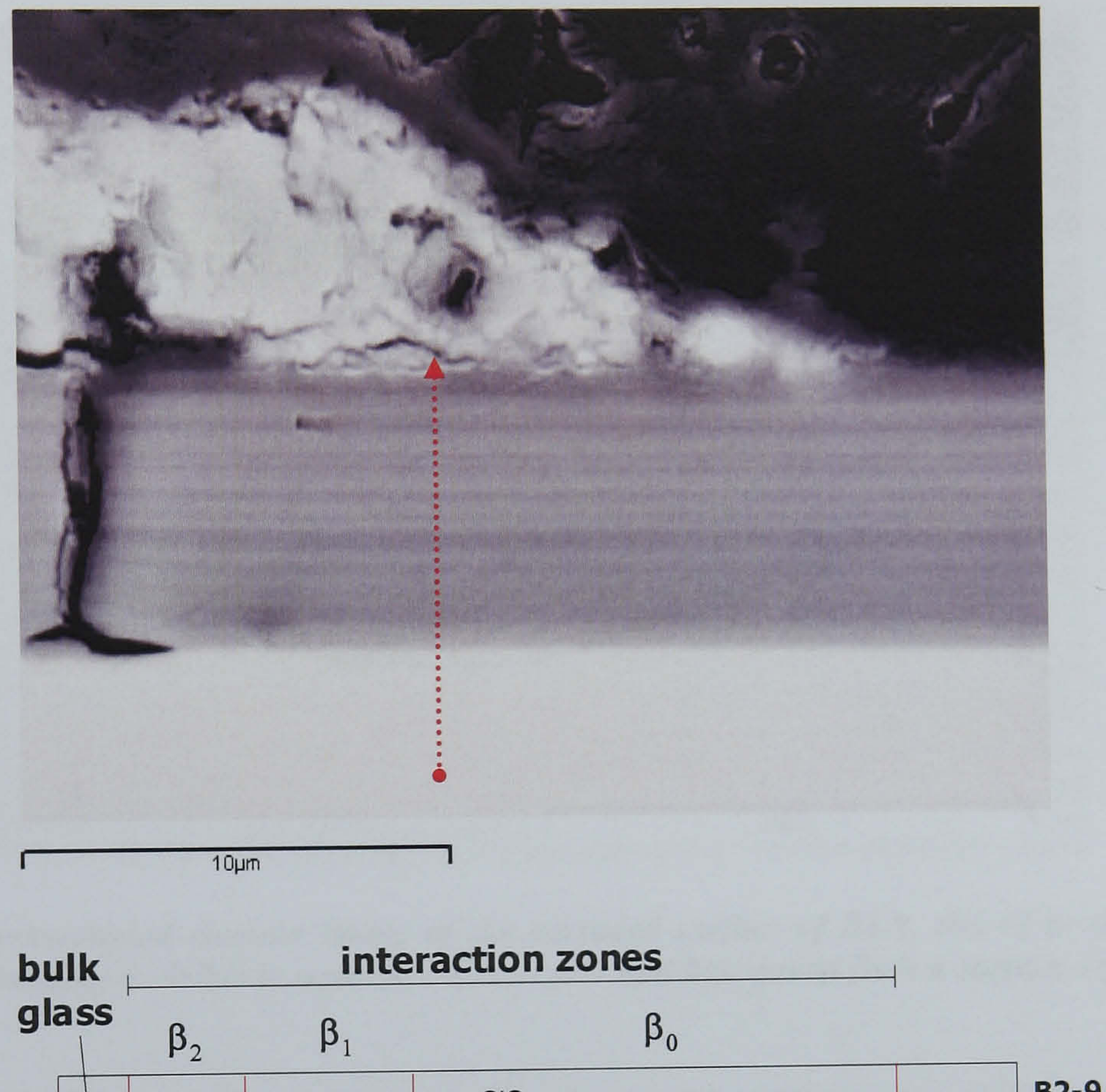


Figure 8-11: backscattered electron image of the corrosion crust formed on B2-9, viewed in cross-section (top). The dotted red arrow indicates the length and direction of the linescan, the data for which is given below the image.

8.1.3 B3 (18th Century composition)

B3 is a KLS glass similar in composition to B2 except in particular for the presence of 4.6wt% P_2O_5. Newton[2] had chosen to bury this composition because the original piece of which B3 is a replica had produced a finely laminated corrosion crust upon excavation. Compositional banding of the surface crust is visible in B3-9 (Figure 8-12), although no clearly multilayered corrosion product was found on B3-1 or B3-9 (B3-32 unfortunately was not recovered from the burial site in 2002).

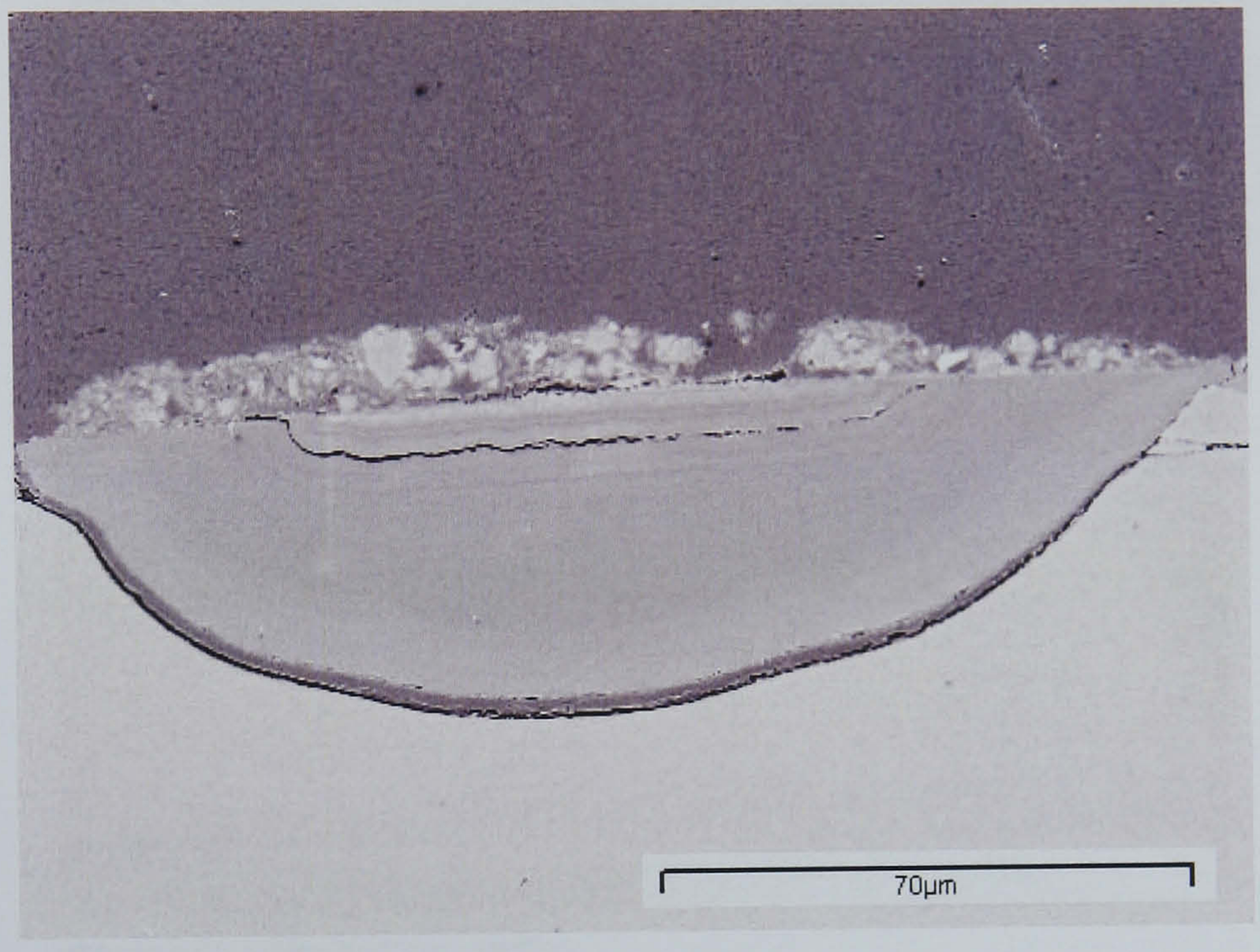


Figure 8-12: backscattered electron image of the corroded surface of B3-9, viewed in cross-section. Compositional banding is visible in a portion of the crust that has spread from a surface defect.

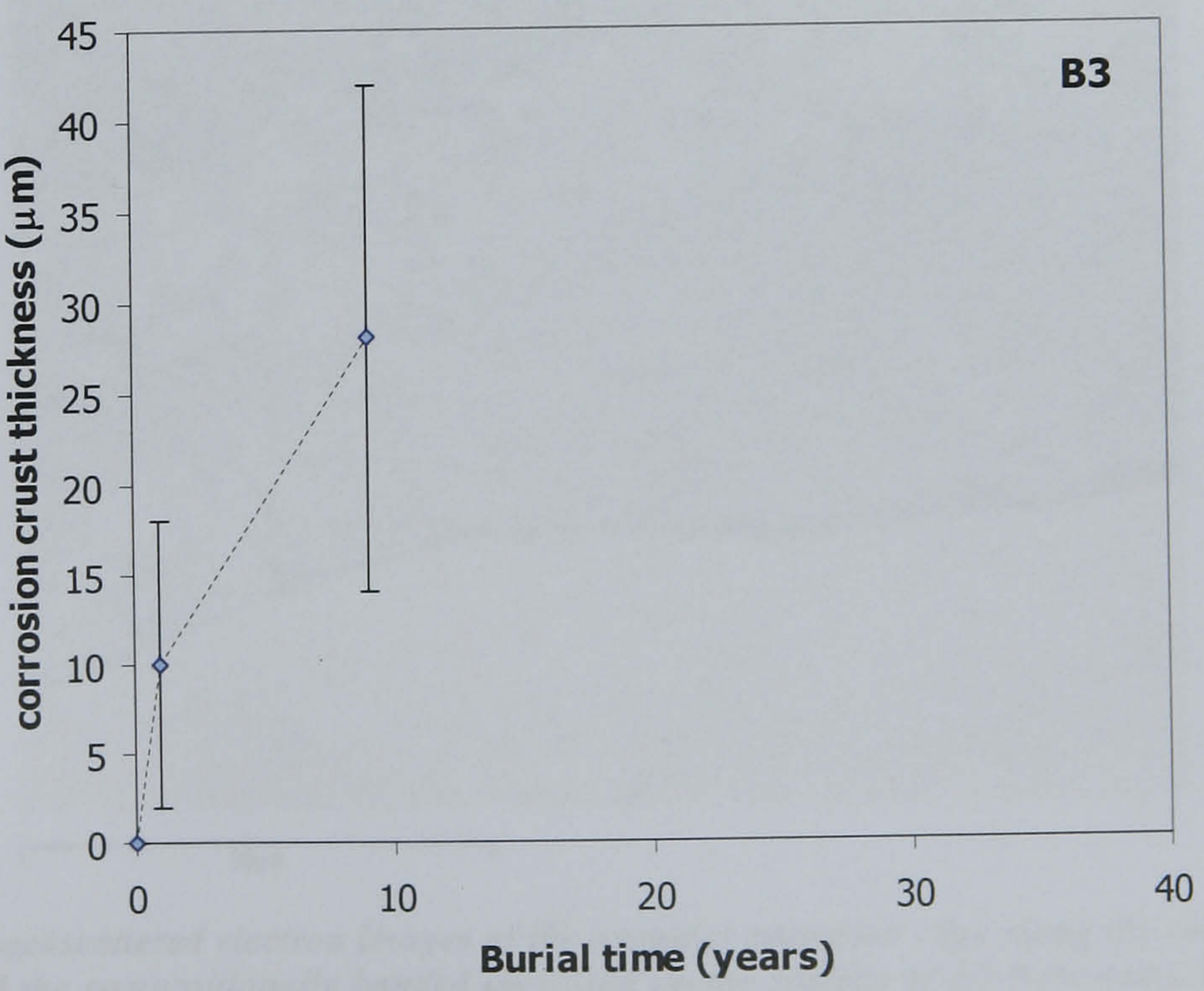


Figure 8-13: corrosion crust thickness versus burial time for B3 glasses.

The thickness of the corrosion crust increased with increasing burial time (Figure 8-13); the crust on B3-1 varied in thickness between 2μm and 20μm and after 9 years of burial this had increased to over 40μm in sections, particularly at points where corrosion had formed hemispherically from the surface (see Section 2.7.3.1), presumably starting at a defect. An example of such a formation is shown in Figure 8-12. The increased extent of corrosion over time for B3 suggests, unlike B2, that the rate of degradation was not slowed by the presence of a corrosion crust.

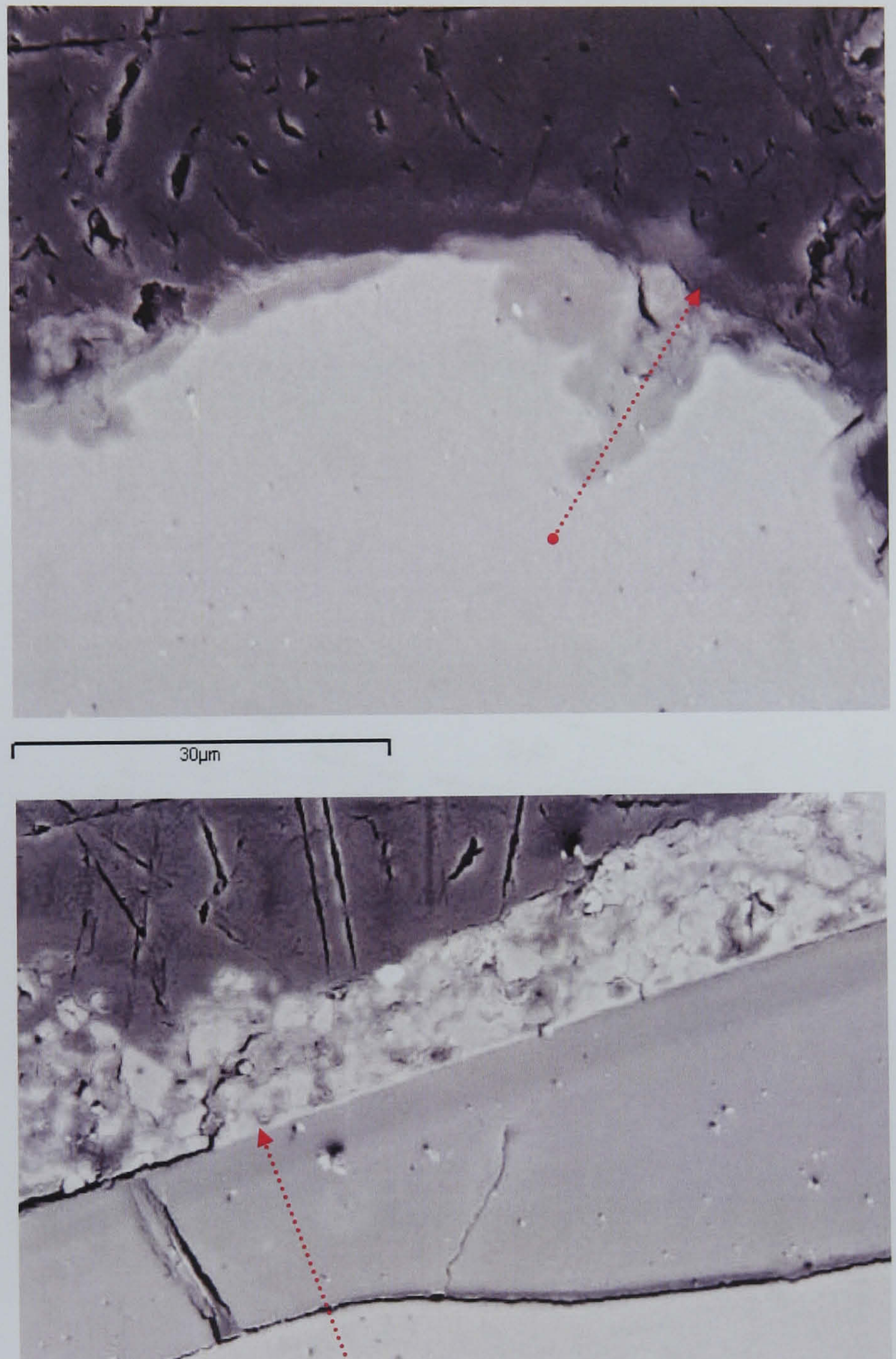


Figure 8-14: backscattered electron images of the irregular corrosion edge along the rough surface of B3-1 (top) and the compositionally banded corrosion on the surface of B3-9 (bottom), both viewed in cross-section. Red arrows in the images indicate direction and length of linescans, the data for which is shown in Figure 8-15.

8.1.3.1 Compositional characteristics

Linescans across the surface of B3-1 and B3-9 are indicated on backscattered electron images in Figure 8-14 and the data is shown in Figure 8-15. The nature of the corrosion on B3 is similar to B2 in that a large increase in SiO_2 concentration is accompanied by depletion of RO and R_2O species and enrichment of Al and Fe. In B3-1, the leaching of monovalent and divalent cations occurs significantly in only the outer 5μm of a 20μm-thick β_1 depletion zone. There is no loss of P_2O_5 across this region. After 9 years of burial however, a discrete, banded crust has formed. The fully leached layer (β_0) is separated from the unreacted glass by a gradient zone (β_1) approximately 2μm thick. P^{5+} has also leached completely out of the crust. The outer edge of the crust, visible in backscattered electron mode, is poorer in Ca than the rest of the crust presumably because it is adjacent to Ca-rich deposits adhering to the surface.

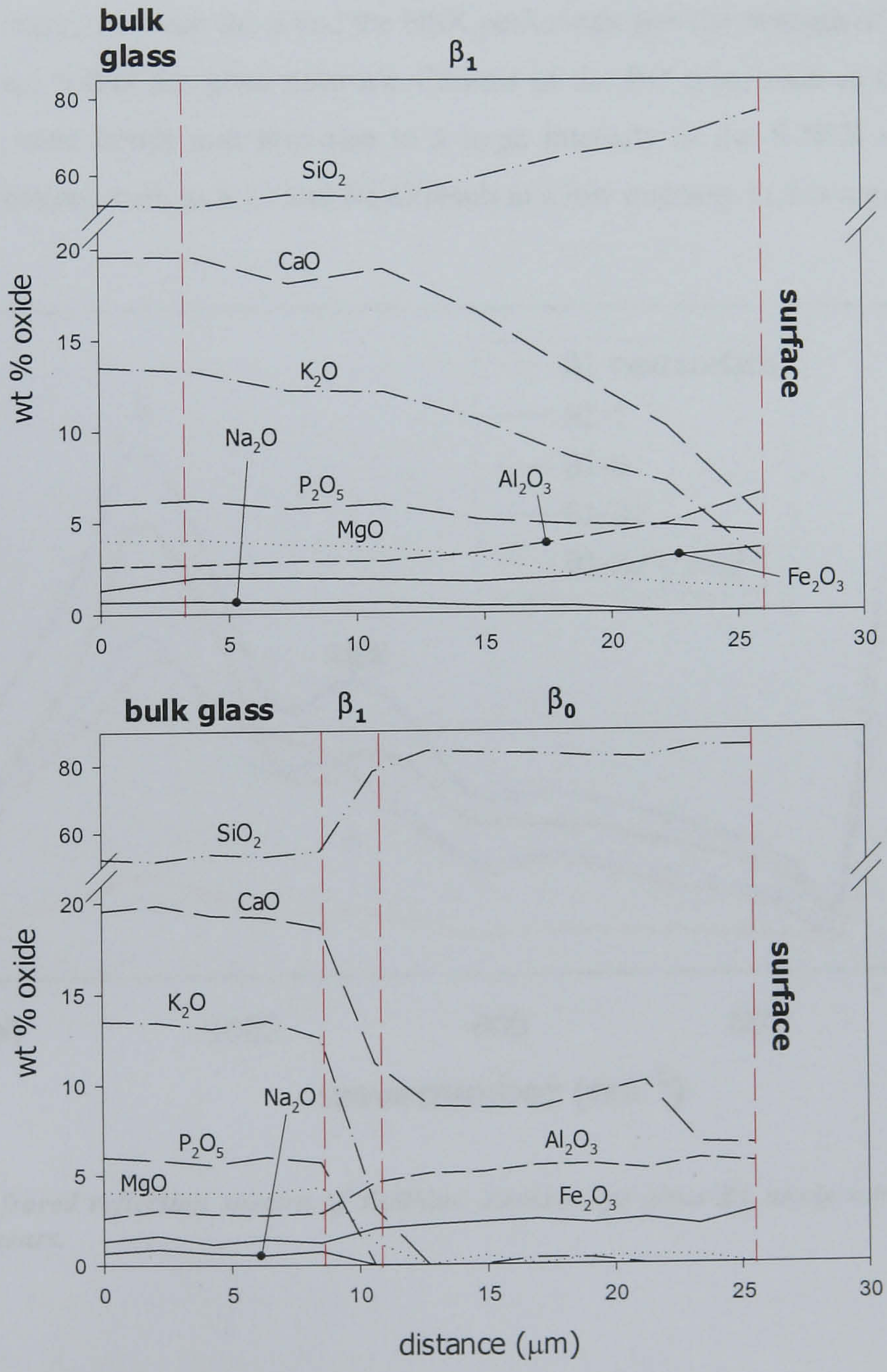


Figure 8-15: results for linescans indicated in Figure 8-14 on B3-1 (top) and B3-9 (bottom). A fully leached outer layer is present after 9 years.

8.2 Structural characterisation by IRRS

The IR spectra of Ballidon compositions 1,2 and 3 were compared according to burial times. Although the IRRS analyses were conducted prior to chemical characterisation, they are presented here for more complete interpretation in light of previously discussed chemical data.

Both the position and amplitude of the Si-O stretch peak (S) maximum indicate the extent of glass corrosion[3]. When the amplitude increases and the S maximum shifts to higher wavenumbers, selective leaching is the primary mode of corrosion, resulting in the development of a silica-rich surface layer. The disappearance of the Si non-bridging peak (NSX) accompanies this reaction. A decrease in the amplitude of the S peak with no change in wavenumber is indicative of surface roughening due to network glass dissolution (i.e. destruction of the silica-rich layer) or to precipitation of a new phase on the surface. The intensity of the region between the S and the NSX peaks indicates the strength of bonding of the modifying cations within the glass network. Cations of the RO type, such as CaO and MgO, produce strong ionic bonds and give rise to a large intensity in the S-NSX region whereas weakly bonded cations such as K_2O and Na_2O result in a low intensity in this region.

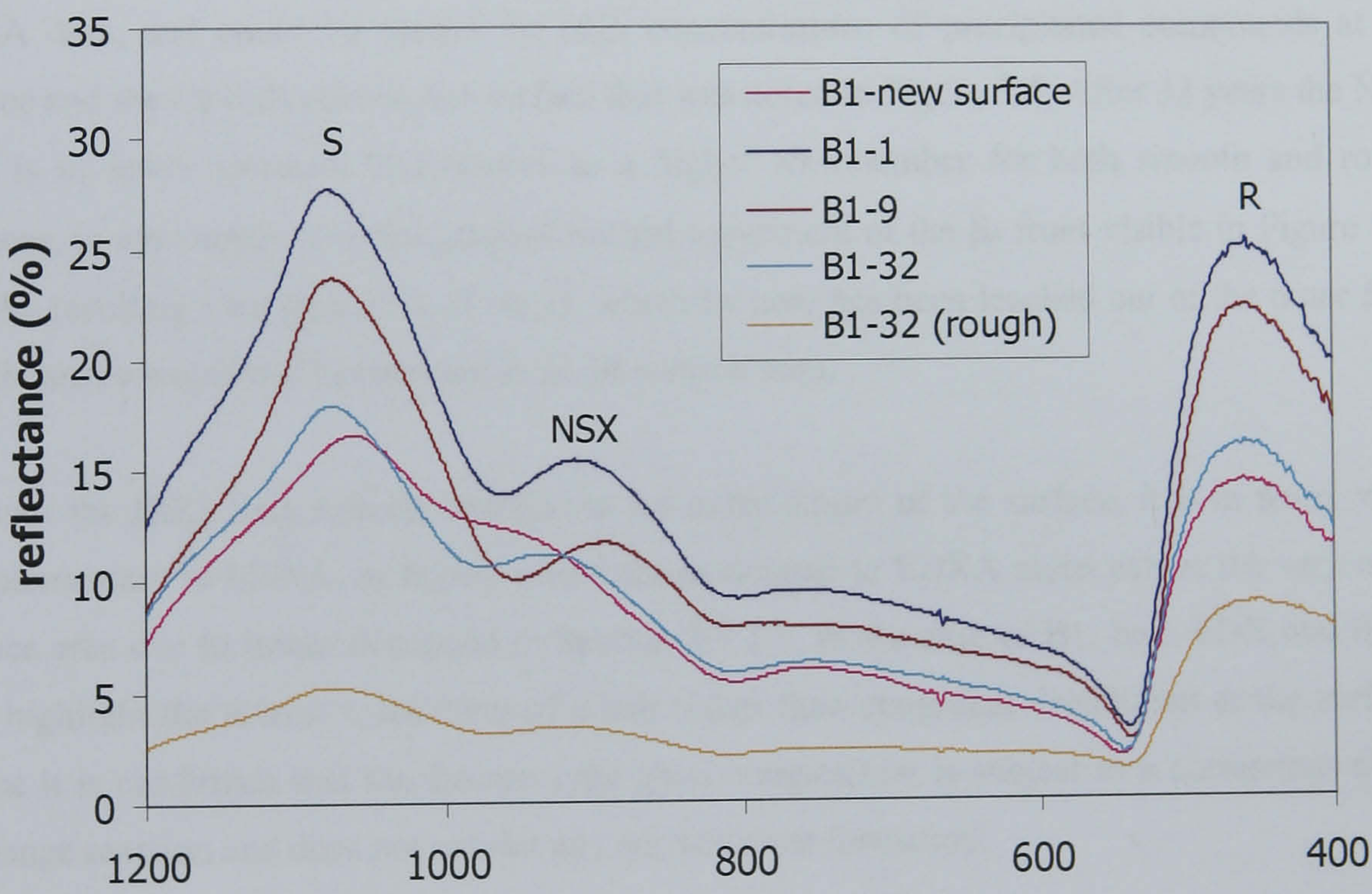


Figure 8-16: infrared reflection spectra of Ballidon Roman type glass B1 newly revealed and buried for 1, 9 and 32 years.

8.2.1.1 B1

IR spectra for B1 glasses are shown in Figure 8-16. The new surface shows an S peak maximum at 1062cm^{-1} and a broad NSX shoulder at 960cm^{-1}. The exposure to groundwater has resulted in shifts in the S peak, which increases in wavenumber to 1082cm^{-1} after 1 year, and stabilises thereafter at 1076cm^{-1}. The initial increase in intensity of the S peak is offset by a net decrease with the passing years of burial. This is reflected in the R peak, which changes in intensity and wavenumber accordingly. The initial increase in peak intensity suggests that surface roughening remains minimal, or at least smaller than silica enrichment effects due to selective alkali depletion (Na in the case of B1). The effect of surface roughness on spectral reflection is clearly visible when the two surfaces analysed from B1-32 are compared: all peaks are significantly suppressed for one of the faces on B1-32 that was roughened prior to burial with respect to a smooth surface on the same piece but no change in S peak wavenumber is recorded.

The NSX peak shifts to lower wavenumbers and becomes more pronounced after 1 and 9 years; this would suggest a simultaneous surface enrichment in mobile RO species (because high intensity in the S-NSX region is due to the presence of RO and not R_2O), in conjunction with the Si enrichment that is predicted from the S peak wavenumber increase and indicated by the EDXA data, and could be caused by high concentrations of precipitated compounds at the surface and the Ca-rich skin on the surface that was noted in Figure 8-5. After 32 years the NSX peak is of lower intensity and returns to a higher wavenumber for both smooth and rough surfaces, in agreement with the gradual inward movement of the β_0 front visible in Figure 8-5, and the resulting total depletion of Na_2O, which by now has been leached out of the outer 5μm and therefore would not be detected in an IR surface scan.

Because the IRRS data reflects changes in the outer 0.5μm of the surface, it is in many ways complementary to EDXA, as higher errors are associated to EDXA scans across the very outer surface area due to issues discussed in Section 4.5.1.1. In the case of B1, both EDX and IRRS data highlight the selective leaching of alkali rather than congruent dissolution at the surface. Hence it is confirmed that the Roman type glass composition is subject to a continuous alkali exchange reaction and does not exhibit any surface crust formation.

8.2.1.2 B2

IR spectra for B2 glasses are shown in Figure 8-17. B2-1 and B2-9 had a layer of soil adhering to the surface, which could have helped to lower the reflectance and interfere with peak maxima. An IR spectrum of soil (included in Figure 8-17) was taken in order to measure the level of interference. Spectra for B2-1 and B2-9 are slightly affected in the region 1000-

1050cm^{-1} (S peak) and 880-890cm^{-1} (NSX peak) but in particular in the region 400-600cm^{-1}, which made measurement of the R peak problematic.

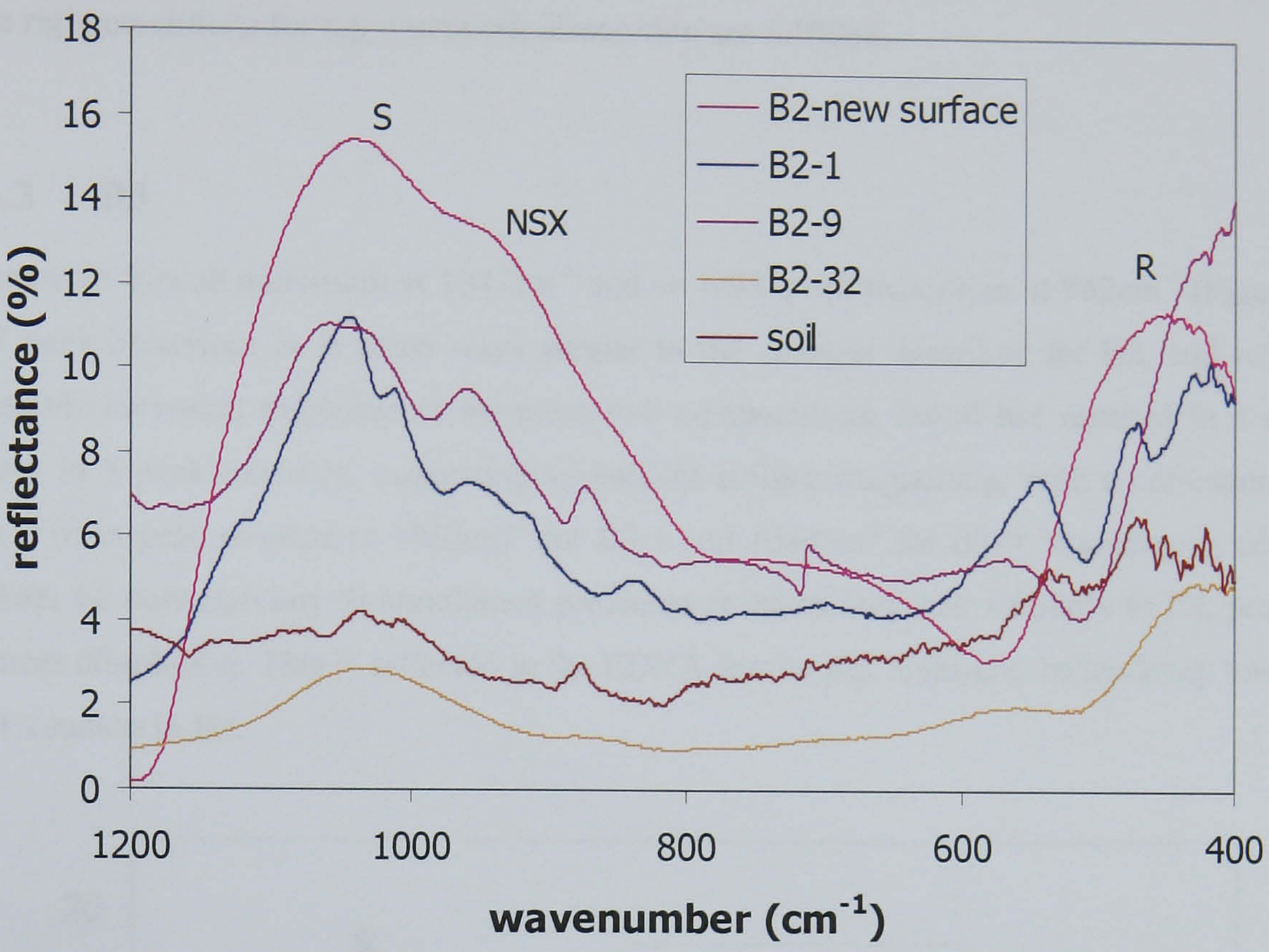


Figure 8-17: infrared reflection spectra of Ballidon medieval type glass B2 newly revealed and buried for 1,9 and 32 years.

Unaltered B2 glass shows peak maxima at 1039cm^{-1} for S and at 941cm^{-1} for NSX. S peak intensity decreases dramatically after 1 year and decreases further after that, accompanied by small increases in peak wavenumber up to 1045 cm^{-1}. Minor Si enrichment at the surface of B2 is thus overshadowed by the progressive surface roughening effects that suppress the spectral reflectance. As the roughening is caused by congruent dissolution of the network, IRRS results point to the same corrosion mechanism as predicted from the EDX data in Section 8.1.2.1, despite the Si-rich exterior that was found in that case.

The NSX peak becomes more pronounced for B2-1 and B2-9 and stabilises at higher wavenumbers (957cm^{-1} and 955 cm^{-1} respectively), confirming that alkali removal in the outer 0.5μm has already reached completion after 1 year. The dissolution front in fact has moved several μm inwards and so the original outer surface is expected to remain relatively stable in composition. B2-32, however, shows a suppressed NSX peak at 927cm^{-1}, suggesting that some alkali enrichment of the surface has taken place. Again, this may be due to deposited salts or precipitated compounds but unfortunately no EDX data was available for comparative clarification.

EDX and IRRS results for B2 point to rapid alkali exchange advancing in conjunction with congruent dissolution, which are the mechanisms expected to form a hydrated corrosion crust. The dissolution front remains closely behind the ion exchange reaction front, suggesting that for B2 the right conditions for rapid network dissolution are fulfilled.

8.2.1.3 B3

B3 shows an S peak maximum at 1047cm^{-1} and an NSX peak maximum at 942cm^{-1} (Figure 8-18). S peak behaviour is in some ways similar to the changes described for B2, and reflects comparable corrosion mechanisms for these two compositions; burial has resulted in a sharp decrease in S peak intensity, suggesting significant surface roughening, with a corresponding minor shift in peak position to 1053cm^{-1} for B3-1 and 1044cm^{-1} for B3-9. Roughening effects, therefore, far outweigh any Si enrichment predicted at the surface and, similarly to B2, point to congruent dissolution. This is reflected in the EDXA results that highlight the tendency towards crust formation in B3.

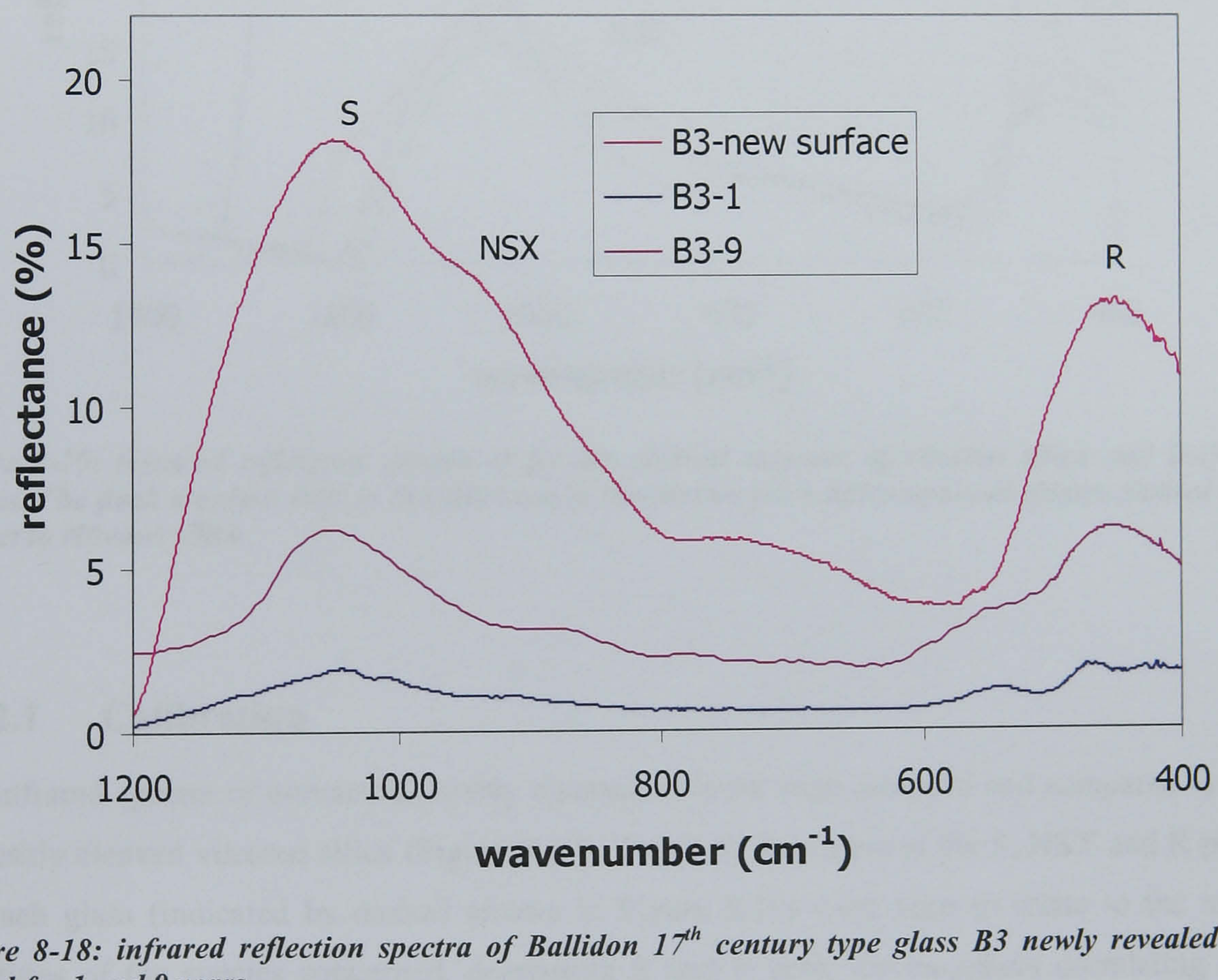


Figure 8-18: infrared reflection spectra of Ballidon 17th century type glass B3 newly revealed and buried for 1 and 9 years.

The NSX peak is reduced after 1 year and almost disappears after 9 years, although the shift to lower wavenumbers (to 918cm^{-1} for B3-1 and 887cm^{-1} for B3-9) points to alkali enrichment at the surface. Again this may be due to alkali-rich deposits at the surface. Soil interference made accurate measurement of the B3-9 R peak unattainable.

8.2.2 Quantification of peak shifts

As outlined in Section 4.5.3.2, the S peak shifts are linearly related to the SiO_2 content of the glass independently of surface roughness[4] (in other words irrespective of spectral suppression). Sanders *et al.*[5] have shown that the location and intensity of the NSX peak is linearly related to the mol.% of R_2O + RO species present in the glass structure. On this basis, quantification of the peak shifts recorded for the Ballidon glasses was attempted and subsequently compared to EDXA results in order to assess the validity of the data obtained by this method.

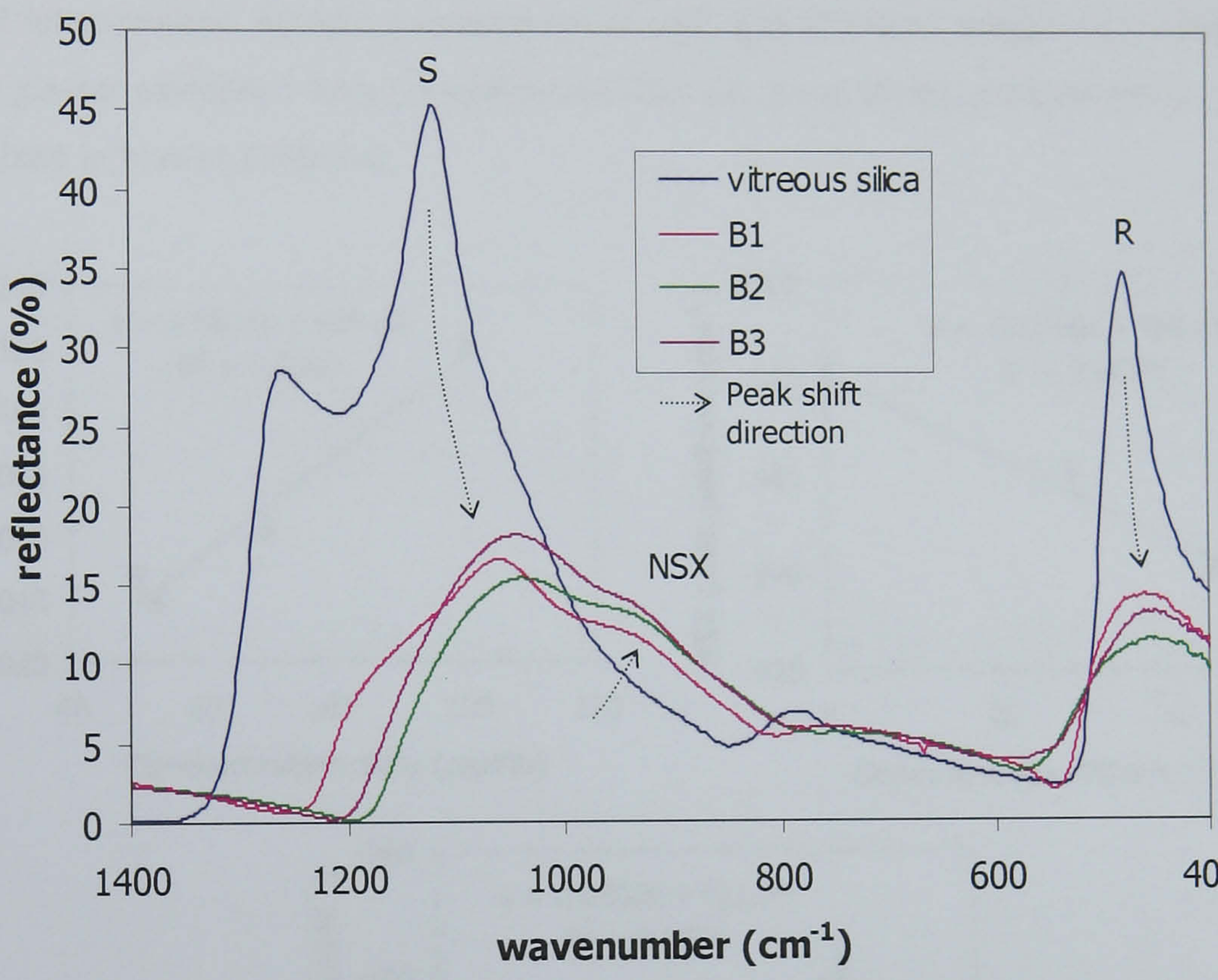


Figure 8-19: infrared reflection spectra of freshly cleaved surfaces of vitreous silica and Ballidon glasses. The peak maxima shift in the direction of the arrows for multicomponent glasses studied with respect to vitreous silica.

8.2.2.1 Calibration

The infrared spectra of unreacted, freshly cleaved surfaces were recorded and compared to that of freshly cleaved vitreous silica (Figure 8-19). The shift directions of the S, NSX and R peaks for each glass (indicated by dashed arrows in Figure 8-19) were seen to relate to the molar quantities of the species concerned, decreasing S and R peak wavenumbers correlating with falling SiO_2 content and decreasing NSX peak positions agreeing with increasing RO + R_2O content. Calibration lines for S, R and NSX peak shifts are shown in Figure 8-20. They were extrapolated for B1, B2 and B3 from plots of each peak wavenumber against molar contents of SiO_2 and RO+R_2O species with R^2 correlation coefficients of 0.96 or higher. The total molar RO+R_2O content was calculated by simple addition of individual molar oxide quantities. The 'SiO_2' total included only the original molar SiO_2 content of the glass, as it is unclear from the

literature how the presence of other network forming species (P^{5+}) and intermediate ions such as Al^{3+} or Fe^{3+} that affect the glass bonding structure is reflected in IR spectra (these constituents often constitute part of the 'silica' totals for compositional calculations in glasses where they are deemed to act principally as network formers). This is in part because experimental IR studies on glass corrosion have often made use of simple glasses of a binary or ternary nature. As the adjusted totals for SiO_2* which included molar Fe_2O_3, Al_2O_3 and P_2O_5 contents, gave an almost identical fit for the S peak ($R^2 = 0.9606$), suggesting that these components bear little influence on the nature of S peak variation, it was decided to discard these oxides for the purpose of spectral interpretation. Molar concentrations of SiO_2 and $RO+R_2O$ species of unaltered B1, B2 and B3 glasses calculated from the calibration lines are given in red and total molar contents are highlighted in blue in Table 8-2.

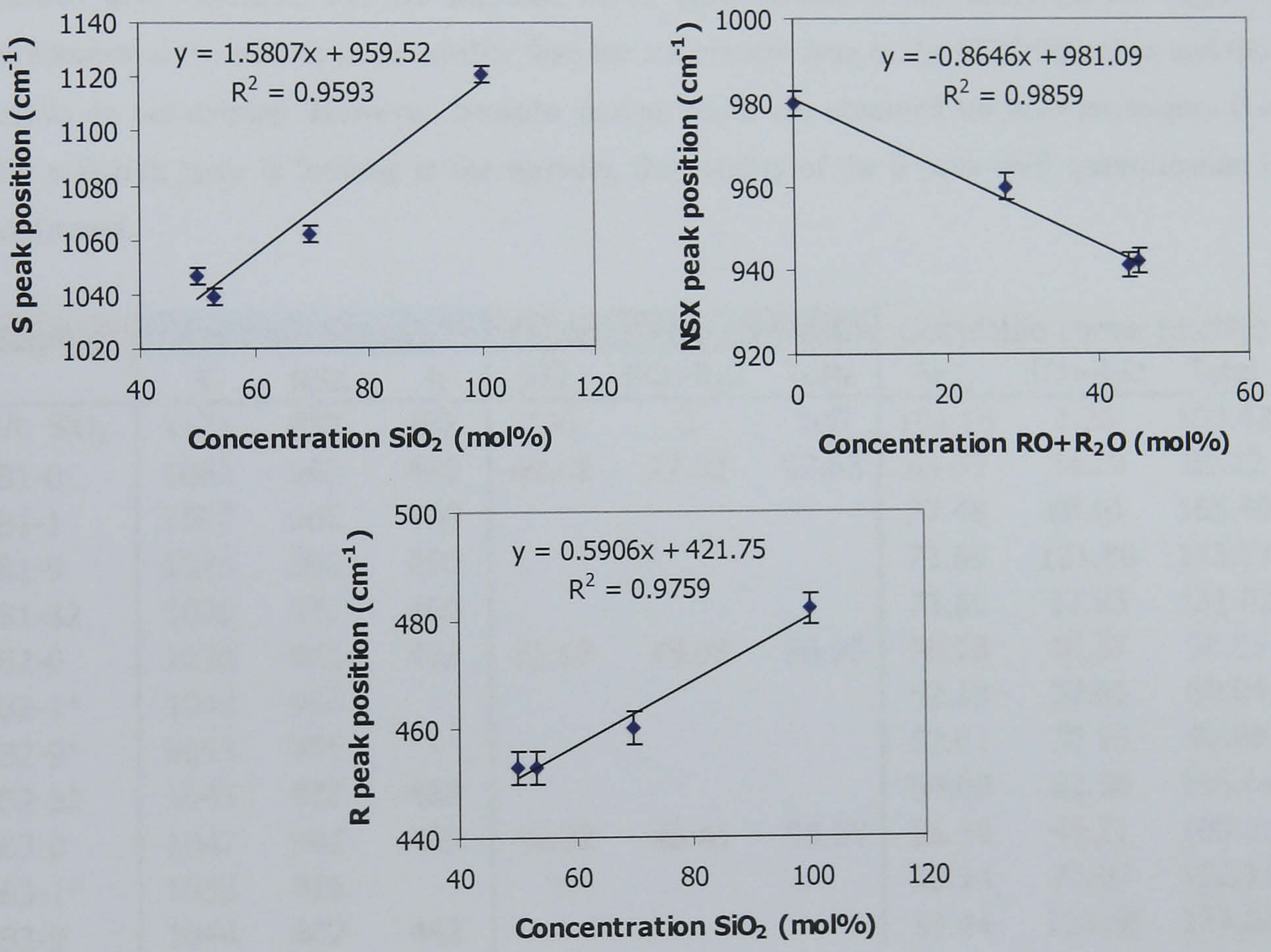


Figure 8-20: IR peak shift calibration curves plotted using three Ballidon glass compositions, as measured by EDXA, and vitreous silica for S peak or Si-O-Si stretching curve (a); NSX peak or Si-O-X stretching curve (b); R peak or Si-O rocking curve (c).

Results for unreacted surfaces are within a few percent of reported molar compositions with totals of SiO_2 and $RO+R_2O$ contents correlating well with the published Ballidon compositions. The linear dependence of peak shifts is maintained in this case irrespective of RO or R_2O cation type and suggests that, from a structural point of view at least, the different cations are equivalent as they form a bond with silica that vibrates in the same way.

8.2.2.2 Interpretation and comparison with EDXA

The corresponding compositional shifts, as determined by the calibration procedure outlined above, are given in the right-hand columns of Table 8-2 and compared to corresponding molar concentrations as determined by EDXA for B1, B2 and B3 in Figures 8-21 to 8-23. Quantification of the R peak shift was not attempted because of problems in determining the R peak location for B2 and B3. Some positive and negative points of note are to be drawn from the results.

In B1 the SiO_2 content is seen to rise and stabilise at the surface to 73.7 mol% in good agreement with EDXA data. SiO_2 results obtained by EDX and IRRS for B1 overlap with each other within experimental error and underline the validity of multi-technique evaluation of leached glass surfaces. For B2 and B3, where crust formation has occurred, the slight Si enrichment at the surface is far smaller than the enrichment seen in the EDX linescans, and thus results do not overlap. However, because similar trends are observed for both techniques (i.e. that a Si-rich layer is forming at the surface), the validity of the S peak shift quantification is confirmed.

Sample	Peak positions (cm^{-1})			Reported comp. (mol%)			Calculated comp. (mol%)		
	S	NSX	R	SiO_2	$RO+R_2O$	Total	SiO_2	$RO+R_2O$	Total
Vt. SiO_2	1121	980	482	100	0	100	102.16	1.26	103.42
B1-0	1062	960	460	69.82	27.83	97.65	64.83	24.39	89.22
B1-1	1082	905	460				77.48	88.01	165.49
B1-9	1076	893	460				73.69	101.89	175.57
B1-32	1076	931	460				73.69	57.93	131.62
B2-0	1039	941	453	52.97	43.98	96.95	50.28	46.37	96.65
B2-1*	1042	957	-				52.18	27.86	80.04
B2-9*	1043	955	-				52.81	30.18	82.99
B2-32	1045	927	450				54.08	62.56	116.64
B3-0	1047	942	453	49.82	45.41	95.23	55.34	45.21	100.55
B3-1*	1053	918	-				59.14	72.97	132.11
B3-9	1044	887	462				53.44	118.58	172.03

Table 8-2: peak maxima for Ballidon IR spectra, with reported and corresponding calculated molar oxide concentrations after calibration.* denotes soil contamination.

Problems in interpretation arise however when the NSX peak is quantified for the corroded specimens; several values for the NSX peak maximum for corroded B1 and B3 glasses lie at such lower wavenumbers than for their unreacted counterparts that the extrapolated data gives $RO+R_2O$ contents in the range of 75-118%, which when summed to the 50-75mol% SiO_2 content extrapolated from the S peak shifts produce unacceptable molar totals far above 100%. More significantly, the calculated compositional NSX peak shift data predicts a major surface enrichment in RO and R_2O species for B1 and B3, in stark contrast to the leaching process

identified from the EDXA results. The NSX calibration cannot therefore be considered valid for the glasses in question, even though the molar $RO+R_2O$ compositional results for B2 agree well with respective EDXA data.

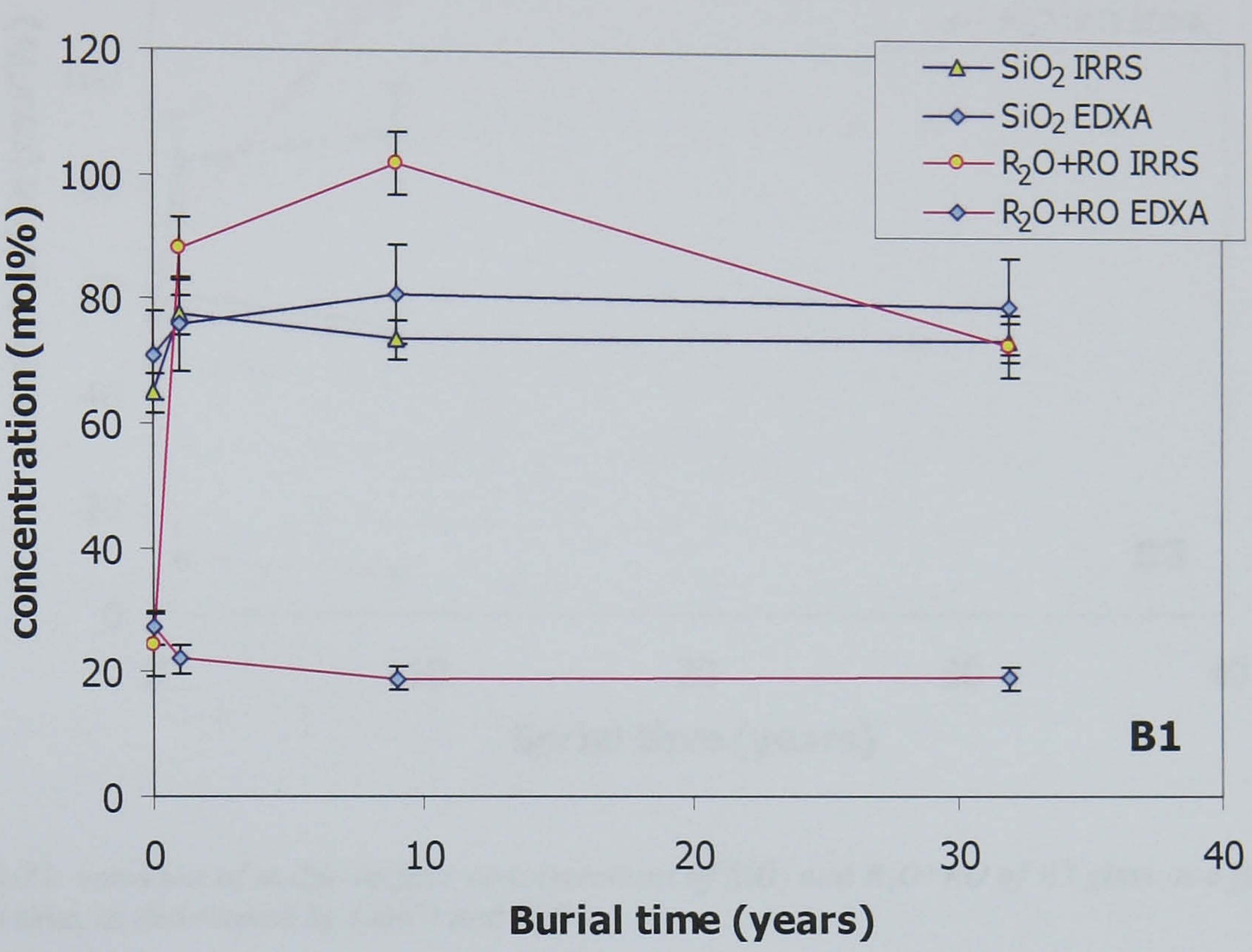


Figure 8-21: variation of molar surface concentrations of SiO_2 and R_2O+RO of B1 glass as a function of burial time, as determined by EDXA and IRRS.

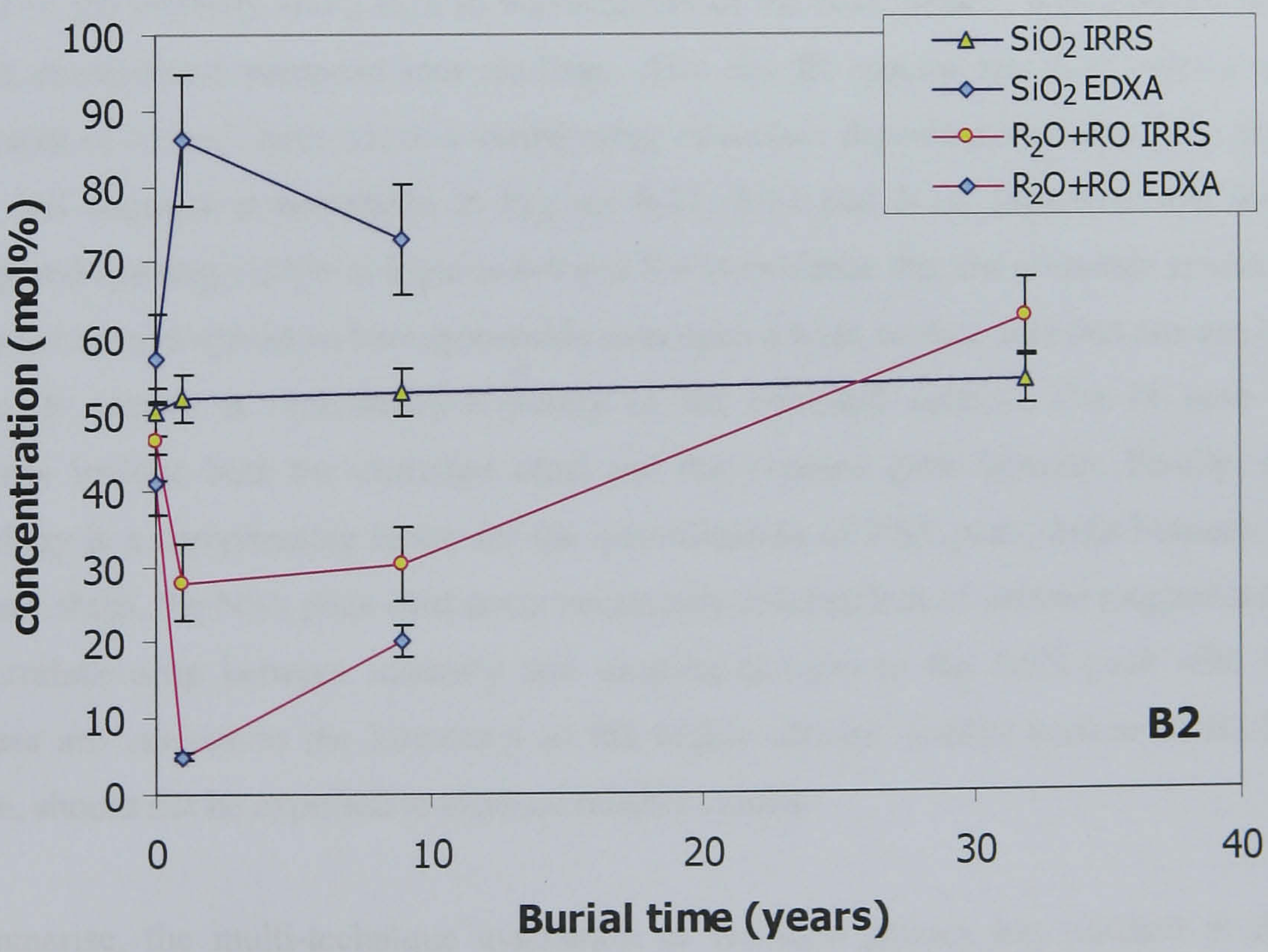


Figure 8-22: variation of molar surface concentrations of SiO_2 and R_2O+RO of B2 glass as a function of burial time, as determined by EDXA and IRRS.

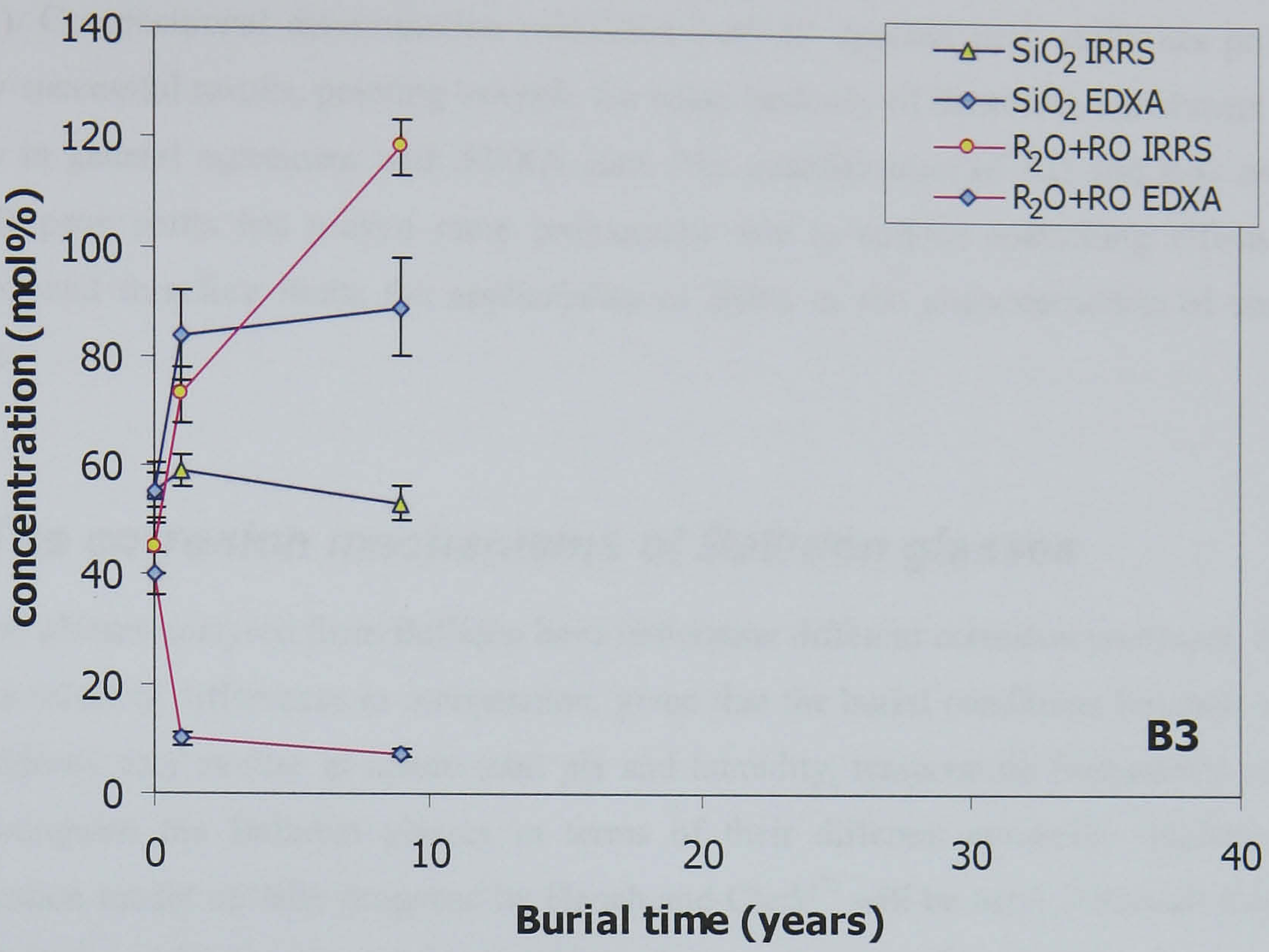


Figure 8-23: variation of molar surface concentrations of SiO_2 and R_2O+RO of B3 glass as a function of burial time, as determined by EDXA and IRRS.

Possible reasons for this are outlined here. Exchange of H^+ ions from water or water vapour with R^+ or R^{2+} ions from the glass, as is the case for corroded Ballidon glasses, results in a decrease in the intensity and a shift in wavenumber of the NSX peak[6], which would interfere with the extrapolated compositional readings. Also the IR spectra are taken over a sample surface area of >1mm^2, over which a varied range of surface deposits are present. The extent of surface soil deposits is noticeable in Figures 8-11, 8-12 and 8-14. Moreover, the localised cracking and spalling visible in Figures 8-6 and 8-8 is evidence that the corrosion products that form do not remain spread so homogeneously over such a wide surface area that one can be sure that the IR spectra is representative purely of the corroded surface. The IR scan would necessarily include both the corroded crust and the exposed glass beneath. Finally, surface morphology is a complicating factor for the quantification of NSX peak shifts because, unlike the S peak shifts, the NSX peak shift is not necessarily independent of surface roughness (in fact the interrelationship between intensity and location changes in the NSX peak with surface roughness are unclear in the literature) so the highly altered, spalled surface of B2-32, for example, should not be expected to produce reliable results.

To summarise, the multi-technique evaluation of Ballidon glasses has resulted in detailed characterisation of corroded glass surfaces. Comparative EDXA and IRRS data has allowed the principal corrosion mechanisms at work in each composition to be established, both in the outer

0.5μm of the surface (IRRS) and through the corroded profile viewed in polished cross-section (EDXA). Compositional determination calculated from IR spectral peak shifts has produced partially successful results, pointing towards the same tendency of Si surface enrichment on all samples in general agreement with EDXA data. The quantification of RO and R_2O contents using IR peak shifts has proven more problematic due to surface coarsening effects upon corrosion and therefore limits the applicability of IRRS in the characterisation of corroded surfaces.

8.3 The corrosion mechanisms of Ballidon glasses

The three glasses analysed from Ballidon have undergone different corrosion processes, that are largely a result of differences in composition, given that the burial conditions for each have to be considered very similar in nature (soil pH and humidity, temperature fluctuations etc). To help distinguish the Ballidon glasses in terms of their different corrosion mechanisms, a classification model initially proposed by Hench and Clark[7] will be used. Although published in 1978, their model is still widely applied to glass studies in order to differentiate between corroded silicate glass surface types. They distinguished six* characteristic types of silicate glass surfaces categorised in terms of SiO_2 profiles across the surface that could be related to different corrosion mechanisms. The six surface types are shown in Figure 8-24 and explained below.

1) A Type I has undergone a thin, less than 50Å, surface layer hydration. As no significant compositional change by either loss of alkali or silica network dissolution has occurred, the surface composition is almost identical to the bulk composition. Vitreous silica is an example of a Type I surface, which indicates the most durable types of glass exposed to solution with neutral pH. It is highly unlikely that there are any ancient glasses with a Type I surface.
2) A Type II surface possesses a silica-rich protective film due to selective alkali-ion removal without any damage to the silica network. Dealkalisation of glasses that have low concentrations of alkali results in a Type II surface. A glass with this type of surface is reasonably durable, particularly when the solution pH remains below 9.
3) Type III glass surfaces form protective films that can render them very durable in all solution types. Type IIIA can be produced by adding Al_2O_3 or P_2O_5 to a glass composition, which causes the formation of dual protective surface layers such as alumino-silicate or calcium-phosphate species on top of a silica-rich layer. Type IIIB is characterised by the formation of multiple protective layers composed of oxides,

* In the first publication only five surface types were distinguished. A revised model including type IIIB was published the following year in 1979[8].

hydroxides and hydrated silicates (although they are only detected on modern nuclear waste glasses and not ancient compositions). These protective films can be produced by dealkalisation or precipitation from solution.

4) Type IV glasses also have a silica-rich film. However, the silica concentration is insufficient to protect the glass from rapid attack by dealkalisation or network dissolution. Silicate glasses that are low in silica tend to have Type IV surfaces.
5) Type V surfaces are found in glasses where congruent dissolution is accompanied by nearly equal loss of alkali and silica, in other words where the glass is soluble in the leaching solution. Because of the uniform attack, the surface composition of Type V glass is equivalent to the bulk composition. Silicate glasses exposed to conditions with pH>9-10 tend towards Type V behaviour, hence surfaces of this type tend to favour pit formation as local concentration of alkali causes pH values to rise in excess of 9-10. As a result they are very susceptible to scratching and abrasion.

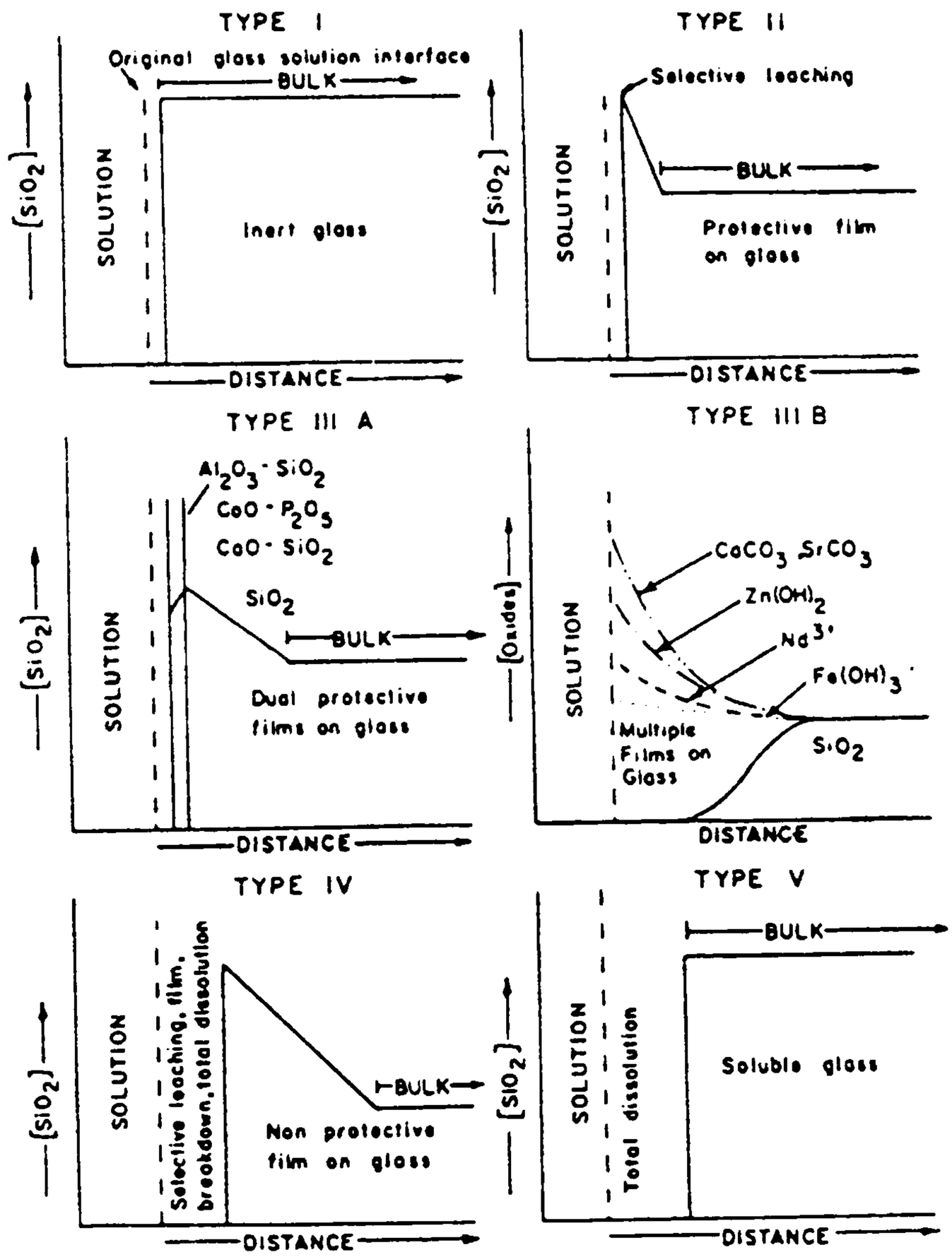


Figure 8-24: six types of corroded glass surface defined by Hench and Clark[8].

B1 is predicted to be the most thermodynamically stable of the three glasses analysed because of its 69.8mol% SiO_2 content. The number of Si-O-Si bonds in the structure prevents the glass network dissolving rapidly, even once complete leaching has taken place. A Type II surface is produced and maintained on B1 as selective leaching of Na is the main reaction occurring. It is unclear whether the fully leached surface in B1-9 and B1-32 is a result of silica-rich compounds reprecipitated from solution or whether it simply represents the hydrated remainder of the original structure after all the leachable constituents have been lost into solution. Whichever the case, the calcium-silicate skin that is formed at the fully leached surface acts as a protective layer to slow the rate of dissolution, whereas ion exchange continues unhindered into the glass. This conclusion concurs firstly with Newton's observations[9] that many Roman glasses exhibit a Type II surface and secondly with Cox and Pollard's findings[10] that at least 0.5mm of surface need to be removed from Roman glasses in order to obtain satisfactory quantitative bulk data, due to the extended Na leaching profile they observed. That a 0.3-0.4mm Na leaching profile was established on a Roman type glass after only 32 years of burial at Ballidon suggests that the alkaline burial conditions there favour relatively rapid alkali exchange, possibly favoured by the completion of leaching at the surface, which may have allowed a far greater quantity of water to penetrate into the structure than before.

B2 and B3 have much lower SiO_2 contents (52.97 and 49.82mol% respectively) than B1 and are thus predicted to be much less stable than B1. It is widely known that medieval KLS glasses are poorly durable and the often-severe decay of medieval stained glass church windows, to name an example, is a thriving area of international research[11]. Both B2 and B3 have formed crusts according to a Type IV surface formation; surface silica enrichment is not enough to prevent total dissolution of the network and reprecipitation of an alumino-ferro-silicate complex. The corrosion behaviour of both compositions also borders on Type V, as alkali extraction and network dissolution are seen to propagate together, leaving only a 2μm thick reaction zone between unaltered glass and fully dissolved crust. The main distinguishing feature between B2 and B3 is that the crust formation has halted in B2 in favour of compositional banding within the crust and localised pitting, whereas the B3 crust has continued to increase with increasing burial time. The P_2O_5 component in B3 may have prevented initial alkali loss during the first year of burial but it has leached out with the other mobile species after 9 years and does not help to form a protective coating.

As all three glasses are compositionally of a mixed alkali nature, the corrosion behaviour is further complicated by the interaction of Na^+ and K^+ ions during the leaching process. This and other observations on Ballidon glasses will be discussed in greater depth once corroded glasses from Raqqa have been presented.

8.4 Bibliography

1. Newton, R.G., *A Summary of the Progress of the Ballidon Glass Burial Experiment.* Glass Technology, 1981. **22**(1): p. 42-45.

2. Newton, R.G., *The Ballidon Glass Burial Experiment.* Glass Technology, 1985. **26**(6): p. 293.

3. Dilmore, M.F., D.E. Clark, and L.L. Hench, *Corrosion Behavior of Lithia Disilicate Glass in Aqueous Solutions of Aluminum Compounds.* Ceramic Bulletin, 1979. **58**(11): p. 1111-1118.

4. Clark, D.E., et al., *Quantitative Analysis of Corroded Glass Using Infrared Frequency Shifts.* Glass Technology, 1977. **18**(4): p. 121-124.

5. Sanders, D.M., W.B. Person, and L.L. Hench, *Quantitative Analysis of Glass Structure with the Use of Infrared Reflection Spectra.* Applied Spectrscopy, 1974. **28**(3): p. 247-255.

6. Hench, L.L., R.G. Newton, and S. Bernstein, *Use of Infrared Reflection Spectroscopy in Analysis of Durability of Medieval Glasses, with Some Comments on Conservation Procedures.* Glass Technology, 1979. **20**(4): p. 144-148.

7. Hench, L.L. and D.E. Clark, *Physical Chemistry of Glass Surfaces.* Journal of Non-Crystalline Solids, 1978. **28**: p. 83-105.

8. Clark, D.E., C.G. Pantano, and L.L. Hench, *Corrosion of Glass*. 1979, New York: Books for Industry and The Glass Industry.

9. Newton, R.G. and S. Davison, *Conservation of glass*. 1989, London: Butterworth-Heinemann.

10. Cox, A. and A.M. Pollard, *X-Ray Fluorescence Analysis of Ancient Glass: the Importance of Sample Preparation.* Archaeometry, 1977. **19**: p. 45-54.

11. Bernardi, A. and F. Becherini, *Vidrio Project: a New Approach to the Study of Ancient Stained Glass Window Deterioration.* Rivista della Stazione Sperimentale del Vetro, 2002. **32**(4): p. 28-39.

Chapter 9

The corrosion of buried glasses

Part 2: Raqqa

In contrast to the three Ballidon glass types discussed in Chapter 8, the corrosion morphologies presented by excavated glasses from Raqqa are distinctly more complex. This complexity first of all reflects over 1000 years of burial, time enough for geochemical processes to reach stable conditions, and secondly the more complex compositions of these ancient glasses with respect to the modern replicas buried at Ballidon. The study nonetheless poses an excellent opportunity to establish the role of minor fluctuations in composition on corrosion evolved over much longer burial times and, through the use of high-resolution imaging techniques, to provide a plausible explanation for the regularly spaced lamellar crusts frequently observed in archaeological glasses.

Corroded Raqqa glasses were characterised using optical microscopy, FE-SEM with EDX, SIM and FIB-SIMS. IRRS was not attempted given the advanced stages of specimen decay and for reasons discussed in Section 8.2.2.2.

9.1 Corrosion vs. compositional type

In the immediate post excavation phase it had been observed that glasses exhibited varying degrees of corrosion, ranging from seemingly unaltered surfaces and thin surface laminae to thick opalescent crusts. Once it emerged that the state of glass corrosion could be broadly related to compositional type, representative samples of types 3, 2 and 1 were chosen for further analysis. It was felt that no composition was truly 'representative' of type 4 due to the chemical variation observed within this group, and thus, for comparative purposes, no samples were selected from this compositional type.

It has been argued in previous sections that, with the use of a variety of compositional types from a variety of raw ingredients, noticeable performance-related differences would have been observed during glassmaking processes at Raqqa, reflecting most importantly melting temperatures and workable viscosity ranges. The typological distinction of compositional

groups carries forward to corrosion related phenomena; on the four samples analysed in detail a wide array of morphological features was observed, which correlated to observed compositional groups.

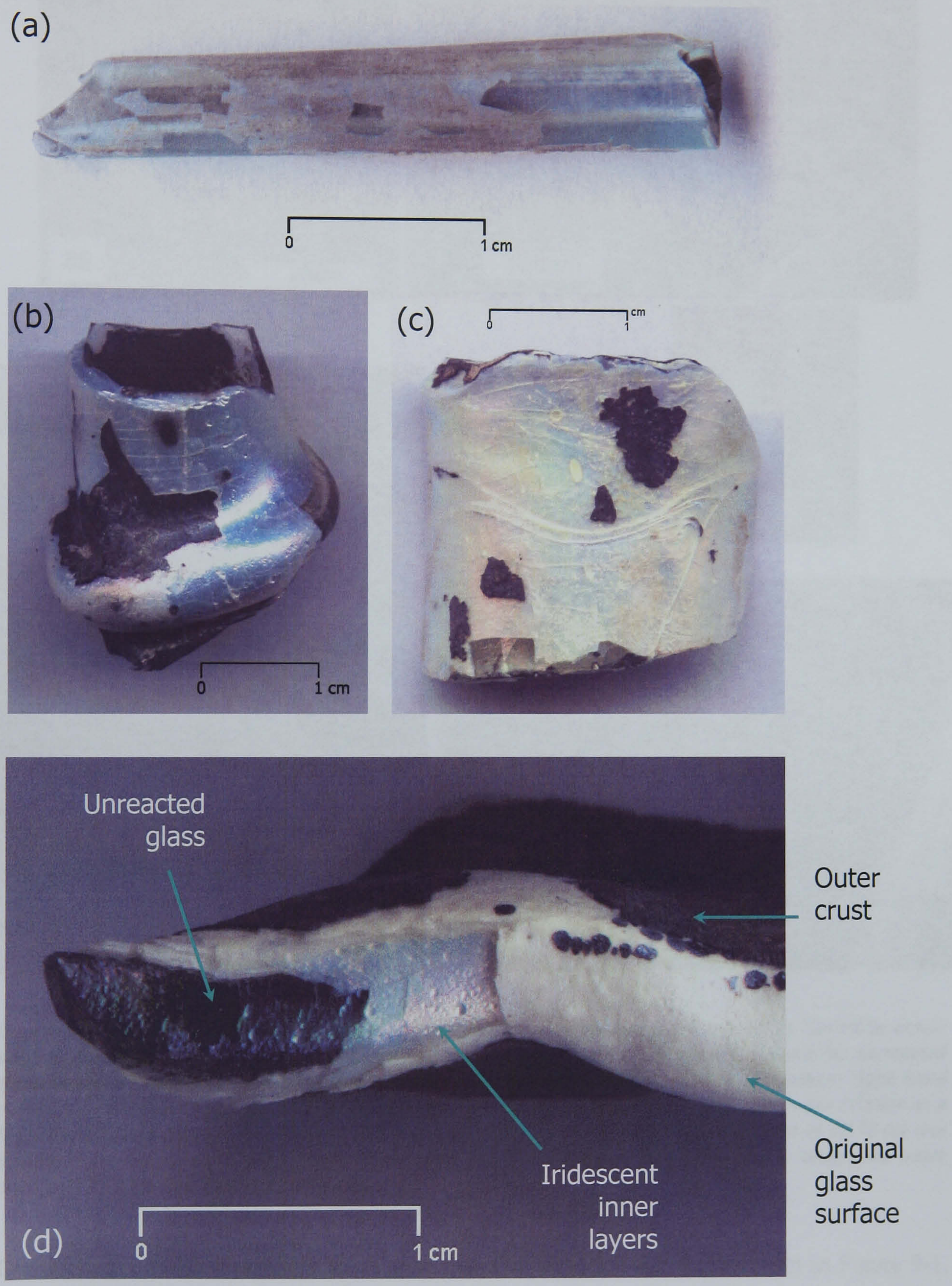


Figure 9-1: the variety of degree of corrosion visible on the surfaces of Raqqa samples. (a) LMG type 3 TZ85 showed some surface opacity and a thin white film; (b) HMG type 1 TZ76 presented a dark crust above a thick iridescent white skin; (c) type 2 TZ79 showed a dark outer crust over an opalescent white skin; (d) HMG type 1 TZ78 also presented a dark crust above a thick iridescent white skin. As the crust was removed, an iridescent pitted skin was seen to adhere to the glass beneath.

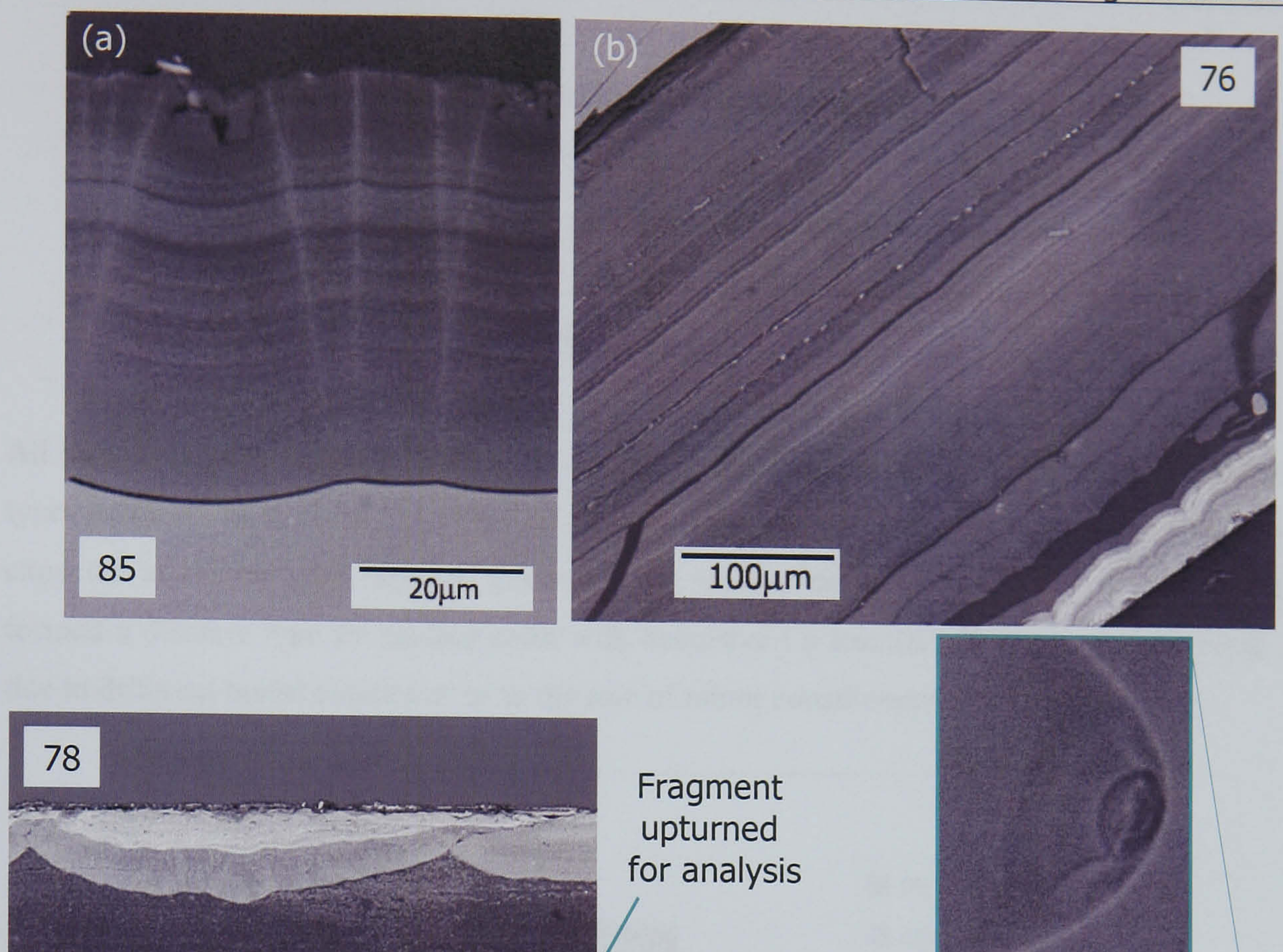


Figure 9-2: backscattered electron images of corrosion crusts on four Raqqa samples viewed in cross-section. Crusts (a) and (c) are viewed with the outer edge uppermost in the image and the unreacted glass beneath. Crusts (b) and (d) are rotated so that the outer edge appears in the bottom right hand corner and the glass top left. TZ85 (a) is the only sample not to exhibit Mn-rich outer edge (visible as a brightly banded layer at the outer extremity of each crust). The top portion of the crust of TZ78 (c) was upturned for microscopic inspection. Nucleation points of internal plugs are visible under the outer crust of TZ79 (d) and are magnified (inset).

Corroded specimens representative of compositional types 1,2 and 3 are shown in Figure 9-1. Type 3 LMG samples were either largely uncorroded or exhibited a thin, pale surface patina. Type 1 and type 2 HMG specimens were covered with a brightly iridescent thick skin that on the outside edge showed a dark opaque crust. This reaction product was readily removed with a scalpel to reveal the following macroscopic features (visible in Figure 9-1d):

- A dark opaque outer crust on the outermost surface
- A smooth thick white crust underneath
- A finely pitted iridescent crust below the surface
- A finely cracked and pitted iridescent crust near the reaction front
- The unreacted glass surface beneath

All samples analysed showed a type IV or type V corrosion behaviour, according to the surface types outlined in Section 8.3. This is curious particularly for the type 3 LMG, which was expected to exhibit a Na depleted gradient zone, in accordance with a type II surface, but had formed a discrete type IV surface crust with extensive Ca loss (see Table 9-1). This could be due to different burial conditions or to the role of minor constituents in the composition.

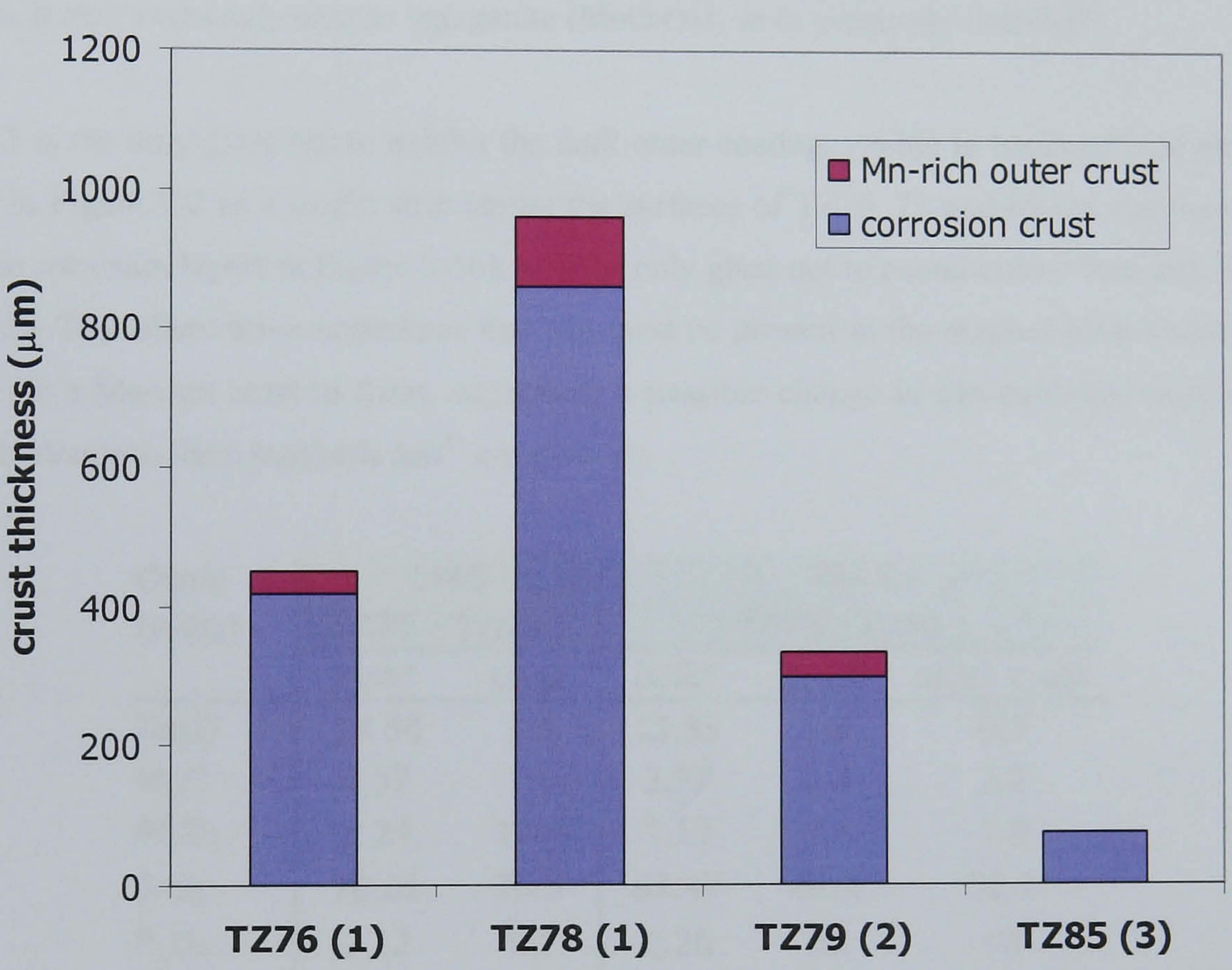


Figure 9-3: comparative graph of average crust thickness (with sample type in brackets) for four corroded Raqqa glasses.

Backscattered electron images of corrosion crusts in cross-section are shown in Figure 9-2 for four samples, along with a comparative graph of average crust thickness in Figure 9-3. Macroscopically, crust characteristics relate to compositional type. The slower rate of decay for the type 3 glass is clear; the corrosion crust on TZ85 is at most only 75μm thick, a fraction of the values for the other crusts, which reach over 1mm in thickness. Even though corrosion rates are susceptible to sample size (expressed as exposed surface area to solution volume, SA/V), sample shape and individual burial history[1], and thus corrosion crust thickness cannot

constitute a strictly accurate means of comparison in the case of Raqqa glasses, results nevertheless point to decreasing chemical durability from type 3 through type 2 to type 1. A distinction in chemical durability between the Raqqa compositional types will become more evident in Section 9-7.

As mentioned in Section 2.7.3.4, Mn infiltrations are a reason for irregularities in the weathering crusts observed in buried glasses. A dark outer crust is often found in corroded specimens[2]. Newton and Davison[3] state that the phenomenon of darkening or browning is the result of the formation in the glass surface of compounds of Mn. The polyvalent nature of Mn is well documented and explains why the element forms such significant deposits at the surface. Manganese deposits at the surface result through the oxidation of MnO to form hausmannite (Mn_3O_4) with the production of a superficial brown or black layer of complex manganese oxides. It may eventually alter to manganite ($MnO{\cdot}OH$) or to pyrolusite (MnO_2)[4].

Type 3 is the only glass not to exhibit the dark outer coating, visible in backscattered electron mode in Figure 9-2 as a bright strip across the surfaces of TZ76, 78 and 85 (cf. the outermost surface corrosion layers in Figure 2-16), and the only glass not to contain more than trace levels of MnO. This observation underlines that Mn must be present in the original glass structure in order for a Mn-rich crust to form, suggesting a possible change in Mn oxidation state as the glass hydrates to form insoluble Mn^{3+} compounds.

Oxide (wt%)	**LMG TZ85 - type 3**		**HMG TZ78 - type 1**		
	bulk*	crust	bulk*	crust	outer crust
Na_2O	14.54	1.6	13.55	1.8	0.7
MgO	0.57	1.1	3.57	0.3	2.2
Al_2O_3	3.24	12.4	1.12	4.7	1.9
SiO_2	70.01	76.5	67.47	81.3	36.1
P_2O_5	0.12	nd	0.26	nd	nd
Cl	0.11	0.3	0.12	1.8	2.1
SO_3	0.83	nd	0.96	3.4	1.1
K_2O	0.52	5.2	2.51	1.6	2.7
CaO	9.49	2.5	8.23	2.8	3.8
TiO_2	0.05	nd	0.06	nd	0.9
Fe_2O_3	0.37	0.4	0.34	1.2	1.3
MnO	nd	nd	1.62	1.1	47.2
Total	99.85	100.0	99.81	100.0	100.0

Table 9-1: average compositions of unaltered and corroded regions of typical LMG and HMG samples from Raqqa. Data for corroded areas is normalised EDXA. * denotes EPMA.

XRD analysis conducted on crust fragments from TZ78 and TZ79 revealed no peaks and thus no discernible crystal phases. The crusts possess a completely amorphous structure. EDXA data of corrosion crusts is given in Table 9-1 for LMG type 3 (TZ85) and HMG type 1 (TZ78) samples, along with unaltered compositions as established by EPMA. Both crusts are significantly depleted in the main modifier, Na_2O, and the stabiliser CaO and are enriched in SiO_2, Al_2O_3 and Fe_2O_3. However, the nature of the crust is distinct for the two types and reflects compositional differences; the HMG crust is clearly lamellar in structure, highly porous and presents an outer surface significantly enriched in Mn (47.2wt% MnO).

The LMG crust has none of these features (although compositional banding is visible in Figure 9-2a, the crust has a continuous structure and no separate layers could be identified), is enriched in K_2O and MgO and exhibits what appear to be channels flowing from the dissolution front to the outer surface. These channels were found to be rich in SiO_2 so appear to aid the transport of dissolved species away from the reaction zone through the crust, which is otherwise only slightly enriched in SiO_2 compared to its HMG counterpart in favour of Al_2O_3. This, and the enrichment of K_2O in the LMG crust, would suggest that the crust itself is not the fully dissolved and reprecipitated porous product of congruent dissolution but the skeletal remains of a partially dissolved glass network depleted in Na and modifiers. The fact that larger K^+ ions have failed to diffuse through this structure would suggest that ionic movement through the crust is very limited. If the crust is indeed porous in nature, the pore size must be so small that the migration of K^+ and Mg^{2+} ions is hindered. This would help to slow the ion exchange reaction rate and would explain why an expected type II surface behaviour is not seen in this typical Roman composition. Slow transport rates from the reaction zone would favour a type IV mechanism with selective leaching and partial dissolution occurring at the reaction front.

Sample ID	Sample Type	Avg crust thickness (μm)	Single layer thickness (μm)	Number of layers
76	1	460	0.7±0.15	430±10
78	1	940	0.75±0.15	950±20
79	2	300	0.6±0.1	420±35
85	3	65	-	-

Table 9-2: average crust thickness, individual layer thickness and number of layers in the crust of the four Raqqa samples inspected.

Results of average crust thickness, layer thickness and number of layers are given in Table 9-2 for the four crusted samples. TZ76 and TZ78 are almost identical in composition, yet they exhibit very differing extents of lamellar formation. Over 950 layers were counted in the crust of TZ78, over twice the number counted in TZ76 and, unless both the internal and external

surfaces of the circular profile of TZ76 are taken cumulatively into account, there is no plausible explanation for this discrepancy other than the significant contribution that sample size and shape play in surface degradation. Surface area to solution volume (SA/V) ratios, however, are not influential in a natural groundwater environment because, when in permanent contact with aqueous solution in the soil, SA/V is assumed to be $\rightarrow 0$. The importance of sample shape would help in clarifying the low number of layers (420±35) observed in TZ79: this sample also sports a round profile and therefore exhibits corrosion in its inner and outer surfaces.

9.2 Growth irregularities

The majority of the surfaces inspected showed regular crust formation that consisted of a regular lamellar pattern spreading inwards from the original glass surface in HMG and a banded crust in LMG. However, different sample characteristics led to a wide array of irregular forms of corrosion, making accurate calculation of corrosion rates problematic.

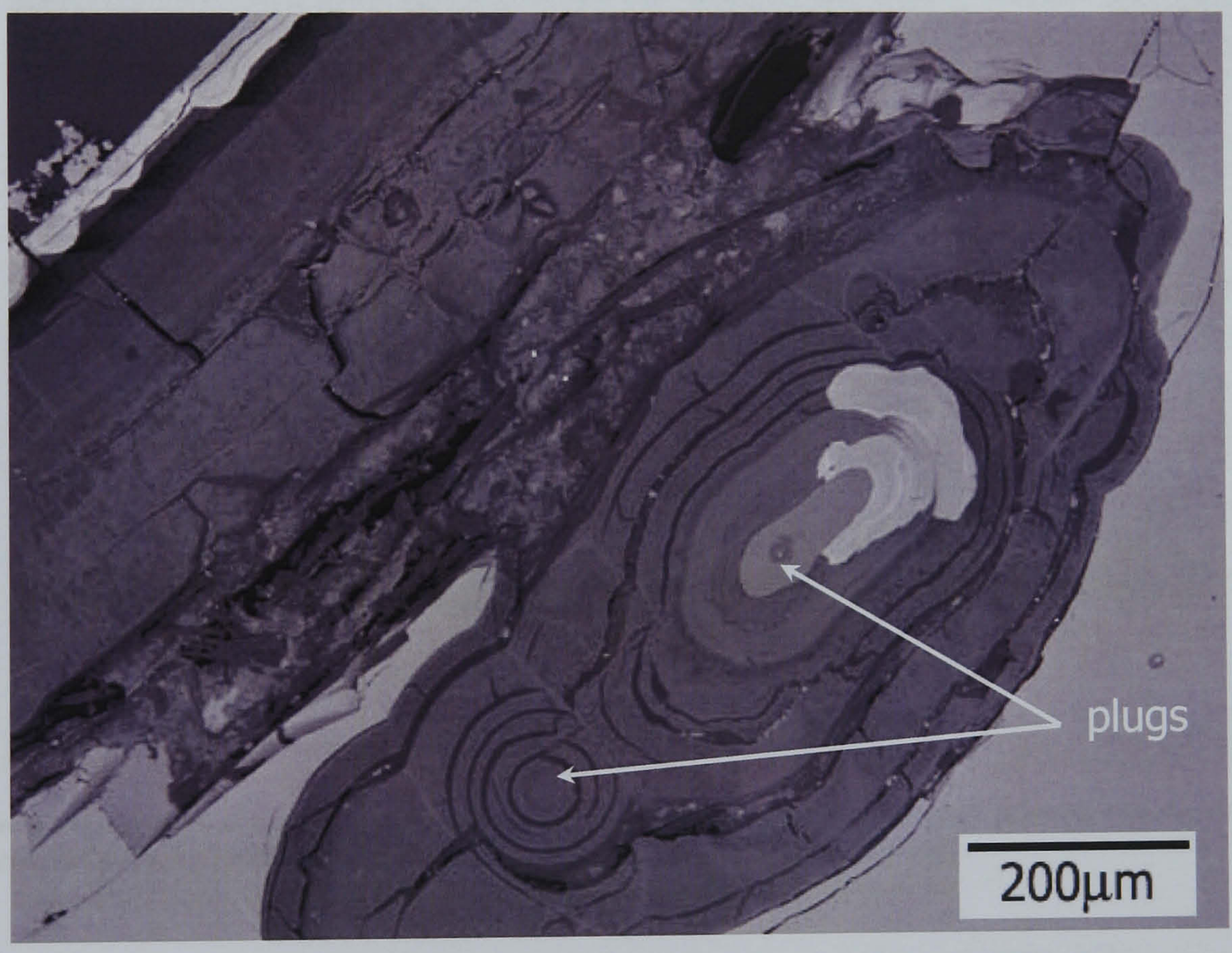


Figure 9-4: backscattered electron image showing internal plug formation in TZ79. The centre of the plug growth is now infiltrated with Mn compounds. Corrosion has irradiated outwards away from the plug centre.

It must be pointed out here for the sake of clarity how the term 'growth' can describe the progressive dissolution and condensation of silicate species at increasing distances into the glass from the surface. Lamellar corrosion is actually forming or 'growing' inwards as the reaction propagates deeper into the glass structure. Given the widespread use of the term 'growth' in the

literature in reference to layered corrosion processes, it is used here to indicate the inward evolution or development of corrosion with time.

9.2.1 Plugs

Plugs are inhomogeneities in the glass structure that act as nucleating centres for corrosion[5]. Initial growth stems from irregularities at the surface and proceeds inwards in a periodic manner. However, when the irregularities are located inside the glass they interfere with regular formation[6]. A vivid example of a plug in TZ79 is presented in Figure 9-4. Underneath the regular crust on the outer surface a separate growth has irradiated from two centres, one of which is immediately surrounded by Mn-rich material. The plug has presumably formed after Mn-rich solutions infiltrated down cracks that opened in the strained structure. The cracks can be seen propagating away from the outer edges of the plug growth in Figure 9-4.

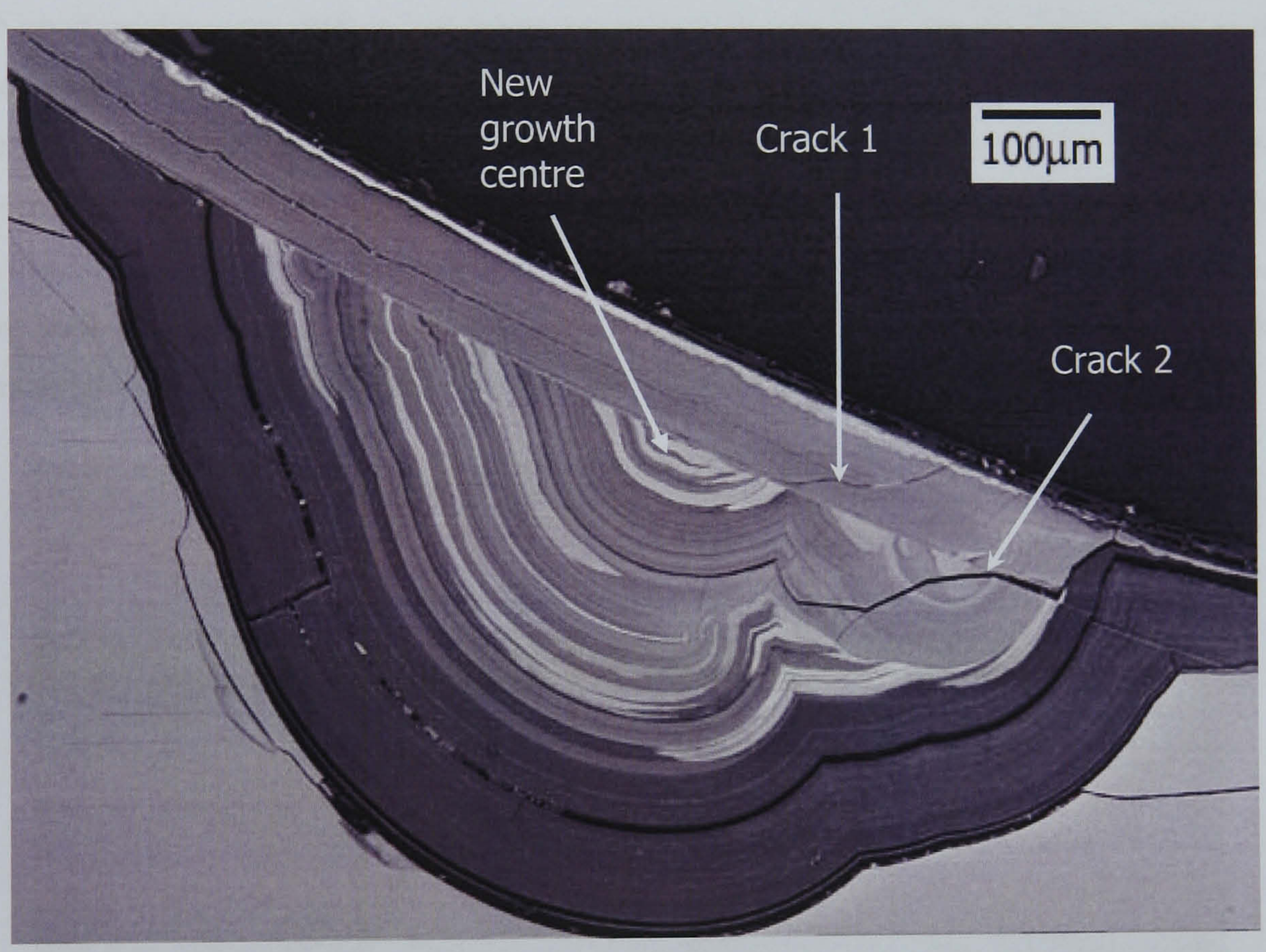


Figure 9-5: backscattered electron image of corrosion on TZ76. The appealing formation is due to two cracks and successive Mn infiltration. Crack 1 formed previous to the second.

A rather more spectacular example has formed on the inner surface of TZ76 and is shown in Figure 9-5. A crack forming in the regular outer layers (Crack 1 in Figure 9-5) would have allowed Mn infiltration and the birth of a new corrosion centre underneath the layers. A second crack (Crack 2) must have occurred at a later stage as it runs along the line formed by successive layers of growth from the plug centre and presumably allowed the Mn-rich deposits to form deeper inside the glass. Crack 2 also separates the plug growth on the right hand side from a compositionally distinct layered growth, which presumably formed at a subsequent stage around its edge. It is not clear why there is no Mn present in these innermost layers and why

crystals have precipitated within a third crack spanning along the darker formation. Nevertheless, the study of plug formation allows part of the corrosion history of the sample to be understood and raises the question as to why a glass would crack under burial conditions.

9.2.2 The effect of residual stresses

The answer may be found when the production history of the samples is considered. The melted goblet stem (TZ76) and the glass moil (TZ 79) both have rounded profiles and when cross-sectioned revealed different corrosion morphologies on the inner and outer crusts in backscattered electron mode. A section of TZ79 in backscattered electron mode in Figure 9-6 shows both crusted surfaces. The inner crust shows highly irregular growth irradiating from plugs under the surface whereas the outer crust follows a much more regular pattern (the Mn-rich crust on the outer surface had fallen away from this area). Again, the bright areas in the inner crust plugs are Mn-rich and have formed around cracks entering the corrosion crust. The fact that cracks are spontaneously occurring only on the inside of the piece indicates the presence of residual compressive stresses in the glass structure that would be concentrated on the inner surface. As alkali depletion and hydration cause local shrinkage, further stresses would have been introduced into the structure until it failed locally and allowed cracks to propagate from stress centres at the surface.

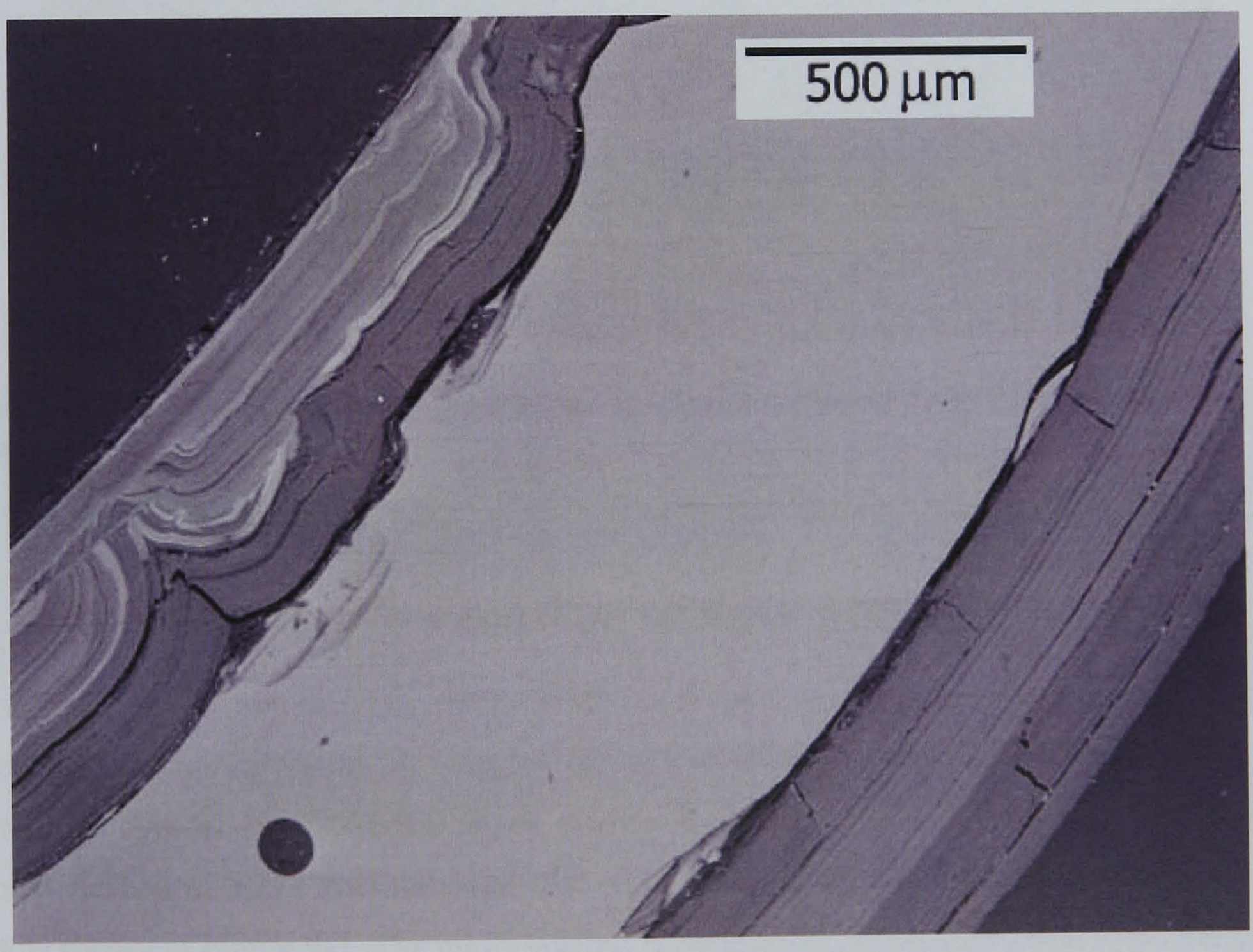


Figure 9-6: backscattered electron image of inner (left) and outer (right) crusts of TZ79. If both surfaces are taken into account, the overall number of layers approximates that of TZ78.

Alts and Strehlow[7] report experimental observations of frozen stresses in sodium-silicate glasses in cases where the cooling rate has not allowed for complete network rearrangement to

an equilibrium structure. The evolution of corrosion structures thus can yield clues as to the cooling regime that archaeological glasses have been subject to; neither TZ76 nor TZ79 would have been annealed because of the residual stresses exhibited through the corrosion morphology. A melted stem and a glass moil would in fact have presumably been discarded as production waste and thus are expected to have cooled rapidly, in air or by quenching. The only sample that showed no irregular cracking or plug growth was the melted lump (TZ78). Presumably then the piece was either annealed or allowed to cool in a furnace as part of disused batch residue. This is reflected in the regularity of lamellar corrosion over the entire surface. As TZ78 showed such regular layered formation, it was selected as the glass best suited for further investigation and for the examination of individual corrosion layers.

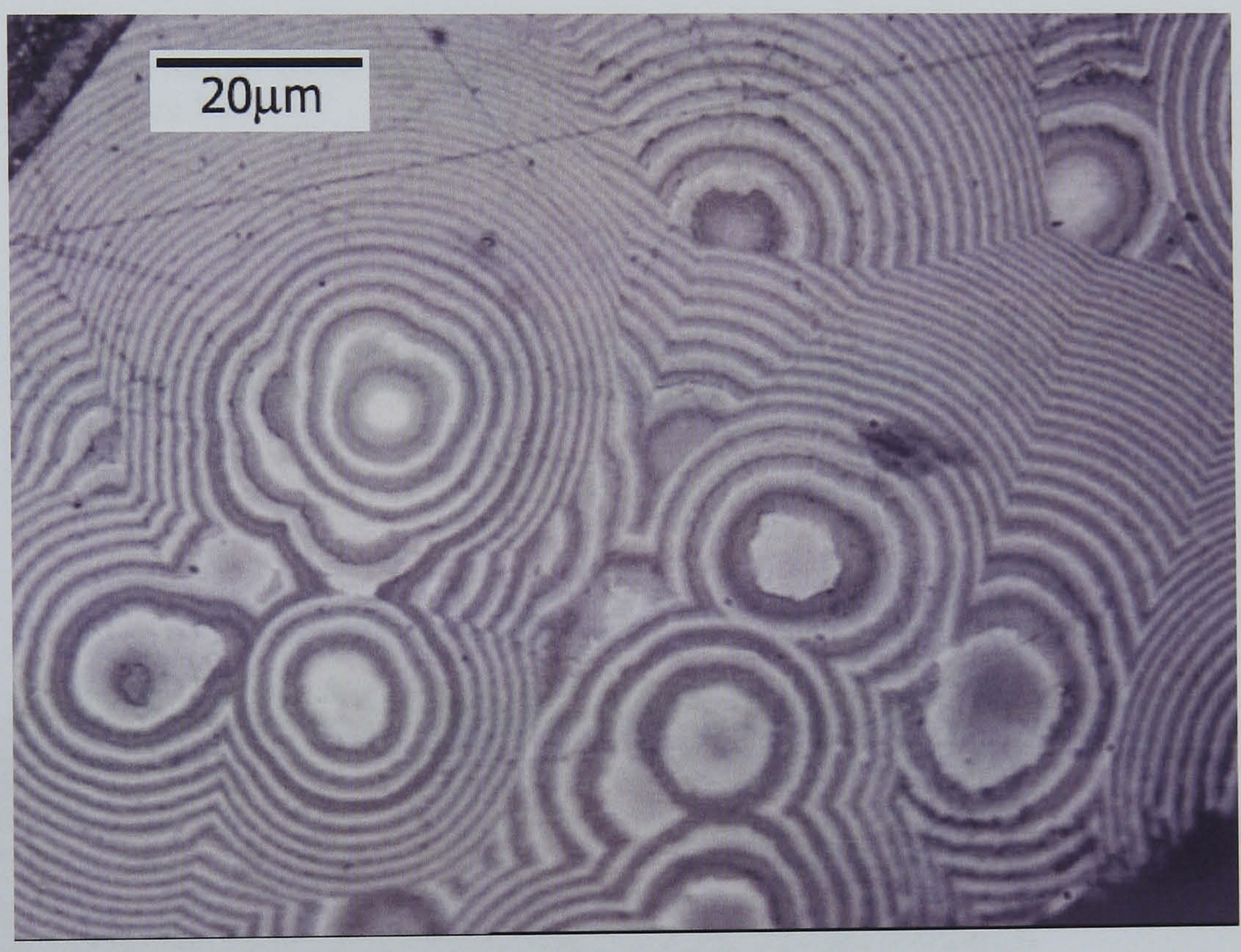


Figure 9-7: optical micrograph showing the truncated outer surface of TZ78. Hemispherical growth of layers is visible.

9.3 The macroscopic evolution of layer growth

As outlined in Section 2.7.3.1, decay starts at defects in the glass surface, which act as nucleating sites for corrosion, and layered formations irradiate deeper into the glass from these points. The typical hemispherical layer growth from the surface became visible when the topmost surface of TZ78 was removed. An optical micrograph of the polished sub-surface of TZ78 is shown in Figure 9-7. The multi-layered surface structure produces thin film interference patterns in which diffraction of light gives rise to the iridescent appearance of layered corrosion on glasses[8].

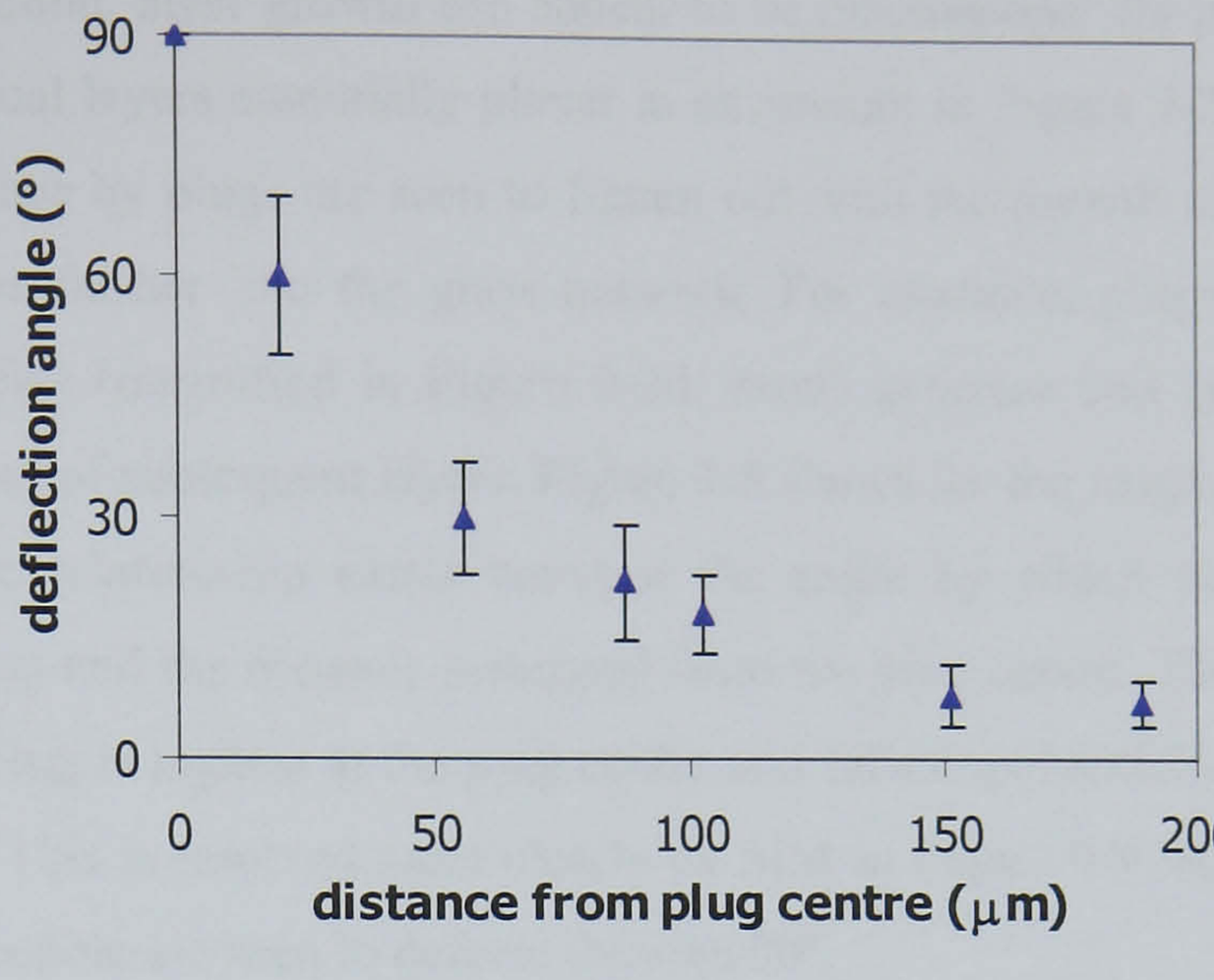


Figure 9-8: deformation angle as single layer plane traverses growth fault stemming from plug magnified in Figure 9-2d.

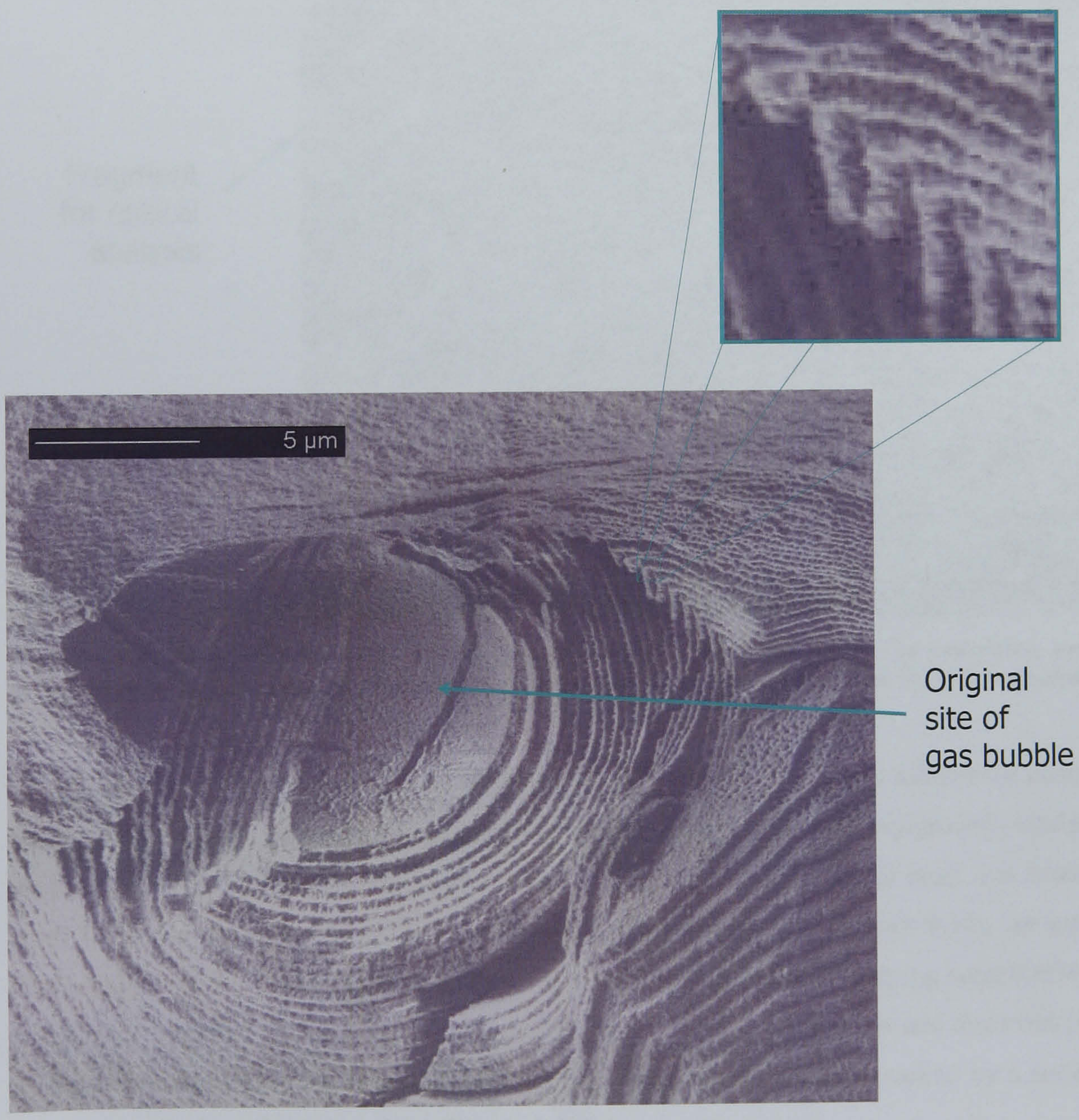


Figure 9-9: ion-induced secondary electron image of layers forming around a dissolved gas bubble. Layer formation is seen to deform by as much as 90° (inset).

Viewed in cross-section, layer growth can appear to be macroscopically parallel to the original surface and individual layers essentially planar in extension; in Figure 9-2c undulating patterns initiated at the surface by plugs are seen to flatten out with the growth of successive layers as the reaction reaches further into the glass network. For example, plugs created in TZ79 by dissolved gas bubbles (magnified in Figure 9-2d, inset) generate new growth directions that deform the formation of subsequent layers. Figure 9-8 shows for the magnified plug in Figure 9-2d that a parabolic relationship exists between the angle by which planar layer growth is deflected by the plug and the distance measured from the plug centre. The growth deformation introduced by the plug is highest at the plug centre and falls exponentially as the distance from the plug increases. This is resolved more clearly by SIM in Figure 9-9: layers forming adjacent to a dissolved gas bubble are seen to deform through 90°.

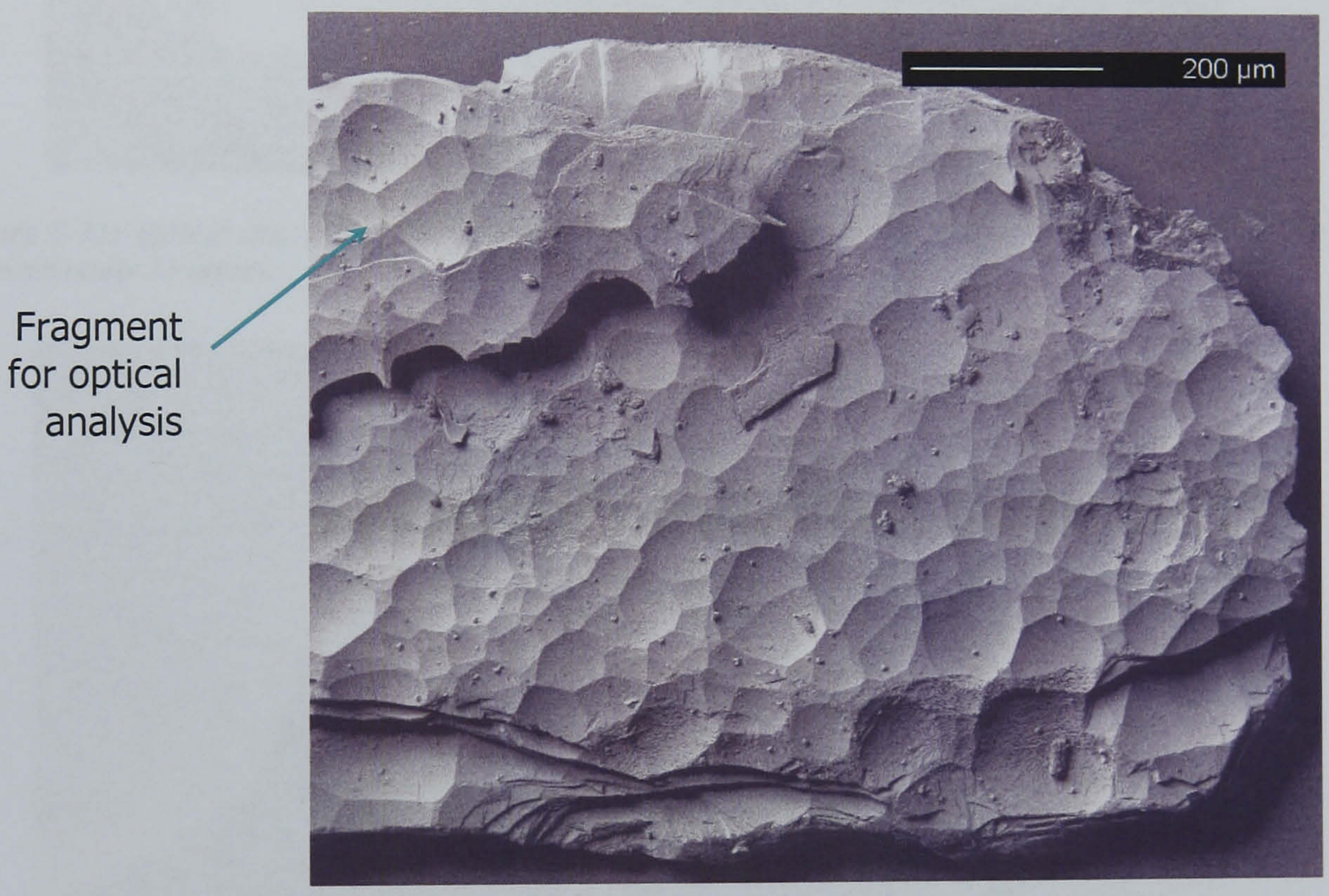


Figure 9-10: secondary ion image of the upturned crust detached from TZ78. The undulating nature of the exposed surface is visible. A fragment detached for optical analysis (Figure 9-11) is indicated.

Macroscopically, layer growth cannot therefore be truly 'flat' but it closely follows the contours of the previous layer with a natural tendency to flatten out an angle/boundary/growth imbalance, presumably for reasons of energy minimisation. When the outer portion of crust was detached from TZ78 (indicated in Figure 9-2b), upturned and viewed by SIM (Figure 9-10), the surface was highly irregular and undulated, with scale and depth of undulation varying considerably. A translucent fragment approximately 15 layers thick was detached from this and observed under an optical microscope. The layers composing the fragment were clearly marked by a series of growth boundaries initiated at plugs (Figure 9-11).

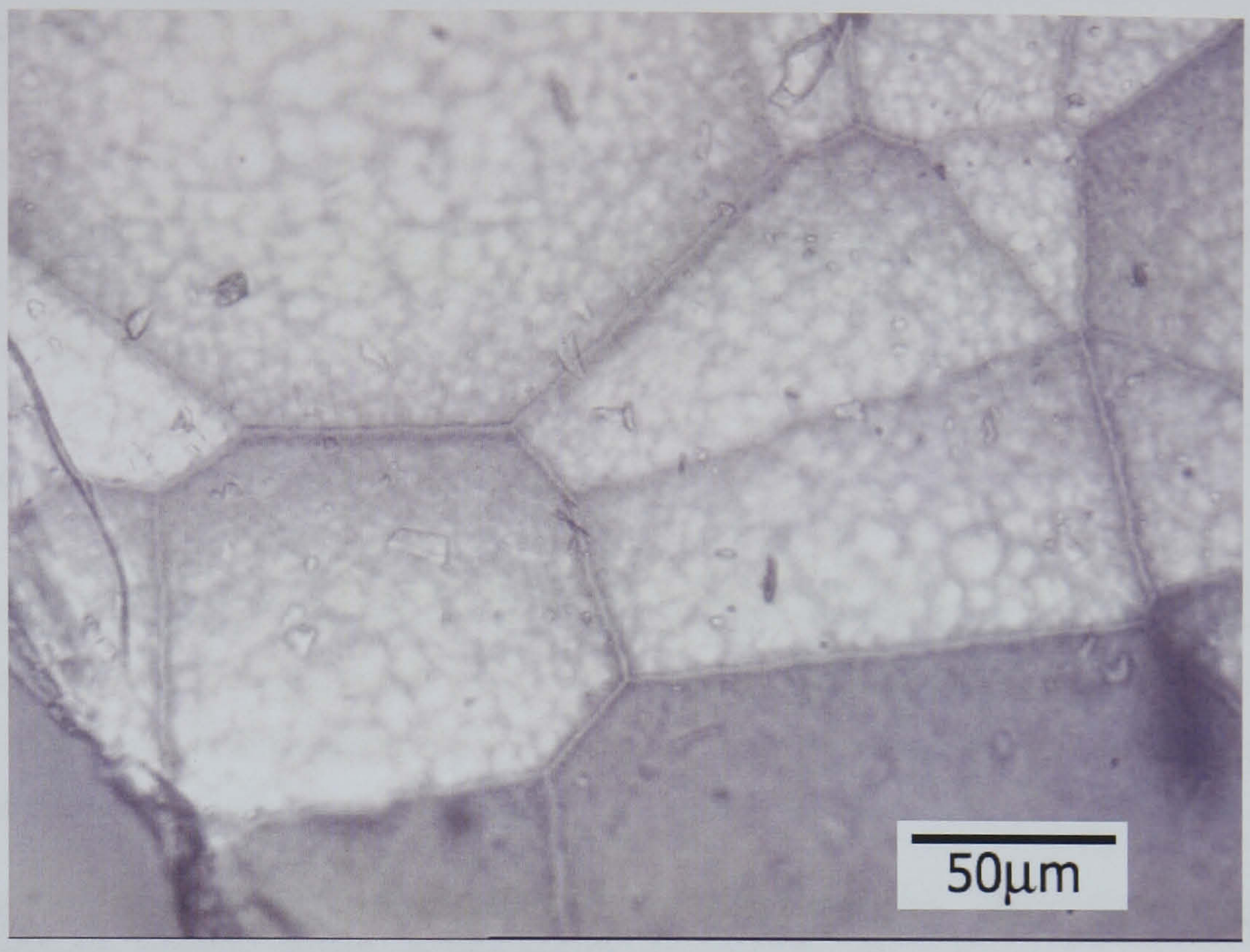


Figure 9-11: optical micrograph of a translucent fragment of the corrosion crust on TZ78. Width approximately 15 layers.

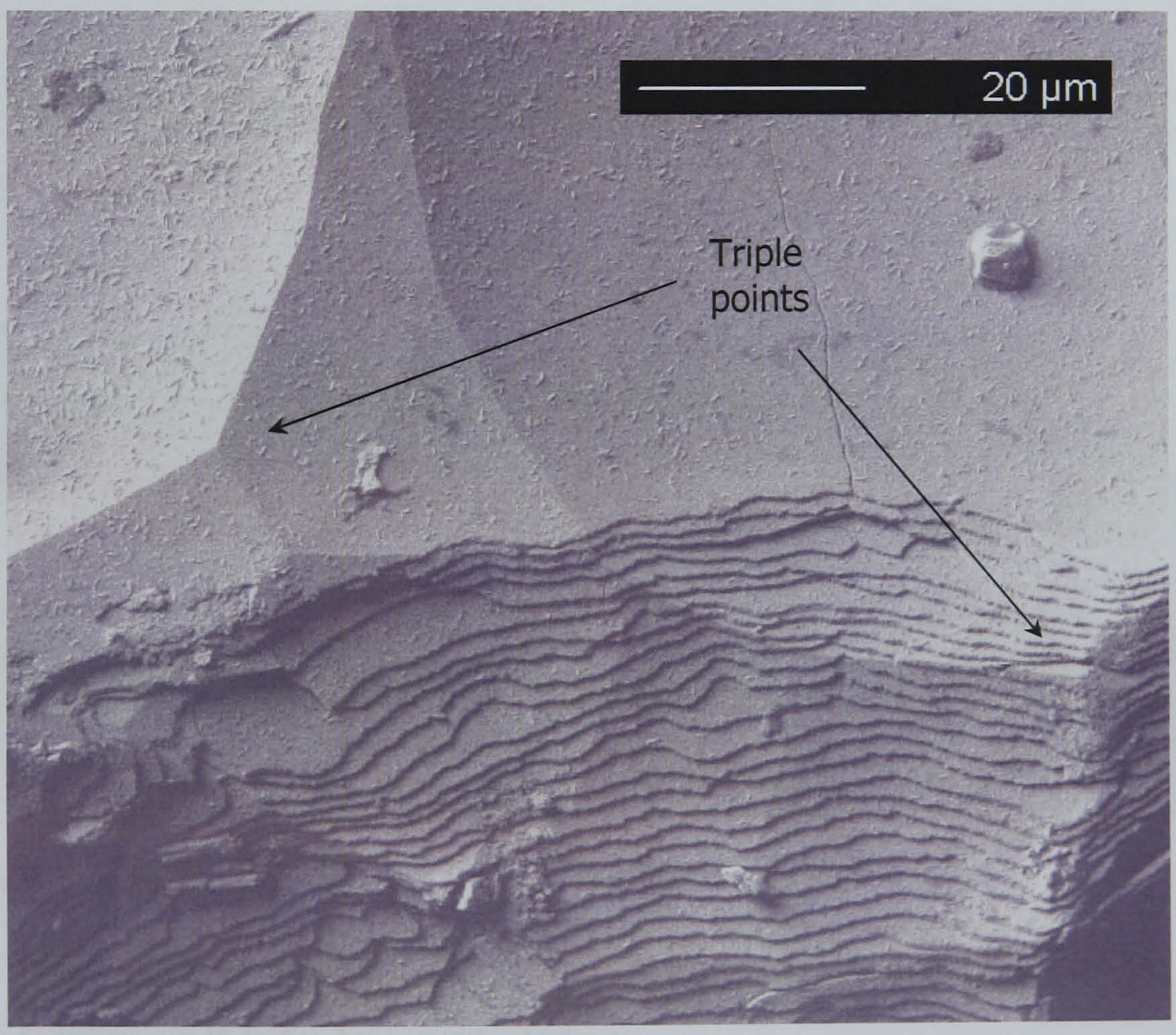


Figure 9-12: secondary ion image of the edge of the upturned crust in Figure 9-10 reveals single layers at higher magnification. Triple points are the intersection of three kinks.

This idea is validated by Figure 9-12, a close-up of an exposed edge in Figure 9-10. The kink formed at the point where two spherical growth patterns meet constitutes an axis around which subsequent layers are forced to bend. The contours of the topmost layer are defined by the layers below (bearing in mind that the crust is upturned and therefore the topmost layer in the image is the most recently formed). Nine layers below, the intersection of three spherical growth patterns (labelled as a triple point on the right in the figure) influences the growth of successive layers. Similarly, the triple point on the left of the image would influence a layer growing subsequently to the topmost layer in the figure.

The pattern reflects the hemispherical nature of growth radiating from nucleation points. And because the initial reaction stems from preferential attack at surface irregularities, the very nature of the crust is microscopically undulated in a complex manner, particularly in the case of ancient glasses that contained bubbles.

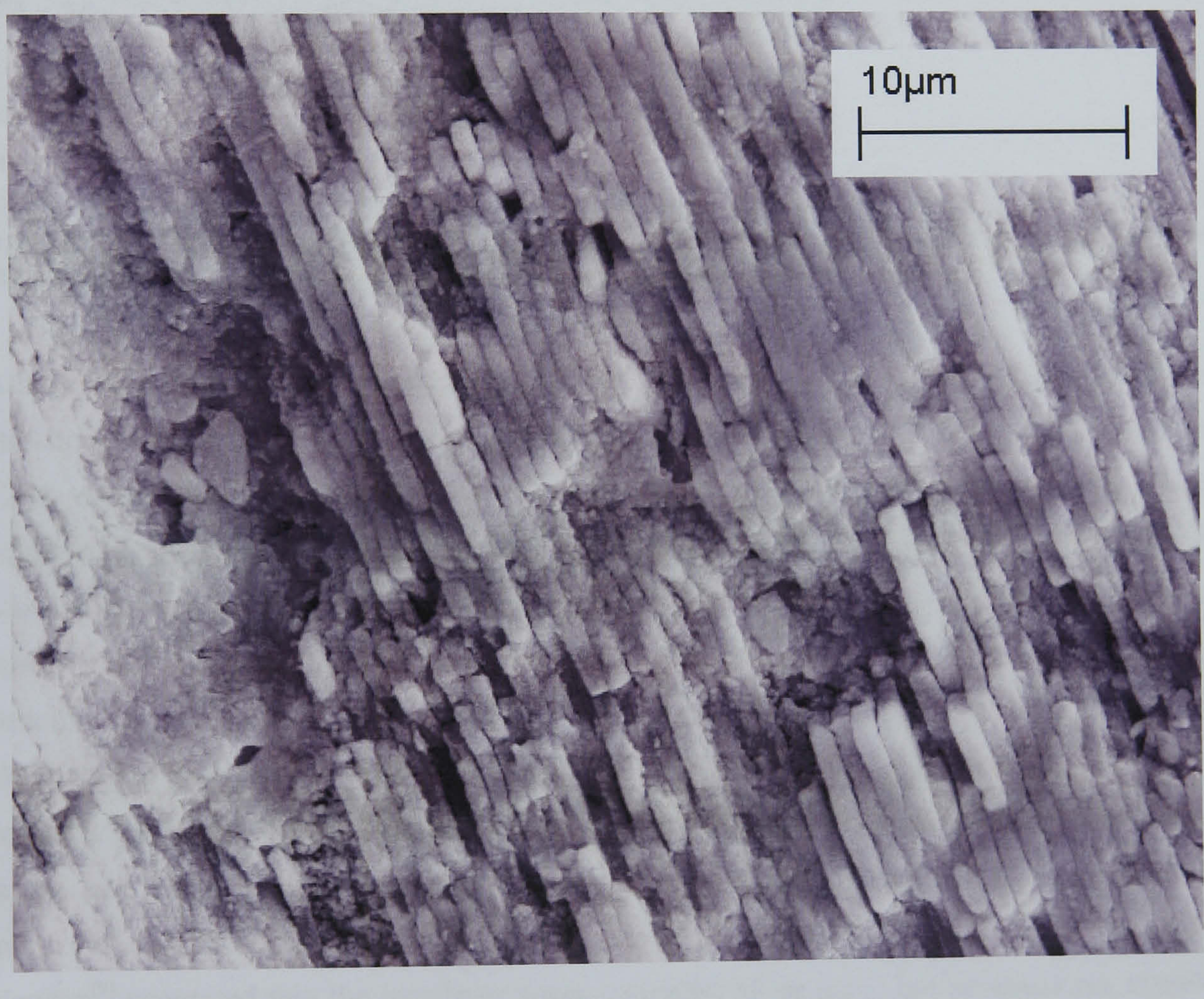


Figure 9-13: secondary electron image of layers from TZ78 in cross-section.

9.4 Layer and interlayer structure

As outlined in Section 2.7.3.1, corrosion layers in buried glasses are highly porous in nature but the reasons why they form are not clear. It is intended that the characterisation of individual layers, through the application of high-resolution ion and electron microscopy, will aid in the

further understanding of the nature and structure of corrosion layers. It will be argued here that individual layer thickness is dependent upon composition.

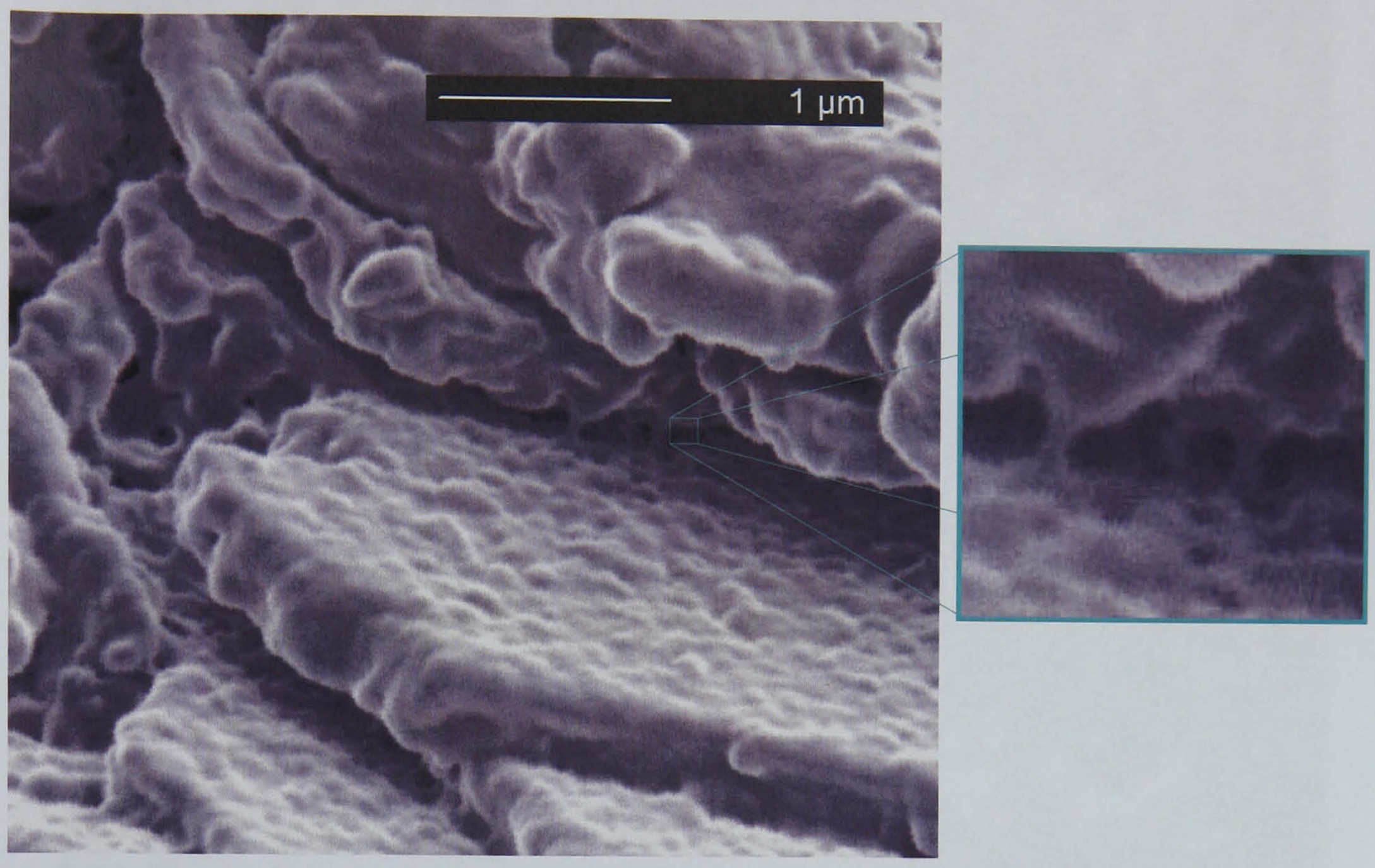


Figure 9-14: the upper surface of an individual corrosion layer revealed by SIM, tilted at 20°. The layers are connected by a series of thin strands that bridge between one layer and the next (magnified, inset).

Although single layers form along directions dictated by the layer previous to it, individual layer thickness was found to remain approximately constant throughout the entirety of the crusts. TZ78 was mounted and polished in cross-section, revealing the multitude of evenly spaced, adjacent layers in secondary electron mode (Figure 9-13). A single layer from TZ78 tilted at 20° was visualised using SIM and is shown in Figure 9-14. The exposed layer has an uneven, rather lumpy surface, suggesting that the precipitated silica-rich material is essentially granular in structure (cf. Figure 2-18). Very thin fibrous strands are also visible in Figure 9-14, bridging the physical gap between the central layer and its direct neighbours. This network of 'bridges' connecting adjacent layers is more clearly resolved in Figure 9-15, at a point where several layers had fractured along the same vertical plane and could be tilted 45° into view. An interlayer distance of approximately 100nm separates layers 0.7µm thick from each other. Newton[9] suggested that the interlayer space consisted of air gaps, but he could not visualise this in cross-section because he thought the space had filled with material from the polishing operation. No sample preparation has occurred here, and a zone with a highly porous foam-like structure is visible between layers.

To understand the nature of the interlayer material, a low intensity (10pA) focused ion beam was rastered for 10 seconds across an 8x5µm area of polished layers on TZ78 in cross-section.

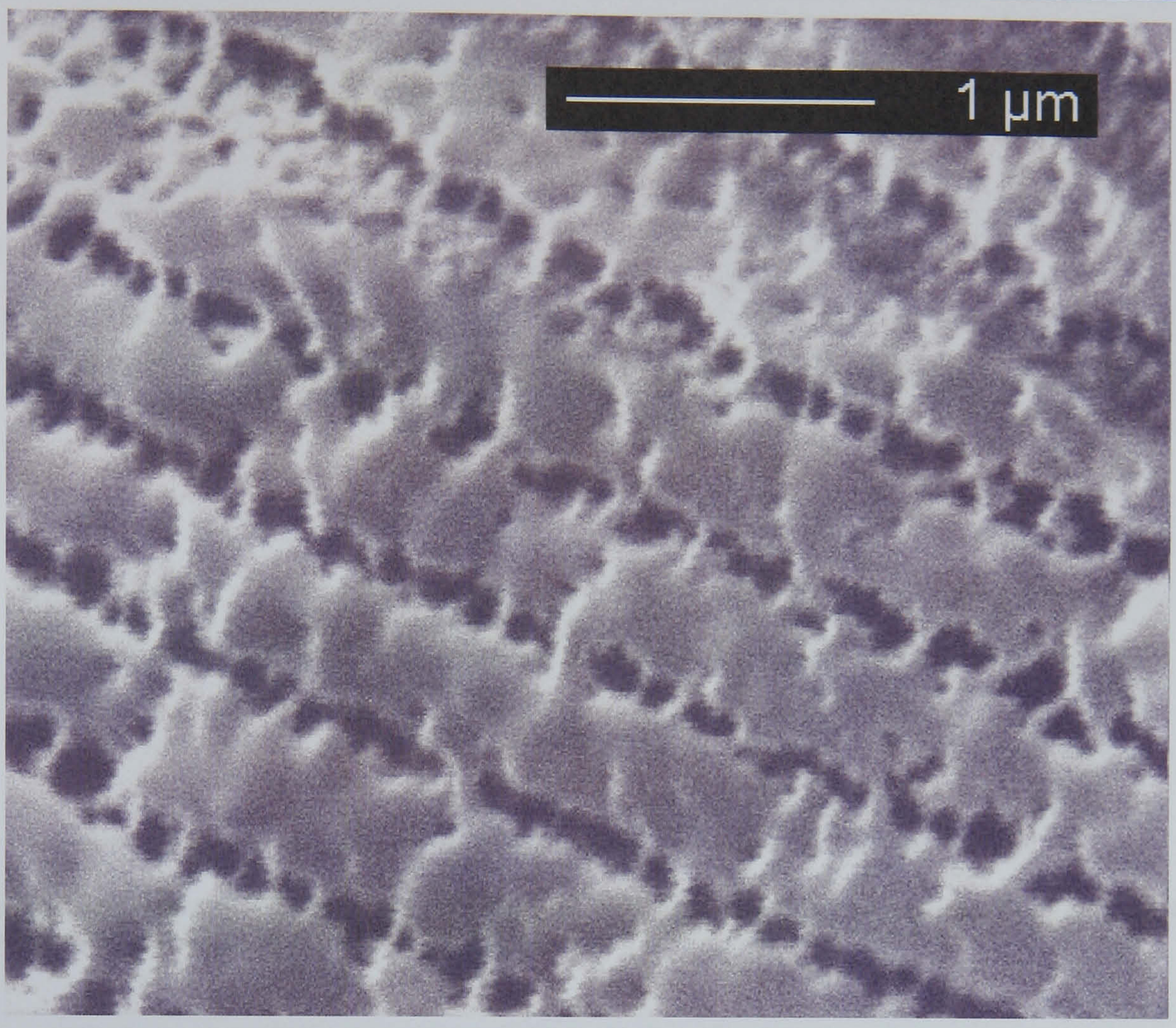


Figure 9-15: ion-induced secondary electron image of stacked layers on TZ78, tilted at 45°. A network of connecting 'bridges' is again visible between individual layers.

This revealed (Figure 9-16) previously unexposed layers and interlayer spacings beneath the polished exterior so that contamination from the polishing procedure was minimised (although it cannot be ruled out). By rastering across the polished surface with a 10pA beam for 30 seconds all the interlayer material was preferentially sputtered away, leaving the layers themselves largely intact (Figure 9-17). This indicates a significant difference in density between the material composing the layers and that within the interlayer area, and goes some way to demonstrating the existence of an interlayer deposit with a constitution as regular as the layers themselves.

9.5 Characterisation of the reaction front

A problem in assessing the reaction zone of corroded ancient glasses is that, due to their often advanced state of degradation, the corrosion product readily peels away from the unaltered body as soon as the glass is unearthed and begins to dry. Mounting in resin and polishing certainly does not improve the chances of finding an intact reaction zone. Referring to Figure 9-2, it can be seen that in all four cases the crust had separated from the body prior to analysis.

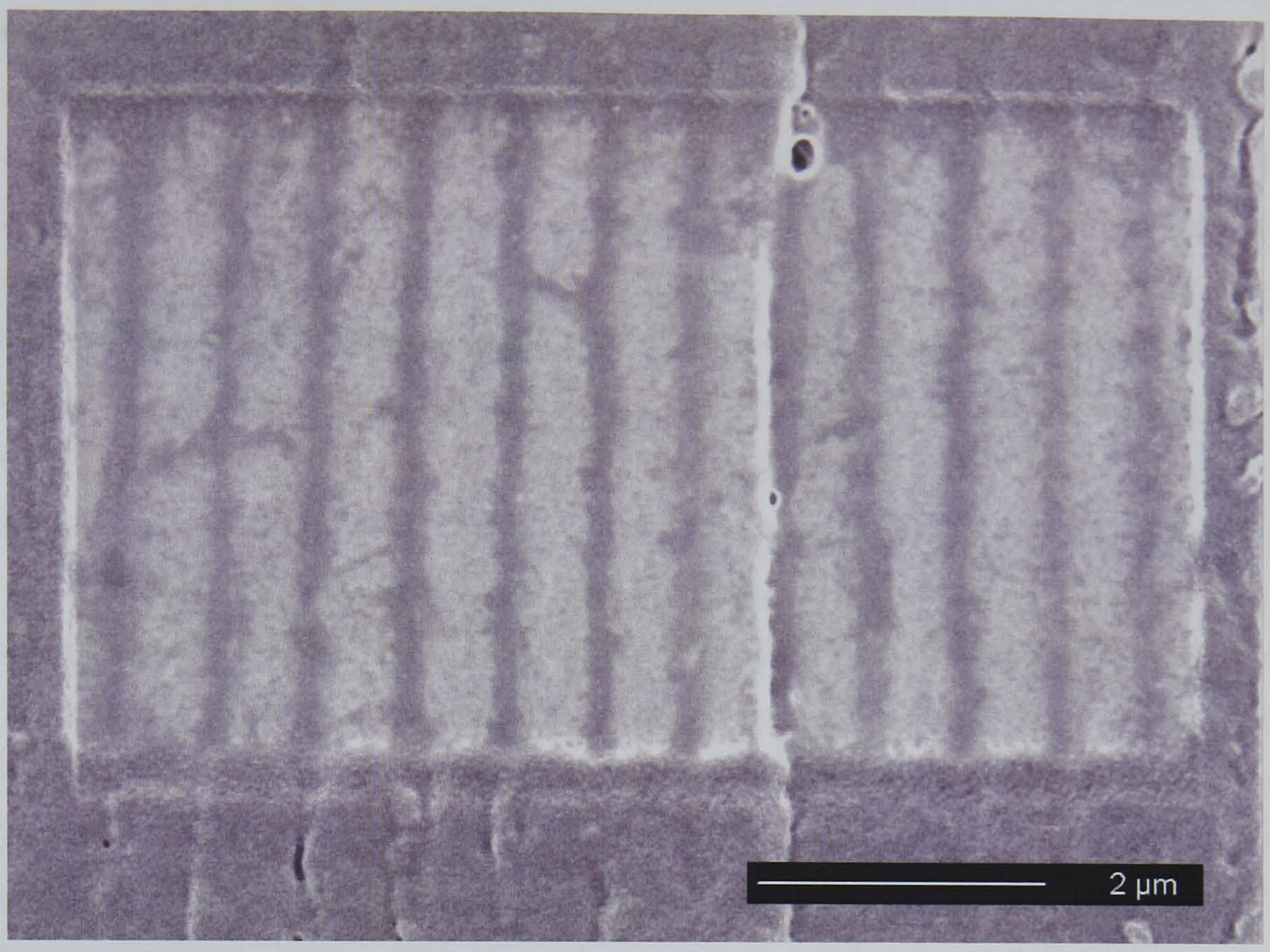


Figure 9-16: ion-induced secondary electron image of layers on TZ78 in cross-section revealed after exposure to a 10pA focused ion beam for 10 seconds.

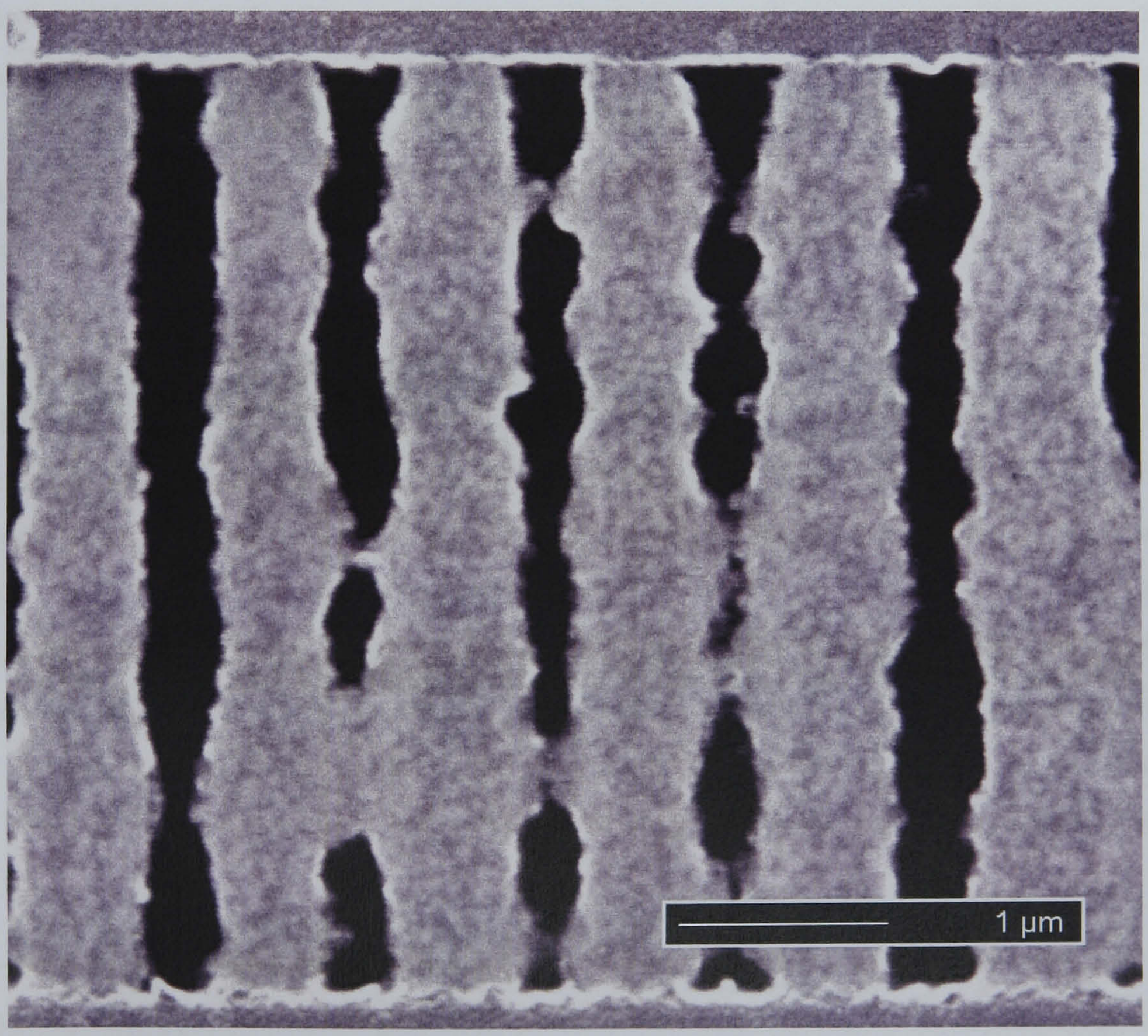


Figure 9-17: ion-induced secondary electron image of layers on TZ78 in cross-section revealed after exposure to a 10pA focused ion beam for 30 seconds.

However, one corner of TZ78 was identified complete with five undisturbed innermost layers beyond the crack that separates the rest of the crust from the glass. Because the cross-sectional upper surface of the inner layers (visible in the backscattered electron image, Figure 9-18) is situated fractionally below the surrounding polished surfaces, their structural integrity is maintained. Remarkably, there is reason to believe that these layers have formed *after* excavation; one partially formed and four fully formed layers are observed in Figure 9-18, which reflect approximately six years of growth at the rate calculated for TZ78 (a total of 950 layers over 1200 years of burial for an estimated formation time of 1.26 years/layer). As Tell Zujaj was excavated in the summer campaign of 1995 and TZ78 was mounted for analysis in late 2001, it can be argued that the layers indeed have grown within this six-year time frame and would explain why they are situated beyond the crack that separates the rest of the crust. It does not however explain why such a formation is present only in one corner of the sample. Similar self-propagating reactions in glasses are not unheard of; Newton[10] reports an experiment in which the leached layer in soda glass fibres was found to change even when the glass was stored in a desiccator*. The same sample was examined 12 months after the images in Figures 9-18 to 9-20 were taken and additional layer growth was not observed, suggesting either that the layers did not form after burial or that the exposure to UHV conditions and storage in a desiccator has either stopped or retarded the reaction. Ultimately, the 'frozen' corrosion reaction in Figure 9-18, independently of the reasons and timescale behind its formation, provides a tantalising opportunity for the detailed characterisation of active layered corrosion formation in progress.

A strip 1.6-1.7μm thick in the glass ahead of the reaction front appears bright in the backscattered electron image. Elemental mapping of Figure 9-18 (shown immediately underneath the figure) revealed the strip to correspond to the corrosion reaction zone (β_1 in Wicks' model outlined in Section 2.7.3.3); Si intensity is highest in the region at the expense of Na, Mg, Ca and K. Higher O intensity within the region suggests hydration of the glass and increased hydroxyl activity. Al and Fe are distributed evenly across the whole area. A linescan was conducted from the unreacted bulk across the reaction zone and precipitated layers and is shown in Figure 9-19. The EDXA data reveals that the gradient zone is actually over 2μm thick and can be viewed at higher magnification as the inner limit of variable contrast in the glass. It is preceded by a thin (~1μm) Na depletion front (β_2). The darker band across the gradient zone does not clearly correlate to the data, although a slight Mn enrichment is recorded at this point. The layers are almost totally depleted in RO and R_2O species and are composed of alumino-

* Obviously this hypothesis has massive implications for the Ballidon data, as the earliest samples were unearthed over 30 years ago and their storage history since then is not fully documented. The point deserves further investigation.

ferro-silicate compounds, in an analogous way to B2 and B3 discussed in the previous chapter. Congruent dissolution is thus observed at the glass reaction front.

As with previously examined layered formations in TZ78, the periodicity of the four fully formed layers is remarkable. They are clearly separated from each other by an interlayer gap of 100-180nm and vary in thickness between 0.8 and 1μm, slightly thicker than the majority of layers observed in the rest of the crust. From the constant 90° angle formed around the corner of TZ78 in the top left of Figure 9-18 it can be assumed that the reaction front is progressing at constant velocity through the glass along the direction of layer growth. The reaction is therefore proceeding under steady state conditions.

The partially formed innermost layer is only 0.7μm thick and holds the key to interpreting the dynamics of the corrosion process. Figure 9-20 is a high magnification secondary electron image of the area in question that demonstrates the structure of the innermost portion of this layer to be glassy and not granular in nature. This corresponds to the gel layer that exhibits a clear, smooth boundary with undissolved, depleted glass to the left (the bright strip between the glass and the gel layer in Figure 9-20 is thought to be an edge effect and not a structural feature) and an irregular, jagged boundary with precipitated granules that constitute the layers on the right. The gel layer forms a compositional continuum across this region, as it is not distinguishable from the rest of the precipitated layer in backscattered electron mode (in Figure 9-18 and Figure 9-19). The diameter of granules ranges from 50 to 100nm. The large granule visible on the right edge of the gel layer could be surface debris, as it appears very different in size and shape to the otherwise homogeneous size and structure of precipitated nanogranules. The interlayer gap is now resolved as consisting of a single row of deposited granules.

9.6 Interpreting periodic glass dissolution reactions

The evidence presented up to the current point suggests that regular lamellar formation in buried glasses is the result of a periodic chemical reaction rather than the result of a mechanical separation due to compressive stresses. Although spontaneous cracking had been observed in TZ76 and TZ79, this was due to residual stresses in the glass and had not been necessarily induced by alkali leaching. The reasons behind the recurring nature of such a corrosion reaction are not clearly understood. For any one glass, corrosion layers are formed consecutively through the concomitant depletion of alkali ions, breakdown of the silicate network and redeposition of complex amorphous silicate compounds across a uniform depth in such a manner that the same conditions prevail at the undissolved surface or at the reaction interface both at the start and at the conclusion of the process.

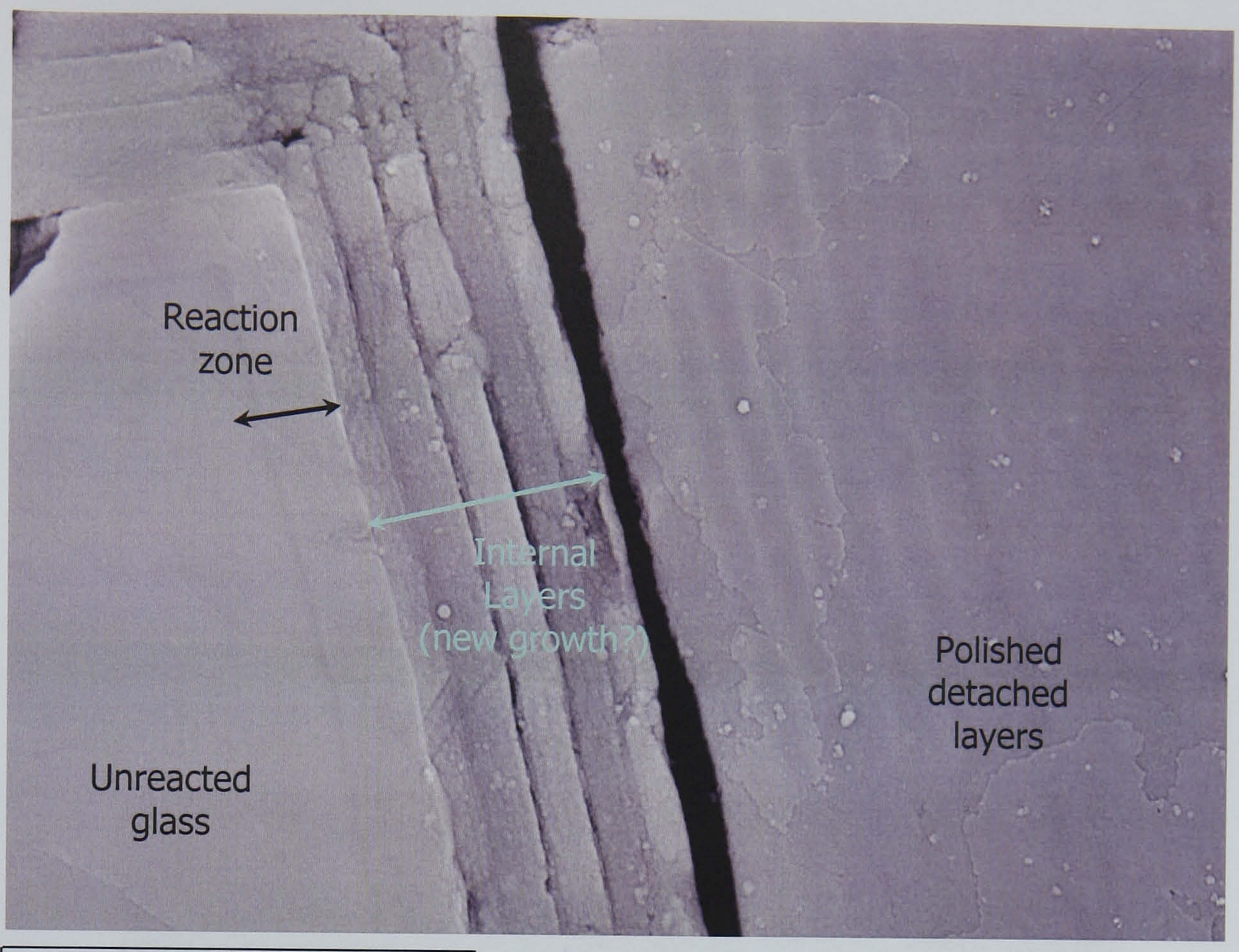
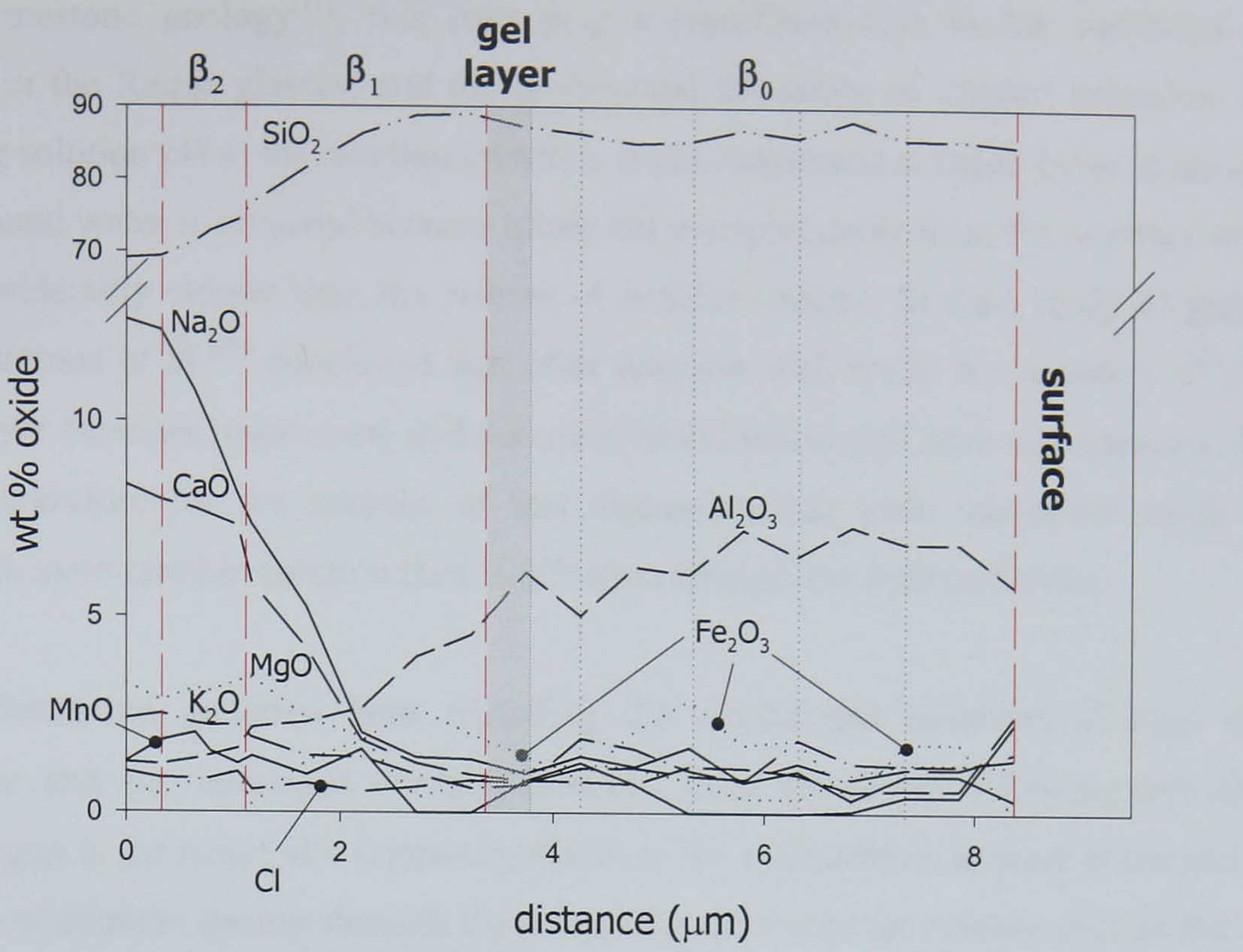


Figure 9-18: backscattered electron image of the most recently formed layers and the active reaction front at the innermost surface of TZ78. An elemental map of the area shows increased Si and O intensity in the reaction zone at the expense of Na, Ca, Mg and K. Al and Fe are seen to remain constant throughout.



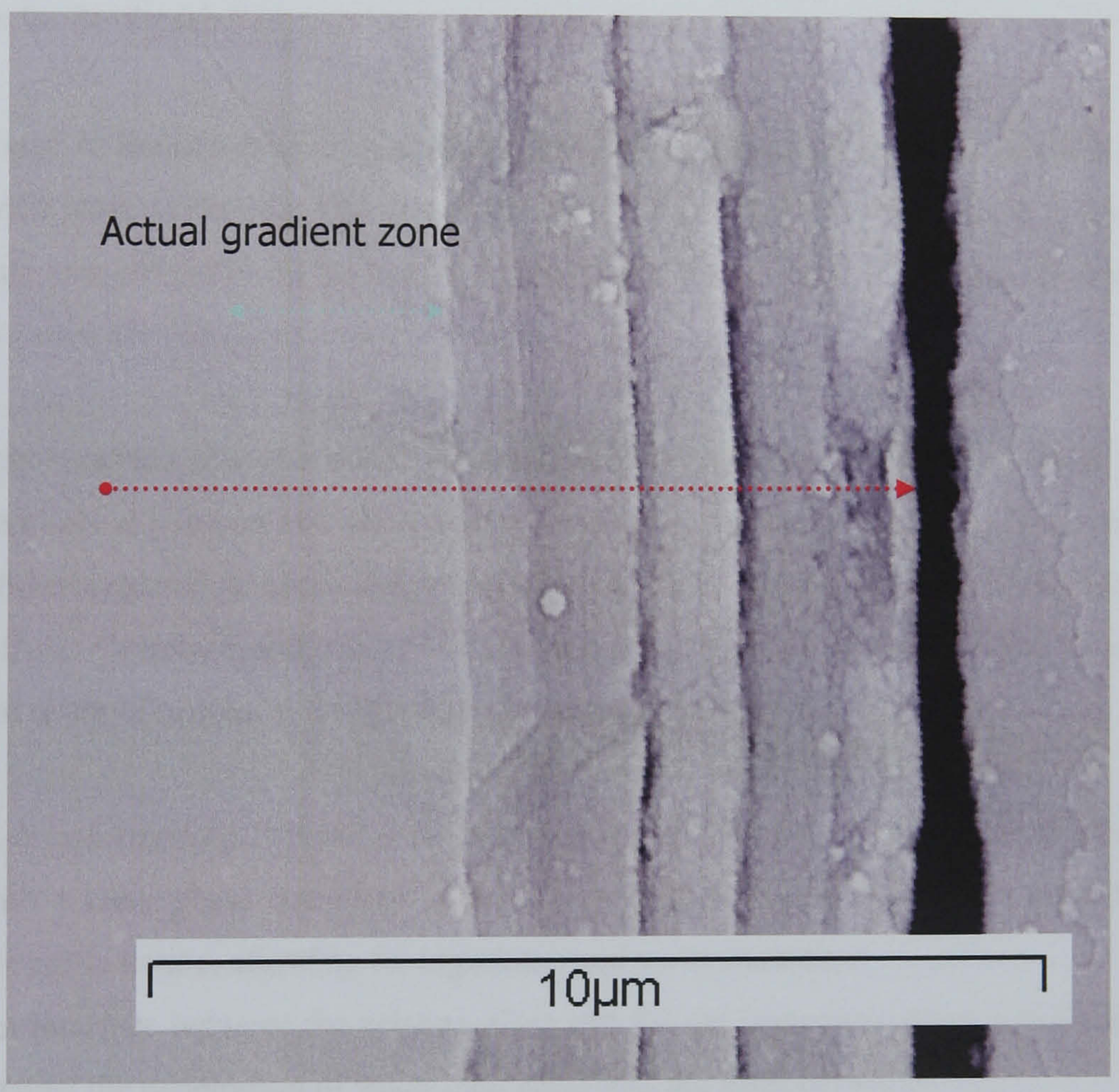


Figure 9-19: EDXA linescan data (top) across cross-sectional layers in Figure 9-18 revealing a gradient zone ahead of the dissolution front. The gel layer visible in Figure 9-20 is shaded grey. The gradient zone is visible in the backscattered electron image (bottom) of the area because of the variation in contrast it produces. The red arrow indicates length and direction of the linescan.

As outlined in Section 2.7.3.2, the solubility of silica in aqueous solutions increases sharply at pH levels ≥9. As the soil pH at Raqqa is almost universally alkaline, given the local

gypsum/limestone geology[11], this may play a significant role in the corrosion processes observed in the Raqqa glasses, and the preferential formation of crusted corrosion. However, increasing solution pH at the reaction interface is not considered a major factor in buried glasses where ground water is involved because alkali ion transport away from the interface would need to be considerably slower than the release of soluble species. In their study of glass surface layers Doremus *et al.*[12] concluded that after reaction with water the structure of a hydrated surface layer becomes more open, and that ionic mobilities in this layer are increased. It must be assumed therefore for the purpose of this discussion that ionic movement away from the interface is more rapid in solution than is diffusion through the hydrated glass.

Novel information gathered here regarding the nature and structure of both the layers themselves and the interlayer material between them raises the following hypothesis: the interlayer gap is the result of a temporary hiatus in the redeposition process at the end of which a build up of alkaline species through the continuing ion exchange reaction creates the necessary conditions for the dissolution reaction to commence once again.

As mentioned in Section 2.7.4.2, a prerequisite for crust formation in buried silicate glasses is that every Si atom in the glass be associated with a basic ion as its second neighbour, which corresponds to a ~66mol% SiO_2 content. This figure becomes important when the dynamics of glass dissolution are considered more closely.

It is widely reported that the initial dissolution is characterised by ion exchange processes between protons in solution and glass network modifier cations, resulting in the formation of a hydrated layer depleted in alkali metal and alkaline earth cations, through which the aqueous species diffuse. Grambow and Müller[13] have indicated three key factors to glass dissolution in their recent study of nuclear waste glass performance predictions:

a) A transformed (gel) layer is formed if sufficient network bonds are hydrolysed, often with a clear phase boundary to the glassy phase. The transformed surface layers are porous in nature, allowing for high ionic and water mobility.
b) An interface between the pristine glass and the gel layer constitutes a diffusion barrier against the penetration of water molecules into the glass network.
c) This diffusion barrier is hydrated glass and, in contrast to the gel layer, can be considered as part of the glass phase. The gel layer is a new phase replacing the glass phase. The matrix dissolution front is then the interface between the water/alkali diffusion profile and the transformed layer.

They redefine the glass dissolution reactions (equations 2-30 to 2-32) in Section 2.7.3 as follows:

$\vec{A}_1$ $$(\equiv Si-O^{\delta-}\ Na^{\delta+}) + H_2O_{(gl)} \rightarrow (\equiv Si-OH) + Na^+_{(gl)} + OH^-_{(gl)} \quad [9.1]$$

$\vec{A}_2$ $$OH^-_{(gl)} + (\equiv Si-O-Si\equiv) \rightarrow (\equiv Si-OH) + (\equiv Si-O^-) \quad [9.2]$$

$\overleftarrow{A}$ $$(\equiv Si-O^-) + Na^+_{(gl)} \rightarrow (\equiv Si-O^{\delta-}\ Na^{\delta+}) \quad [9.3]$$

B $$(\equiv Si-O^-) + H_2O_{(gl)} \rightarrow (\equiv Si-OH) + OH^-_{(gl)} \quad [9.4]$$

C $$Na^+_{(gl)} + H^+_{(aq)} \rightarrow Na^+_{(aq)} + H^+_{(gl)} \quad [9.5]$$

Where: 'gl' indicates a mobile phase in the slightly porous hydrated glass and 'aq' denotes a mobile ion in the interfacial aqueous solution.

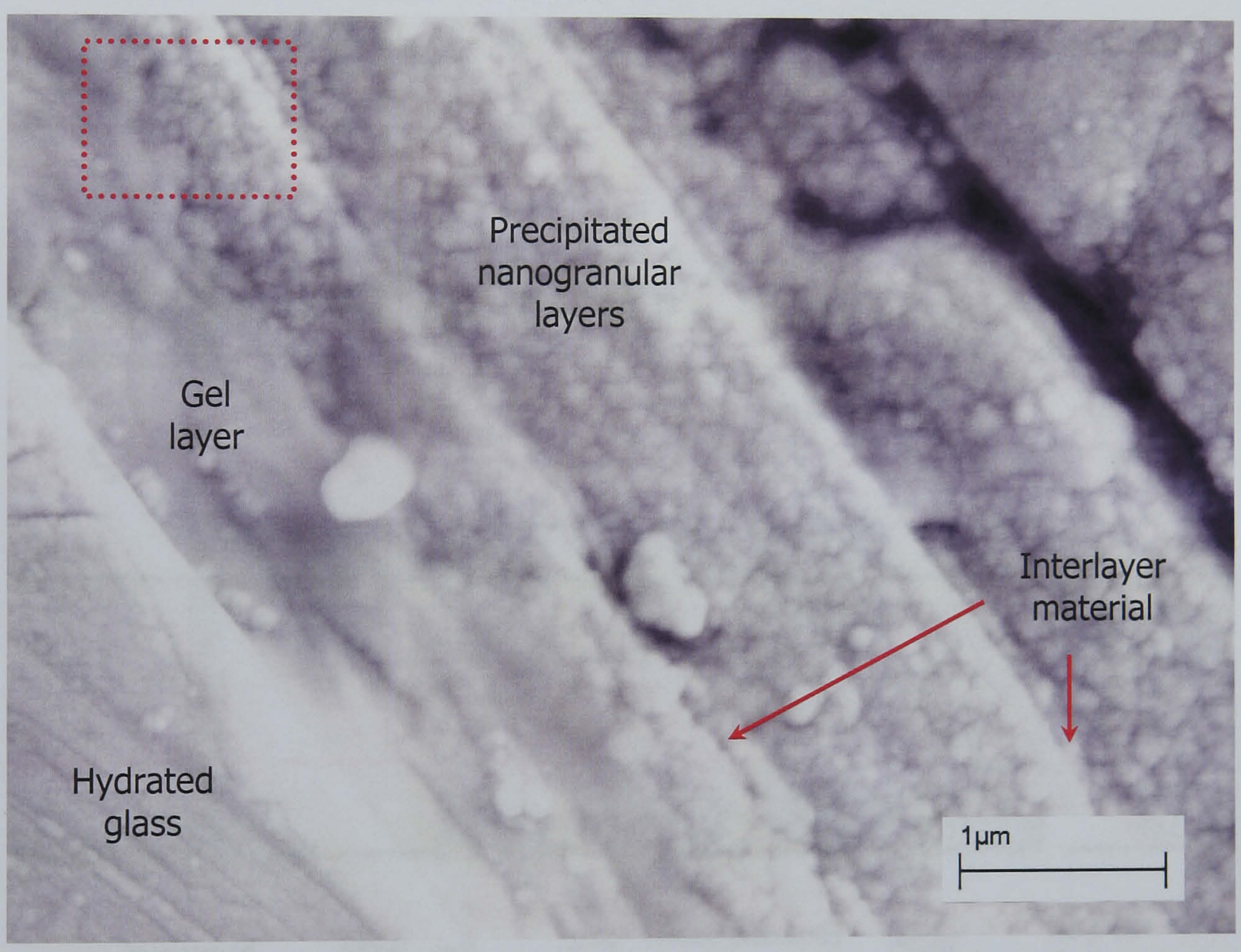
The redefinition works on the basis that molecular water is not an inert diffusing species but that it reacts with the glass network. The net result of both partial forward reactions A_1 and A_2 and the back reaction A (equation 9.3) remains the hydrolysis of siloxane bonds, as with the original reactions in equations 2-30 to 2-32. However, only a fraction of Na may become released as a NaOH ion pair because a significant quantity of Na is immobilized by back reaction A in the hydrated glass and cannot diffuse out. This is because $\equiv SiO^-$ groups are unstable in the hydrated glass and $OH^-_{(gl)}$ is highly reactive with the glass network, so the back reaction A is favoured over competing reaction B. Na diffusion into the interfacial solution takes place preponderantly through a direct ion exchange reaction with H^+ ions, reaction C, which is driven by chemical potential differences between the outermost surface species and solution species. The authors conclude that the liberation of a hydroxyl group leads to instantaneous dissolution of network siloxane bonds (reactions A_1 and A_2) and instantaneous Na^+/H^+ ion exchange equilibrium at the hydrated glass/gel layer interface (back reaction A and C). The surface region is thus chemically stable by definition.

Let us consider the case of crusted glasses, i.e. those that contain 66mol% SiO_2 or less, and imagine, for the sake of argument, a pristine surface in contact with groundwater. Every molecule of water that reacts with the glass network causes an alkaline cation to be freed, a hydroxyl group to be liberated and a siloxane group to be instantaneously disrupted, leaving only one undisturbed siloxane group in the adjacent region. This leads to a greater degree of network breakdown per molecule of reacting water entering the structure than, say, a glass containing 75mol% SiO_2, so that a gel layer is created more rapidly at the surface and over a shorter distance into the glass. The ensuing interface between the pristine glass and the gel

layer, which slows further water diffusion into the network, is therefore characterised by a steeper concentration gradient of soluble species being leached into solution.



Figure 9-20: the nanogranular consistency of the layers becomes clear in a secondary electron image of the reaction front in TZ78, visible in backscattered electron mode in Figures 9-18 and 9-19. The glassy nature of the gel layer is also clearly distinguishable. Undissolved glass is located in the bottom left corner with a half-formed layer attached to it. A 1μm-long region of the dissolution boundary to the right of the gel layer is highlighted by a red border and magnified above (inset), showing the regular 50-100nm grain size of precipitated products and the uneven edge between the gel layer and precipitated corrosion products.



The formation of a protective barrier (point b, above) constitutes the main rate-limiting factor in the long-term corrosion of buried glasses[1]. However, because the ion exchange equilibrium is driven by chemical potentials across the interfacial area, the increased concentration gradient across it will ensure that diffusion of alkali ions into solution and water molecules into the glass continues, increasing the depletion depth of alkali species and extending the gel layer.

Referring back to Figures 9-19 and 9-20, the gel layer is seen to correspond chemically to the region just ahead of the Si maximum at the outer edge of the gradient zone. The undissolved

glass in front is therefore at its most depleted point at the interface with the gel layer. The gel layer itself corresponds to a peak in Al values, as the element precipitates back out of solution in the form of alumino-ferro-silicate nanogranules. Na, Mg and Ca are significantly depleted over 1μm into the glass ahead of the gel layer, so diffusion would be slowed considerably because of the extra distance that water molecules would need to travel in order for the exchange processes to continue. The gel layer by now has become significantly enriched in Si and the ensuing build up of silicate species in solution would favour recondensation until the gel layer shortens in thickness to previous levels or until the concentration of Si in solution falls below its solubility limits. It is possible to envisage at such a point a period of gradual build-up of Si in solution as the alkali diffusion reaction returns to dominate and the gel layer moves progressively forwards into the glass, in which there is no recondensation of silicate compounds. This would correspond to the interlayer gap.

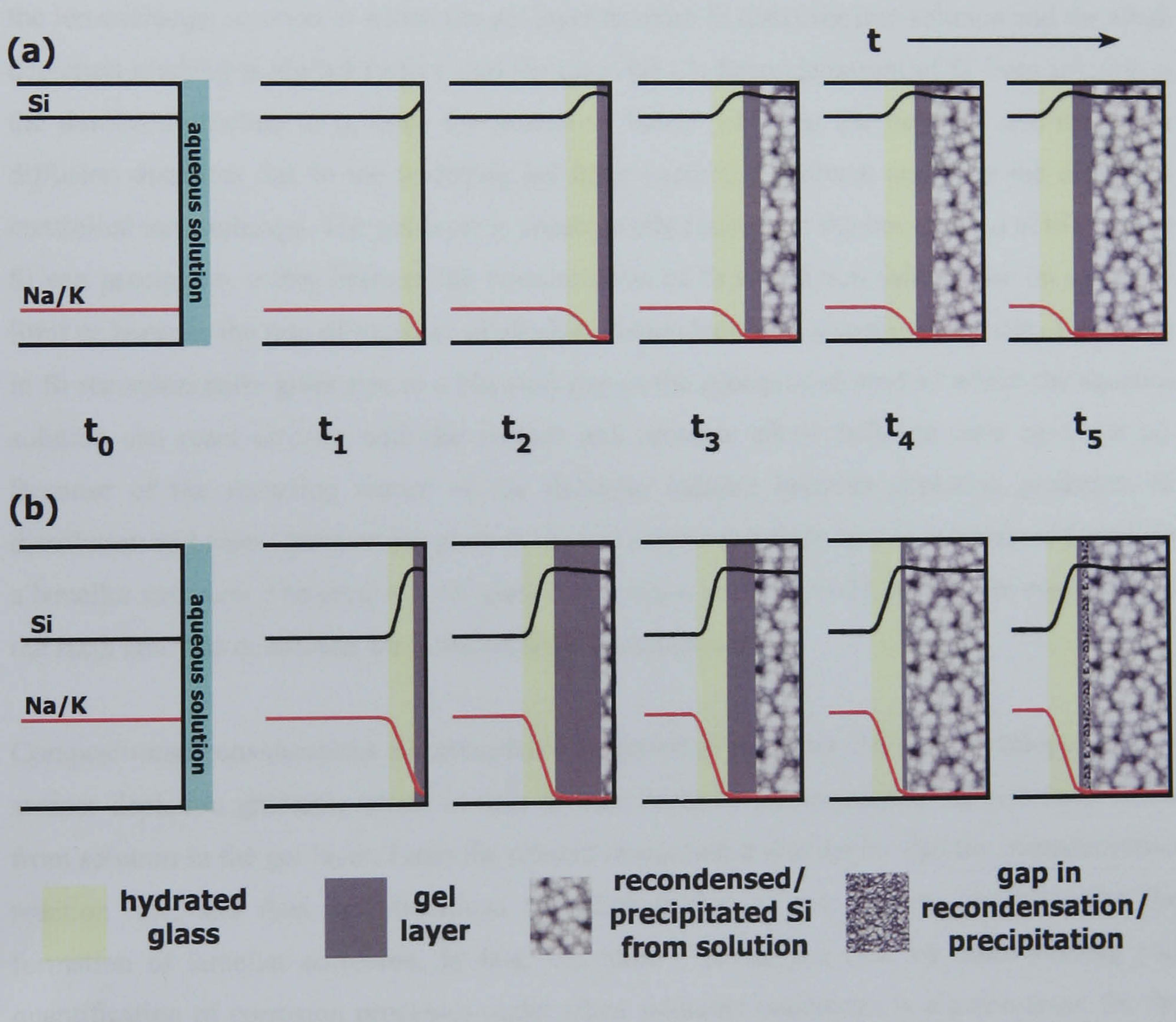


***Figure 9-21:** schematic diagram illustrating the compositional dependence of layered corrosion in buried glasses. Specimens* a *and* b, *where* C_{R+}(b)>C_{R+}(a), *are in permanent contact with groundwater. Glass* a *hydrates* (t_1), *forming a gel layer* (t_2) *that maintains a constant thickness as the corrosion reactions propagate into the glass* (t_3-t_5). *The higher alkali content of* b *leads to a steeper leaching gradient and a more rapidly formed gel layer* (t_1). *The greater chemical imbalance across the gradient causes the gel layer to increase in size until diffusion across it is significantly slowed* (t_2). *Si recondenses from solution, reducing the width of the gel layer* (t_3). *At such a point Si either falls below solubility limits and is retained in solution or the recondensation rate falls below the diffusion reaction rate in such a way that recondensation momentaily stops* (t_4) *until the depletion profile is restored to previous values* (t_5). *Water and other lighter compounds infiltrate the highly porous area and kick-start the diffusion reaction over again. Hence the reaction is of a recurring nature.*

The process is summed up schematically in Figure 9-21: two glasses, *a* and *b*, where $C_{R+(b)}>C_{R+(a)}$, in other words where *b* contains a higher quantity of alkali than *a*, are subjected to permanent contact with groundwater at time t_0. The different mechanisms are illustrated through the evolution of Si and alkali profiles with time. After five subsequent time intervals (labelled t_1-t_5) a steady state congruent dissolution reaction dominates in *a*; an alkali gradient is established by t_1 and is then followed by the formation of a gel layer as the network dissolves (at t_2), leading to the progressive condensation of silicate species once local saturation limits are surpassed (t_3). The dissolution and condensation reactions propagate into the glass at the same rate (t_4 and t_5), so that the gel layer maintains a constant thickness.

A discrete layer has formed in *b*, however. This is because of the larger alkali content of glass *b*; a gel layer is established relatively quickly (at t_1) and the steeper concentration gradient drives the ion exchange reaction to widen the gel layer as more Si dissolves into solution and the alkali depletion gradient is shifted further into the glass (at t_2). Recondensation of Si from solution is the dominant reaction at t_3, once the protective barrier effect at the interface and the larger diffusion distances due to the widening gel layer become significant and slow the diffusion-controlled ion exchange. The gel layer is subsequently reduced in thickness (at t_4) until no more Si can precipitate, either because the concentration of Si in solution falls below its solubility limit or because the rate of increase of alkali diffusion increases sharply once more. The pause in Si recondensation gives rise to a physical gap in the precipitated product where the aqueous solution can react directly with the surface and promote alkali diffusion over again (at t_5). Because of the recurring nature of the dynamic balance between depletion gradients, Si dissolution and reprecipitation for glass *b*, the gap occurs at evenly spaced intervals and leads to a lamellar structure. The gradients for glass *b* at t_1 and t_5 in Figure 9-21, in fact, are equivalent to the sixth and thus conditions for a self-repeating reaction are met.

Compositional considerations are considered therefore to influence the early development of a steeper depletion gradient, which in turn favours rapid recondensation of silicate compounds from solution in the gel layer. From the present discussion it also seems that the recondensation reaction rate, and thus the conditions for silica saturation, are vital to understanding the formation of lamellar corrosion. In fact, Grambow[1] points out that the understanding and quantification of corrosion processes under silica saturated conditions is a prerequisite for the long-term prediction of glass behaviour.

9.7 Thermodynamic approach to layer formation

In order to corroborate the ideas expressed on cyclic glass corrosion reactions, the durability of Raqqa and Ballidon glasses was assessed in terms of the thermodynamic characteristics of their

constituent oxides, according to the model developed by Jantzen and Plodinec[14] as outlined in Section 2.7.2.1, and compared to previously published studies on layered corroded glasses.

9.7.1 Methodology

Images of layered crusts on KLS and SLS glasses from a selection of published papers[6, 9, 15-17] were chosen for inspection where satisfactory details were given about chemical composition in order to calculate NBO fractions and ten or more layers could be clearly visible adjacent to one another in cross-section. This because the perceived thickness of layers varies according to the viewing angle, as is the case for Figure 9-7. Because the layers radiate hemispherically from plugs above the truncated surface, they appear to decrease in thickness whereas it is the growth angle that varies with respect to the planar polished surface.

Oxide (mol%)	this study					published literature						
	TZ76	TZ78	TZ79	TZ143	TF208	SC1 [a]	EP1 [a]	RA3 [a]	HLS [b]	AMS4 [c]	ZZ [d]	J1 [e]
Na_2O	13.25	13.08	15.25	14.57	11.72	1.76	2.38	2.94	0.73	3.95	2.05	16.16
MgO	5.37	5.29	3.74	4.67	4.72	10.38	11.13	10.16	8.63	3.80	10.55	0.30
Al_2O_3	0.65	0.66	0.96	0.93	0.73	0.82	0.54	0.77	2.21	2.04	0.68	1.49
SiO_2	66.96	67.21	69.40	68.01	69.65	50.55	60.84	52.15	49.85	62.18	63.05	70.34
P_2O_5	0.10	0.11	0.15	0.12	0.12	2.90	1.30	2.98	2.09	0.99	1.65	0.04
Cl	1.56	1.61	1.37	1.02	1.30	nd	nd	nd	nd	nd	nd	1.37
SO_3	0.11	0.09	0.18	0.22	0.12	nd	nd	nd	nd	0.08	nd	0.08
K_2O	1.57	1.59	1.43	1.93	1.21	11.13	7.56	11.38	11.21	1.30	8.55	0.52
CaO	8.92	8.78	5.66	6.98	9.12	21.22	14.90	17.96	24.80	24.13	13.46	9.09
MnO	1.29	1.36	1.60	1.20	1.08	1.00	1.04	1.37	nd	0.95	nd	0.34
Fe_2O_3	0.13	0.13	0.22	0.26	0.16	0.24	0.31	0.28	0.48	0.58	nd	0.19
NBO	0.59	0.59	0.53	0.57	0.54	0.89	0.72	0.86	0.85	0.63	0.68	0.50
ΔG_0 (kcal/mol)	-4.95	-4.87	-4.48	-4.92	-3.96	-11.74	-7.42	-11.56	-11.15	-5.22	-7.24	-4.08
ALT (µm)	0.7	0.75	0.6	0.65	0.7	3.8	2.75	3.7	4.6	1.2	2.25	0.7

Table 9-3: molar compositions, non-bridging oxygen (NBO) bond fraction, ΔG_0 and average layer thickness (ALT) for five corroded Raqqa glasses from the present study and seven glasses from published studies. [a] Cox and Ford[15]; [b] Newton, 1972[9]; [c] Cox and Ford[16]; [d] Cox and Ford[6]; [e] Janssens et al[17].

All images were scanned and layers measured digitally with image processing software. Averages of layer thickness were taken from five separate layers. Because the uncertainty in the measuring process is prone to several sources of inaccuracy, cumulative error bars have been added to the data. Layer thickness was also measured in the corrosion crusts of fragments TZ143 and TF208 as 0.65±0.1 and 0.7±0.15 respectively. Compositions were converted to molar percentages and the total fraction of non-bridging oxygen bonds in the structure calculated. These values are reported for published glasses along with the relevant publication sources in Table 9-3.

9.7.2 The relationship between glass stability and layer thickness

Calculated NBO values for corroded Raqqa and published layered glasses correlate linearly to calculated free energy of hydration within upper and lower limits established by Jantzen and Plodinec for a range of natural, medieval and nuclear waste glasses (Figure 9-22). The thermodynamic stability is therefore seen to decrease linearly as the fraction of non-bridging oxygen bonds increases. Figure 9-23 is a plot of NBO fraction against average layer thickness. The latter is seen to increase linearly with increasing fraction of non-bridging oxygen bonds. As a result of this relationship, the layer thickness correlates to the SiO_2 content (Figure 9-24) with an R^2 linear correlation coefficient of 0.93, and subsequently to the $RO+R_2O$ content of the glasses involved (Figure 9-25) with an R^2 value of 0.94, as this corresponds closely to the remainder of the composition (excluding Al, Fe, P, S and Cl). The y-axis intercept of the trendline in Figure 9-24 suggests an approximate value of 71.8 mol% SiO_2 as the upper limit for layer formation. Given that all five layered Raqqa crusts have between 67 and 70 mol% SiO_2 contents, El-Shamy's reported experimental upper limit of ~66 mol% SiO_2 for crust formation should be increased in the context of long-term corrosion of buried glasses.

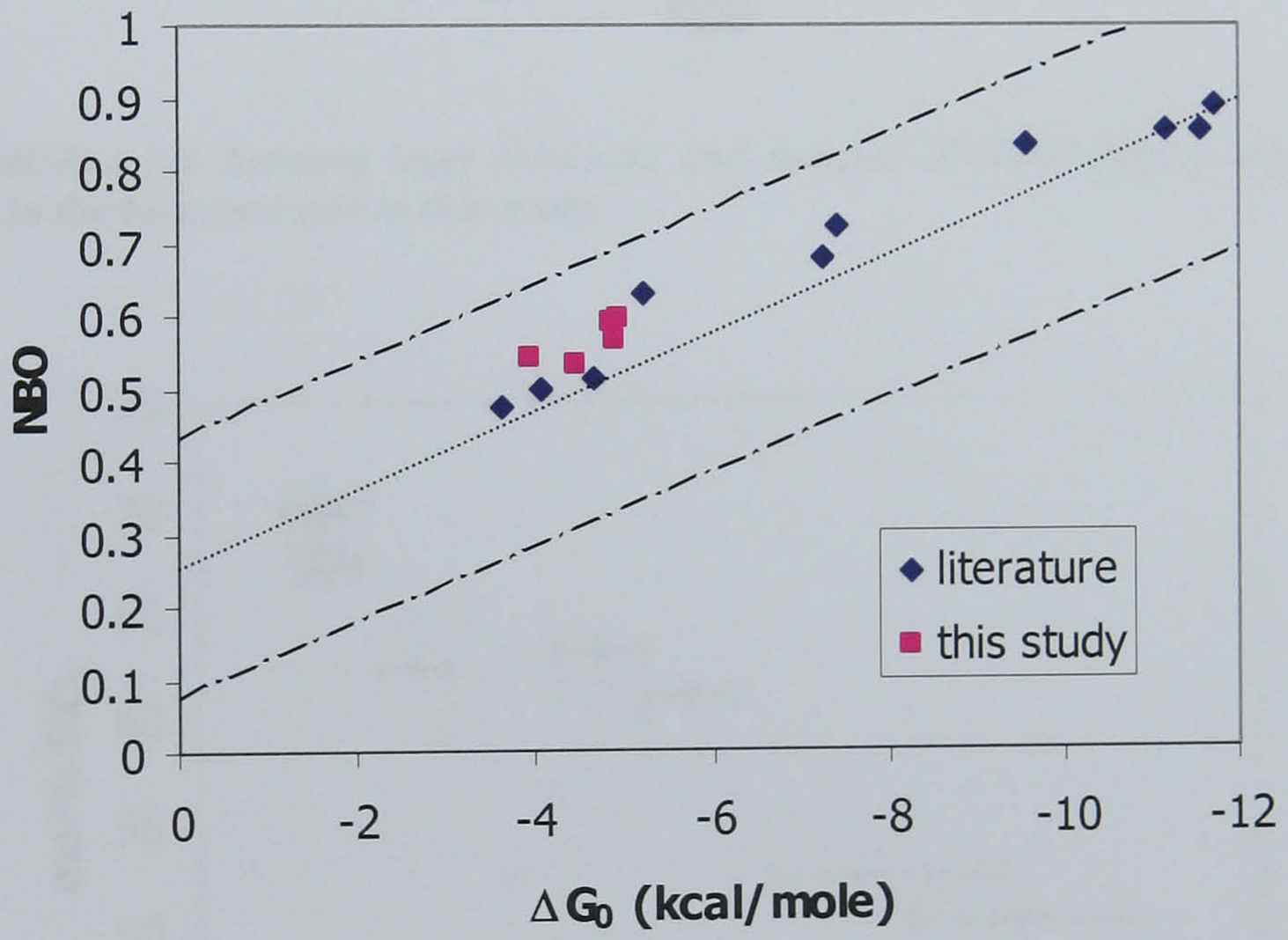


Figure 9-22: relationship between the calculated free energy of hydration and the number of non-bridging oxygen bonds for crusted glasses in the literature and in this study. The dashed lines correspond to the limits of correlation found by Jantzen and Plodinec[14].

The above observations have implications on the formation of lamellar corrosion crusts. As a linear relationship is observed between the molar concentration of leaching species and layer thickness, it supports the conclusion that the concentration gradients in the gradient zone in the corrosion reaction and the subsequent width of the gel layer influence the quantity of glass that is dissolved before dissolution comes to a temporary halt. The y-axis intercept of the trendline in Figure 9-25 suggests an approximate lower limit of $RO+R_2O$ content of 25.8mol% for

periodic layered corrosion. It can be extrapolated from the above data that, for glasses containing less than this amount, the gradient at the reaction boundary will not provide a chemical driving force strong enough to temporarily stop silica dissolution and recondensation, and thus a continuous crust will be favoured.

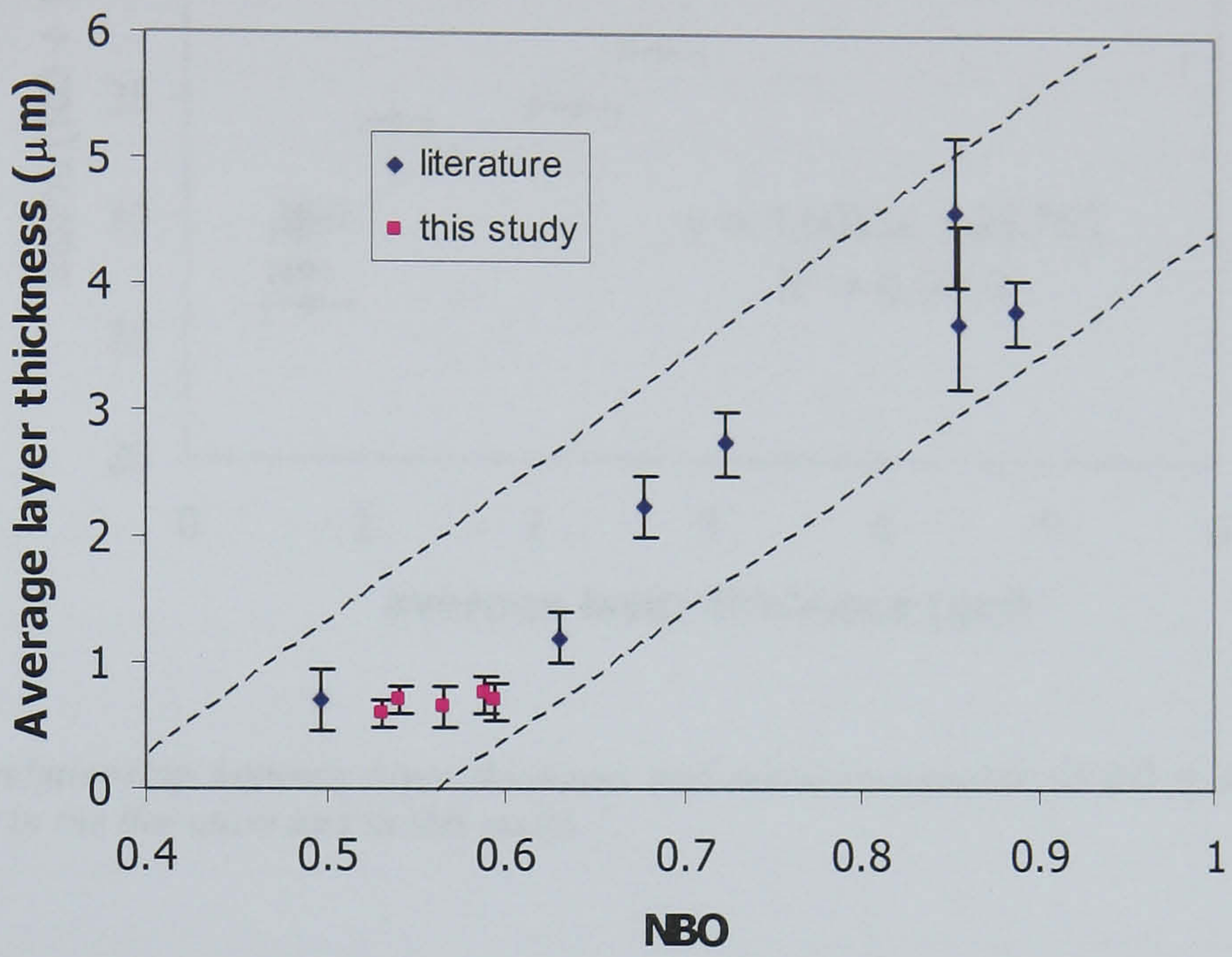


Figure 9-23: relationship between layer thickness and number of non-bridging oxygen bonds for crusted glasses in the literature and in this study.

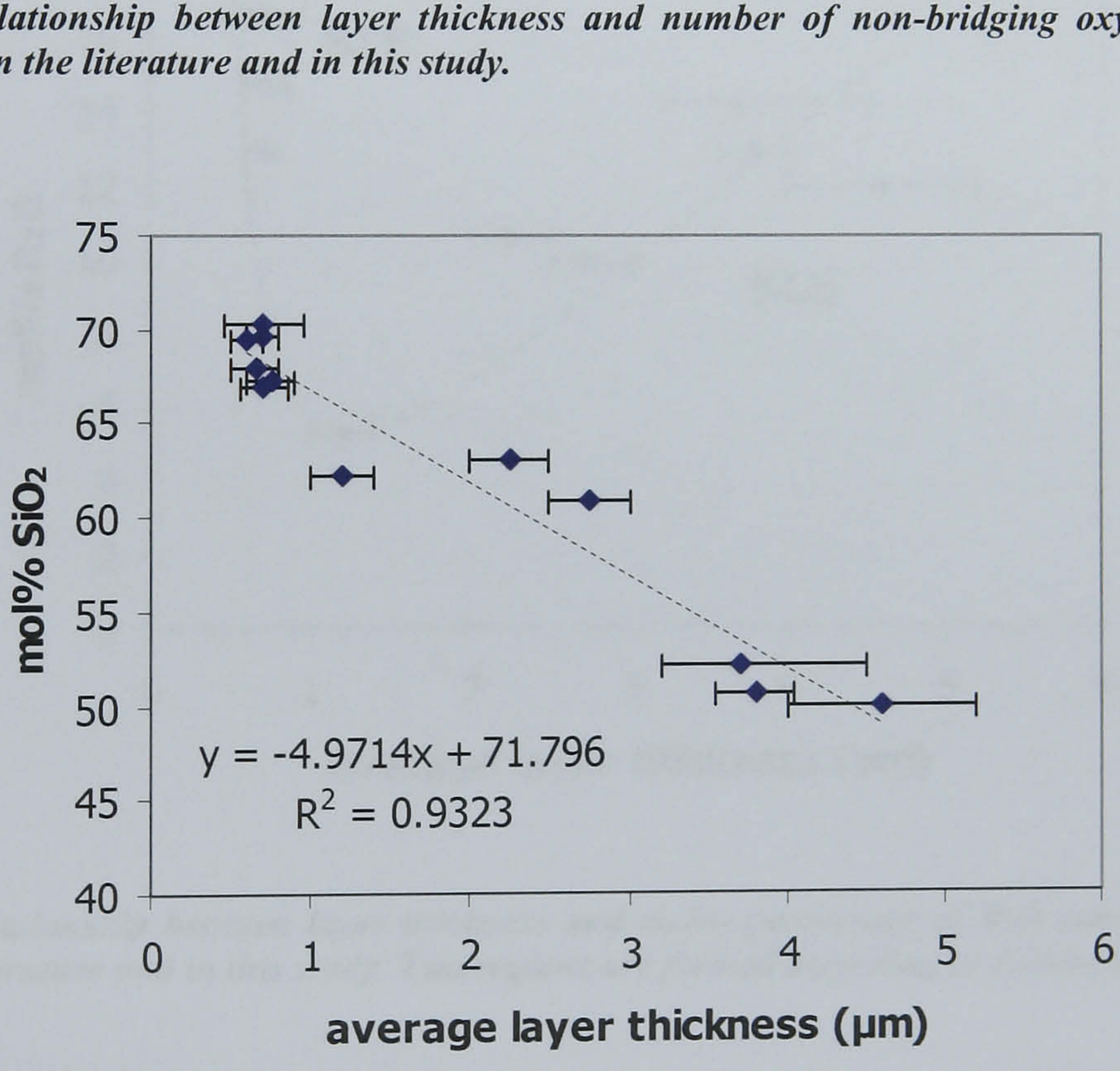


Figure 9-24: relationship between layer thickness and molar percentage of SiO_2 for crusted glasses in the literature and in this study.

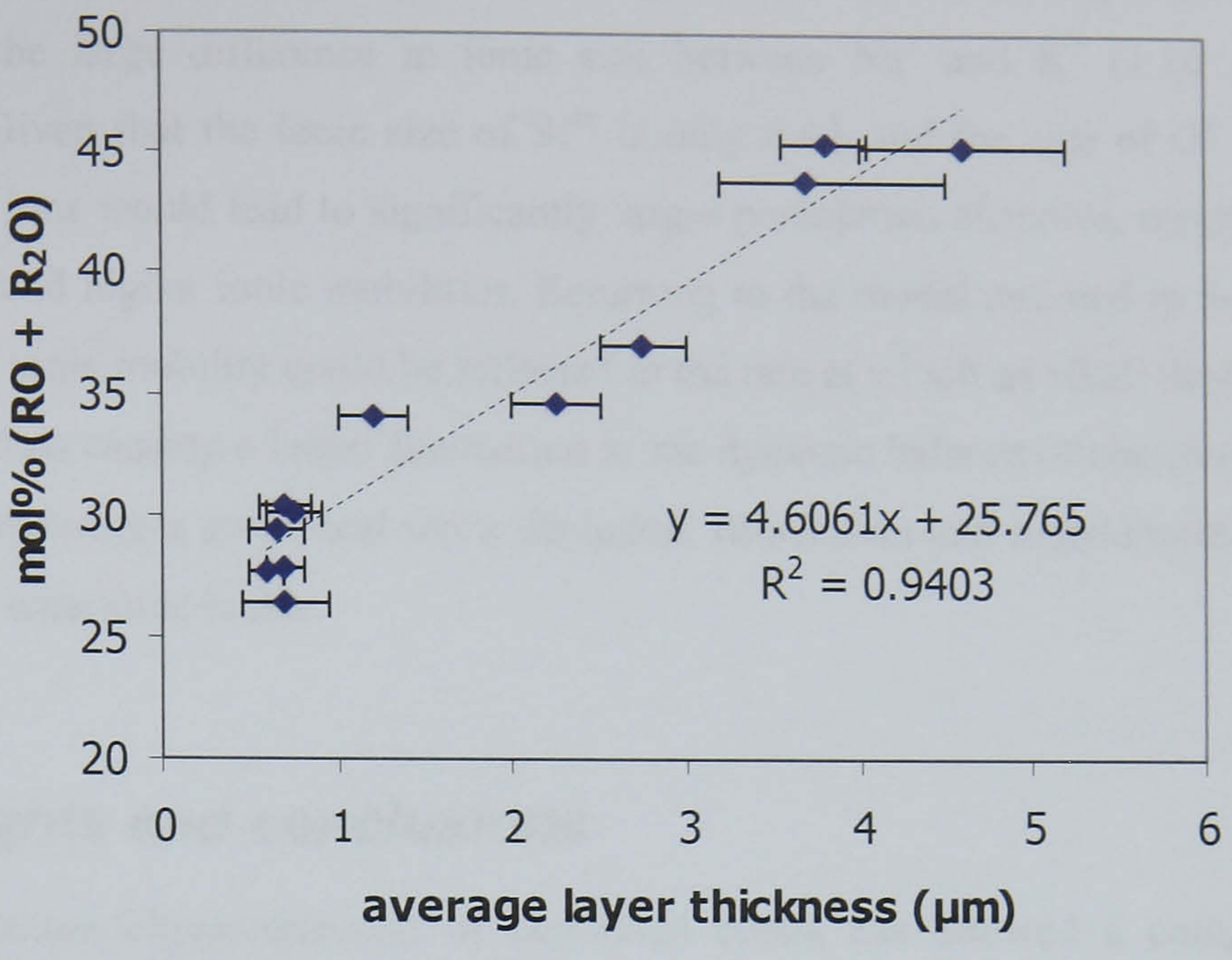


Figure 9-25: relationship between layer thickness and molar percentage of RO + R_2O content for crusted glasses in the literature and in this study.

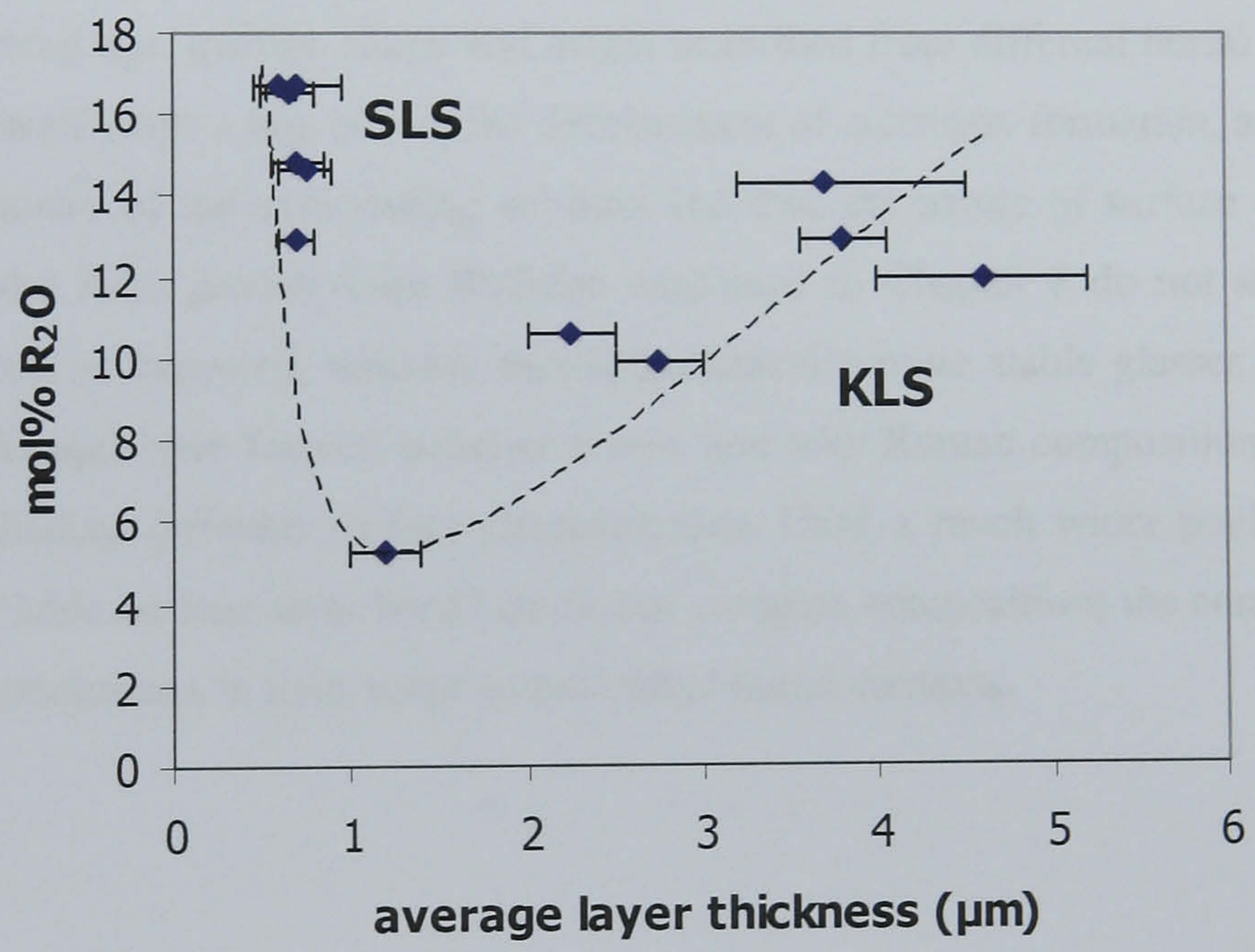


Figure 9-26: relationship between layer thickness and molar percentage of R_2O content for crusted glasses in the literature and in this study. Two regions are formed according to dominant alkali type.

As the linear relationship has been found valid for layer thickness against RO+R_2O content, which is considered as a single quantity, it does not take into account the observed differences in durability between KLS and SLS glasses, in other words the different impact that the dominant alkali ion has on layer formation, and does not take into account the mixed alkali effect. This is partly resolved in a plot of average layer thickness against R_2O content, shown in Figure 9-26. SLS glasses tend to form corrosion layers approximately 1µm thick or less,

whereas for KLS glasses single layers over 5μm thick have been reported. This can be explained by the large difference in ionic size between Na^+ and K^+ (1.16 Å and 1.52Å respectively). Given that the ionic size of Si^{4+} is only 0.4Å and the size of O^{2-} is 1.26Å, the leaching of K^+ ions would lead to significantly larger percolation channels, resulting in a more open structure and higher ionic mobilities. Returning to the model outlined in Section 9.6, the implications of ionic mobility could be reflected in the rate at which an alkali depletion gradient is established, thus causing a larger fluctuation in the dynamic balance of chemical forces at the interface and requiring a great deal more depletion, dissolution and recondensation before the expected layer-separating hiatus.

9.8 Thoughts and conclusions

The high-resolution characterisation of laminated crusts has allowed a composition-based approach to be developed as an explanation for the formation of periodically layered glass corrosion in long-term burial environments. However, given the highly complex chemical nature of the glasses examined and the vast number of variables acting upon them, it is by no means straightforward to accurately compare the nature of corrosion phenomena observed on glasses of differing age, quality, shape and origin unearthed from different burial contexts. The burial context itself plays a key role in the development of corrosion formation, as it influences the electrochemistry of the surrounding solution and thus the nature of surface deposits. This may explain why KLS glasses from Ballidon examined in Chapter 8 do not show a clearly lamellar structure as expected, whereas thermodynamically more stable glasses from a desert environment (Raqqa) have formed lamellar crusts, and why Roman compositions from Raqqa and Ballidon display different surface characteristics. Until a much wider pool of published research is available on long-term burial studies of complex compositions the complexity of the subject limits conclusions in their scope to individual burial contexts.

9.9 Bibliography

1. Grambow, B., *Geochemical Approach to Glass Dissolution*, in *Corrosion of Glass, Ceramics and Ceramic Superconductors*, D.E. Clark and B.K. Zoitos, Editors. 1992, Noyes Publications: New Jersey. p. 124-152.

2. Doménech-Carbó, A., M.T. Doménech-Carbó, and L. Osete-Cortina, *Identification of Manganese(IV) Centers in Archaeological Glass Using Microsample Coatings Attached to Polymer Film Electrodes.* Electroanalysis, 2001. **13**(11): p. 927-935.

3. Newton, R.G. and S. Davison, *Conservation of glass*. 1989, London: Butterworth-Heinemann.

4. Deer, W.A., R.A. Howie, and J. Zussman, *An Introduction to the Rock Forming Minerals*. 1966, London: Longman.

5. Cox, G.A. and A.-R. Khooli, *The Natural Corrosion of Glass: The Formation and Structure of Plugs.* Glass Technology, 1992. **33**(2): p. 60-62.

6. Cox, G.A. and B.A. Ford, *The Influence of Inhomogeneities in Glass on the Morphology of the Weathering Layers.* Glass Technology, 1989. **30**(3): p. 113-114.

7. Alts, T. and P. Strehlow, *Frozen Deformations, Frozen Stresses, and Structure-Induced Na Distributions in Sodium-Silicate Glasses.* Journal of Thermal Stresses, 1984. **7**: p. 317-359.

8. Lampropoulos, V., A. Kalagri, and L. Valsamis. *An Attempt to Face the Problem of Iridescence on Archaeological Glass*. in *Hyalos Vitrum Glass: History, Technology and Conservation of Glass and Vitreous Materials in the Hellenic World*. 2002. Athens: Glasnet Publications. p. 311-316.

9. Newton, R.G., *Stereoscan Views of Weathering Layers on a Piece of Ancient Glass.* Glass Technology, 1972. **13**(2): p. 54-56.

10. Newton, R.G., *The Durability of Glass - A Review.* Glass Technology, 1985. **26**(1): p. 21-38.

11. Gardner, A., *pers. comm.* 2003.

12. Doremus, R.H., et al., *Reaction of Water With Glass: Influence of a Transformed Surface Layer.* Journal of Materials Science, 1983. **18**: p. 612-622.

13. Grambow, B. and R. Müller, *First-Order Dissolution Rate Law and the Role of Surface Layers in Glass Performance Assessment.* Journal of Nuclear Materials, 2001. **298**: p. 112-124.

14. Jantzen, C.M. and M.J. Plodinec, *Thermodynamic Model of Natural, Medieval and Nuclear Waste Glass Durability.* Journal of Non-Crystalline Solids, 1984. **67**: p. 207-223.

15. Cox, G.A. and B.A. Ford, *The Long-Term Corrosion of Glass by Groundwater.* Journal of Materials Science, 1993. **28**: p. 5637-5647.

16. Cox, G.A. and B.A. Ford, *The Corrosion of Glass on the Sea Bed.* Journal of Materials Science, 1989. **24**: p. 3146-3153.

17. Janssens, K., et al., *Corrosion Phenomena in Electron, Proton and Synchroton X-ray Microprobe Analysis of Roman Glass from Qumran, Jordan.* Nuclear Instruments and Methods in Physics Research B, 1996. **109/110**: p. 690-695.

Chapter 10

Conclusions and suggestions for further work

A multi-technique approach, including FE-SEM-EDXA, SIM, EPMA, ICP-AES, IRRS, DSC, XRD and DTA/TGA, has been used throughout the present study for the analysis of ancient and modern replica glasses from archaeological burial contexts. The novel application of high-resolution FE-SEM and SIM to archaeometric studies has proved a valuable tool for the characterisation of corrosion mechanisms on buried glasses to a sub-micron level.

Compositional studies of over 250 glass fragments excavated from three 8th-12th century AD glassmaking contexts at the ancient industrial site of Raqqa, Syria, have shown that, of the major groupings to emerge, types 1 and 3 represent glass traditions that adhere to specific recipes and controlled manufacturing techniques. Characterisation and interpretation of such a large quantity of glass and glassmaking remains from a single archaeological site has not been attempted before. The 'late Roman' type 3 LMG composition is replaced almost entirely by the typical Islamic type 1 HMG by the 11th century AD. The transition indicates the re-introduction of a plant ash based recipe and the use of crushed quartz as opposed to a natron based recipe mixed with sand. The *Salicornia* ash collected from Raqqa was not of the expected composition to form type 1 glass, and therefore is not indicative of a local plant ash source.

Replica glasses mirroring the major LMG and HMG compositional types have highlighted differences in T_g, viscosity and fining properties, engendering the idea that technological considerations related to the glassmaking process could have contributed to the aforementioned compositional shift. Three mathematical methods were used for viscosity calculations and proved in good enough agreement with each other to allow for the high temperature modelling of LMG and HMG properties.

The characteristic compositional scattering that forms type 4 supports the hypothesis that the group is the result of the implementation of new raw materials that took place at a time of technological change. Experimentation with colour related to the re-introduction of manganese to the glassmaking process is suggested from the discussion of compositional results from

Raqqa. The possible influence of the Islamic chemist Jabir Ibn-Haiyan on glassmaking at Raqqa is speculated on the basis of the clear differences in manganese recorded between contemporary LMG and HMG compositional groups.

The characterisation of primary production waste from 12th century Tell Belor at Raqqa has shed light on melting temperatures and length of exposure to high temperature regimes, which relate to glassmaking processes there. Microscopic inspection of casting surfaces and furnace debris, backed up by experimental casts, has highlighted the clear microstructural differences that exist between them. This is significant as differences are not clearly distinguishable by eye. The high temperature interactions observed at glass-furnace interfaces are accompanied by the nucleation and growth of wollastonite and diopside crystals, which have allowed the minimum time of exposure to the tank furnace heating cycle to be calculated by applying an experimental model of wollastonite growth in SLS glasses.

The multi-technique evaluation of corrosion characteristics has been applied, firstly to glasses from Ballidon and subsequently to glasses from Raqqa, so that a methodology for the micron-scale characterisation of corrosion crusts could be established. Glasses from Ballidon buried for 1, 9 and 32 years have proved a valuable tool for assessing the validity of IRRS for the analysis of corroded glass surfaces. The mock Roman SLS Ballidon composition, B1, exhibits type II surface morphology, whereas the KLS glasses, B2 and B3, show type IV surfaces with compositionally banded corrosion crusts.

Raqqa glasses have been found to exhibit type IV to type V surface morphologies. The corrosion crusts of Raqqa glasses are not macroscopically homogeneous in composition or structure and have been influenced by composition, sample morphology and production history. Type 1 and type 2 both exhibit extensive lamellar corrosion crusts whereas type 3 shows less degradation with compositional banding but no discernable layering in the crust. All the glasses inspected that contain manganese exhibit manganese-rich dark outer crusts. Type 1 and type 2 individual layer thickness has been measured in the order of 0.6-0.8μm. A linear relationship has been found between individual layer thickness of KLS and SLS glasses and molar SiO_2 content (and correspondingly between layer thickness and molar $RO+R_2O$ content), which suggests the influence of the leaching R^+ and R^{2+} cations in establishing the layer thickness. It has been argued that the thickness of single weathering layers is related to composition. This has not been observed before.

The investigation of an undisturbed corner of a corroded type 1 Raqqa glass has unveiled the active reaction front. The microstructure of the weathering crust consists of a highly porous conglomeration of granules 50-100nm in diameter. The gel layer situated at the interface

between the hydrated glass and the condensed species has been seen to be essentially glassy in nature. A model for the periodic formation of lamellar corrosion has thus been proposed, based on the influence of increasing alkali on gel layer growth and recondensation rate. A hiatus in the precipitation of ferro-alumino-silicate species from the gel layer has been put forward as the reason behind periodic layer formation. A dynamic imbalance between the gel layer thickness and the ion exchange front, caused by excess alkali content, is implied as the necessary condition for the periodic reaction.

10.1 Suggestions for further work

Due to the variety of avenues pursued in this study, there is much scope for further work. The three points that I think lie closest to the aims of the present work and therefore deserve most attention are outlined below.

10.1.1 Trace element analysis

The chemical characterisation of Raqqa glasses, now that distinct groupings have emerged from the sizeable database, would benefit enormously from trace element analysis. The characterisation down to trace element level of a selection of Raqqa glasses is hoped to confirm the compositional groupings, and to allow a more in-depth look at which elements can be attributed the different raw ingredients involved. Prohibitively high operational costs prevented the use of LA-ICP-MS facilities located at the Natural History Museum, London, during this project although the technique remains the most promising step towards a more complete classification of glass from Raqqa.

10.1.2 FIB-SIMS issues

The characterisation of individual weathering layers using FIB-SIMS did not prove possible. Depth profiling with the micro-machining possibilities that the technique has to offer was not found to yield reproducible data because the FEI T200 used in this project has not been designed to contemporaneously deal with an add-on SIMS detector and an add-on charge neutralizer for the analysis of rough, non-conductive surfaces. Further work with fine-tuning of the FIB-SIMS should be geared towards providing a methodology for analytical data reproducibility.

It is also suggested that further SIMS characterisation work be coupled with the Atomika 6500 SIMS apparatus in the Surface Analysis Laboratory in the Materials Department (Imperial College). An ongoing project with the Atomika 6500 is seeking to characterise the leaching of alkali in the outer 20-50nm of chemically unstable glass surfaces and thus a methodology for the quantitative evaluation of glass surfaces using SIMS is concurrently under development.

10.1.3 Structural characterisation of glass corrosion

Now that a gel layer of sub-micron proportions can be visualised with high-resolution microscopy, its characterisation becomes a major aim. Infrared techniques can be used to assess the structure of the gel, and possibly of single particulates, in order to better understand the chemistry of the reaction front. The presence and activity of H^+ and Si-OH, expressed for example in terms of a plot of intensity or concentration versus distance across the interface, would ultimately allow the more detailed reconstruction of the reaction front and the modelling of pH across it. The Spectratech IRRS facility in the Materials Department (Imperial College) can be adapted for use with optical lenses to limit data acquisition to tiny areas so that the reaction front may be structurally characterised.

Open questions remain regarding the nature of precipitated compounds from the gel layer. The nanogranular structure of recondensed species suggests a possible overlap with sol-gel technology; uniform silica particles can be obtained at room temperature from the condensation of tetraethoxy silane (TEOS) to form hydroxylated monomers[1] with the general reaction:

$$Si(OR)_4 + 2H_2O \Rightarrow (OH)_2 - Si - (OR)_2 \qquad [10\text{-}1]$$

Provided the gel layer is hydrated, water may be used for the condensation of silicate monomers in a similar way. The assessment of condensation rates and silica saturation conditions in the gel layer are thus important considerations. A series of properly annealed experimental replica glasses, buried and monitored under known conditions, could permit the characterisation of the reaction front *in situ*, and thus the assessment of how the gel layer develops with time for different compositions in the same burial context.

10.2 Bibliography

1. Garofalini, S.H., *Simulation of the Sol-Gel Process*, in *Sol-Gel Technology for Thin Films, Fibers, Preforms, Electronics and Specialty Shapes*, L.C. Klein, Editor. 1988, Noyes: New Jersey. p. 16-49.

Appendix 1

Full compositional results are presented overleaf for all Raqqa glasses analysed in this thesis. Samples from Tell Zujaj and Tell Fukhkhar have been analysed by EPMA and those from Tell Belor by SEM-EDXA. The corroded Raqqa glasses studied in Chapter 9 are highlighted in red.

Samples are labelled according to site, type, colour and hue, according to the lists below. Chemical compositions are given in wt% oxide. *nd* denotes not detected. Cr_2O_3, Sb_2O_3 and NiO were searched for by EPMA but were not detected. SiO_2 contents for EPMA data have been normalised to 100% (shown as SiO_2*) to account for the 6% spread in analytical totals. EDXA results are normalised compositions.

Site colour code

Tell Zujaj	
Tell Fukhkhar	
Tell Belor	

Sample types

1	vessel rim/handle/base
2	flask/bottle/jug/beaker/ewer
3	other vessel fragments
4	cast glass
5	window glass
6	goblet
7	mould blown bowl
8	bracelet/bangle
9	furnace glass
10	production waste
11	frit

Glass colours

A	aqua
B	blue
BR	brown
C	colourless
G	green
GY	grey
P	purple
R	red
T	turquiose
Y	yellow

Hues

d-	dark
p-	pale
O-	opaque
aG	amber (green)
eG	emerald (green)
oG	olive (green)
cB	cobalt (blue)

#	Type	Colour	Na_2O	MgO	Al_2O_3	SiO_2*	P_2O_5	SO_3	Cl	K_2O	CaO	TiO_2	MnO	Fe_2O_3	BaO	PbO	Other oxides
76	1	C	13.73	3.62	1.11	67.23	0.23	0.15	0.93	2.48	8.36	0.06	1.53	0.36	nd	0.09	
77	9	P	15.18	2.47	1.90	67.87	0.39	0.21	0.74	2.12	5.37	0.09	2.65	0.85	0.05	nd	0.06 CoO
78	10	pG	13.55	3.57	1.12	67.47	0.26	0.12	0.96	2.51	8.23	0.06	1.62	0.34	0.06	0.05	
79	10	pG	15.61	2.49	1.62	68.86	0.34	0.24	0.80	2.22	5.24	0.07	1.88	0.58	nd	nd	
80	10	pG	15.81	2.50	1.58	68.14	0.39	0.23	0.89	2.31	5.35	0.09	1.93	0.62	0.05	0.05	
81	10	P	13.38	3.45	1.13	67.41	0.32	0.12	0.87	2.43	9.04	0.06	1.29	0.37	nd	nd	
82	9	Y/G	13.82	3.23	1.01	66.07	0.30	0.15	0.89	2.58	9.42	0.06	1.92	0.43	0.05	0.05	
83	10	C	13.55	3.59	1.14	67.77	0.27	0.15	0.79	2.52	8.10	0.06	0.87	0.97	0.05	nd	0.07 CuO; 0.08 ZnO
84	10	G	13.36	4.22	1.97	64.82	0.33	0.18	0.69	2.34	9.29	0.12	1.60	0.90	nd	0.09	0.05 ZnO
85	10	A	14.54	0.57	3.24	70.00	0.12	0.11	0.83	0.52	9.49	0.05	nd	0.37	0.05	0.07	
86	4	T	14.82	1.06	2.39	69.29	0.21	0.12	0.81	1.04	7.62	0.07	0.15	0.56	0.05	0.18	1.43 CuO; 0.06 ZnO; 0.10 SnO
87	9	G	12.77	4.75	3.47	63.34	0.31	0.15	0.57	2.97	8.79	0.18	0.75	1.69	0.06	nd	0.06 ZnO
88	2	pG	14.77	4.53	3.03	62.34	0.29	0.30	0.78	1.87	8.27	0.13	2.34	1.17	0.05	nd	0.06 CoO
89	2	A	12.75	0.74	3.19	72.46	0.07	nd	0.89	0.58	8.68	0.06	nd	0.44	nd	nd	
90	2	C	12.85	5.32	1.06	70.92	0.06	0.28	0.63	2.11	6.05	nd	0.24	0.26	nd	0.06	
91	6	pG	13.16	6.33	1.26	69.51	0.13	0.26	0.48	3.03	4.70	0.05	0.59	0.33	0.05	nd	
92	6	A	13.96	0.60	3.26	70.74	0.09	nd	0.83	0.59	9.36	0.06	nd	0.35	0.06	nd	
93	6	B	14.61	8.05	1.31	65.10	0.14	0.32	0.47	3.12	5.88	0.07	0.27	0.42	nd	0.07	
94	6	pG	17.10	7.57	1.09	64.02	0.12	0.27	0.70	3.31	4.46	nd	0.88	0.34	nd	nd	0.06 As_2O_3
95	6	pG	13.74	0.57	3.38	68.81	0.17	0.18	0.69	0.50	11.32	0.07	nd	0.32	0.05	nd	
102	2	pG	14.63	4.29	2.78	64.50	0.29	0.18	0.64	2.63	7.75	0.13	0.89	0.95	nd	0.11	0.08 CuO
104	3	pG	13.66	4.41	2.96	65.19	0.36	0.21	0.59	3.99	6.79	0.13	0.30	1.16	0.05	nd	0.05 CoO
104*	3	G	13.72	4.10	2.39	67.44	0.32	0.21	0.50	4.20	5.89	0.11	nd	0.88	0.05	0.08	
105	7	pG	13.38	4.50	2.08	69.10	0.26	0.17	0.52	3.20	5.65	0.10	nd	0.85	nd	0.06	
106	7	pG	13.41	4.54	2.08	69.04	0.27	0.18	0.53	3.25	5.61	0.07	0.05	0.79	nd	0.06	
107	7	pG	13.16	5.75	2.21	68.30	0.26	0.24	0.40	2.75	5.73	0.13	nd	0.91	nd	nd	
108	1	A	13.64	0.52	3.22	70.66	0.15	0.06	0.86	0.47	9.86	0.05	nd	0.37	0.05	nd	
109	1	pG	13.40	0.47	3.09	72.97	0.07	0.06	0.78	0.45	8.18	0.06	nd	0.29	0.05	nd	
110	1	A	12.57	0.50	3.14	72.04	0.09	nd	0.74	0.48	9.75	0.05	nd	0.38	0.05	0.08	
104A	1	pG	12.74	5.10	1.57	70.87	0.12	0.21	0.41	3.42	4.52	0.06	0.29	0.51	nd	0.05	
105B	1	BR	15.05	0.97	3.42	67.19	0.22	nd	0.80	0.73	10.90	0.07	nd	0.47	0.06	0.05	
105C	1	pG	14.17	1.98	2.87	69.56	0.12	0.08	0.59	1.28	8.51	0.05	0.09	0.48	0.06	0.09	

#	Type	Colour	Na_2O	MgO	Al_2O_3	SiO_2*	P_2O_5	SO_3	Cl	K_2O	CaO	TiO_2	MnO	Fe_2O_3	BaO	PbO	Other oxides
106A	1	pG	14.73	6.20	1.51	68.60	0.12	0.21	0.61	2.82	4.32	0.07	0.18	0.47	0.05	nd	0.05 As_2O_3
107A	1	pG	14.51	6.24	1.53	68.78	0.11	0.21	0.59	2.75	4.35	0.07	0.21	0.49	nd	0.06	
108A	1	pG	13.16	0.50	3.14	71.76	0.07	0.18	0.67	0.46	9.49	nd	nd	0.33	0.05	nd	
109A	1	pG	13.96	4.52	1.70	69.15	0.16	0.12	0.68	3.09	4.41	0.07	1.30	0.60	0.05	0.07	
110A	1	pG	12.92	0.44	3.03	73.63	0.06	nd	0.72	0.44	8.16	0.05	nd	0.31	0.05	nd	
111A	1	oG	14.62	4.75	2.58	64.06	0.22	0.21	0.50	2.59	7.31	0.11	1.97	0.89	0.06	nd	
112A	1	pG	12.76	0.68	3.21	73.16	0.05	nd	0.82	0.58	8.17	0.05	nd	0.40	0.05	nd	
113A	7	pG	14.27	4.07	2.57	66.37	0.30	0.24	0.46	3.53	6.35	0.11	0.40	1.11	nd	nd	
114A	3	pG	13.35	0.78	3.51	72.96	nd	0.06	0.84	0.52	7.12	0.07	nd	0.45	0.06	0.13	
115	3	oG	15.72	3.74	3.64	64.78	0.25	0.20	0.56	3.13	6.74	0.11	nd	0.95	nd	nd	
116	3	G	14.47	3.40	1.40	68.22	0.26	0.23	0.73	2.35	6.62	0.08	1.36	0.76	0.06	nd	
117	7	pG	14.77	4.15	1.92	68.06	0.29	0.23	0.60	3.82	5.00	0.07	0.21	0.77	0.05	nd	
118	3	dB	12.80	3.11	1.85	69.59	0.17	nd	0.80	1.59	5.11	0.05	1.10	2.95	0.05	nd	
119	7	pG	14.16	4.33	1.81	69.28	0.24	0.17	0.57	3.65	4.88	0.07	0.05	0.67	nd	0.05	
120	7	pG	13.34	5.03	2.73	67.09	0.22	0.18	0.49	3.15	6.27	0.13	0.10	1.04	0.05	nd	0.05 As_2O_3
121	3	pG	15.08	0.65	3.29	69.70	0.06	0.11	0.72	0.47	9.45	0.06	nd	0.32	0.06	nd	
122	1	pG	13.13	3.51	2.57	69.70	0.28	0.08	0.66	3.13	5.52	0.13	0.14	1.06	nd	nd	
123	1	pG	12.67	5.48	1.42	71.77	0.11	0.09	0.58	2.60	4.15	0.06	0.53	0.45	nd	nd	
124	1	oG	14.64	3.75	3.88	65.27	0.34	0.17	0.50	3.12	6.47	0.15	0.15	1.42	0.05	nd	
125	1	pG	15.30	0.58	3.17	71.10	0.09	0.12	0.77	0.51	7.77	0.06	nd	0.32	0.06	nd	
126	1	pG	13.07	4.16	2.06	70.72	0.19	0.11	0.65	2.20	4.49	0.08	1.04	0.87	0.06	0.07	
127	1	pG	14.53	6.53	1.47	67.53	0.09	0.24	0.47	2.92	5.05	nd	0.54	0.45	0.05	nd	0.05 As_2O_3
128	1	pG	14.74	0.91	3.39	69.34	0.17	nd	0.41	0.73	9.51	0.07	nd	0.55	0.05	nd	
129	1	pG	13.76	5.32	2.27	67.32	0.22	0.18	0.52	2.83	6.14	0.11	0.23	0.91	nd	nd	
130	3	C	13.51	3.00	1.05	69.02	0.21	0.11	0.84	2.49	7.48	0.05	1.75	0.30	0.05	nd	0.05 As_2O_3
131	3	pB	12.70	3.24	2.86	68.62	0.13	0.05	0.76	1.81	6.23	0.12	0.63	2.19	nd	0.10	0.10 CoO; 0.37 CuO; 0.06 ZnO
132	3	dB	12.54	3.04	1.87	69.56	0.16	nd	0.77	1.59	5.18	0.07	1.05	3.07	0.05	0.18	0.15 CoO; 0.59 CuO; 0.06 ZnO
133	3	B	13.62	3.04	3.21	66.91	0.17	0.09	0.74	2.55	6.60	0.09	0.09	1.91	0.07	nd	0.21 CoO; 0.33 CuO; 0.29 ZnO
134	3	dG	13.55	4.60	2.77	65.68	0.23	0.15	0.69	2.65	5.84	0.08	2.59	0.99	0.11	nd	
135	1	pG	14.76	4.22	2.69	64.40	0.24	0.12	0.51	2.52	8.45	0.10	0.84	0.98	0.06	0.08	
136	1	C	14.08	3.69	0.87	67.52	0.25	0.14	0.87	2.40	8.40	nd	1.34	0.28	0.05	nd	
137	1	pG	14.24	4.61	5.32	59.53	0.34	0.26	0.56	3.35	8.27	0.20	0.83	2.29	0.06	nd	

#	Type	Colour	Na_2O	MgO	Al_2O_3	SiO_2*	P_2O_5	SO_3	Cl	K_2O	CaO	TiO_2	MnO	Fe_2O_3	BaO	PbO	Other oxides
138	1	pG	14.46	0.59	3.11	69.75	0.10	0.15	0.68	0.57	10.04	nd	nd	0.37	0.05	nd	
139	1	A	13.66	0.49	3.02	73.06	0.05	0.06	0.80	0.42	7.73	0.05	nd	0.34	0.05	0.12	0.07 ZnO
140	1	pG	15.43	0.45	2.88	71.13	0.10	0.17	0.62	0.44	8.32	nd	nd	0.25	0.06	nd	
141	1	pG	14.30	4.19	2.63	65.72	0.30	0.24	0.48	3.66	6.56	0.13	0.44	1.14	nd	0.05	
142	1	pG	12.11	3.04	1.16	69.76	0.21	0.05	0.81	2.30	7.94	0.06	2.07	0.43	0.05	nd	
143	1	pG	14.92	3.11	1.56	67.48	0.29	0.29	0.60	3.00	6.47	0.09	1.41	0.69	0.06	nd	
144	1	pG	12.43	0.77	3.13	73.66	0.18	0.06	0.72	0.55	7.87	0.05	nd	0.40	0.05	0.06	
145	1	C	15.25	0.53	3.12	71.17	0.08	0.06	0.89	0.52	7.86	nd	nd	0.33	0.05	nd	0.05 ZnO
146	1	A	13.70	0.51	3.08	71.12	0.13	0.24	0.61	0.47	9.68	nd	nd	0.29	nd	nd	
147	1	pP	13.32	3.30	0.88	68.78	0.24	0.14	0.82	2.54	8.12	0.06	1.43	0.31	nd	nd	
148	1	pG	12.91	0.54	3.15	72.58	0.07	0.09	0.53	0.56	8.81	0.08	nd	0.53	0.05	nd	
149	1	C	12.88	0.48	3.12	71.84	0.09	0.18	0.67	0.46	9.71	nd	nd	0.31	0.05	0.07	
150	1	pG	13.86	0.54	2.66	73.23	nd	0.06	0.72	0.47	7.75	0.05	nd	0.43	0.06	nd	
151	1	pG	13.11	4.58	1.55	71.02	0.16	0.12	0.69	2.97	4.22	0.07	0.75	0.50	0.05	0.06	
152	1	pG	13.45	1.43	2.95	70.06	0.14	nd	0.60	1.06	9.31	0.06	0.17	0.60	0.05	nd	0.05 CoO
153	1	C	13.95	5.03	1.77	68.21	0.20	0.17	0.66	2.99	4.55	0.09	1.62	0.63	0.06	nd	
154	1	pG	13.60	1.41	2.99	70.46	0.12	0.05	0.65	0.97	8.83	0.07	0.17	0.53	0.05	0.07	
155	1	pG	12.67	4.46	2.02	70.82	0.17	0.15	0.60	2.80	5.01	0.09	0.21	0.86	0.05	nd	0.07 ZnO
156	1	C	14.43	0.69	3.20	68.23	0.06	0.12	0.67	0.52	11.44	nd	nd	0.44	0.06	0.08	
157	1	A	13.21	0.48	3.18	71.92	0.10	0.12	0.68	0.49	9.32	nd	nd	0.33	0.05	nd	
158	1	pG	15.91	0.61	3.14	70.13	0.05	0.15	0.85	0.54	7.97	0.05	nd	0.37	0.06	0.10	
159	1	A	12.55	0.47	3.10	73.61	0.07	0.05	0.84	0.40	8.41	nd	nd	0.26	0.08	nd	
160	1	pG	14.54	0.61	3.21	70.48	0.12	0.09	0.80	0.61	8.84	nd	nd	0.43	0.06	0.11	0.05 CoO
161	1	pG	13.20	0.53	3.21	72.10	0.09	0.05	0.84	0.49	8.89	nd	nd	0.35	0.05	nd	
162	1	A	13.94	1.86	2.79	70.20	0.10	0.08	0.64	1.03	8.60	0.06	0.12	0.43	0.05	0.05	
163	1	pG	13.74	1.23	2.98	70.66	0.12	nd	0.54	0.86	8.77	0.07	0.15	0.65	0.06	nd	
164	1	pG	13.25	3.23	0.86	69.01	0.24	0.15	0.84	2.51	8.08	0.06	1.41	0.26	nd	nd	
165	1	pG	13.32	3.87	2.04	68.53	0.23	0.14	0.60	3.35	4.96	0.10	1.80	0.86	0.08	0.08	
166	1	A	13.45	1.34	2.83	71.11	0.11	0.05	0.62	0.84	8.90	0.07	0.07	0.42	0.06	0.11	
167	1	pG	13.40	1.32	2.97	69.94	0.10	0.05	0.49	0.88	9.79	0.07	0.15	0.52	0.05	0.21	0.05 ZnO
168	1	oG	13.73	2.32	3.53	67.31	0.28	0.09	0.53	2.30	8.27	0.12	0.13	1.21	0.06	0.12	
169	1	A	14.26	0.52	4.62	69.91	0.10	0.24	0.68	0.48	8.75	nd	0.05	0.21	0.05	nd	0.06 CuO

#	Type	Colour	Na_2O	MgO	Al_2O_3	SiO_2*	P_2O_5	SO_3	Cl	K_2O	CaO	TiO_2	MnO	Fe_2O_3	BaO	PbO	Other oxides
170	1	oG	15.01	4.28	4.24	62.03	0.39	0.15	0.65	3.38	7.63	0.19	0.19	1.71	0.06	nd	
171	1	pG	12.86	3.83	1.08	67.39	0.30	0.12	0.73	2.58	8.98	0.06	1.49	0.40	nd	nd	
172	1	oG	14.73	3.72	4.22	63.84	0.40	0.21	0.51	3.41	7.01	0.16	0.06	1.54	0.05	0.05	
173	1	oG	14.64	4.63	3.65	63.66	0.47	0.15	0.56	2.64	7.54	0.15	0.51	1.29	nd	nd	
174	1	pG	15.74	3.08	3.26	62.93	0.28	0.29	0.85	2.49	7.85	0.12	1.80	1.02	0.07	nd	0.07 CoO; 0.09 ZnO
175	1	oG	14.33	0.69	3.42	69.13	0.07	0.11	0.71	0.55	10.43	0.05	nd	0.41	0.06	nd	
176	1	C	12.83	5.51	1.14	70.40	0.09	0.25	0.67	2.04	6.40	nd	0.27	0.30	nd	nd	
177	1	pB	12.92	0.41	3.21	74.93	0.05	0.06	0.79	0.50	6.59	0.05	nd	0.32	0.05	nd	
178	1	pG	13.37	1.00	3.11	73.25	0.09	0.05	0.70	0.73	6.98	0.07	0.09	0.41	0.07	nd	
179	1	pG	13.28	0.48	3.37	72.14	0.14	nd	0.86	0.50	8.65	0.07	nd	0.32	0.06	nd	
180	1	C	14.96	0.49	3.09	70.23	0.06	0.15	0.66	0.48	9.36	0.05	nd	0.32	0.07	nd	
181	1	pG	13.41	0.68	3.45	71.58	0.09	0.08	0.83	0.53	8.77	0.05	nd	0.39	0.07	nd	
182	1	pG	15.82	3.72	1.08	64.30	0.34	0.20	0.92	2.48	9.98	0.05	0.64	0.35	0.06	nd	
183	1	A	12.38	0.48	3.28	73.39	0.05	0.06	0.83	0.58	8.54	nd	nd	0.28	nd	nd	
184	1	A	13.33	0.45	2.98	72.97	0.06	0.08	0.83	1.04	7.71	0.05	nd	0.36	0.06	nd	
185	1	A	15.72	0.61	3.38	68.58	0.06	0.14	0.83	0.51	9.57	0.05	nd	0.38	0.06	nd	
186	1	pG	14.67	6.06	1.69	67.41	0.14	0.34	0.52	3.37	3.79	0.09	1.21	0.53	0.05	nd	
187	1	C	14.24	5.56	1.76	67.04	0.16	0.27	0.47	3.00	4.86	0.08	1.76	0.61	0.07	nd	
188	10	pG	12.55	2.83	1.39	70.95	0.44	0.17	0.86	4.45	5.72	0.06	nd	0.43	nd	nd	
189	8	dBR	20.63	4.69	5.73	59.97	0.19	0.20	0.51	2.23	4.22	0.18	nd	1.21	0.07	nd	
190	6	A	12.95	0.50	3.16	70.70	0.08	0.08	0.65	0.42	10.89	0.06	nd	0.37	0.05	nd	
192	2	G	12.72	2.90	1.51	68.05	0.29	nd	0.61	2.15	10.38	0.07	0.11	0.97	nd	0.07	
193	2	pG	14.68	5.30	2.24	65.33	0.22	0.23	0.59	3.06	5.94	0.09	1.35	0.79	0.06	nd	
194	2	pG	14.28	5.06	1.65	67.83	0.14	0.11	0.93	1.52	5.10	0.06	2.66	0.50	0.08	nd	
195	2	A	12.93	0.51	3.18	71.16	0.12	0.17	0.68	0.45	10.30	nd	nd	0.35	0.05	nd	
196	2	pG	13.36	3.54	1.23	67.44	0.27	0.14	0.90	2.47	8.28	0.07	1.77	0.37	0.06	nd	
197	2	pG	13.74	3.58	1.17	67.33	0.26	0.21	0.80	2.12	8.46	0.07	1.58	0.57	0.05	nd	
198	2	A	13.18	0.61	3.24	71.07	0.19	0.09	0.89	0.59	9.57	0.07	nd	0.39	0.05	nd	
199	2	A	13.15	0.47	3.18	72.61	0.10	0.21	0.60	0.43	8.73	nd	nd	0.32	0.06	nd	
200	2	pG	14.30	0.53	3.20	70.73	0.09	0.06	0.80	0.58	9.19	0.05	nd	0.35	0.05	nd	
201	2	A	12.89	0.76	3.45	71.87	0.06	0.12	0.74	0.55	8.97	nd	nd	0.39	0.06	nd	

#	Type	Colour	Na_2O	MgO	Al_2O_3	SiO_2*	P_2O_5	SO_3	Cl	K_2O	CaO	TiO_2	MnO	Fe_2O_3	BaO	PbO	Other oxides
202	2	C	12.15	3.39	1.35	65.17	0.25	0.20	0.73	2.87	11.28	0.07	1.80	0.54	0.06	0.08	
203	2	C	12.37	3.34	1.27	65.92	0.24	0.21	0.70	2.78	10.74	0.07	1.70	0.55	0.05	nd	
204	2	pG	14.12	3.07	0.81	66.44	0.28	0.26	0.74	2.95	10.33	0.05	0.55	0.33	0.05	nd	
205	2	B	13.44	0.88	2.98	70.69	0.09	0.06	0.64	0.73	8.60	0.06	nd	0.83	0.05	0.14	0.13 CoO; 0.14 CuO; 0.52 ZnO
206	2	pG	11.93	2.67	0.91	70.47	0.28	0.18	0.72	3.17	8.73	0.06	0.47	0.25	nd	0.11	
207	2	BR	13.58	3.80	2.15	69.00	0.38	0.12	0.60	1.65	6.31	0.21	nd	2.02	0.05	nd	
208	2	C	12.14	3.18	1.25	69.90	0.28	0.17	0.77	1.90	8.55	0.07	1.28	0.43	0.05	nd	
209	2	pB	12.13	3.73	1.20	68.01	0.28	0.11	0.68	2.47	9.46	0.07	0.19	1.27	nd	nd	0.07 CoO; 0.14 CuO; 0.15 ZnO
211	2	pG	12.40	3.32	1.15	66.84	0.29	0.17	0.75	2.97	10.48	0.06	0.99	0.42	0.05	nd	
212	2	pB	11.82	3.58	1.33	66.91	0.27	0.15	0.59	2.24	11.05	0.07	0.67	0.98	0.06	0.07	0.06 CoO; 0.11 CuO
213	2	cB	10.91	3.35	1.41	68.14	0.28	0.11	0.62	2.34	10.00	0.07	1.18	1.16	0.05	0.07	0.13 CuO; 0.13 ZnO
214	2	pP	11.97	3.10	1.28	67.18	0.27	0.21	0.74	2.52	11.10	0.06	1.05	0.41	0.05	0.06	
215	2	B	11.10	3.02	1.32	69.92	0.28	0.17	0.68	2.22	9.15	0.07	1.38	0.52	0.07	nd	
216	2	cB	11.44	2.75	1.03	69.95	0.28	0.14	0.82	2.93	8.75	0.06	1.35	0.33	0.06	nd	0.05 ZnO
218	2	cB	10.81	3.16	1.43	67.92	0.29	0.12	0.65	2.25	10.87	0.07	1.10	0.96	0.05	0.06	0.15 ZnO
219	2	pG	12.36	3.67	1.09	66.40	0.23	0.24	0.68	2.09	11.84	0.06	0.93	0.33	0.05	nd	
220	2	cB	13.90	3.94	1.26	66.11	0.30	0.18	0.79	3.00	9.47	0.08	0.24	0.55	nd	nd	
221	2	C	12.06	3.28	1.12	66.54	0.27	0.18	0.71	2.87	11.20	0.05	1.20	0.42	0.05	0.05	
222	2	pG	12.79	3.85	1.18	67.03	0.25	0.17	0.79	2.29	9.79	0.07	1.28	0.39	0.06	nd	
224	2	pG	11.60	3.34	1.10	69.36	0.29	0.18	0.79	2.00	9.95	0.07	0.82	0.38	0.05	nd	
225	2	pG	11.94	3.56	1.24	68.67	0.27	0.21	0.74	2.72	8.81	0.07	1.00	0.64	0.05	nd	
227	2	pG	14.03	3.14	0.77	66.35	0.30	0.21	0.83	2.92	10.31	0.07	0.60	0.32	nd	nd	
229	2	pG	13.56	3.61	1.11	67.31	0.26	0.14	0.79	2.66	9.14	0.06	0.80	0.41	0.06	nd	
231	2	pG	11.77	2.89	1.08	70.74	0.26	0.14	0.74	2.17	8.36	0.07	1.34	0.34	0.05	nd	0.06 ZnO
232	2	pG	11.32	3.34	1.32	65.98	0.34	0.23	0.71	2.73	12.05	0.07	1.20	0.53	0.06	0.06	
233	2	C	10.47	3.36	1.32	68.12	0.32	0.12	0.83	2.68	10.95	0.07	1.18	0.49	nd	nd	
234	2	pG	11.95	3.36	1.16	67.04	0.30	0.14	0.77	2.77	10.64	0.07	1.19	0.47	0.06	nd	
235	2	pG	13.04	3.25	1.15	68.69	0.31	0.19	0.88	2.54	9.05	0.05	0.34	0.34	nd	nd	
236	2	pG	15.28	1.91	1.09	72.14	nd	0.17	0.05	0.15	8.82	nd	nd	0.14	0.05	nd	0.09 As_2O_3
238	2	pG	11.02	3.46	1.49	64.94	0.28	0.11	0.47	2.24	11.79	0.07	3.03	0.88	0.07	nd	0.09 ZnO
239	2	A	14.63	0.69	3.26	67.97	0.09	0.09	0.70	0.49	11.29	nd	nd	0.45	0.07	0.09	
240	10	pG	10.54	3.45	1.31	67.89	0.33	0.15	0.79	2.61	10.61	0.07	1.69	0.45	0.05	nd	

#	Type	Colour	Na_2O	MgO	Al_2O_3	SiO_2*	P_2O_5	SO_3	Cl	K_2O	CaO	TiO_2	MnO	Fe_2O_3	BaO	PbO	Other oxides
241	2	pG	12.98	3.31	1.13	67.39	0.27	0.14	0.89	2.22	9.44	0.06	1.55	0.44	0.05	nd	0.07 ZnO
243	2	pG	11.40	3.17	1.34	68.58	0.28	0.15	0.70	2.16	9.94	0.05	1.67	0.52	nd	nd	
245	2	pG	12.62	3.36	1.19	66.92	0.25	0.18	0.76	2.78	10.44	0.06	0.93	0.41	nd	nd	
246	2	pG	11.53	3.07	1.29	69.72	0.26	0.12	0.71	2.20	8.95	0.07	1.48	0.47	0.06	nd	
247	2	pG	13.75	3.71	1.19	66.66	0.29	0.14	0.79	2.66	9.29	0.07	0.91	0.42	0.05	0.06	
248	2	pP	13.47	3.69	1.14	65.77	0.28	0.17	0.76	2.55	10.39	0.06	1.20	0.39	0.05	nd	
249	2	B	13.92	3.73	1.34	65.44	0.29	0.18	0.67	2.24	10.08	0.07	0.86	0.92	0.05	nd	0.06 CoO; 0.12 CuO
250	2	B	11.03	3.31	1.49	66.32	0.25	0.17	0.64	2.25	11.66	0.07	1.12	1.19	0.06	nd	0.18 CuO; 0.16 ZnO
251	2	P	13.19	3.33	1.25	65.96	0.24	0.29	0.75	2.29	10.20	0.07	1.86	0.48	0.06	nd	
252	2	C	12.31	3.48	1.26	68.19	0.28	0.17	0.69	2.66	9.28	0.07	1.01	0.41	0.05	nd	
253	2	pG	12.60	0.49	3.11	72.87	0.07	nd	0.80	0.60	8.94	nd	nd	0.33	0.06	nd	
254	2	B	12.87	3.51	1.20	66.63	0.25	0.12	0.75	1.92	11.27	0.06	0.26	0.87	0.05	nd	0.09 ZnO
255	2	P	11.55	3.10	1.36	69.16	0.31	0.14	0.74	2.18	9.07	0.08	1.48	0.51	0.05	0.15	0.08 As_2O_3
256	2	pG	12.36	3.32	1.22	68.59	0.30	0.18	0.80	2.52	8.89	0.06	0.96	0.47	0.05	0.09	0.06 CuO
257	2	pG	10.33	3.54	1.30	68.51	0.13	0.11	0.89	2.31	11.26	0.07	1.07	0.38	0.05	nd	
258	2	pP	11.81	3.42	1.25	66.97	0.27	0.18	0.68	2.58	10.23	0.07	1.93	0.39	0.06	0.10	
260	1	B	11.91	3.65	1.42	66.00	0.28	0.17	0.65	2.28	11.66	0.06	0.76	0.91	0.06	nd	0.09 CuO
261	1	B	12.94	3.52	1.20	66.94	0.27	0.14	0.74	2.00	10.77	0.07	0.30	0.84	0.06	0.10	0.06 CoO; 0.05 ZnO
262	4	OY	12.18	0.62	2.50	56.63	0.10	0.11	0.78	0.64	7.38	0.06	0.09	0.42	0.07	14.93	1.08 CuO; 0.08 ZnO; 2.35 SnO
263	8	dBR	17.29	3.15	1.80	67.62	0.31	0.21	0.92	2.10	5.27	0.11	0.05	1.04	nd	0.09	
264	8	dBR	18.08	3.07	1.99	66.41	0.29	0.26	0.77	2.49	5.04	0.13	nd	1.26	0.05	0.10	
265	8	dBR	20.02	5.52	3.88	60.40	0.27	0.18	0.38	1.97	5.84	0.13	nd	1.18	0.05	0.07	
266	8	dBR	15.08	2.89	1.69	67.20	0.31	0.11	1.03	2.15	6.34	0.11	0.37	2.50	0.05	0.12	0.05 CuO
267	8	oG	12.79	3.61	2.94	67.17	0.37	0.11	0.82	1.79	8.03	0.15	0.06	1.91	0.05	0.06	0.08 As_2O_3
268	8	dG	15.03	4.29	1.82	65.74	0.51	0.11	0.91	2.37	6.41	0.08	0.20	2.15	0.06	0.24	
269	8	dG	15.04	4.30	1.77	66.17	0.45	0.09	0.91	2.42	6.39	0.08	0.23	2.04	nd	nd	
270	8	B	15.50	4.10	3.78	61.35	0.60	0.18	0.96	2.69	8.01	0.17	0.12	2.36	0.05	nd	
271	8	dBR	13.16	5.06	2.12	67.76	0.70	0.06	0.98	1.80	6.50	0.10	0.09	1.47	nd	nd	
272	9	pG	12.39	3.59	1.71	66.25	0.25	0.15	0.64	2.38	10.59	0.08	1.13	0.72	0.05	nd	
273	9	pG	14.54	0.57	3.01	71.26	0.05	0.17	0.69	0.49	8.64	0.06	nd	0.39	0.05	0.05	
274	9	pG	11.75	3.40	1.30	66.68	0.34	0.23	0.75	2.76	11.28	0.07	0.88	0.50	0.05	nd	
275	9	pG	11.73	3.84	1.61	66.78	0.25	0.18	0.63	2.17	10.51	0.08	1.30	0.73	nd	nd	

#	Type	Colour	Na_2O	MgO	Al_2O_3	SiO_2*	P_2O_5	SO_3	Cl	K_2O	CaO	TiO_2	MnO	Fe_2O_3	BaO	PbO	Other oxides
277	2	pG	14.77	5.72	0.95	68.97	0.10	0.21	0.68	2.21	5.68	nd	0.26	0.26	nd	0.14	
278	2	pG	11.99	2.92	1.04	70.46	0.28	0.15	0.75	2.95	8.51	0.05	0.52	0.31	0.05	nd	
279	2	pB	13.89	4.56	1.72	69.04	0.20	0.11	0.62	3.12	4.42	0.08	1.32	0.74	0.05	nd	
280	2	pG	12.59	3.67	1.02	68.13	0.25	0.17	0.76	2.06	10.05	0.05	0.78	0.33	nd	0.09	
2	9	pG	10.9	3.3	1.2	70.5	nd	nd	0.6	2.4	9.4	nd	1.7	nd	nd	nd	
5	9	dBR	13.6	5.0	1.4	66.3	0.4	0.3	0.7	3.0	6.3	nd	2.4	0.6	nd	nd	
6	9	pG	11.7	2.9	0.9	70.7	0.3	0.1	0.7	2.8	7.7	nd	1.8	0.5	nd	nd	
7	9	dG	9.7	2.8	0.8	72.6	nd	nd	0.6	2.7	8.7	nd	2.1	nd	nd	nd	
14	9	G/P	12.1	2.1	2.2	66.2	0.4	0.4	0.6	3.2	7.9	0.2	3.4	1.3	nd	nd	
22a	3	pG	12.7	2.7	0.5	69.7	0.3	nd	0.9	2.9	8.0	nd	1.8	0.5	nd	nd	
22b	3	pG	12.0	2.8	1.2	68.0	0.2	0.2	1.2	3.3	9.1	nd	1.7	0.4	nd	nd	
22c	3	pG	12.3	2.9	1.3	69.5	0.1	0.1	0.9	2.8	7.7	nd	1.6	0.7	nd	nd	
22d	3	pG	11.6	3.2	1.1	67.7	0.2	0.1	0.9	3.4	9.2	0.2	1.9	0.4	nd	nd	
22e	3	pG	11.8	5.4	1.7	66.9	0.1	0.2	0.7	3.5	5.9	0.1	2.7	1.1	nd	nd	
22f	3	pG	10.3	3.0	1.0	68.1	0.2	nd	0.7	3.0	12.5	0.3	0.0	0.8	nd	nd	
22g	3	G/B	11.8	2.1	1.5	68.8	0.2	0.2	0.9	3.5	6.2	0.3	1.4	3.0	nd	nd	
22h	3	dG	12.2	0.1	2.2	70.6	0.1	0.1	1.1	0.3	11.4	0.5	0.1	1.2	nd	nd	
22i	3	pG	12.5	2.8	1.2	69.6	nd	nd	0.8	2.9	7.9	nd	1.5	0.6	nd	nd	
22j	3	pG	12.2	3.1	1.1	68.5	0.2	nd	0.8	3.4	9.0	0.2	1.0	0.5	nd	nd	
22k	3	pG	11.9	3.1	0.8	68.1	0.4	0.1	0.9	3.6	8.7	0.2	1.6	0.5	nd	nd	

List of publications

1. McLoughlin, S.D., et al., *On Technological Change in Islamic Glass Production at Raqqa, Syria.* Glass News, 2000(9): p. 4-5.

2. Henderson, J. and S.D. McLoughlin. *Glass Production in al-Raqqa: Experimentation and Technological Changes*. in *Annales 15th Congress AIHV*. 2001. New York - Corning: Nottingham AIHV Press. p. 144-148.

3. Henderson, J., S.D. McLoughlin, and D.S. McPhail, *Radical Changes in Islamic Glass Technology: Evidence for Conservatism and Experimentation with New Glass Recipes from Early and Middle Islamic Raqqa, Syria.* Archaeometry, in press.

4. McLoughlin, S.D., D.S. McPhail, and J. Henderson, *The Weathering of Archaeological Glass from Raqqa, Syria: a New Perspective Using Scanning Ion Microscopy.* Proceedings of the 33rd International Archaeometry Symposium, in press.

5. McLoughlin, S.D. and I. Notingher, *The Ballidon Experiment: New Results on the Long-Term Corrosion of Buried Glasses*. in prep.

List of figures and table captions

Figure 2-1: the silica tetrahedron.

Figure 2-2: the molecular structure of quartz, silica glass, soda-silica glass and Roman glass.

Figure 2-3: schematic diagram of the MRN model of glass structure.

Figure 2-4: present day natron traders in the Wadi Natrun, Egypt.

Figure 2-5: the variation of MgO and K_2O as a function of alkali source.

Figure 2-6: the five main categories of Western ancient glass.

Figure 2-7: age ranges in which the major chemical glass compositions were produced in antiquity and medieval times.

Figure 2-8: reconstitution of the plan and the section of a tank furnace from Bet Eli'ezer, Israel.

Figure 2-9: viscosity-temperature plots for a range of commercial silicate glasses.

Figure 2-10: temperature change caused by an increase of 0.01 mole oxide/mole SiO_2 at different viscosities.

Figure 2-11: viscosity versus temperature in relation to glassmaking processes.

Figure 2-12: the temperature dependence of nucleation rate and growth rate of crystals in glasses.

Figure 2-13: liquidus of the ternary SLS system of particular relevance to glass technology.

Figure 2-14: model for the precipitation of one of the constituents of a liquid mixture.

Figure 2-15: stability diagram of quartz and vitreous silica.

Figure 2-16: optical micrograph of a section through a KLS window glass buried for 288 years.

Figure 2-17: electron image of individual corrosion layers on the KLS glass in figure 2-16.

Figure 2-18: an individual corrosion layer of a corroded 10th century Carolingian glass.

Figure 2-19: the main structural features of the altered layers found on buried glasses.

Figure 3-1: political map of the Middle East.

Figure 3-2: a Corona satellite image taken in 1967.

Figure 3-3: furnace base chunks found at Tell Belor.

Figure 3-4: TB2, an example of type A production waste.

Figure 3-5: samples TB9, TB5 and TB6 of production waste type A.

Figure 3-6: type B production waste furnace floor lumps that TB13 and TB14 were sampled from.

Figure 3-7: samples TB13, TB14 and TB7 of production waste type B.

Figure 3-8: typical appearance of Salicornia plant gathered Raqqa.

Figure 4-1:overview of experimental procedure for all samples in this study.

Figure 4-2: schematic of electric and magnetic fields that cause the plasma gas in ICP-AES.

Figure 4-3: the LEO 1525 FE-SEM workstation.

Figure 4-4: effects of the interaction of an electron beam with a solid.

Figure 4-5: results of particle size analysis of powders used to make replica glasses.

Figure 4-6: illustration of the casting process.

Figure 4-7: backscattered electron image of a polished cross-section of corroded crust on sample B2-9.

Figure 4-8: backscattered electron image showing five points of a linescan conducted across the outermost depleted edge of B2-32.

Figure 4-9: data from the linescan in figure 4-8.

Figure 4-10: diagram illustrating the increasing errors involved in wt% determination of SiO2 as the atomic% of C detected by EDXA increases.

Figure 4-11: schematic diagram of an ion column in a focused ion beam spectrometer.

Figure 4-12: the ion column and main chamber of the FEI Strata T200 FIB workstation.

Figure 4-13: a typical liquid-metal ion source substrate.

Figure 4-14: schematic of the sputtering process that occurs during ion beam bombardment.

Figure 4-15: schematic of the operation of electron beam charge neutralisation.

Figure 4-16: operating range of the electron gun.

Figure 4-17: positive mass spectrum of B3-9.

Figure 4-18: positive mass spectrum of a polished section of sample TZ143.

Figure 4-19: secondary ion image of a 40x40μm crater, viewed at 28°, on sample B3-9.

Figure 4-20: infrared reflection spectra of vitreous silica compared to a KLS glass before and after corrosion.

Figure 5-1: MgO vs. Al_2O_3 for 127 Tell Zujaj glass fragments.

Figure 5-2: MgO vs. Al_2O_3 for 67 Tell Fukhkhar glass fragments.

Figure 5-3: MgO vs. Al_2O_3 for 15 Tell Belor glass fragments.

Figure 5-4: MgO vs. Al_2O_3 for primary and secondary production waste evidence from three Tells at Raqqa.

Figure 5-5: MgO vs. K_2O for Raqqa glasses divided by compositional grouping.

Figure 5-6: SiO2 vs. Na2O for Raqqa glasses divided by compositional grouping.

Figure 5-7: P2O5 vs. CaO for Raqqa glasses divided by compositional grouping.

Figure 5-8: logarithmic plot of Al_2O_3 vs. Fe_2O_3 and TiO_2 for unintentionally coloured type 4 glasses.

Figure 5-9: Al_2O_3 vs. Fe_2O_3 for Raqqa glasses divided by compositional grouping and coloration.

Figure 5-10: Fe_2O_3 vs. MnO for coloured Raqqa glasses.

Figure 6-1: 3-D scatter plot of MgO, K_2O and Al_2O_3 levels for Raqqa LMG type 3 and HMG type 1.

Figure 6-2: calculated viscosity-temperature curves for the replica type 1 HMG composition.

Figure 6-3: calculated viscosity-temperature curves for the replica type 3 LMG composition.

Figure 6-4: DSC curves of type 1 and type 3 replica glasses.

Figure 6-5: DSC curves of Raqqa samples TZ145 and TF 211.

Figure 6-6: results of casting experiment for type 1 and type 3 replica glasses.

Figure 6-7: results of fining experiment for type 1 and type 3 replica glasses.

Figure 6-8: measured densities of type 1 and type 3 replica glasses against time held at 1200°C.

Figure 6-9: cast glass from Raqqa for floor tile and tessera production with respective moulds.

Figure 7-1: cross-section of TB6 showing reaction zone below interface.

Figure 7-2: the different phases in the reaction zone of TB6 at higher magnification.

Figure 7-3: the minute granular phase at the reaction zone.

Figure 7-4: XRD results on the base of TB6.

Figure 7-5: sample TB2 in polished cross-section.

Figure 7-6: backscattered electron image of the base of TB2.

Figure 7-7: backscattered electron image of the glass-substrate interface of TB2.

Figure 7-8: magnified cross-section of TB5.

Figure 7-9: backscattered electron image of the base of TB5.

Figure 7-10: backscattered electron image of the cracks induced by wollastonite precipitation in TB5.

Figure 7-11: magnified cross-section of TB9.

Figure 7-12: backscattered electron image of the top edge of TB9.

Figure 7-13: close-up of previous figure.

Figure 7-14: backscattered electron image of the reacted base of a SLS glass cast on to a $CaCO_3$ base.

Figure 7-15: backscattered electron image of TB14 in cross-section.

Figure 7-16: magnified cross-section of sample TB13.

Figure 7-17: results of linescan a in figure 7-15.

Figure 7-18: results of linescan b in figure 7-15.

Figure 7-19: backscattered electron image of crystals nucleated in TB13.

Figure 7-20: EDXA data of linescan across glass-substrate interface in TB7.

Figure 7-21: backscattered electron image of wollastonite and diopside crystals growing above the glass-substrate boundary in TB7.

Figure 7-22: backscattered electron images of the microstructure of TB19y and TB19g.

Figure 7-23: DTA scans of yellow brick TB19y and green brick TB19g.

Figure 7-24: TGA scans of yellow brick TB19y and green brick TB19g.

Figure 7-25: DTA results on fragments of production waste type A, B and C.

Figure 7-26: TGA results on fragments of production waste types A, B and C.

Figure 7-27: monoclinic unit cell structure of diopside.

Figure 7-28: chain structure of diopside and wollastonite.

Figure 7-29: phase diagram for the CaMgSi2O6-CaFeSi2O6 (diopside-hedenbergite) system.

Figure 7-30: smoothed EDXA data of the first 400μm of the linescan in figure 7-20 across diopsde and wollastonite crystals in glass in TB7.

Figure 7-31: transmitted light photomicrographs of wollastonite structures in TB14 in thin section.

Figure 7-32: calculated growth rates of precipitated wollastonite crystals using viscosity values from the Lakatos model.

Figure 7-33: calculated growth rates of precipitated wollastonite crystals using viscosity values from the Urbain model.

Figure 7-34: the temperature variation during the seven-day firing of large bricks in a 13th century tile kiln.

Figure 8-1: optical micrograph of filled scratches and lightly banded structure on the surface of B1-32.

Figure 8-2: Na depleted layer thickness versus burial time for B1 samples.

Figure 8-3: backscattered electron image of the outer surface of B1-32 in cross-section.

Figure 8-4: linescan across a 400μm-wide area of the Na depleted region of B1-32 in figure 8-3.

Figure 8-5: comparative linescan across the outer 10μm of the surfaces of B1-1, B1-9 and B1-32.

Figure 8-6: secondary ion image of cracked crusted surface of B2-1.

Figure 8-7: optical micrograph of cracked crusted surface with filled scratches on the surface of B2-9.

Figure 8-8: secondary ion image of cracked crusted surface of B2-32.

Figure 8-9: corrosion crust thickness versus burial time for B2 glasses.

Figure 8-10: backscattered electron image of the corrosion crust formed on B2-1.

Figure 8-11: backscattered electron image of the corrosion crust formed on B2-9.

Figure 8-12: backscattered electron image of the corroded surface of B3-9.

Figure 8-13: corrosion crust thickness versus burial time for B3 glasses.

Figure 8-14: backscattered electron images of the irregular corrosion edge along the rough surface of B3-1 and the compositionally banded corrosion on the surface of B3-9.

Figure 8-15: results for linescans indicated in figure 8-14 on B3-1 and B3-9.

Figure 8-16: infrared reflection spectra of Ballidon Roman type glass B1.

Figure 8-17: infrared reflection spectra of Ballidon medieval type glass B2.

Figure 8-18: infrared reflection spectra of Ballidon 17th century type glass B3.

Figure 8-19: infrared reflection spectra of freshly cleaved surfaces of vitreous silica and Ballidon glasses.

Figure 8-20: peak shift calibration curves plotted using three Ballidon glasses and vitreous silica for S peak, NSX peak and R peak.

Figure 8-21: variation of molar surface concentrations of SiO_2 and R_2O+RO of B1 glass as a function of burial time, as determined by EDXA and IRRS.

Figure 8-22: variation of molar surface concentrations of SiO_2 and R_2O+RO of B2 glass as a function of burial time, as determined by EDXA and IRRS.

Figure 8-23: variation of molar surface concentrations of SiO_2 and R_2O+RO of B3 glass as a function of burial time, as determined by EDXA and IRRS.

Figure 8-24: six types of corroded glass surface.

Figure 9-1:the variety of degree of corrosion visible on the surfaces of Raqqa samples.

Figure 9-2: backscattered electron image of corrosion crusts on four Raqqa samples viewed in cross-section.

Figure 9-3: comparative graph of average crust thickness for four corroded Raqqa samples.

Figure 9-4: backscattered electron image showing internal plug formation in TZ79.

Figure 9-5: backscattered electron image of corrosion on TZ76.

Figure 9-6: backscattered electron image of inner and outer crusts of TZ79.

Figure 9-7: optical micrograph showing hemispherical growth of layers on TZ78, seen in cross-section truncated through outer surface.

Figure 9-8: deformation angle as single layer plane traverses growth fault stemming from plug.

Figure 9-9: secondary electron ion beam image of layers forming around a dissolved gas bubble.

Figure 9-10: secondary ion image of the upturned crust detached from TZ78.

Figure 9-11: optical micrograph of a translucent fragment of the corrosion crust on TZ78.

Figure 9-12: secondary ion image of the edge of the upturned crust in figure 9-10.

Figure 9-13: secondary electron image of layers from TZ78 in cross-section.

Figure 9-14: the upper surface of an individual corrosion layer revealed by SIM.

Figure 9-15: secondary electron ion beam image of stacked layers on TZ78.

Figure 9-16: secondary electron ion beam image of layers on TZ78 in cross-section revealed after exposure to a 10pA ion beam for 10 seconds.

Figure 9-17: secondary electron ion beam image of layers on TZ78 in cross-section revealed after exposure to a 10pA ion beam for 30 seconds.

Figure 9-18: backscattered electron image of the most recently formed layers and the active corrosion front at the innermost surface of TZ78.

Figure 9-19: EDXA linescan data across cross-sectional layers in figure 9-18.

Figure 9-20: secondary electron image of the reaction front in TZ78.

Figure 9-21: schematic diagram illustrating the way in which corrosion forms in buried glasses.

Figure 9-22: relationship between the calculated free energy of hydration and the number of non-bridging oxygen bonds for crusted glasses in the literature and in this study.

Figure 9-23: relationship between layer thickness and the number of non-bridging oxygen bonds for crusted glasses in the literature and in this study.

Figure 9-24: relationship between layer thickness and molar percentage of SiO_2 for crusted glasses in the literature and in this study.

Figure 9-25: relationship between layer thickness and molar percentage of $RO+R_2O$ content for crusted glasses in the literature and in this study.

Figure 9-26: relationship between layer thickness and molar percentage of R_2O content for crusted glasses in the literature and in this study.

Table 2-1: the range of analytical techniques applicable to the study of glasses.

Table 2-2: comparison of crystallisation and melting characteristics between GeO_2 and $Na_2O{\cdot}SiO_2$.

Table 2-3: composition range of industrial SLS glasses studied by Guillemet and Denoncin.

Table 2-4: calculated free energies of hydration for glass components.

Table 3-1: reported compositions of glasses recovered from Ballidon.

Table 4-1:results of EPMA and SEM calibration with Corning B glass standard

Table 4-2: calibration of SiO_2 totals across separate EPMA sessions.

Table 4-3: an illustration of the method for data conversion followed in this study.

Table 4-4: target compositions for type 1 HMG and type 3 LMG replicas.

Table 4-5: batch compositions used to make 100g of type 1 HMG and type 3 LMG replicas.

Table 5-1: mean values and standard deviations of the twelve major components of type 3 and type 1 glasses from Tell Zujaj and subtype 1 glasses from Tell Fukhkhar and Tell Belor.

Table 6-1: ICP-AES results for Salicornia ash collected at Raqqa.

Table 6-2: ICP-AES results for TA1 Salicornia ash with missing values from EDXA.

Table 6-3: target compositions of type 1 and type 3 glasses and ICP-AES results of prepared samples.

Table 6-4: theoretical working point, softening point and annealing temperature for type 1 and type 3 replica glasses.

Table 7-1: normalised EDXA data of glass above and below reaction boundary of TB6.

Table 7-2: EDXA elemental percentages of dark mottled phase and wollastonite growth around reaction zone of TB6.

Table 7-3: normalised EDXA results for phases in the base and matrix composition of TB2.

Table 7-4: normalised EDXA results for glass in TB2 at different points above the interface.

Table 7-5: normalised EDXA results for phases in the base and for the glass composition of TB5.

Table 7-6: EDXA elemental percentages for gypsum and augite crystals identified at the base and upper surface of TB9 respectively.

Table 7-7: normalised EDXA results for the vitreous matrix and the upper augite-rich layer of TB9.

Table 7-8: normalised EDXA results of the reacted base of a SLS glass cast on to a $CaCO_3$ base at 1400°C.

Table 7-9: normalised EDXA results of glass and substrate at different points in TB13 and TB14 and ICP analysis of substrate base from TB13.

Table 7-10: normalised EDXA results of precipitated crystals, glass and substrate at different points in TB7.

Table 7-11: normalised EDXA results of TB19 yellow and green bricks.

Table 7-12: molar fraction of CaO, the derived liquidus temperature and corresponding calculated viscosity for seven glasses showing wollastonite precipitation.

Table 7-13:the maximum observed length of wollastonite needles in five Raqqa glasses.

Table 8-1: reported compositions of Ballidon glasses B1, B2 and B3 and corresponding normalised bulk EDXA results in this study.

Table 8-2: peak maxima for Ballidon IR spectra with reported and corresponding calculated molar oxide concentrations after calibration.

Table 9-1: average compositions of unaltered and corroded regions of typical LMG and HMG samples from Raqqa.

Table 9-2: average crust thickness, individual layer thickness and number of layers for four Raqqa samples.

Table 9-3: molar compositions, non-bridging oxygen (NBO) bond fraction, ΔG_0 and average layer thickness for five corroded Raqqa glasses and seven glasses from published studies.